AMS on ISS

Construction of a particle physics detector on the International Space Station

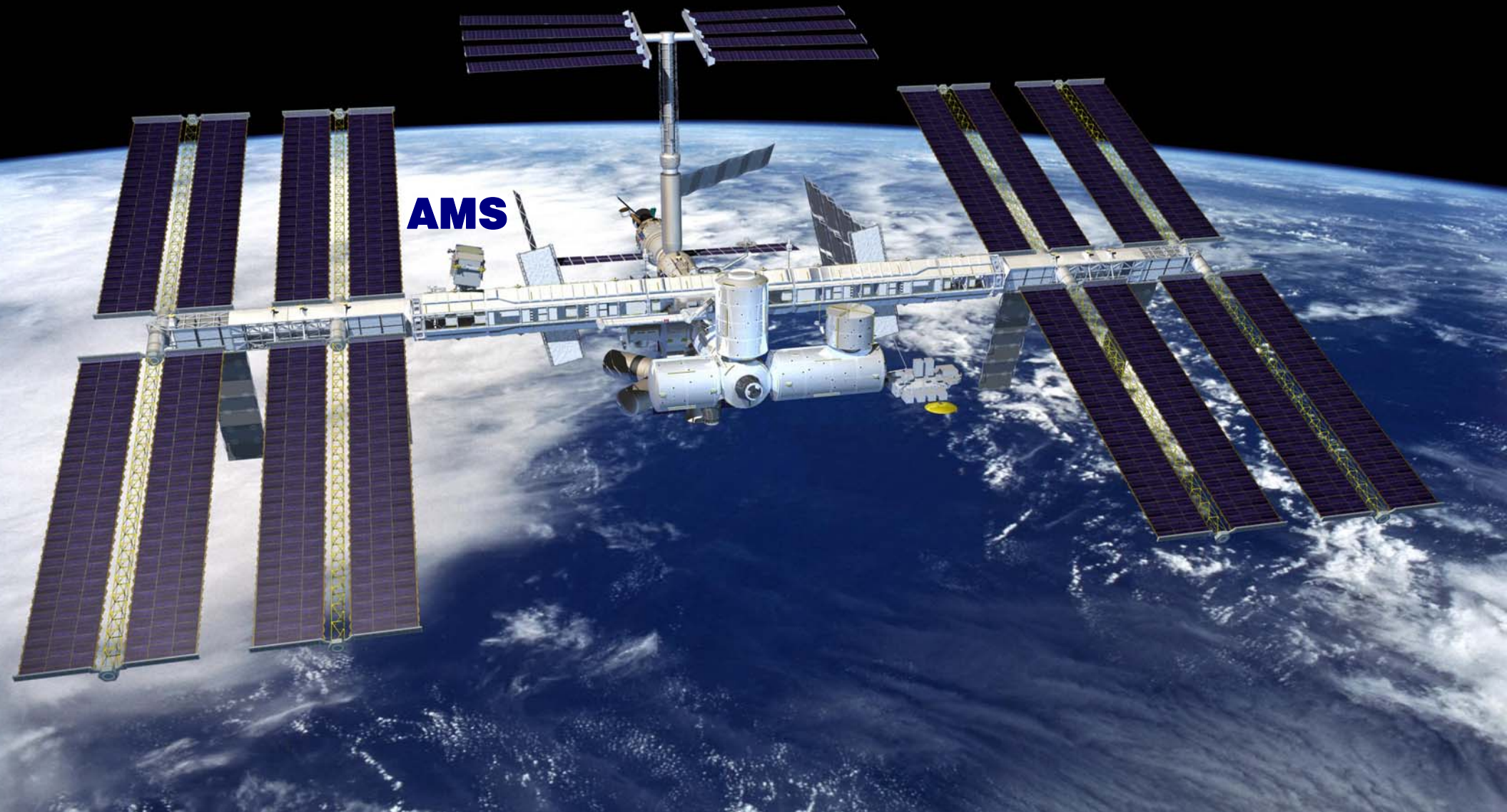

AMS on ISS
Construction of a particle physics detector on the International Space Station

The AMS Collaboration

C.H. Chung, S. Fopp, Th. Kirn, W. Karpinski, K. Lübelsmeyer, S. Schael, A. Schultz von Dratzig, G. Schwering, Th. Siedenburg, R. Siedling, W. Wallraff, M. Wlochal
I. Physikalisches Institut, RWTH, D-52056 Aachen, Germany

H.-B. Broeker, V. Commichau, G. Fluegge, K. Hangarter
III. Physikalisches Institut, RWTH, D-52056 Aachen, Germany

Jes Madsen
Department of Physics and Astronomy, University of Aarhus, DK-8000 Aarhus C, Denmark

H. Boer Rookhuizen, C. Snippe, B. Verlaat
National Institute for Nuclear Physics and High Energy Physics, NIKHEF, NL-1098 SJ Amsterdam, The Netherlands

C. Adloff, F. Cadoux, G. Coignet, L. Girard, C. Goy, R. Hermel, R. Kossakowski , J. Pochon, S. Rosier-Lees, J.-P. Vialle
Laboratoire d'Annecy-le-Vieux de Physique des Particules, LAPP, F-74941 Annecy-le-Vieux CEDEX, France

A. Pevsner
Johns Hopkins University, Baltimore, MD 21218, USA

S.B. Bai, Y.Q. Feng, F. Gao, X.J. Han, K. Luo, F.X. Shen, R.H. Wei, S.H. Xiang, L.J. Xu, S. Yang, Z.H. Zhu
Beijing Institute of Spacecraft Environment Engineering, BISEE, 100029 Beijing, China

Z.G. Chen, C.M. Li, N. Li, X.B. Peng, J.G. Tang
Chinese Academy of Launching Vehicle Technology, CALT, 100076 Beijing, China

Y.M. Dai, N.H. Song, Q.L. Wang, Y.J. Yu
Institute of Electrical Engineering, IEE, Chinese Academy of Sciences, 100080 Beijing, China

G.M. Chen, H.S. Chen, Z.H. Li, Y.S. Lu, X.W. Tang, C.G. Yang, M. Yang, Z.Q. Yu, H.L. Zhuang
Institute of High Energy Physics, IHEP, Chinese Academy of Sciences, 100039 Beijing, China

M. Basile[1),2)], V. Bindi[1),2)], D. Casadei[1),2)], F. Cindolo[1)], A. Contin[1),2)], A. Evangelista[1)], S. Finelli[1)], F. Giovacchini[1),2)], C. Guandalini[1)], G. Laurenti[1)], G. Levi[1),2)], M. Lolli[1)], R. Martelli[1),2)], L. Quadrani[1),2)], F. Palmonari[1),2)], G. Sartorelli[1),2)], C. Sbarra[1),2)], A. Zichichi[1),2)], A. Zucchini[1)]
University of Bologna and INFN-Sezione di Bologna, I-40126 Bologna, Italy
[1)] *INFN-Sezione di Bologna,* [2)] *Universita' di Bologna*

N. Dinu[1)], M. Ionica[2)], R. Ionica[3)], F. Manolescu[1)], O. Maris[1)], A. Mihul[4)]
Institute of Microtechnology, Institute for Space Sciences and University of Bucharest, R-76900 Bucharest, Romania
[1)] *Institute for Space Science, ISS,* [2)] *Institute for Microtechnology, IMT,* [3)] *University Politechnica, UPB,* [4)] *University of Bucharest, UB*

R. Becker, U. Becker, P. Berges, J.D. Burger, X.D. Cai, M. Capell, G. Carosi, V. Choutko, B. Demirkoz, P. Dennett, F.J. Eppling, P.H. Fisher, A. Klimentov, A. Koulemzine, A. Kounine, V. Koutsenko, A. Lebedev, B. Monreal, A. Rozhkov, K. Scholberg, Samuel C.C. Ting, S.M. Ting, M. Steuer, S. Xiao, S.D. Xu, M. Vergain, Y. Wang, X.Z. Wang
Massachusetts Institute of Technology, MIT, Cambridge, MA 02139, USA

Y.H. Chang, C.H. Lin
National Central University, Chung-Li, Taiwan 32054

A. Malinine, E.-S. Seo
IPST, University of Maryland, College Park, MD 20742, USA

R. Sagdeev
East-West Center for Space Science, University of Maryland, College Park, MD 20742, USA

H. Ahmed, C.H. Chung, G.N. Kim, M.W. Lee, W.H. Park, J.W. Shin, D. Son, K.W. Sung, N. Tasneem
CHEP, Kyungpook National University, 702-701 Daegu, South Korea

A.A.M. Delil, A. Pauw, G. van Donk, J. van Es, A.A. Woering
National Aerospace Laboratory, NLR, NL-1 8300 AD Emmeloord, The Netherlands

G. Castellini[1),2)]
CNR-IROE, I-50125 Florence, Italy
[1)] INFN, Sezione di Bologna, [2)] INAF,CNR, Firenze

J. Trümper
Max-Planck Institut für extraterrestrische Physik, D-85740 Garching, Germany

Ph. Azzarello, Ph. Bouvier, M. Bourquin, E. Cortina, D. Haas, H. Hakobyan, C. Leluc, S. Natale, M. Paniccia, E. Perrin, M. Pohl, D. Rapin, C.M. Ting, M. Willenbrock
DPNC, Université de Genevè, CH-1211 Genevè 4, Switzerland

S. Breon
NASA Goddard Space Flight Center, GSFC, Greenbelt, MD 20771, USA

B. Baret, A. Barrau, G. Boudoul, M. Buénerd, L. Derome, K. Protasov, M. Vargas-Trevino, O. Véziant
Laboratoire de Physique Subatomique et de Cosmologie, LPSC, IN2P3/CNRS and Université J. Fourier, F-38026 Grenoble, France

K.H. Guo, Z.H. He, Y.H. Huang, X.H. Jiang, T.X. Li , S.S. Lu, J.Q. Ni, X.M. Qi, S.J. Yu, N.S. Xu
Sun Yat-sen University, Guangzhou, 510275, China

C.-R. Chen, C. Hsiao, L.C. Lee, J.-R. Tsai
National Space Program Office, NSPO, Hsin-Chu, Taiwan 300

L. Cheng, Z.G. Guo, K. Li, T. Luan, L.Q. Wang
Shandong University, Jinan, Shandong, 250100, China

W. de Boer, F. Hauler, L. Jungermann, C. Sander, M. Schmanau, V. Zhukov
IEKP, University of Karlsruhe, D-76128 Karlsruhe, Germany
A. Mujunen, J. Ritakari
Metsahovi Radio Observatory, Helsinki University of Technology, FIN-02540 Kylmala, Finland

F. Barao[1),2)], G. Barreira[1)], M. Pimenta[1),2)], P. Goncalves[1)], L. Arruda[1)], R. Pereira[1)]
Laboratorio de Instrumentacao e Fisica Experimental de Particulas, LIP, P-1000 Lisboa, Portugal
[1)] *LIP, Av. Elias Garcia, 14 1-andar 1000 Lisboa,* [2)] *IST, Av. Rovisco Pais, 1049 Lisboa*

Y.-J. Fanchiang, H. Jinchi, Y.-T. Ting
Chung-Shan Institute of Science and Technology, CSIST, Lung-Tan, Tao Yuan 325, Taiwan

M. Aguilar-Benítez, J. Alcaraz, J. Berdugo, J. Casaus, J. De Vicente, C. Díaz, L. García-Tabarés, E. Lanciotti, G. Martínez, C. Palomares, C. Maña, J. Marín, M. Molla, E. Sanchez, S. Sanz, I. Sevilla, F. Toral, A. Torrento, C. Vazquez
Centro de Investigaciones Energéticas, Medioambientales y Tecnológicas, CIEMAT, E-28040 Madrid, Spain

A. Menchaca Rocha
Instituto de Fisica, Universidad Nacional Autónoma de México, UNAM, Mexico D. F., 01000 Mexico

G. Boella[1),2)], M. J. Boschini[1),2)], M. Gervasi[1),2)], D. Grandi[1),2)], D. Pedrini[1),2)], S. Pensotti [1),2)], P.G. Rancoita[1)], L. Rossi [1)], G. Volpini[1),2)]
University of Milano-Bicocca and INFN-Sezione di Milano, I-20133 Milan, Italy
[1)] *INFN-Sezione di Milano,* [2)] *Universita' di Milano*

J. Bolmont, A. Jacholkowska, M. Sapinski, C. Zurbach
Groupe d'Astroparticules de Montpellier, GAM, IN2P3/CNRS-Universite Montpellier II, F-34095 Montpellier, France

E. Chumilov, Yu. Galaktionov, V. Plyaskin, A. Suvorov
Institute of Theoretical and Experimental Physics, ITEP, Moscow, 117259 Russia

I. Mitrofanov
Institute for Space Research, IKI, Russian Academy of Sciences, Moscow, 117810 Russia

A. Grechko, S. Vostrikov, N. Chernoplekov
Kurchatov Institute, Moscow, 123182 Russia

G. Bashindzhagyan, M. Merkin, M. Panasyuk
Skobeltsyn Institute of Nuclear Physics, Lomonosov Moscow State University, Moscow, 119992, Russia

J. Gong, G.Q. Gu, J.Q. Li , Q. Li , J.Z. Luo, Q. Meng, L.G. Shuai, H. Yi, C.R. Zou
Southeast University, Nanjing 210096, China

A. Chikanian, E. Finch, R. Majka, J. Sandweiss
Physics Department, Yale University, New Haven, CT 06520, USA

B. Alpat[1)], G. Ambrosi[1)], A. Damiamo[2)], A. Piluso[2)], R. Battiston[1),2)], B. Bertucci[1),2)], S. Bizzaglia[1)], S. Blasko[1),2)], W.J. Burger[1)], D. Caraffini[1),2)], C. Cecchi[1),2)], G. Esposito[1),2)], E. Fiandrini [1),2)], E. Fiori[1),2)], G. Lamanna[3)], M. Menichelli[1)], M. Pauluzzi[1),2)], P. Zuccon[1)], A. Papi[1)], M. Bizzarri[1),2)], L. Di Massso[1),2)], G. Scolieri[1)], S. Qiu[4)]
INFN-Sezione di Perugia and Universitá Degli Studi di Perugia, I-06100 Perugia, Italy
[1)] *INFN, Sezione di Perugia,* [2)] *Universita' di Perugia,* [3)] *Present address CPPM, Marseille, France,* [4)] *Present address China*

F. Cervelli[1)], St. Di Falco[1),2)], St. Galeotti[1)], F. Gherarducci[1)], M. Incagli[1)], T. Lomtadze[1)], C. Magazzù[1)], A. Orsini[1)], E. Pedreschi[1)], M. Piendibene[1)], F. Pilo[1),2)], F. Spinella[1),2)], C. Vannini[1)]
INFN-Sezione di Pisa and Universitá di Pisa, I-56100 Pisa, Italy
[1)] *INFN-Sezione di Pisa,* [2)] *Universita' di Pisa*

F. Bracciaferri , M. Conte, S. Di Pippo
Agenzia Spaziale Italiana, ASI, I-00198 Roma, Italy

A. Agneni[3),4)], St. Baccaro[1),4)], A. Bartoloni [1),2)], B. Borgia[1),2)], C. Bosio[1),2)], C. Gargiulo[1),2)], S. Gentile[1),2)], M. Montecchi[1),4)], A. Paolozzi[1),3)], P. Rapagnani[1),2)], E. Valente[1)]
INFN-Sezione di Roma and Universitá di Roma "La Sapienza", I-00185 Roma, Italy
[1)] *INFN, Sezione di Roma,* [2)] *Universita' di Roma,* [3)] *Dip. Ingegneria Aerospaziale, Roma,* [4)] *ENEA, Roma*

J. Yang, K. Kim
Ewha Womens University, 120-750 Seoul, South Korea

W.J. Ding, A.Z. Gu, Z.J. Jin, W.S. Lin, Q.J. Pang, W.X. Qiao, J.H. Shi, Y.M. Shi, R.S. Wang, S.W. Xie, Q.H. Ye
Shanghai Jiaotong University, SJTU, Shanghai 200030, China

E. Falchini[1),2)], P. Maestro[1),2)], P.S. Marrocchesi[1),2)]
INFN-Sezione di Siena and Universita' di Siena, I- 53100 Siena
[1)] *INFN-Sezione di Siena,* [2)] Universita' di Siena

C.E. Lin, Y.-C. Chao
Dept. of Aeronautics and Astronautics, National Cheng Kung University, NCKU, Tainan, 701 Taiwan

S.C. Lee, Y. Lei, Z. Ren, C. Wan, Y. Zhou
Institute of Physics, Academia Sinica, Taipei 11529, Taiwan

R.H. O'Neal, Jr.
AstroParticle and Cosmic Radiation Detector Research and Development Laboratory, Florida A&M University, Tallahassee, FL 32307, USA

R.J. Garcia Lopez, C. Delgado
Instituto de Astrofisica de Canarias, E-38205 La Laguna, Tenerife, Spain

A. Monfardini, P. Trampus
Center for Adanced Research in Space Optics, CARSO, 34012 Trieste, Italy

T. Eronen, T. Laitinen, E. Riihonen, J. Torsti, E. Valtonen
University of Turku, FIN-20014 Turku, Finland

H. Anderhub, A. Biland, H. Hofer, F. Pauss, J. Ulbricht, G. Viertel
Eidgenössische Technische Hochschule, ETH Zürich, CH-8093 Zürich, Switzerland

Contents

Introduction: The Alpha Magnetic Spectrometer (AMS)

AMS is a particle physics experiment in space. The purpose is to perform accurate, high statistics, long duration measurements of energetic (up to multi-TeV) primary charged cosmic ray spectra in space. Some of the physics goals are:

(1) **Dark Matter**: There are many theoretical suggestions that particles predicted by SUSY theories, for example the neutralino χ, are a component of the Dark Matter which constitutes one quarter of the mass of the universe [1]. Collisions of dark matter in the galactic halo produce $\bar{p}$, e^+ and γ via:

$$\chi + \chi \rightarrow \bar{p} + \ldots$$
$$\rightarrow e^+ + \ldots$$
$$\rightarrow \gamma + \ldots$$

The $\bar{p}$, e^+ and γ from these collisions will produce deviations from the smooth energy spectra. Therefore, the precision measurement of the $\bar{p}$, e^+ and γ spectra will enable us to establish whether SUSY particles are the origin of Dark Matter. There are also predictions that antideuterons can be produced from the collision of SUSY particles, which we will detect [2].

(2) **Antimatter**: The strong evidence which supports the Big Bang theory of the origin of the universe requires matter and antimatter to be equally abundant at the very hot beginning. The absence of sharp annihilation γ ray peaks excludes the presence of large quantities of antimatter within our cluster of galaxies. However there is no direct experimental evidence regarding the remainder (10^8) of the universe.

Theories (based on a new type of CP-violation, Baryon Violation, the Standard Model, and Grand Unification) which predict either the existence of antimatter in segregated domains or the total absence of antimatter, are highly speculative. To date, there is no evidence of a new type of CP-violation (neither from BaBar nor Belle) or proton decay. These theories have no firm foundation in experimental data.

The resolution of this important problem will require further data: from the current generation of particle colliders and the B Factories at SLAC and in Japan to improve our understanding of CP-violation; from the upgraded Tevatron and the LHC to provide clues to the correct extension or modification of the Standard Model; from the excellent proton decay experiments to improve our understanding of proton stability and from this experiment to improve (by a factor of 10^3) the observational basis of our understanding of the matter-antimatter balance in the universe.

(3) **Cosmic rays**: AMS will collect ~ 10^9 nuclei and isotopes (D, He, Li, Be, B, C …Fe). Among the interesting issues in physics are:

Accurate determination of the ratio of boron to carbon over a wide range of energies provides crucial information regarding the propagation of cosmic rays in the galaxy. In particular, the ratio of ^{10}Be (mean lifetime of 2.3 x 10^6 years) to the stable ^{9}Be will enable us to extend the low-energy measurements of the Ulysses satellite to higher energies and to provide important information on the understanding of cosmic ray propagation.

In the last half century, there have been many fundamental discoveries in astrophysics measuring microwaves, X-rays and gamma rays. Some examples include:

(i) the discovery of pulsars by Ryle and Hewish [3](Nobel Prize, 1974).

(ii) the discovery of microwave background radiation by Penzias and Wilson [4](Nobel Prize, 1978).

(iii) the discovery of new types of pulsars, which has opened up possibilities for the study of gravitational radiation phenomena, by Hulse and Taylor [5](Nobel Prize, 1993).

(iv) the many discoveries of ROSAT [6], COS-B [7], COBE [8], CGRO [9], ASCA [10], RXTE [11] and the Hubble Space Telescope [12].

In recent years, there have been many outstanding experiments with balloons (BESS [13], IMAX [14], HEAT [15], CAPRICE [16], WIZARD [17], MASS [18], the RICH Experiment [19], etc.) and accurate non-magnetic experiments on satellites (HEAO-3-C2 [20], Ariel-5,6 [21], ACE [22], EPACT [23], Ulysses [24], Voyager 1 and 2 [25], etc.). In addition, there are ingenious ground-base experiments such as CASA [26], GRAND and the future P. Auger project [27], and underground experiments including IMB, MACRO [28], Soudan-2 [29], Super Kamyokande [30]. The results of these experiments have and will continue to provide important information on the understanding of the origin of cosmic rays.

Figure 1 shows the worldwide participation in AMS. Appendix C lists the universities and institutes collaborating in AMS.

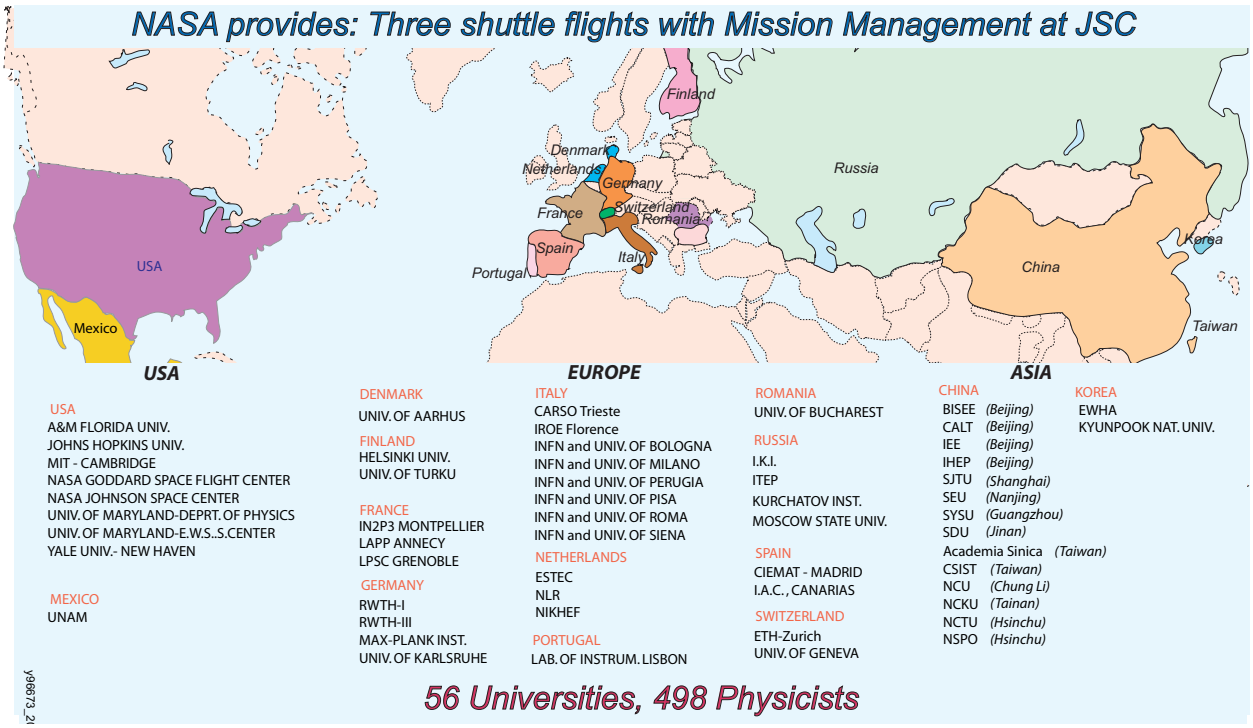

Figure 1: Participation in AMS from the U.S.A., Europe and Asia.

To perform a high accuracy measurement of the spectra of energetic charged particles in space, we have designed the AMS detector based on experience and observations from experiments to study rare signals among intense backgrounds, such as the study of leptonic decays of vector mesons from $\gamma + N \rightarrow N + (\rho, \omega, \phi \rightarrow e^+e^-)$ at DESY [31] and the discovery of the J particle from $p + N \rightarrow J (\rightarrow e^+e^-) + ...$ [32] combined with the precision measurements made in the study of Z decays [33]. These experiments were successful because they have:

(a) Minimal material in the particle trajectory so that the material itself is not a source of background nor a source of large angle nuclear scattering;

(b) Many repeated measurements of momentum and velocity so as to ensure that background particles which had experienced large angle nuclear scattering from the detector itself be swept away by the spectrometer and not confused with the signal.

It was the strict adherence to these techniques that ensured that a background rejection of 10^{10} was indeed possible and made these experiments successful. AMS is designed following the same principals. Figure 2 shows the AMS-02 detector configuration for the International Space Station (ISS).

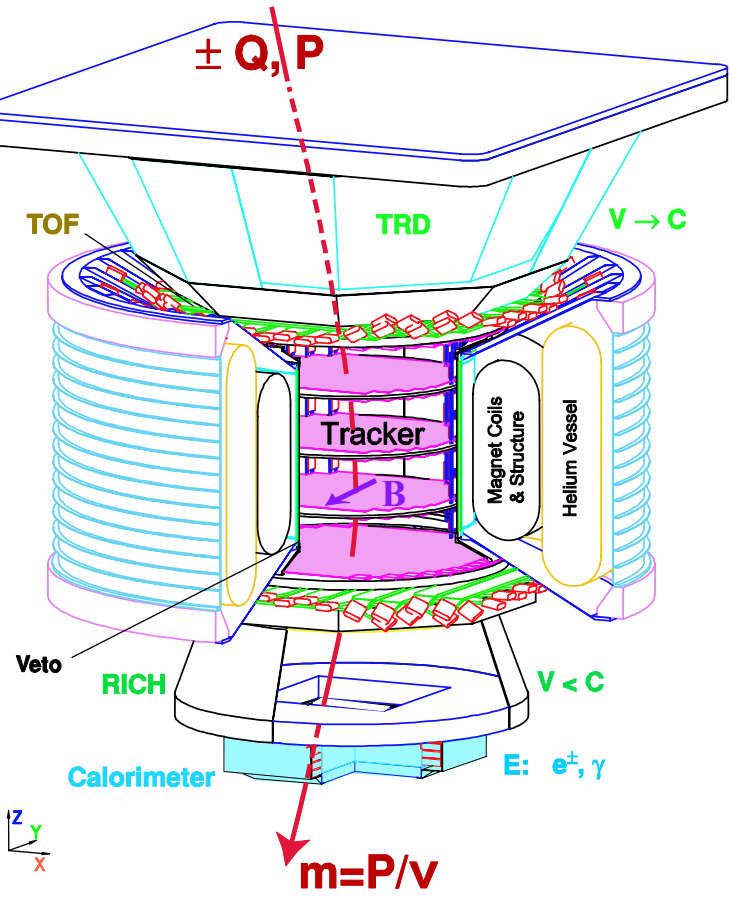

Figure 2: A TeV Detector in Space: AMS-02 on the Space Station.
The value of |Q| is measured independently in Tracker, RICH and TOF. The signed charge, ±Q, and the momentum of the particle, P, are measured by the 8 layers of doubled-sided silicon tracker in the magnet. The velocity, $\beta = v/c$, is measured by the TOF, TRD and RICH.

On the ISS, AMS contains the following main components:

(1) A twenty layer Transition Radiation Detector (TRD) which identifies electrons and positrons with a measured rejection factor against hadrons of 10^3 to 10^2 from 1.5 GeV to 300 GeV.

(2) Four layers of Time of Flight (TOF) hodoscopes that provide precision time of flight measurements (~ 120 picoseconds) and dE/dX measurements.

(3) The superconducting magnet, which provides a bending power of $BL^2 = 0.86\ Tm^2$.

(4) Eight layers (6.45 m^2) of silicon tracker, which provide a proton rigidity (= momentum/charge) resolution of 20% at 0.5 TV and a helium (He) resolution of 20% at 1 TV. Figure 3 shows the calculated rigidity resolution of AMS-02.

(5) Veto, or anticoincidence, counters (ACC) which ensure that only particles passing through the magnet aperture will be accepted.

(6) A Ring Imaging Cerenkov Counter (RICH), which measures the velocity (to 0.1%) and charge |Z| of particles or nuclei. This information, together with the measurement of momentum in the tracker, will enable AMS to unambiguously determine the mass of these particles and nuclei.

(7) A 3-D sampling calorimeter (ECAL) made out of 16.7 X_o (radiation lengths) of lead and scintillating fibers which measures the energy of gamma rays, electrons and positrons and distinguishes electrons and positrons from hadrons with a rejection of 10^4 in the range between 1.5 GeV to 1 TeV.

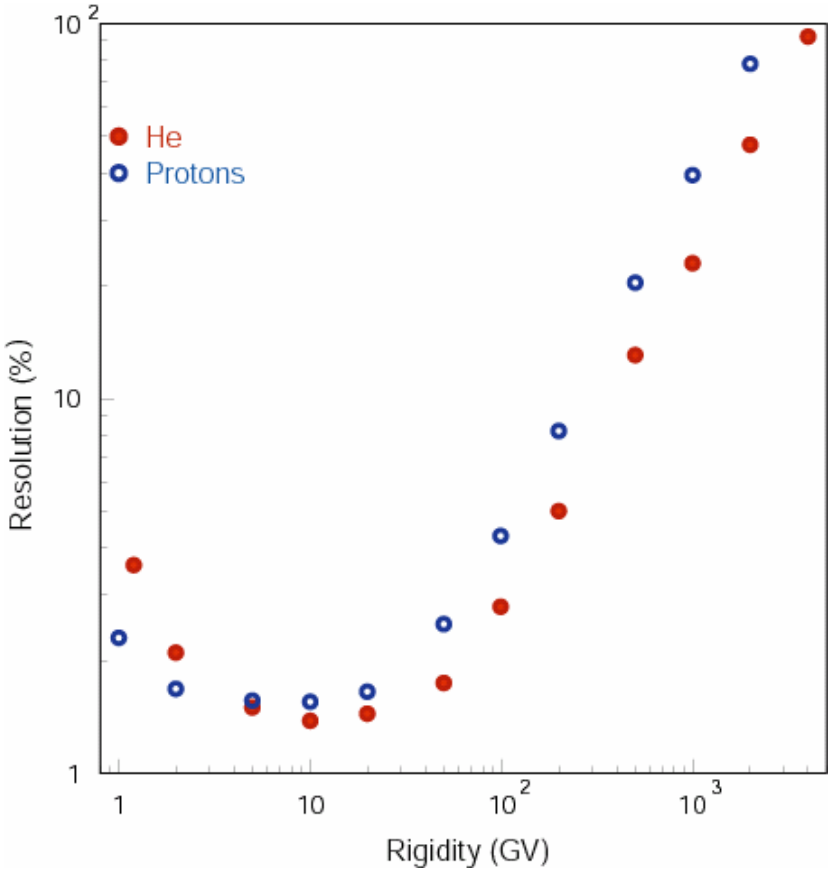

Figure 3: Rigidity Resolution of protons and He in AMS-02.

By installing a Star Tracker (which provides an angular resolution of a few arc seconds), AMS will become a sensitive high energy (up to 300 GeV) gamma ray detector. The measurement of $\gamma \rightarrow e^+ e^-$ will be done by the method similar to the one used in earlier work at DESY:

- No signal in the top layers of the TRD and in the Veto Counters.
- Trajectory in the magnet measuring the opening angle and momentum of e^+,e^- from $\gamma \rightarrow e^+ e^-$ [34].
- Energy measurement of the e^+ and e^- in the ECAL.

Independently, γ can be measured directly in the ECAL by selecting events with:

- No signal in TRD and Tracker, TOF and Anticoincidence Counters.
- One large electromagnetic shower in the ECAL pointing towards the other detectors.

Figure 4 shows a NASA computer simulation of AMS-02 installed on the International Space Station. AMS is the only approved and scheduled large scale physics experiment on the International Space Station.

References

[1] J. Ellis *et al.*, Phys. Lett. **B214** (1998) 3;
M. Turner and F. Wilczek, Phys. Rev. **D42** (1990) 4;
E.A. Baltz and J. Edsjo, Phys. Rev. **D59** (1999) 23511;
T. Moroi and L. Randall, Nuc. Phys. **B570** (2000) 455.

[2] P. Salati, *et al.*, Nucl.Phys.Proc.Suppl. **81** (2000) 37.

[3] M. Ryle and A.Hevish, Nobel Foundation Directory (2003).

[4] P.L. Kapista, A.Penzias and R.W. Wilson, Nobel Foundation Directory (2003).

[5] R.A. Hulse and J. Taylor, Nobel Foundation Directory (2003).

The experiments noted have published many valuable papers, which are listed at the noted URLs:

[6] http://heasarc.gsfc.nasa.gov/docs/rosat/rosgof.html

[7] http://heasarc.gsfc.nasa.gov/docs/cosb/cosb.html

[8] http://lambda.gsfc.nasa.gov/product/cobe/

[9] http://heasarc.gsfc.nasa.gov/docs/cgro/cgro.html

[10] http://heasarc.gsfc.nasa.gov/docs/asca/ascagof.html

[11] http://heasarc.gsfc.nasa.gov/docs/xte/xte_1st.html

[12] http://hubble.nasa.gov/

[13] http://lheawww.gsfc.nasa.gov/docs/gamcosray/hecr/BESS/BESS.html;
H. Matsunaga *et al.*, Phys. Rev. Lett. **81** (1998) 4052;
A. Moiseev *et al.*, Astrophysical Journal **474** (1997) 489;
S. Orito *et al.*, Proceedings of ICHEP, Vancouver (1998);
J.F. Ormes *et al.*, Ap. J. Lett. **482** (1997) L187;
T. Saeki *et al.*, Phys. Lett. **B422** (1998) 319;
E.S. Seo *et al.*, 25th ICRC **5** (1997) 373;
A. Yamamoto *et al.*, Advances in Space Research **14** (2) (1995) 75;
K. Yoshimura *et al.*, Phys. Rev. Lett. **75** (1996) 3792.

[14] http://ida1.physik.uni-siegen.de/IMAX.html;
J. W. Mitchell *et al.,* 23rd ICRC **1** (1993) 519.

[15] Barwick *et al*., NIM **400** (1997) 34.

[16] http://ida1.physik.uni-siegen.de/caprice.html;
M. Boezio *et al.,* Ap. J. **532** (2000) 653;
M. Boezio *et al.,* Phys. Rev. **D62** (2000) 032007
J. Kremer *et al.,* Phys. Rev. Lett. **83,** # 21 (1999) 4241;
M. Boezio *et al.,* Phys. Rev. Lett. **82,** # 24 (1999) 4757;
T. Francke *et al.,* 26th ICRC **2** (1999) 80;
M. Boezio *et al.,* Ap. J. **518** (1999) 457
G. Barbiellini *et al.,* 25th ICRC **6** (1997) 317;
G. Barbiellini *et al.,* 25th ICRC **3** (1997) 369;
G. Barbiellini *et al.,* 25th ICRC **4** (1997) 217;
G. Barbiellini *et al.,* 25th ICRC **4** (1997) 221;
G. Barbiellini *et al.,* 25th ICRC **3** (1997) 377;
M. Boezio *et al.,* AP. J. **487** (1997) 415;
G. Barbiellini *et al.,* A&A **309** (1996) L15;
G. Barbiellini *et al.,* Nucl. Instr. Meth. **A371** (1996) 169;
M. Bocciolini *et al.,* Nucl. Instr. Meth. **A370** (1996) 403;
G. Barbiellini *et al.,* 24th ICRC **3** (1995) 80;
G. Barbiellini *et al.,* 24th ICRC **3** (1995) 657;
P. Carlson *et al.,* Nucl. Instr. Meth. **A349** (1994) 577;
P. Carlson *et al.,* 23rd ICRC **2** (1993) 504.

[17] http://ida1.physik.uni-siegen.de/Mass2.html;
C. Grimani *et al.,* A&A **392** (2002) 287;
M. Circella *et al.,* 26th ICRC (1999) SH.3.6.18;
G. Basini *et al.,* 26th ICRC (1999) OG.1.1.21;
R. Bellotti *et al.,* Phys. Rev. D **60** (1999) 052002;
M. Circella *et al.,* 25th ICRC **6** (1997) 381;
M. Hof *et al.,* Ap. J. **467** (1996) L33;
G.Basini *et al.,* 24th ICRC **3** (1995) 1;
C.Grimani *et al.,* 24th ICRC **4** (1995) 1029;
G.Basini *et al.,* 24th ICRC **1** (1995) 585;
P.Papini *et al.,* 24th ICRC **4** (1995) 1033;
M. Hof *et al.,* 24th ICRC **3** (1995) 60;
G. Basini *et al.,* 23rd ICRC **3** (1993) 773.

[18] http://flaco.nmsu.edu;
M. Hof *et al.,* Ap. J. **467** (1996) 33.

[19] D.Ellithorpe, PhD Thesis, U. of Chicago (1998).

[20] http://heasarc.gsfc.nasa.gov/docs/heao3/heao3.html;
W.A. Mahoney *et al.,* Nucl. Instr. Meth. **178** (1980) 363.

[21] http://www.skyrocket.de/space/doc_sdat/ariel-5.htm;
K.A. Pounds, RAS Quarterly **27** (1986) 435.
P.H. Fowler *et al.,* 17th ICRC (1983)

[22] http://www.srl.caltech.edu/ACE/;
Space Science Reviews **86** (1998) 1/4.

[23] http://lheawww.gsfc.nasa.gov/docs/gamcosray/lecr/EPACT/epact.html;
D.V. Reames et al., Adv. Space Res. **19.5** (1997) 809.

[24] http://helio.estec.esa.nl/ulysses/;
D.D. Barbosa and M.G. Kivelson, Science **257** (1992) 1487.

[25] http://voyager.jpl.nasa.gov/index.html;
http://voyager.jpl.nasa.gov/science/bibliography_crs.html.

[26] P.H. Fowler *et al.,* Astro. Part. Phys. **15** (2001) 49.

[27] http://www.auger.org/;
http://www.auger.org/admin/DesignReport/index.html.

[28] C. De Marzo et al., Nuovo Cimento **9C** (1986) 281.

[29] Oliver *et al.,* Nucl. Instr. Meth. **A276** (1989) 371.

[30] http://www-sk.icrr.u-tokyo.ac.jp/doc/sk;
The Super-Kamiokande Collaboration, Phys. Rev. Lett. **81** (1998) 1562.

[31] J.G. Asbury *et al.,* Phys. Rev. Lett. **18**, 2 (1967) 65;
J.G. Asbury *et al.,* Phys. Rev. Lett. **19**, 15 (1967) 869;
U. Becker *et al.,* Phys. Rev. Lett. **21**, 21 (1968) 1504;
H. Alvensleben *et al.,* Phys. Rev. Lett. **27**, 13 (1971) 888.

[32] J.J. Aubert *et al.,* Phys. Rev. Lett. **33**, 23 (1974) 1404.

[33] For example, L3 Collaboration, Nucl. Instr. Meth. A **289** (1990) 35.

[34] R.Battiston *et al.*, Astro. Part. Phys. **13** (2000) 51.

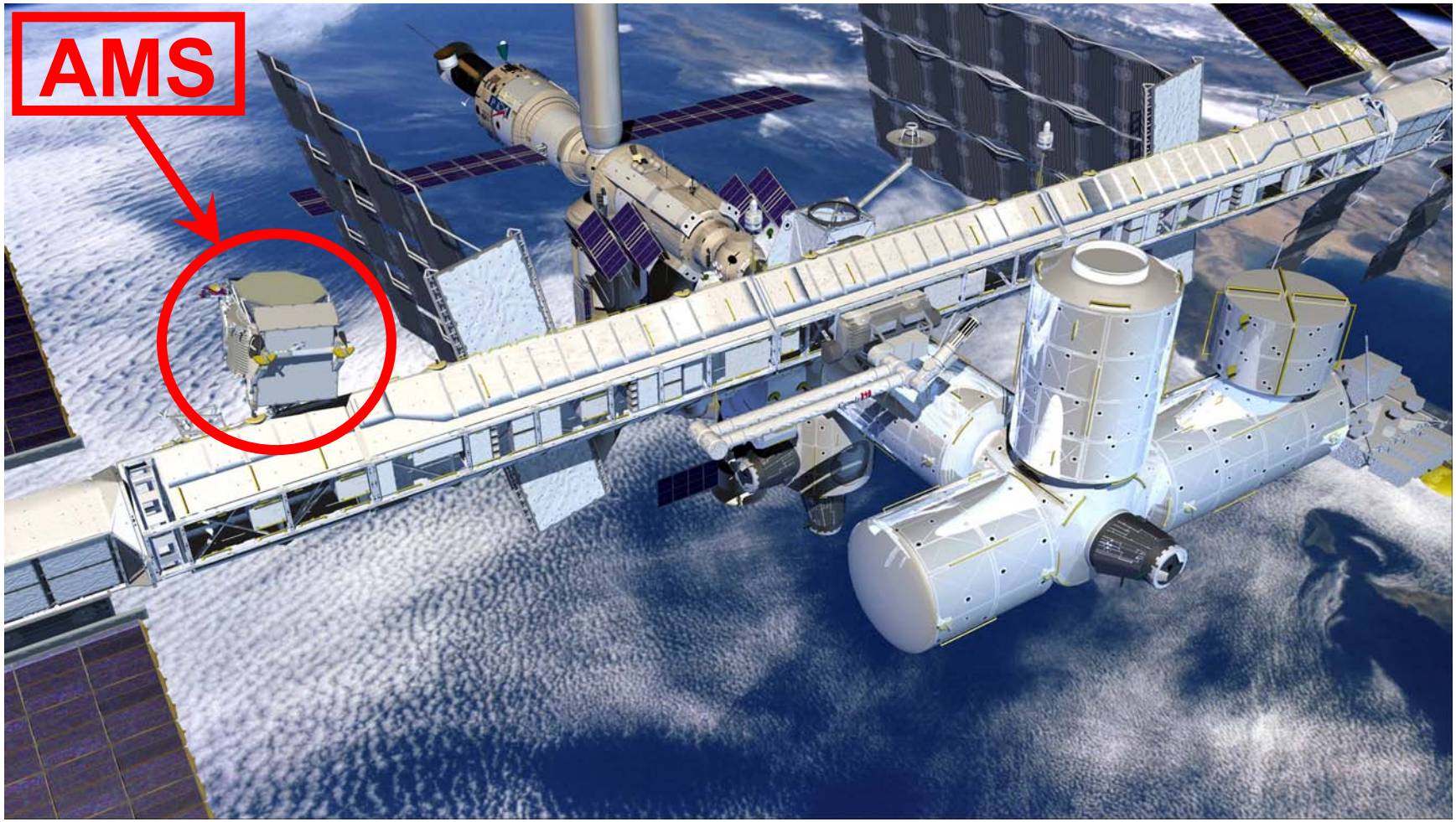

Figure 4: View of AMS on the ISS.

Chapter One: AMS-01, engineering flight on the Space Shuttle

Before installation on the Space Station, AMS performed an engineering flight on the Space Shuttle to ensure that:

- The AMS experiment can function properly in space; in vacuum with orbital temperature changes from −65 to 40 °C and in the intense radiation background (which contains heavy nuclei causing single event latch-up in chips).
- The detector can withstand the tremendous vibrations (150 dB) and acceleration (3 g) at launch and the deacceleration (6.5 g) at landing;

This mission was subsequently referred to as AMS-01. The experimental configuration is shown in Figure 1.1.

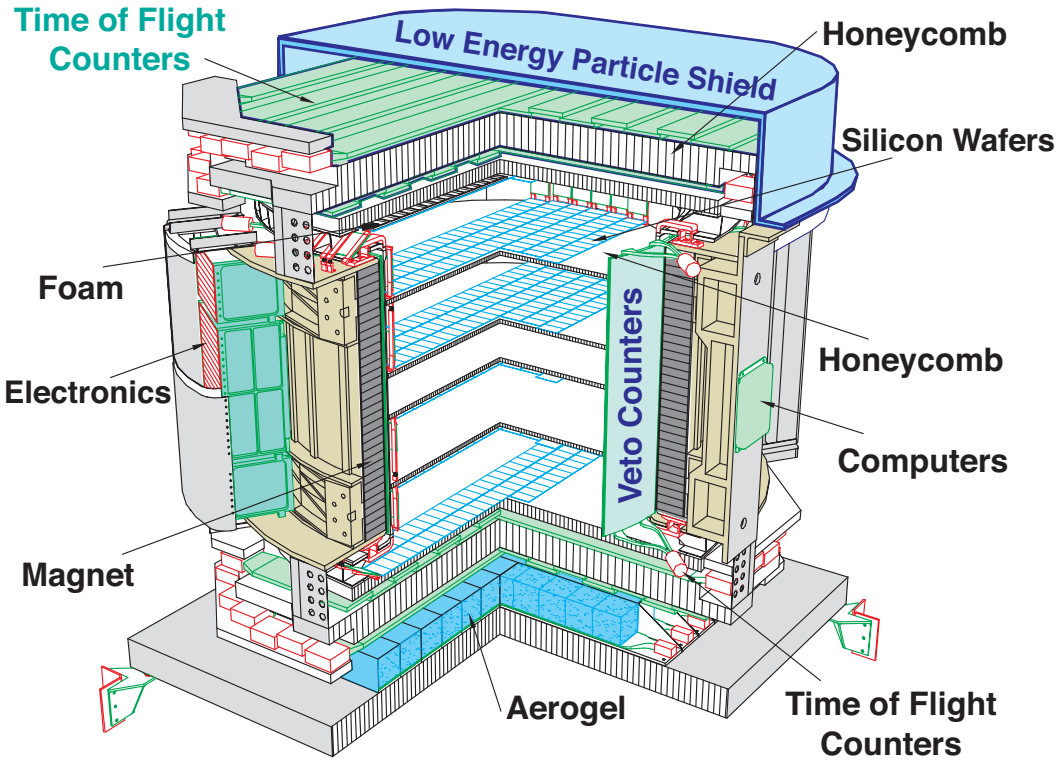

Figure 1.1: AMS-01, the configuration for the Space Shuttle flight.

1.1 Construction of the AMS-01 magnet

The AMS-01 magnet was made from 64 high-grade Nd-Fe-B sectors. Each sector was composed of 100 (2" x 2" x 1") blocks. Figure 1.2 shows the arrangement of the field direction of the 64 sectors. The highest grade Nd-Fe-B blocks, with an energy level of $(BH)_{max}$ = 50 x 10^6 GOe, were used. This

configuration produced a dipole field of 1.5 kG and a negligible dipole moment[1]. In addition, the flux leakage[2] at a 2-meter distance from the center of the magnet is 3 G.

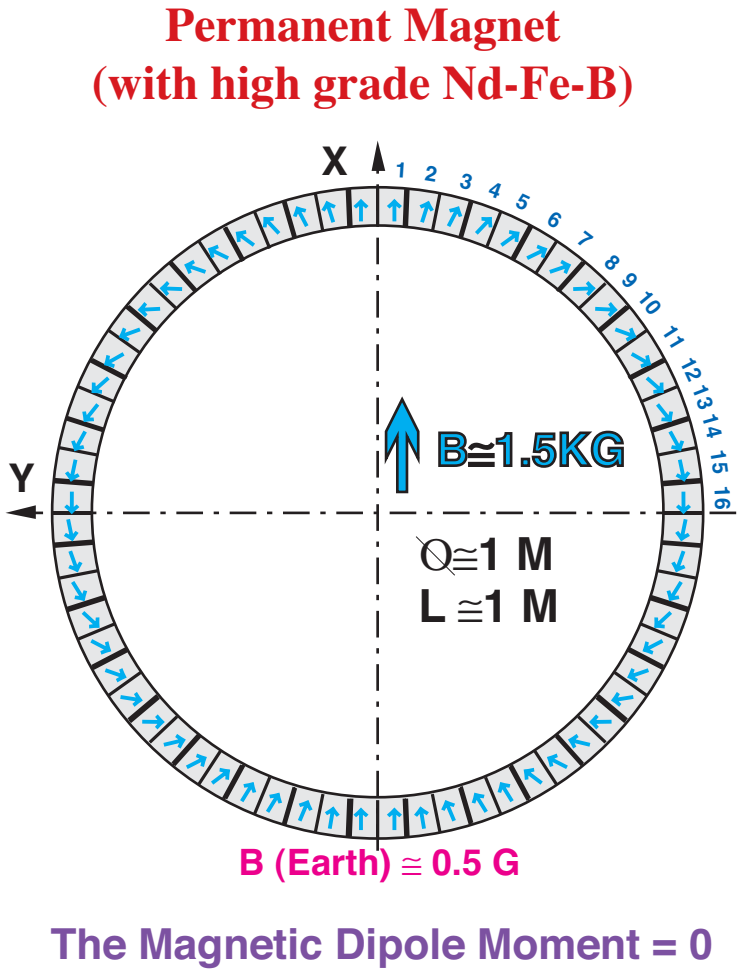

Figure 1.2: Magnetic field orientation of the AMS-01 magnet.

Before the construction of the full scale magnets, a 1:3 scale magnet was built to confirm and measure the field inside the magnet, the dipole moment and the flux leakage. Then three full scale magnets were built:

(i) the first magnet was used in acceleration and vibration tests for space qualification;

(ii) the second magnet was the flight magnet;

(iii) the third magnet was built without glue for NASA safety tests.

Figure 1.3 shows the dimensions of the AMS-01 flight magnet. As shown in Figures 1.4 and 1.5, these magnets were subjected to a full battery of space qualification testing.

The third full scale magnet was built because of the lack of knowledge of the glue performance over an extended period of time in the space environment. It was built without using any glue to be tested to destruction to ensure that AMS could be returned on the Shuttle to Earth even if the glue completely failed while on orbit.

---

[1] The geomagnetic field is 0.5 G on the surface and varies when on orbit. A strong dipole moment would result in an undesirable force on the space shuttle or the space station.

[2] NASA requires the leakage field to be < 300G so as not to interfere with the life support system of the astronauts.

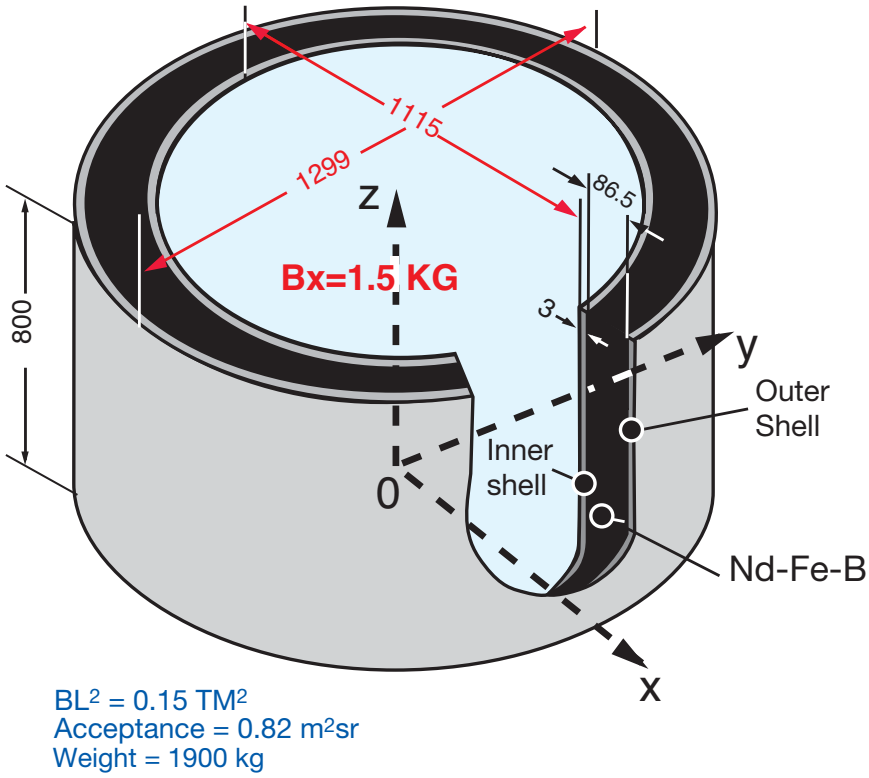

Figure 1.3: Properties of the AMS-01 flight magnet.

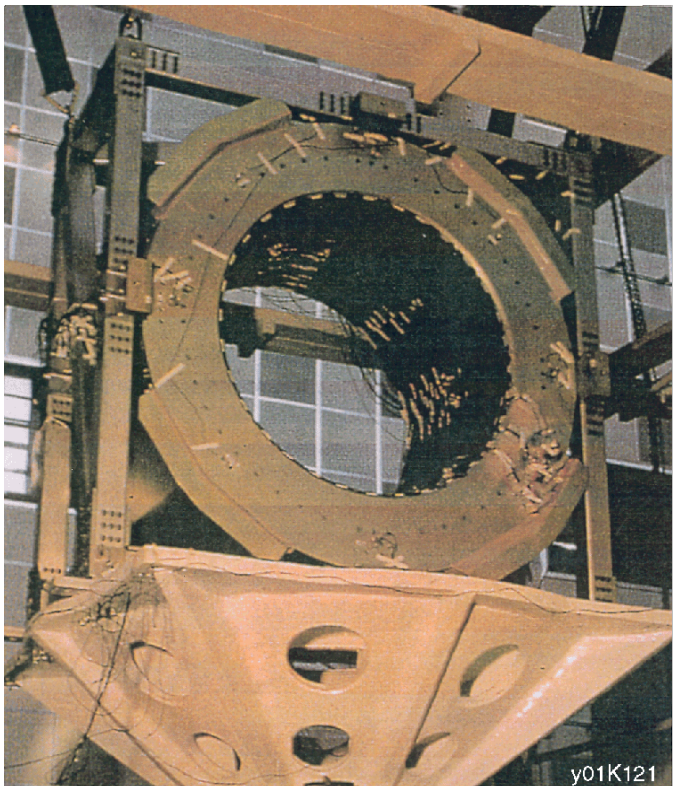

Figure 1.4: AMS-01 magnet during vibration tests at the Beijing Institute of Spacecraft Environment and Engineering in Beijing, China.

Figure 1.4: AMS-01 magnet undergoing centrifuge (static load) testing at the Laboratory for Centrifugal Modeling in Beijing, China.

1.2 AMS-01 Silicon Tracker

Figure 1.6 shows the location of the six planes of the Silicon Tracker (T1-T6) in AMS-01.

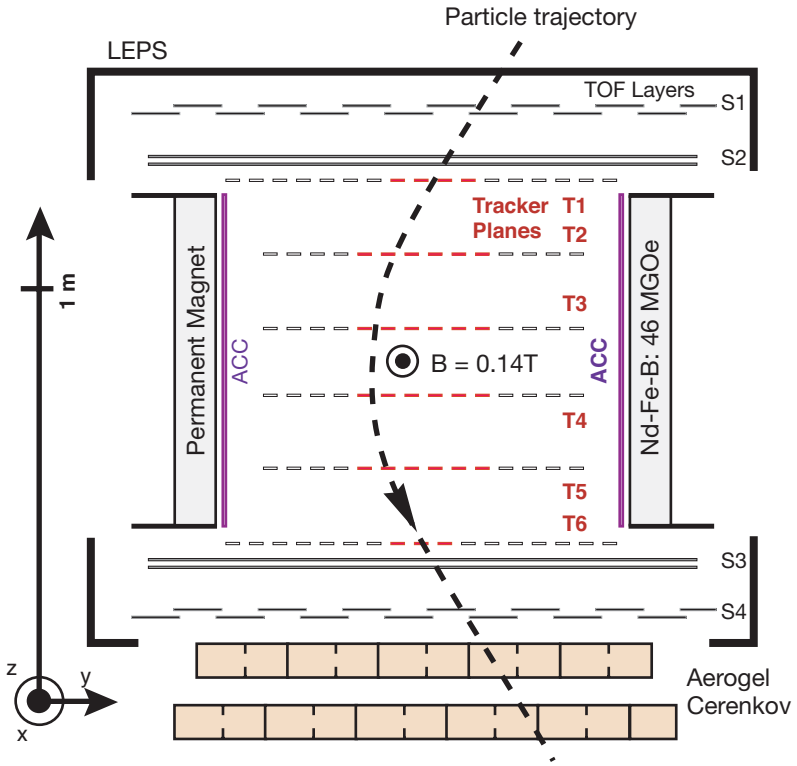

Figure 1.6: Location of the Silicon Tracker in AMS-01.
For this engineering flight 3 of the 6 m^2 of silicon were installed, as shown in red.

The design and construction of the Tracker benefited from the construction and operational experience of the Silicon Microvertex Detector (SMD) at the L3 experiment. For the AMS-01 shuttle flight, 3 m^2 of double-sided silicon sensors were implemented, a total of 70,000 readout channels. The resolution was 10 μm in the bending plane and 30 μm in the non-bending plane, or $\Delta P/P = 7\%$ at 10 GeV.

The silicon ladders were wrapped in an ultra-thin copper coated electromagnetic shield. The ladders went through electromagnetic (EM) compatibility tests in the kHz, MHz and GHz ranges to establish EM immunity levels. The completed ladders were assembled on six thin honeycomb plates with a combined thickness, in radiation lengths, of $X/X_0 < 3.2\%$. Each plate, measuring 1 m in diameter, contained precision holes for attaching the silicon ladders and ensuring their flatness to 80 μm. They were designed to allow the ladders to be aligned independently of temperature, humidity and air pressure changes.

Figure 1.7 shows the integration of the silicon ladders on one of the six plates. The support structure for the six planes, also shown in Figure 1.8, was made from a carbon composite material to be light-tight and equipped with a cooling system that removes heat produced by the tracker's front-end electronics.

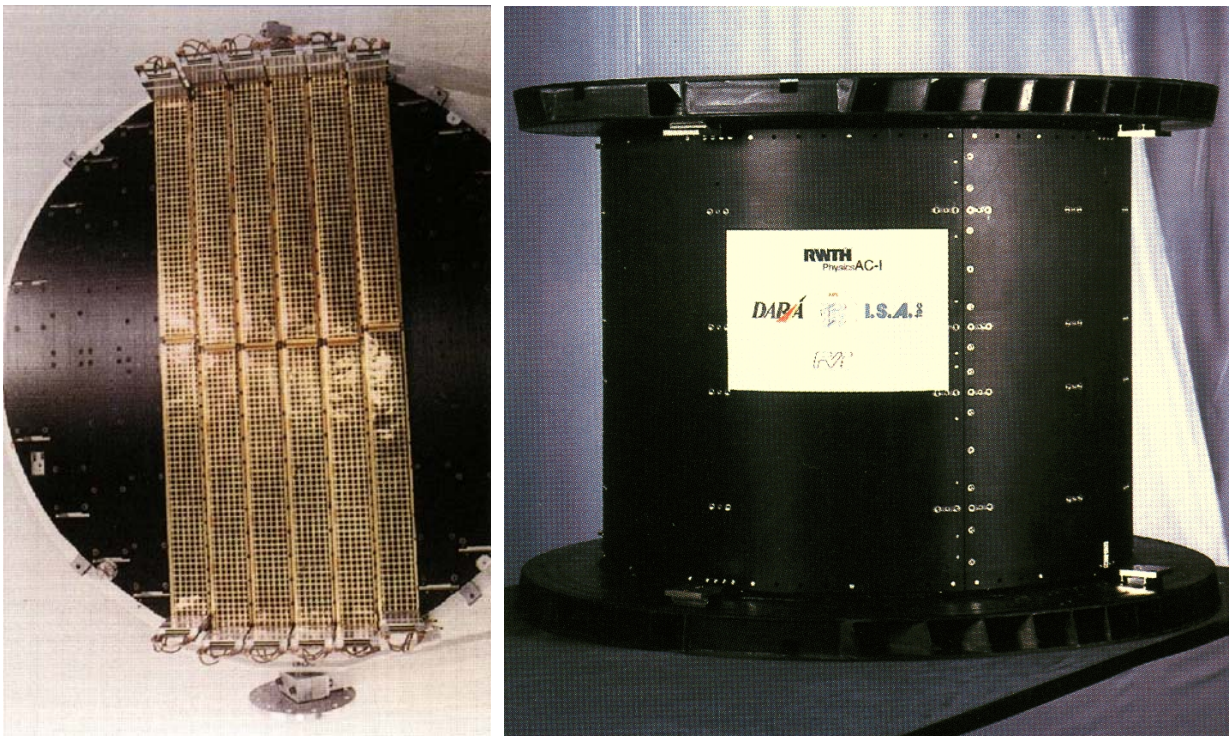

Figure 1.7: Integration of silicon ladders on one of six ultralight plates (left). Final preassembled silicon tracker carbon-fiber composite (CFC) mechanical structure including the CFC upper and lower support flanges (right).

To ensure that the AMS-01 detector had the desired accuracy, an infrared laser alignment system was developed. The laser beams partially ionize the silicon as they traverse the Tracker planes. The system provides positional accuracy of a passing particle through each of the six planes to within a few microns. This system is shown in Figure 1.8.

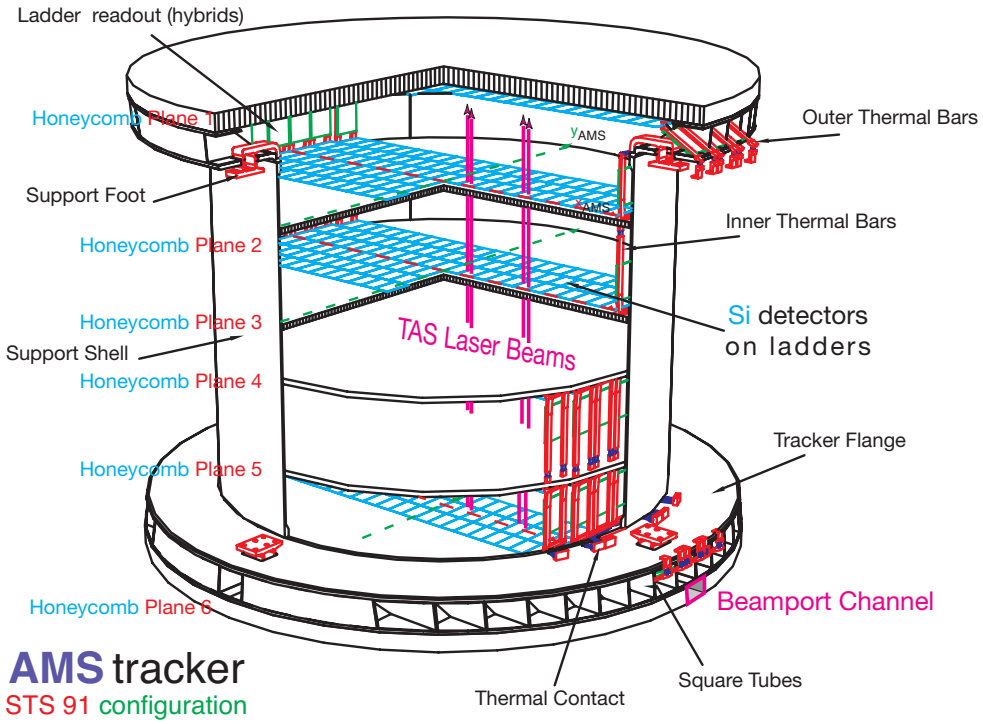

Figure 1.8: Laser alignment system for the AMS-01 Tracker.

The front-end electronics of the Tracker were made of very low noise VLSI units. Each channel consists of a sample and hold low-noise charge preamplifier. They are read out sequentially at speeds up to 5 MHz. The data reduction electronics for the Tracker were specially designed to be light weight and use minimum power. The ladders and all the data reduction systems went through vigorous space qualification testing including acceleration, vibration, thermal vacuum and temperature tolerance.

The ladders were tested in a heavy ion test beam at the Gesellschaft für Schwerionenforschung (GSI) Darmstadt, Germany, with H, He, Li and C. Figure 1.9 demonstrates the dE/dX response linearity in minimum ionizing particle (MIP) equivalents.

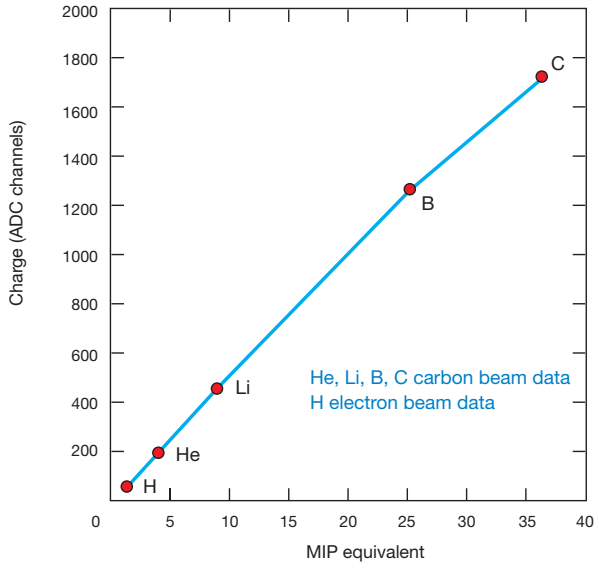

Figure 1.9: Response of AMS-01 Silicon Ladders.

1.3 AMS-01 Counters

AMS-01 contained three types of counters: Veto, Time of Flight and Aerogel Cerenkov.

1.3.1 The veto counters

These counters consisted of a cylindrical shell made of 16 modules of plastic scintillator surrounding the Silicon Tracker inside the magnet. Their function, in conjunction with the Time of Flight Counters, is to provide anti-coincidence protection against background particles entering the sides of the AMS apparatus or generated within AMS. Such events can create confusion in the event reconstruction or timing from the Time of Flight System. There is one photomultiplier tube at each end of the scintillator. Because of the very limited space available and to maintain mechanical stability, thin (1 mm diameter) double clad wavelength shifter fibers were used to guide the light to the photomultiplier tubes (see Figure 1.10). The figure also shows the final assembly of the counters inside the magnet, supported by a specially made carbon-composite reinforced cylinder. The veto counters were close to 100% efficient.

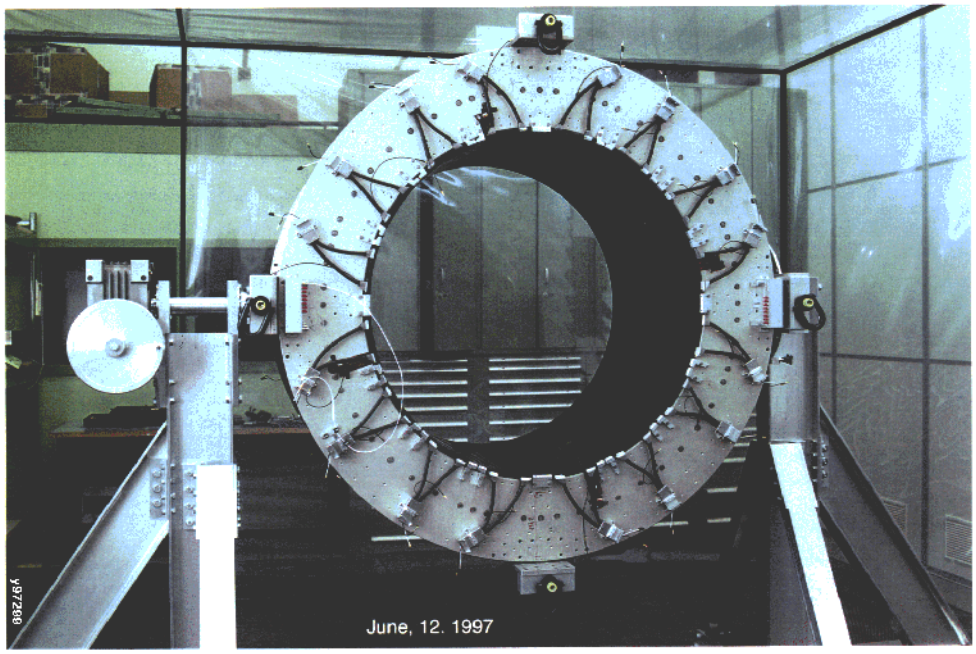

Figure 1.10: Final flight assembly of the 16 module veto counter system in the AMS-01 magnet at ETH-Zürich. The carbon fiber reinforcement cylinder is visible inside.

1.3.2 The AMS-01 Time of Flight hodoscopes

The Time of Flight System provides the first-level trigger, measures the time of flight to an accuracy of ~ 100 ps and measures dE/dX to determine the absolute charge (Z). The four layers of Time of Flight Counters (S1-S4) each contain 14 scintillator hodoscopes (paddles). Each hodoscope is viewed by three photomultipliers at each end, as shown in Figure 1.11.

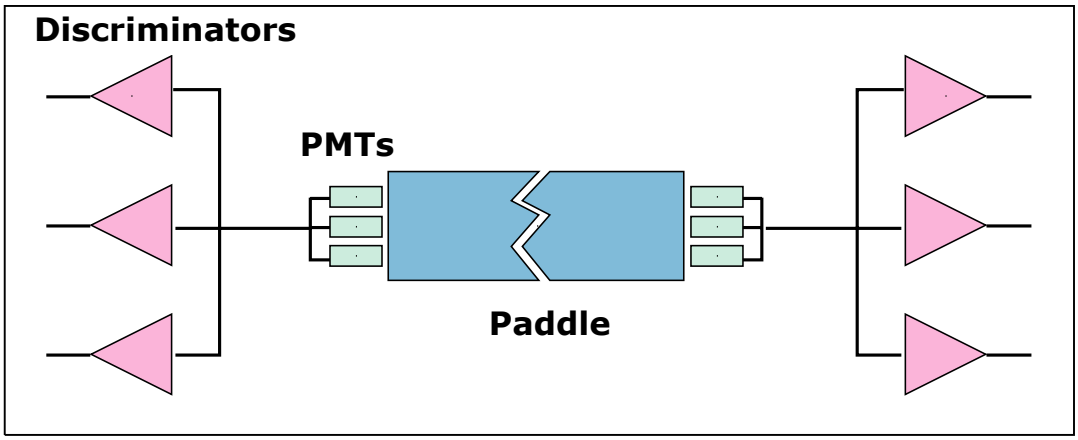

Figure 1.11: Schematic of AMS-01 Time of Flight counter design.

The Time of Flight elements underwent extensive calibration and space qualification tests including vibration and thermal vacuum tests in the Italian aerospace industry. The thermal vacuum tests were intended to check and correct any potential hazardous electrical discharge in space. Figure 1.12 shows the Time of Flight counters installed into AMS-01.

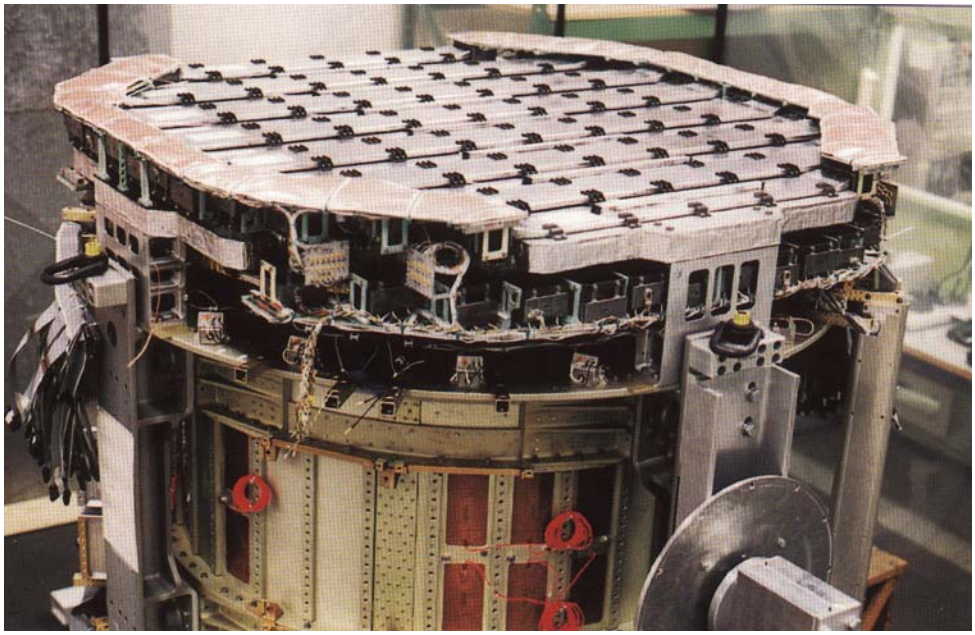

Figure 1.12: Mounting of Time of Flight on AMS-01.

1.3.3 Aerogel Cerenkov Counter

For the AMS-01 Shuttle flight we replaced the RICH and ECAL with Aerogel Cerenkov Counters which had a refractive index n = 1.04. The Aerogel counters were made out of two superimposed layers of cells 11 x 11 cm^2, each layer consisting of 80 (top) and 88 (bottom) cells of Aerogel blocks. The cell design is shown in Figure 1.13. Each cell was individually coupled to two photomultiplier tubes which detect Cerenkov light from electrons (from 2.1 MeV), pions (from 560 MeV) and protons (from 4.05 GeV). This information enabled us to identify antiprotons up to 4 GeV.

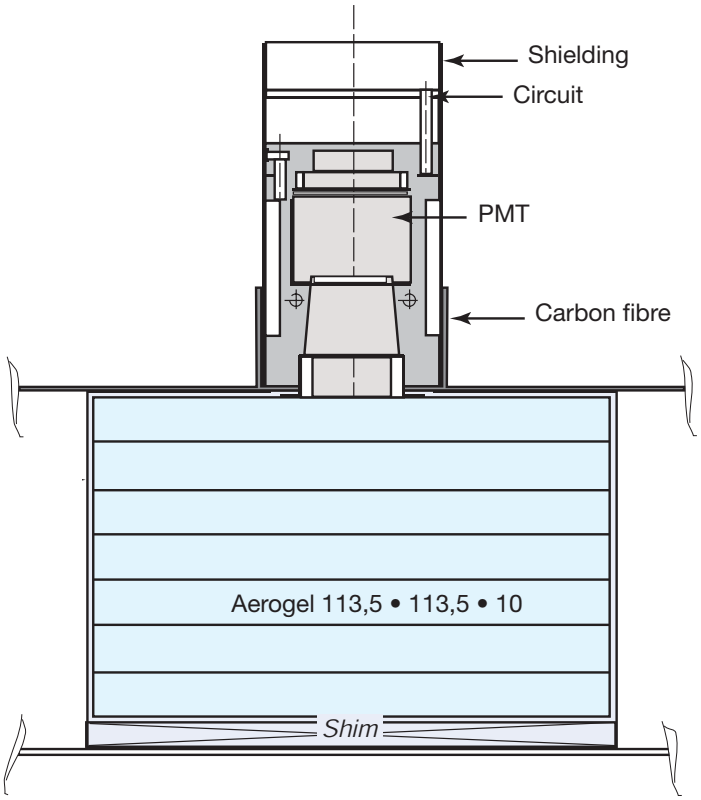

Figure 1.13: A cell of the Aerogel Counter.

1.4 AMS-01 Electronics

The electronics for AMS is derived from our experience in instrumenting terrestrial particle physics detectors. Much care and attention are necessary to ensure that these particle physics electronics can be used in space. There are 70,000 channels of tracker signals which provide a coordinate accuracy of 10 μm. There are four layers of Time of Flight hodoscopes providing a time resolution of ~ 100 ps. Both the Silicon Tracker and Time of Flight counters also provide independent dE/dX measurements to identify particle charge. Because of power and weight restrictions, all the electronics were specially designed, manufactured and space qualified by AMS institutions and aerospace industries in Europe and Asia.

Figure 1.14 shows an overview of the AMS-01 electronics design which is based on multiple redundancies to safeguard against the loss of data in space. To space qualify the electronics, the system went through extensive tests which included: vibration, temperature, thermal vacuum, radiation and electromagnetic compatibility. The radiation tests were specially carried out at Dubna and these tests were particularly important to ensure there would be no single event latch up in space. Table 1.1 shows the beam and energy used in these tests. The space qualification tests (vibration, temperature ...) were carried out at the Max Plank Institute for Extraterrestrial Physics in Germany and at the Chung-Shan Institute of Science and Technology (CSIST) in Taiwan; the latter of which also manufactured most of the electronic units.

Beam	Energy (MeV)
Ne	270
Au	460
Kr	430

Table 1.1: Beam characteristics used for AMS-01 electronic component tests at Dubna.

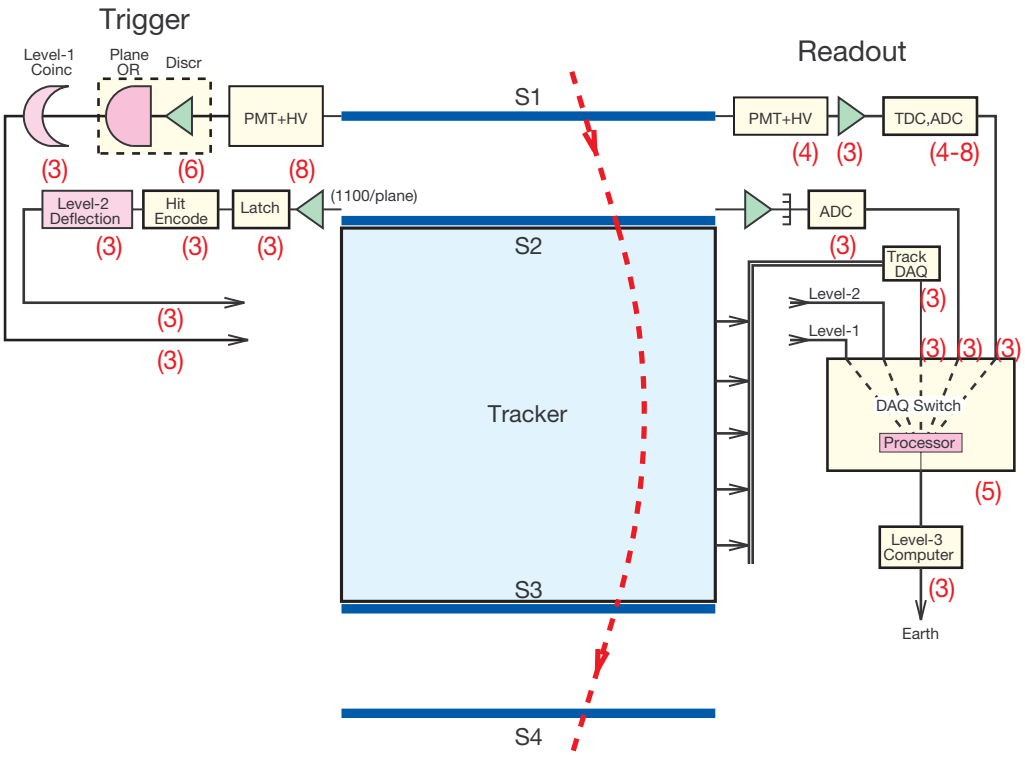

Figure 1.14: AMS-01 electronics. The numbers of redundant elements are given parenthetically.

1.5 AMS-01 Operations

AMS-01 was launched on the Shuttle Discovery (STS-91 flight) on 2 June 1998. During the ten-day mission of Discovery, AMS was allocated 100 hours of primary time to perform system tests. The rest of the time, Discovery was used for docking and transferring logistic support with the MIR space station. Figure 1.15 shows the lift-off of Shuttle Discovery with AMS-01 on board. The photograph in Figure 1.16, taken from MIR shortly before docking, shows AMS-01 at the rear of the Shuttle cargo bay.

Figure 1.15: The launch of the Space Shuttle *Discovery* with AMS-01 on board.

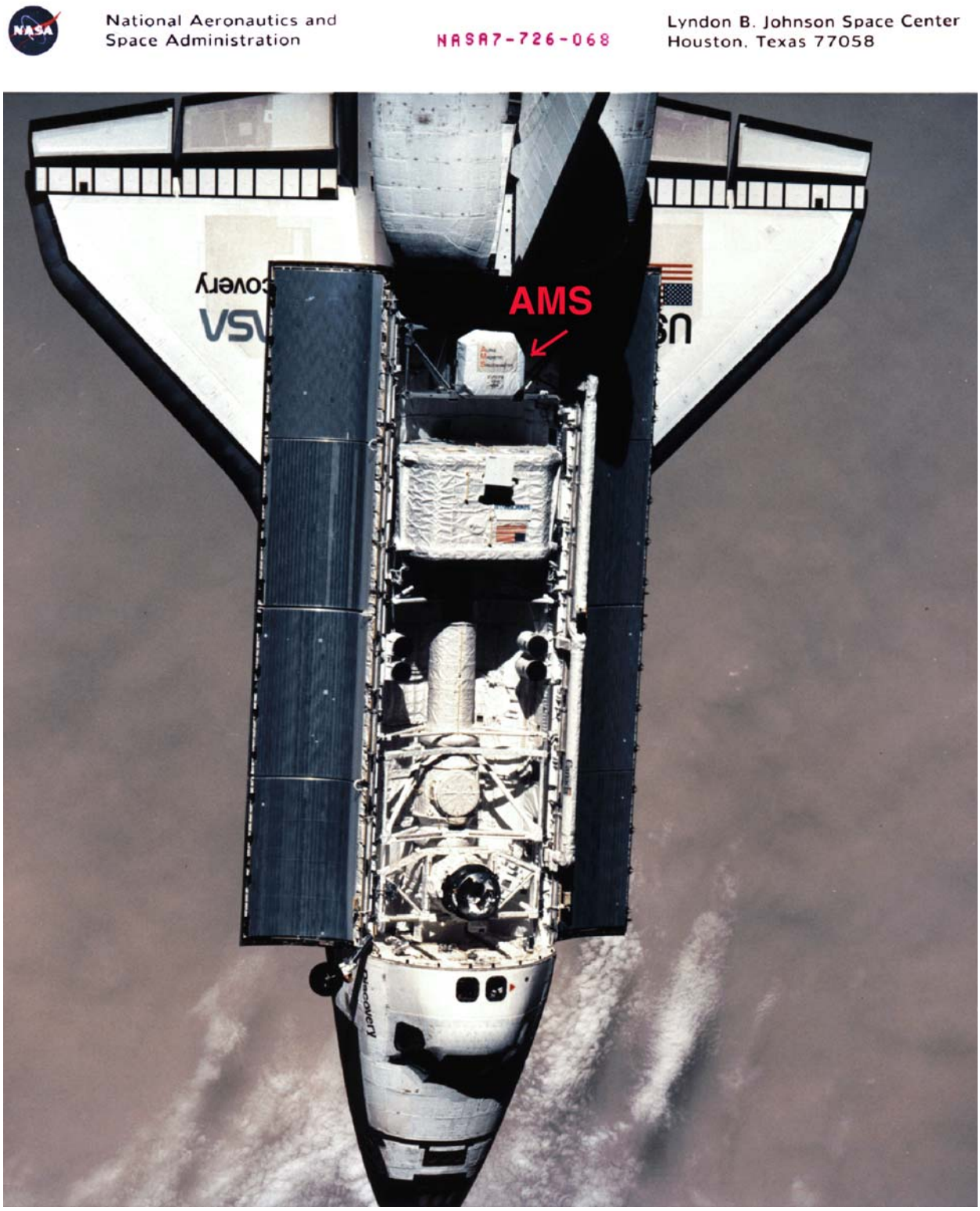

Figure 1.16: *Discovery* with AMS-01 seen from MIR.

1.6 Physics results of AMS-01

From the STS-91 flight of AMS-01, we gained experience and knowledge on how to execute a particle physics experiment in space. The construction of the complete detector which will be deployed on the Space Station benefits from this practical understanding of the technical capabilities and performance of each component under actual flight conditions.

Two hours after the shuttle lift-off on 2 June 1998, we began performing tests on AMS. Figure 1.17a shows the on-orbit Silicon Tracker displacement from the measurement of the laser alignment system. Figure 1.17b shows the same measurement when AMS was on the launch pad. Comparing these two measurements indicates that the relative alignment of the tracker layers was monitored with an accuracy of 3 μm. The AMS Digital Data Recorder was activated in the Shuttle crew compartment ensuring that all data were being recorded.

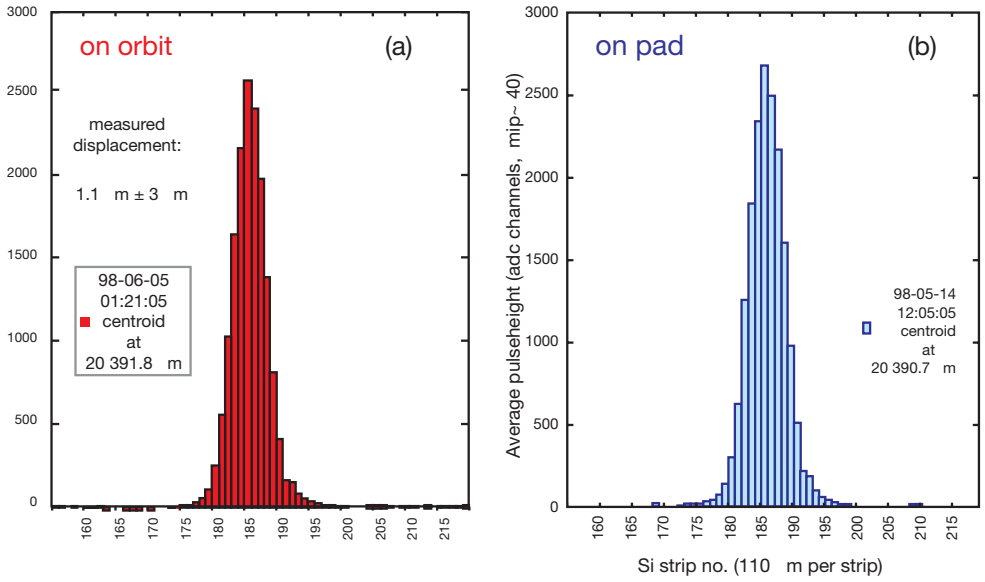

Figure 1.17: Laser displacement measured in orbit (a) and on launch pad (b).

During flight, the detector was located in the payload bay of the space shuttle and operated in vacuum. Events were triggered by the coincidence of signals in all four TOF planes consistent with the passage of a charged particle through the active tracker volume. Triggers with a coincident signal from the Veto Counters were rejected. The detector performance as well as temperature and magnetic field were monitored continuously. A total of 100 million triggers were recorded.

After the flight, AMS-01 was checked again. The detector was placed in a heavy ion (He, C) beam from 1.0 to 5.6 GV at 600 different incident angles. This test was done with a total of 45 million events and was carried out at GSI-Darmstadt. Figure 1.18 shows the location of AMS at the GSI ion accelerator and Figure 1.19 shows one of the carbon-beam test results.

After GSI, the detector was placed in a proton and pion beam at CERN, with momentum from 2 to 14 GeV at 1200 different incident angles. This test was done with a total of 100 million events.

The continued monitoring of AMS-01 confirmed that the detector performance before, during and after the flight remained the same. In particular, the alignment error of the silicon tracker was controlled to be less 5 μm through out.

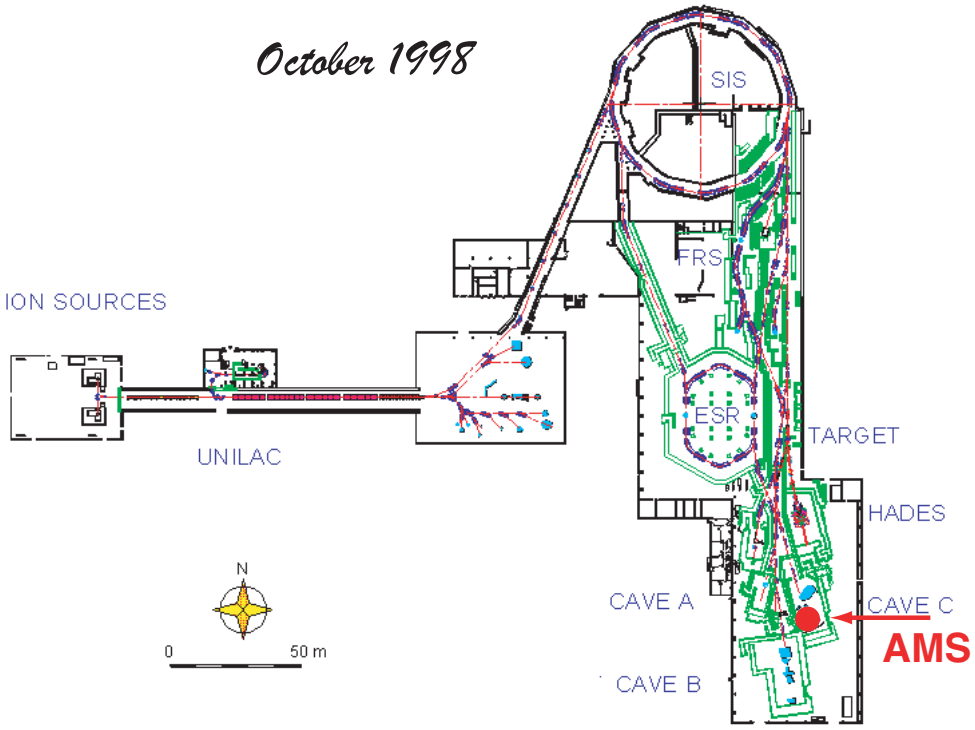

Figure 1.18: Location of AMS at the GSI Ion Accelerator.

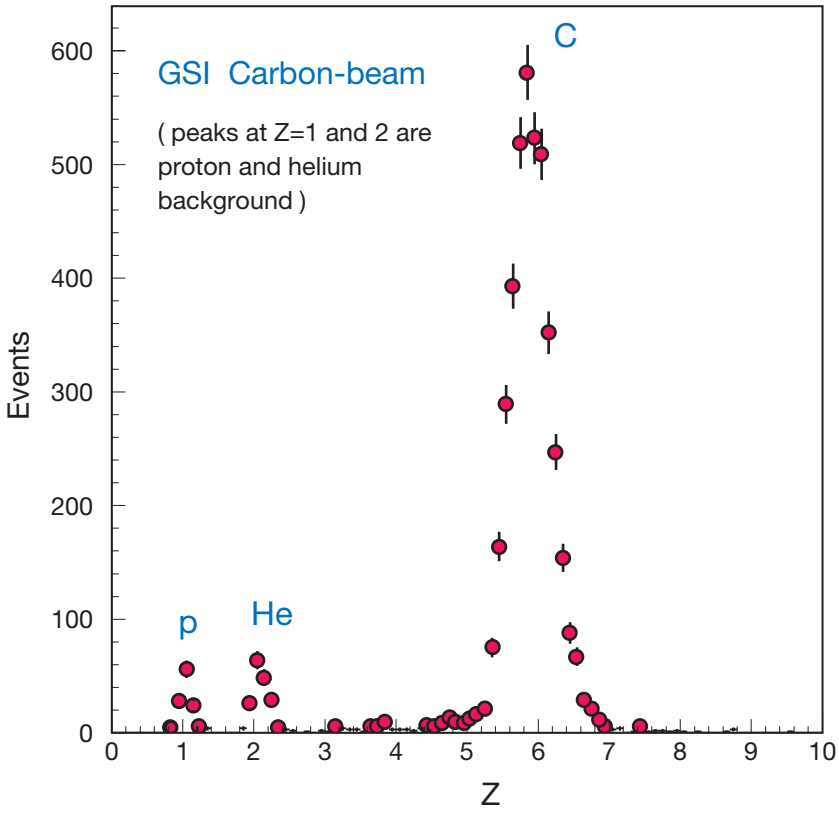

Figure 1.19: Results of tests of AMS-01with the GSI carbon beam.

Though the first flight was an engineering flight, over 100 million events were collected. In addition to validating the AMS concept, analysis of these events led to the following significant results:

- **Search for antihelium in cosmic rays**

A total of 2.86 x 10^6 helium nuclei with rigidities up to 140 GV were observed. No antihelium nuclei were detected at any rigidity. The most precise upper limit on the ratio of the flux of antihelium to the flux of helium of less than 1.1 x 10^{-6} is obtained.

- **Protons in near earth orbit**

The proton spectrum in the kinetic energy range 0.1 to 200 GeV was measured. Above the geomagnetic cutoff, the observed spectrum is parameterized by a power law. Below the geomagnetic cutoff, a substantial second spectrum was observed. Most of these second spectrum protons follow a complicated trajectory and originate from a restricted geographic region.

- **Leptons in near earth orbit**

The lepton spectra in the kinetic energy ranges 0.2 to 40 GeV for e^- and 0.2 to 3 GeV for e^+ were measured. From the origin of the leptons two distinct spectra were observed: a higher energy spectrum and a substantial second spectrum with positrons much more abundant than electrons. Tracing leptons from the second spectra shows that most of these leptons travel for an extended period of time in the geomagnetic field and that the e^+ and e^- originate from two complementary geographic regions.

- **Cosmic protons**:

The precise primary proton spectrum in the kinetic energy range 0.2 to 200 GeV was accurately measured. It is an important input to atmospheric neutrino estimations.

- **Helium in near earth orbit**:

The helium spectrum from 0.1 to 100 GeV/nucleon was measured. Above the geomagnetic cutoff, the spectrum is parameterized by a power law. Below the geomagnetic cutoff, a second helium spectrum was observed. In the second helium spectra over the energy range 0.1 to 1.2 GeV/nucleon, in the geomagnetic latitude from –0.4 to +0.4 rad, the flux was measured to be (6.3 ±0.9) x 10^{-3} /(m^2sec sr) and, contrary to expectations, more than ninety percent of the helium was determined to be ^{3}He (at the 90% C.L.).

- **Deuterons in near earth orbit**:

A total of 1 x 10^4 deuterium nuclei in the energy range 0.1 to 1.0 GeV/nucleon were observed allowing the first accurate test of galactic confinement models.

- **Search for antideuterium in cosmic rays:**

In a total of 1 x 10^4 deuterium nuclei in the momentum range 1 to 3 GeV/c no antideuterium nuclei were detected at any momentum. The most precise limit on the flux of antideuterium of less than 1 x 10^{-4} has been obtained.

- **Study of trapped and quasi-trapped high energy Cosmic Rays in near earth orbit:**

Detailed analysis of the particles below geomagnetic cutoff have established the existence of permanently trapped high energy p, e^+ and e^- with trajectories crossing the South Atlantic Anomaly.

Five papers covering the first five results have been published in Physics Letters B. At the invitation of the editor, we have also published a Physics Report on the construction of AMS-01 and all of the physics, including results on deuterium and antiprotons. Other publications are in preparation. A bibliography is included in Appendix B.

Chapter Two: AMS-02, particle physics on the International Space Station

AMS is scheduled to be installed on the Space Station in April 2007 for a period of three to five years. This configuration of AMS, AMS-02, is shown in Figure 2.1. As will be described in the following sections, the construction of the detector is progressing well. Because this is the major scientific experiment on the Space Station, NASA is following the progress of AMS with detailed reviews concerning the design and construction, safety and ground operations to ensure the detector can be launched in April 2007.

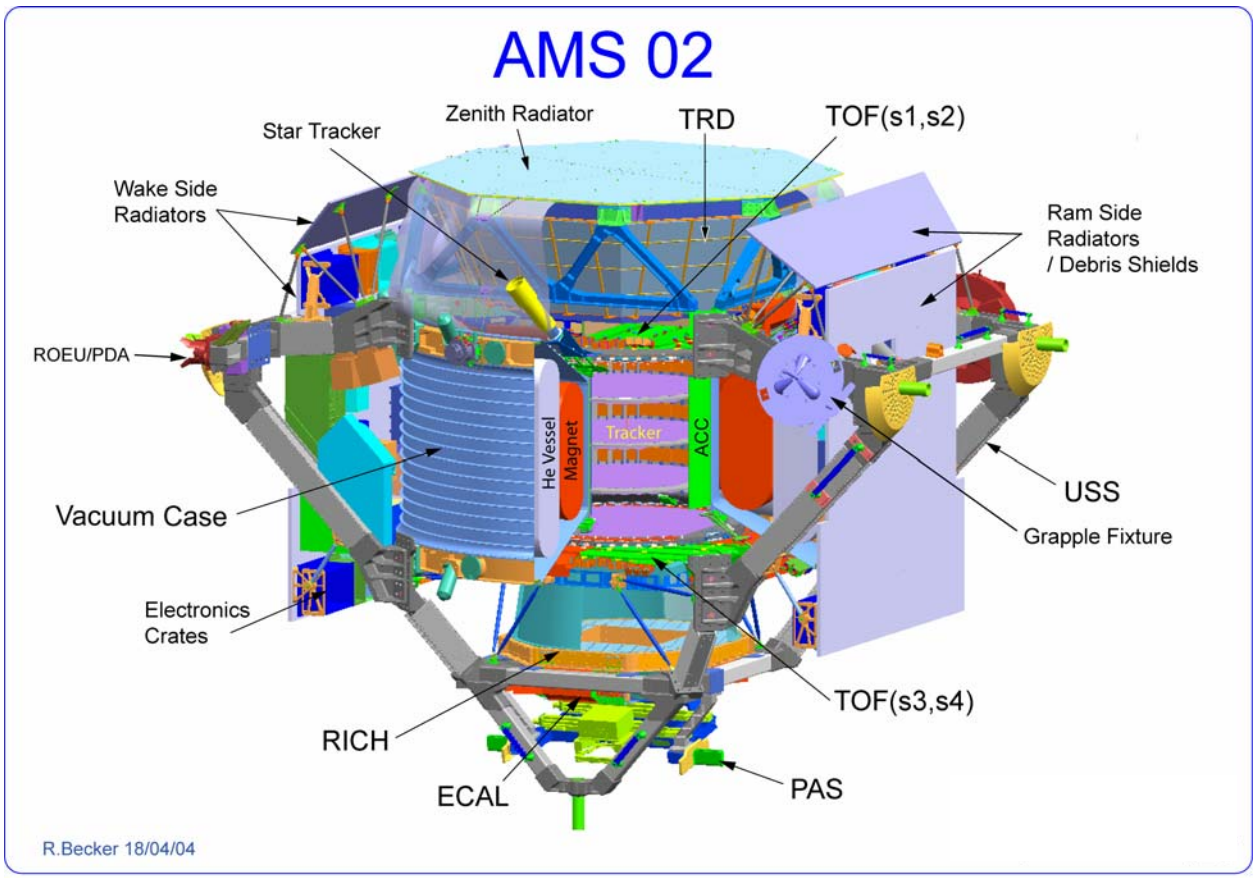

Figure 2.1: The Alpha Magnetic Spectrometer (AMS) as it will appear on the ISS (AMS-02). In addition to the detector elements of Figure 2, this figure shows the structural interface (USS) which connects the detector to the shuttle and to the ISS, the thermal radiators, debris shields, the electronics crate racks and the location of the Cryomagnet Avionics Box (CAB).

2.1 Cryomagnet

The purpose of the superconducting magnet is to extend the energy range of our measurements of particles and nuclei to the multi-TeV region [1,2]. The AMS-02 magnet design is under the overall responsibility of ETH-Zürich and MIT. The magnet design was based on the following technical considerations:

(i) Experience in designing and manufacturing the AMS-01 magnet which was 10 times safer than stress limits allowed.

(ii) The result of many years of intensive R&D collaboration between ETH and the R&D group of Oxford Instruments Ltd. to design a magnet with the following properties :

- Identical field configuration to the AMS-01 magnet to maintain mechanical stability and follow NASA safety standards, as shown in Figure 2.2.
- Minimized heat loss (~100 mW) and minimized quench probability.

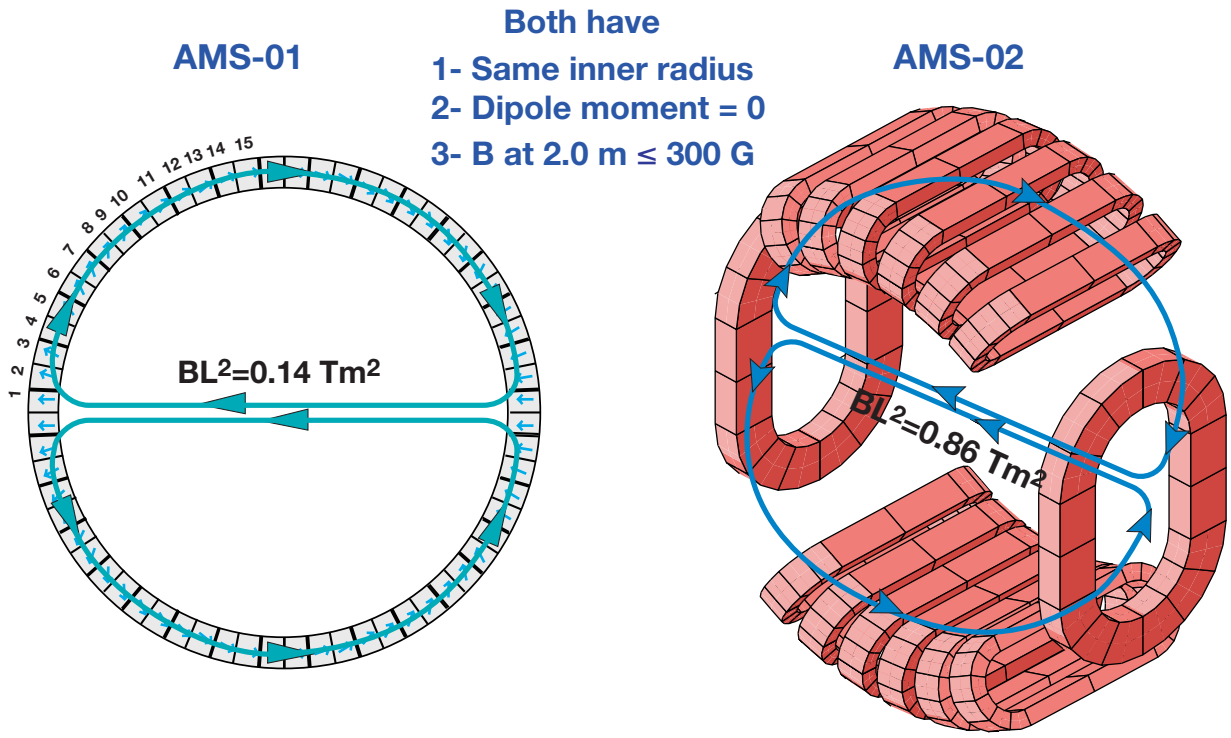

Figure 2.2: Identical magnetic field configuration between AMS-01 and AMS-02 magnets.

(iii) We have chosen to have the magnet built by experts from the Oxford Instruments R&D group, who have an excellent record to produce highly reliable magnets running in persistent mode without quench. This group has produced the 8 OSCAR magnets (2.36 Tesla) used in cyclotrons in Japan and England and which have operated for close to 30 years without any quench. This group also built the CLEO magnet at CORNELL and the CLAS torus at Jefferson Laboratory and the KLOE magnet in Frascati. All are large, high-field, special-purpose magnets which have operated for years without quench.

To ensure that these experts are able to devote all their efforts to the construction of the AMS-02 magnet, we have supported a new company: Space Cryomagnetics Ltd., entirely staffed by the experts of the Oxford Instruments R&D group and entirely dedicated to the AMS-02 magnet.

(iv) Most importantly, we are using a new, small cross-section, aluminium stabilized conductor developed and mass-produced by the ETH-Zurich magnet group [1,2]. Based on test results, this conductor reduces the quench probability by a factor of 2000. ETH has pioneered many of the key technologies for producing Al stabilized conductors [1,2,3]. Aluminium stabilized conductor is now widely used in high energy physics (HEP) detectors [4]. Figure 2.3 shows the non-destructive quality control apparatus developed at ETH. It consists of an ultrasonic phased array which ensures the continuous bonding between the superconductor and the high purity Al (see Figure 2.7). It also includes a laser dimension measuring system and an eddy current check for quality control. The system shown in Figure 2.3 ensures that Al stabilized superconducting cable can be produced uniformly and reliably with lengths up to 2.5 km.

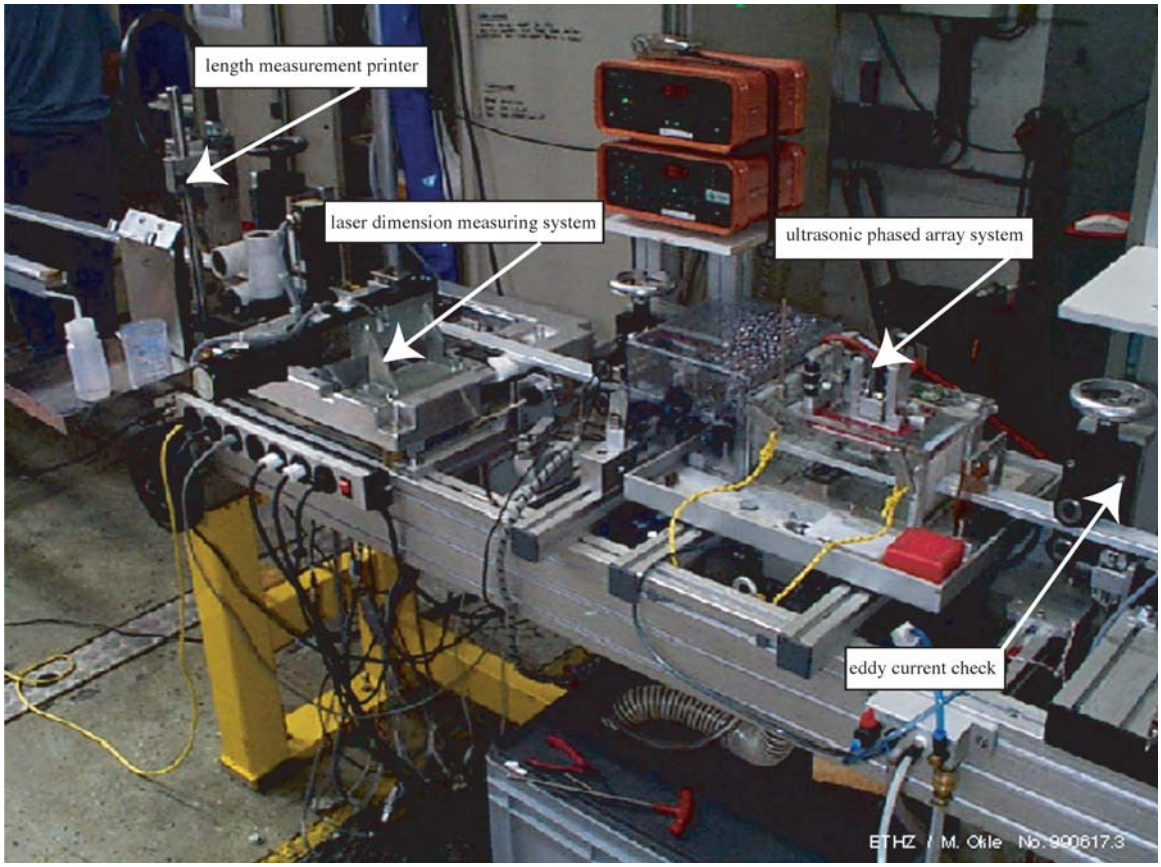

Figure 2.3:Technology developed at ETH for producing high quality Al stabilized superconducting cable.

Two identical magnets are being built. One is the flight magnet and the other is used for space qualification tests. The magnet has no magnetic field during the shuttle launch and landing and so there is no force among the coils, hence for the test magnet the coils are replaced by mass equivalents.

The magnet system [1], as shown in Figures 2.4 and 2.5, consists of superconducting coils, a superfluid helium vessel and a cryogenic system, all enclosed in a vacuum tank. Outside of the vacuum tank are supporting electronics, located in the Cryomagnet Avionics Box (CAB), valves and cabling. The vacuum tank is toroidal with inner diameter of 1.1 m, outer diameter of 2.7 m and a length of the central cylinder surrounding the tracker of 0.9 m.

The magnet operates at a temperature of 1.8 K, cooled by superfluid helium stored in the vessel. It is launched at the operating temperature, with the vessel full of 2500 litres of superfluid helium. The

magnet will be launched with no field, it will be charged only after installation on the ISS. Because of parasitic heat loads, the helium will gradually boil away throughout the lifetime of the experiment. After the project time of 3 to 5 years, the helium will be used up and the magnet will warm up and no longer be operable.

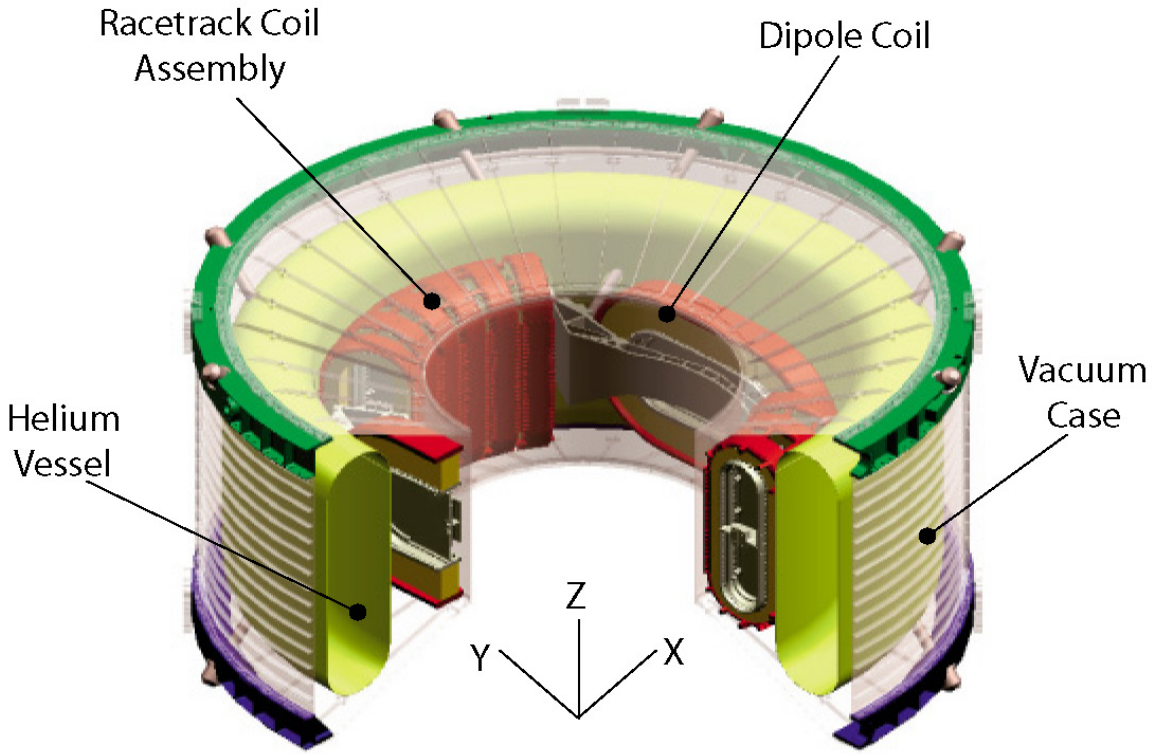

Figure 2.4: AMS-02 superconducting magnet layout.

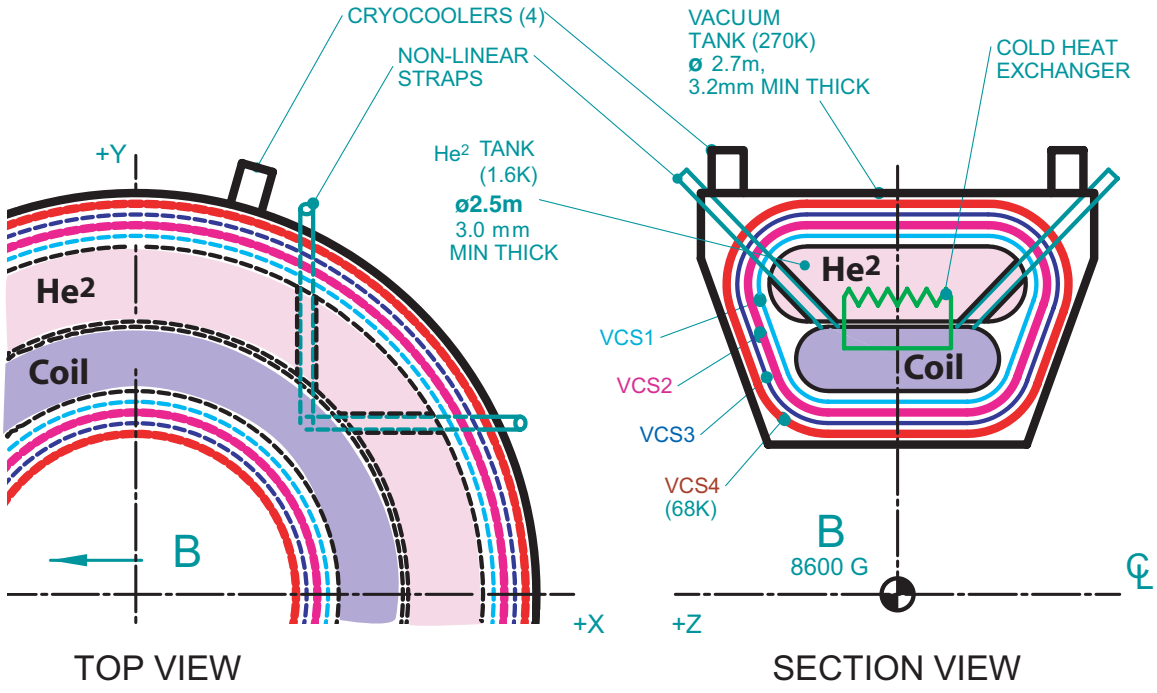

Figure 2.5: Sectional view of the AMS-02 superconducting magnet (VCS – Vapor Cooled Shield)**.**

2.1.1 Magnet Coil System

The coil system consists of a set of 14 superconducting coils arranged, as shown in Figure 2.4, around the inner cylinder of the vacuum tank. The coil set has been designed to give the maximum field in the appropriate direction inside the bore tube, while minimising the stray field outside the magnet.

As seen from Figure 2.6, the single large pair of coils generates the magnetic dipole field perpendicular to the experiment axis. The twelve smaller flux return coils control the stray field and, with this geometry, they also contribute to the useful dipole field. Figure 2.6 also shows the strength and direction of the magnetic field within the set of coils. The magnetic flux density at the geometric centre of the system is 0.86 T. Table 2.1 summarizes some of the magnet parameters.

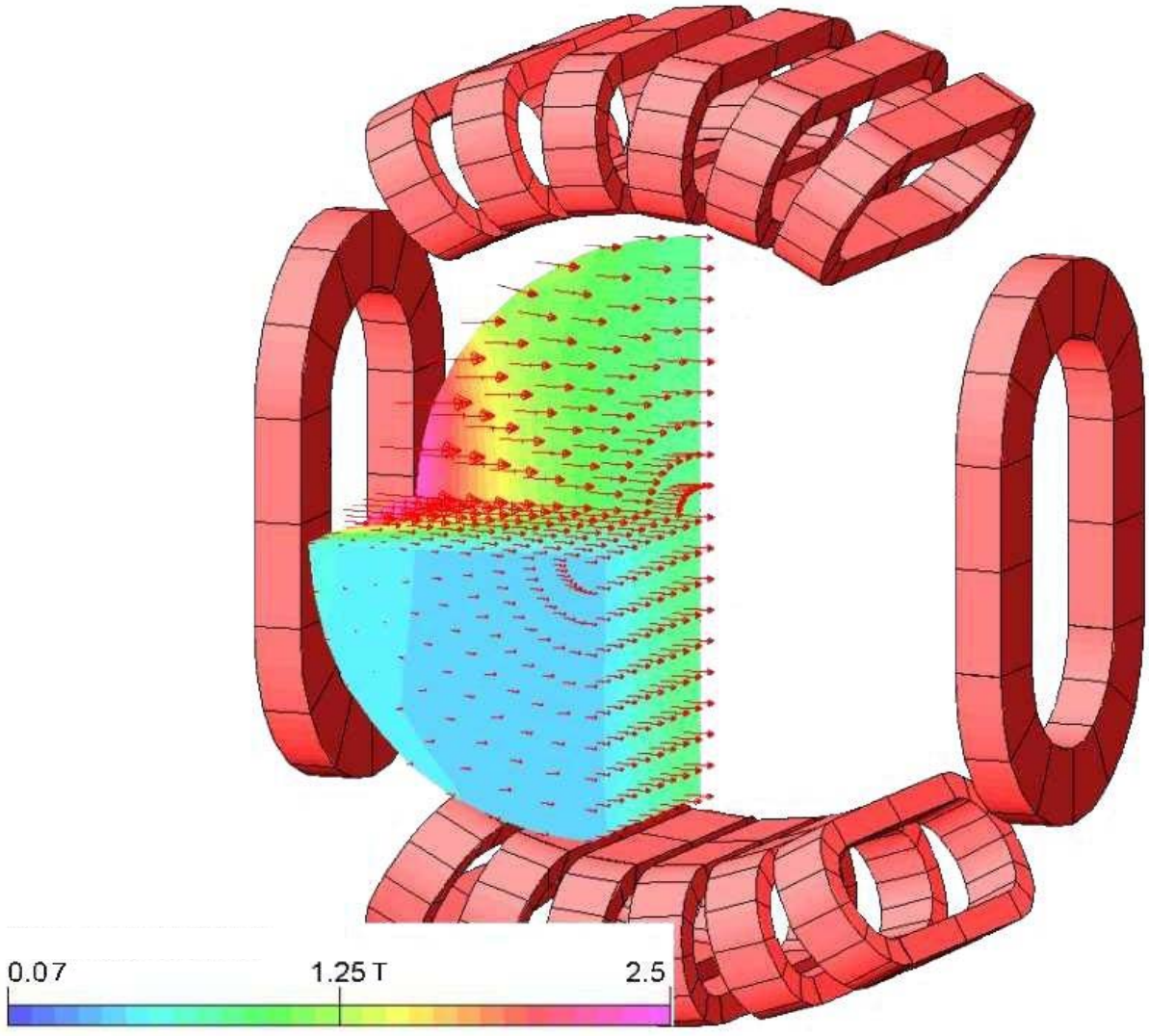

Figure 2.6: Coil arrangement of the AMS-02 superconducting magnet, showing the two large dipole coils and the 12 smaller flux return coils and the field map inside the magnet bore.

Central Magnetic Field B_X (0,0) [T]	0.860
Dipole Bending Power [Tm^2]	0.862
Maximum Stray Magnetic Field at R=2.3 m [mT]	15.2
Maximum Stray Magnetic Field at Y=2.3 m [mT]	7.6
Maximum Stray Magnetic Field at R=3.0 m [mT]	3.9
Peak Magnetic Field on the Dipole Coils [T]	6.59
Peak Magnetic Field on the Racetrack Coils [T]	5.91
Maximum Torque in geomagnetic field [Nm]	0.272
Nominal Operating Magnet Current [A]	459.5
Stored Energy [MJ]	5.15
Nominal Magnet Inductance [H]	48

Table 2.1: AMS-02 Cryomagnet parameters.

The superconducting wire for the AMS magnet was developed specifically to meet the requirements of the AMS cryomagnet by ETH-Zürich [2]. The current is carried by tiny (22.4 μm diameter) filaments of niobium titanium (NbTi) which - given the magnetic flux and current densities within the coils – carries the current without resistance provided the temperature is kept below 4.0 K. Because pure NbTi has rather low thermal conductivity, it is prone to instability. This can be overcome if it is in intimate contact with a material which has a high thermal conductivity at the cryogenic operating temperature, such as a pure metal. For this reason, the NbTi filaments are embedded in a copper matrix, which is encased in high-purity aluminium. The copper is required for manufacturing reasons, but the aluminium is extremely conductive and much less dense, thus providing maximum thermal stability for minimum weight.

Figure 2.7 shows a cross section of the aluminium-stabilized conductors developed by the ETH group and a magnified section through the wire. The diameter of the round copper strand at the centre is 0.76 mm, and the aluminium dimensions are 2.0 mm x 1.5 mm. The current density in the superconductor is 2300 A/mm^2 or 157 A/mm^2 including the aluminium.

To manufacture the coils, the superconducting wire was first cleaned then insulated using 85 μm thick polyester tape. Each coil was wound separately onto an aluminium former from a single length of conductor before being impregnated under vacuum with epoxy resin. The impregnation process gives the coils mechanical integrity, and also provides electrical insulation between turns and layers. After completion, each coil is tested individually under conditions as representative as possible of flight, to test the integrity of the design and the quality of the build, as shown in Figure 2.8.

Each of the two larger (dipole) coils, which generate most of the useful field, has 3360 turns, and the 12 smaller (flux return) coils each have 1457 turns. The 14 coils are connected in series, with a single conductor joint between each pair of adjacent coils. The current when the magnet is operating is 459.5 A.

All of the coils have been manufactured and tested (see Figure 2.9).

If magnet coils are not well designed, heating in a quench can be so rapid that the conductor may actually melt in the region where the quench began. Another problem can occur in systems consisting of a number of coils, where quenching of one coil - and the collapse of its associated magnetic field – can lead to increased current flow and field in other coils coupled by mutual inductance. In some cases this can lead to excessive stresses within the windings and between the coils.

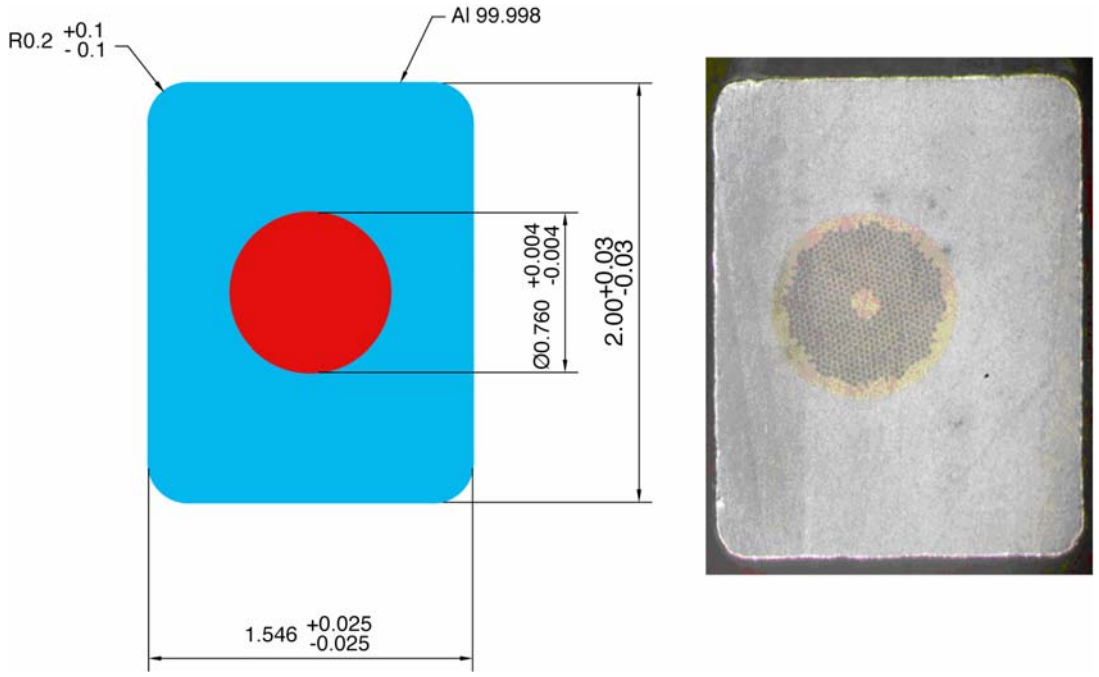

Figure 2.7: Cross sections of the Aluminum stabilized NbTi/copper composite conductor. Dimensions in mm.

Figure 2.8: Testing the coils to flight loads.

Figure 2.9: Arrangement of the completed 2 dipole coils, 12 flux return coils and structural members in roughly the positions they will have in the flight magnet.

The AMS magnet has been specifically designed to avoid these hazards. The aluminium-stabilised conductor is sufficiently conductive that the coils are very stable. If a quench does occur, the heat generated is conducted throughout the coil so quickly that the peak temperatures reached are not hazardous. Because all 14 coils are connected in series they have to carry the same current at all times, so there is no danger of magnetically induced stresses causing damage. However, the coils are not very closely coupled thermally. This means that a quench in one coil, leading to a rise in temperature, will not necessarily propagate to any of the others. If this were allowed to happen, the entire stored energy of the magnet (5 MJ) could be dissipated as heat in the coil which quenched. While the temperatures reached in that coil would not be dangerous, sufficient thermal stresses could be induced (by differential thermal contraction between parts of the coil) that the performance of the coil might be permanently reduced. For this reason, all the coils are constantly monitored by an electronic protection system. If the onset of a quench is detected in any coil, heaters are powered in the other coils to quench all 14 simultaneously. This distributes the stored energy between the coils, preventing any single coil from taking a disproportionate amount of energy which could otherwise result in degradation. The operation of these quench heaters is an important part of the testing and qualification procedure for the magnet coils.

2.1.2 Mechanical System

The mechanical loads on the system are either magnetic or inertial. Magnetic loads apply whenever the magnet is charged, and can be between or within coils. Significant inertial loads are applied during launch, re-entry and landing of the Space Shuttle. But, because the magnet will not be charged during launch or landing, magnetic and inertial loads are never superimposed.

In general, the magnetic loads are much greater than the inertial loads. All magnetic loads are reacted within the structure of the coil set, and none are transmitted to the vacuum tank or other parts of the AMS system. These loads are resisted by components made from high strength aerospace grade aluminium alloy, chiefly 6061-T6.

Each coil is subject to internal forces as a result of its own magnetic field. In general, these are burst forces, trying to expand the racetrack-shaped coil into a ring. These loads are in the plane of the coil, and are resisted by the former on which the coil was wound. In addition, each coil is attracted or repelled by all the other coils in the magnet. This leads to a relatively complicated load system on some of the coils, with forces perpendicular to the plane of the coil.

The magnetic loads are quite large: the two dipole coils feel a net attraction to each other of around 250 tonnes. During individual coil testing, each coil is charged until some part of the winding is subject to the same force it will experience in flight.

The cold mass of the magnet is more than 2000 kg. This has to be supported from the experiment structure (in particular the vacuum tank), which is at ambient temperature (~270±40 K). The design of the support straps is therefore crucial, as they have to be able to carry the load without conducting significant heat across the large temperature gradient.

During normal operation on the ground, inertial loads are relatively small: once on orbit they disappear altogether. At these times, the function of the straps is only to position the magnet correctly within the vacuum tank. During launch and landing, however, inertial loads and vibration become very significant. Now the straps have to resist large forces, and also require high stiffness to prevent low frequency resonance which could lead to mechanical damage.

For high strength and stiffness, the straps need large cross-sections. However, this inevitably leads to high levels of heat conduction, which would reduce the endurance of the superfluid helium system and thus shorten the life of the experiment. For minimum heat conduction, the straps need to be very thin, but this gives poor strength, low stiffness and a low resonant frequency.

The straps have been designed to satisfy all of these requirements. Each consists of a pair of composite bands connected in parallel. One band is thin, with low stiffness and strength, and is permanently connected between the cold mass and the vacuum tank. The other band is much thicker and stronger, but possesses a passive disconnect feature. This means that it only forms a thermal path between the vacuum tank and the magnet during launch and landing. At other times (when it is not needed), differential thermal contraction between the bands and the removal of the high inertial load cause the disconnect to open, dramatically reducing the thermal conduction of the support.

A total of 16 straps support the magnet from the vacuum tank (see Figure 2.10). During normal operations on the ground or in space, only the low-stiffness band is engaged, and the heat conduction is very low (less than 3 mW per support). During launch, the high-stiffness band engages as well. The conducted heat load is much higher but because the launch takes only a few minutes the effect on the overall endurance of the system is not significant.

The dual stiffness characteristic of the straps makes their behaviour non-linear and, as major structural components of the magnet system, they have been subject to special scrutiny and testing, particularly testing to failure to understand the safety margins (see Figure 2.11).

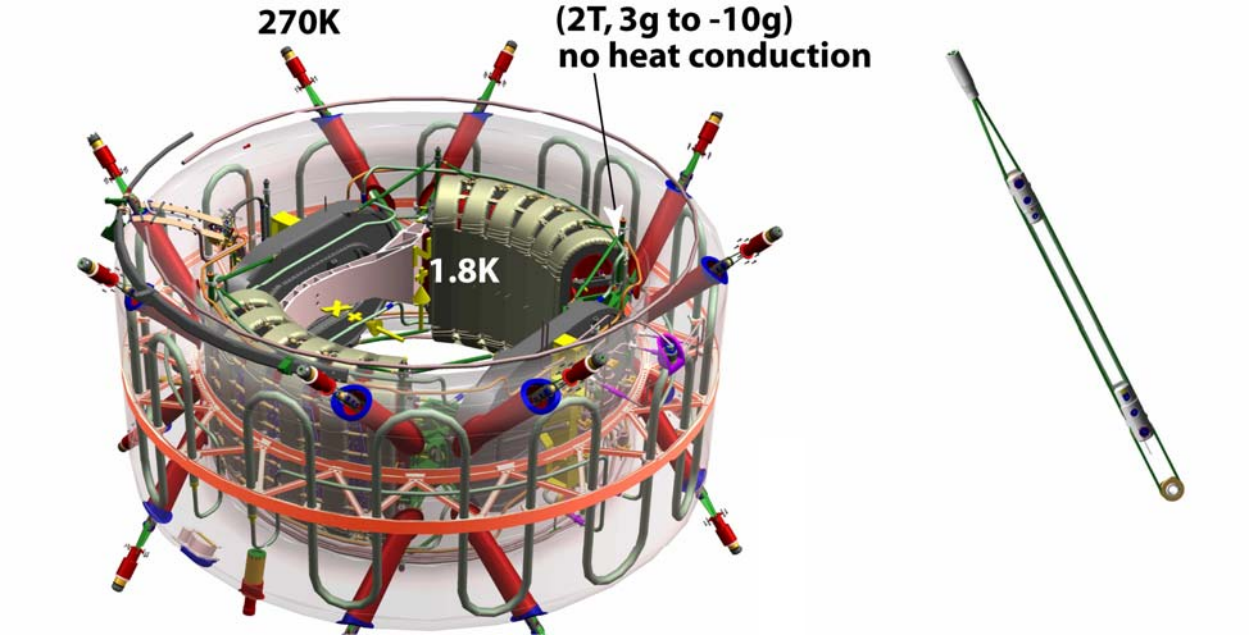

Figure 2.10: The Magnet support straps. The cold mass at 1.8 K has to be supported to the vacuum case which is at approximately 270 K. This is achieved by 16 straps, which hold the 2 ton cold mass in position during launch (acceleration 3g) and landing (deceleration 10g). In space, the straps are designed to be nearly disconnected so as to not transfer heat from the vacuum case to the cold mass.

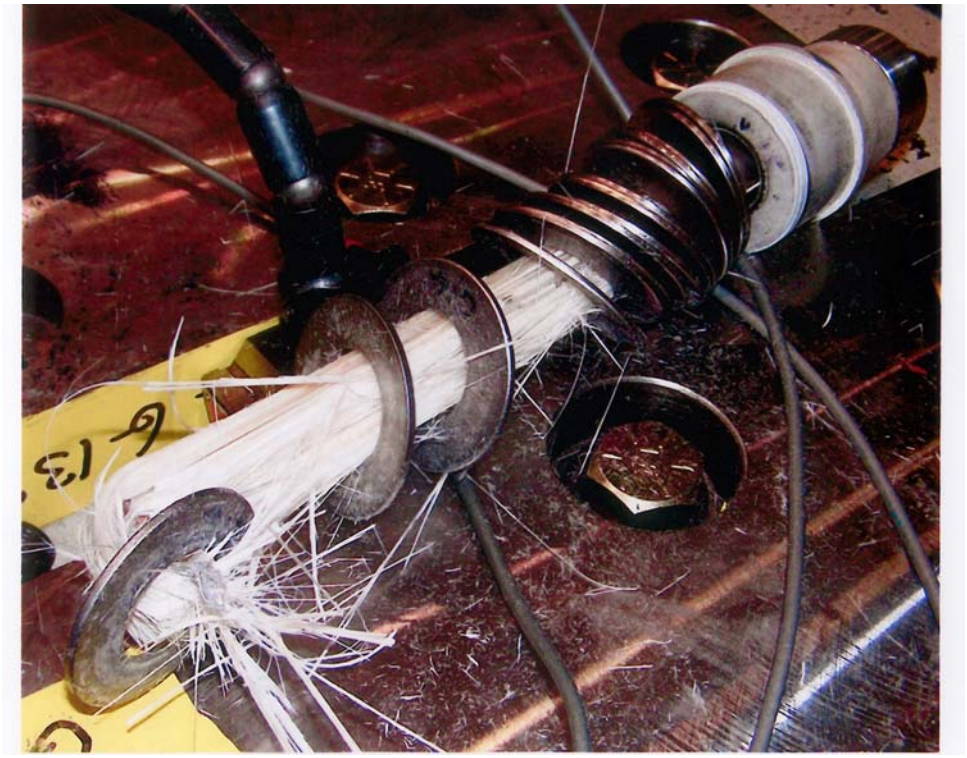

Figure 2.11: .Testing of strap to failure to understand the critical failure mode. Assembly failure caused by failure of the glass fiber "bod", other damage observed caused by impact loading as strap failed, not by static loading.

2.1.3 Cryogenic System

The cooling of terrestrial superconducting magnets using liquid helium is a well-established technology, but there is little experience of helium cryogenics in space. Apart from a few very small-scale experiments, the only major missions involving liquid helium have been the Infrared Astronomical Satellite (IRAS) [5], the Cosmic Background Explorer (COBE) [6], the Infrared Space Observatory (ISO) [7] and the Superfluid Helium On-Orbit Transfer demonstration (SHOOT) [8].

The cryogenic system for the AMS magnet combines technologies from terrestrial magnet cryogenics and space cryogenics to meet the particular challenges of the Space Shuttle launch and the environment of the ISS [9]. It maintains the magnet at a temperature of 1.8 K, under all operating conditions, for the duration of the experiment. It therefore has to be able to store enough helium to last the entire mission, to transfer any heat from the cold components to the helium, to allow the magnet to be charged and discharged safely from the external power supply, and to re-cool the magnet after a quench. On the ground, it also has to control the cool down of the magnet from ambient temperature.

Figure 2.12 shows all the elements of the AMS-02 cryogenics system, including the passive phase separator (PPS), which removes the gaseous He which is then used to cool the 4 vapour cooled shields, the two thermo-mechanical pumps (TMP), one to cool down the magnet in the unlikely event of a quench and the other to cool down the current leads during magnet charging and discharging, the helium gas pressure activated cold valves which operate at 1.8 K, the warm valves outside the vacuum tank which operate at ambient temperature but with cold He gas flowing through them and the burst disks (0.8, 3, 10 and 20 bar) for safety. The valves are implemented redundantly in parallel (for example DV06A, B), or series (DV16A, B) or both (DV15A, B, C, D).

i) Helium Management and Endurance

Liquid helium (^{4}He) can exist in two forms. Normal liquid helium behaves in a conventional manner. But if it is cooled below 2.17 K, some of its properties change dramatically as it becomes a superfluid. In particular, its viscosity falls almost to zero, and its apparent thermal conductivity increases by many orders of magnitude.

The AMS magnet is cooled by superfluid helium. There are two main reasons for this. Firstly, the specific latent heat and density of superfluid helium are both higher than in normal liquid helium. Since the amount of cryogen that can be carried is limited by the size of the helium vessel, this gives a useful endurance benefit (there is a greater mass of helium, and each kilogram has a higher cooling capability). Secondly, in zero gravity there can be no convection currents. In normal liquid helium this can result in thermal stratification, making it difficult to ensure that all parts of the system are fully cold. In the superfluid state, however, the very high thermal conductivity makes it impossible for the helium to support large temperature gradients, so the system remains isothermal.

Superfluid helium is obtained by reducing the pressure above a vessel of normal liquid helium. The boiling point of helium at atmospheric pressure is 4.2 K, and this can be reduced to 1.8 K if the absolute pressure is reduced to 16 mbar. On the ground, this pressure reduction is achieved using large vacuum pumps to remove helium vapour. Once on orbit, the vacuum of space itself is used as a pump, and the low temperature can be achieved simply by venting the helium vessel to space.

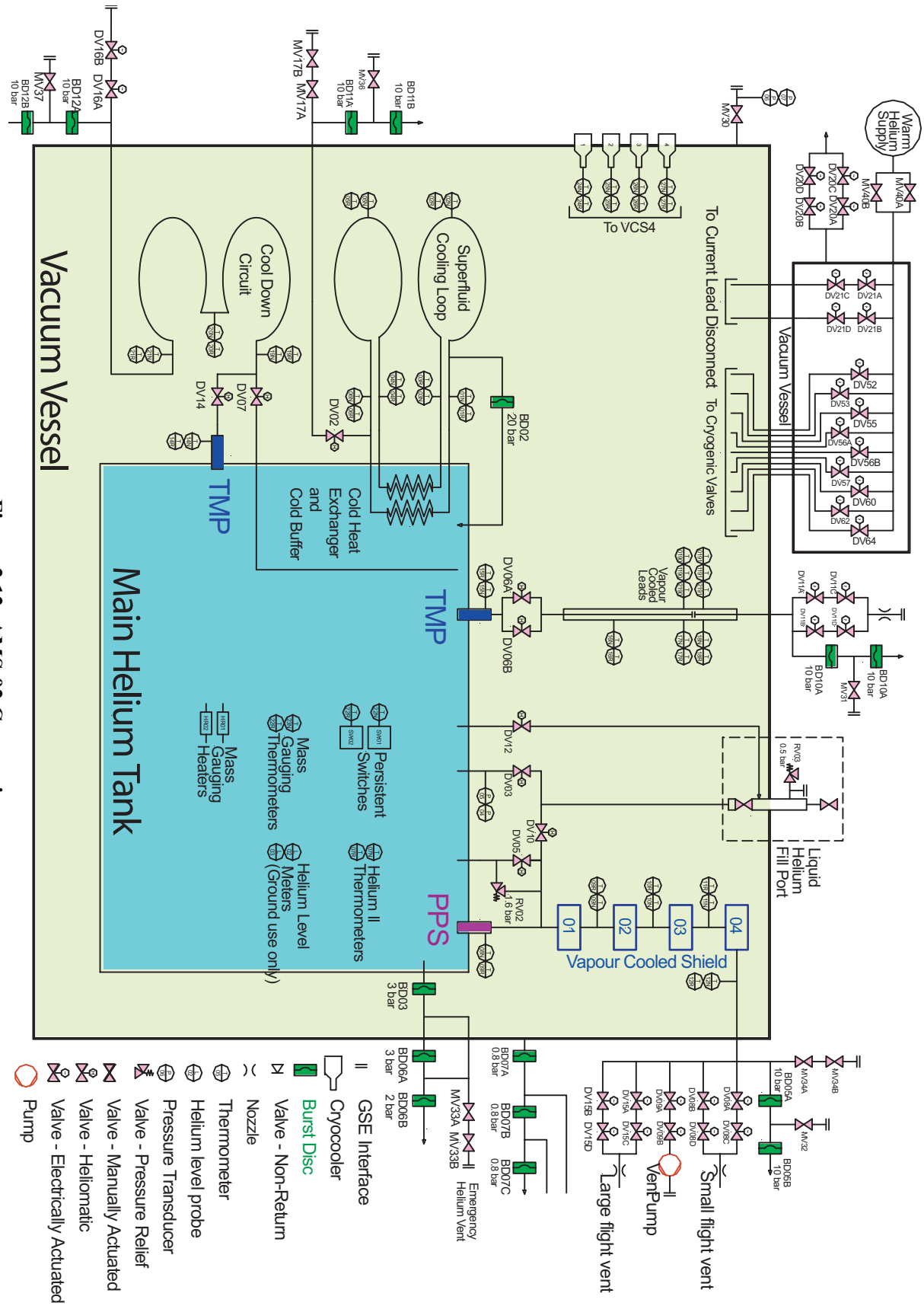

Figure 2.12: AMS-02 Cryogenics

ii) Helium Vessel

The helium vessel is a toroidal tank, with inner and outer diameters of 1.92 m and 2.58 m, length 1.18 m and volume 2500 litres. It is a fully welded construction of aluminium alloy 5083-H321. For maximum strength and minimum weight, both cylinders are ribbed and they are joined together by cross-bracing at the mid-plane.

The sixteen support straps have to pass through the volume occupied by the helium vessel as they support the coils from the outer cylinder of the enclosing vacuum tank. Because a high heat load would result if the straps came into contact with the helium itself, the vessel is equipped with 16 tubes which pass completely through it. These allow the straps to pass through the vessel while remaining in vacuum.

Figure 2.13 shows the construction of the vacuum tank and Figure 2.14 shows the welding of the He tank.

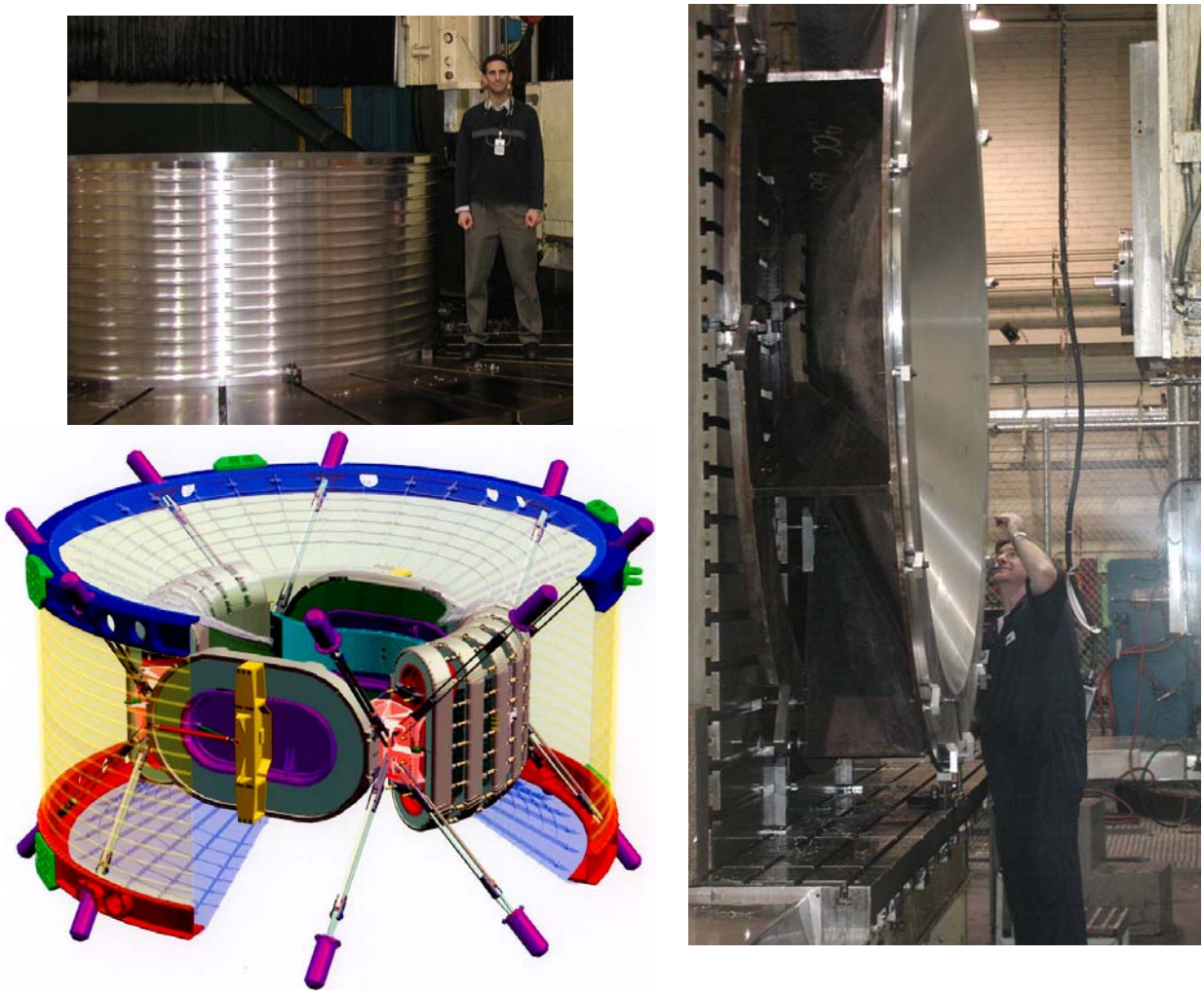

Figure 2.13: Construction of the vacuum tank, also showing the location of the support straps.

Figure 2.14: Welding of the He tank.

iii) Phase Separation

The heat which leaks into the system is transferred to the helium in the 2500 litre vessel, which is the ultimate low temperature heat sink for the system where the heat is dissipated by boiling the superfluid helium. For efficient use of the helium, the gas which is generated has to be separated from the liquid and used to remove heat from other parts of the system. On the ground, phase separation can be achieved simply by placing the vapour vent at the highest point in the vessel: gravity will then ensure that the liquid remains at the bottom and the vapour is released from the top. In space this approach clearly will not work, so the system uses a special zero-gravity passive phase separator (PPS) [10] developed by Linde in Germany. The phase separator is similar in construction to that used on ISO, consisting of a porous plug of sintered stainless steel in a steel housing. In flight, a slight (~30 mK) temperature difference is maintained between the two faces of the plug. The separator takes advantage of the thermo-mechanical effect [11] that superfluid He liquid moves from cold regions to hot regions, thus the He gas can be removed and the superfluid He liquid retained, see Figure 2.15. The phase separator for AMS has been tested (see Figure 2.16) and is ready for welding into the helium vessel.

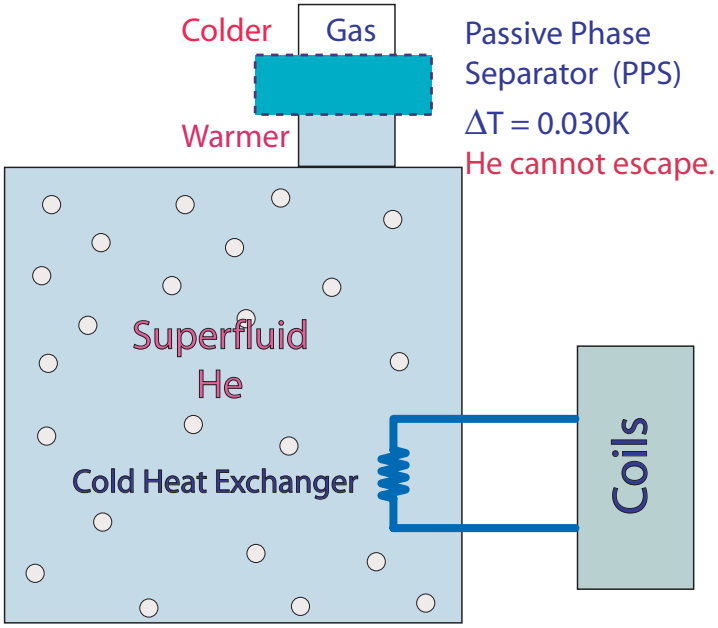

Figure 2.15: Schematic of the principal of phase separation as used in AMS-02.

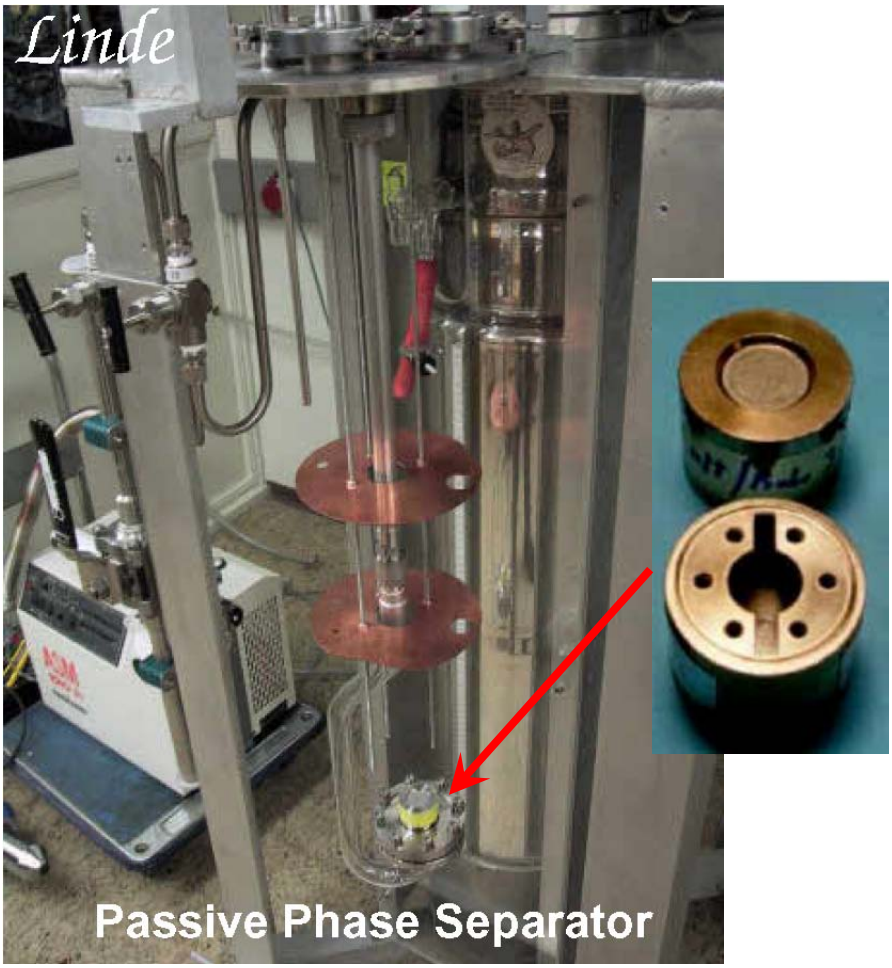

Figure 2.16: Passive phase separator under test at Linde, Germany.

iv) Vapour Cooled Shields (VCS)

A series of four concentric shields completely encloses the magnet and helium vessel (see Figure 2.5). By cooling these shields with the vapour from the helium vessel (separated by the phase separator, PP), the heat leak into the coldest parts of the system is dramatically reduced, and thus the lifetime of the experiment increased. The vapour flows through pipes connected to the shields, removing radiated heat as well as intercepting conducted heat from the support straps and other components.

The design of the shields is particularly challenging, as there is very little space available for them. To maximise the useful field in the bore of the magnet system, the coils have to be large, and also as close as possible to the inner surface of the vacuum tank. Likewise, the helium vessel has to be large to be able to carry the maximum volume of superfluid helium.

Two of the shields are rigid, consisting of variable-thickness aluminium honeycomb with fibreglass skins. These are designed for minimum thickness while retaining sufficient strength to withstand launch and landing loads. The other two shields are flexible, made from thin sheets of soft aluminium. Figure 2.17 shows one of the completed (honeycomb) shields.

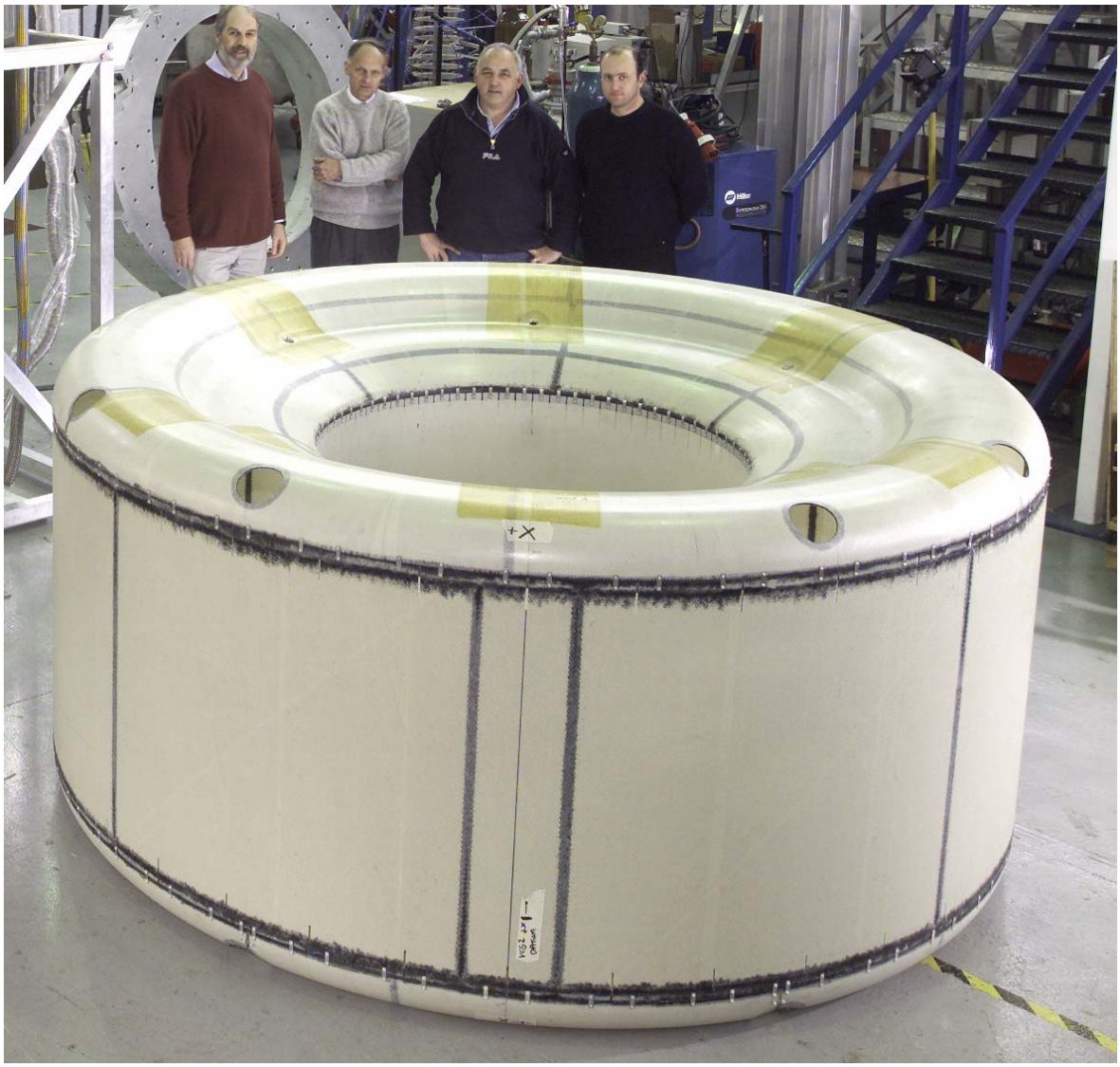

Figure 2.17: One of the four vapour cooled shields ready for installation.

v) Cryocoolers

Cryocooler technology has made great progress in recent years but, for fundamental thermodynamic reasons, coolers capable of reaching temperatures approaching 1.8 K require extremely large amounts of power at ambient temperature to be able to provide significant cooling. This power is not available on the ISS, so it is not feasible to provide mechanical cooling to the magnet itself. However, the heat load to the 1.8 K parts of the system can be reduced significantly if heat is removed at a higher temperature.

For this reason, four Stirling cycle coolers are connected to the outer vapour cooled shield. The coolers are qualified and tested (see Figure 2.18) by a team at NASA Goddard Space Flight Center, and are expected to remove a total of about 12 W at 68 K. This should be sufficient to reduce the rate of consumption of superfluid helium by a factor of four. A high (~92%) efficiency power supply to drive, control and monitor the coolers has been developed by ETH-Zürich, MIT and RWTH-Aachen. One of the initial concerns over the cryocoolers was whether their performance might be compromised by the presence of the magnetic field. However, testing carried out by NASA at MIT [12] has demonstrated that the cryocoolers can be operated without problems or degradation in the stray field generated by the magnet in the locations where they are installed.

Each cooler consumes 100 W, which, along with the heat removed from the cryogenic system, is conducted using a dual redundant capillary pumped loop to a quarter panel zenith facing radiator on the top of the experiment (see § 2.9).

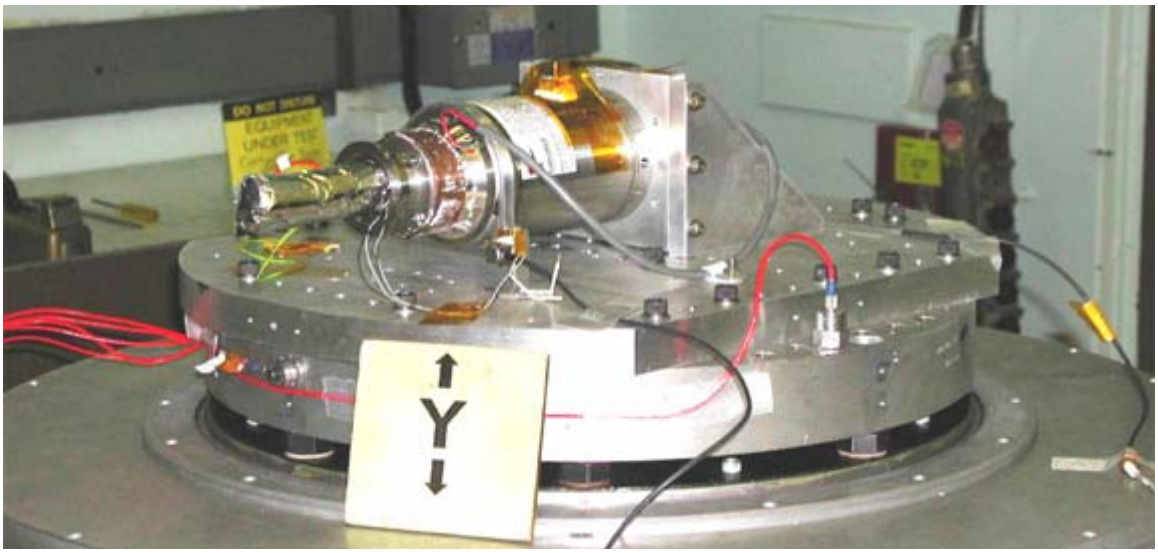

Figure 2.18: Vibration test of Cryocooler at NASA-GSFC.

vi) Mass Gauging

In zero gravity there is no clearly defined liquid level, so conventional helium level probes cannot be used. Instead, a calorimetric method is used to determine the mass of helium in the tank. Detailed analysis of this technique has been published [13] but the principle is simple. A small heat pulse is applied to the helium while the temperature is monitored some distance away in the vessel by an accurate thermometer. Because of the high thermal conductivity of the superfluid, the helium in the vessel is isothermal. The heat pulse is therefore manifest not by local boiling of helium but by a small rise in the temperature of the entire helium bath, measured by the thermometer. Knowing the energy dissipated by the heater and the temperature rise in the bath, the mass of helium can be deduced.

The mass gauging system for AMS is similar to the one used on ISO [7] and has been developed by Linde, Germany. The performance depends critically on the accuracy of the temperature measurement, and is therefore limited by the electronics. Two redundant mass gauges will be used on AMS. Both have been tested and qualified.

vii) Coil Cooling System

The most obvious feature about the cooling system is that the coils are dry; they are not mounted inside the helium vessel, see Figure 2.19. There are two reasons for this. Firstly, if the coils were inside the helium space, the geometry of the vessel itself would become very complicated, and this would add considerable mass. Secondly, and more importantly, it must be possible to recover from a magnet quench in space (however unlikely this may be) by re-cooling the magnet using the onboard helium. If a magnet immersed in helium quenches, the heat transfer is so rapid that the helium quickly pressurises and is lost through the vessel pressure relief devices.

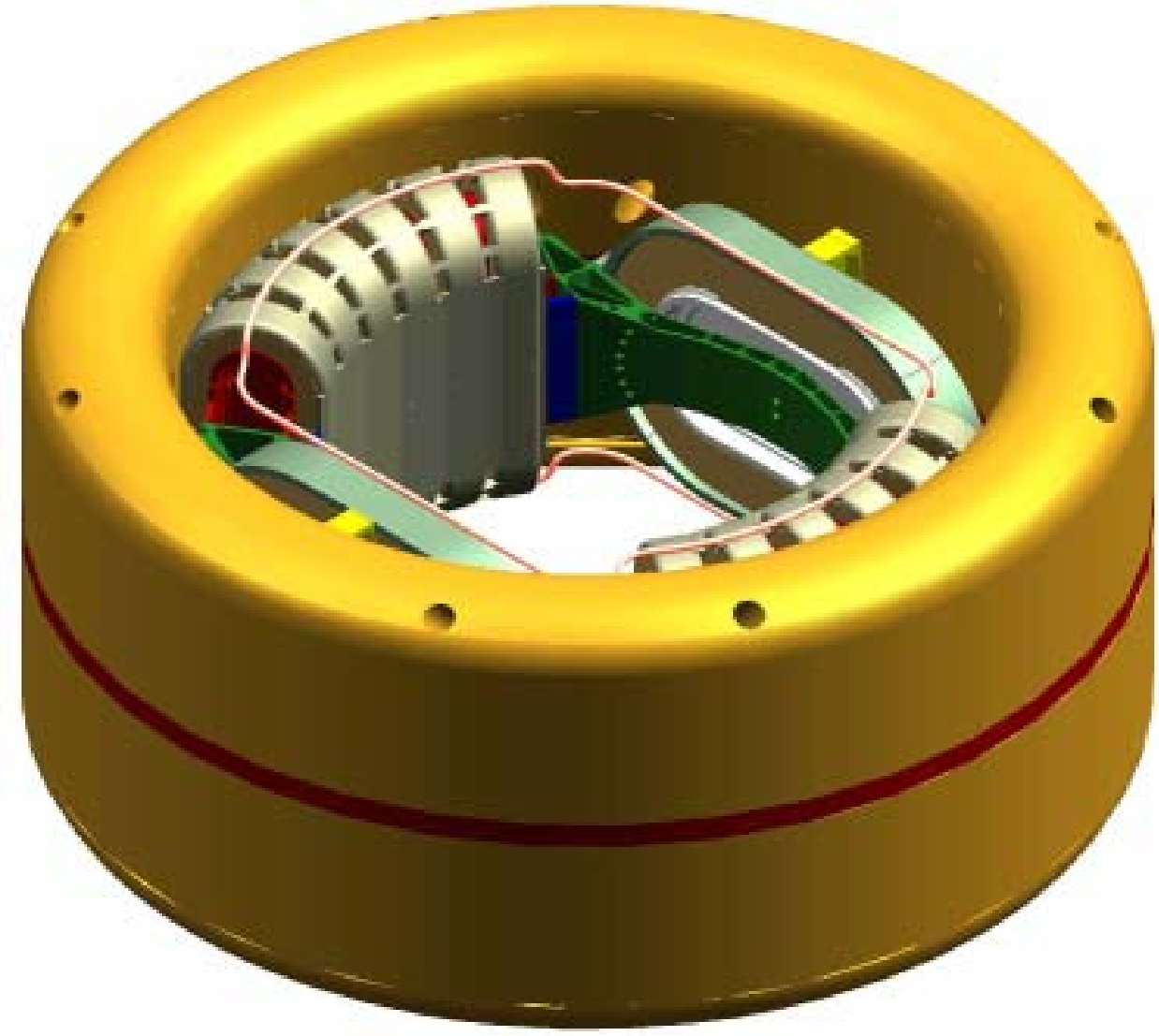

Figure 2.19: Arrangement of the coils surrounded by the He tank.

If the coils cannot be physically inside the helium vessel, they must be cooled instead by conduction to the superfluid helium. The ideal conductor would have very high thermal conductivity at very low temperatures (to remove steady state and charging heat loads from the coils) but much lower conductivity at higher temperatures (to avoid transferring heat too quickly to the superfluid following a quench). Fortunately, helium itself fulfils both these requirements, having extremely high thermal conductivity below 2.17 K but relatively low conductivity above this temperature.

The coil cooling scheme, based on this principle, is shown schematically in Figure 2.20. Each coil is connected at two positions to a thermal bus bar which consists of a copper pipe filled with superfluid helium. This helium is at a pressure of around 1 bar, so that it is supercooled and boiling is suppressed. Part of the thermal bus bar is inside the main superfluid helium vessel and so acts as a heat exchanger (see Figure 2.12). Heat radiated to (or generated in) the coils is transferred by Gorter-Mellink conduction (the heat transfer mechanism in superfluid helium) through the superfluid helium in the thermal bus bar and is dissipated by boiling the helium in the vessel.

The copper pipe forms a sealed circuit, filled with helium while the magnet is being cooled down, but there is no net flow through it. Analysis of the flow of heat around the thermal bus bar requires the solution of the non-linear differential equations describing Gorter-Mellink conduction. The methodology used in this case was based on that developed by Mord and Snyder [14] and adapted for the AMS geometry.

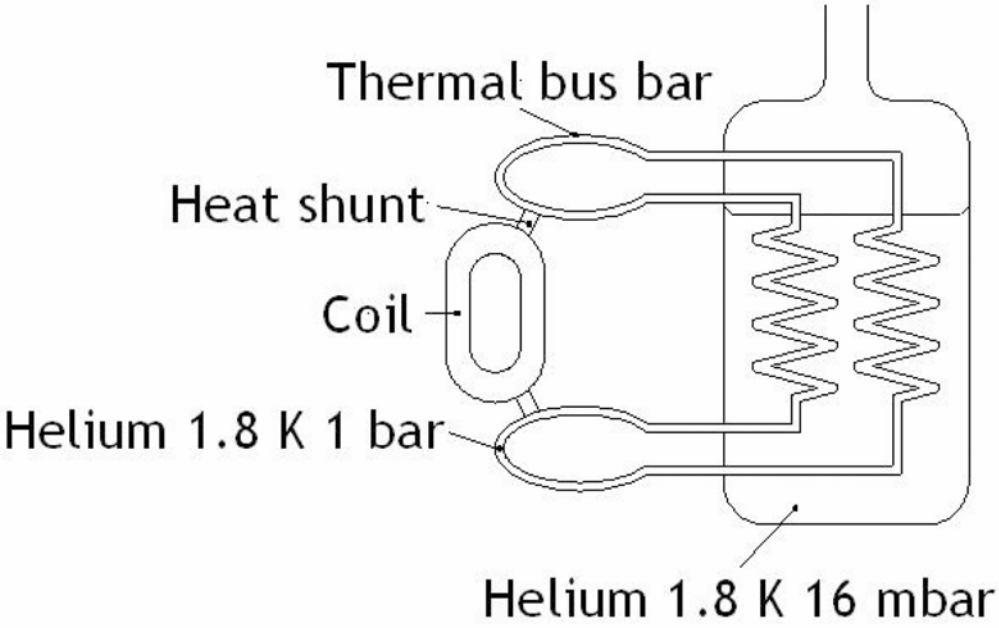

Figure 2.20: Principal of AMS-02 coil cooling system.

viii) Current Supply

The magnet can be operated at currents up to 459.5 A. It is equipped with persistent switches which, when closed, form a superconducting link across the terminals of the magnet. This allows it to continue to operate, once charged, in persistent mode without connection to the external power supply. The leads, which supply current from the power supply to the magnet, are therefore only used for charging or discharging: since the magnet will mostly be operated at a constant field, the leads will be used only rarely.

For this reason, the leads are designed for minimum heat leak when they are carrying no current. This makes them less efficient during charging but, because their overall duty cycle is very small, results in total in much reduced helium consumption. To achieve this, the cross section of the leads is relatively small. When the magnet field is constant and the leads carry no current, the conducted heat load is therefore minimised. During charging, the leads generate a substantial amount of Ohmic heating because their resistance is rather high. This heat can only be removed by helium from the superfluid helium vessel. However, the vessel itself operates at a pressure of just 16 mbar, which is not high enough to ensure a sufficient flow of helium.

A thermo-mechanical pump (TMP) is therefore mounted in the superfluid helium vessel. The TMP is used to pump helium from the vessel through the current leads to provide cooling when required (see Figure 2.12). The TMP operates like the PPS in reverse. A small heater is used to induce a slight temperature difference across the TMP, but with the warmer side towards the current leads and the cooler side towards the He vessel, causing sufficient He to be pumped out to cool the leads. TMP technology in space was first demonstrated by NASA in the SHOOT demonstration but the TMP for AMS differs in details of its operation, and is developed by the Institut für Luft und Kältetechnik (ILK), Dresden, Germany [15].

A further reduction in the heat conducted by the current leads when the magnetic field is constant (no current through the leads) is given by a disconnect feature near the warm end of the leads. This device provides a complete thermal and electrical break in the leads when the persistent switch is closed (see Figure 2.21).

ix) Cryogenic Ground Support Equipment

To cool the magnet and fill the He tank a substantial amount of cryogenic ground support equipment (CGSE) is being provided by Shanghai Jiao Tung University (SJTU), ETH, MIT and the Kurchatov Institute. The 2 ton cold mass has to be cooled from 300 K to 1.8 K while maintaining a temperature gradient of less than 50 K and the 2500 liter tank must be filled with superfluid He at a pressure of 16 mbar. In addition, to support the installation and testing of AMS-02 in various locales (see § 2.10 and 2.11) the system must be portable. To maintain the reliability of the system, the system must be very clean and the He filtered to 0.5 μm (nominal grade).

The CGSE scheme is depicted in Figure 2.21. Cooling proceeds in three phases: from 300 K to 90 K using liquid nitrogen externally to cool gaseous He which circulates through the internal system, from 90 K to 4.2 K using gaseous and liquid He and from 4.2 K to the working point of 1.8 K by pumping. From room temperature to the operational condition the three phases together are estimated to take less than three weeks and require 2.4 tons of N_2 and 1 ton of He. Subsequently the He tank can be topped off, for example while AMS is installed in the space shuttle on the launch pad, using just the equipment indicated. All equipment is manufactured under strict quality and cleanliness controls.

x) Cryogenic Safety

Any large cryogenic vessel has to be viewed as a potential safety hazard, particularly when it is in an enclosed space such as the payload bay of the Space Shuttle. Safety of the AMS magnet has to be assured in ground handling operations, during launch, on orbit and during landing. All cryogenic volumes, as well as the vacuum tank, are protected by burst discs to prevent excessive pressures building up in any fault conditions. Some of the burst discs have to operate at temperatures below 2 K, and these have been the subject of a special development and testing programme.

In addition, extra protection is provided to mitigate the effect of a catastrophic loss of vacuum. This could be caused, during ground handling operations, by a serious rupture of the vacuum case. If the vacuum case had a large puncture, air could rush through the gap and condense on the surface of the helium vessel. This would result in rapid pressurisation and venting of the helium in the vessel. To slow

down the rates of pressurisation and venting (making the pressure relief path smaller and more manageable) a 3 mm layer of lightweight cryogenic insulation will be applied to the outside surface of the helium vessel. Carefully constructed experiments have shown that this insulation reduces the heat flux to the superfluid helium by a factor of 8 following a sudden, total loss of vacuum.

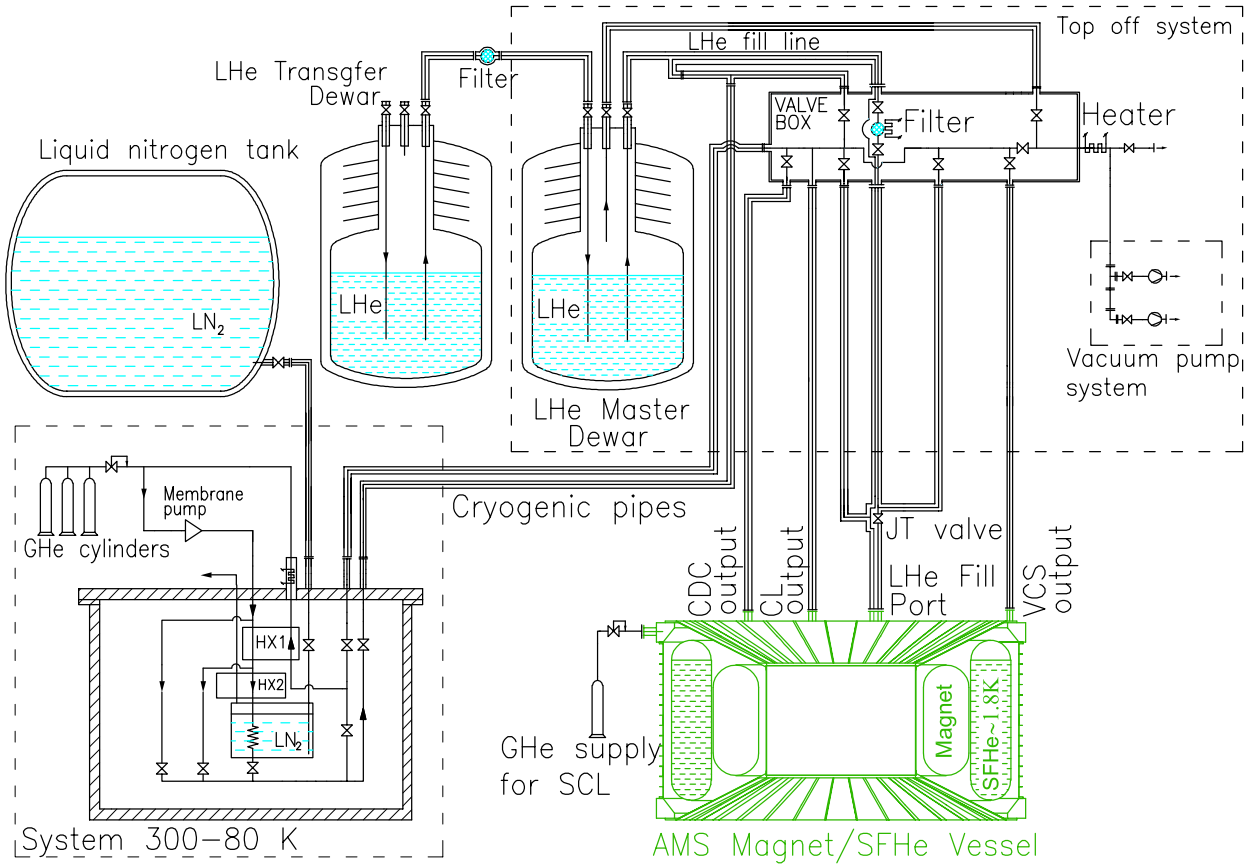

Figure 2.21: Cryogenic Ground Support Equipment schematic. The equipment in the upper right is also used to top off the He tank and is designed to be compact and portable.

2.1.4 Cryomagnet Avionics

The electronics to power, monitor and control the magnet is housed primarily inside the Cryomagnet Avionics Box (CAB) under the responsibility of CIEMAT and MIT. As illustrated in Figure 2.22, this avionics includes:

a) the Cryomagnet Current Source (CCS) and precision shunt, used to charge the magnet,

b) the dump diode arrays mounted on the port and starboard USS (CDDP and CDDS), which dissipate the energy stored in the magnet when it is ramping down,

c) the Cryomagnet Self Protection (CSP), used to detect and protect the magnet in case of a quench or the loss of power or communications,

d) the dual redundant uninterruptible power supplies (UPS), which power the self protection functions,

e) the Cryomagnet Controller and Signal Conditioner (CCSC), which gather the monitoring data from the rest of the avionics data and forwards it to the JMDC (see § 2.8) and receives and executes commands from the JMDC,

f) the Power Switches module, which activates valves and heaters as directed by the CCSC, and

g) the Cryocooler electronics box (CCEB), (see § 2.1.3.v).

Figure 2.22 also shows the major electrical features of the magnet which include the superconducting coils with a load of zero ohms and an inductance of 48 henries (see § 2.1.1), the persistent switch and mechanical disconnecting current leads (§ 2.1.3.viii), the quench heaters (§ 2.1.1), warm and cryogenic valves and associated temperature, pressure and voltage sensors (§ 2.1.3). Additional sensors are located within the CAB itself.

Operationally, the magnet will be launched cold but at zero field and charged only after installation on the ISS. Charged or not, the CCSC will continuously monitor the magnet state and relay these readings through the AMS CAN bus housekeeping network to the JMDC. Altogether about 150 values are monitored including 23 prime and 23 redundant cryogenic temperature measurements based on CERNOX sensors, which cover ranges from 1.4 to 400 K with accuracies down to 1 mK. These exacting measurements allow the proper functioning of the cryogenics and magnet to be accurately controlled. The information will then flow to ACOP, the AMS computer inside the ISS, and through the NASA air to ground links to the POCC, the AMS ground operations center. Commands follow the reverse path to reach the CCSC, which then initiates the appropriate action within the CAB and the magnet.

The magnet is charged by the CCS. After various checks to ensure, for example, that the magnet coils are superconducting, the complete charging operation consists of five phases: preparation, output voltage limited charging, power limited charging, current limited charging and disconnection. To prepare the magnet for charging, the current leads are cooled by He vapor generated by the differentially heating the associated TMP, the superconducting persistent switch is "opened" by heating it into the normal state and the current leads are mechanically connected. The CCS then draws power directly from the ISS 120 VDC “A” feed and it is converted to a maximum of 10 VDC using six DC-DC converters in parallel. The resulting current flows through the precision shunt to the current leads and serially through all the magnet coils and back. In the third phase the power drawn from the ISS is limited to 1875 W and the current in the coils continues to increase while the output voltage drops. Then the target coil current of 459.5 A, as monitored by the precision shunt is smoothly approached. After the target current is reached the persistent switch is allowed to cool and it again becomes superconducting and the current is trapped within the closed circuit of the magnet coils plus switch. Then the current leads are disconnected and no longer need to be cooled by the TMP and the CCS is shutdown. In total the charging process is estimated to take less then 2 hours.

Ramping down the magnet current is less complicated. The CCS remains powered off and disconnected, the current leads are cooled and connected and the persistent switch is again driven open. The current in the magnet coils then flows through the dump diodes (CDD-P,-S) which are mounted directly on the Unique Support Structure (USS) and the stored magnetic energy is converted into heat dissipated by these diodes. To dissipate the 5 MJ stored in the magnet is estimated to take less than 1.5 hours.

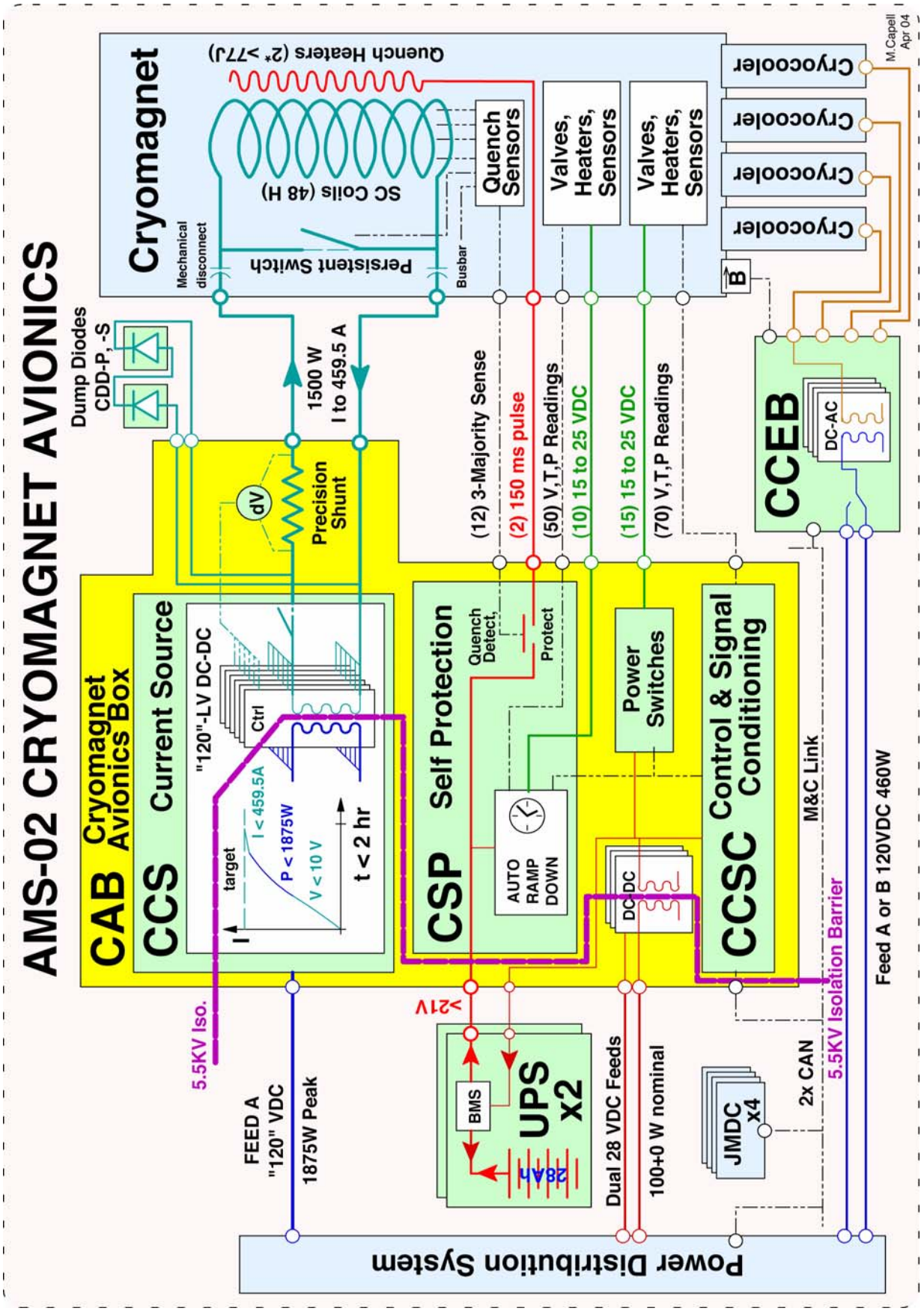

Figure 2.22: AMS-02 Cryomagnet Avionics

The CSP has two overlapping functions: to detect and protect the magnet should a quench occur and to automatically ramp down the magnet after a fixed delay should either power or communication to the experiment be interrupted. As noted in § 2.1.1, an uncontrolled quench, though unlikely, could damage the magnet. If the onset of a quench is detected, as indicated by a voltage drop anywhere over the coils or persistent switch, a fast pulse of energy is required to fire the quench heaters wound within each coil and dissipate the stored magnetic energy evenly over the cold mass. As the power level required is never available from the ISS, this energy is drained directly from the UPS to the quench heaters. If, during a charge or discharge operation, the current leads start to overheat, they can also be damaged quite rapidly, so current lead temperature sensors are also tied into the quench heater trigger.

It should be stressed that, owing to the advanced properties of the AMS superconductor and the cryogenics design, none of these conditions, including a spontaneous magnet quench, is anticipated to occur on orbit. However, should it ever happen, this design ensures that the magnet will not be damaged and that, after re-cooling, it can be recharged and the mission can proceed successfully. In any case, no hazard will be presented.

When charged, the magnet current would continue to circulate indefinitely, even if the experiment was powered down or the command path to the experiment was broken. To obviate concerns arising from this when attached to the ISS, the CSP also contains an auto ramp down timer. In the event that no external communication is received for 8 hours the CSP initiates the ramp down sequence, while continuing to monitor and protect against a quench. Consequently, even in the event that power or communication to AMS is interrupted, after 8+1.5 hours the magnet is guaranteed to be at zero field.

A critical element of the magnet avionics is then the Uninterruptible Power Supply (UPS), which provides the power to the CSP and through the CSP to the quench heaters, in the unlikely event of a quench. After an extensive investigation of capacitors and battery technologies it was determined that only the highest quality Lithium-Ion cells would fulfill the requirements of energy density, thermal operating range and rate of discharge, as well as reliable and safe operation on orbit. These cells are being produced by Yardney/Lithion. They are based on the mechanical design space proven in the Mars Lander and Exploration Rover programs and the cell chemistry used in the B2 Bomber upgrade. In addition they are supplied with a Battery Management Systems (BMS) adapted for the AMS-02 requirements from a space qualified system developed for JPL. The BMS ensures that the eight cell battery is neither over charged nor over discharged, both of which could reduce the battery capabilities, though with the implemented mechanics and chemistry neither condition would be a hazard. However, as even the highest reliability batteries may not perform at full capacity at end of life, two UPS (cell pack plus BMS) will be installed on AMS-02. Either is sufficient to meet the requirements.

Owing to the amount of stored power and because the CCS within the CAB is connected directly to the ISS power bus, detailed analysis has been done to ensure proper grounding and isolation, both against possible breakdowns and against electromagnetic interference within the CAB, between the CAB and the rest of AMS, and between the CAB and the ISS.

The level of space qualification required for the CAB project is significantly more stringent then for the bulk of the electronics in AMS-02. From design and procurement through production and testing the CAB will use space quality techniques. The entire CAB has been designed to be single fault tolerant and certain critical blocks have been replicated to allow successful operation after multiple faults. For example, should one of the six primary DC-DC converters fail in the CCS, the remaining five are sufficient to reach full field. Even if a second converter were to fail, the field value could reach over 80% of nominal. As another example, the target current is obtained by using the median result between three independent circuits which compare the voltage drop measured across the precision shunt to a reference voltage, where each circuit is fed by an independently generated reference. Also, the control, signal condition blocks of the CCSC and the power switching are redundantly duplicated and cross strapped, with the primary and redundant sides being independently powered with dedicated converters and 28 VDC feeds.

2.1.5 Test Results

All parts of the AMS magnet system are subject to a battery of tests to ensure their quality and integrity, and their suitability for the mission.

i) Coil Tests

Every one of the 14 superconducting coils will have been tested before assembly into the final magnet configuration. All twelve of the flux return coils have been tested successfully, and the first of the two dipole coils is undergoing final preparations for testing. A special test facility has been constructed (Figure 2.23) which allows the coil to be operated under cryogenic conditions as close as possible to flight. In particular, the coil is mounted in a vacuum space, and is cooled by a thermal bus bar of the same construction as the one in the flight system.

Figure 2.23: Coil test facility.

Although the maximum current in the fully-assembled magnet system is 459.5 A, individual coils are tested to different currents. This is because the distribution of magnetic field is different when a coil is tested in isolation. The coils have therefore been tested at currents high enough that some part of the

coil is subject to the same stress that it will experience in the full configuration. If the test current was higher, then this part of the coil would be over-stressed. In practice, this means that some of the flux return coils are tested at 600 A, others at 562 A and the dipole coils at 335 A.

The procedure for testing the flux return coils was to charge to the maximum current (600 A or 562 A), then reduce to 459.5 A. With the coil held at this current, the quench heater was powered at 200 W for a controlled time period. Heater pulses were applied in increments of 10 ms until the coil quenched. After the quench, the coil was re-cooled and charged again to 459.5 A, to check that there was no damage. The two dipole coils will follow a similar testing procedure. Completion of all coil testing is expected in the first half of 2004.

ii) Coil Cooling System Tests

A full-scale replica of the superfluid thermal bus bar system outlined above was designed and assembled. The replica consisted of a thermal bus bar in the form of a 20 m long sealed copper pipe with a 15 mm bore. Part of the pipe was inside a 200 litre helium vessel to provide a cold heat exchanger: the rest was in the vacuum space.

The copper pipe was connected to an external, clean supply of helium. The vessel was cooled down and filled with liquid helium which was then further cooled to 1.8 K by pumping. Helium was drawn into the copper pipe due to the cooling, but the pressure was maintained at around 1 bar. Eventually, the 200 litre vessel contained boiling superfluid helium at 1.8 K and 16 mbar, and the pipe was filled with supercooled helium at 1.8 K and 1 bar.

Heaters on the part of the thermal bus bar outside the helium vessel were then used to simulate the heat load due to the magnet coils being charged. Up to 6 W could be generated by the heaters and transferred by Gorter-Mellink conduction through the thermal bus bar to be dissipated in the vessel of boiling helium. If the heaters were used to generate more power, the Gorter-Mellink conduction broke down: the thermal bus bar was unable to transfer the heat and the temperatures within it began to rise rapidly. These results corresponded to the calculations carried out before the tests.

iii) Cryogenic Safety Tests

A series of experiments has been carried out to determine what happens in the event either of a catastrophic loss of vacuum or of a much smaller vacuum leak. A test facility was designed and assembled in which either of these scenarios could be investigated on a small scale. The test facility contained a 12 litre helium vessel, together with a system of valves, sensors and high-speed data acquisition. To carry out a test, the 12 litre vessel was filled with superfluid helium at 1.8 K. A fast-acting valve was then used to open a large hole in the insulating vacuum to simulate a catastrophic leak, or a very small hole to simulate a small leak. By monitoring the rise of pressure and temperature, and the rate of change of mass of the vessel, the heat flux and venting rate could be calculated.

These results can be extrapolated directly to the AMS magnet, and have been used to qualify the cryogenic system for flight on the Space Shuttle.

In addition to these investigations, tests have also been carried out on prototype burst discs. Discs for protecting the vacuum tank have undergone vibration testing followed by controlled bursts. These tests have shown that the discs are not affected by the levels of vibration encountered during a launch. Further tests have been carried out on discs for protecting the helium vessel, which operate at 1.8 K. These discs have been shown to have extremely good leak tightness against superfluid helium. Although the burst pressure is increased as a result of the low temperature, this increase has been found to be predictable and reproducible. The next planned test is a vibration test under cryogenic conditions, followed by a controlled burst.

iv) Avionics

In addition to extensive testing with the magnet, the CAB will undergo the full battery of space qualification procedures for avionics listed in detailed in § 2.8. The UPS have an even more rigorous series of tests at both the cell (currently in progress) and battery levels to ensure that they are safe and reliable under all conditions.

The magnet has passed a special NASA Safety Review. Figure 2.24 shows the assembly of the flux return coils.

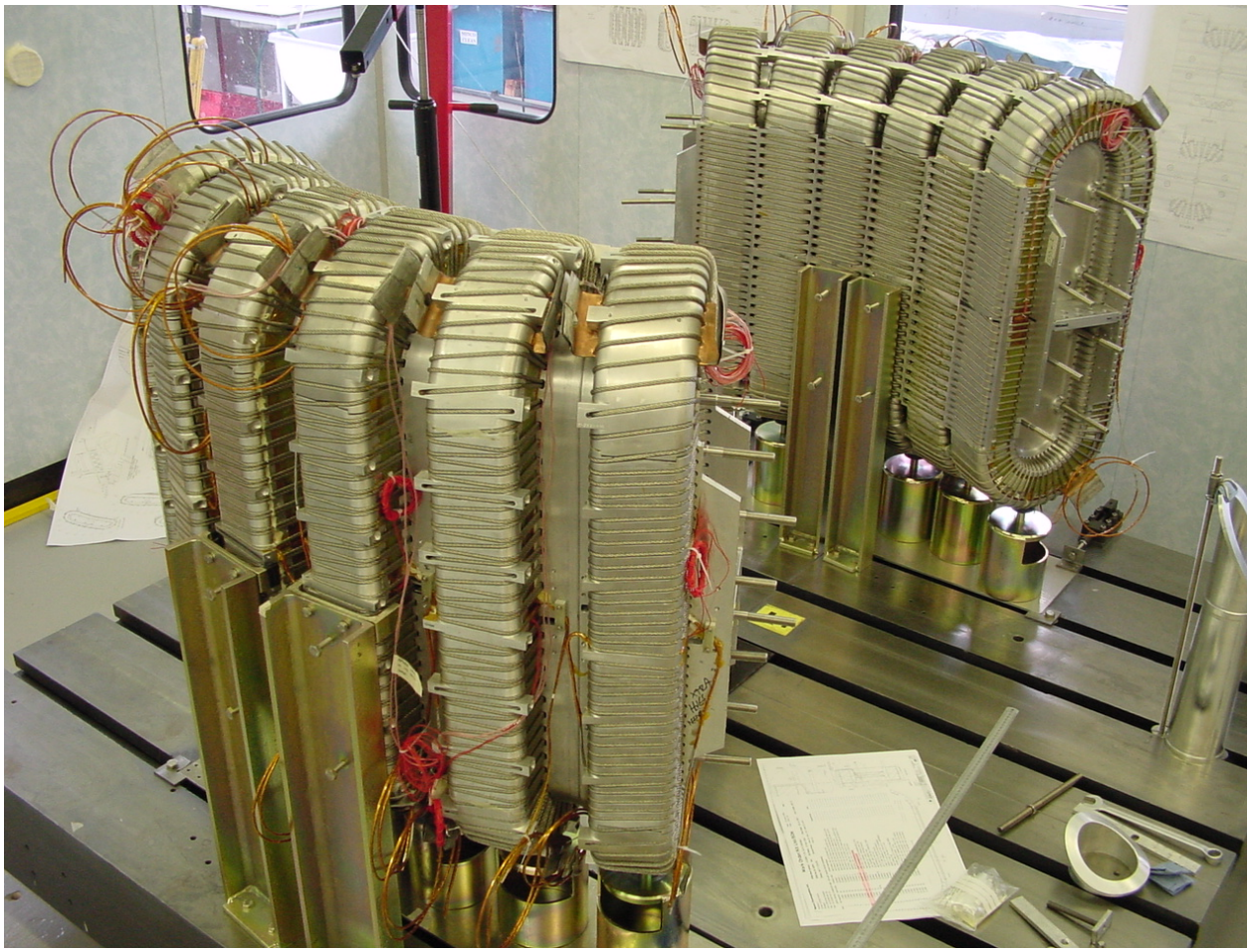

Figure 2.24: Coil Assembly.

2.1.6 References

[1] B. Blau, E. Ettlinger, S. Harrison *et al.*, "The AMS02 superconducting magnet for astrophysical research", Gravitation and cosmology **5** (2000), Supplement pp. 1.

[2] B. Blau, S. Harrison, H. Hofer *et al.* "The superconducting magnet system of AMS-02 – a particle physics detector to be operated on the International Space Station", IEEE Transactions on Applied Superconductivity **12** (2002) 349.

[3] G. Baccaglioni, B. Blau *et al.*, "Production and Qualification of 40 km of Al-stabilized NbTi Cable for the ATLAS Experiment at CERN", IEEE Trans. On Applied Superconductivity, **12.1** (2002) 1215.

[4] L. Rossi, "Superconducting accelerators and detectors", Cryogenics **43** (2003) 281, see § 6.

[5] F. M. Ohlen, Astronomy and Astrophysics Supplement Series, **65.4** (1986) 607, and references therein.

[6] S. M. Volz *et al.*, "Cryogenic on-orbit performance of the NASA Cosmic Background Explorer (COBE)", SPIE Vol. 1340 Cryogenic Optical Systems and Instruments IV (1990).

[7] M. F. Kesseler *et al.*, The ISO Handbook, Vol I "ISO - Mission & Satellite Overview", ESA SAI/2000-035/Dc, Ver. 2 (Nov 2003).

[8] M. J. DiPirro *et al.*, "The transfer of superfluid helium in space", Cryogenics 1994 vol. 34 ICEC supplement.

[9] S. Harrison, E. Ettlinger, G. Kaiser, *et al.* "Cryogenic system for a large superconducting magnet in space", IEEE Transactions on Applied Superconductivity Vol. 13 pp. 1381-1384.

[10] A. Nekano, D. Petrac and C. Paine, "He II liquid/vapour phase separator for large dynamic range operation", Cryogenics Vol. 36, pp. 823-827.

[11] A. Kent, "Experimental low-temperature physics", Macmillan, pp. 54-57.

[12] S. Breon *et al.*, "Operation of a Sunpower M87 cryocooler in a magnetic field", Cryocoolers 12, Edited by Ron Ross, Jr., Kluwer Academic/Plenum Publishers, pp. 761-769, 2003.

[13] M. DiPirro, P. Shirron and J. Tuttle "Mass gauging and thermometry on the superfluid helium on-orbit transfer flight demonstration", Advances in Cryogenic Engineering Vol. 39, pp. 129-136, 1994.

[14] A. Mord and H. Snyder, "Self-driven cooling loop for a large superconducting magnet in space", Cryogenics Vol. 32, pp. 205-211, 1992.

[15] G. Kaiser *et al.*, "Thermo-mechanical superfluid helium pumps for Alpha Magnetic Spectrometer (AMS-02) mission", Proceedings of the 19th International Cryogenic Engineering Conference, pp. 523-526.

2.2 The Transition Radiation Detector (TRD)

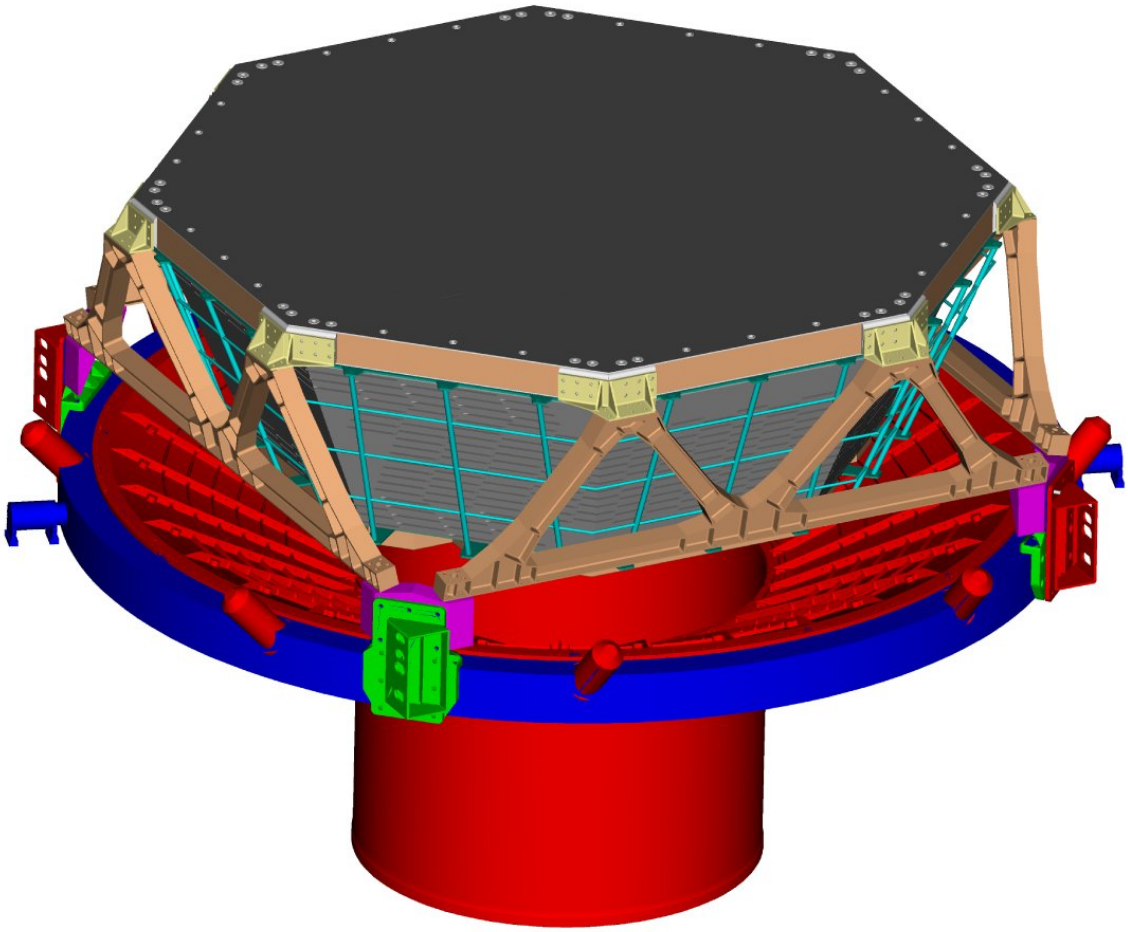

Figure 2.25: Computer generated view of the TRD on top of the magnet vacuum case.

Transition radiation [1] is the electromagnetic radiation that is emitted when charged particles transverse the boundary between two media with different dielectric properties ε_1 and ε_2. It is the result of the reformation of the particle's field when traveling from medium with ε_1 to a medium with ε_2. The probability for a particle to emit a TR photon at a single interface is very small (10^{-2}). This can be significantly enhanced by a multilayer structure. For the AMS-02, the Transition Radiation Detector (TRD) is realized by a 20 mm thick fleece which is used as radiator.

The AMS-02 Transition Radiation Detector is under construction at RWTH-Aachen. The DAQ electronics and power systems are under test by TH-Karlsruhe, Chung Shan Institute of Science and Technology (CSIST) and Kyungpook National University. The gas system is being built by MIT with electronics from INFN Rome.

Figure 2.25 shows the TRD on top of the magnet vacuum case. A charged particle traversing this detector produces characteristic electromagnetic radiation depending on its mass and energy. Since the particle momentum is determined with the AMS-02 silicon tracker by measuring the trajectory inside the magnet, the detected transition radiation (TR) can be used to distinguish between particles of different masses, like positrons and protons.

The TR photons are detected in straw tubes, filled with a Xe:CO_2 (80%:20%) gas mixture (see Figure 2.26) and operated at 1600 V. With a probability of about 50% TR photons are produced in the 20 mm thick fleece and detected by the straw. The principal of TRDs is very well understood and they are used in large particle physics experiments (ATLAS [2] at CERN, HERA-B [3] at DESY). The new challenge is to operate such a large gas detector safely and reliably in space.

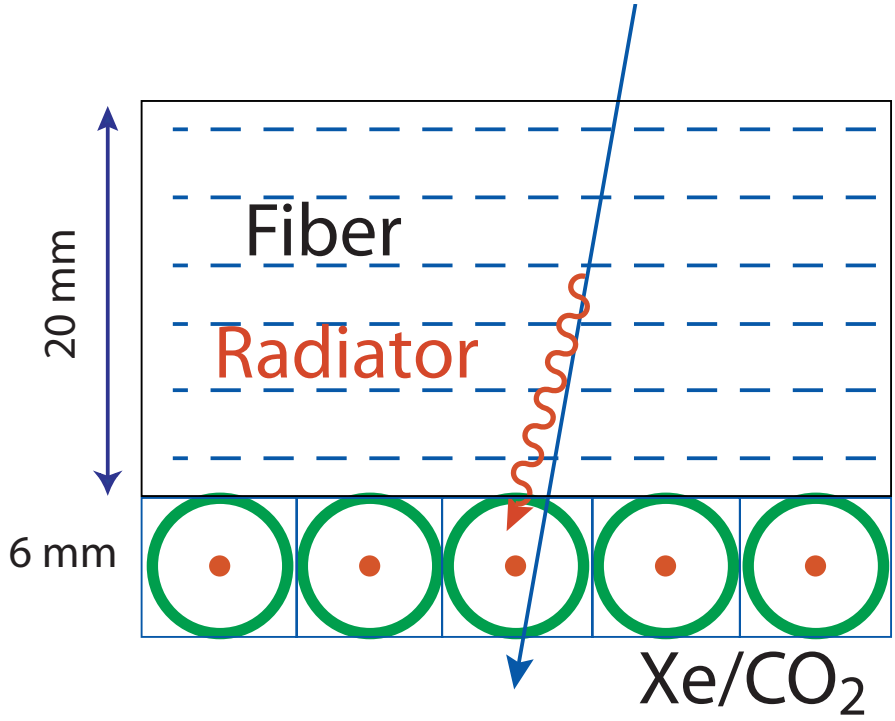

Figure 2.26: The operating principal of the AMS-02 Transition Radiation Detector.

2.2.1 Mechanical Structure

In total 328 TRD modules, each containing 16 straws, of lengths between 0.8 and 2 m are arranged in 20 layers each with 20 mm of 0.06 g/cm^3 polypropylene/polyethylene 10 μm fiber fleece. The lower and upper four layers are oriented parallel to the AMS-02 magnetic field while the middle 12 layers run perpendicular to provide 3D tracking. They are supported by a conical octagon, as shown in Figure 2.27, made of aluminum-honeycomb walls with carbon-fiber skins and bulkheads. A mechanical precision of better than 100 μm assures gas gain homogeneity better than 1%. On the outside of the conical octagon structure a grid structure (see Figure 2.25), built out of carbon fiber tubes, will be attached to support the services (gas tubes, HV cables, signal cables).

A coupled load analysis of the entire TRD structure [4] has been carried out by means of a detailed Finite Element Calculation. As the result of the modal analysis the first natural eigen-frequency turns out to be 54 Hz, above the required 50 Hz. Figure 2.28 shows, for the most critical direction z, the relative displacements. Various experimental tests (see Figure 2.29) have been used to verify material properties and analytical calculations [5].

Figure 2.27: The TRD Octagon Support Structure.

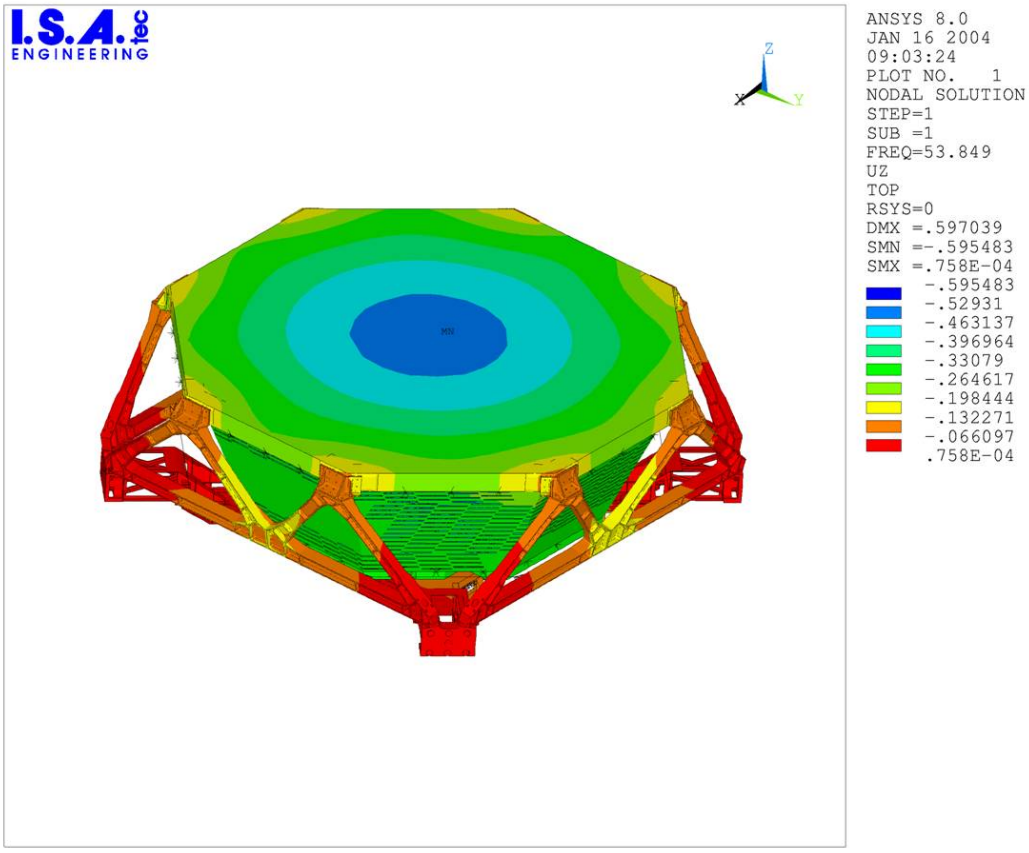

Figure 2.28: TRD modal analysis results.

Figure 2.29: Vibration test stand loaded with a TRD straw module at RWTH-Aachen.

As shown in Figure 2.30, the 16 straws in each module are built out of two overlapping kapton strips covered with aluminum and graphite on one side and polyethylene on the backside and are wound back-to-back and heat sealed to form straw tubes of 2.2 m in length, 6 mm in diameter and 72 μm wall thickness. Sixteen straws are used to build a module. Six longitudinal carbon stiffeners and additional carbon strips running across the module every 10 cm assure mechanical rigidity to withstand launch vibrations. The straws are closed with two polycarbonate endpieces, which provide the gas-supply and center the Cu-Te crimp-plugs [6] to hold the 30 μm gold plated tungsten wires tensioned with 1 N. The precision of the wire positioning was verified with a high-resolution computer-tomography-scan as shown in Figure 2.31 and was found to be within 30 μm.

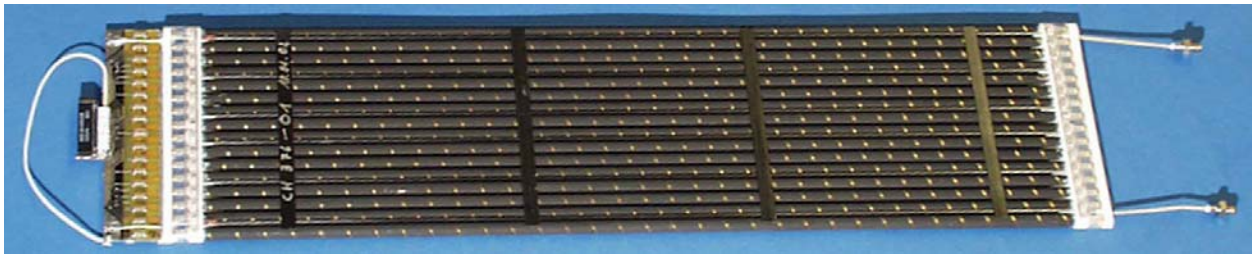

Figure 2.30: AMS-02 TRD module with 16 straw tubes.

Figure 2.31: TRD Module Computer Tomography. The straw walls and the central wires are clearly visible.

The optimized AMS-02 TRD design with a diameter of 2.2 m and 5248 straw tubes arranged in 20 layers weighs less than 500 kg (see Table 2.2).

Component	Weight [kg]
Radiator	60
Straw Tube Modules	54
Octagon	114
Support,Shielding and Services	100
$Xe:CO_2$	54
Gas System	63
Crate Electronics	53
Total	**498**

Table 2.2: Breakdown of the TRD weight.

2.2.2 Module Construction and Quality Control

The gas tightness of the straw modules is the most critical design issue. The available supplies of gas, 49.5 kg of Xe and 4.5 kg of CO_2, will have to last for three years of operation. Using as standard conditions 1 bar and 298 K, this corresponds to 8420 l of Xe and 2530 l of CO_2. The CO_2 leak rate for one meter of strawtube was measured to be 0.23×10^{6} l mbar/s with the TRD gas $Xe:CO_2$ 80:20 mixture (Figure 2.32). This leak rate is attributed to diffusion through the straw walls. It corresponds to 1.85×10^{5} l mbar/s per module-meter or 9.3×10^{-3} l mbar/s for the full TRD (500 module meters). A single poly-carbonate endpiece has a CO_2 leak rate of 0.9×10^{-5} l mbar/s, for all 328*2 endpieces this totals to 5.9×10^{-3} l mbar/s. Summing, the total TRD CO_2 leak rate of 1.5×10^{-2} l mbar/s would correspond to a loss of CO_2 over 3 years of 287 l or a "safety factor" of 8.8 with respect to the CO_2 supply. Fabricated TRD modules are accepted if they have with a CO_2 safety factor better than 4. This can only be assured by testing each of the 5248 straws individually before producing a module [7].

A single straw test stand (Figure 2.33) has been developed where helium is used to achieve fast and accurate measurements. Per meter of module, a helium leak rate of 10×10^{-5} l mbar/s corresponds to the target safety factor of 4 for CO_2 (Figure 2.34). A straw is glued gas tight at one end using a brass plug. A steel tube is glued to the other end, serving as a gas inlet. The straw is placed inside an external volume which is made gas tight with a lid and O-ring. This volume is connected to a reference volume via a valve and a differential pressure sensor. The volumes are in thermal contact and the temperature is monitored. After installation, the valve is opened briefly to equalize the pressure between the two volumes. Then the straw is filled with helium at a pressure of 2.8 bar. Helium gas enters the external volume due to diffusion through the straw walls or due to macroscopic leaks. The differential pressure increase is measured and the leak rate can be determined after a period of 5 minutes (Figure 2.35).

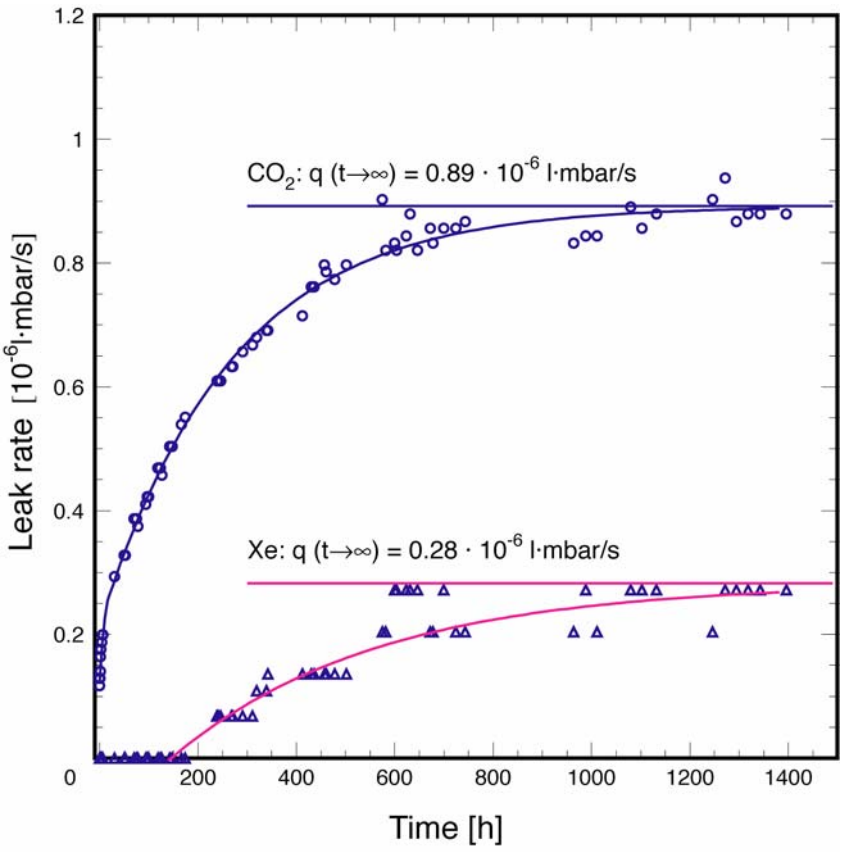

Figure 2.32: Xe:CO_2 leak rate measured with a mass spectrometer with three 1.3 m long straws.

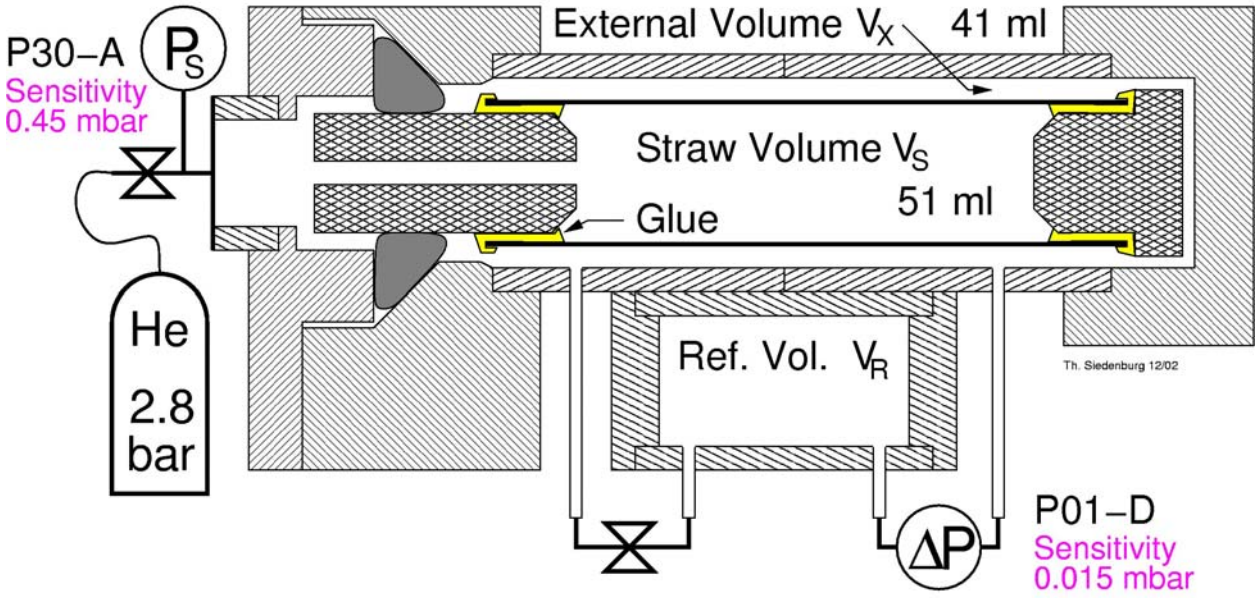

Figure 2.33: AMS-02 TRD single straw test stand.

A detailed description of the straw module production can be found in [8,9]. After fabrication all straw modules undergo the following tests:

- Pressure drop test: The CO_2 leak rate of each straw module is measured by a pressure drop test at 1.7 bar in a vacuum vessel. As shown in Figure 2.36, the safety factor averaged over all modules selected for flight is 7.9. This would allow up to 20 years of operation on the ISS.
- Dark current: The straws must operate without any significant (< 1 nA) dark current at a high voltage of 1500 V with Ar:CO_2 (80:20).
- ^{55}Fe gas gain homogeneity (Figure 2.37): The gas gain as a function of the position along the straws is measured for each straw of the module while it is mounted on a precision granite block to ensure flatness. The straw signals are caused by converted 5.9 keV photons from an ^{55}Fe source. The measured gas gain dispersion is required to be less than 1.5 %.

Space qualification tests have been carried out for eight 0.7 m long straw modules. The modules underwent vibration tests (a 0.5 g sine sweep followed by a 6.8 g_{rms} random test followed again by a 0.5 g sine sweep), 8 cycle thermo-vacuum tests (see Figure 2.38), between −40 and +60 °C, followed again by vibration tests. No significant changes in gas tightness, gas gain or eigen-frequencies were observed.

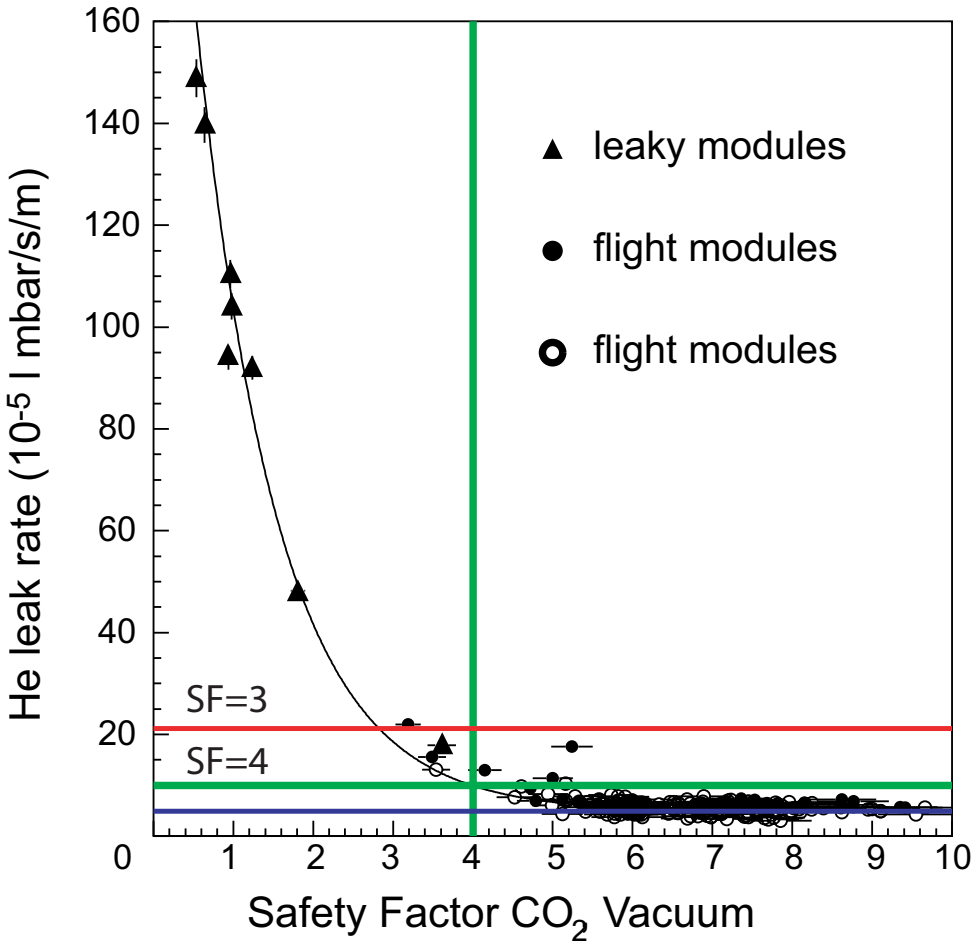

Figure 2.34: Correlation between measured He and CO_2 leak rates for modules that underwent different processing methods. The open circles represent modules where the individual straws were tested before assembly, for the modules denoted by closed circles they were not. Note that only modules with a safety factor greater than 4 are used for flight.

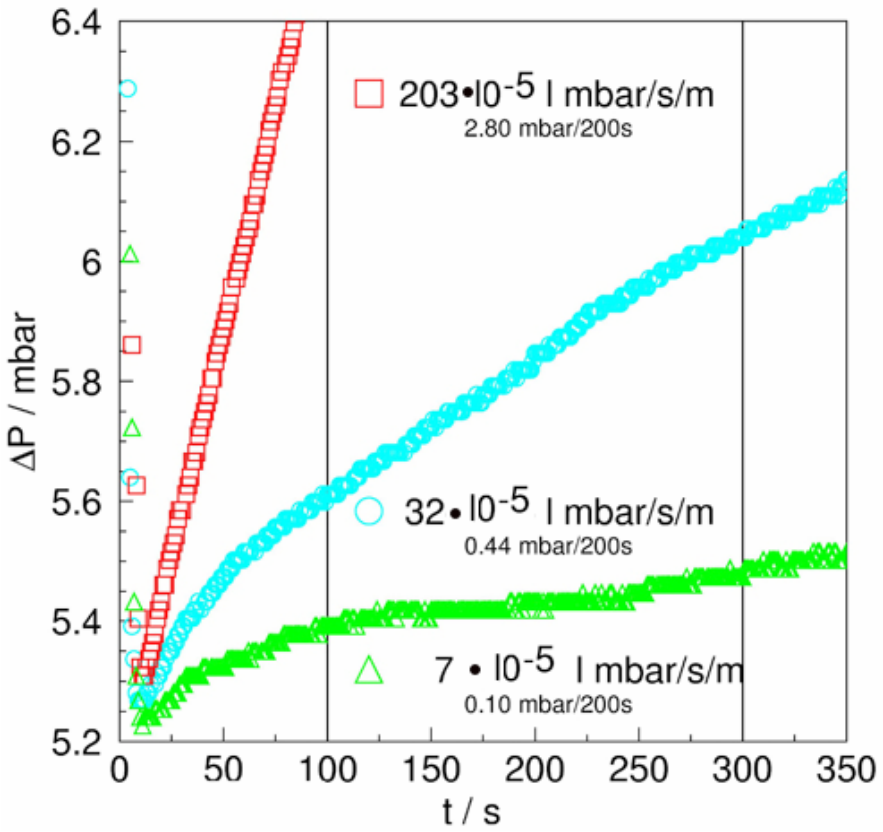

Figure 2.35: Leak rate measurement of 3 straws, one acceptable, two above the limit 10x10^{-5} l mbar/s/m (safety factor 4).

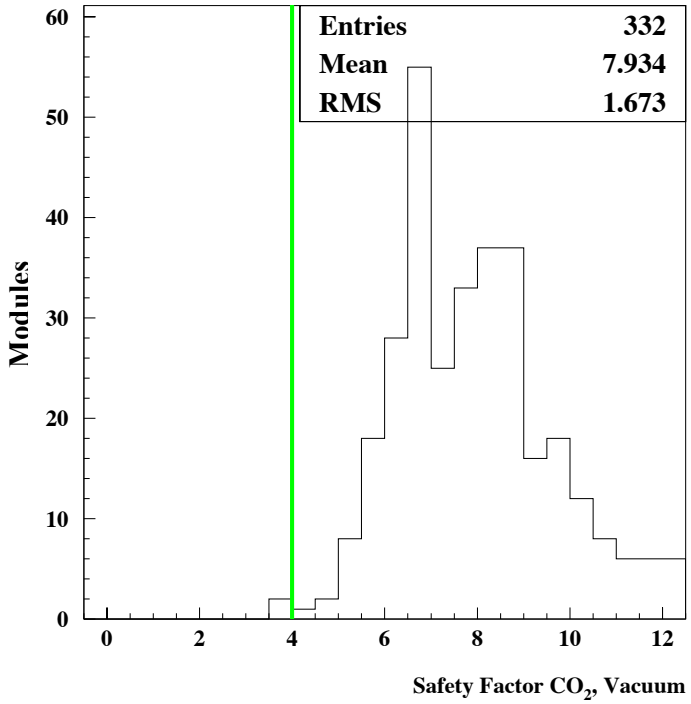

Figure 2.36: Straw module production: safety factor CO_2.

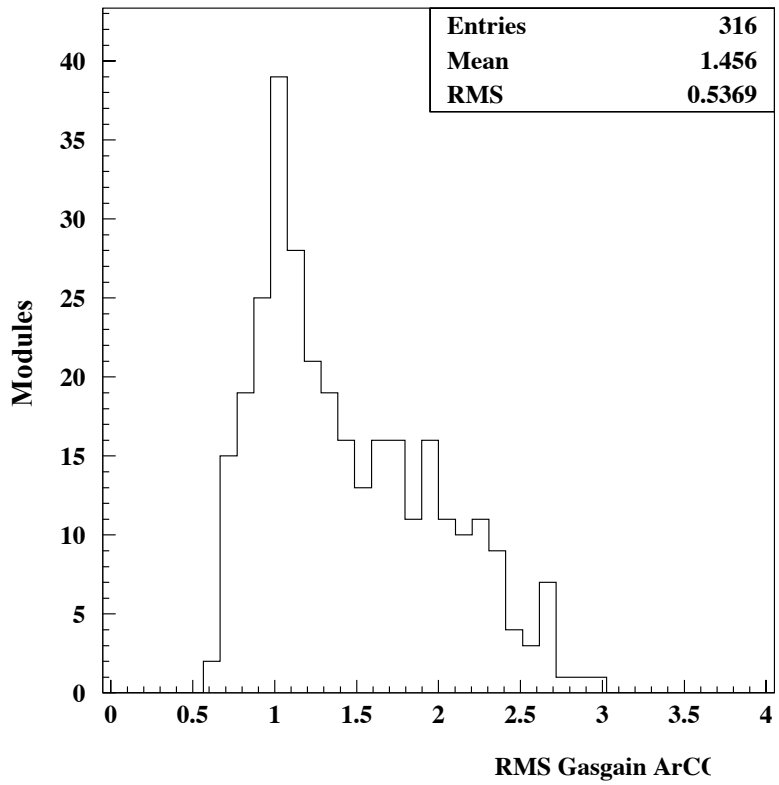

Figure 2.37: Straw module production status: Gas gain homogeneity using Ar:CO_2 (80:20) at a nominal gas gain of 3000.

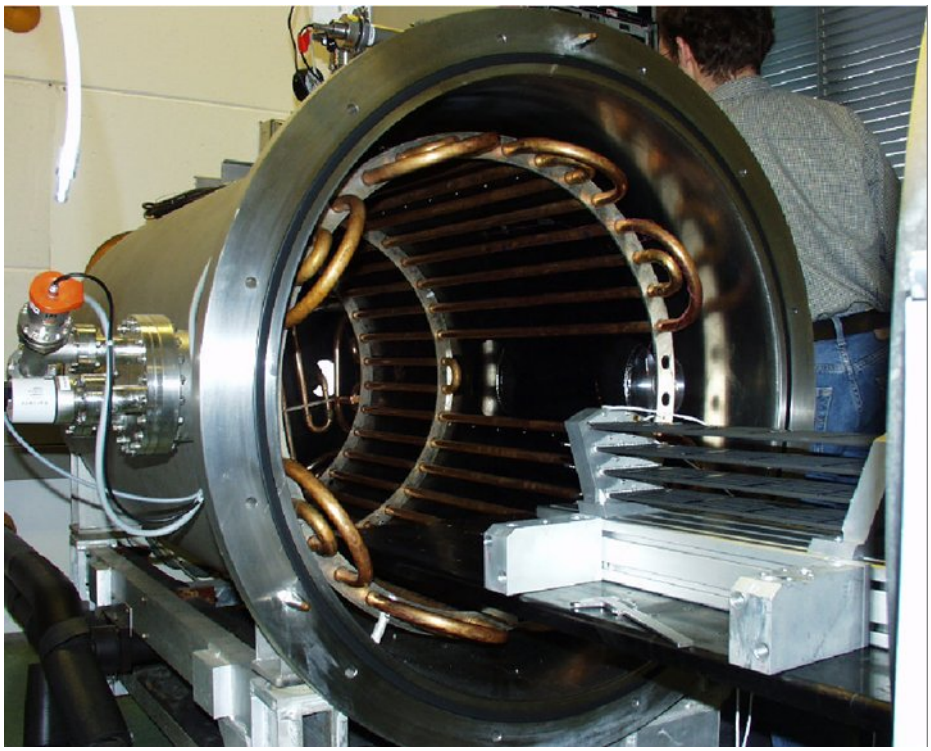

Figure 2.38: TRD thermal vacuum test of 4 straw detector modules.

2.2.3 TRD Electronics

To separate protons from positrons, etc, anode signals from ionization losses alone have to be distinguished efficiently from signals containing both this energy deposit and absorbed TR photons with a pulse height readout. The signals of all straw tubes are digitized after a signal from the general AMS trigger and filtered in the first step of data reduction. Only good hits, defined as 3σ above the noise level or about one tenth the signal left by a singly charged minimum ionizing particle (MIP), are sent to the higher levels system of AMS data acquisition (DAQ) system.

The DAQ system of the TRD, Figure 2.39, is divided into front end electronics, which are mounted directly on the detector, two U-Crates, which host the DAQ and slow control boards and two UPDs in which the 28 VDC supplied from the PDS is transformed in to the low voltages needed by the other TRD electronics.

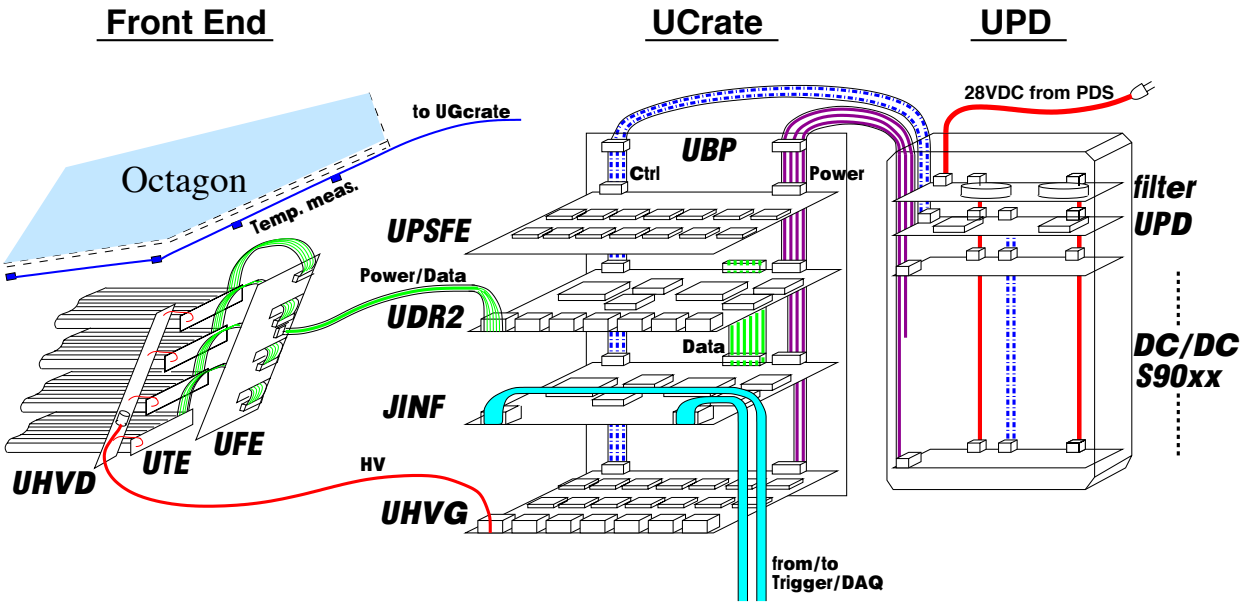

Figure 2.39: Overview of the TRD data acquisition system.

Altogether this electronics consumes less than 100 W (20, 42 and 35 W in the front end, U-Crates and UPDs) to power, readout and control the 5248 channels of the TRD. The front end electronics is developed, built and tested in Aachen. The U-Crate and UPD are jointly developed by Aachen, Karlsruhe and MIT and will be produced and space qualified at the Chung-Shan Institute of Science and Technology (CSIST), Taiwan. The various steps of the development from first prototypes through the qualification of the flight units are described in §2.8.5.

i) Front End electronics

Each of the 328 straw modules is equipped with a UTE board which distributes the HV to the signal wires and brings out the signals via a short sixteen fold twisted pair cable to the front end board (UFE). Four straw modules with their UTE boards are combined in a group or "tower". Each of the 82 towers is supplied by a separate HV channel and read out by one UFE board. The HV for a tower arrives at a UHVD board and is distributed to the four UTE boards.

The UFE board, shown in Figure 2.40, is based on VA analog multiplexers [10]. It is equipped with a serial 12-bit analog to digital converters (ADC) and covers a dynamic range of 40 MIPs (at a gas gain of 3000). The readout time, including the digitization of the 64 connected channels, is 87 μs.

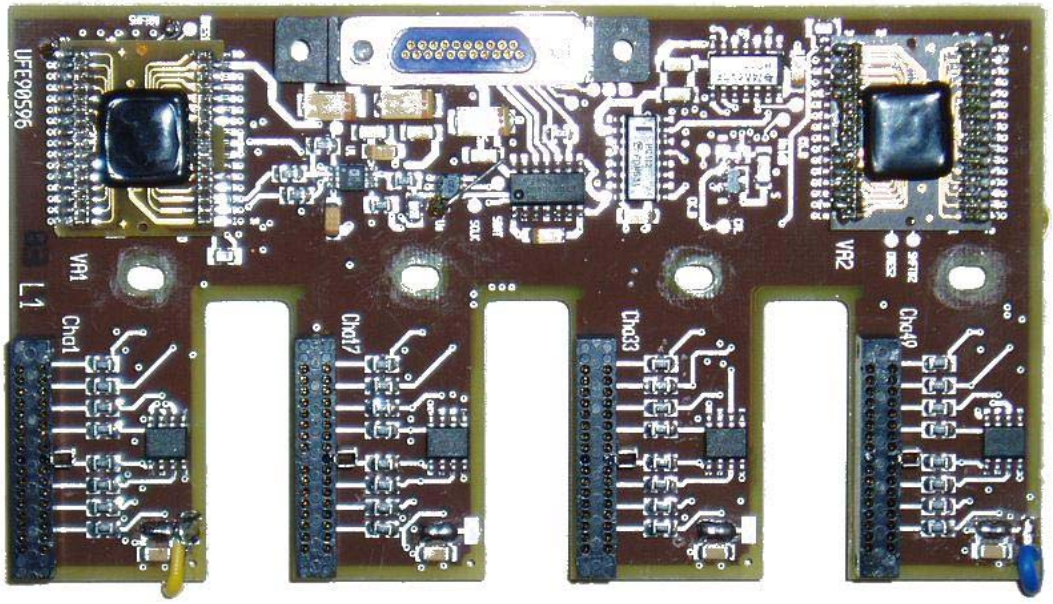

Figure 2.40: TRD Frontend readout board, UFE.

The mounting of the front end electronics directly on the octagon, inside the multi-layer insulation (MLI), assures an electrical shielding which keeps the noise level below 2 ADC channels. The dissipated heat keeps the mean TRD temperature between −15 and +35 °C. All the front end boards have been space-qualified with the strawtube modules. In addition to vibration and thermal vacuum tests, the electromagnetic interference was measured with four 1.4 m modules mounted in a carbon-fiber/aluminum-honeycomb box (as the TRD octagon) wrapped in MLI foil. This included high frequency emission and susceptibility studies. Figure 2.41 shows an acceptable TRD frontend readout emission spectrum after appropriate shielding.

Temperature measurements inside the octagon are made with digital temperature sensors (Dallas DS18S20), which are attached to the UG-Crate (see § 2.2.5.i).

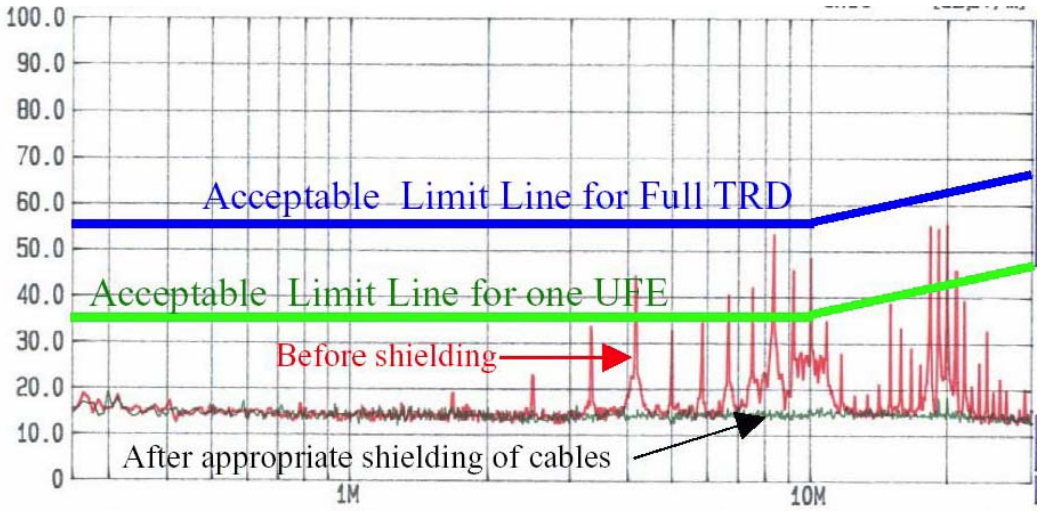

Figure 2.41: TRD Frontend electromagnetic emission test results.

ii) U-Crate

Each of the two U-Crates contains the data acquisition system, the distribution of low and high voltage to the front end electronics and the control of all boards and voltages for half the TRD. The front end electronics is connected to six boards (UDR2) which provide the first level of data reduction. This type of board consists of a dual redundant common digital part (CDP) and a detector dependant part (DDP).

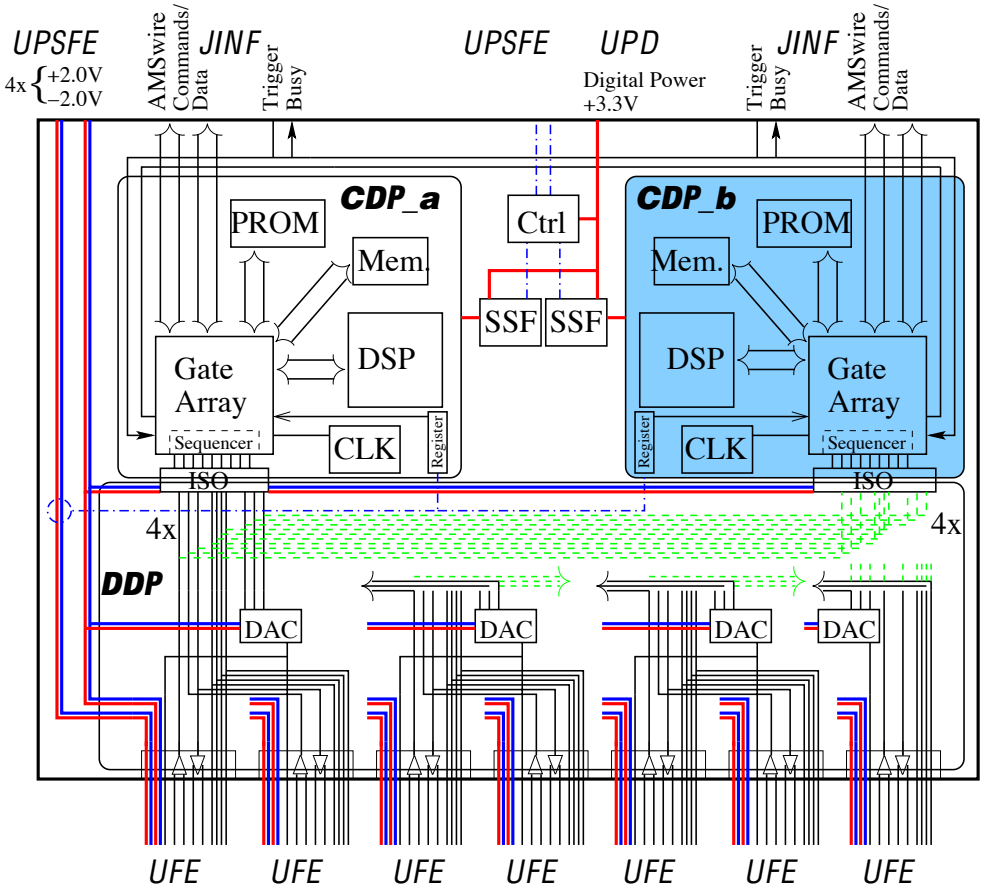

Figure 2.42: Design of the TRD data reduction board, UDR2.

The CDP communicates with the higher levels of the AMS DAQ system via a high speed serial link, AMSwire, through the JINF board. The DDP is an interface between the common digital part of the UDR2 and the UFE boards. Here the signals for the readout sequence are transferred to the UFE board via decoupling chips (ISO) to adjust the different voltage levels of the CDP (+3.3 VDC) and the front end (±2.0 VDC). A digital to analog converter (DAC) for calibration procedures is also included. For each trigger, each UDR2 reads the data of 7 UFEs (448 12 bit words) and performs data reduction by pedestal subtraction and zero suppression and attaches a geographical address. Because of the arrangement of the readout in 4 layer towers, typically only one UFE per UDR2 will have valid hits.

Other boards in each of the U-Crates generate and control stable low and high voltages for the 41 towers. This is arranged in three power groups, each containing 13 or 14 towers, two UDR2s, one UPSFE, for the low voltage control and two UHVG for the high voltage generation. The UPSFE consists of seven dual redundant linear regulators (LR) which stabilize the voltages delivered to the UFE and protect against over current and under voltage. Each LR can be switched off via a command. The UHVG boards contain seven dual redundant Cockroft-Walton elevators in which 120 VDC is multiplied in a 16

stage diode capacitor cascade. Control is provided by an MHV100 application specific integrated circuit (ASIC), developed by LeCroy Research Systems specifically for AMS.

The JINF board also serves as a command and monitoring interface to the UPSFE, UHVG and the UPD using 6 serial busses.

iii) UPD

The UPD hosts an input/output filter (S9011B) at the 28VDC feed input side, a double redundant controller board (S9011AU) and DC-DC converters. One S9053 generates +3.3 VDC for all digital parts in the Ucrate and the S9011AU. Three S9048 generate ±2.6 VDC for the frontend and the DDP. Three S9056 generate +120 VDC as input voltage to the Cockroft-Walton elevator and +5.0 VDC for the MHV controller. All the DC-DC converters are dual redundant units. The active unit can is controlled and monitored by the S9011AU.

2.2.4 Thermal Model

The thermal stability of the TRD is essential for the performance of the detector as temperature variations change the gas density and hence the gas gain. To keep these variations below the few percent level, comparable to the module to module inter-calibration uncertainties discussed below, temperature gradients within the TRD should not exceed ±1 °C. The thermal control study has been performed by OHB System, Bremen, Germany.

To keep the spatial and temporal orbit temperature gradient below 1 °C the TRD will be fully covered in multi-layer-insulation (MLI), including the front end electronics. A thermal simulation for orbit parameters which will give the highest TRD temperature swing as shown in Figure 2.43 proves the effectiveness of this approach. Nonetheless, this will be backed up by a full scale thermal vacuum test.

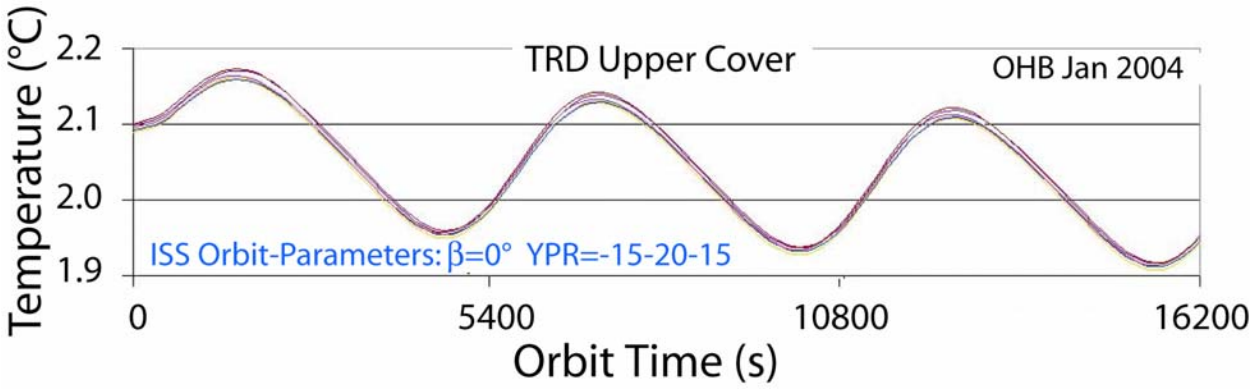

Figure 2.43: TRD thermal simulation.

2.2.5 Gas System

The general layout of the AMS-02 TRD gas system is shown in Figure 2.44. Box S holds the Xe and CO_2 storage vessels with sufficient gas for the 3-5 year AMS-02 mission with a safety margin of four. It provides Box C with premixed gas from a limited transfer volume (~1 liter) under computer control daily. Box C contains pumps and valves to control the gas circulation. It also monitors gas quality. Manifolds distribute the gas to the 5248 proportional wire tubes, which are arranged in 41 parallel segments.

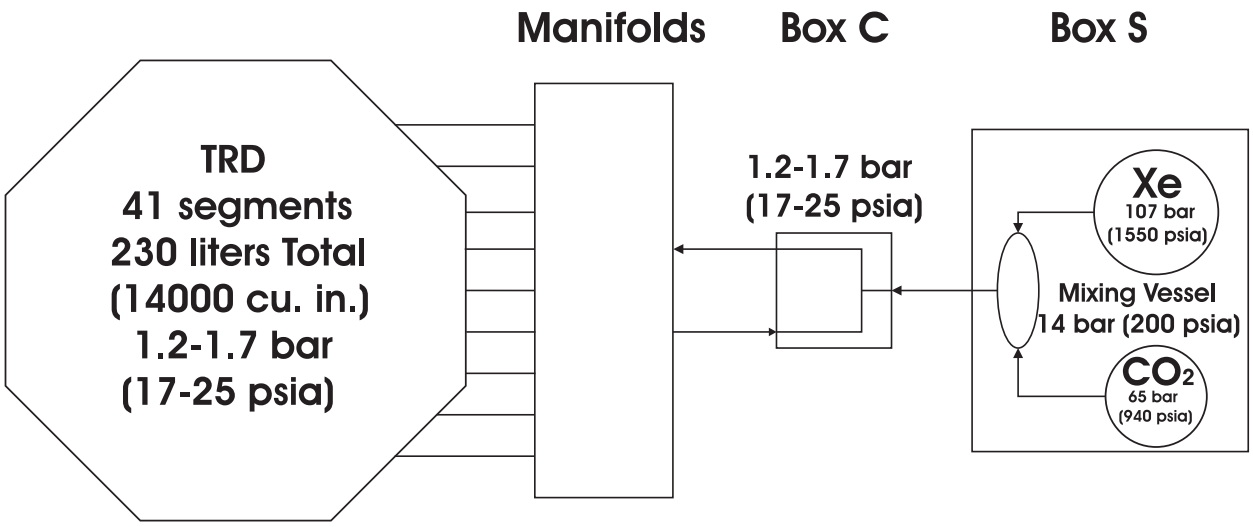

Figure 2.44: AMS-02 TRD gas system general layout.

Boxes S and C are mounted behind a debris shield on the USS on the wake side of AMS (Figure 2.45). The manifolds are mounted on the upper parts of the ram and wake sides of the TRD octagon, inside its thermal enclosure. To keep the solenoid valves in Boxes S and C above 5 °C, the assembly is enclosed in MLI and the valve blocks are fitted with heaters. Heaters are also mounted on the gas tanks to keep them above the critical temperatures of Xe (17 °C) and CO_2 (31 °C), so that the amount of gas remaining can be measured by the pressure.

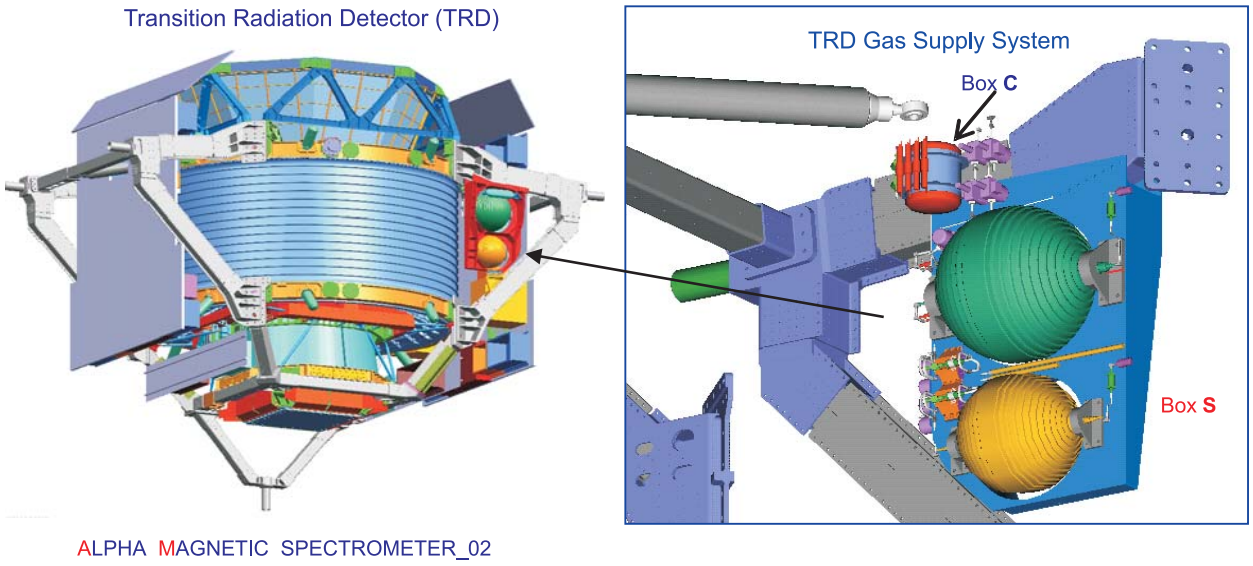

Figure 2.45: Location of TRD Gas system elements

The schematic for Box S is shown in Figure 2.46. Two storage vessels store the xenon and carbon dioxide separately. Two mixing circuits convey the gases to the mixing vessel where the 4:1 mixture is made using partial pressures in P2a and P2b. A system of valves then allows the transfer of the gas from the mixing vessel to Box C. At all points, the valves have a two fold redundancy.

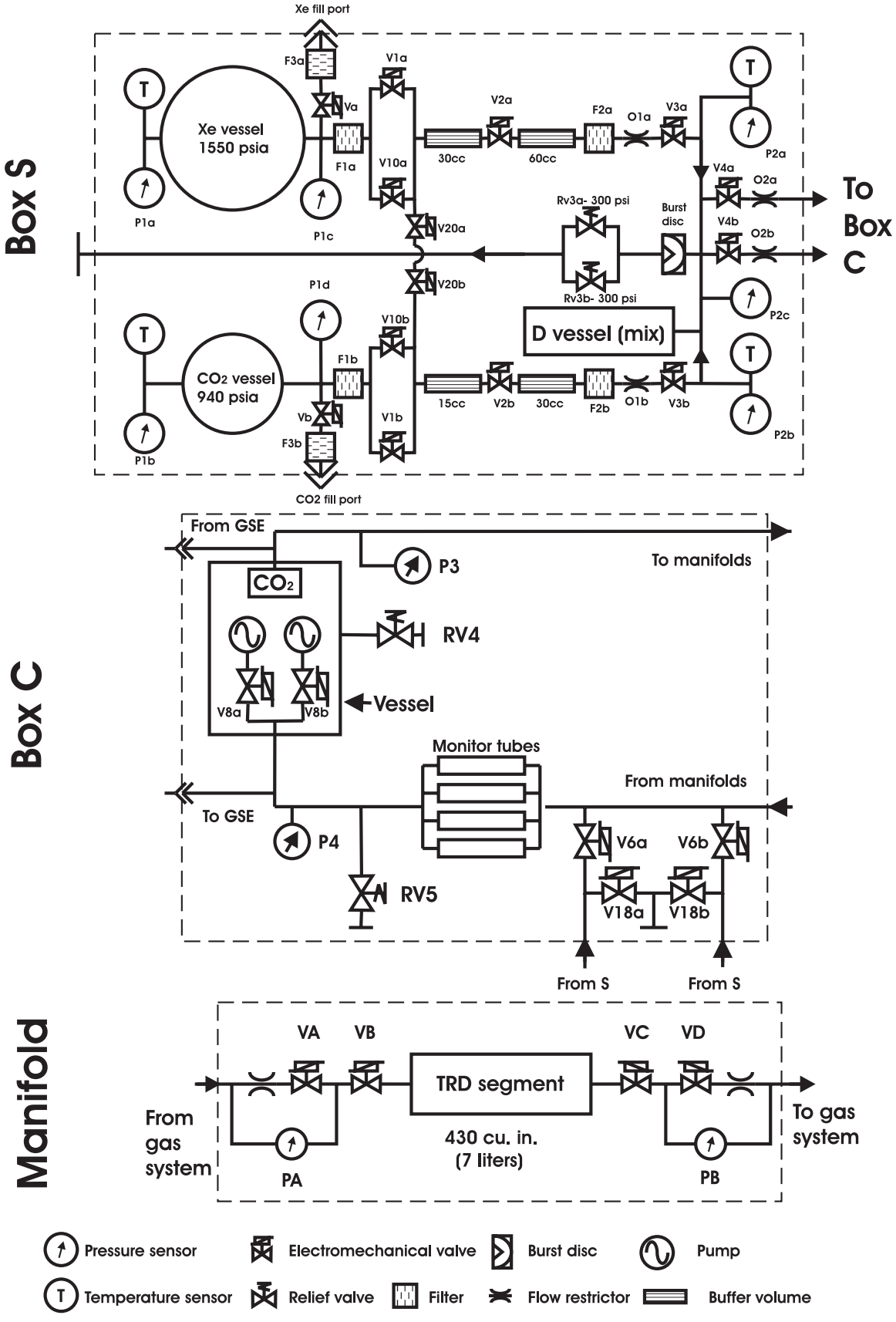

Figure 2.46: Schematics of Box S, Box C, and one of the 41 Manifold segments.

Leak-before-burst vessels ensure safety in the event of high temperatures causing over pressure in the vessels during a time when gas cannot be vented, such as when the system has no electrical power.

Figure 2.46 also shows the Box C schematic. Gas from Box S passes through the transfer valves V6a and V6b. One of two pumps circulate the gas through the TRD volume in order to keep the gas mixed and allow the CO_2 sensor and gain monitor tubes to assess the properties of the gas. The pumps and CO_2 sensor are mounted inside a gas tight vessel; in the event of a pump or valve failure, pressure integrity of the system will not be lost.

One of the 41 manifold segments is shown schematically at the bottom of Figure 2.46. Each manifold segment has two bi-stable valves and one pressure sensor at each end. The valves allow the isolation of a TRD segment in case a leak occurs and the pressure sensors allow detection of leaks from pressure differential caused by abnormal flow. All valves are computer controlled: If there is a large leak in any segment, that segment is closed by the control computer. If there is a large pressure drop at P3 or P4 in Box C, all valves are closed by the gas system electronics, even if the computer is not running.

i) TRD Gas system electronics

The gas control system of the TRD is an essential for the performance of the detector. To obtain the required discriminating power, a stringent control of gas parameters is necessary. For example, a 3 °C change of temperature causes 1% gas density variation, which corresponds approximately to 5% gain variation. Therefore the design of the control system meets tight requirements for safety and reliability [12]. The general layout of the control system is shown in Figure 2.47. The system is designed in three levels. At the lowest level, hardware interlocks ensure that the system will maintain the gas in the TRD in a good condition, preventing any uncontrolled leaks, overpressures, etc. The next level, which operates in the USCM, allows the system to autonomously optimize the performance of the gas parameters within strict limits. The third level operates in the main computer (JMDC) for high level monitoring and control.

The JMDC is discussed in § 2.8. The USCM, developed by RWTH Aachen, is connected to the JMDC via a dual redundant CAN serial bus and to the gas system control electronics via a dedicated custom bus. The USCM contains the monitor program, which tests the status information of the gas system against preset conditions and, as required, executes commands. The conditions and commands are stored in form of decision tables.

The UGBS, UGBC, UGFV and UGPS boards provide the electronic interface between the USCM and the electromechanical gas system devices. The UGBS controls the operations of Box S, providing the correct gas mixture to refill the TRD and monitoring the pressure and filling status. It will shut the gas system down safely in case of power or communications failure. In case of overpressure a relief valve will be opened. The UGBC in connected to Box C. It runs the pump, activates valves to refill the TRD and reads out the gas pressures monitors. In the case of an unexpected power or communications interruption it will safely shutdown the system and generates a High Voltage system shutdown signal to the UHVG in the U-Crates. In case of overpressure a relief valve will be opened. The UGFV and UGPS controls and monitors the isolation valves, pressure sensors and temperature sensors of TRD manifolds. It will control the flow of gas through the TRD modules, detect and then isolate any leaking segments.

The UGPD contains a filter for the 28 VDC input from the PDS, a control board and the DC-DC converters necessary to provide voltage and current to operate valves, pumps and other parts of the TRD gas system and the command electronics.

All control and monitor electronics operate in the stray field form the AMS magnet of ~180 G.

The entire TRD gas system electronics is dual redundant at the board level. The system can continue to operate properly even in the event of multiple failures in different types of boards. To implement this feature, for every board in operation, the *hot board,* a standby unit, the *cold board,* is provided (Figure 2.48).

The engineering modules of the control electronics (Figure 2.49) have been thoroughly tested with the actual parts of the gas system.

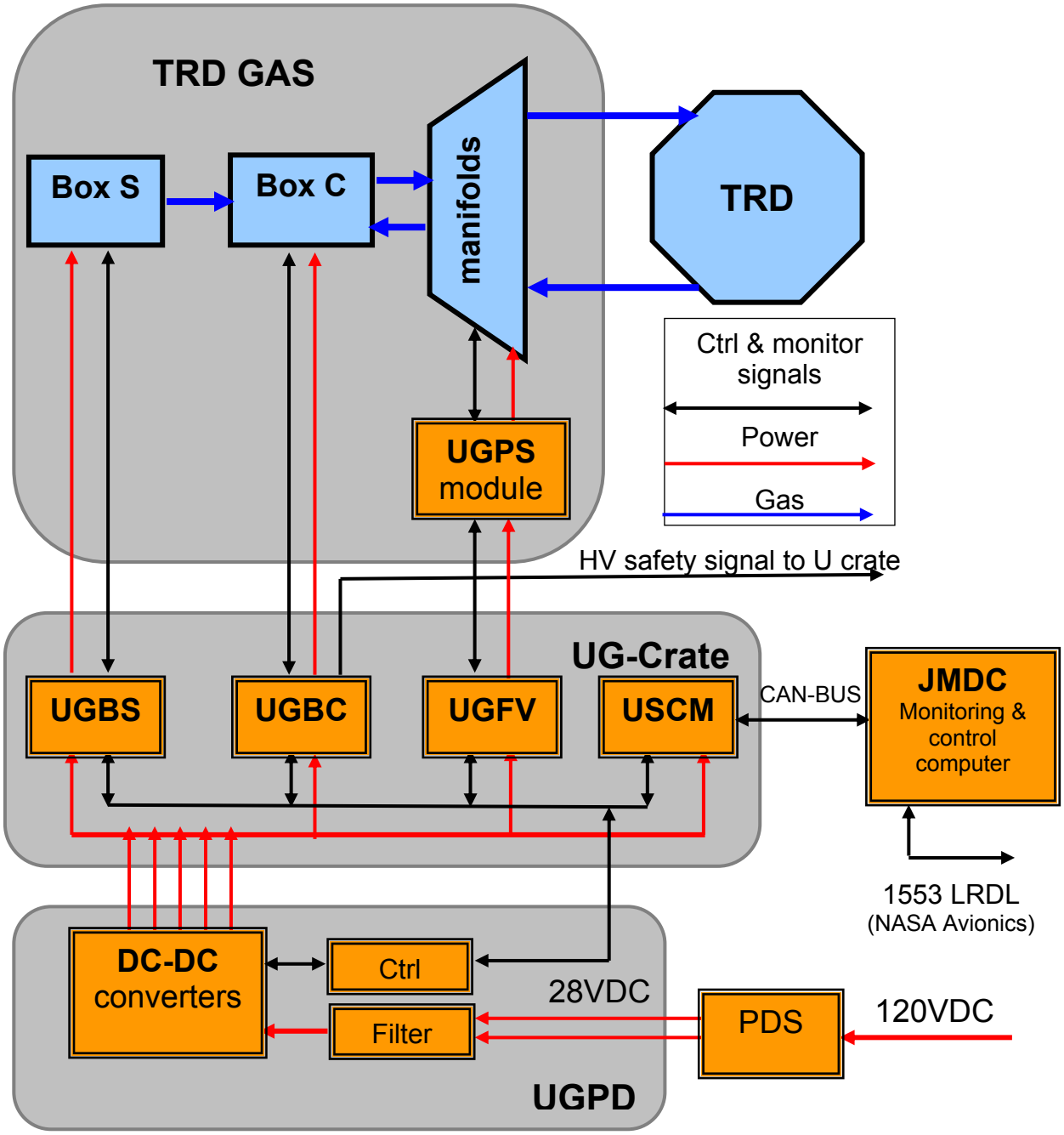

Figure 2.47: TRD gas system command and control architecture.

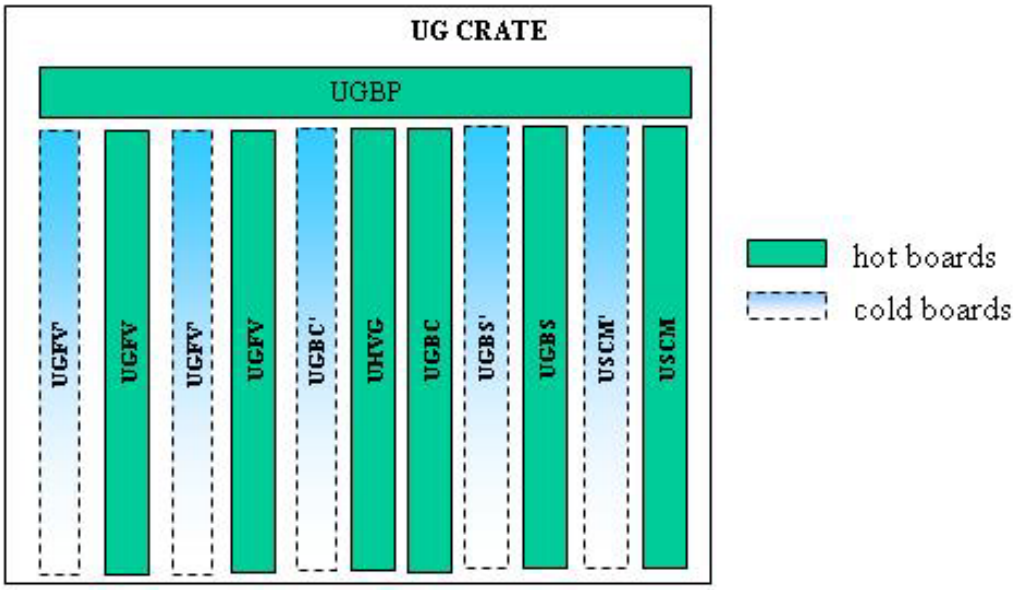

Figure 2.48: Boards in the TRD gas system electronics crate, UG-Crate.

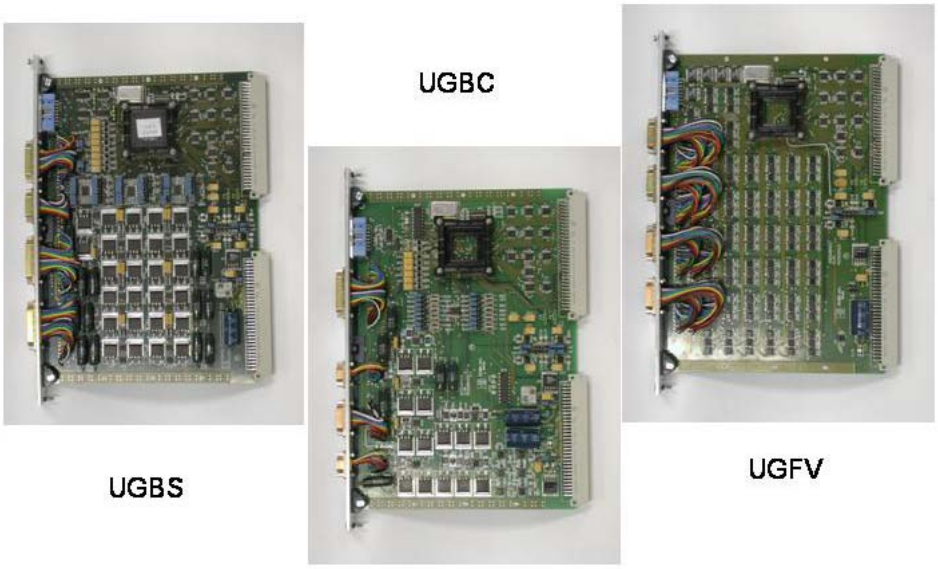

Figure 2.49: TRD gas system electronics boards.

ii) Box S Tests

Component tests have been carried out over the past three years on the space qualified valves, the pressure sensors and all the inline gas fittings (flow restrictors, filters, buffer volumes and mechanics fittings). The valves and sensors have been tested and operation verified over the operating temperature range (0 to +40 °C) and the survival range (−20 to +65 °C). All tests were carried out at maximum expected operating pressure.

Two vibration tests have been carried out on the storage system engineering model at ENEA, Cassaccia, Italy with the INFN Roma group to ensure the mechanical integrity of the system and the functionality of the components after launch as well as to validate the finite element calculation.

The system as tested is shown in Figure 2.50. The test procedure was to perform first a sine sweep, followed by a random vibration and a final sine sweep, all along the same coordinate axis. This procedure was carried out five times: once along the Z axis and twice each along X and Y. After each series of three vibrations, a functional test was performed on the gas circuits to make sure all the mechanical elements still function. In each case, comparison of the sine sweep carried out before and after the random vibration showed there had been no change in the eigenfrequencies of the system and hence no change in structural integrity. The lowest eigenfrequency was found to be above 71 Hz, well above the range of vibrations experienced during launch (Figure 2.51) [11].

Using an engineering model of the control electronics, all components of Box S were successfully operated under autonomous computer control during several mixing cycles (Figure 2.52).

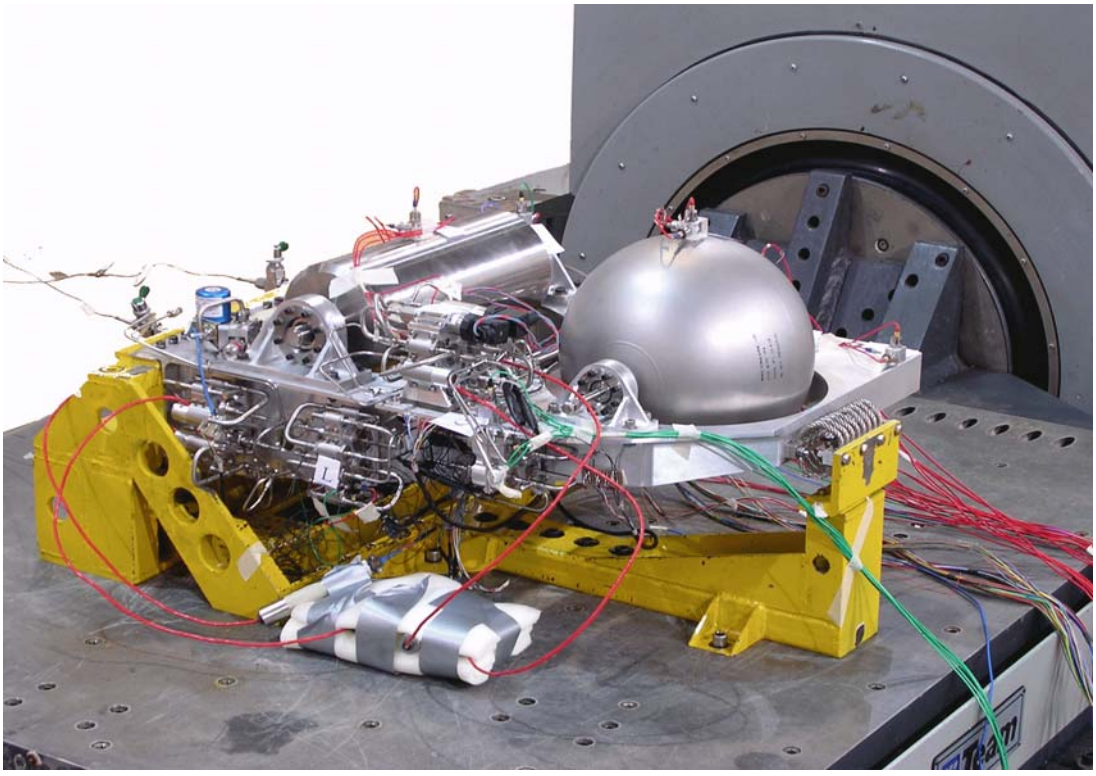

Figure 2.50: Box S engineering prototype and test fixture (yellow) mounted o ***71 Hz***

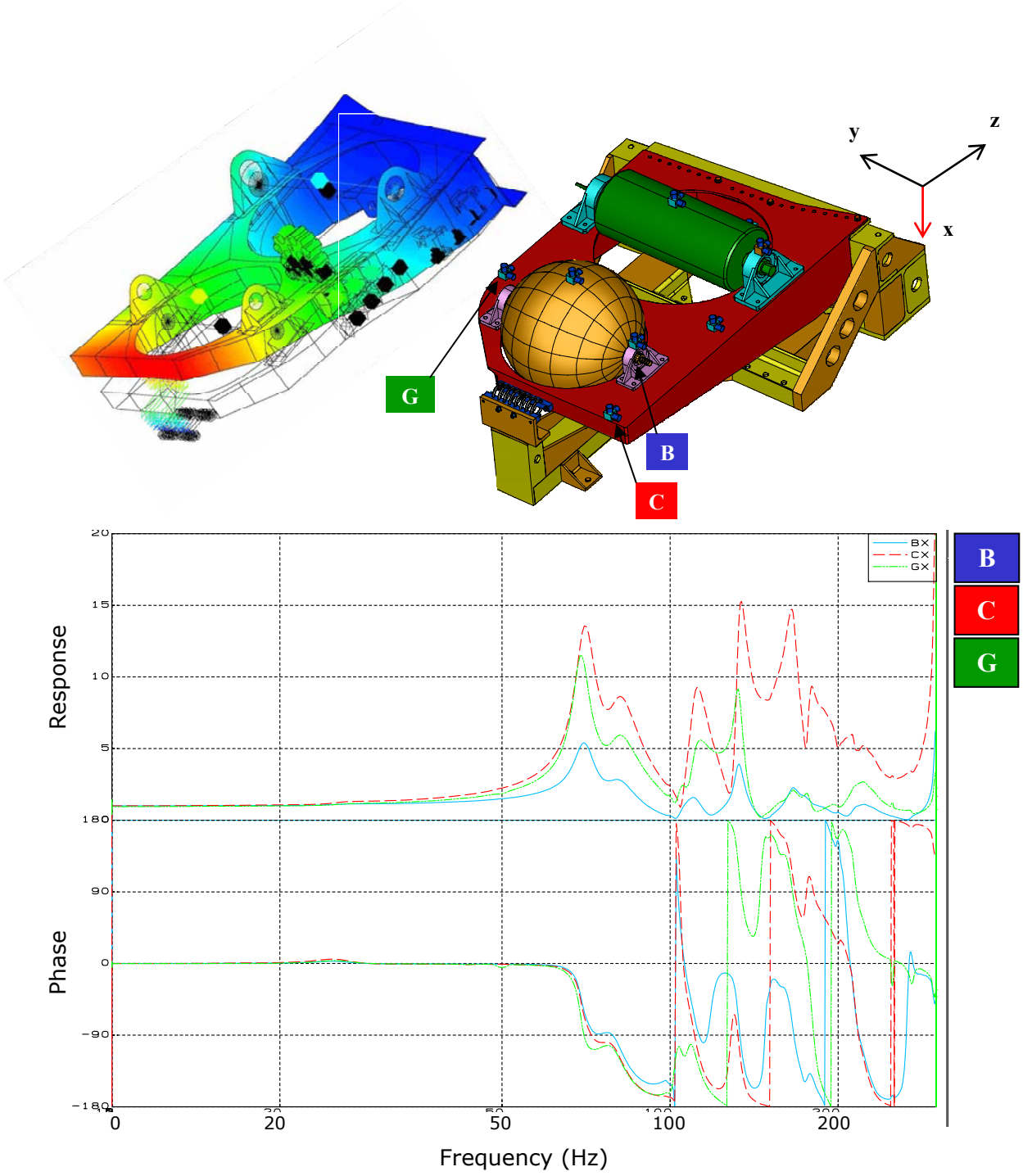

Figure 2.51: Vibration testing of the Box S mechanics. The figure in the upper left shows the results of finite element modeling and the figure on the upper right the locations of the accelerometers during the test. The upper half of the graph shows response to the excitations in the lower half during an x-axis sine sweep.

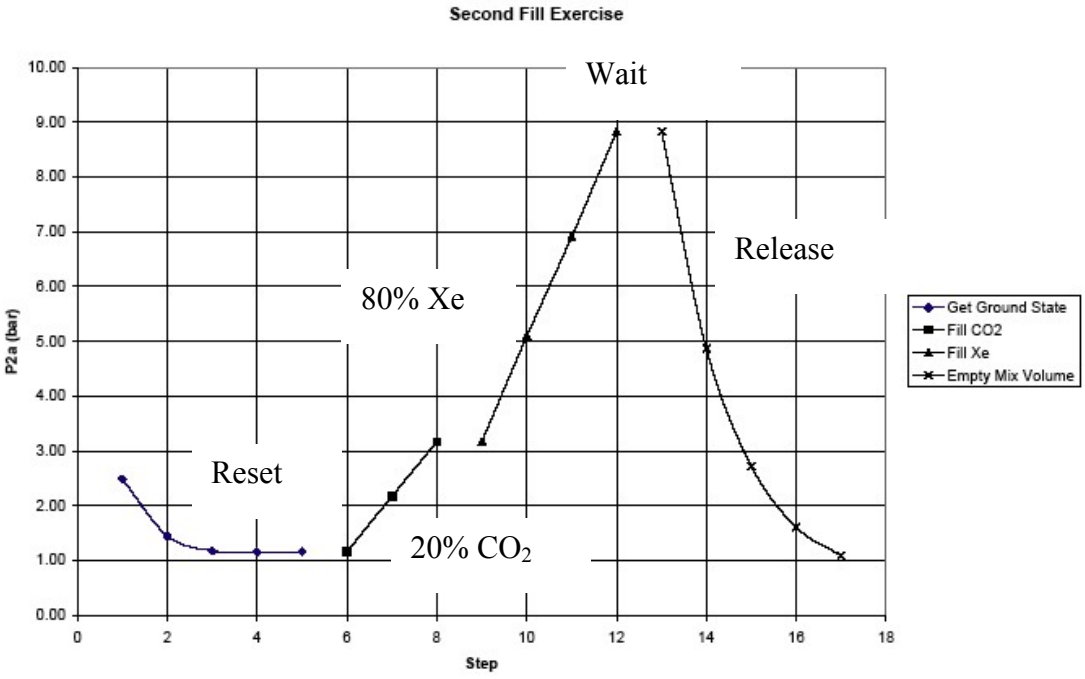

Figure 2.52: Fill cycle using electronics under computer control for Box S. Pressure measurements show the buildup of gas while mixing and then a release simulating filling.

iii) Box C Tests

The circulation system contains two circulation pumps with accompanying valves inside a steel vessel. The functioning of the pumps over the full temperature range has been tested in a cold box. They function with a slight (10%) change in current. The valves have also been tested over the entire range and are found to work down to –15 °C (Figure 2.53), well below the minimal operational temperature of 0 °C.

The monitor tube assembly has also been tested by making gain measurements with Ar:CO_2 and Xe:CO_2 (80:20). The measured gas parameters match the known values well and the monitor tube system performs reliably. The spirometer, which is used to measure the CO_2 content by measuring sound velocity, has been temperature cycled over the survival range many times and continues to work.

The engineering model of Box C has been assembled with all internal components planned for flight, Figure 2.54. A test article for the close-out welds has been made and the first weld test performed. Functional tests of the vessel have been carried out and all the internal components perform well. A first temperature cycle test of the engineering version of the vessel has been carried out successfully. As expected, the pump draws somewhat more current at low temperatures. In this test the valves continued to operate at –20 °C ambient.

iv) Manifold tests

The valves and pressure sensors have been successfully qualified over their temperature range and a manifold assembly was vibration tested at RWTH. With the addition of 1.3 mm Vacoflux shielding, they have successfully passed a functional test in the 200 G magnetic field which correspond to their operational environment.

The manifold assemblies have been tested using the engineering model of electronics controlled as for flight. Each valve in a valve set was cycled under 1 bar of argon and the pressure sensors read out after each cycle. In all cases, the valves and pressure sensors functioned as expected.

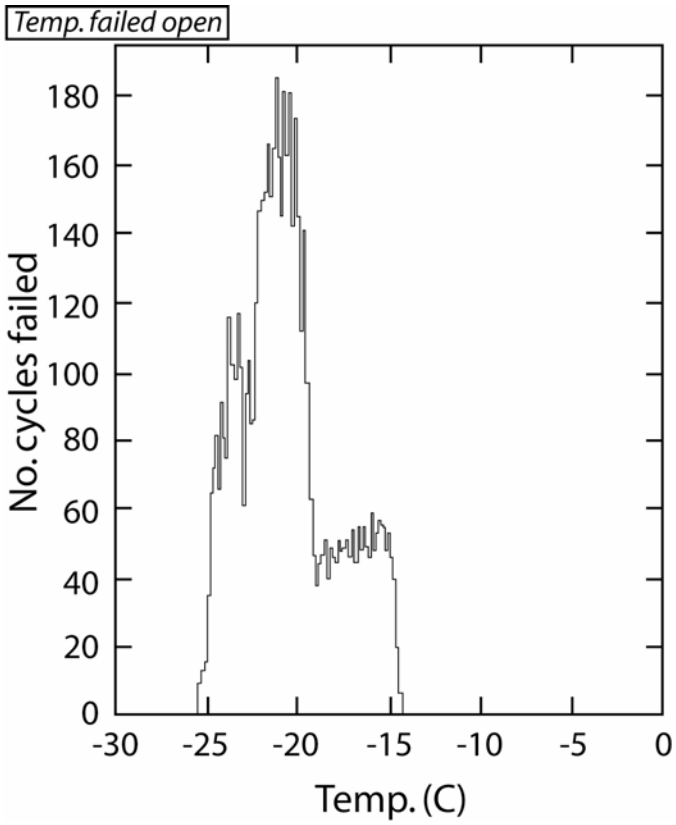

Figure 2.53: Histogram of temperatures at which the valve failed to open (minimum operating temperature is 0 °C).

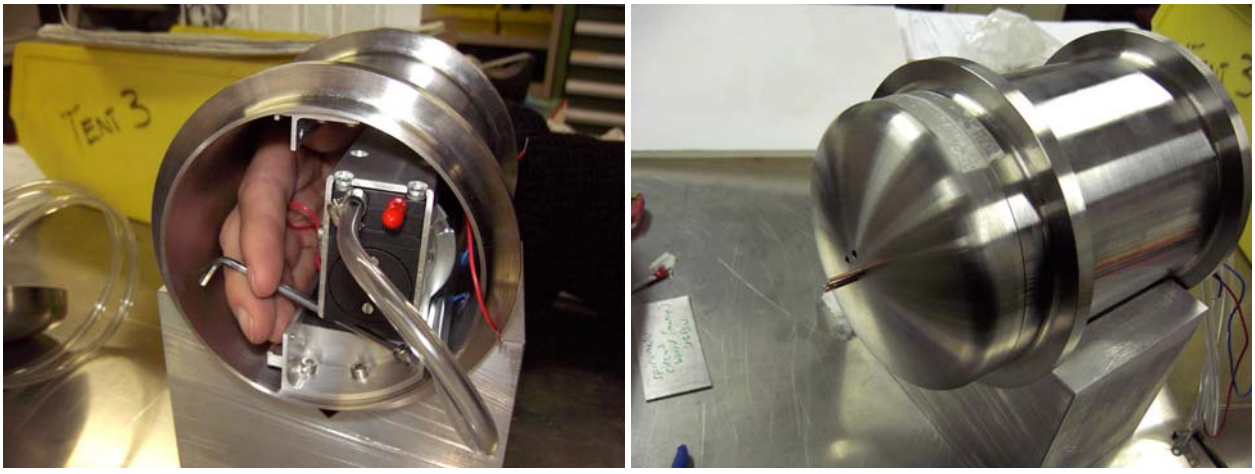

Figure 2.54: Left - Engineering model of Box C vessel with pump visible at in the opening. Right - Vessel with end cap in place and gas feedthrough.

2.2.6 TRD Prototype Performance

To verify the proton rejection power of the AMS-02 TRD design a full 20 layer prototype was built with 40 modules of 40 cm in length arranged in two adjacent towers, equipped with VA analog multiplexer based frontend electronics. In Figure 2.55 the gas panel supplying six chains can also be seen.

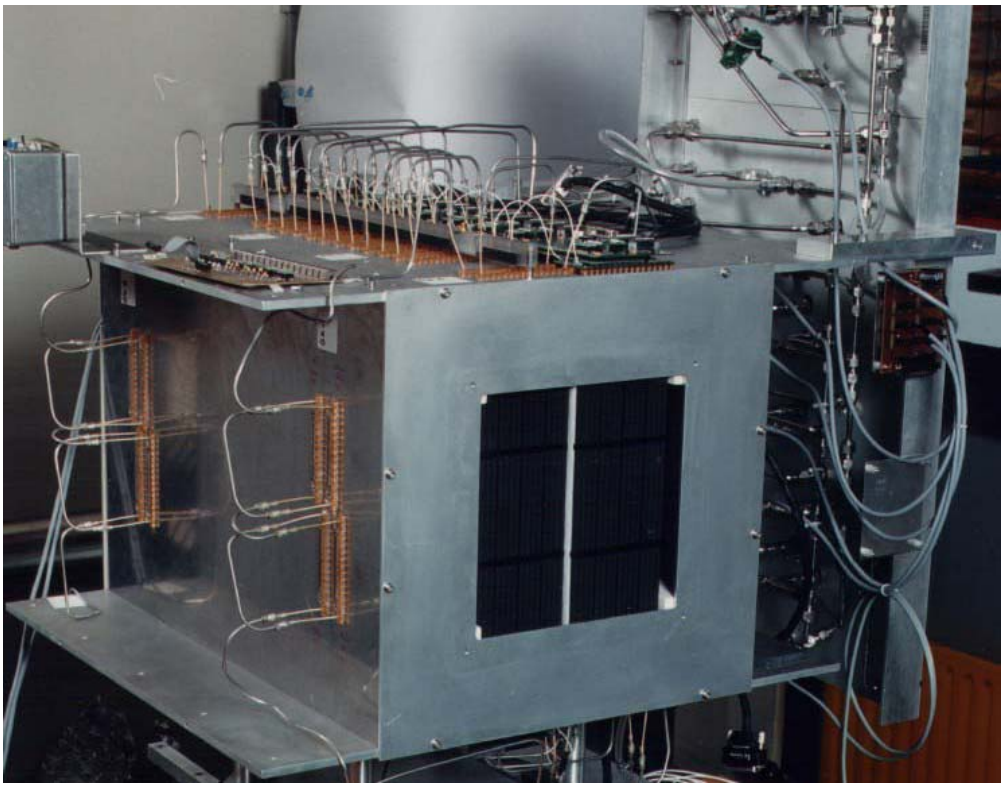

Figure 2.55: AMS-02 TRD 20 layer prototype.

This setup was used in the CERN T9, X7 and H6 beam lines to record 3 million tracks [13]. The particle trigger with scintillator panels and threshold or differential Cerenkov counters allowed the selection of electrons, muons and pions up to 100 GeV and protons up to 250 GeV. The data preprocessing verified the low noise level with pedestal widths below 2 ADC channels and an inter-calibration precision below 2% achievable with 5000 tracks. The gas gain-density correlation at 1470 V (gas gain 5000) was determined to be $\Delta G/G = -5.5\ \Delta\rho/\rho$. The absolute energy scale was calibrated with an ^{55}Fe source.

MC simulation studies are used to optimize the detector design. They are based on the proven Geant3 [14] detector simulation package with additional code [15] to include TR photon generation and absorption [16] and to improve the simulation of dE/dX Landau-fluctuations in thin gas layers [17]. The test beam data are used to tune the MC parameters to describe our detector response. Figure 2.56 shows the energy spectra measured for all wires in isolated single track events. The proton spectrum shows the expected Landau fluctuations. For electrons an enhancement due to the transition radiation component is clearly visible above 6 keV.

To analyze the test beam results, protons are separated from electrons with a likelihood algorithm. The energy spectra in Figure 2.56 are used as probability densities $p(E)$. With each energy deposit E_i in n tubes on the reconstructed track, normalized probability products are defined as $P_{e,p} = \sqrt[n]{\prod_1^n p_{e,p}(E_i)}$.

With a likelihood defined as: $L = P_e/(P_e + P_p)$ the proton rejection factor is determined as the inverse proton selection efficiency with a likelihood cut set for an electron efficiency of 90%. For proton beam energies between 15 and 250 GeV the proton rejection is well above 100 as shown in Figure 2.57.

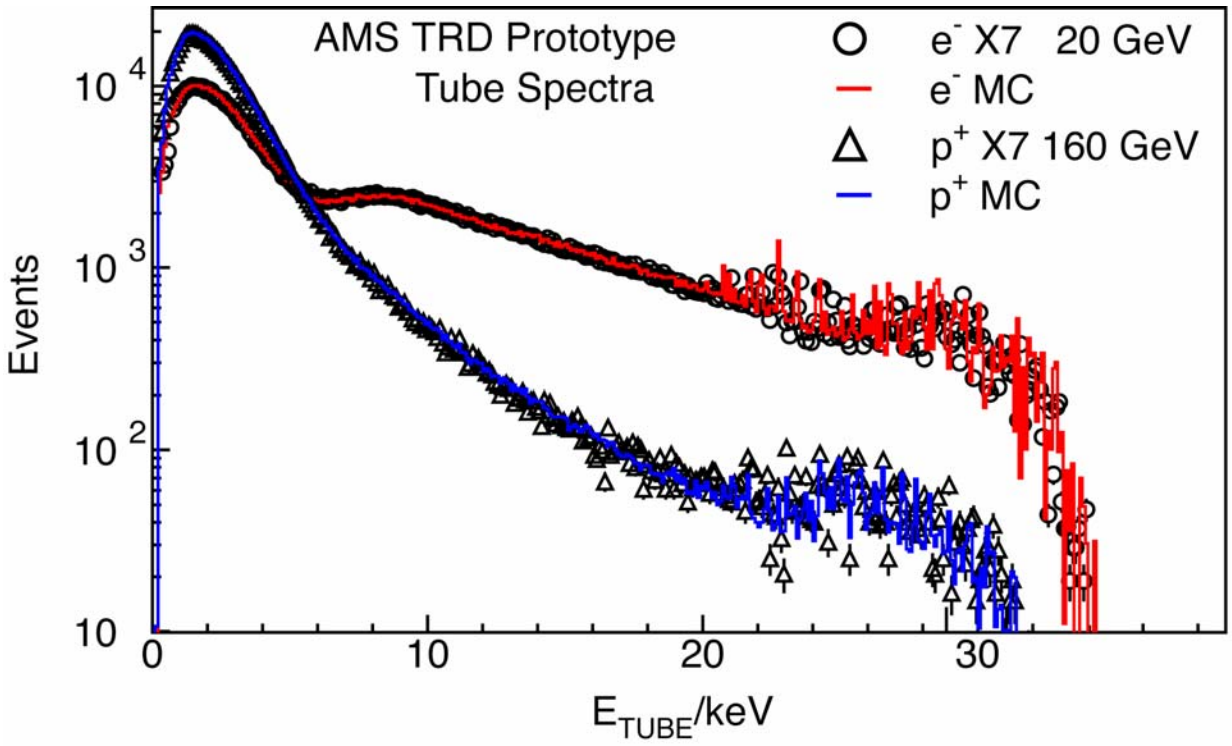

Figure 2.56: Clean single track energy spectra.

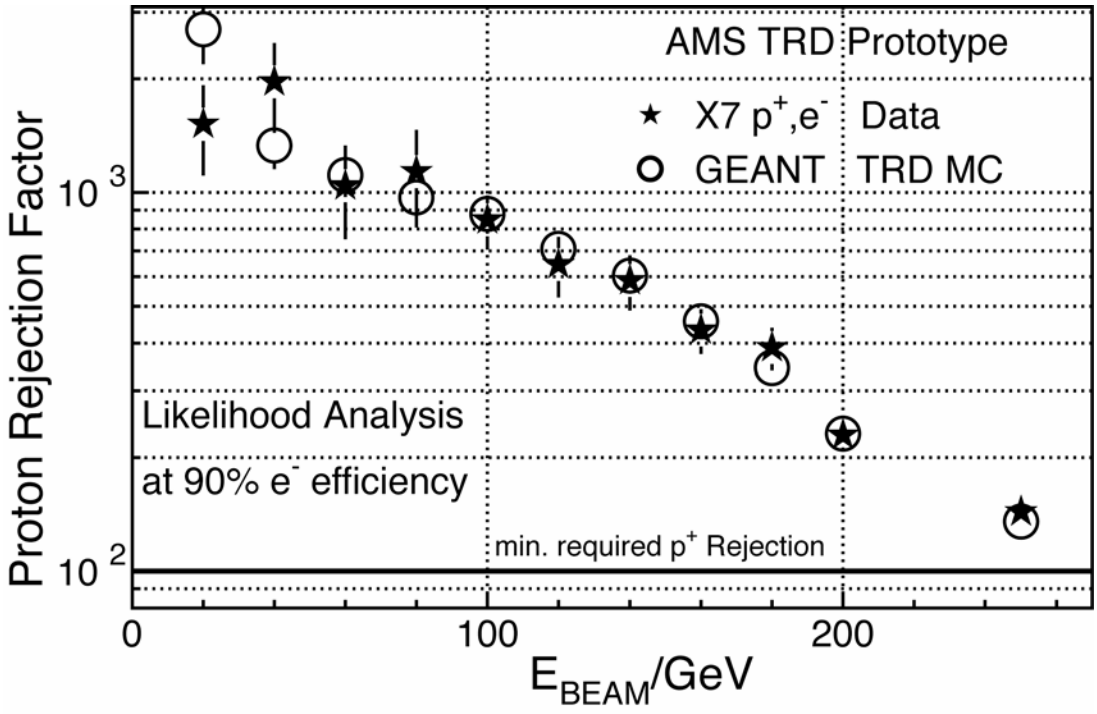

Figure 2.57: AMS-02 TRD proton rejection.

2.2.7 References

[1] I. Frank, V. Ginzburg, J. Phys. **9** (1945) 353.

[2] ATLAS TDR 5, Vol.2, CERN/LHCC/97-17.

[3] HERA-B, DESY-PRC 00/04, 2000.

[4] "AMS-02 Structural Verification Plan", JSC-28792, Rev. C.

[5] *Space Qualification of the AMS-02 Transition Radiation Detector,* to be submitted to NIM A.

[6] R. Bock *et al.*, NIM A **336** (1993) 128.

[7] *Construction of Straw Detector Modules for the AMS-02 Transition Radiation Detector*, to be submitted to NIM A.

[8] Th. Kirn *et al., Status of AMS-TRD-Straw modules*, Conf. Proc. TRDs for the 3rd millennium, Bari 2003, sub. NIM A.

[9] Th. Kirn *et al.*, Frascati Physics Series Vol. **XXV** (2001), 161-172.

[10] F. Hauler, *The AMS-02 Transition Radiation Detector for the International Space Station*, Conf. Proc. IEEE NSS 2003, sub. IEEE NS.

[11] A.Bartoloni, *The AMS-02 TRD gas Control System;* NIM A**518** (2003) 143.

[12] C.Gargiulo *et al.*, *The Mechanical Design of a Gas Supply and Mixing System for AMS-02;* Proc. IAC-03-J.P. 11; 54th Int. Astronautica Conf. September 2003, Bremen, Germany.

[13] *Performance of the AMS-02 Transition Radiation Detector*, to be submitted to NIM A.

[14] R. Brun *et al*., GEANT. CERN DD/EE/84-1 (Geant 3.21 Revised 1987).

[15] V. Egorytchev, V. Saveliev, S.J. Aplin, Nucl. Instr. and Meth. A **453** (2000) 346.

[16] M. Cherry, Phys. Rev. D **10** (1974) 3594.

[17] V. Ermilova *et al.,* NIM A **145** (1977) 555.

2.3 Silicon Tracker

The AMS-01 Silicon Tracker [1] was the first application in space of the high precision silicon technology developed for position measurements in accelerator experiments [2]. The high modularity, low voltage levels (<100 V), and gas-free operation of the device is well suited to operation in space. The 1998 shuttle test flight demonstrated both the successful adaptation of the technology to the space environment and the feasibility of large area detectors.

The AMS-02 Silicon Tracker design and construction is under the overall responsibility of INFN-Perugia. The assembly of the silicon ladders, which represents a substantial part of the construction effort, is performed at INFN-Perugia, University of Geneva and at an Italian industrial research facility[1] operating under an ASI contract. Personnel of the University of Bucharest and of ISS-Bucharest contributed to the silicon ladder assembly. The Tracker mechanical support as well as the Tracker laser alignment system are designed and built by Aachen. The DAQ electronics and power systems were developed at the University of Geneva and INFN-Perugia in collaboration with MIT and CSIST and will be fabricated at CSIST. The online data reduction software is developed at Monpellier. The Tracker Thermal Control System is designed and built by NLR in collaboration with the University of Geneva, Sun Yat-sen University, Guangzhou, and INFN-Perugia.

Silicon micro-strip sensors were originally developed for vertex detectors in colliding-beam experiments in order to provide a few high precision position measurements near the interaction point. The AMS application differs considerably. The tracking information is provided uniquely by the silicon sensors, which implies a large surface area and higher inter-strip capacitances. The major challenges were to maintain the required mechanical precision and low-noise performance in the large scale application, and to do so in outer space.

2.3.1 Silicon Sensors

The silicon tracker is composed of 41.360 x 72.045 x 0.300 mm^3 double-sided silicon micro-strip sensors. The n-type, high resistivity (> 6 kΩ) sensors are biased with the punch-through technique and p^+ blocking strips, implanted on the n-side, are used to minimize the influence of surface charge on the position measurement obtained from the ohmic side [3]. The sensor design uses capacitive charge coupling [4] with implantation (readout) strip pitches of 27.5 (110) μm for the p-side and 104 (208) μm for the n-side. The finer pitch p-side strips are used to measure the bending, or *y*, coordinate and the orthogonal n-side strips measure *x*. Figure 2.58 shows the sensor layout.

The ionization loss of singly charged particles traversing the fully depleted, reverse-biased 300±10 μm thick sensor is described by a Landau distribution [5]. The peak energy loss of a singly-charged, minimum ionizing particle at normal incidence produces 22,000 electron-hole pairs. The opposite sign +/- charge carriers drift rapidly (10-25 ns) in the electric field to the two surfaces (p/n) where the accumulated charge on the metalized strips (p^+/n^+) is fed to the front-end electronics. The position of the particle is determined by the relative signal levels observed at the readout strip positions. At the single sensor level, the position resolution depends on the sampling pitch and the signal-to-noise performance.

[1] G&A Engineering; Localita' Miole; I-67063 Oricola.

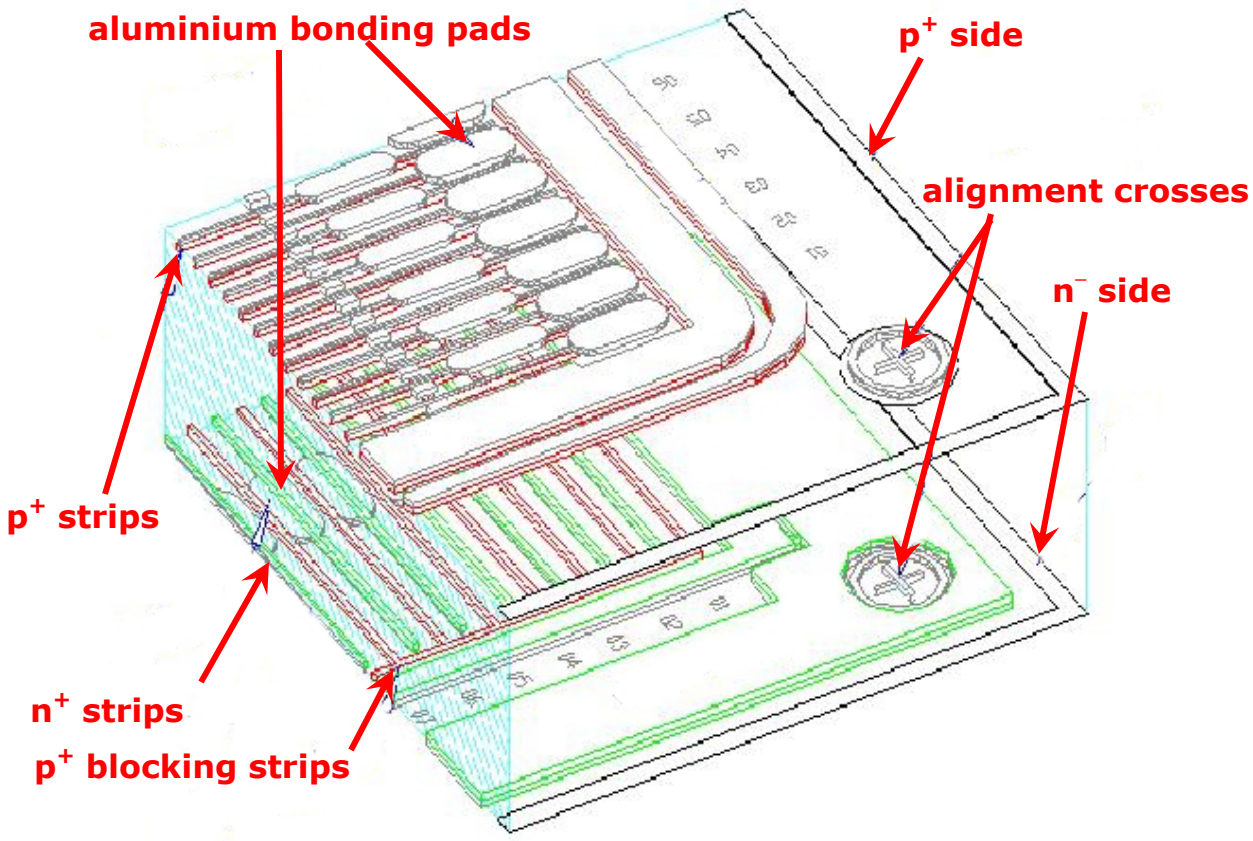

Figure 2.58: Layout of the double-sided silicon micro-strip sensor.

The sensors have been produced at silicon foundries located in Switzerland[2] and Italy[3] using identical geometries and processing procedures. Over 4000 sensors have been produced to select the ~ 2500 sensors of the very high quality required to assemble the Silicon Tracker units (ladders). All the sensors were tested both at the foundry as well as at INFN-Perugia and the Italian industrial facility to ensure that electrical parameters were within space qualification specifications and that the number of noisy strips was less than 0.06%. Over 2 x 10^7 electrical measurements have been performed using four automatic test stations. The data were stored in a database and used to select the silicon detectors to be used in assembling the Tracker. The long term electrical stability of the silicon detectors was studied at the Moscow State University. This large number of sensors makes the Silicon Tracker the largest precision tracking detector ever built for a space application.

2.3.2 Ladders

Figure 2.59 shows the principal elements of the silicon ladder and the main components of the readout hybrids. Thin-film, 50 µm Upilex is used extensively in the ladder [6]. A metalized Upilex film, glued directly to the silicon sensors, serves as a routing cable to bring the n-side signals to the n-side front end hybrid, which is located at the ladder end closest to the magnet wall. The flexible Upilex film and a second short Upilex film joining the p-side strips to their hybrid allow the hybrids to be placed back-to-back, perpendicular to the detection plane, thus minimizing the material in the sensitive region of the

[2] Colibrys SA ; Maladière 83, CH-2007 Neuchâtel.
[3] ITC-irst; Via Sommarive 18; I-38050 Povo.

tracker. Finally, an electromagnetic shield in the form of a doubly-metalized Upilex film surrounds each ladder.

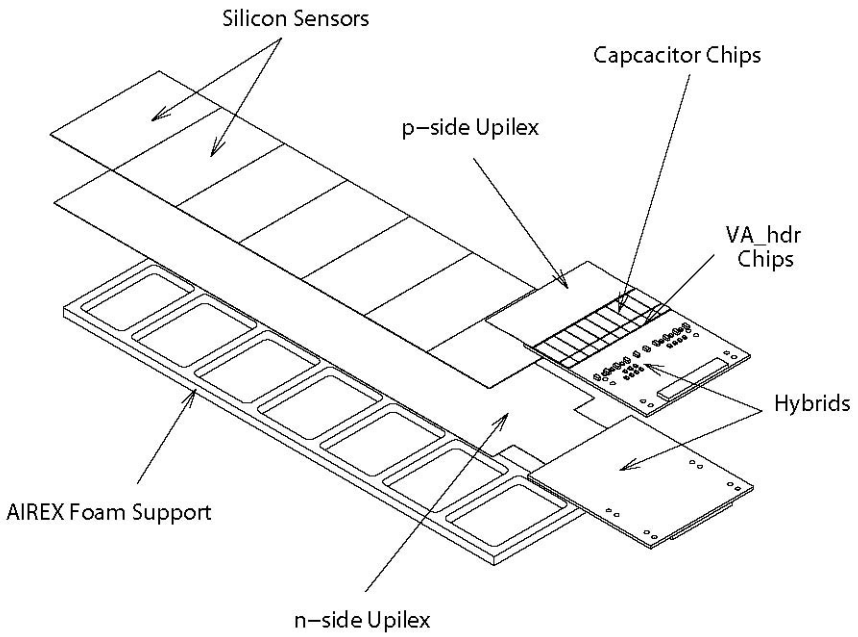

Figure 2.59: The principal components of the silicon ladder.

The silicon sensors of each ladder are supported by a 5 mm thick Airex[4] foam that is glued to the n-side Upilex film. The exposed surface of the foam is covered with a 100 μm thick layer of carbon fiber. Small 5 mm^3 aluminum frames are glued to the carbon fiber surface; the exact number depends on the ladder length. The aluminum frames contain a screw fixation hole which is used to attach the ladder to its tracker plane.

The principal goals of the ladder fabrication are to guarantee the required precision for the relative alignment of the silicon sensors (<5μm), and minimize the degradation of the electrical performance due to handling and ultra-sonic bonding. Ladder fabrication was organized between three centers operating with identical procedures derived from the AMS-01 [7] and located at INFN-Perugia (in collaboration with the University of Bucharest), the University of Geneva (in collaboration with ETH-Zürich), and the Italian industrial research center operating under an ASI contract. These centers used state of the art facilities in class 10.000 clean rooms and following strict quality control procedures. The silicon sensors were cut with a mechanical accuracy of < 5 μm (rms) at a facility in Finland [5] operated under contract to the University of Turku.

The alignment precision is provided by the mechanical precision of the jigs (1-2 μm) and the precision of the sensor cut (< 5 μm). During fabrication the sensor positions on a ladder are recorded with a 3D semiautomatic measuring machine. The results for the sensor alignment for 125 (of 192) AMS-02 ladders are shown in Figure 2.60. A particular effort has been made to maintain the low noise by passivation of the silicon and by optimization of the ladder assembly procedure.

[4] Airex R82; Alcan Airex AG Specialty Foams; CH-5643 Sins.
[5] Selmic Oy; Lumikontie 1; 94600 Kemi, Finland.

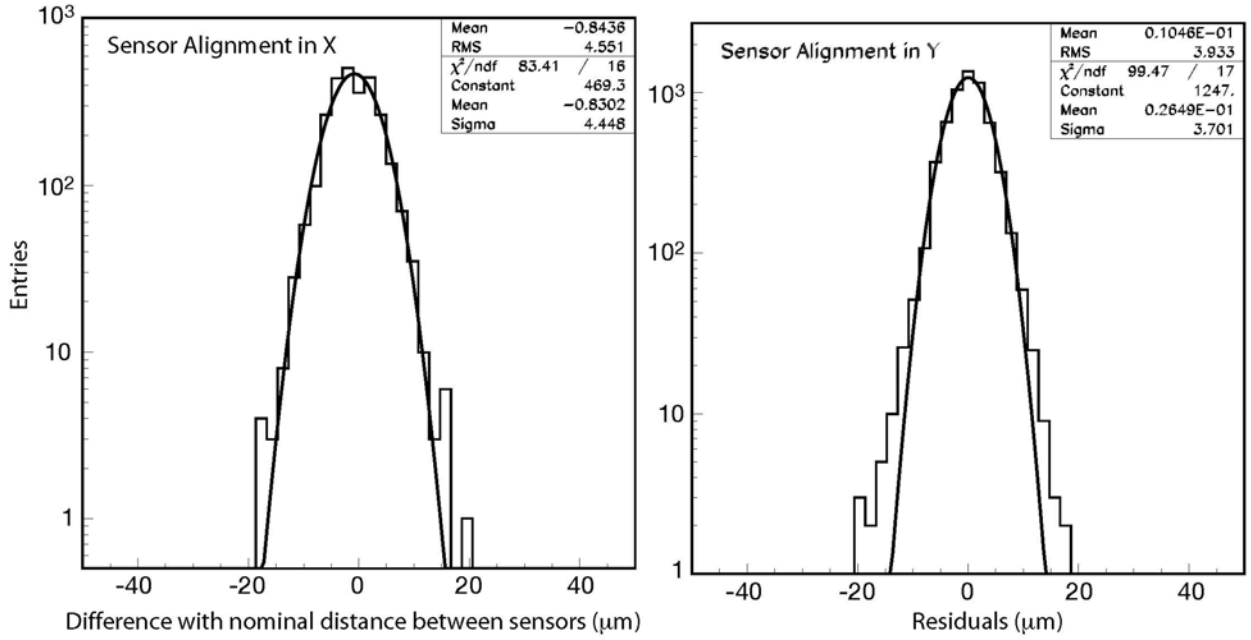

Figure 2.60: Assembly precision of 125 AMS-02 ladders: distribution of the measured differences of the distance between adjacent sensors and the nominal distance, 640 μm including a 40 μm gap between sensors (left), and the residual distribution of the sensor positions about the line fits defining the ladder axis parallel to the magnetic field (right).

2.3.3 Tracker Support Structure

The tracker support structure, developed by RWTH-Aachen, is divided into three sections: a carbon fiber cylindrical shell which supports the planes 2 to 4 located inside the magnet, and two carbon fiber flanges which support the exterior planes 1 and 5. With respect to the AMS-01 configuration, the number of silicon layers has been increased from 6 to 8 by suppressing one internal plane and equipping both sides of the remaining three internal planes with silicon ladders.

The tracker planes located inside (outside) the magnet are the same as those used for AMS-01, produced under contact to ETH- Zürich[6]. They have a composite structure with two 220 (700) μm thick layers of carbon fiber surrounding a 12 (40) mm thick, low density aluminum honeycomb interior, $\rho = 16.02\ (32.0)\ kg/m^3$. The diameter of the interior (exterior) planes is 1.0 (1.4) m. The AMS-01 interior planes have been modified to accommodate the second layer of ladders; the latter increases the material thickness of an interior plane to 1% of a radiation length at normal incidence. In view of the marginal increase of the plane hermeticity, and the very significant complication of the mechanical design, there is no overlap between the ladders in the planes of the tracker.

When ladders equipping a full tracker plane are produced, they are integrated onto the corresponding support plane. Supervision, quality control and traceability are ensured by a database developed for that purpose. The activities start with acceptance tests of the ladders arriving from all production lines and then proceed in steps toward integration of the complete detector.

The first step is the completion of the ladder itself with support feet, hybrid cover and electromagnetic shielding. Figure 2.61 shows two ladders at the end of this operation, ready to be installed on a support plane.

[6] Oerlikon Contraves; Birchstrasse 155; CH-8050 Zürich.

Tracker assembly and cabling operations then start by mounting ladders onto the support planes. The bare honeycomb plane is first installed on an assembly jig which allows rotation of the plane and easy access to both sides. The thermal bar assemblies are then installed. Their mechanical compatibility with the cooling loop interface is tested. The first side can then be equipped with ladders. Installation of the second layer on the other side is more delicate since one has access from only one side for fixation. A strict sequence of assembly and tests must therefore be followed to ensure that no inaccessible ladder has to be changed. The assembled plane is finally stored in a light-tight container under dry nitrogen.

Figure 2.62 shows the first two fully equipped inner planes. A complete series of electrical tests has been completed for both planes; ladder quality did not degrade during integration.

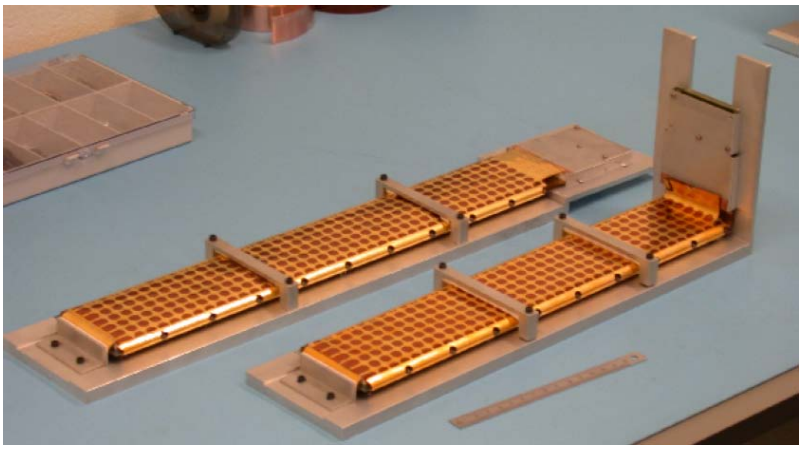

Figure 2.61: Two AMS-02 ladders ready to be mounted on the support plane.

Figure 2.62: Plane numbers 2 (above) and 3 (below) completely equipped with ladders.

2.3.4 Electronics

The silicon sensors are grouped together, for readout and biasing, in ladders of different lengths to match the cylindrical geometry of the AMS magnet. The maximum combined strip length in the silicon for a single readout channel is 60 cm. The relatively large input capacitance (30-180 pF), as well as the need for a high dynamic range (<100 MIPs), led to the development of a new front-end readout chip based on the low-noise Viking design [8], the VA_hdr[7] [9]. As for the ladders and support structure, the tracker electronics is an upgraded and updated version of the circuits developed for AMS-01 [10].

Each of the 64 channels of the VA_hdr chip consists of a charge sensitive amplifier, a CR-RC semi-Gaussian shaper, and a sample-and-hold stage. An analog multiplexer, shift register and buffer are incorporated in the chip for sequential data output at a maximum clock frequency of 10 MHz. The equivalent noise charge as a function of capacitance load C_{det} has been measured to be $(350+4C_{det}/pF)$ e^- at a 6 μs peaking time and nominal bias currents. The VA_hdr chips are operated at a lower bias current resulting in a peaking time of 3-4 μs and average power consumption 0.7 mW per channel. The single channel response of the VA_hdr chip has been measured to be linear up to ~75 MIPs. The strips of the silicon sensors are ac-coupled to the VA_hdr via 700 pF capacitor chips[8]. Both the VA_hdr chips and the capacitor chips are housed on the Tracker Front End board (TFE) that also contains a resistor network to furnish the VA_hdr operating currents, a receiver chip for digital control signals and a low power analog amplifier for the current-to-voltage conversion.

The readout and power distribution system of the tracker detector is composed of a total of 232 boards divided into 8 sections. Each section takes its power from an independent 28 V line coming from the Power Distribution System (PDS) and provides the readout, data compression and power supplies for 24 silicon sensor ladders. As shown in Figure 2.63, each section is composed of readout crate (T-Crate) and a power conversion and distribution unit (TPD). The T-Crate hosts the 12 readout and data reduction boards (TDR2, each containing two TDR circuits), the linear post-regulator boards (4 TPSFE, 2 TBS) and the interface to the slow control and the higher level of the DAQ chain (JINF). The TPD contains an input filter (S9011B[9]), a slow control interface (S9011AT) and 8 dual DC-DC converters for the generation of the different voltages needed to operate the detector system, of three types (S9051, S9053, S9055). The high performance DC-DC converters were custom developed after an extensive investigation and provide high efficiency and very low noise to meet the system requirements.

In the readout crate, in addition to the JINF, there are three types of cards:

- Four TPSFE, which regulate the S9051 outputs to provide a stabilized and filtered ±2.1 V for powering the front-end circuits on the TFE attached to six ladders. The status of each linear regulator (12 per TPSFE) can be monitored and controlled via commands on the LeCroy bus. Over current protection is implemented in burp mode: the linear regulator tries to recover automatically after the current limit is passed.

- Two TBS, which produce the bias for the silicon detectors and the ground levels for the n-side front-end electronics. The default value of the bias voltage is 80 V, matching the value measured on the bare silicon wafers. A lower value of 60 V can be set in order to accommodate ladders with different bias characteristics. The linear regulators of the card have a 500 μA current limit (fold back mode), one for each side (p or n) of six ladders. In order to monitor the dark current of each ladder, a current measuring system of each bias line is also implemented, with interface to the slow control system.

- Twelve TDR2 cards each containing two TDR circuits. The TDR performs the digitization, calibration and data reduction for one ladder. Figure 2.64 shows a schematic view of the readout with the lines connected to a TFE pair on the left and JINF and power systems on the right.

[7] IDE AS; Veritasveien 9; N-1323 Hovik.
[8] Colibrys SA ; Maladière 83, CH-2007 Neuchâtel.
[9] Part numbers like S90nnxyz refer to designs from CAEN Aerospace; via Vetraia 11; I-55049 Viareggio.

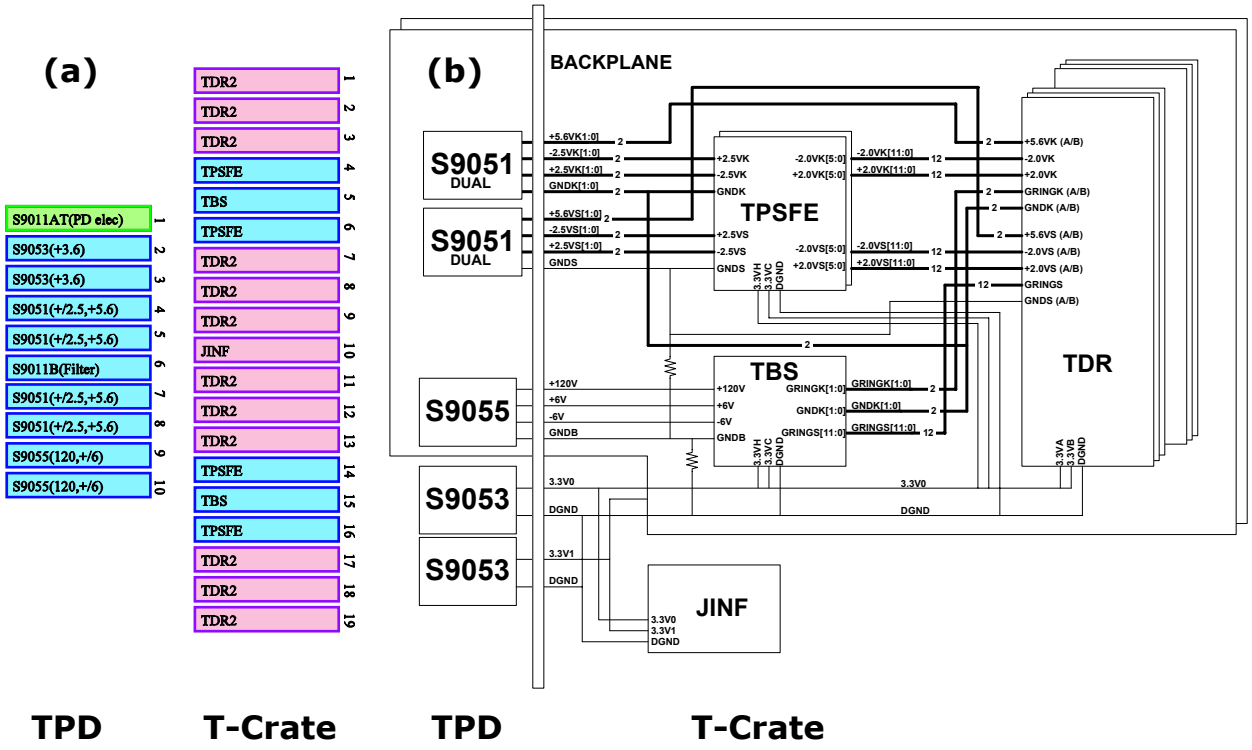

Figure 2.63: Layout of boards in TPD and Tracker Crates (a), Tracker power scheme (b).

One half of a TDR2 board is pictured in Figure 2.65. Each p-side (n-side) TFE is connected to a TDR through a 21 (19) line quasi-coaxial cable with a mean length of 2.5 meters[10]. Digitization is performed on the TDR with a 12-bit, 5 MHz analog-to-digital converter (ADC, ADS803E) that is coupled through a set of digital isolators (ADuM1100B) to a Common Digital Part (CDP), described in § 2.8 and composed by a data buffer, a programmable gate array chip, which controls the VA_hdr chips and the data buffer, and a Digital Signal Processor (DSP) for calibration and data reduction. The reduction algorithm is based one used in AMS-01 and achieves the required average compression ratio of 600 at rates above 3 KHz.

The DC-DC converters contained in the TPD are described in Table 2.3. In addition, the box contains a S9011AT module to control and monitor the DC-DC converters and interface to the JINF and an S9011B input/output common and differential mode filter qualified to work in magnetic fields up to 500 G. The S9053, S9055 and S9011AT are operated in cold redundancy.

Qty	Module	Voltages	Load	Ripple (<20 Mhz)	Regulation	Efficiency
4	S9051	±2.5, 5.6	TDR2 analog and front end	< 15 mVpp	Cross: < 5%	78%
2	S9053	+3.4	Crate digital	< 20 mVpp	Load: 4%	79%
2	S9055	+120, ±6	Silicon bias	< 20 mVpp	Cross: 1% on 120V	n/a

Table 2.3: TPD DC-DC converter properties.

[10] G&A Engineering; Localita' Miole; I-67063 Oricola.

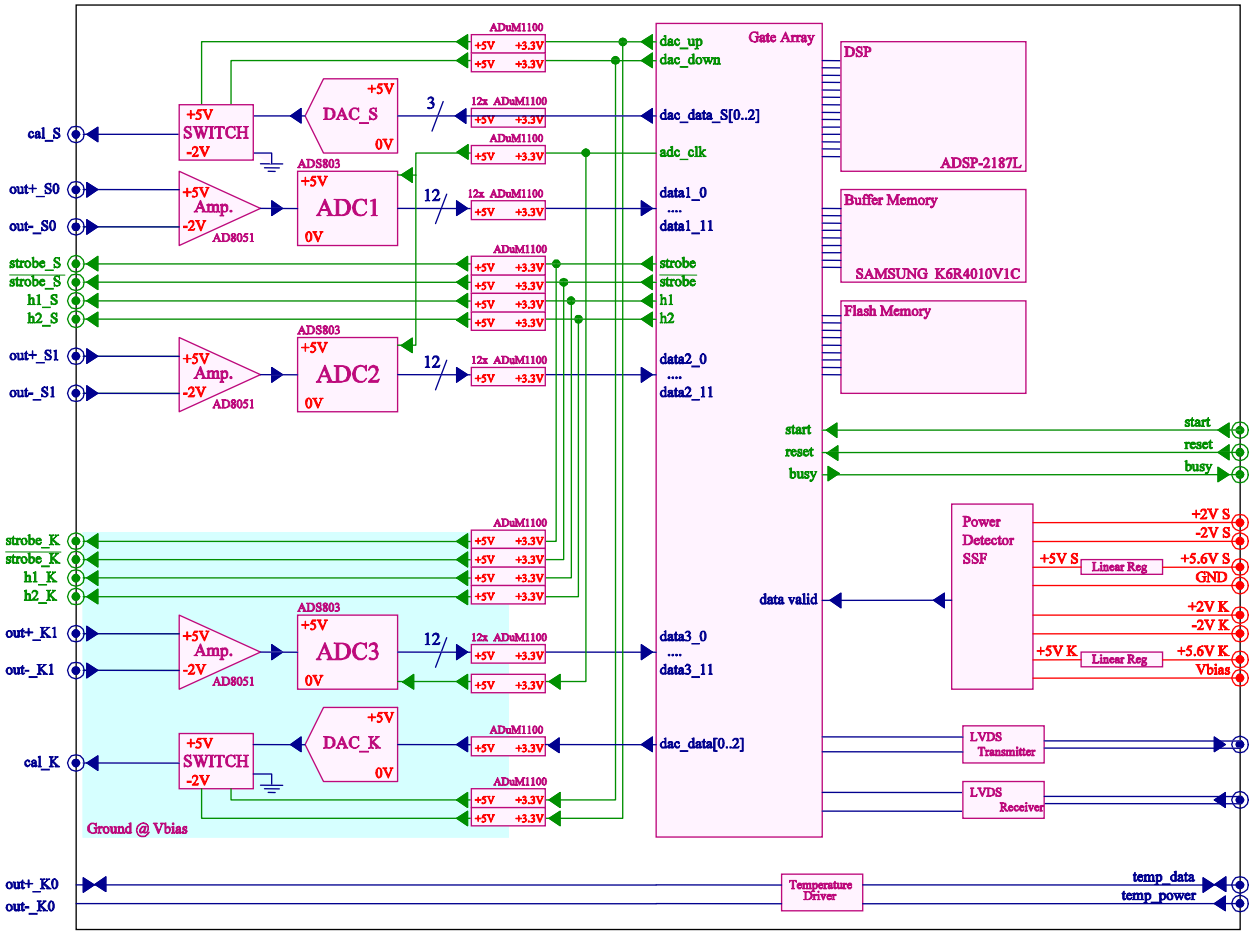

Figure 2.64: Schematic of the TDR (Tracker Data Reduction) circuit.

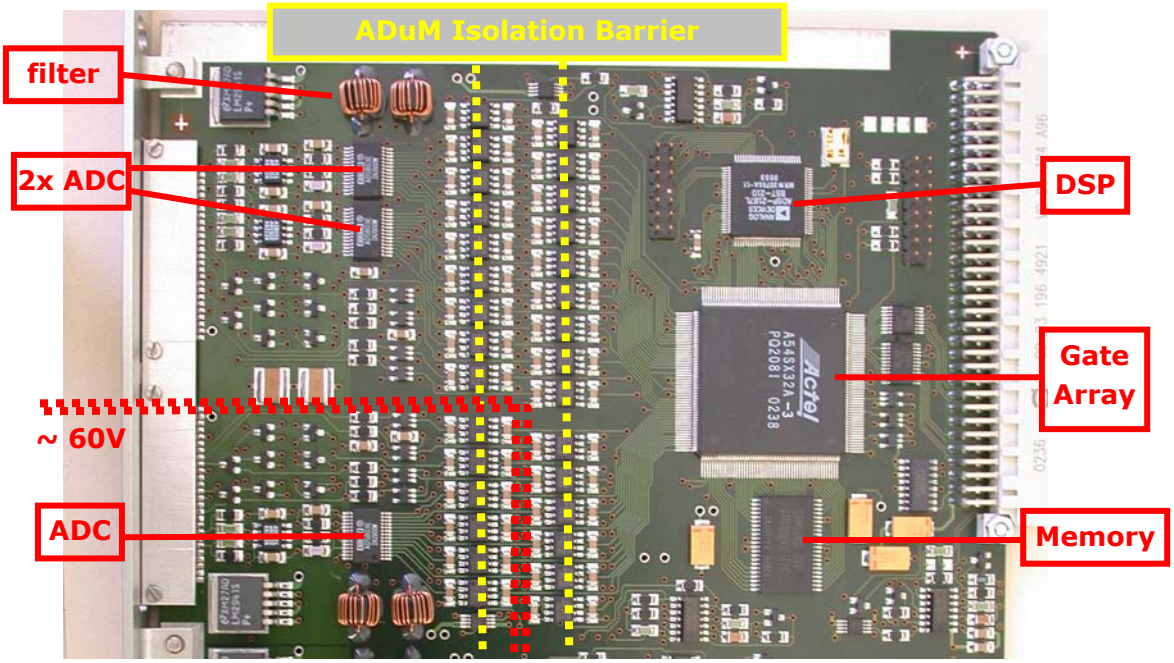

Figure 2.65: One half of a flight quality TDR2 board.

2.3.5 Tracker Thermal Control System

The hybrids are mounted on carbon fiber-metal cooling bars, which evacuate the heat generated by the front-end electronics inside the magnet. The presence of the superconducting magnet requires an active cooling system for the tracker.

The AMS-02 Tracker Thermal Control System (TTCS), developed by NLR in collaboration with the University of Geneva, NIKHEF, Sun Yat-sen University and INFN-Perugia, is schematically shown in Figure 2.66, and the locations of the principal elements in Figure 2.67. It is a two-phase, mechanically pumped loop system. The cooling liquid, CO_2 at about 80 bar pressure, is circulated by a pump. It enters into the tracker volume at a temperature just below the boiling point, as controlled by pre-heaters, and passes by thermal bars on the outer and outermost inner planes, where the heat from front-end hybrids is collected in series. At each heat input, a small fraction of the liquid is evaporated. By the last hybrid up to 30% of the fluid has been vaporized. The evaporator circuit is split into upper and lower loops to cool the upper and lower layers of the tracker. In this manner, the tracker volume is isothermally cooled and the cooling hardware located in the tracker volume minimized.

Outside of the tracker volume, the fluid passes through a heat exchanger to keep the incoming fluid just at the boiling point while minimizing the pre-heater power required. It is then directed to condensers on the tracker thermal wake and ram radiator panels facing deep space. There, the vapor/liquid mixture is cooled to below the boiling point, and then returns to the pump input, closing the circuit. Ammonia heat pipes embedded in the radiators increase their effectiveness. The relative flow of fluid to the wake and ram radiators is self-adjusting, the fluid will preferentially flow towards the cooler radiator.

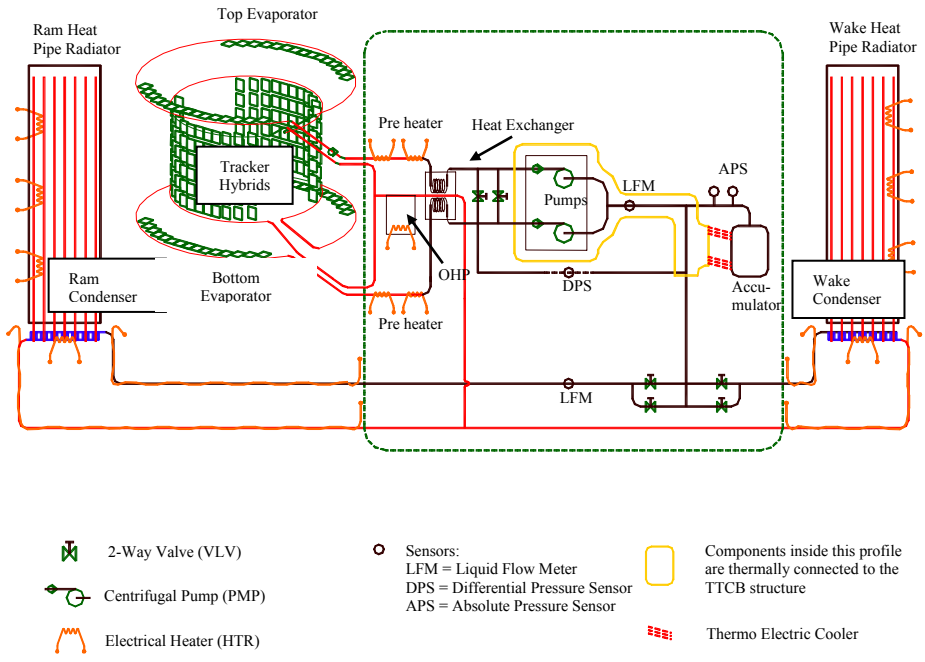

Figure 2.66: Schematic of the primary Tracker Thermal Control System loop.

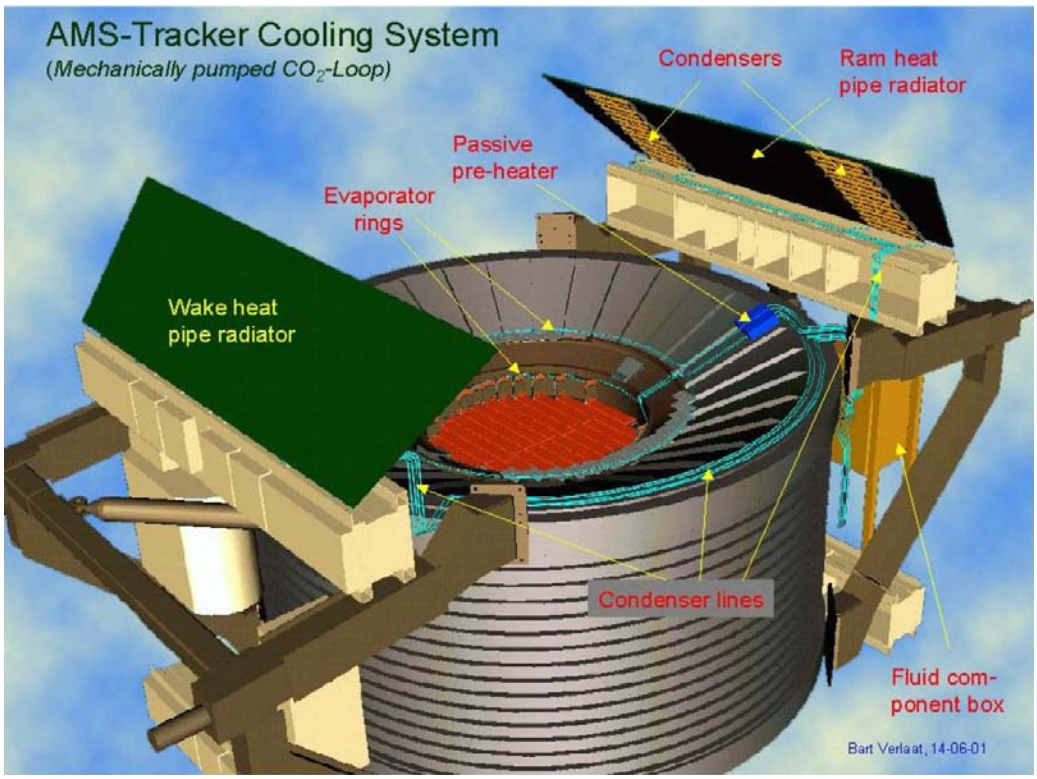

Figure 2.67: Locations of the principal elements of the Tracker Thermal Control System.

To adjust the temperature set point of the system, an accumulator regulated by a thermo-electric (Peltier) element controls the amount of CO_2 in the loop. The accumulator is also equipped with override heaters to prevent cavitation in the pump. The system is implemented with a series of control valves, flow meters and temperature and pressure monitors to optimize the operation. Typical flow rates are 2 g/s with a set point of 0 °C.

For redundancy there are two hydro-dynamically separate loops - the primary loop and the secondary. Loop elements (pumps, etc.) are mounted correspondingly in boxes (TTCB-P,-S) on the port and starboard USS members.

In this system, the pump is clearly a critical element. Each loop is equipped with two redundant pumps. The candidate pump for the system is an adapted version of that used for the NASA Mars missions (Pathfinder, etc.)[11].

Figure 2.68 shows the details of the evaporator layout within the tracker volume and Figure 2.69 shows a prototype of the evaporator loop and thermal connections to the thermal bars and hybrids. The inner diameter of the evaporator is 2.6 mm and the total loop length is 10 m. Heat collected at the inner tracker planes is transported by thermal bars to the top and bottom inner evaporator rings.

The heat exchanger reduces the amount of pre-heater power required. The effect of the heat exchanger (HX) was calculated using a SINDA-FLUINT thermo-hydraulic model[12], including the two-phase flow in the plumbing and using environmental heat fluxes as boundaries conditions. The design is shown in Figure 2.70 and a protoflight version in Figure 2.71. It is a plate type heat exchanger with two cold passages for the sub-cooled branches and one hot passage for the evaporator outlet. This plate heat exchanger design meets the requirements of high pressure (160 bar), low-pressure drop, leak tightness and easy modification to add more plates and adjust the plate design based on test results. The contribution of

[11] Pacific Design Technologies, Inc.; 72 Santa Felicia Drive; Goleta, CA 93117.
[12] Cullimore & Ring Technologies, Inc.; Littleton, CO.

the heat exchanger to the overall system pressure head is negligible; ~5 mbar at the two-phase side and 1 mbar on the liquid side. First tests with the heat exchanger show a better performance than predicted by the model further reducing the required pre-heater power.

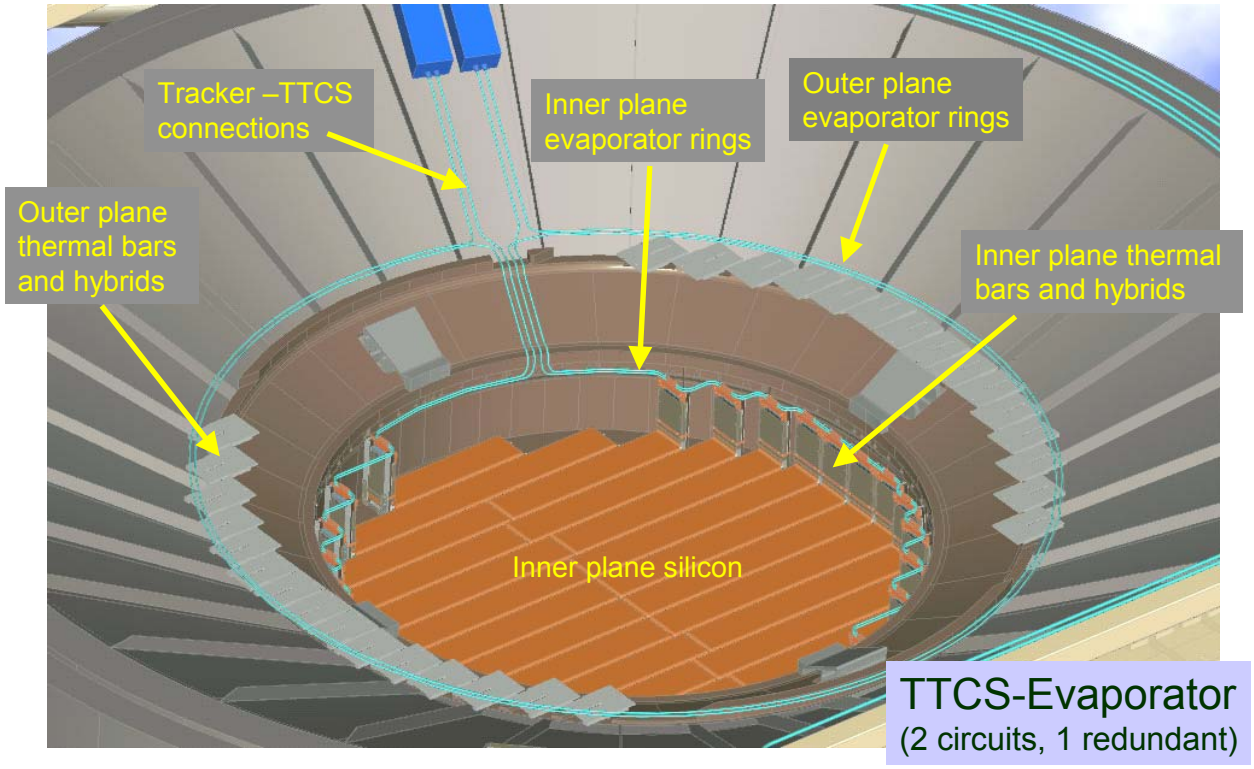

Figure 2.68: Evaporator installation details.

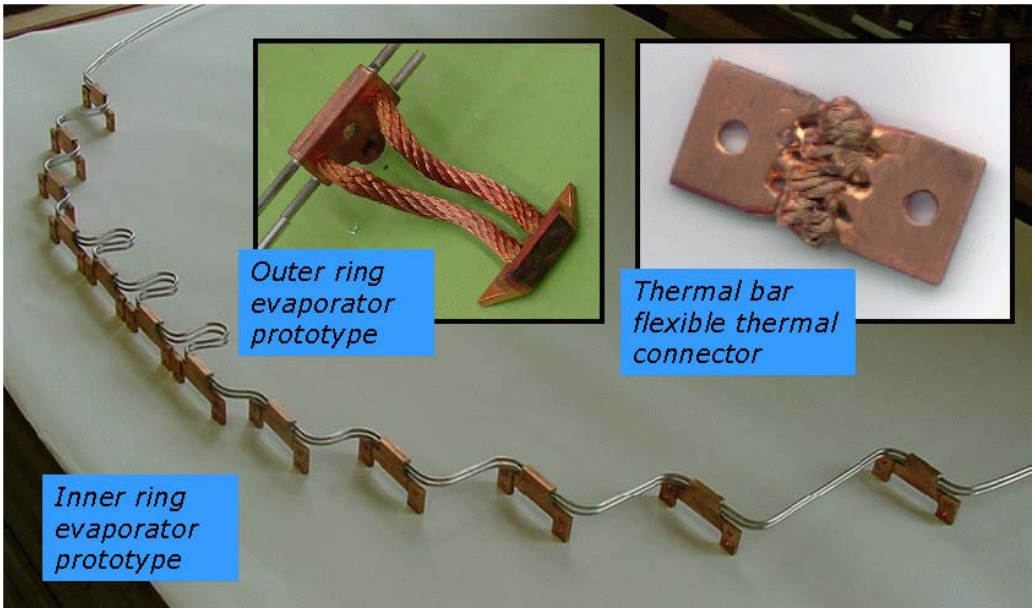

Figure 2.69: Evaporator prototypes.

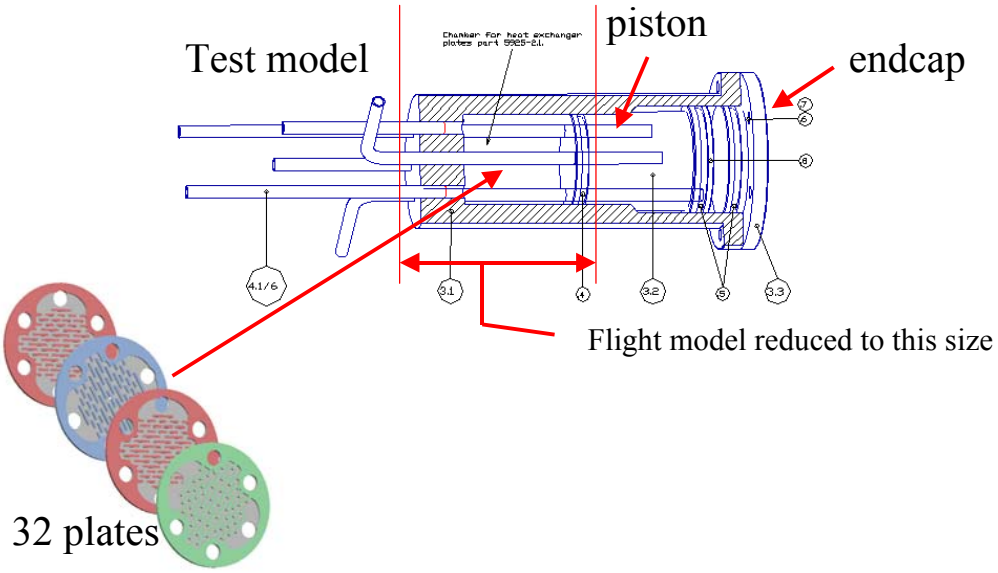

Figure 2.70: Design of the heat exchanger (HX).

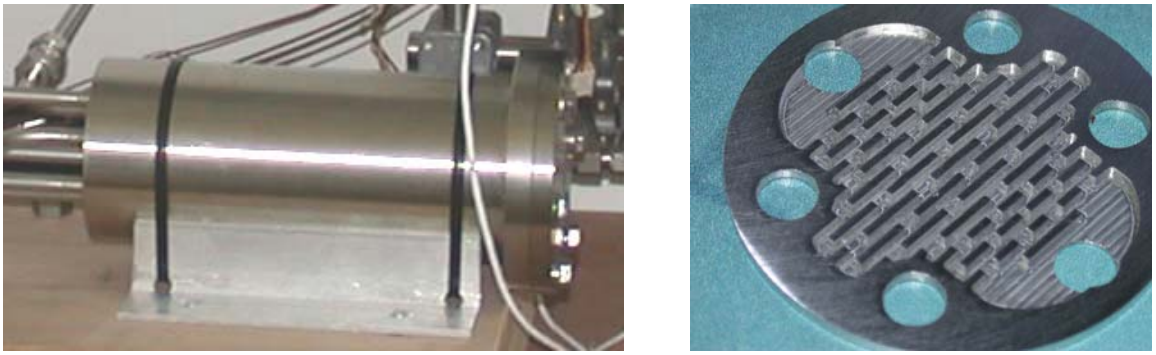

Figure 2.71: Protoflight heat exchanger elements.

To reject the heat to deep space the loops are each connected to the ram and wake heat pipe radiators using special condensers (see Figure 2.72). Due to the required design pressure (160 bar) special attention had to be given to the in- and outlet orifices. Figure 2.73 shows a condenser assembly. A heat pipe like profile is used in which the vapor core is filled with a solid rod, in this way creating 16 parallel condenser channels. A point of concern is the possible freezing of CO_2 in case of a complete power down of AMS. Uncontrolled melting can cause liquid enclosures and therefore high pressures. By reducing the inlet and outlet orifice volumes it is expected that the induced pressures will stay below the design pressure. Additional tests are in progress to verify this.

Prototypes of the critical parts of the evaporator loop have been successfully produced. A full-scale inner ring was manufactured and tested in a full-scale bread board model of the system. Several different prototypes of the thermal flex connectors, which connect the thermal bars together, have been made for production optimization.

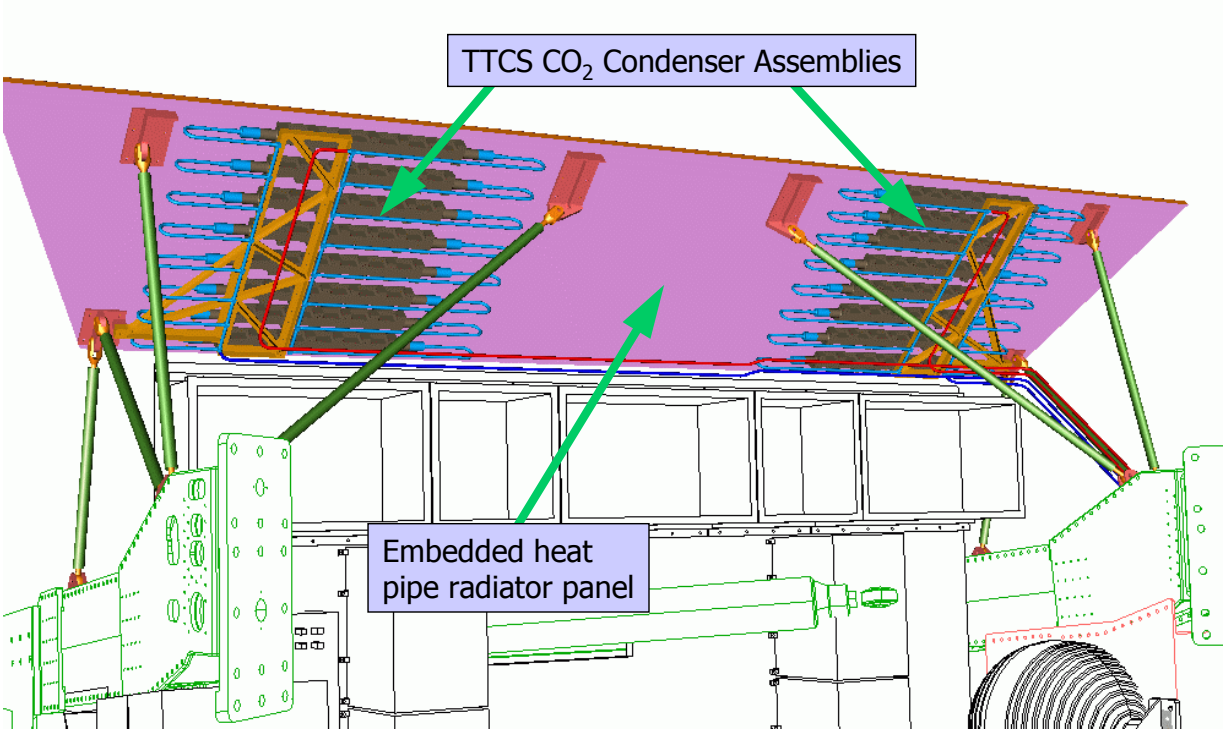

Figure 2.72: Condenser locations on one heat pipe radiator.

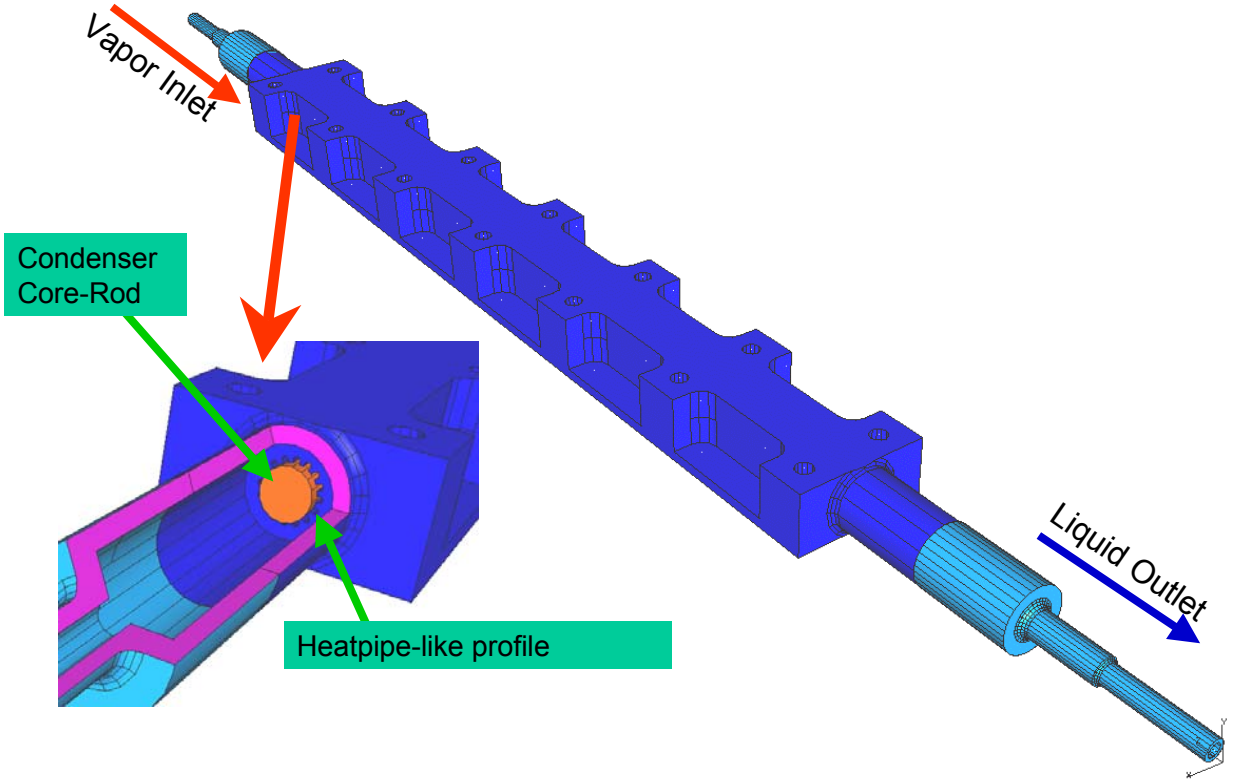

Figure 2.73: Condenser design.

2.3.6 Laser Alignment System

Space based particle detection systems have to cope with a far wider range of environmental conditions than those at accelerators. This concerns notably the vibrations during the transport before deployment and the rapid periodic changes in the thermal settings due to solar radiation and cooling while in the shadow of Earth. With the AMS-02 silicon tracker, charged particle tracks are traced at 8 space points in a ~1 m^3 sized B-field to an accuracy of better than 10 μm.

With AMS-01 it was found that the carbon fiber tracker support structure is stable at the 15 μm level but that excursions up to 30 μm did occur. These excursions were correlated with changes in the thermal conditions following changes in spacecraft attitude [11, 12]. For long observation periods, the overall system stability is especially important in that it limits the ultimate momentum resolution for high rigidity particles and can introduce dominating systematic errors in the pointing accuracy of the AMS tracker for converted photons, particularly from astrophysical point sources. Sub arc minute precision pointing of weak sources is possible provided sufficiently frequent checks of the tracker geometry can be performed with laser beams and stiff cosmic tracks without going to a zero field condition.

The alignment system, developed by RWTH-Aachen, provides optically generated signals in the 8 layers of the silicon tracker that mimic straight (infinite rigidity) tracks. It has been shown with AMS-01 [11, 13, 14] that these artificial straight tracks allow the tracing of changes of the tracker geometry with a position (angular) accuracy of better than 5μm (2 μrad). The system uses the same silicon sensors for both particle detection and control of the alignment. It serves to generate position control data within seconds at regular time intervals (4 to 6 times per orbit), for example, while the ISS flies into the shadow of the Earth or comes back into the sunlight.

As shown in Figure 2.74, the AMS-02 tracker is equipped with 2 x 10 pairs of alignment control beams. The beams are narrow (diameter < 0.5 mm) and of small divergence (< 1 mrad). The beams enter the tracker volume through 2 x 5 beamport boxes (LBBX) mounted on the outer face of the two outer tracker support plates. The photons of these beams are generated with laser diodes mounted outside of the tracker volume and are brought practically loss free to the LBBX via mono-mode optical fibers. The pulse length is less then the electronics integration time so that the repetition rate is limited only by the readout. The wave length of these beams, 1082 nm, has been chosen such as to penetrate all 8 Si detector layers of the tracker at once. At this wavelength only a small fraction of the generated photons are absorbed (10% in the 300μm-thick Si sensor), however the reflection at the Si surface has to be suppressed in order to overcome the intensity limitations in recording the alignment beams due to the strong effective attenuation (factor of ~10 per Si layer) caused by the high refractive index (dielectric constant) of Si. Furthermore the transparency of the Si particle detector surfaces is obstructed by the aluminized readout strips. In consequence, the tracker sensors on the alignment beams have been equipped with anti-reflective coatings (SiO_2 and Si_3N_4) optimized for the wavelength chosen (residual reflectivity ~ 1%). In addition, the readout strip metallization width was reduced to 10μm width in the coated areas and the other implants not metallized. Together these measures have resulted in a transparency of the alignment sensors of 50% [15] and the 8th layer of the tracker receives about 0.8% of the intensity coming out of the LBBX. With high quality DBR diodes the very high electro-optical efficiency allows for comfortably large photon fluxes even during small signal (100nJ/pulse) operation. This results in signals induced by the laser that can exceed those of Z=26 nuclei in the tracker planes closest to the LBBX.

As shown in Figure 2.75, the laser beam spot covers 10 (5) strips on the p- (n-) side of the sensors. Position changes are determined concurrently for both coordinates from changes of the measured centroids of the laser profiles. Alignment beams are arranged in pairs in order to distinguish between changes in beam geometry and sensor displacements. The figure also shows that, with only a single laser pulse, displacements of 200 μm can be measured with a precision of a few μm.

Laser alignment will be performed coincident with data taking. This allows any possible changes in the tracker geometry, from rapid thermal deformations to long term drift, to be identified and corrected offline.

The AMS approach to silicon tracker alignment control using IR laser beams fulfills the requirements of a space borne experiment. It is light weight (3kg), low power (1mW), low dead time (< 1%) and provides a precision exceeding the tracker resolution (8μm) with less than 100 laser shots. The success of the AMS approach in Si tracker alignment control by IR laser beams has lead the team building the largest Si tracker array [16] to develop a similar system for 10 years of operation at the LHC.

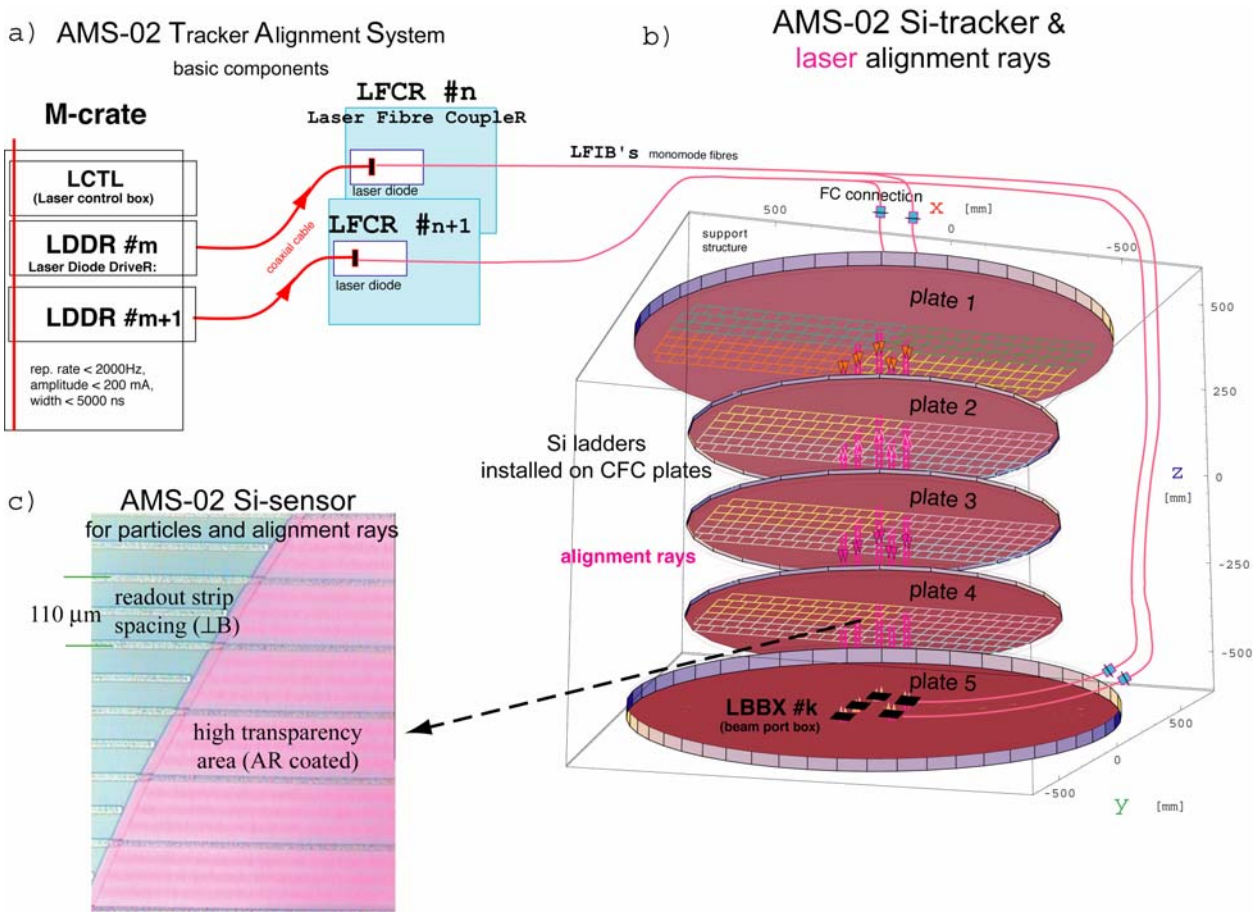

Figure 2.74: AMS-02 silicon tracker laser alignment system overview (a). Geometry of upward and downward going laser beams (b). Microphotograph of an Anti Reflective area (c).

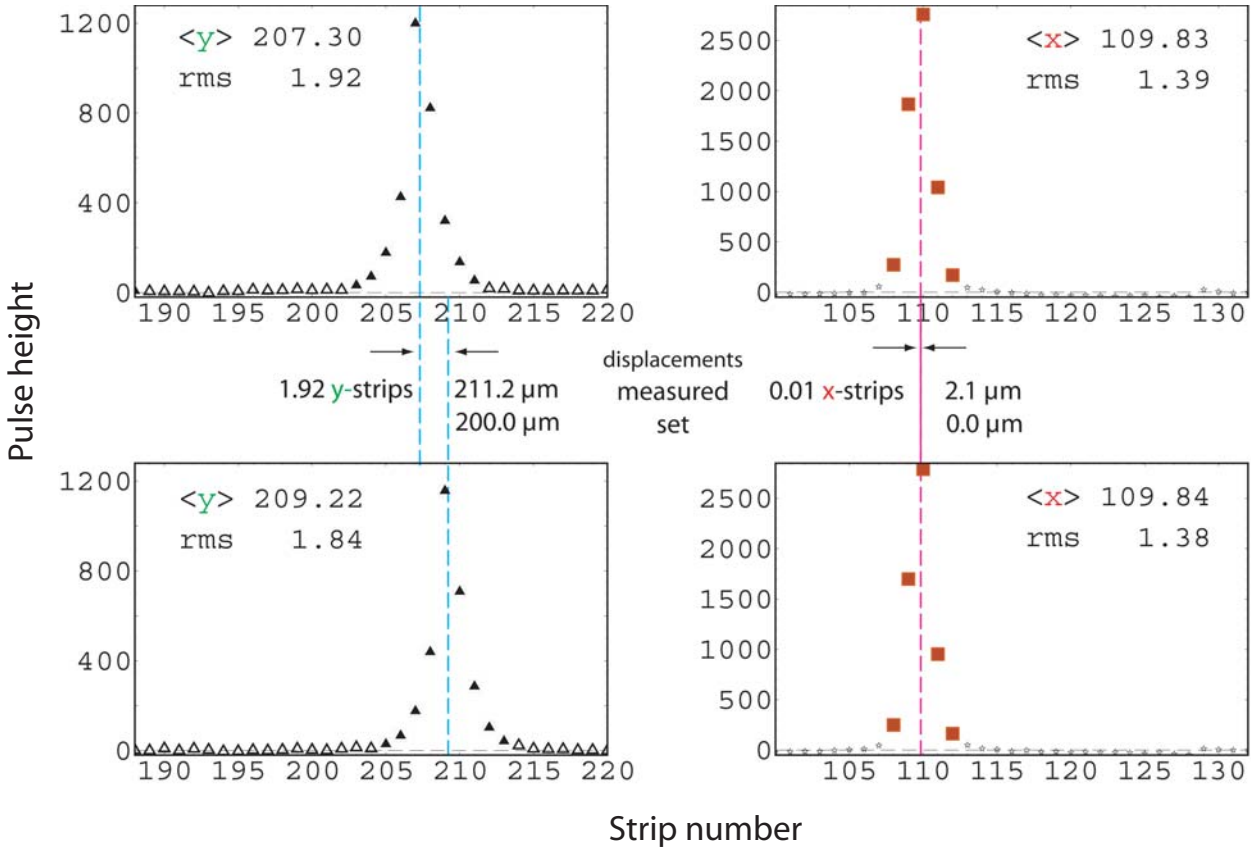

Figure 2.75: Single pulse laser beam profiles observed with the standard AMS-02 readout chain on flight ladders for the y (plots on the left) and x (plots on the right) coordinates. Between the upper and lower measurements the beam was stepped by 200 µm in y. In y coordinate the reconstruction precision is dominated by the stepping accuracy. In x it is better than 3 µm.

2.3.7 Performance Tests

An extensive series of tests have been performed to verify the performance of the AMS-02 silicon tracker. These include bench tests at the ladder by ladder level and beam tests with minimum ionizing particles, light ions and heavy ions.

An important modification with respect to the original design was the increase by a factor of two in the implantation pitch on the n-side of the silicon sensors. The presence of four p^+ blocking strips in the 208 µm readout gap of the AMS-01 sensors resulted in a 35 % lower signal level at normal incidence for tracks passing in the middle of the readout gap [17], and consequently on average, a 20 % lower signal level for the singly-charged particles compared to the p-side performance. Moreover, the silicon manufacturing process has been improved with a significant reduction in the noise level on both silicon readout sides. A comparison of the noise levels of the AMS-01 and AMS-02 ladders is presented in Figure 2.76 in terms of average ADC counts: ADC counts: the mean values have improved from 3.2 to 2.4 and from 4.4 to 3.1 for p- and n-sides.

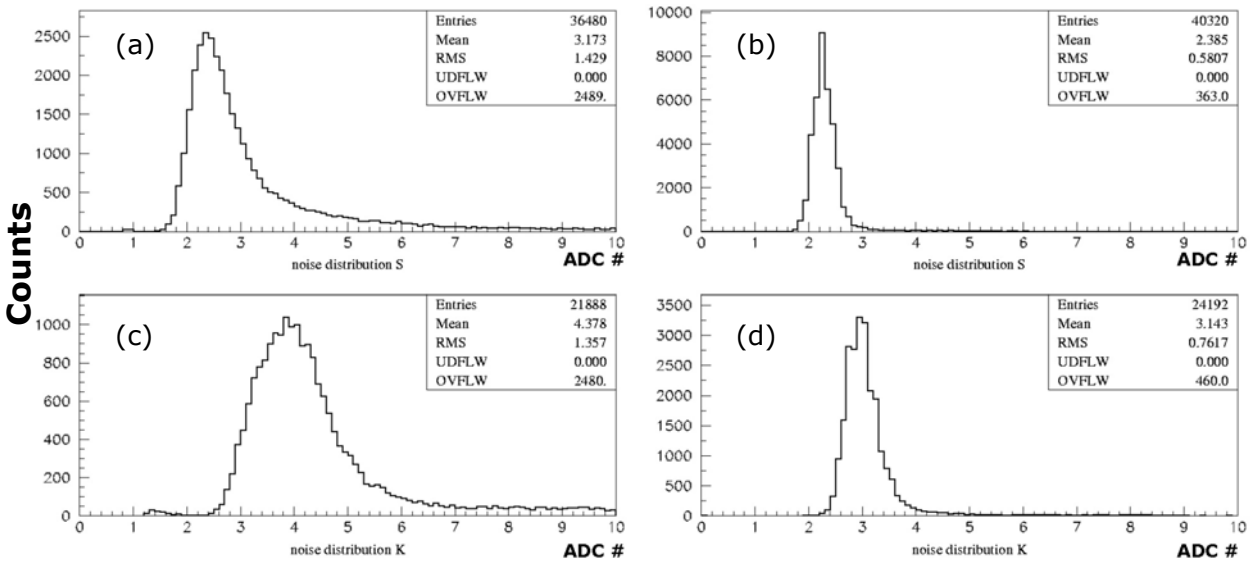

Figure 2.76: Channel noise distribution of ladder p-sides: AMS-01 (a) and AMS-02 (b). Channel noise distribution of ladder n-sides: AMS-01 (c) and AMS-02 (d).

Four AMS-02 ladders were exposed to a 10 GeV/c proton beam at CERN to determine the optimal shaping time for the front-end VA_hdr chip. Figure 2.77 shows the performance of the two sides of the AMS-02 silicon sensors for minimum ionizing protons, for the optimal shaping time of 3.5 μs. The data are described by a Landau distribution convoluted with a Gaussian noise distribution. The fitted widths for the latter are 2.0 and 1.8 ADC counts for the n- and p-sides respectively. In Figure 2.78, the fitted Landau peak values as a function of the shaping time are shown.

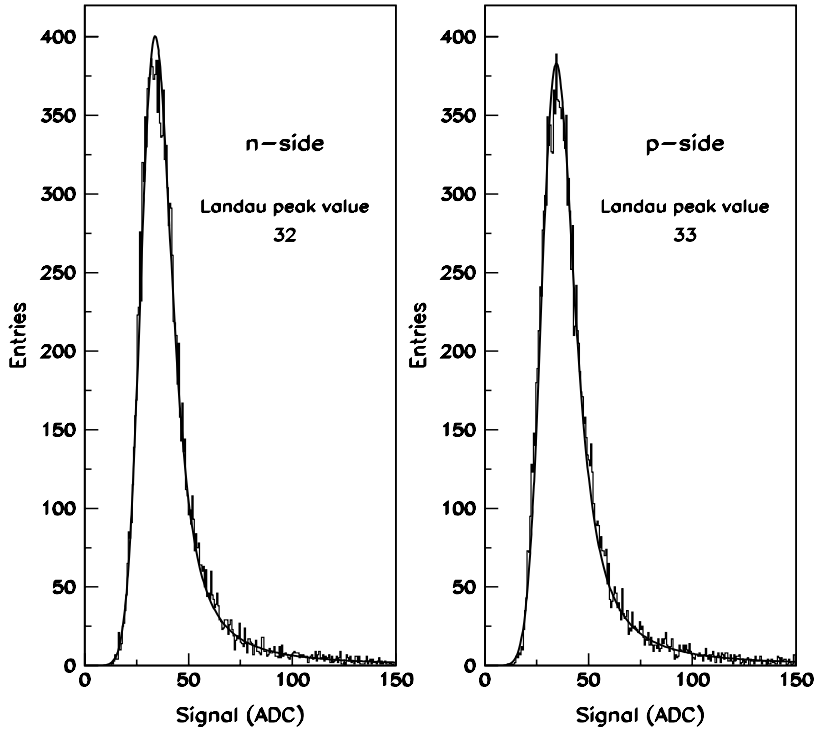

Figure 2.77: AMS-02 silicon tracker performance: signal levels for minimum ionizing protons.

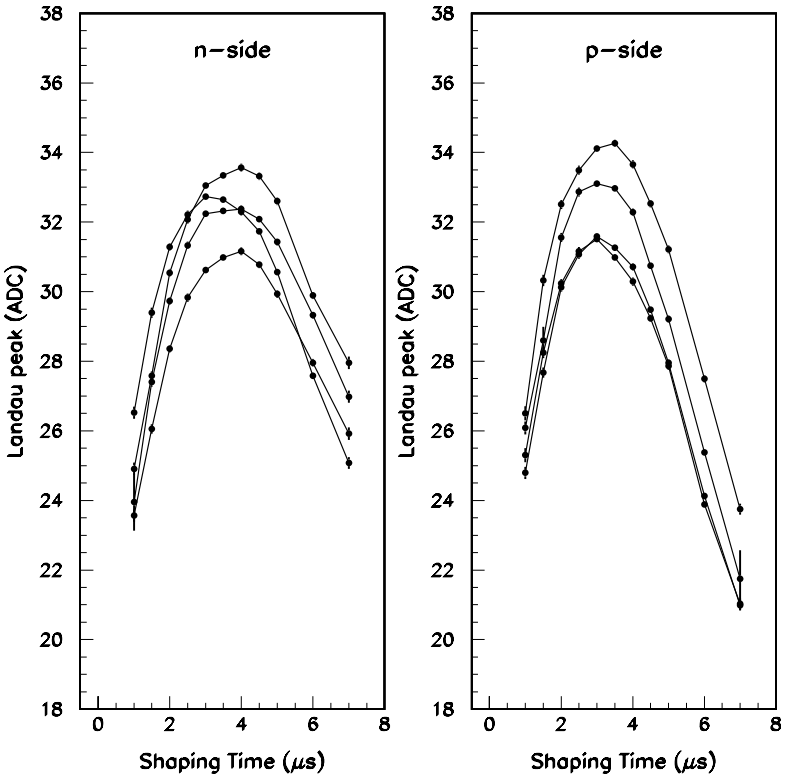

Figure 2.78: Landau peak position for minimum ionizing protons as a function of the VA_hdr shaping time for four AMS-02 silicon ladders.

A measurement of the position resolution was provided by a dedicated setup consisting of a reference telescope composed of four single-sided silicon sensors with 50 μm pitch readout and an AMS-02 prototype ladder. The detectors were placed in 120 GeV muon beam at CERN. Figure 2.79 shows the residual distributions of the ladder, which are described by a Gaussian function and flat background. The widths of the Gaussians are 8.5 and 30 μm respectively for the p- and n-sides.

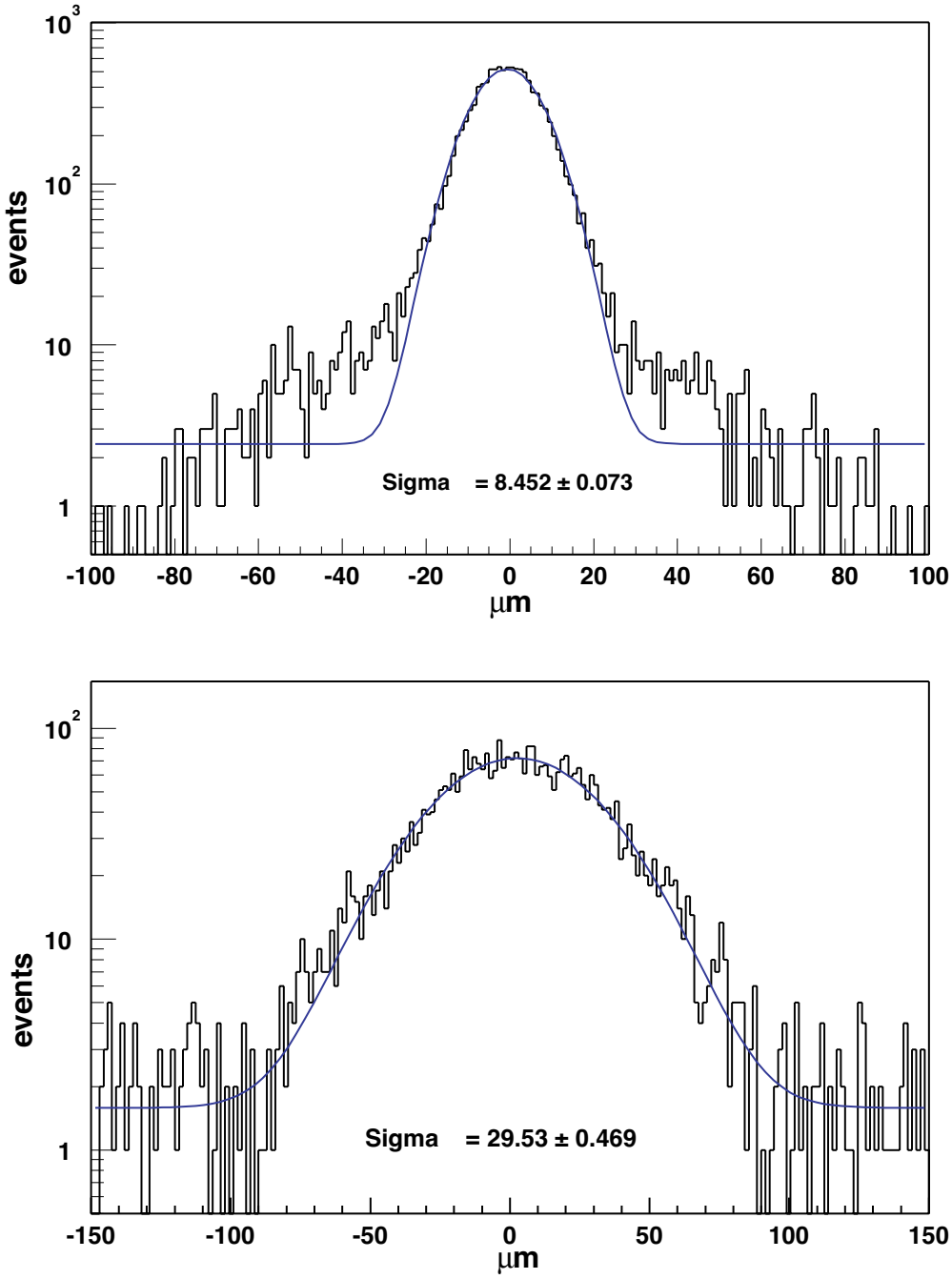

Figure 2.79: Residual distribution of hits on the prototype ladder with respect to the position expected from the reference telescope. The resolution is 8.5 μm on the p-side (top plot) and 30 μm on the n-side (bottom plot).

To study the AMS-02 ladder response to light and heavy ions, six ladders were exposed to an ion beam at CERN in October 2003. A fragmentation beam was produced with primary Indium ions impinging with an energy of 135 GeV/A on a beryllium target. The fragmentation ions could be selected according to their A/Z ratio, and different data samples corresponding to A/Z = 1, A/Z = 2 and A/Z = 2.25, were collected. An independent measurement of the ion charge was also performed by the prototype AMS-02 RICH detector (see § 2.6).

A representative set of two 12-sensor long ladders from each of the three assembly lines was selected from the final AMS-02 production and mounted in a light tight aluminum box orthogonal to the beam. Engineering models of the power supplies were used to supply bias voltage to the silicon sensors as well as low voltages to the front-end hybrids. Three data reduction boards (TDR2) read out two ladders each and transmitted the acquired data to a PC computer running under a Linux operating system. A trigger was provided using a scintillator beam telescope.

The standard data acquisition mode for the tests was in uncompressed mode, to allow the test of different algorithms of common mode noise subtraction, signal finding and clustering.

In each event, a cluster was selected on both the junction (K) and ohmic (S) sides of each ladder by using the following criteria:

- The seed for the cluster is found at the channel *i* with the maximum single channel energy, provided that the signal over noise ratio is above a given threshold. For protons and Z>1 ions the threshold level has been set to 3.5 and 5 respectively.
- The channels adjacent to the cluster seed are associated to the cluster provided that their signal over noise ratio is larger than 0.0 (1.5) for the proton (Z>1) data samples.
- The cluster energy, defined as the sum of energy of channels in a cluster, is larger than 15 ADC counts for S side and 20 ADC counts for K side.

In Figure 2.80 the average cluster energy as a function of the particle's impact position in the readout gap is shown for protons and He, on the S and K sides of a ladder. The impact position is represented by the η parameter, defined as the fractional distance between readout strips of the centre of gravity of the cluster energy. On the K side, an energy loss of 30 % is still present in the central part of the readout gap, for both proton and helium nuclei, however the signal is well above the noise level, insuring a good efficiency for the selection of the proton signal.

To improve the charge measurement, an η dependent correction factor is applied to the measured cluster energy on the K side. In Figure 2.81 the cluster total signal collected on the two sides of a ladder is shown for protons and helium nuclei.

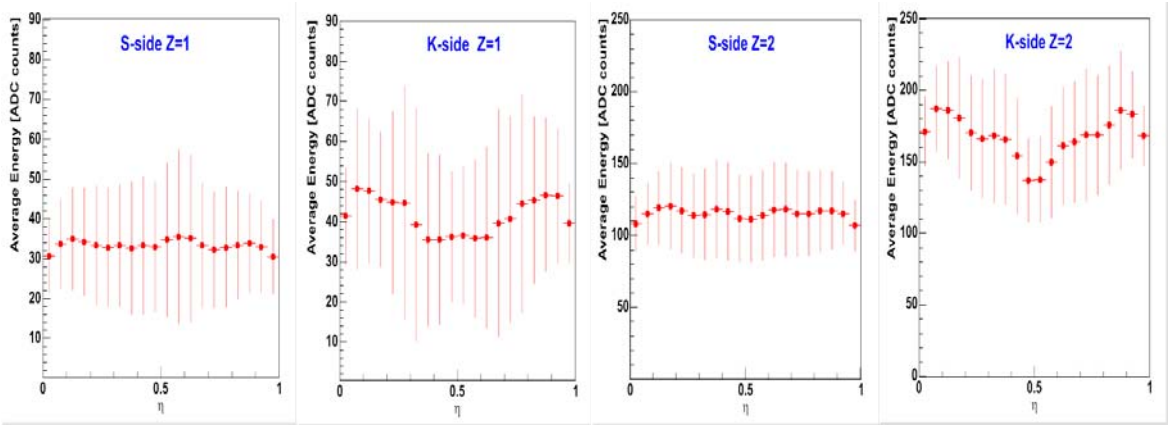

Figure 2.80: Average cluster energy as a function of center-of-gravity of the cluster energy, η, on the S and K sides of a ladder, for protons and helium nuclei.

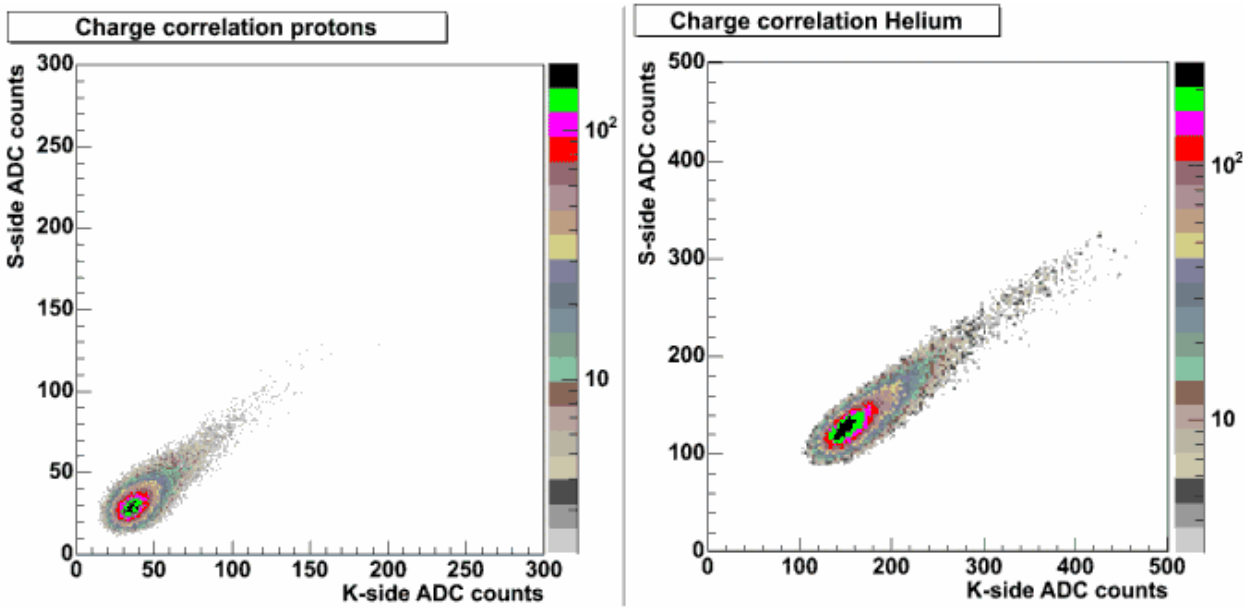

Figure 2.81: Total cluster energy as measured on the S and K sides of the same ladder for protons and helium nuclei.

For both protons and helium, a Landau distribution convoluted with a Gaussian noise distribution describes the cluster energy distribution and can be used to define a probability density function for proton and helium signals as a function of the cluster energy. In Figure 2.82 the probability density functions of proton and helium signals on the S side of a ladder are shown. In the figure, the probabilities of having a proton and a helium signal with a cluster energy below or above a given value of 110 ADC counts are reported as a reference.

At the event level, the measurements performed by *n* different ladders along a track can be used to define the log-likelihood of the event under the proton ($\log L_p^n$) or helium hypothesis ($\log L_{He}^n$) as: $\log L_p^n = \log \prod_i^n f_p(E_i)$; $\log L_{He}^n = \log \prod_i^n f_{He}(E_i)$, where E_i represents the cluster energy measured on ladder *i*, and f_p and f_{He} are the probability density functions for protons and helium shown in Figure 2.82.

A Monte Carlo simulation has been used to evaluate the p/He separation capability using the eight tracker planes. The probability density functions measured in the beam test have been used to simulate the charge deposit in each of the eight tracker planes for 10^8 proton and 10^8 helium events. In each event, the log-likelihood of the event under the proton ($\log L_p^8$) or helium hypothesis ($\log L_{He}^8$) has been calculated, as well as the ratio $R = \log L_p^8 / \log L_{He}^8$. Figure 2.83 shows the distributions of this ratio for proton and helium events for different number of tracker layers crossed. The resulting p/He separation is better than 10^{-6}.

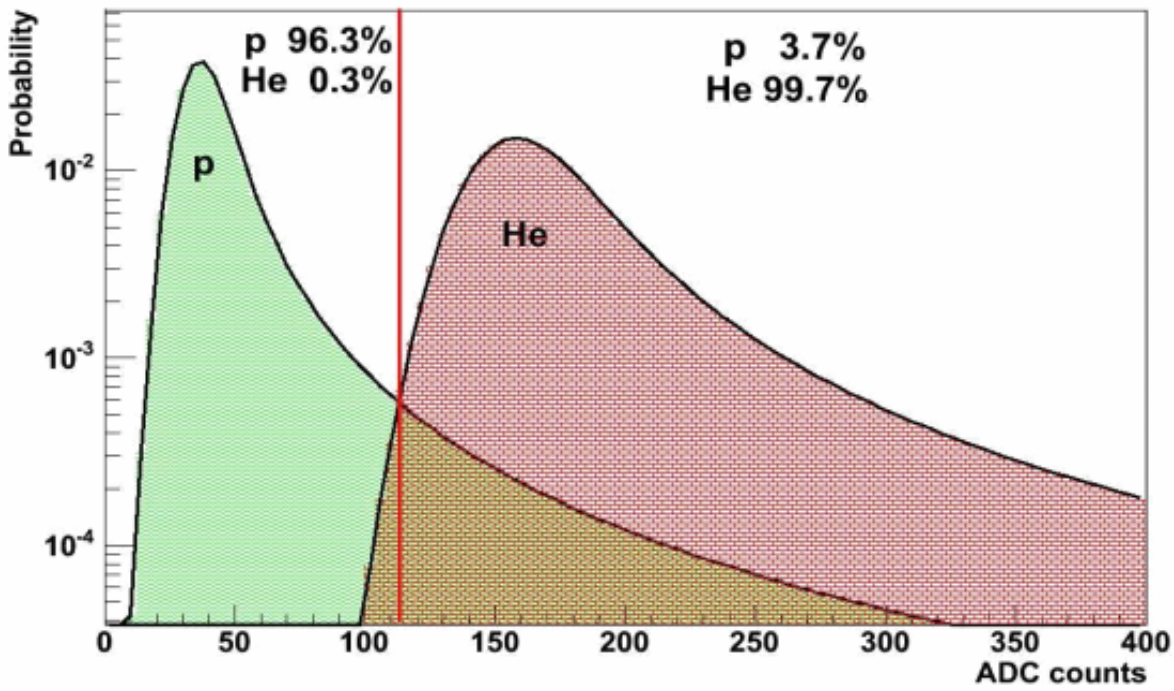

Figure 2.82: Probability density functions for proton and helium signals on a ladder S-side.

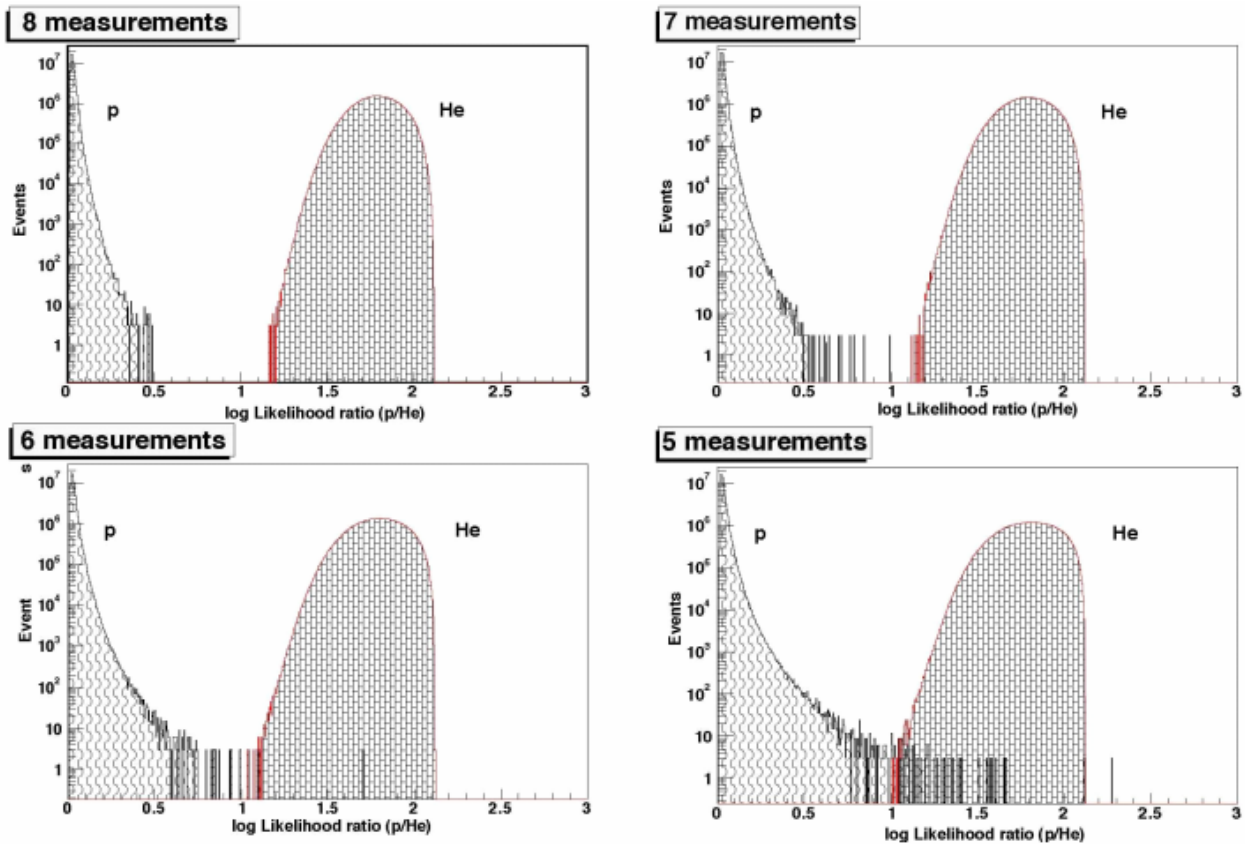

Figure 2.83: Distribution of the log-likelihood ratio p/He for protons and helium events measured in 8, 7, 6 or 5 tracker layers.

The η dependence of the cluster energy observed for protons and He has also been observed for heavier nuclei. In Figure 2.84 the average cluster energy measured on the K side of a ladder as a function of η is reported for different ion charges. The η dependence of the cluster energy varies with ion charge (deposited energy) and the variation is different between the K side and the S side. To improve the charge measurement, an energy and η dependent correction factor is applied to the measured cluster energy. The corrected cluster energy spectrum of a ladder is shown in Figure 2.85. The contribution from individual ions is also shown in this figure. The K side shows a better ion identification capability than the S side. Up to Z = 14, the ion species can be distinguished by a single tracker layer.

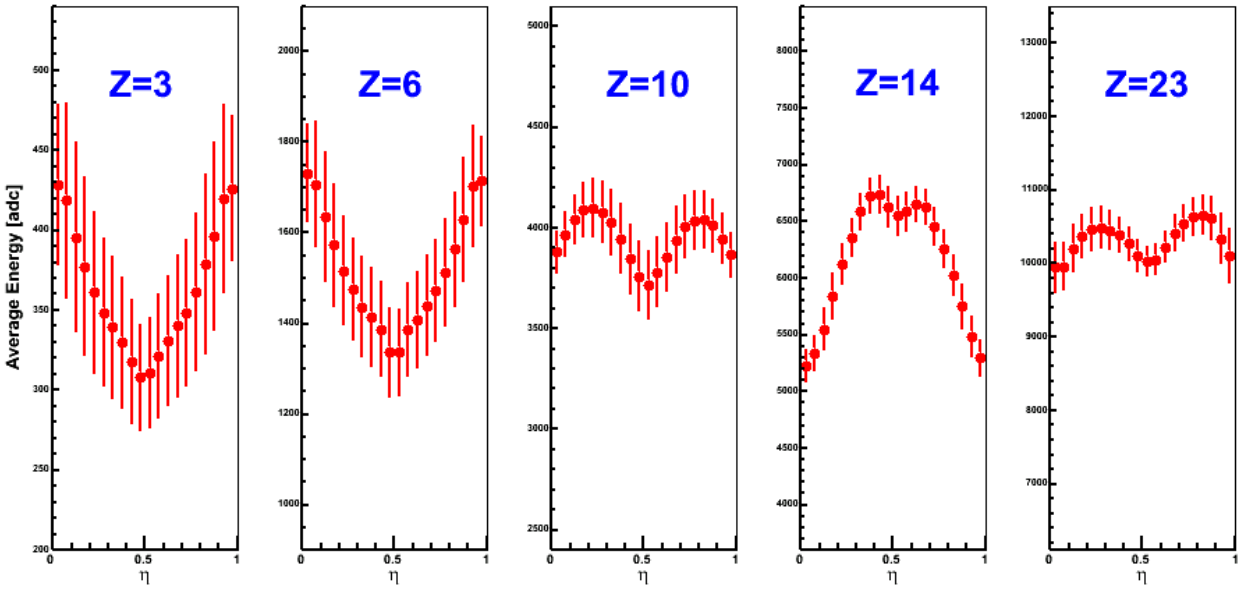

Figure 2.84: Average cluster energy as a function of centre-of-gravity of the cluster energy, η, in different ion types in the K side of a ladder.

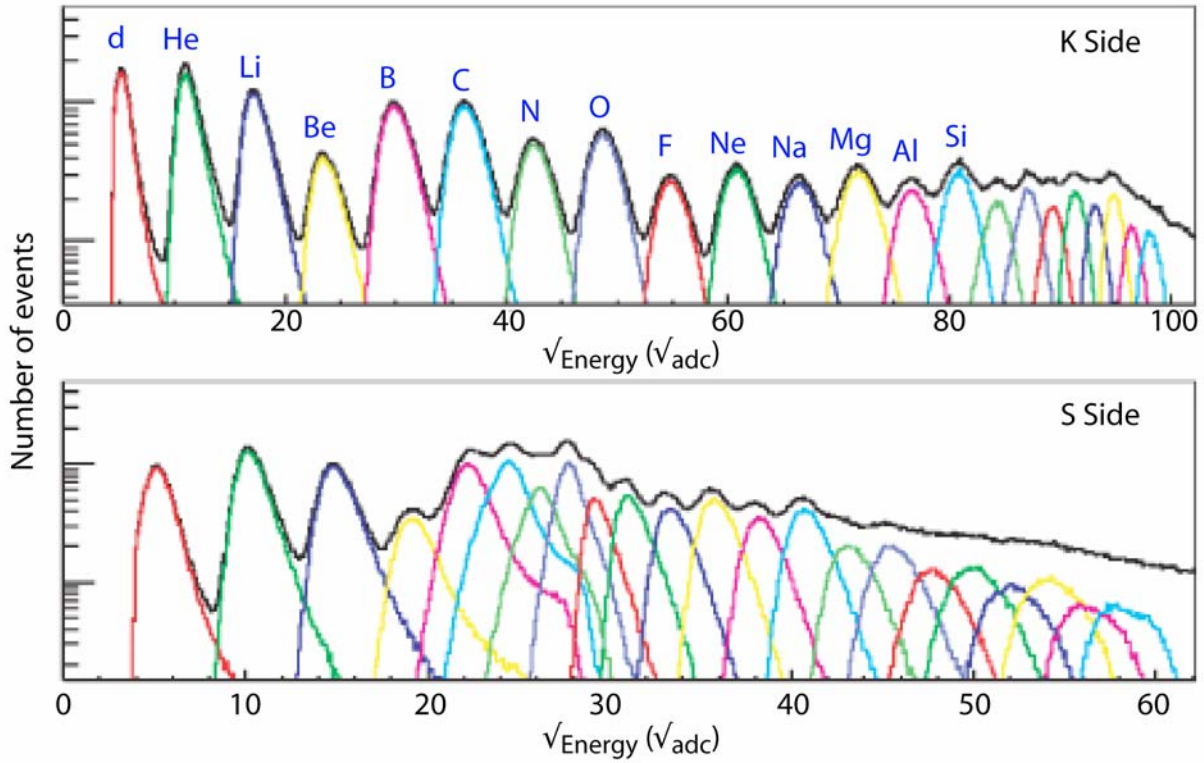

Figure 2.85: Corrected cluster energy spectrum measured in the K and S side of one ladder.

To combine the results from different ladders, the corrected cluster energy has to be transferred into units of charge (Z) to equalize the gains of different VA chips. As an example, the relation of the corrected cluster energy and Z of ladder 1 is shown in Figure 2.86 with the polynomial fit. Similar relations are observed in other ladders. For the K side, the cluster energy introduced by different ions follows a Z^2 dependence, but the slope changes around Z = 12 due to single channel saturation effects in the front end electronics. For the S side, a Z^2 dependence is also observed for the lightest four ions, while a transition region is seen from boron to neon. Above neon, a Z^2 dependence is observed again with a smaller gain until saturation. The results of *Z* measurements from different ladders are combined by the truncated average:

$$\overline{Z} = \frac{1}{n-2}\left[\sum_{i=1}^{n} Z_i - Z^{Max} - Z^{Min}\right]$$

$$\sigma^2\left(\overline{Z}\right) = \frac{1}{n-3}\left[\sum_{i=1}^{n}\left(Z_i - \overline{Z}\right)^2 - \left(Z^{Max} - \overline{Z}\right)^2 - \left(Z^{Min} - \overline{Z}\right)^2\right]$$

where *n* is the number of ladders and is required to be larger than 4. The error on average Z, $\sigma\left(\overline{Z}\right)$, is also calculated event by event. The combined Z measurement is shown for the K side and the S side separately in Figure 2.87. The ion species can be distinguished up to Z = 25 with the K side and to Z = 16 with the S side. These measurements are compared to those of prototype RICH detector in Figure 2.88. An excellent correlation to the RICH Z measurement is seen for both the K side and the S side.

If compared to the precursor AMS-01 mission, the performance of the tracker in terms of signal to noise, position resolution and charge resolution has been greatly enhanced. The increase of silicon layers from 6 to 8, together with the more powerful AMS-02 cryomagnet, has significantly increased the physics reach of the AMS-02 detector, making a wide range of physical phenomena accessible during the AMS-02 mission.

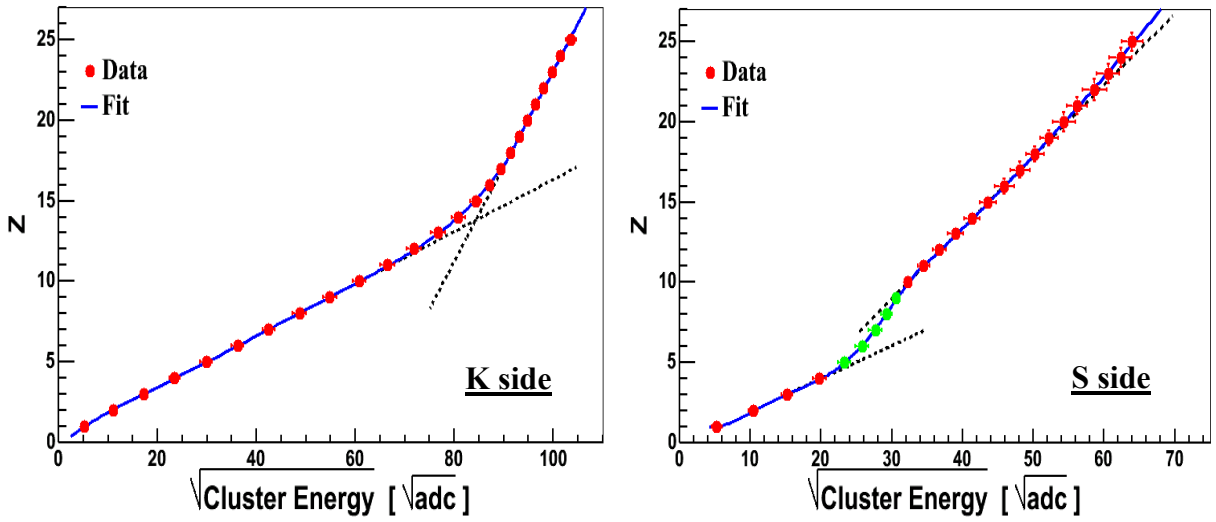

Figure 2.86: Relation of the corrected cluster energy and charge (Z) of ladder 1.

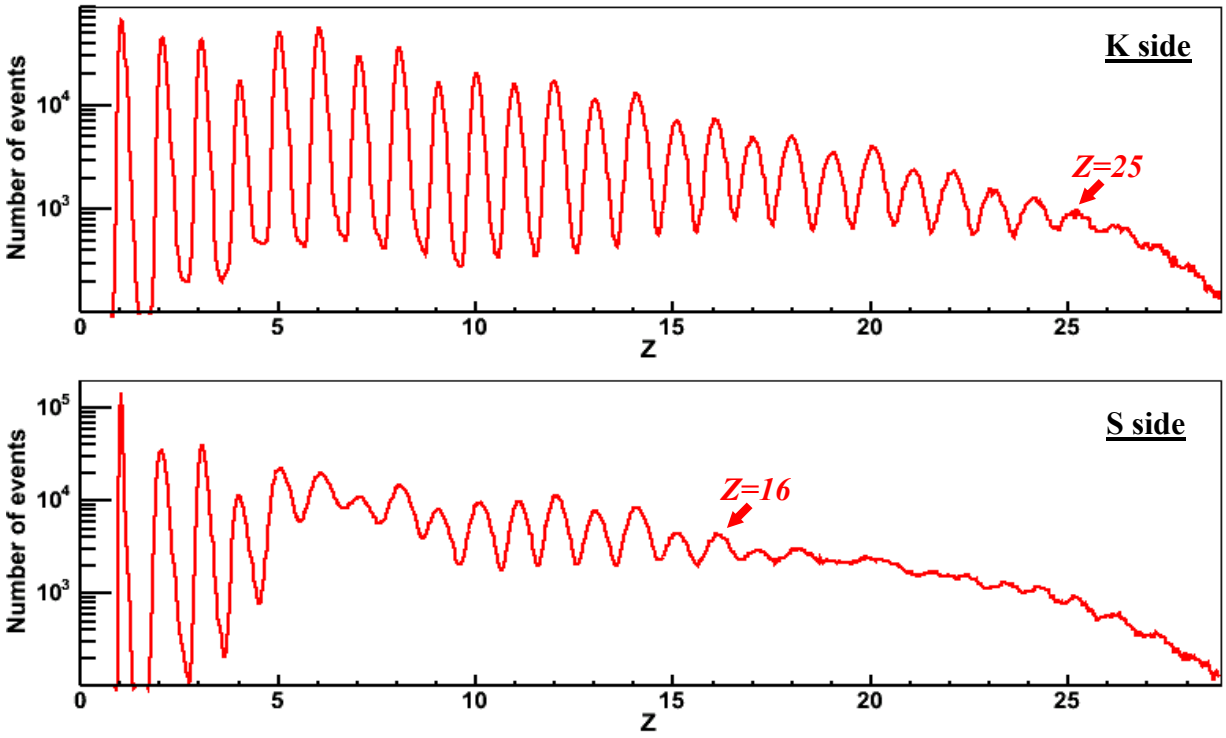

Figure 2.87: Combined Z measurements for 4 or more ladders on the K and S sides.

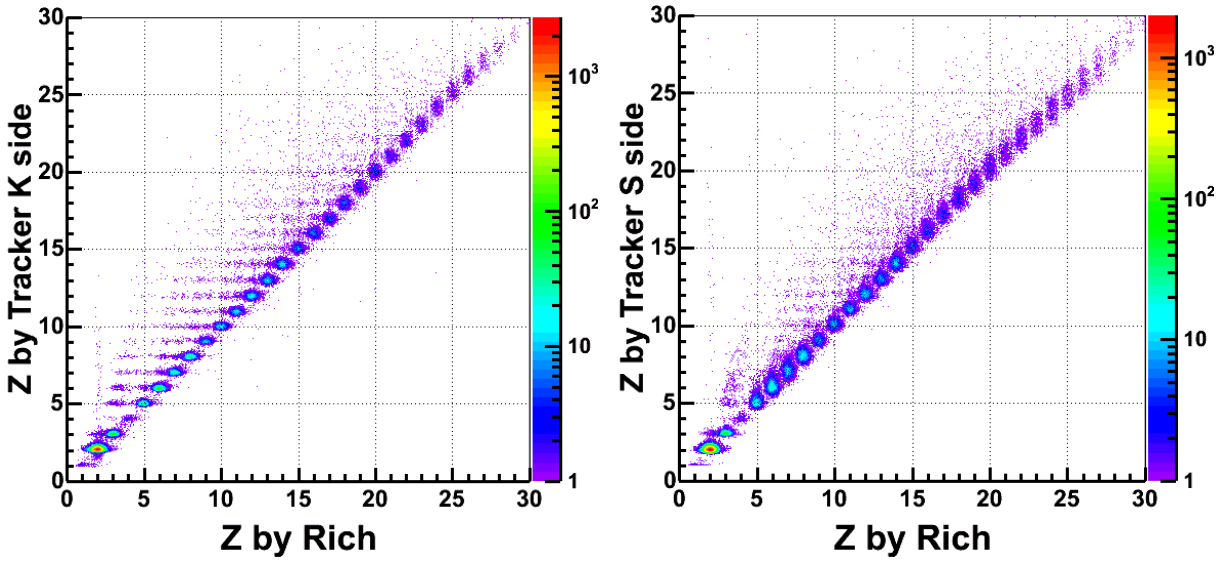

Figure 2.88: Comparisons of charge (Z) measurements by the Tracker and RICH.

2.3.8 References

[1] R. Battiston Nucl.Phys.Proc.Suppl. **44** (1995) 274;
J. Alcaraz *et al.*, Nuovo Cim. **112A** (1999) 1325;
W.J. Burger, Nucl.Phys.Proc.Suppl. **113** (2002)139.

[2] M. Acciarri et al., Nucl. Instr. and Method. A **351** (1994) 300.
G.F. Dalla Betta, et al., Nucl. Instr. and Method. A **431** (1999)83.

[3] G. Batignani et al., Nucl. Instr. and Method. A **277** (1989) 147.

[4] J.B.A. England et al., Nucl. Instr. and Method. A **185** (1981) 43.

[5] J.B. Birk, Proc. Phys. Soc. A **64** (1951) 874.

[6] G. Ambrosi *et al.*, Nucl. Instr. and Meth. A**361** (1995) 97.

[7] M. Pauluzzi, Nucl. Instr. and Meth. A **473** (2001) 67.

[8] O. Toker et al., Nucl. Instr. and Method. A **340** (1994) 572.

[9] B. Alpat et al., Nucl. Instr. and Method. A **446** (2000) 552.

[10] G. Ambrosi, Nucl. Instr. and Method A **435** (1999) 215.

[11] J. Vandenhirtz, Ein Infrarot Laser Positions-Kontroll-System für das AMS Experiment, 2001, PhD thesis, RWTH-Aachen.

[12] W.J. Burger et al., Nucl. Instr. and Method. A **512** (2003) 517.

[13] J. Vandenhirtz et al., Proc. 27th International Cosmic Ray Conference (ICRC2001), D-Hamburg, session OG, **5** (2001) 2197.

[14] W. Wallraff et al., Proc 7th International Conference on Advanced Technology and Particle Physics (ICATPP-7), I-Villa Olmo Como, M. Barone et al. (Eds.), World Scientific, Singapore, ISBN 981-238-180-5, (2002) 149.

[15] V. Vetterle, Silizium Alignment Sensoren für den AMS-02 Tracker auf der ISS, 2001, Diplomarbeit, RWTH-Aachen.

[16] A. Ostaptchouk et al., 9 May 2001, CMS Note 2001/053, CMS – CERN.

[17] J. Alcaraz et al., Il Nuovo Cimento - Vol. 112 A, **11** (2000) 1325.

2.4 Time of Flight (TOF)

Within AMS-02, the Time of Flight (TOF) scintillators provide the fast trigger for charged particles and converted photons, selection, at the trigger level, of particles within the main AMS acceptance, measurement of the particle velocity including the discrimination between upward and downward going particles and a measurement of the absolute charge which complements those made in the other detectors. The TOF system of the AMS-02 detector is being built at the INFN Laboratories in Bologna. It is based on previous well-established techniques [1] able to reach a precision in the time resolution of 100 ps. The design follows the experience gained with the AMS-01 detector [2], modified to take into account the different conditions in AMS-02, in particular, the stronger stray magnetic field at the photomultiplier tubes (PMTs).

The geometrical acceptance of the TOF, and consequently AMS-02 for charged particles, is 0.4 m^2sr, maximizing the sensitivity of the spectrometer in the search for antimatter and other phenomena. This matches the acceptance of the silicon tracker within the magnet. As shown in Figure 2.1 and Figure 2.89, the TOF system is composed of four roughly circular planes of 12 cm wide scintillator paddles, one pair of planes above the magnet, the upper TOF, and one pair below, the lower TOF. Each plane has a sensitive area of 1.2 m^2 and within one plane the paddles are overlapped by 0.5 cm to avoid geometrical inefficiencies. For efficient background rejection and to aid the offline analysis, the paddles in the two adjacent planes are perpendicular. Each paddle is instrumented with two PMTs at each end.

The TOF system provides a very fast and reliable response to the energy loss of charged particles, in order to provide the general data acquisition system (DAQ) with the fast trigger signal (FT), that is used as the reference time for the event (see also § 2.8). The overlapping and crossed paddle geometry of the AMS-02 TOF allows a granularity of about 12 x 12 cm^2 for trigger purposes with ~100% efficiency and a gate of 50 ns.

The resolution in the time of flight needed to satisfy the physics requirements is 120 ps. The scintillator paddles are 1 cm thick, a compromise between minimum thickness and the light output needed to reach this resolution. Downward going charged particles are distinguished from upward going at the level of 10^9.

The system measures the energy loss by a charged particle (to first order proportional to the square of the particle charge) with a resolution sufficient to distinguish nuclei up to charge $Z \sim 20$. Taking into account the attenuation along the counters, and the need to have a good measurement of singly charge particles, a dynamic range of more than 10,000 in the measurement of the pulse height is required. Within AMS-02, this measurement complements those made by the silicon tracker and RICH.

The TOF system meets the requirements imposed by the need to operate several years on orbit. Each paddle is encased in a mechanically robust and light-tight cover and the support structure conforms to the NASA specifications concerning resistance to load and vibrations. The electronics withstands the highly ionizing low Earth orbit environment. Moreover the system guarantees redundancy, with two PMTs on each end of the paddles and double redundant electronics. The system can operate in vacuum over the temperature range –20 to +50 °C; has a weight of less than 280 kg and a power consumption, including all electronics, of less than 170 W. System components have been qualified for use in space and have been tested with particle beams.

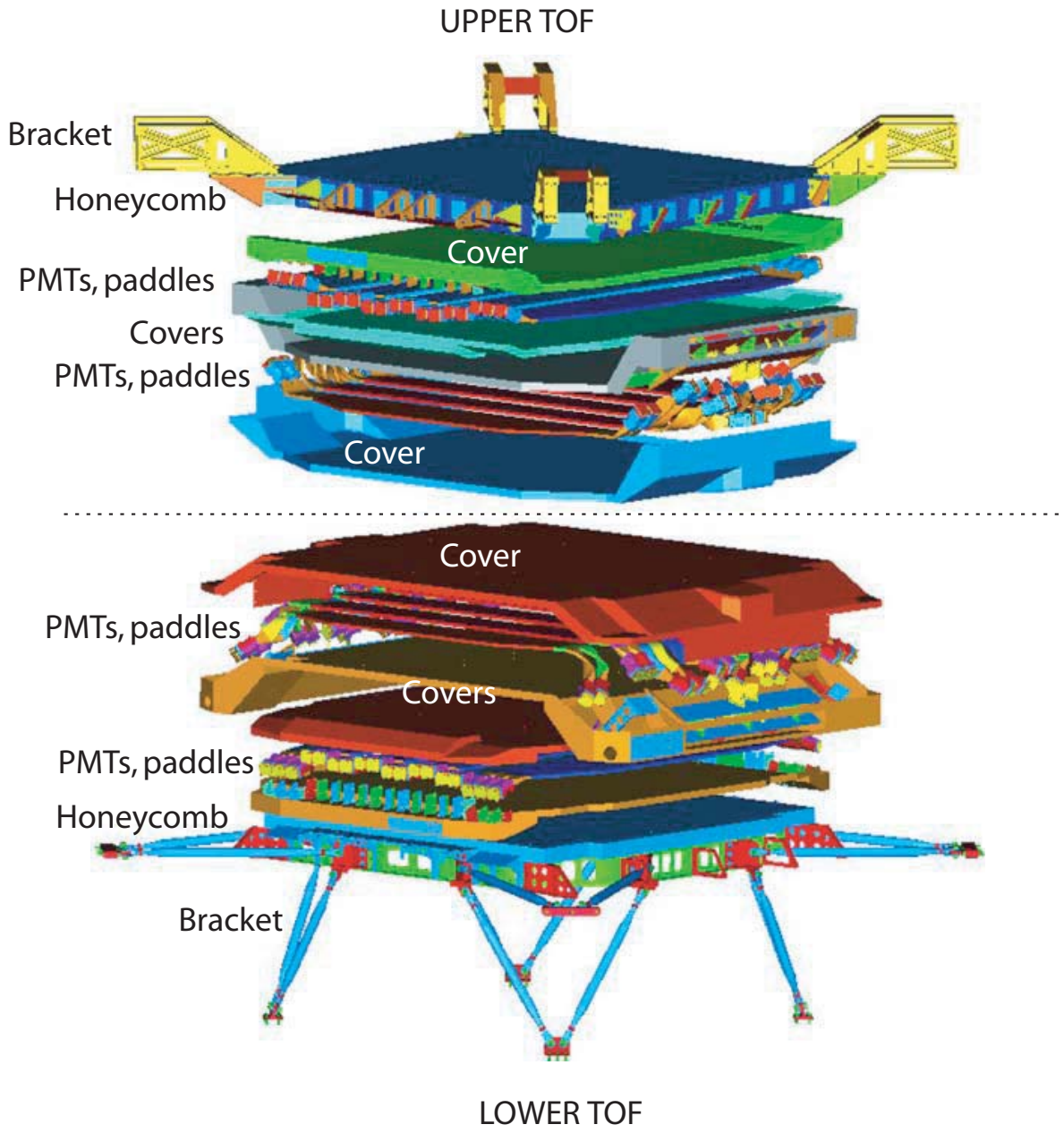

Figure 2.89: Exploded view of the AMS-02 time of flight (TOF) system.

2.4.1 Construction of the TOF

In addition to the requirements to operate reliably in space for 3-5 years and to withstand the launch and landing loads when AMS-02 is in the shuttle, the TOF counters must operate in the stray field of the AMS-02 cryomagnet. Figure 2.90 shows the magnetic field in the region of the TOF planes, which ranges up to 3 kG. The use of magnetic shielding is precluded because of the large weight required and the induced forces on the assembly. Consequently, a thorough investigation selected a PMT which can operate under these conditions – the Hamamatsu R5946 – provided the PMT axis is aligned within 45 degrees of the field direction. This has been a primary design consideration in the construction of the TOF system.

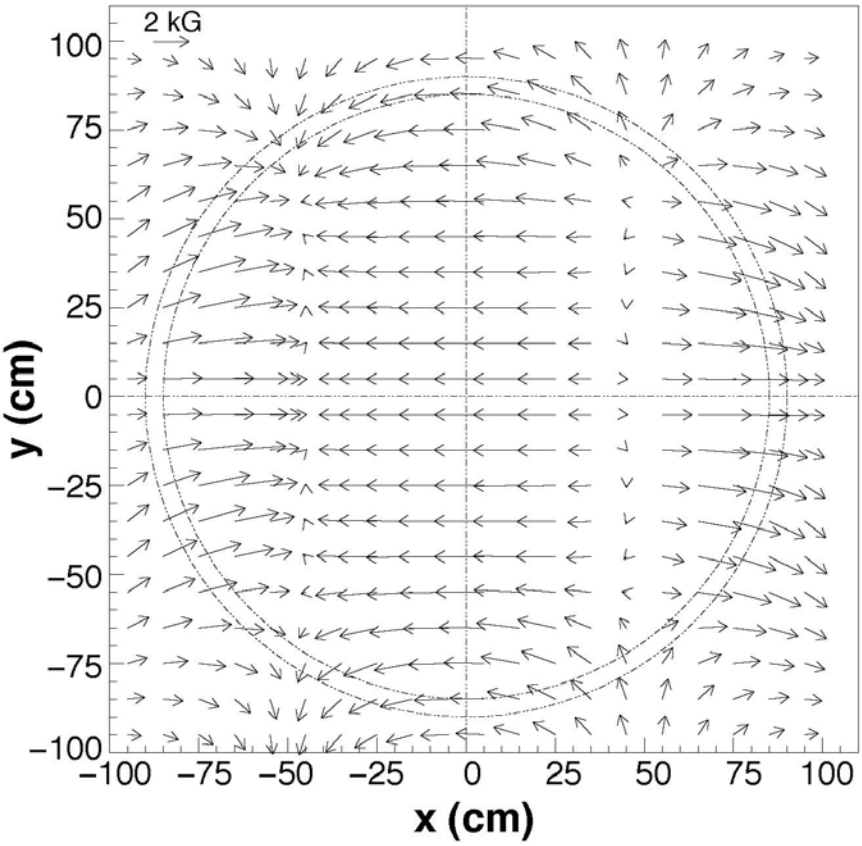

Figure 2.90: Magnetic field at the level of the TOF planes. PMT locations are indicated by the dashed circles.

As shown in Figure 2.91, each of the four planes is composed of 8 or 10 paddles. The paddles are 1 cm thick and 117 to 134 cm long. The edge paddles are trapezoidal with a width of 18.5 to 26.9 cm. The other paddles are 12 cm wide rectangles. As shown in Figure 2.92, each paddle is composed of a central section of ELJEN EJ-200 scintillator adjoined at each end by clear curved or bent light guides up to 15 cm long to align the PMT correctly in the magnetic field and two or three conical light guides which adiabatically match the PMT photocathode areas.

As shown in Figure 2.89, the paddles for the upper (lower) plane pair are mounted on the tracker side of a 10 cm (5 cm) thick honeycomb panel. Carbon fiber enclosures (0.5 and 0.7 mm thick) provide support and light-tightness. Special care is taken to allow these volumes to vent during lift off. These covers also surround and support the PMTs and attached electronics. The upper and lower TOF are each mounted via brackets to the USS, however as the structural requirements and interfaces for the upper and lower assemblies are different, the mounting brackets are different. Figure 2.93 shows finite element model calculation of the displacements for the first mode of the lower TOF, which, at 50 Hz, is well above the frequencies of the shuttle engines.

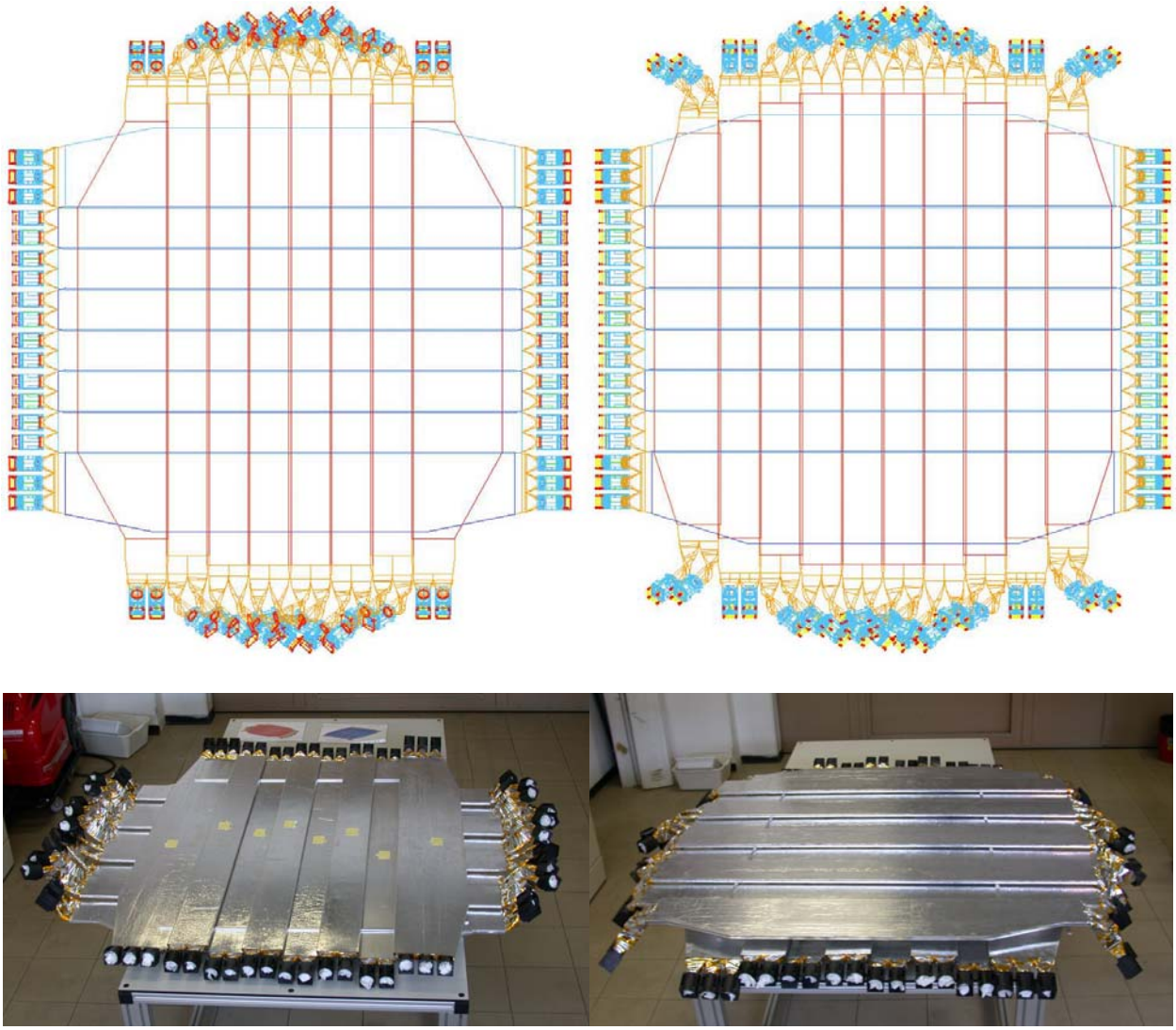

Figure 2.91: Top view of the design and flight paddles during an assembly test of the upper (left) and lower (right) TOF.

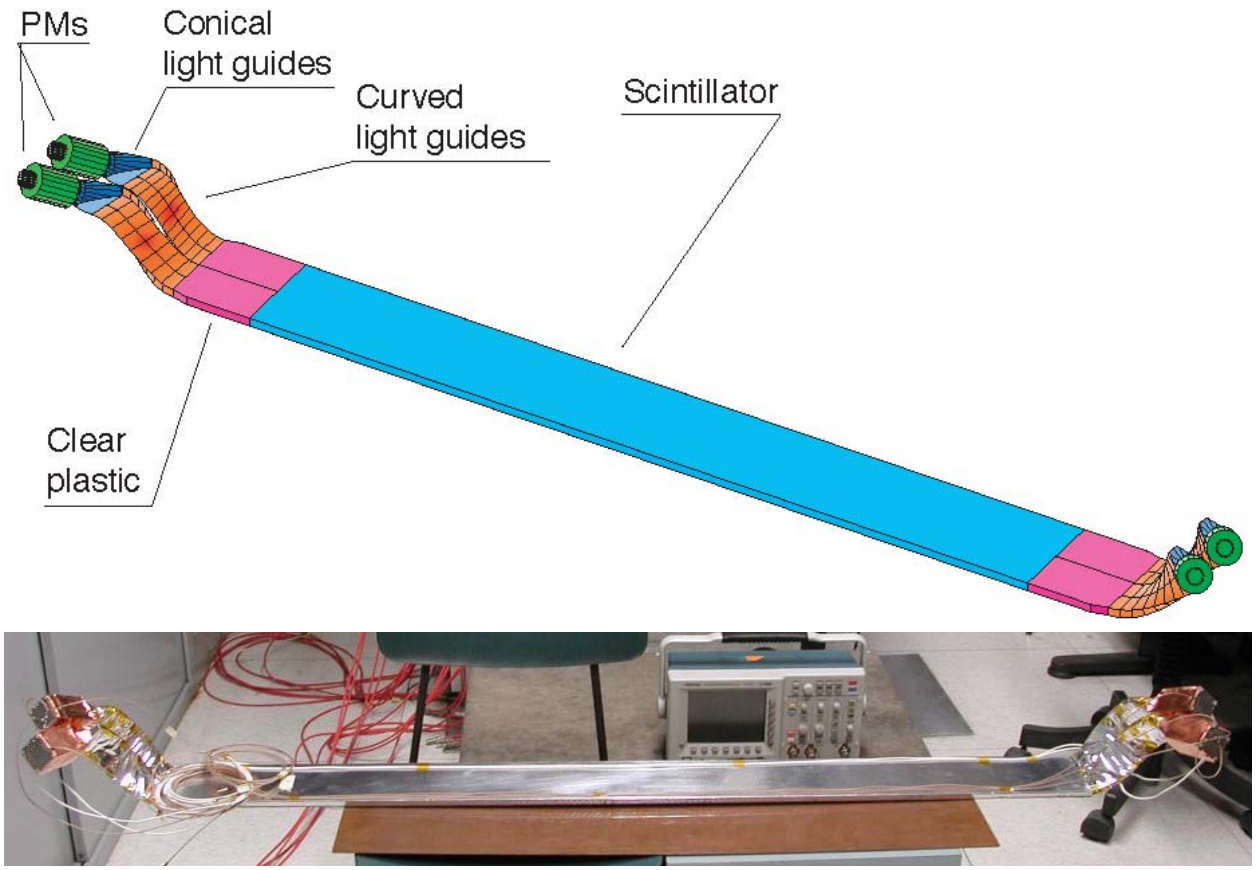

Figure 2.92: Design of a TOF paddle and photograph of an assembled paddle after thermal vacuum and electrostatic discharge tests.

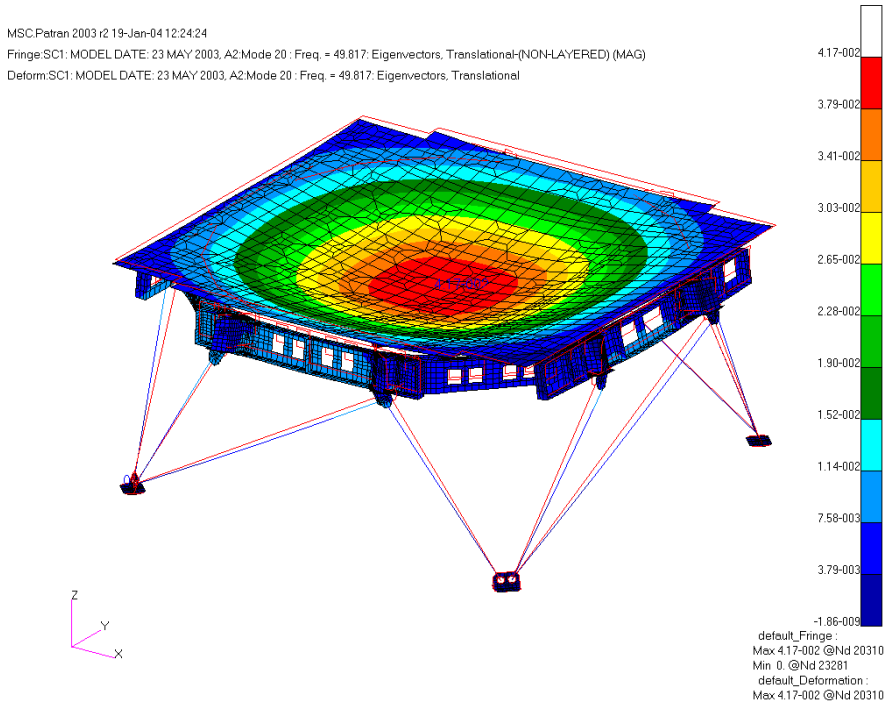

Figure 2.93: Finite element modeling of the lower TOF displacements (in meters).

2.4.2 PMT

In total, the TOF detector is instrumented with 144 Hamamatsu R5946 PMTs. They are cylindrically shaped, ``fine mesh" PMTs and were chosen for their good performance in high magnetic field. The PMT has a bialkali photocathode, a borosilicate glass window and 16 bialkali dynodes. The spectral response ranges from 300 to 600 nm with a maximum response at 420 nm (corresponding to a quantum efficiency of about 20%), which matches the scintillator output. Typical characteristics at 2000 V and 25 °C are: a cathode luminous sensitivity (2856K) of ~80 μA/lm; an anode luminous sensitivity (2856K) of ~80 μA/lm; a gain of 10^6 to 10^7; an anode dark current of ~5.0 nA; transit time of ~7.2 ns.

The effects of magnetic field on this PMT were tested at INFN Bologna [3]. The measurements were made using a red light emitting diode (LED) operated through a CAMAC module. The light was guided to the PMT by two optical fibers. The PMT was placed inside the poles of a 4 kG electromagnet on a translation and rotation stand. The PMT response was measured for different magnetic field values and angles.

Figure 2.94 shows the relative pulse height for different values of the field intensity and for different PMT orientations inside the magnetic field, with respect to zero field. For angles above 45 degrees, the response of the PMTs degrades rapidly if the field is greater than 0.5 to 1 kG. The time response was measured by flashing both the fine mesh PMT and a reference Hamamatsu R5900 PMT with the same LED pulse. Figure 2.95 shows the magnetic field effect on the time measurement. Again, a serious deterioration of the time resolution occurs when the tube is operated at angles above 45 degrees, independently of the applied magnetic field. The transit time variation of the PMTs was measured to be about 2 ps/Volt [4].

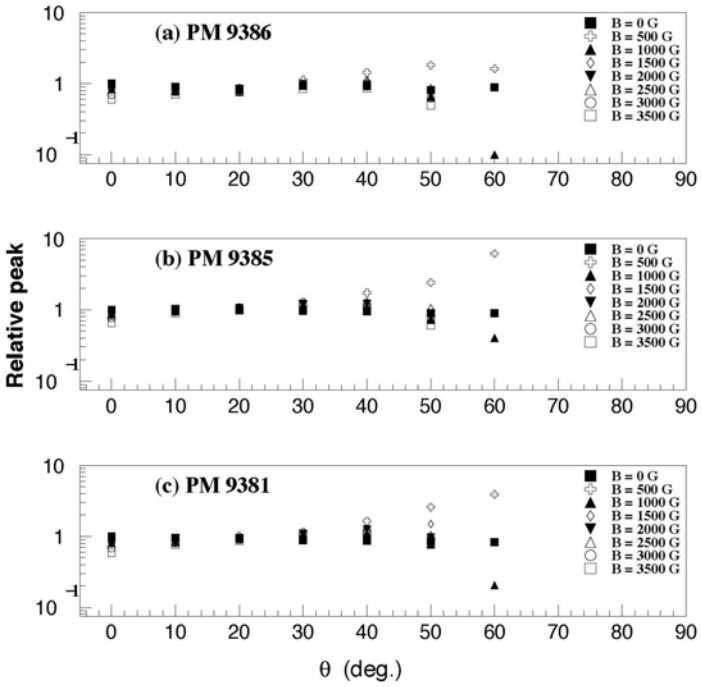

Figure 2.94: Effect of magnetic field on the charge response of R5946 PMTs.

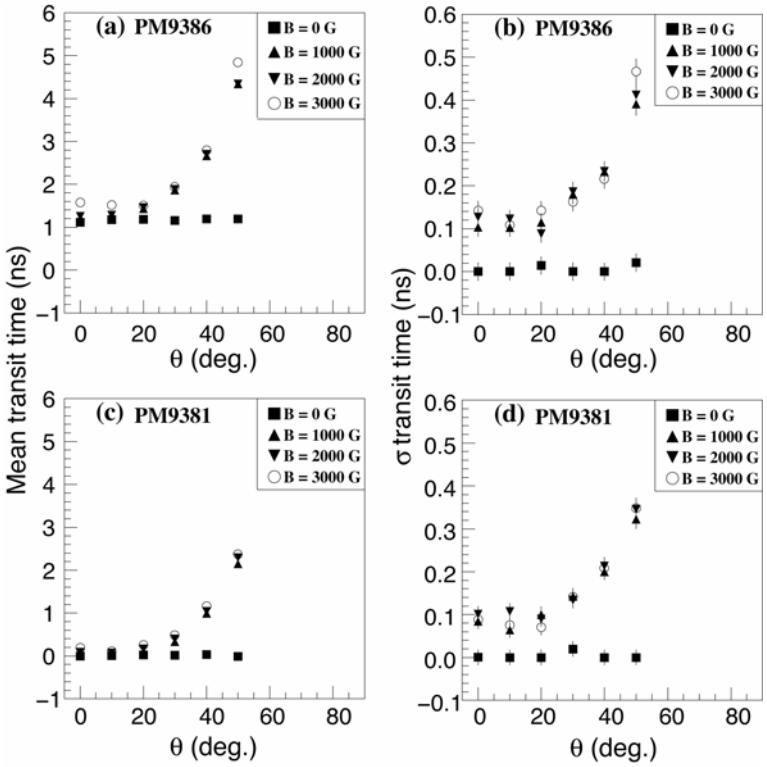

Figure 2.95: Effect of magnetic field on the time response of R5946 PMTs.

To select the flight PMTs, they have all been characterized using the methods developed for AMS-01 [5]. As an example, Figure 2.96 shows the temperature dependence of the gain for two PMTs, measured under vacuum. After calibration, the operating HV for each tube to equalize the response to one minimum ionizing particle (MIP) hitting the center of a counter (~150 mV) was computed [4] and the PMTs grouped so as to have the PMTs at each end of a paddle with similar operating HV (and therefore transit times). A genetic algorithm [6] has been used to determine the best placement of each PMT in the apparatus by means of a likelihood function with parameters including the HV dependence of the gain, slope of the calibration curve, photocathode efficiency, anode to dynode response ratio, magnetic field intensity and direction and light guide transmission properties. High gain PMTs are put at the critical positions, so that their voltage can be increased, if necessary, to compensate for the worsening of their time response during the experiment lifetime [4]. The PMT and counter characteristics are entered into a database from which they have been extracted to support the test beam analysis included below and which will later support the AMS-02 physics analysis.

As shown in Figure 2.97, the PMTs are mounted in a polycarbonate housing which also contains an optical joint between the conical light guide and the PMT window and an 80 MΩ resistor HV divider attached to the base of the PMT. The divider and base are completely potted to avoid corona effects. To ensure proper functioning on orbit, each paddle assembly with the PMTs is subjected to vibration and thermal vacuum space qualification acceptance testing before integration into the planes.

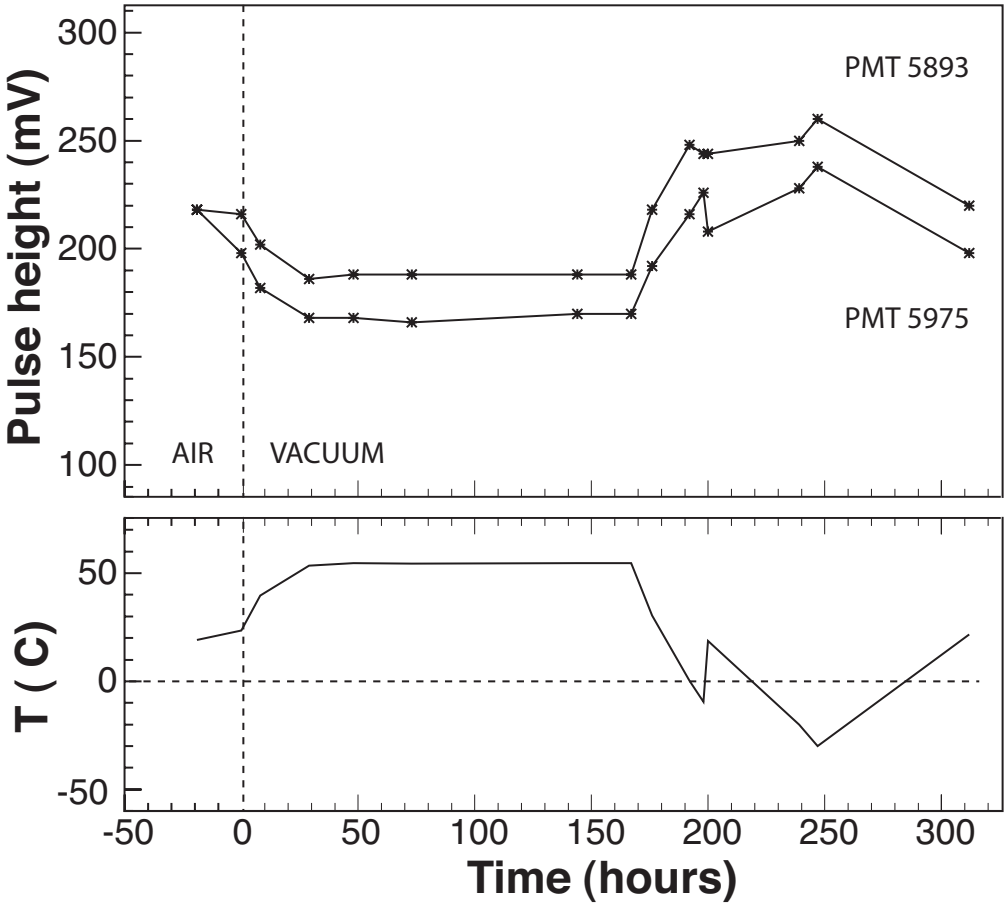

Figure 2.96: PMT response during thermal vacuum testing (upper) and the applied temperature variation (lower).

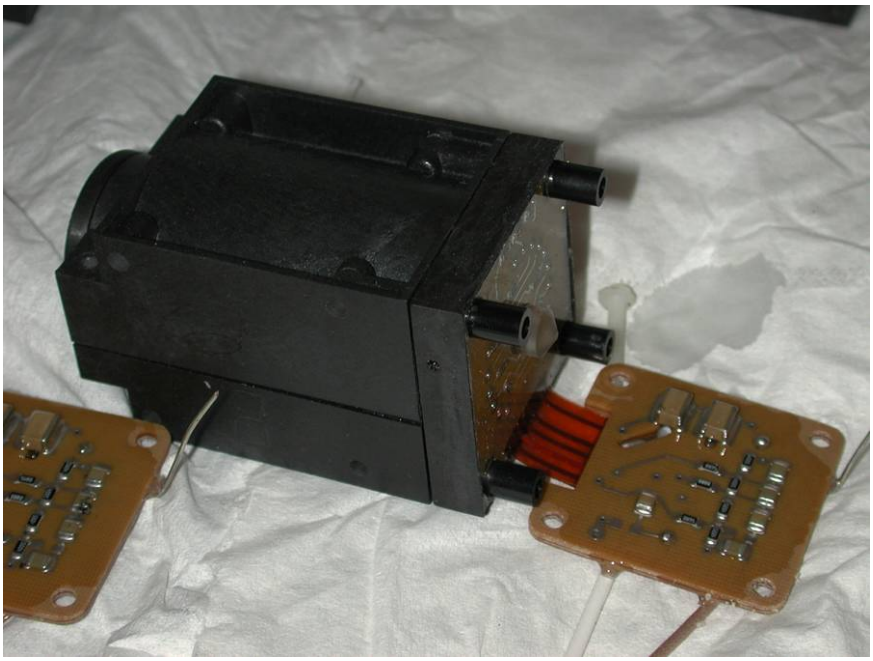

Figure 2.97: PMT in housing with HV divider.

2.4.3 Trigger and Electronics of the TOF and ACC

Within AMS-02, the TOF system provides the first indication that a charged particle has passed through the spectrometer. This is the fast trigger or FT. In addition to the FT, the TOF system also flags cosmic rays with charge greater than one, in order to allow for proton suppression at the trigger level, if necessary, without strongly affecting the measurement of the flux of higher charge ions. Figure 2.98 shows a study using AMS-01 data to simulate the fast trigger efficiency obtained by changing the thresholds on the anode signals, in units of the energy lost by a MIP crossing the center of a counter and requiring hits above threshold in at least three out of four planes. In the study, the threshold was applied separately on each counter end and on the analog sum of the two ends of each counter. The latter solution yielded no improvement and was discarded in favor of the former. A threshold of 3.5 MIP signals can be used to suppress 99% of the protons, while still leaving the efficiency for He and heavier ions untouched.

Figure 2.99 shows the general scheme of the TOF and ACC electronics, which follows the standard AMS-02 system architecture. The system is split into two halves, shown in blue and red, which are operated in cold redundancy. The system has additional degrees of redundancy with two or three PMTs at each end of each paddle, where only one is required, and by having four planes, whereas the timing measurement requires only one plane in each of the upper and lower TOF assemblies. The active half of the electronics is selected by the application of 28V on one or the other feed from the PDS. This voltage powers DC-DC converters to generate the voltages needed by the electronics and HV elevators to power the PMTs. The resulting analog signals from the PMTs split into the two redundant halves, with care having been taken to avoid any interference from one half to the other. The signal is then processed by the front end electronics, the digital results of which are sent via a data reduction module (SDR) directly to the upper levels of the AMS data acquisition system (JINJ). Commands to the system follow the reverse path, from the JINJ to the SDR and then to front end electronics or HV system. Signals to and from the global AMS-02 trigger system (not shown) connect at the front end electronics.

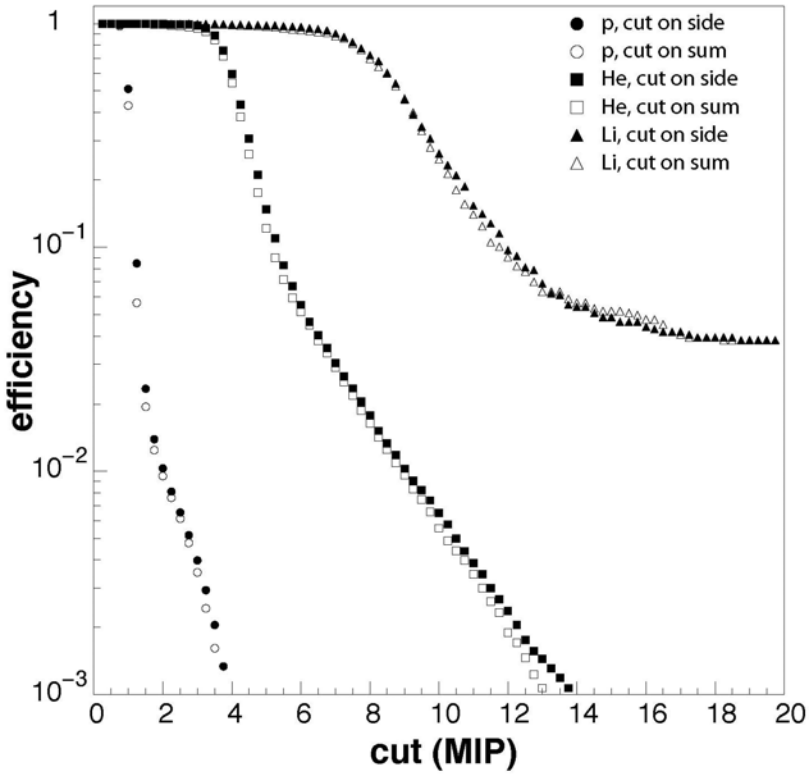

Figure 2.98: Fast trigger efficiency for different ions as a function of threshold applied on the energy loss measured by a single counter at each end or both ends, in units of MIP.

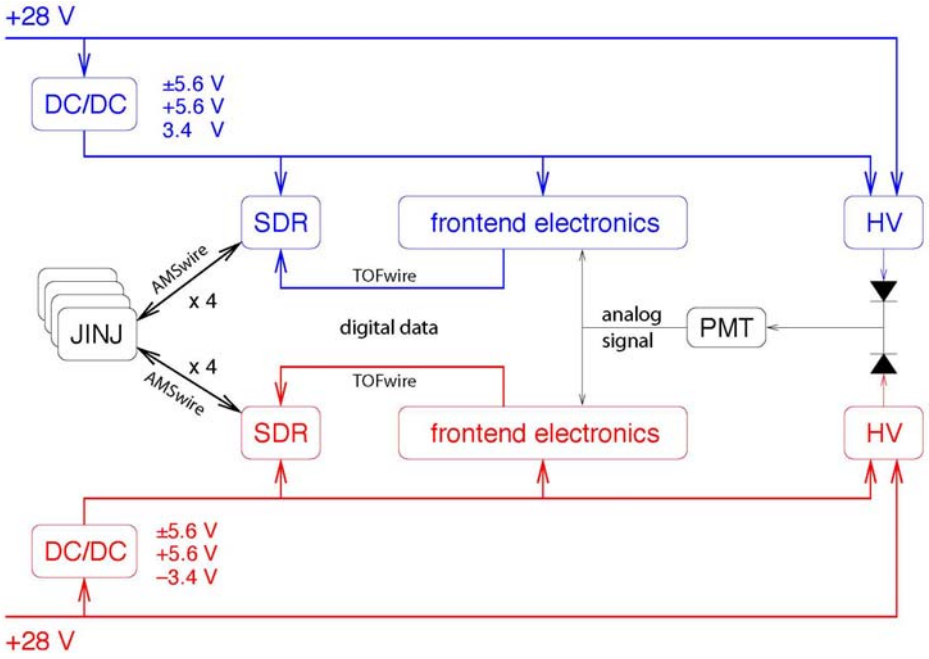

Figure 2.99: TOF and ACC electronics scheme.

The electronics is implemented in four subsystems; each is composed of a standard AMS electronics crate with 7 cards and a backplane (S-Crate), a power distributor containing the DC-DC converters (SPD, located within a TSPD box), a HV brick containing elevators and linear regulators/circuit breakers (SHV) and, for the TOF PMTs only, dynode charge measuring electronics (SFEC). The S-Crate, SPD and SHV are mounted on the main radiators, the SFEC are mounted on the detector, near to the PMTs. Figure 2.100 shows the power distribution, for the active half, within each S-Crate, which houses four SFET2 cards and one each of SDR2, SPT2 and SFEA2 (two redundant SFET modules are mounted on one SFET2 card, etc). Each subsystem is connected to the PMTs located on the adjacent ends of two planes of the upper or lower TOF and the four nearby ACC PMTs mounted on the vacuum case conical flange (see § 2.5).

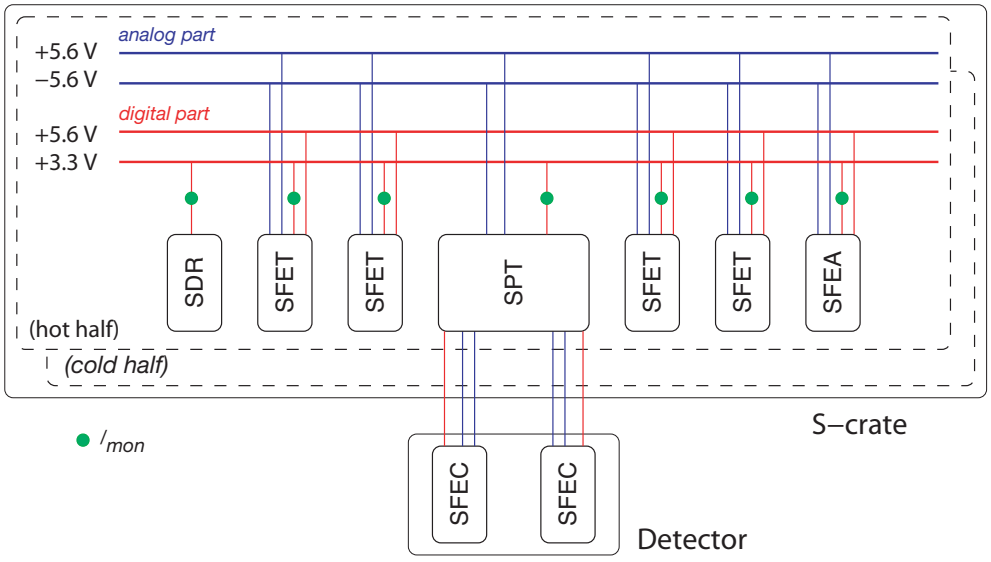

Figure 2.100: TOF and ACC electronics power distribution.

The SFEC boards digitize the anode and dynode signals from each PMT using a circuit developed for the RICH front end electronics (§ 2.6). As in AMS-01, the signals from the PMTs connected to one end of each paddle are combined with a linear adder.

The signal then arrives at the SFET2 card, where it is split into the two redundant SFET modules. Within the active SFET half, the signal is split into three discriminators. A low threshold leg initiates the 40:1 time expansion circuit used to make precise time measurements with minimal skew. A high threshold output is also used in the time expansion logic as well as in a "history" channel to flag out of time particles ($-16 < t < +9$ μs) and as input to the trigger processing. A very high threshold leg is used as a $Z > 1$ flag to the trigger. The outputs of the time expansion and history legs are fed into an octal pipeline time to digital converter (TDC). All of the critical timing circuits are copied from those used successfully in AMS-01, in particular, the low power, high speed discriminator and TDC chips were an MIT development for AMS by LeCroy Research Systems.

The signals from the four ACC PMTs are directed into the SFEA module, where the timing and charge signal processing is similar to that on the SFET. The SFEA can also process two TOF channels as in the SFET.

The SPT module collects and preprocesses the binary signals from the TOF paddles which are then forwarded with the ACC signals to the global AMS-02 trigger (see also § 2.8).

The SPD contains a dual 28V filter plus two redundant pairs of DC-DC converters (S9052, S9074) to supply the low voltages needed by the electronics in the S-Crate and SHV. These converters were specifically developed by MIT-EMI and Bologna to meet the needs of these electronics with minimum weight and maximum efficiency.

The SHV unit supplies up to 40 PMTs with operating high voltages from -1200 V to -2300 V. They were custom developed by the collaboration and a similar, lower voltage, design is used for the RICH and ECAL. Within the SHV, a high voltage elevator receives 28 V and supplies 24 linear regulator channels. Via an attached controller board, both the elevator output voltage and the linear regulator output voltages can be adjusted in steps of 4.5 V or disabled and each output includes resetable over current protection. The controller is attached using the AMS standard LeCroy bus protocol to the SDR for monitoring and commanding.

2.4.4 Space qualification

The TOF system must be able to operate in space for years without human intervention and with temperatures ranging from −20 to +50 °C. In addition, the detector must survive the strong accelerations produced by the shuttle launch, and its performance should not be affected by this vibration. Hence, a series of thermal-vacuum and mechanical tests have been carried out on the TOF system, in addition to the tests on the full AMS-02 detector before flight.

Ten PMTs were tested in a thermal vacuum chamber at a pressure of 10^{-6} to 10^{-7} mbar with the temperature varying between −30 and +55 °C. Four PMTs were equipped with a radioactive β^-source and a small reference scintillator. The dark current was monitored for all PMTs. Figure 2.101 shows the pulse height variation as a function of temperature for 2 of the PMTs (see also Figure 2.96). Each point corresponds to the average of 5000 events measured with an oscilloscope. As shown in the figure, the pulse height (i.e. the gain) of the PMTs is well described by a parabolic dependence on the temperature. The data are in good agreement with the PMT characteristics as given by Hamamatsu. Figure 2.102 shows the variation of the dark current versus temperature for 2 PMTs, which, even at the highest temperature, is always negligible.

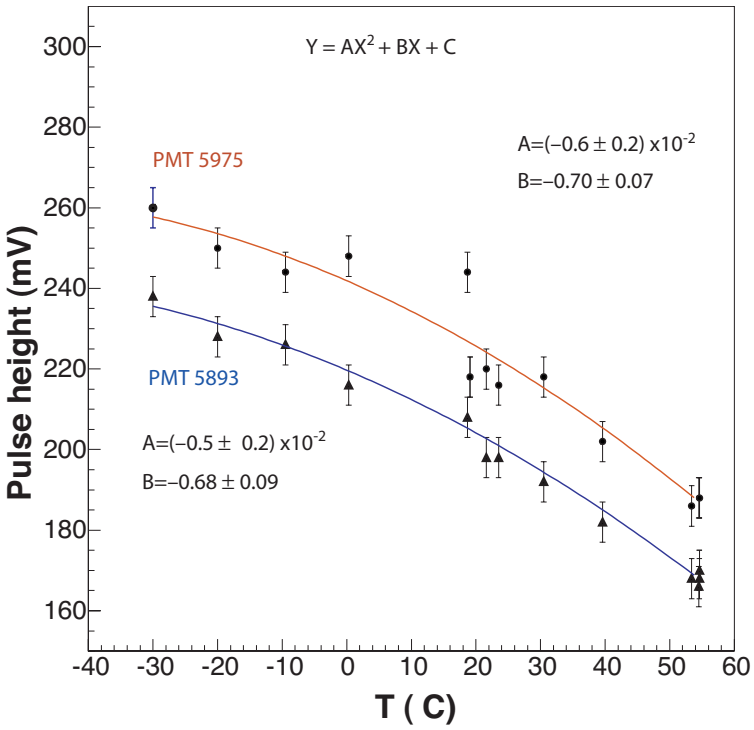

Figure 2.101: PMT response as a function of the temperature in vacuum.

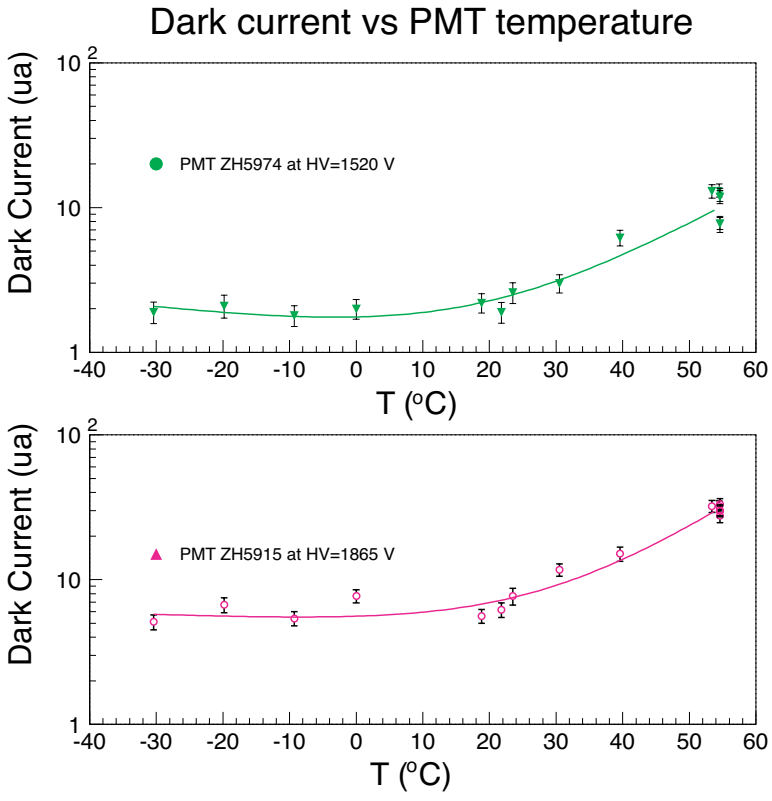

Figure 2.102: PMT dark current as a function of the temperature.

2.4.5 Beam test results

The TOF counters were tested in ion beams at CERN in 2002 and again in 2003. The beams were obtained by the fragmentation of the primary SPS Pb beam at 20 and 158 GeV/c/A against a Be or Pb target, within different momentum per nucleon windows using the H8 selection line. In 2002 the response of the counters were compared to one of the AMS-01 counters. In 2003, four counters with different configurations of the light guides were tested. Preliminary results are presented below.

Figure 2.103 shows the two counters tested in 2003 (C2 and C3) which are the two most challenging light guides with C3 bent and C2 twisted and bent. Counters C1 and C4, before and after C2 and C3 in the beam line, have straight light guides.

The ion charge is well measured by all counters. The measurement from the anode signal of counter C2, in principle the worst one, is shown in Figure 2.104. The charge resolution of C2 for different ions is shown in Figure 2.105 for both the anode and dynode signals summed from two PMTs. Measurements from the 2002 test beam run are compared with those of the AMS-02 RICH element that was also in the beam line in Figure 2.106.

The time of flight measurement between the C2 and C3 counters is shown in Figure 2.107 as a function of the particle charge. As the measurement in AMS-02 will be done with four independent measurements, the time resolution which can be inferred is of the order of 130 ps for a MIP.

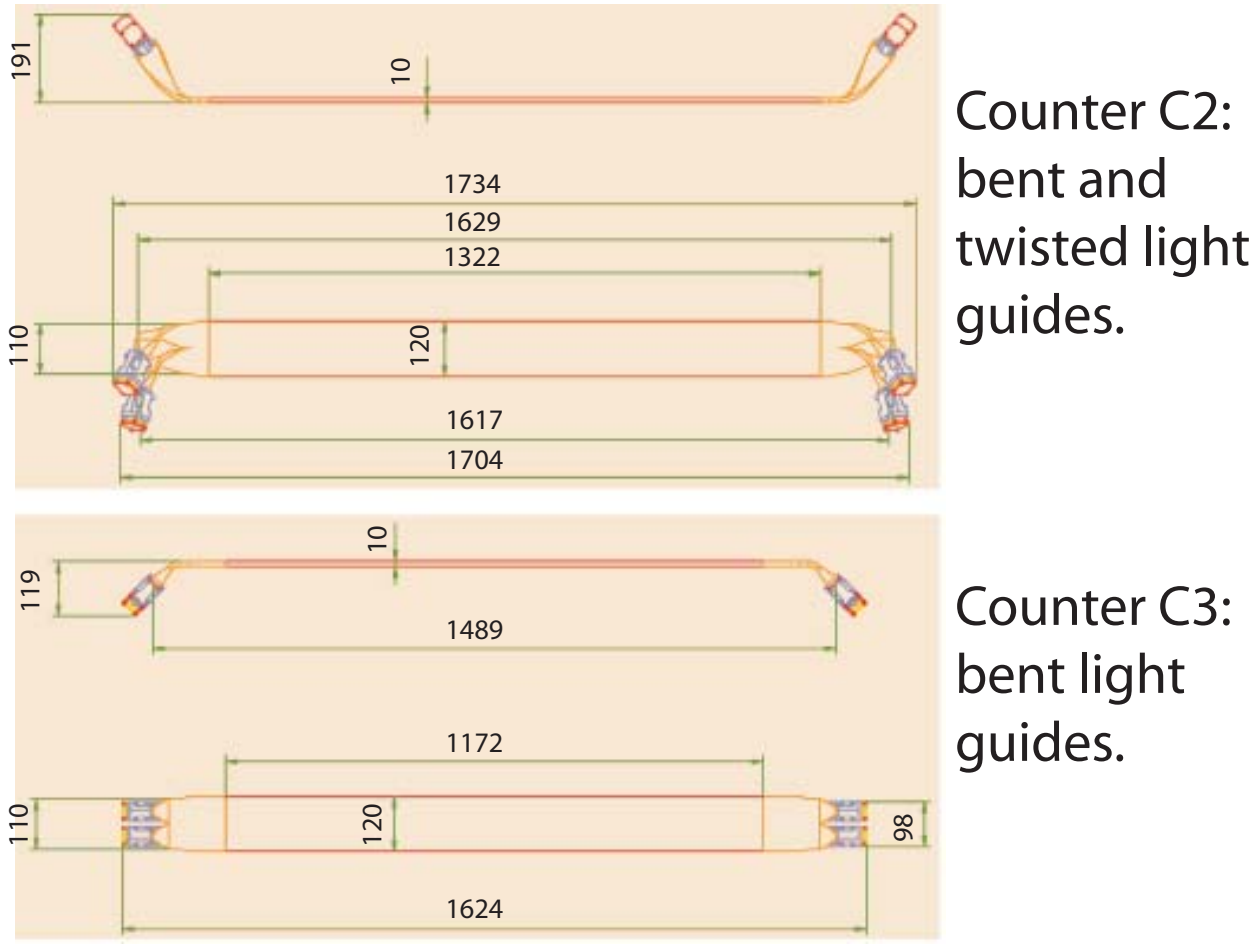

Figure 2.103: The C2 and C3 counters with bent and twisted light guides, tested in an ion beam at the CERN SPS in 2003.

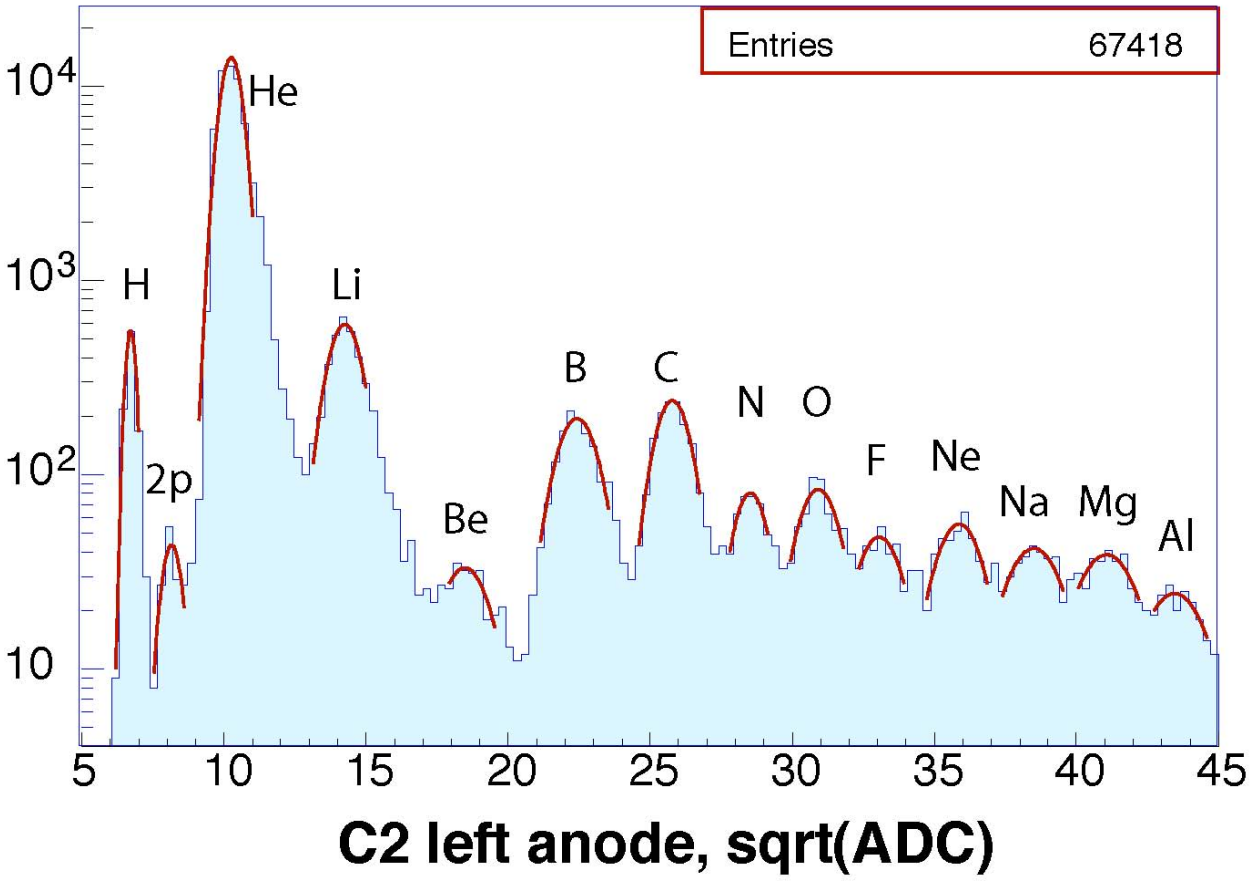

Figure2.104: The square root of the integrated charge measured with anodes and dynodes show peaks corresponding to different beam particles. Peak "2p" is produced by two singly charged particles crossing the scintillator in time.

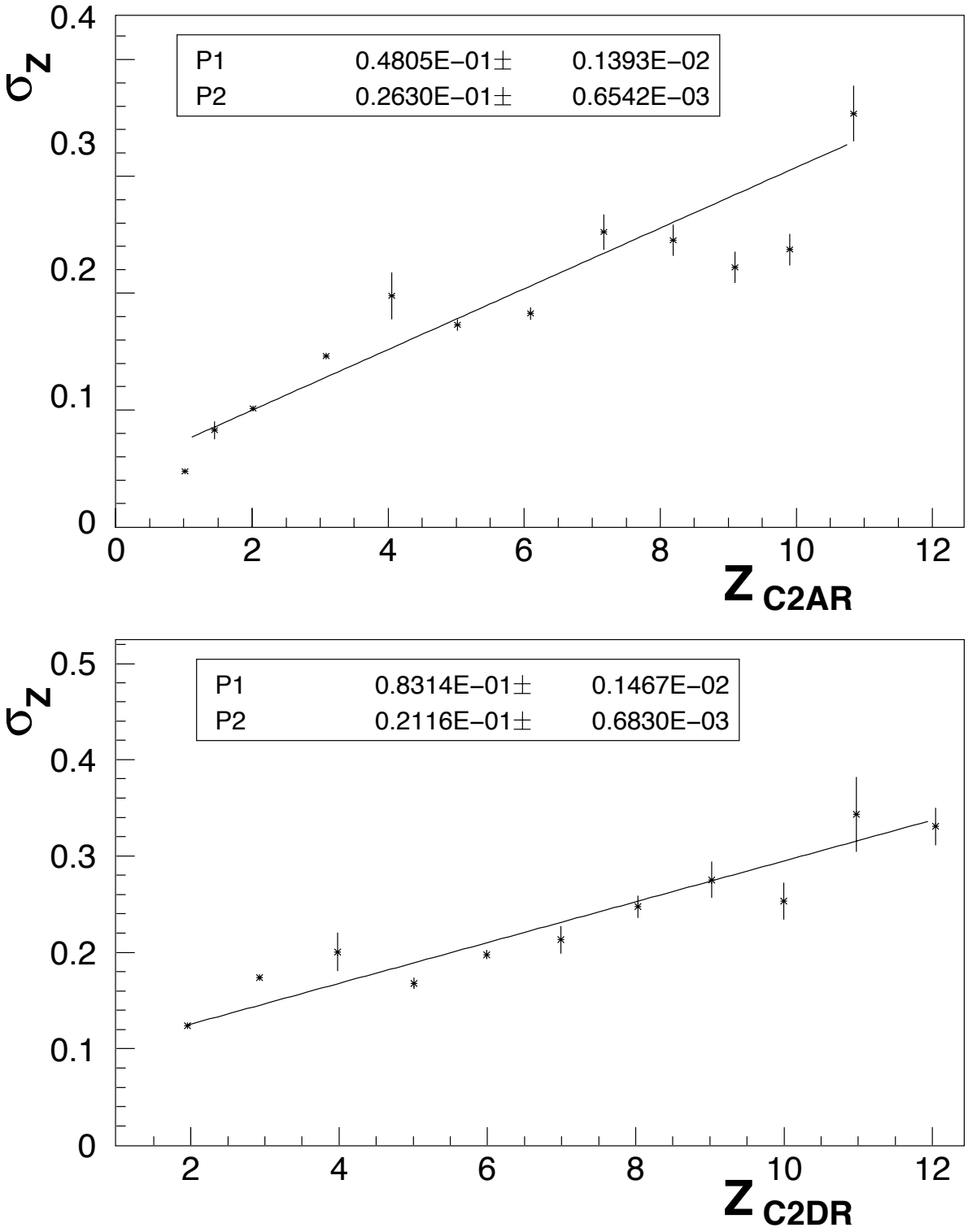

Figure 2.105: C2 charge resolution as a function of the particle charge for anode (above) and dynode (below) signals.

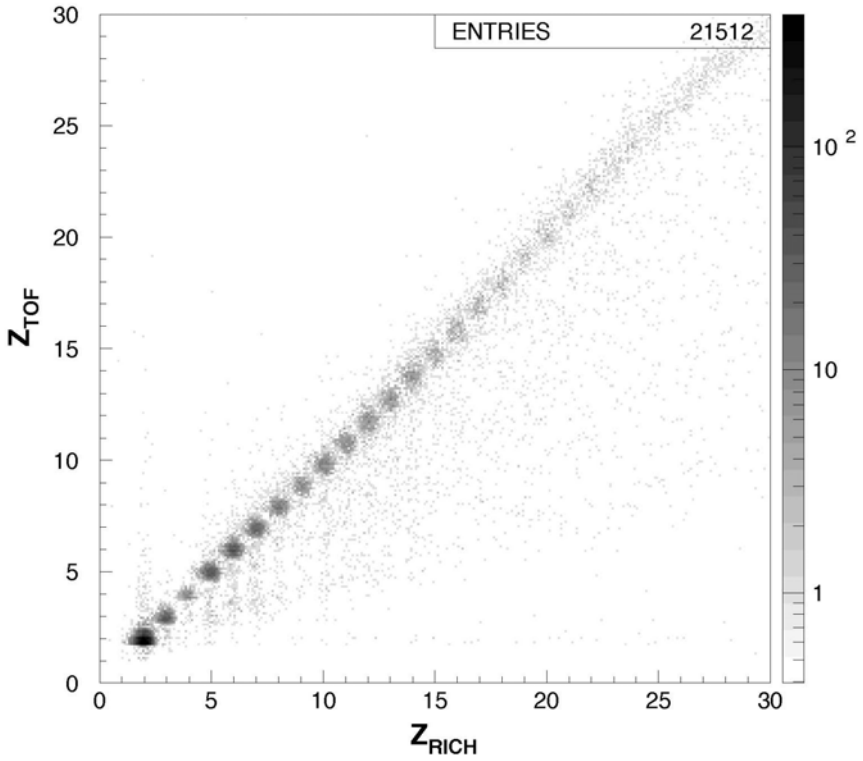

Figure 2.106: Charge measurements by the RICH and TOF (2002 test beam).

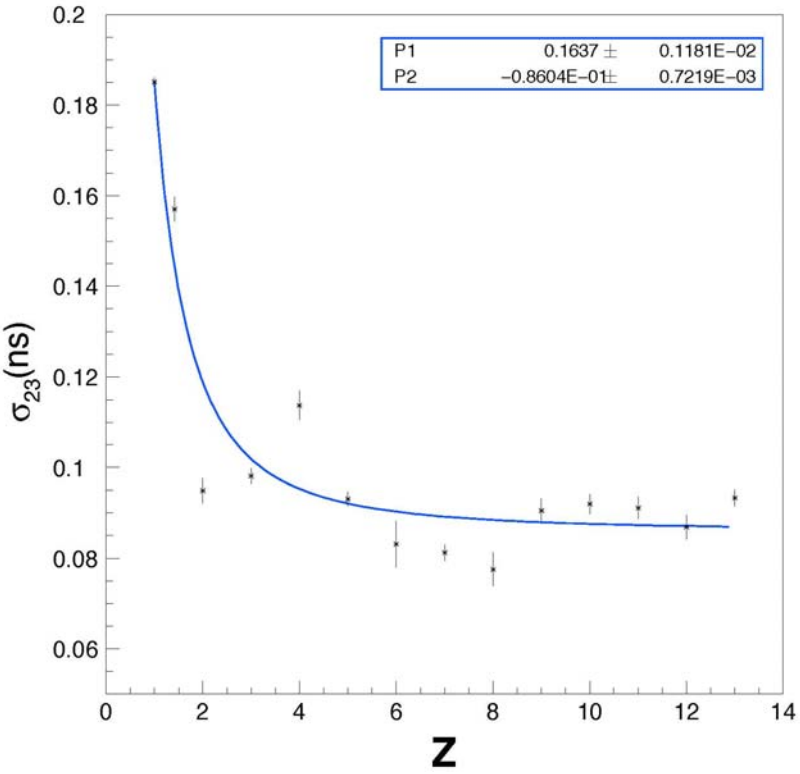

Figure 2.107: Time of Flight Resolution with C2 and C3 vs. particle charge.
(The point at Z = 1.4 corresponds to two peak 2p in Figure 2.104).

2.4.6 References

[1] D. Bollini et al., Nuovo Cimento **61A** (1969) 125;

A. Zichichi, Annals of Physics **66** (1971) 405;

A. Zichichi, "Study of charged final states produced in e^+e^- interactions" in "Elementary processes at High Energy", Academic Press (1971), p. 790;

M. Basile et al., Nucl. Instrum. and Meth. **179** (1981) 477.

[2] D. Alvisi et al., Nucl. Instrum. and Meth. A **437** (1999), 212.

[3] L.Brocco et al., Proc. 27^{th} ICRC (2001) 2193.

[4] G. Levi et al, Proc. 8^{th} ICATPP, Como, Italy, 2003.

[5] B. Bencheikh et al., Nucl. Instrum. and Meth. A **315** (1992) 349.

[6] N.Carota, "Studi per la calibrazione e l'ottimizzazione dei fotomoltiplicatori per i contatori a scintillazione dello spettrometro spaziale AMS-02", Laurea Thesis, Bologna (2002).

2.5 Anticoincidence Counters (ACC)

The AMS-02 Silicon tracker is surrounded by a layer of scintillation counters fitting tightly inside the inner bore of the superconducting magnet (see Figure 2.1), developed by RWTH-Aachen. Sixteen scintillation panels (BICRON BC414) of 8 mm thickness form the ACC (Figure 2.108). The panels dovetail along their vertical joints (Figure 2.108 inserts) to provide hermetic coverage. The ACC detects particles which enter the tracker laterally, outside of the main acceptance. Those particles may confuse the charge determination if they leave hits in the tracker close to the tracks of interest. The ACC scintillation counters are designed such that they can reject unwanted particles with high efficiency. Furthermore the photomultipliers (PMTs) that record the light signals from the ACC panels have to work in a moderate (~1.2 kG) magnetic field at locations on the top of and on the bottom of the magnet vacuum case, approximately 40 cm from the racetrack coils (Figure 2.109). To minimize the impact of this, the mesh PMTs (Hamamatsu R5946) are oriented with their axes parallel to the stray field. The light from the scintillation panels is collected in wavelength shifter fibers (Kuraray Y-11(200)M, diameter 1 mm) embedded in grooves milled into the scintillation panels (Figures 2.108, 2.110 and 2.111). The embedded fibers are collected into 2 output ports of 37 fibers each at both ends of the counters (Figure 2.111). For each panel there are two transition connectors (Figure 2.112), located on the upper and lower conical flanges of the magnet vacuum case. From these transition connectors the light is routed through clear fibers up to the PMTs mounted on the rim of the vacuum case.

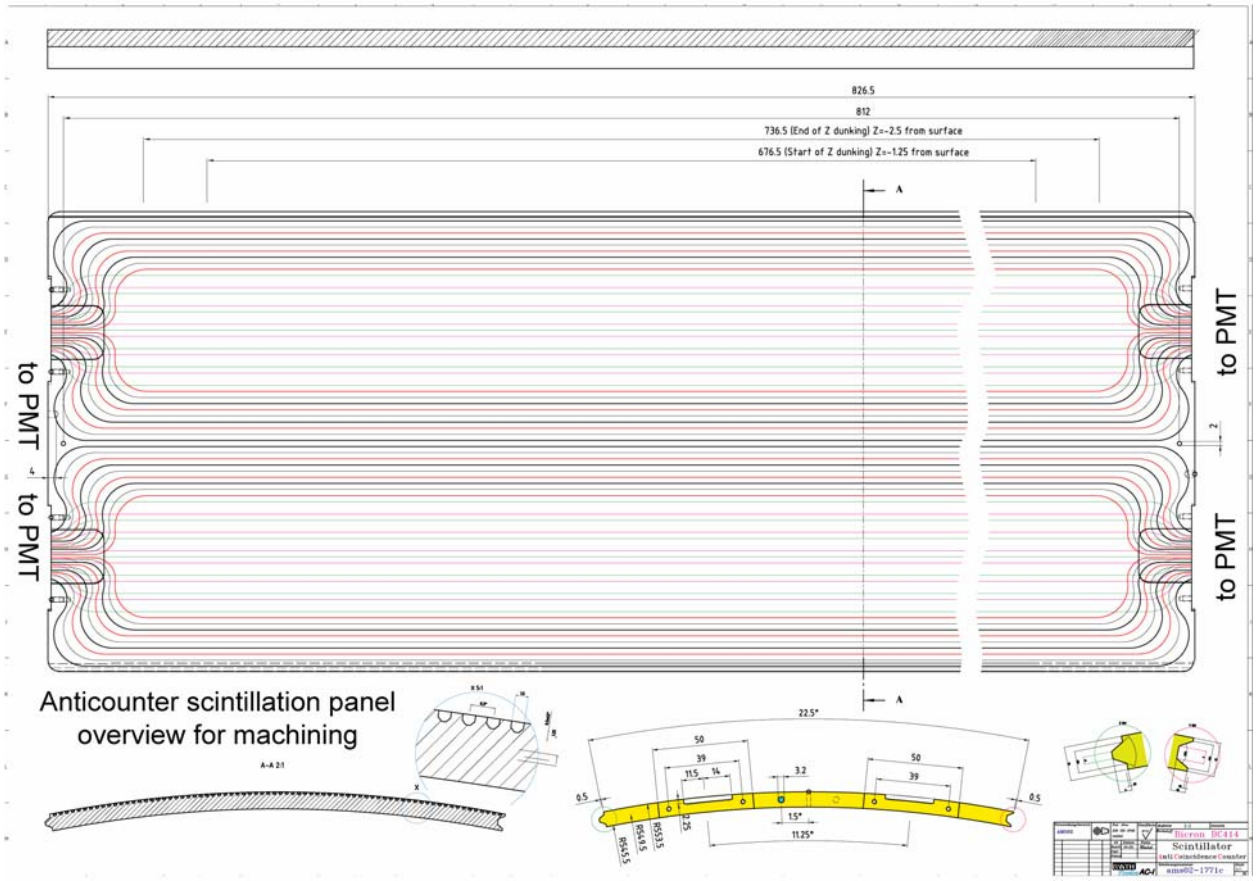

Figure 2.108: Anticounter scintillation panel. The edges are dovetailed for hermeticity.

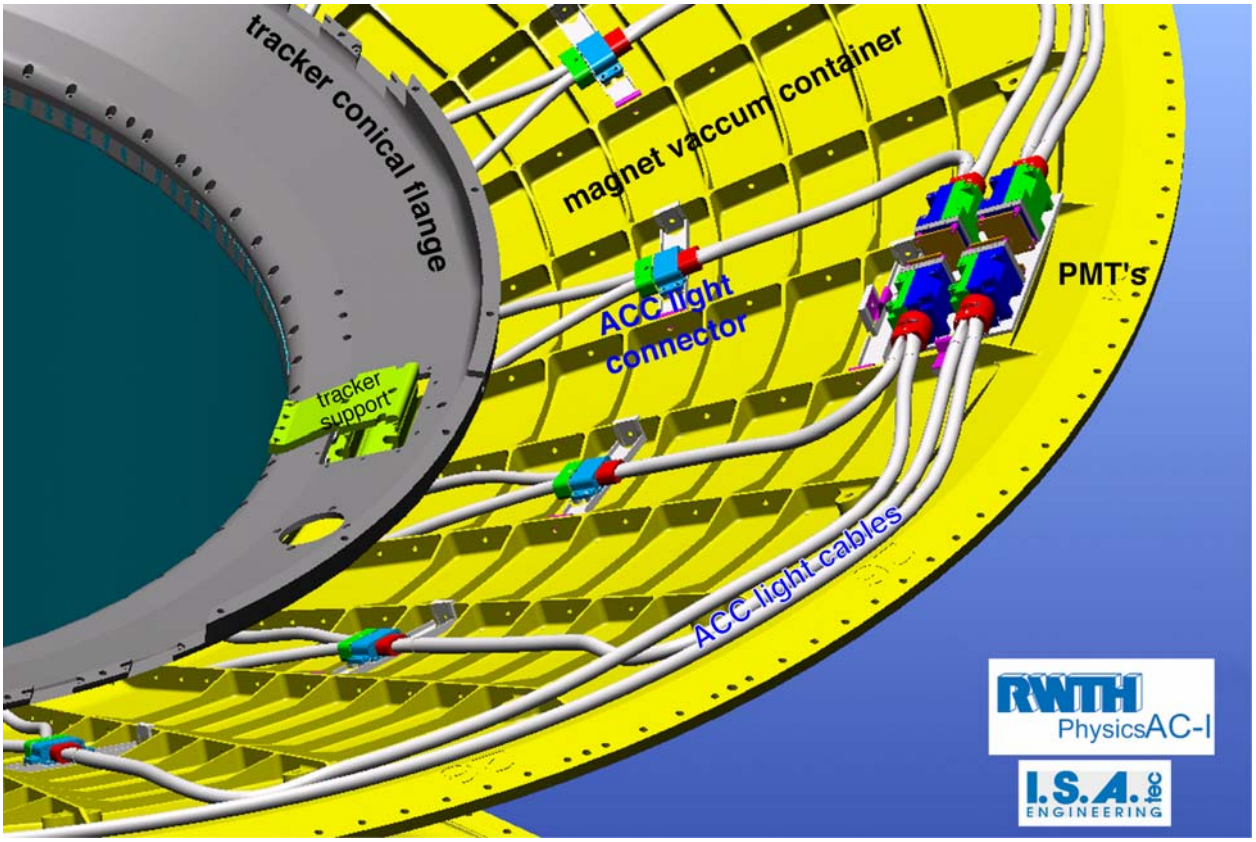

Figure 2.109: ACC light transport system, from the fibers embedded in the panels, through the couplings to the PMTs located on the outer rim of the vacuum case.

The light signal provided by the closely spaced wavelength shifter fibers and transported further on by the clear fibers to the PMTs typically yields 15 to 20 photoelectrons. One track thus results in at least 30 photoelectrons for detection since there are 2 tubes connected to each counter. For minimum ionizing particles at normal incidence to the panels, the mean electrical output charge of the PMTs is 13 pC. The front end electronics of the ACC is identical to that of the TOF system (see § 2.4.3). Signals from the ACC are included in the AMS-02 trigger in order to optimize the trigger performance by rejecting events outside the tracker acceptance.

A prototype counter has been tested with 10 GeV protons at CERN in 2003. Figure 2.113 shows a sample of the pulse height distributions observed within 3 cm of the edge. Figure 2.113a shows the typical upward fluctuations generally observed in energy loss measurements of charged particles. In order to emphasize the low signal behavior, Figure 2.113b, displays the spectrum below the most probable energy loss. Two different trigger conditions are displayed: for the events in red one of adjacent counters was required to have a signal; for the events in yellow only the beam defining counters were required. In the first case, a signal was observed in the counter under test for each of the 350,000 proton events. In the second case approximately 45 events were below threshold (0.6 pC). With this performance, the ACC guarantees that an antimatter signal will not be simulated due to laterally entering particles.

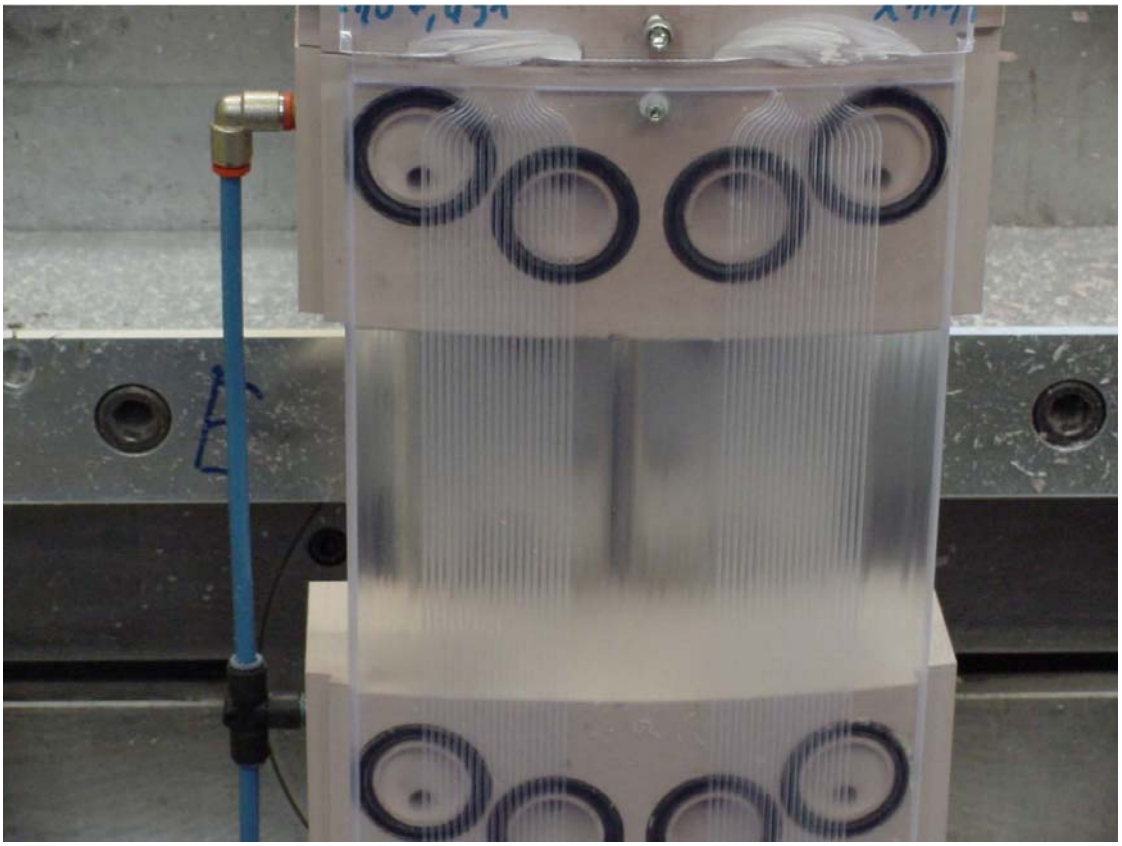

Figure 2.110: ACC during machining of the fiber grooves.

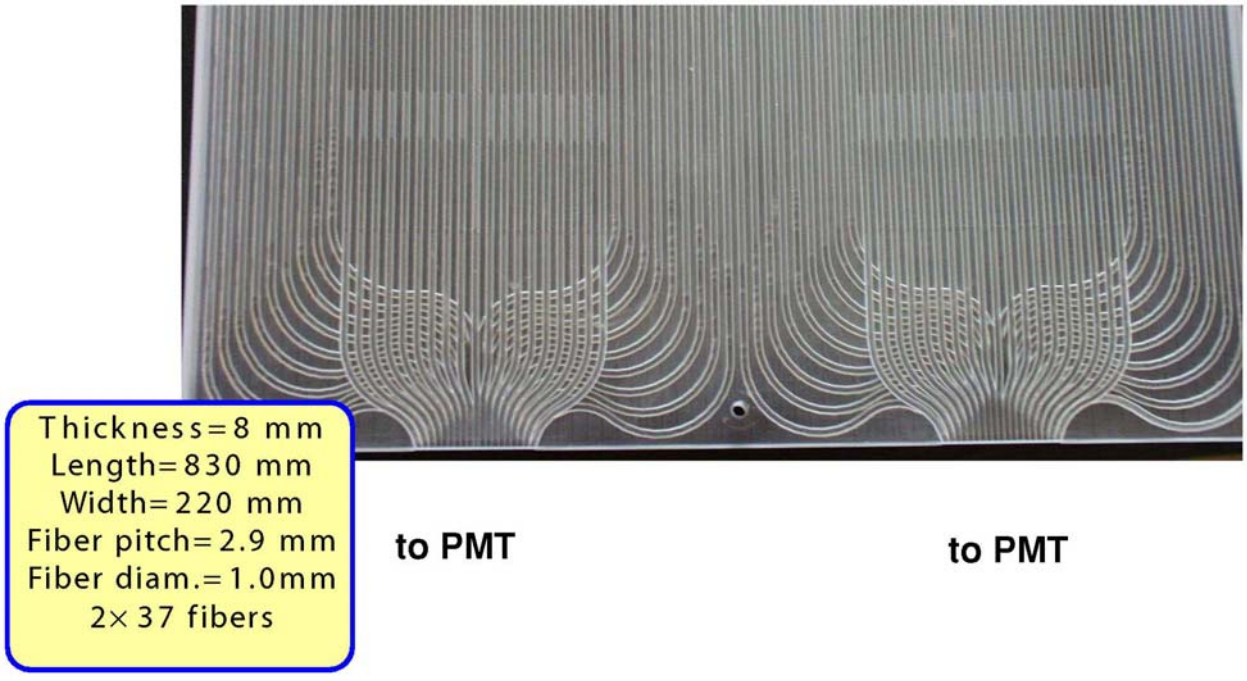

Figure 2.111: Finished ACC panel end.

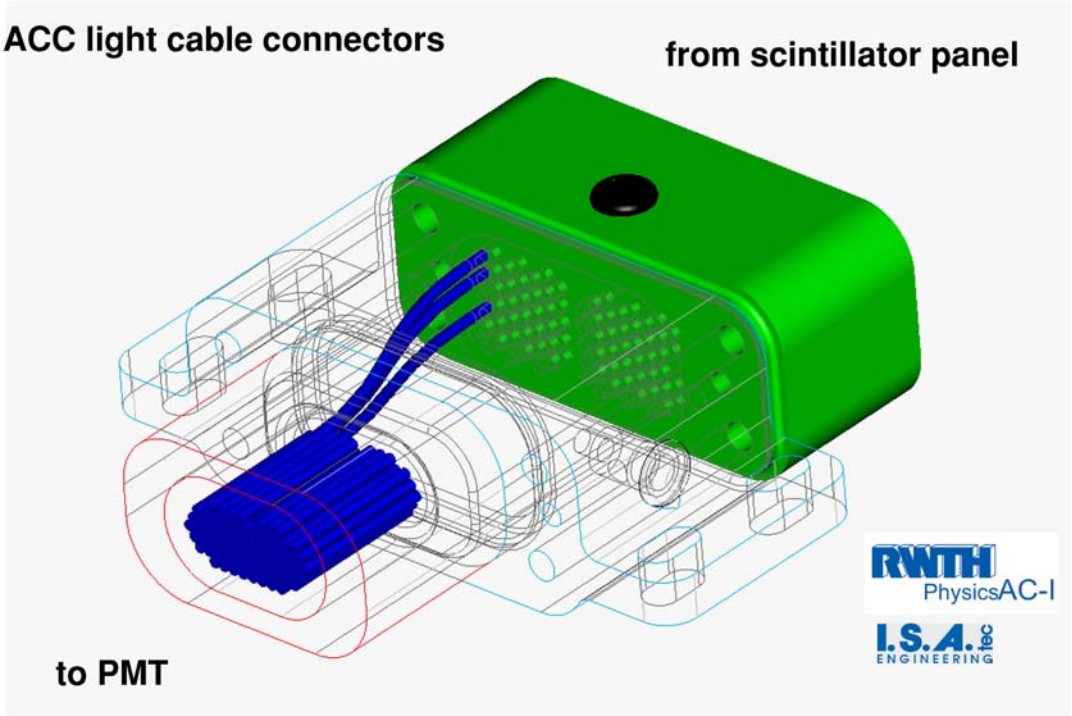

Figure 2.112: ACC light cable connectors, wave length shifter fibers arrive from the panel on the right side, clear fibers continue to the PMT on the left.

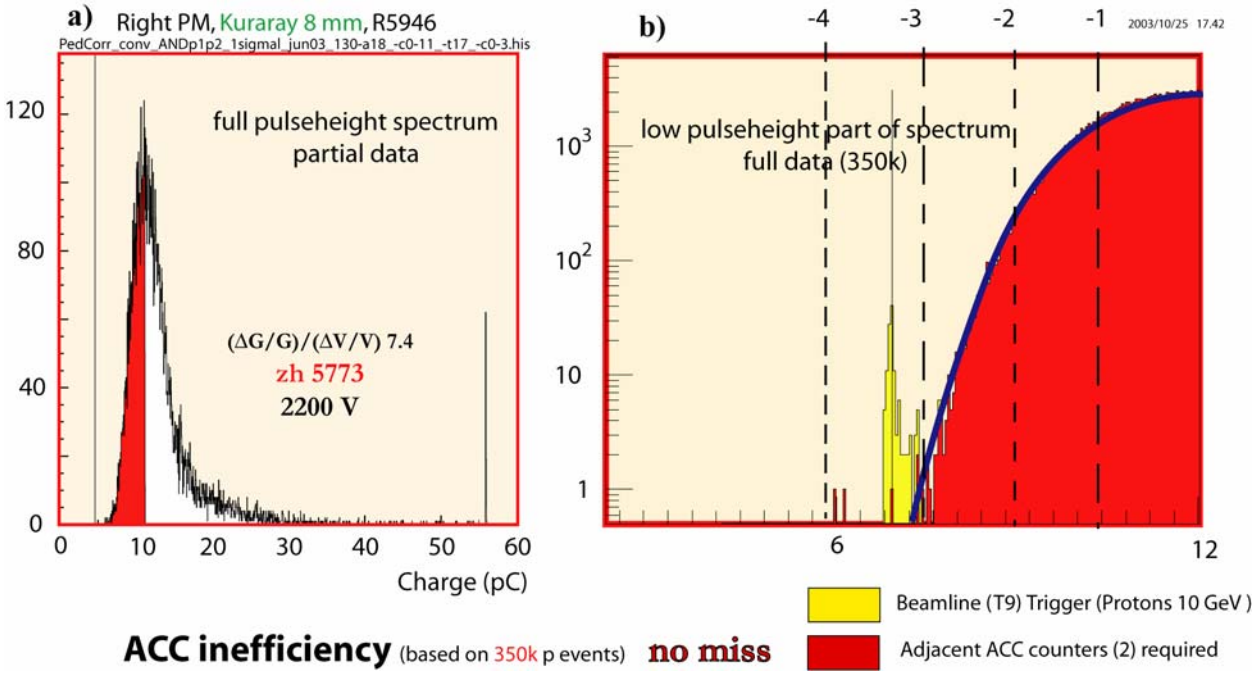

Figure 2.113: ACC prototype test with 10 GeV protons. a) Pulse height spectrum from typical run, counts vs. PMT charge. b) Pulse height spectrum below maximum, counts vs. charge, with tight (red) and loose (yellow) trigger conditions (see text).

2.6 Ring Imaging Cerenkov Detector (RICH)

In order to study fundamental topics in astroparticle physics such as the existence of antimatter or the relative abundances of light isotopes and charged nuclei, it is necessary to have a precise determination of the masses of charged particles. The mass of a particle is related to its momentum, p, and velocity, β, through the expression $m = (p/\beta)\sqrt{1-\beta^2}$ and its determination is based on the measurement of both quantities. In the AMS spectrometer, the momentum is determined from the information provided by the Silicon Tracker with a relative accuracy of ~1% over a wide range of energies. This entails an error of the same order on the mass of the particle so, in order to overcome this uncertainty, the velocity has to be measured with a relative accuracy of about 1 per mil. For this purpose a Ring Imaging Cerenkov Detector (RICH) has been designed with a large geometrical acceptance to operate in the environmental conditions of the outer space.

The determination of the velocity of charged particles is based on the Cerenkov effect. When a charged particle goes through a dielectric material, it induces a macroscopic polarisation. If its velocity is larger than the phase velocity of the electromagnetic field in the material, the change of the dipolar fields with time initiates the emission of electromagnetic radiation. The different monochromatic waves emitted in the optical region of the material form almost the same angle with respect to the velocity of the particle. Therefore, a cone of Cerenkov radiation is created along its trajectory in the material. The properties of this radiation cone depend on the velocity of the charged particle and the refractive index of the material, $n(\omega)$. In particular, for an incoming particle of charge Ze, the half opening angle of the cone is given by $\cos\theta = 1/\beta\, n(\omega)$; the number of radiated photons in a frequency range $d\omega$ for a traversed length dx in the material by $d^2N/d\omega/dx = \alpha Z^2 \sin^2\theta$; and the threshold velocity above which Cerenkov radiation is emitted by $\beta_{\min} = 1/n(\omega)$. Therefore, the velocity is determined from the measurement of the opening angle of the Cerenkov cone and, as a by-product, the number of detected photons will provide an independent estimation of the charge of the incoming particle.

Within AMS-02, as shown in Figure 2.1, the RICH is placed on the lower part of the spectrometer, between the lower Time of Flight Counters and the Electromagnetic Calorimeter. It is being built by INFN-Bologna under contract to the Italian Space Agency (ASI), CIEMAT, Instituto de Astrofisica de Canarias, Lab. Inst. Exp. Particle Physics, U. of Maryland, Florida A&M, Nat. Auto. U. of Mexico and LPSC. As shown in Figure 2.114, the RICH has a truncated conical shape with 60 cm upper radius, 67 cm lower radius, a height of 47 cm and a supporting plate on the top that holds a 3 cm thickness layer of dielectric material (radiator). The lower plane, which has a 64x64 cm^2 square central hole to let particles go unaffected to the Electromagnetic Calorimeter, supports an array of 680 light guides and photomultipliers as well as the front-end electronic boards. A charged particle coming from above first crosses the radiator creating a cone of Cerenkov radiation. Most of the photons go directly to the photon detectors in the lower plane. The other photons are reflected on the lateral surface of the cone and also directed to the photon detectors. At the lower, or image, plane, the photon detectors have light guides attached to photo-multiplier tubes (PMTs). From the spatial coordinates of the photomultiplier pixels and the direction of the incoming particle, the Cerenkov cone is reconstructed and the velocity of the particle determined. Upward going particles do not leave this signal and can thus be unambiguously discriminated.

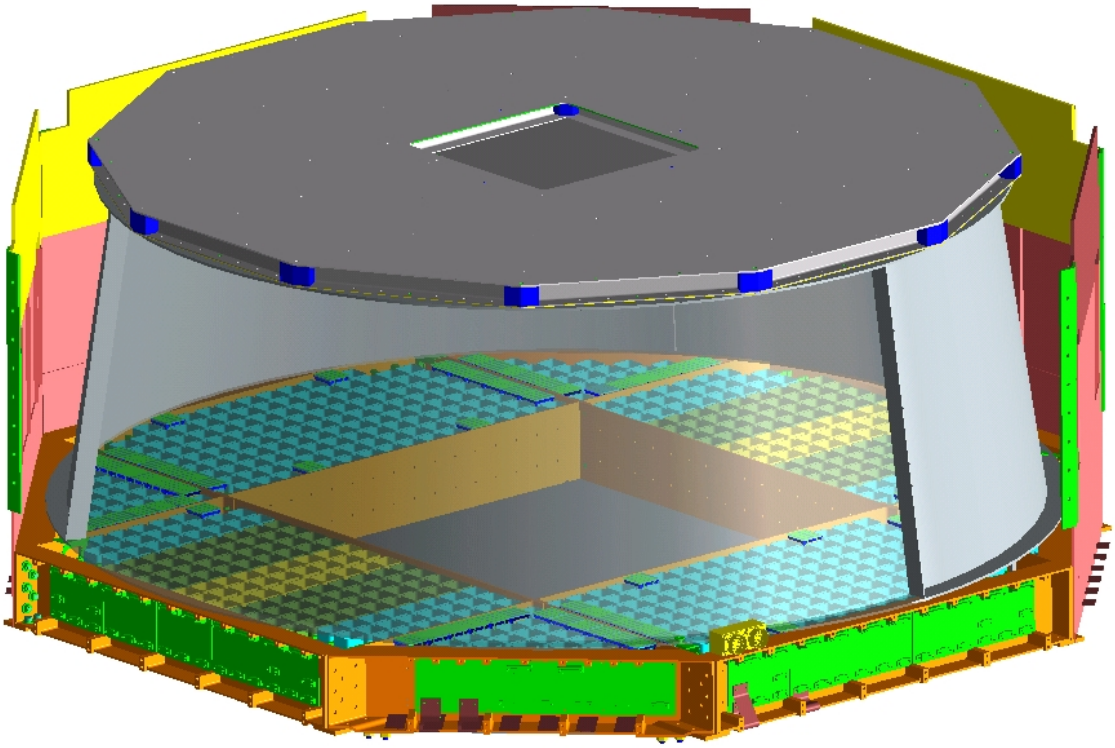

Figure 2.114: The main structural components of the RICH.

2.6.1 Radiator

Several dielectric materials have been considered as possible radiators. Their performance has been analysed by a Monte Carlo simulation and, for the most appropriate ones, tests have been performed with ion beams at CERN and cosmic rays at LPSC (Grenoble). The material that has shown better performance for the experimental goals are silica Aerogels. These compounds are a mixture of $m(SiO_2)$ and $2m(H_2O)$, with m an integer, and have a porous structure with bubbles, most of them of small size compared to optical wavelengths. The refractive index is an average between the ones of air and the mixture and has an almost linear dependence with the density. Thus, with different treatments of the mixture appropriate densities can be selected in the range of 0.1 to 0.3 g cm^{-3} and therefore refractive indices greater than most gases and smaller than most liquids and solids can be obtained. There are two suppliers of high quality Aerogels with the desired properties (see Table 2.4): the Catalysis Institute of Novosibirsk (hereafter referred as CIN), which produces 3 cm thick hydrophilic tiles, and Matsushita Electronic Company (MEC) which produces hydrophobic tiles of 1 cm thickness.

Supplier	Refractive Indices	Clarity (mm^4/cm)	Size (cm^3)	Other features
MEC	1.03 – 1.05	0.007 – 0.013	11.5 x 11.5 x 1	Hydrophobic
CIN	1.03 – 1.05	0.005 – 0.008	11.5 x 11.5 x 3	Hydrophilic

Table 2.4: Properties and manufacturers of high quality silica Aerogel.

Several tiles produced by the two manufacturers have been tested under different external conditions. In particular, mechanical and optical properties such as the refractive index, the transmittance and the light dispersion were analysed by exposing the tiles to thermal and vacuum cycles in order to assess the performance of the radiator under the extreme environmental conditions of outer space. In order to increase the photon detection efficiency for those particles that fall upon the central hole of the detection plane, the central blocks of the radiator are made out of NaF, which has a higher refractive index (n=1.336) and so gives a wider Cerenkov cone. Thus, the mechanical structure of the radiator consists of 80 rectangular blocks of silica Aerogel of 11.5x11.5x3 cm^3 and 16 central blocks of NaF of 8.5x8.5x0.5 cm^3. All the blocks are supported from the bottom by a 1 mm thick layer of methacrylate free of UV absorbing additives that is fixed to the TOF upper supporting plane.

2.6.2 Reflector

About 30% of the Cerenkov photons emerging from the radiator are pointed outside of the photon detector array. A reflector (see Figure 2.115) has been designed to collect those photons in the array. It consists of a supporting structure with a truncated conical shape of 134 and 114 cm lower and upper diameters and a thin film of reflective coating deposited on the inner surface. In order to maintain the 1 per mil velocity resolution, it has been designed with strong requirements on the tolerances as shown in Table 2.5.

Conicity	200 μm
Centering	100 μm
Reflectivity	≥ 85 % (at λ = 420 nm)
Roughness	≤ 150 nm
Slope error	< 1 mrad

Table 2.5: Parameters and designed tolerances for the reflector.

As shown in Figure 2.115, the reflector is produced in 120-degree composite segments, which are framed with composite ribs at the entire perimeter of the mirror. The composite used is BRYTE EX-1515/M55J Laminate with Unidirectional Prepreg glued with MASTER BOND EP30LTE-LO Epoxy Adhesive. The bushing is stainless steel. In order to achieve the reflectivity requirement, the reflective coating is made up of 100 nm of aluminium and 300 nm of SiO_2.

Figure 2.115: The conical reflector of the Cerenkov detector (3 sectors layout).

The reflector is made by a replica technique. The starting point is a mandrel (a die) on which the CFRC plies, which will be the lateral surface of the reflector, are positioned before being cured. The mandrel and plies are oven cured under vacuum and then the surfacing process begins. Using a patented

technique, a thin layer (a few tenths of a millimeter) of resin is poured between the CFRC and the mandrel. After a second cure process, the mechanical part of the lateral surface is ready. It is important to have a mandrel with the exact shape, dimensions and roughness of the reflector to be produced. Afterwards the flanges and the ribs are glued to the lateral surface using the mandrel as a geometrical reference. Following this procedure, the three sectors are produced and then assembled by gluing the vertical ribs using the mandrel as a jig. The final step is the coating made by vacuum deposition of the aluminum and silicon dioxide layers.

The mandrel for the final mirror has been produced (Figure 2.116). Optical measurements have shown that the surface roughness is less than 15 nm and that all the required tolerances are satisfied. It has been used to produce two samples of the reflector (of 30 x 45 cm) to test the optical properties, one of which was used in the prototype tests. The measured roughness of the surface was less than 5.3 nm (rms) and the reflectivity greater than 85% at 420 nm. After these results, one of the three segments of the final mirror has been produced by Composite Mirror Applications Inc. (Tucson, AZ) with a roughness of less than 3.8 nm.

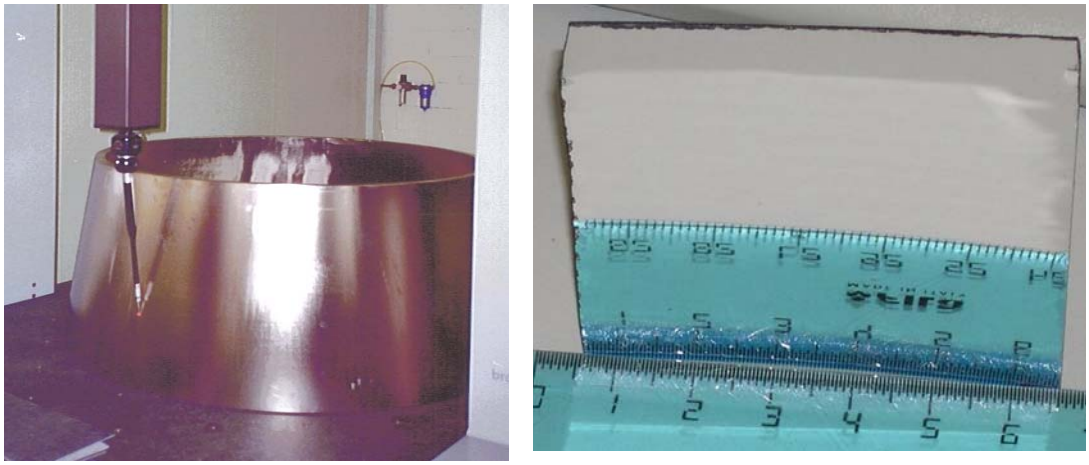

Figure 2.116: Measurement of the mandrel and a sample produced to control the roughness and reflectivity.

2.6.3 Photon detection system

The Cerenkov photons are collected at the bottom of the detector by an array of 680 photomultiplier tubes (PMTs) that withstand moderate magnetic fields. However, the residual field of the superconducting magnet in the region where the photomultipliers are placed is ≈ 300 G so they have to be surrounded by a shielding case and, as a consequence, a light collection system has to be designed in order to direct the Cerenkov photons from the top of the shielding case to the sensitive part of the photomultipliers. Thus each unit of the photon detection system, as shown in Figure 2.117, is composed of a photomultiplier, the shielding, the housing and the light-guides.

To detect the Cerenkov photons, different photomultiplier tubes have been analysed. Most appropriate for the characteristics of this detector is the HAMAMATSU R7600-00-M16 due to the reduced size, fast response under low operational voltage (800 V), large anode uniformity and low sensitivity to external magnetic fields. The Cerenkov photons are detected on the image plane at 40 cm from the radiator material. Therefore the accuracy in the measurement of the velocity depends significantly on the size of the photon sensors. The aforementioned photomultipliers have a multianodic structure with 4 x 4 pixels, each one with a sensitive zone of 4 x 4 mm^2. This guarantees a resolution in the measurement of the velocity of 1 per mil. These PMTs also have a high quantum efficiency (≈20%)

in a range of wavelengths between 300 and 600 nm, well within the optical region of the radiator and where the refractive index is, to a large extent, independent of the photon energy. With this efficiency, for an ultra relativistic particle of charge Z = 1, an average of 8 photons are detected for a radiator with a refractive index of n=1.03. We have analysed each photomultiplier for the detector under single and multiple photon excitations and characterised their response in terms of the gain, the spread of collected charge and the linearity in order to equalize their response within the high voltage range of 750 to 850 V.

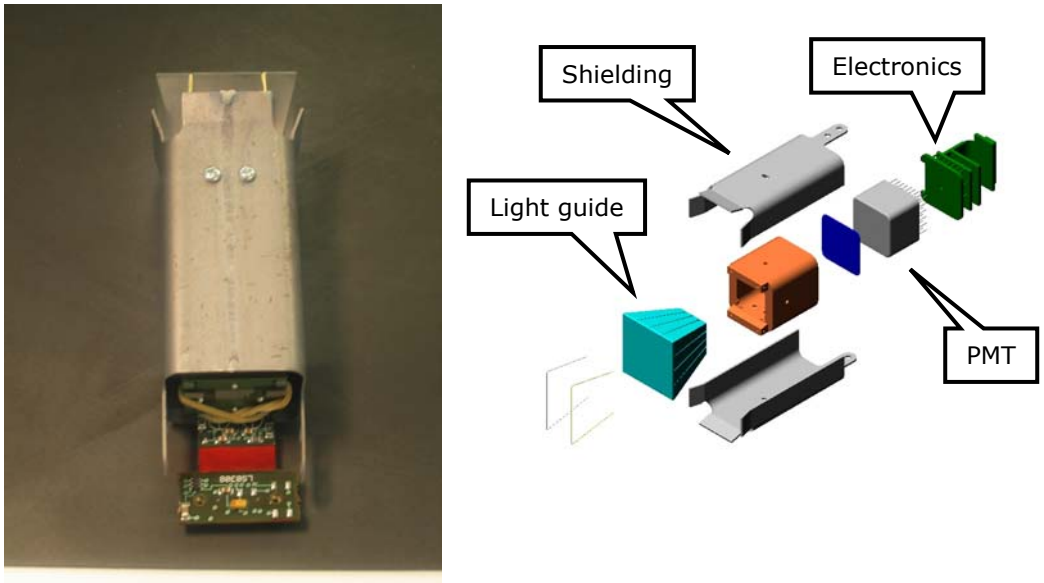

Figure 2.117: The photon detection system and an exploded view of the main components.

To ensure the PMT performance, each one is placed, together with the corresponding front-end electronic boards, inside a cell made of soft iron and VACOFLUX 50, a diamagnetic material that, after proper annealing, provides good shielding in strong magnetic fields. The dimensions of the cells are longer than those of the photomultiplier to avoid boundary effects. Due to the geometry of the array of photomultipliers, they are assembled forming a grid with two different geometries: square (with 143 cells) and triangular (with 27 cells). The different grids are supported by a secondary structure made out of aluminium beams that also hold the frustum of the conical reflector. We have analysed the performance of the shielding cage under an external magnetic field of 300 G (the maximum under which the photomultipliers will have to operate) and different orientations. In the worst case, the inner field was always less than 120 G. Each PMT was tested independently to establish its proper performance under this residual field. As the elements of the grid are fixed together by spot welding, a series of mechanical measurements have been performed to ensure that the thermal stress so induced does not significantly modify the diamagnetic properties of the materials.

The interface between the photomultipliers and the walls of the shielding grid is a polycarbonate box (housing) that also contains the front-end electronics boards. The housing has been designed to ensure the alignment of the photomultiplier pixels and the light guides within the shielding cells. Both are glued to the housing and, in all possible configurations, a correct alignment has been achieved.

The light collection system leads the Cerenkov photons from the top of the shielding case to the sensitive part of the photomultipliers. Different options have been analysed: fiber optic cables, hollow light guides with reflecting inner surfaces and solid light guides working by internal reflection. Detailed Monte Carlo simulations have shown that, for the actual dimensions of the Cerenkov detector and the particular characteristics of the radiator, the solid light guides are the most efficient. However, the optical and mechanical properties of the plastic are crucial for the good performance of the light collection

system. The photomultiplier response has high quantum efficiency for wavelengths between 300 and 600 nm. On the other hand, due to the angular distribution of the incoming photons, the average path length inside the light guides is 3.7 cm. Therefore, we require a transmittance as high as possible over this wavelength interval; in particular, materials free from UV absorbing additives must be used. Furthermore, the refractive index has to be as close as possible to the one of the photomultiplier window ($n = 1.5$), the density low to minimise the weight of the whole structure and the thermal expansion coefficient small to withstand temperature gradients without significant deformation. Many different organic materials have been analysed and DIAKON LG-703 was selected. In order to reduce the losses caused by the different optical interfaces, a thin film (1 mm) optical joint is inserted between the light guides and the photomultiplier window. As shown in Figure 2.118, each photomultiplier has 4 x 4 pixels and every light-guide structure has 16 independent units with 4 different shapes and fills a total volume of 13 cm^3. The optimum dimensions have been determined to maximise the photon collection efficiency. A Monte Carlo simulation of different physical processes has shown that sufficient Cerenkov photons are collected to achieve a resolution in the velocity of charged particles of $\sigma_\beta / \beta \approx 10^{-3}$.

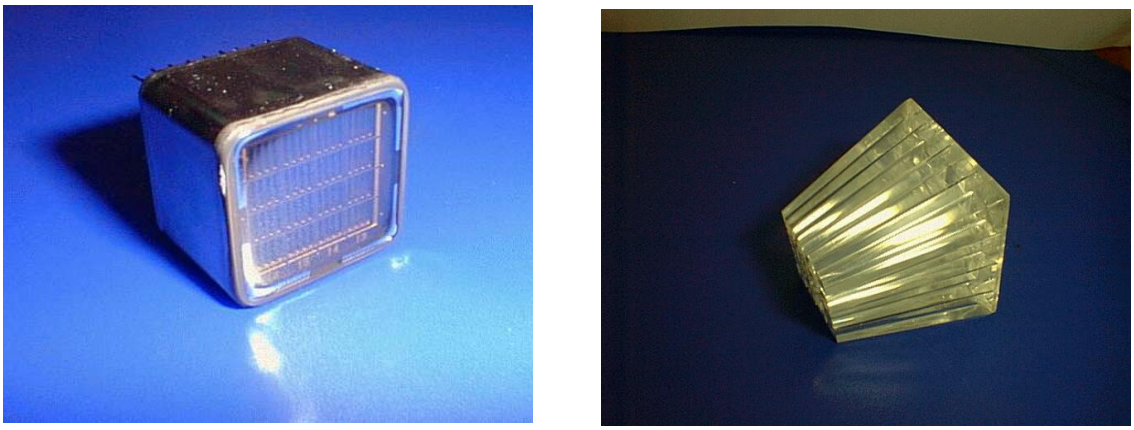

Figure 2.118: PMT showing the 4 x 4 anode structure and a 4 x 4 array of light-guides.

Complete cells, as shown in Figure 2.117, were tested on a vibration table, Figure 2.119, to ensure that the structure will withstand the shuttle take-off. The tested structures broke between 19 and 27 g_{rms}, 3 to 4 times above the required qualification levels. A similar test was performed on an assembly of 8 cells and no mechanical damage was observed.

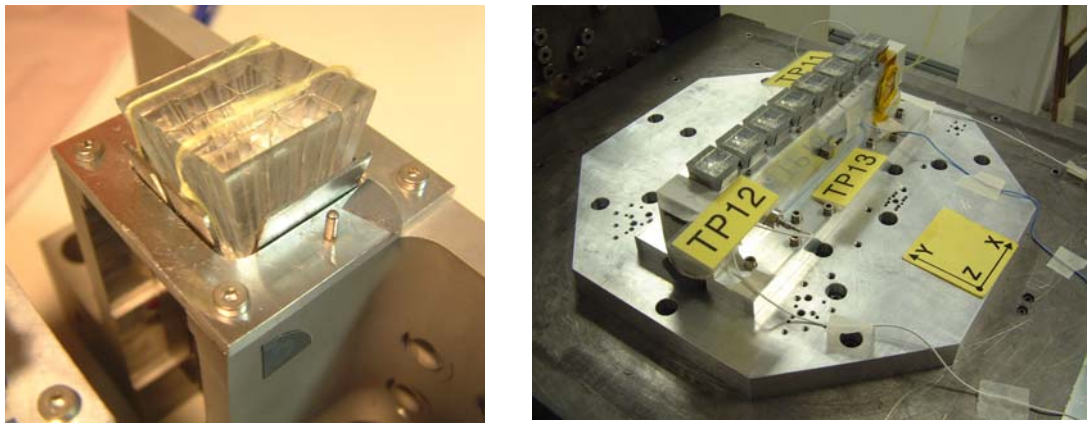

Figure 2.119: Vibration tests of a single cell (left) and of an eight cell array (right).

2.6.4 Electronics

The electronics for the RICH has four main components: front-end electronics, control and signal processing, monitoring and setting of working parameters and power supplies. The front-end electronics consists of printed circuit boards located at the base of each photomultiplier (see Figures 2.117 and 2.120). These provide the HV bias network for the PMT and the conditioning and digitalization of the PMT anode signals. The control and signal processing stage is devoted to the generation of sequences of control signals to drive the front-end electronics and to the collation, reduction and dispatch of digitized results. It consists of a set of 12 electronic boards located on the edge of the detector structure, shown in green in Figure 2.114. These circuits are based on the common digital part (CDP) custom developed for AMS (see § 2.8). The third component deals with the monitoring and the setting of different parameters (like temperature, voltage and current) by means of two electronics boards also mounted on the detector edge. The high voltages required by the photomultipliers are supplied by one type of unit, mounted on the oblique legs of the USS, and a second type, mounted on the main radiators, provides the different low voltages needed for the rest of the electronics.

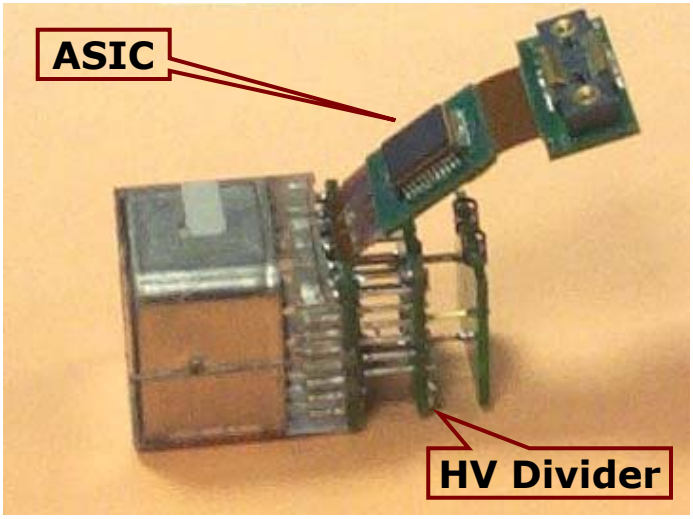

Figure 2.120: RICH front end electronics at the base of the PMT.

i) Front End Electronics

As shown in Figure 2.120, three printed circuit boards mounted on the base of each PMT form an 80 MΩ HV resistor divider which provides the bias for each dynode of the phototube, optimizing the power consumption and maintaining a very high linearity. An application specific integrated circuit (ASIC) is mounted on a forth board connected by a flexible Kapton cable. The ASIC, developed specifically for the AMS-02 RICH, contains 16 channels of a charge sensitive preamplifier which feeds an RC-CR shaper and a sample & hold (S/H) circuit, which fixes the maximum of the shaped signal. In order to increase the resolution for the small signals, an amplifier, which selects between a gain factor 1 or 5, has been added to the chain. A multiplexed output buffer drives the signal through a current to voltage converter shared by the 16 channels out of the ASIC to an analog to digital converter (ADC). This ADC (Analog Devices AD8051A), which is also used in the TRD and ECAL electronics, implements a 12-bit successive approximation at 1 million of samples per second, with low voltage and very low power consumption and serial output.

ii) Control and Signal Processing Stage

The main trigger regulates the sample & hold, the multiplexing and the ADC operations. When the trigger signal arrives, a train of pulses is produced. The leading pulse puts the S/H of the front end stage into sample mode waiting for the peak of the signal. The next pulse puts the S/H into hold mode waiting for the signal to be read out. At the leading edge of each successive pulse the output of each S/H is then sequentially readout. In lock step, the analog to digital conversion is performed using two dedicated clock signals. The first holds the signal at the ADC input while the conversion is performed and the other initiates the conversion. The digitalized signal is then sent to a buffer. Once the conversion process is completed, the 16 S/H in the ASIC are reset and the ADC enters a low power mode until the next trigger. The generation of the control signals and their sequences has been implemented, as shown in Figure 2.121, through an algorithm hardwired into a radiation tolerant, low power and low voltage gate array (ACTEL A54SX72A).

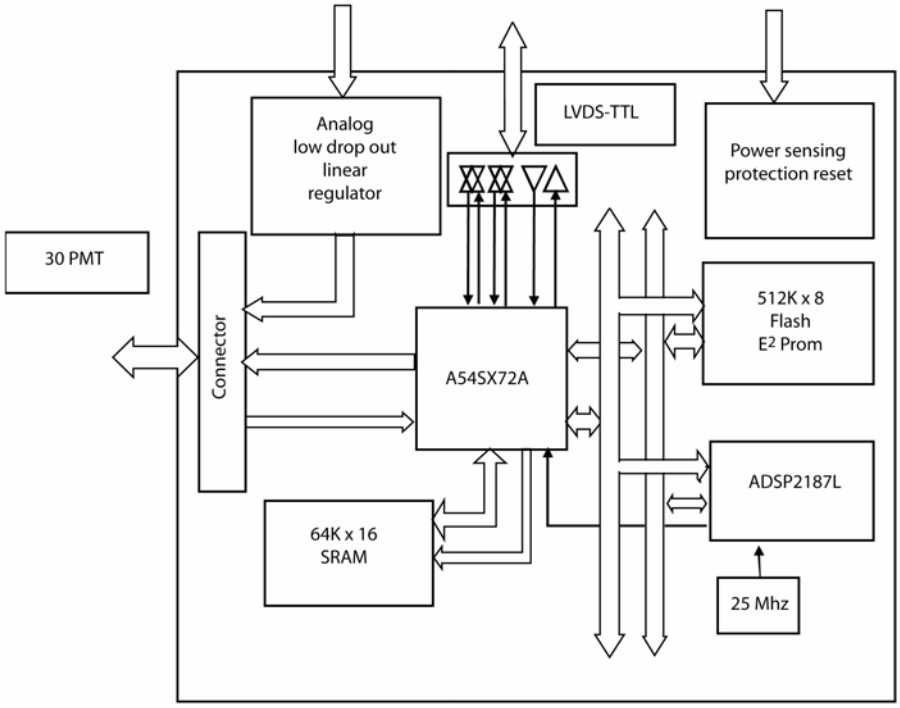

Figure 2.121: RICH Control and signal processing electronics based on CDP design.

Asynchronously with the trigger, the data is extracted from the SRAM buffer into the digital signal processor (DSP), pedestals are subtracted and the result compared to a threshold. The pedestals are related to the electronic offsets on each channel and the threshold is related to electronic noise. Significant data reduction is achieved by rejecting, on a trigger by trigger basis, those channels with amplitudes below threshold. The selected DSP (Analog Devices ADSP2187L-BKST) operates at 50 MIPS and includes 32K words of memory for on chip buffering. Once processed, the data are sent to an output buffer until they are read out by the next level of the data acquisition system.

This next level is like the circuit shown in Figure 2.121 except that the connections to the PMTs are replaced by 100 MHz serial point to point links to each of the data reduction circuits. After collation and buffering the data is sent up to the main data acquisition (see § 2.8). In addition, a set of 1 MHz serial point to point links from the DSP are added to the circuit of Figure 2.121 to collect monitoring data and set voltages, etc, in the associated devices.

iii) Power Supplies

The main features of the two different power supply systems are shown in Table 2.6. Both systems use 28V input. The high voltage system for the RICH provides up to 900 V well regulated and with very low ripple. This voltage is used to bias the PMTs and, due to the dependence of the gain with the voltage, a control and monitoring system is required. The high voltage system is implemented in 4 modules (RHV). Each module contains two voltage elevators in cold redundancy with an output voltage ≤ 900 V. The elevator feeds a set of 40 fully redundant HV regulators with over current protection, also located within the module. Each of these outputs supplies a set of 4 or 5 photomultipliers. The PMT characteristics (gain vs. voltage, etc.) have been matched within each set. The delivered HV can be regulated between 750 and 850 V.

The low voltage system feeds all the electronics but the photomultipliers. As shown in Table 2.6, three different voltages are required. The +3, −2 voltages feed the analog front-end chips and ADCs and the +3.3 voltages feed the digital control and processing part. The RICH low voltage system has 8 boards located in two boxes (ERPD) mounted on the main radiator. Each board (Figure 2.122) has a pair of DC-DC converters, forming, as for the high voltage, a fully redundant system. These were developed specifically to met AMS requirements. They have high efficiency and low noise. Cold redundant regulation of the analog voltages is performed as close as possible to the associated loads.

High Voltage		
Output Voltage	Power required	Ripple
750 to 850 V	7 W	< 20 mV
Low Voltage		
Output Voltage	Power required	Ripple
+3.0 V	20 W	< 5mV
−2.0 V	7 W	< 5 mV
+3.3 V	35 W	<50 mV

Table 2.6: Characteristics of each Power Supply unit.

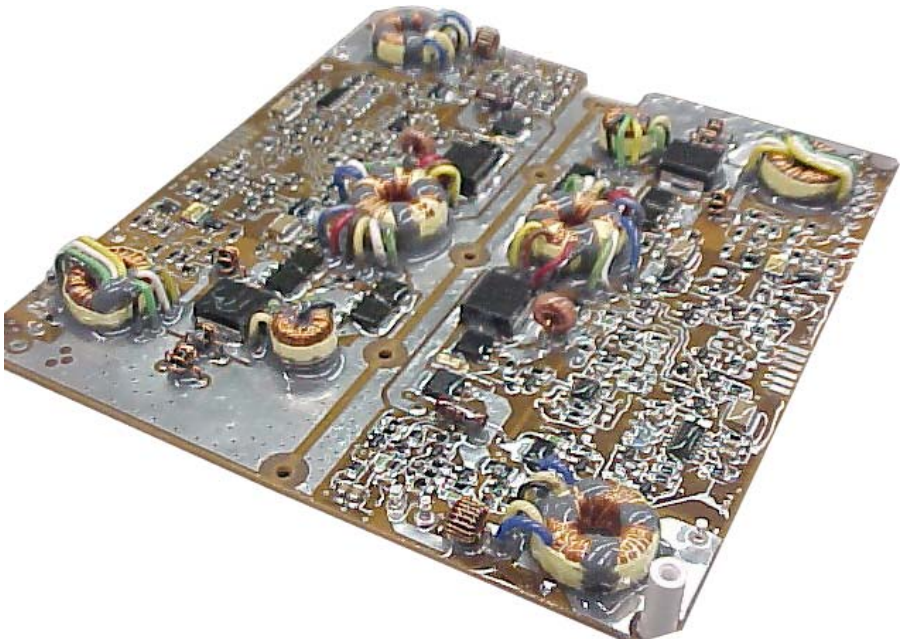

Figure 2.122: DC-DC low voltage converter.

2.6.5 Tests with the RICH prototype

In order to validate the design of the AMS-02 RICH, a prototype (Figure 2.123) with an array of 9 x 11 cells similar to those of the final model has been constructed. The performance of this prototype has been tested with cosmic muons and, in October 2002, it was placed in a beam of secondary ions at the CERN SPS produced by the fragmentation of a Pb beam. The rigidity settings for the fragments on the transport line allow an effective selection of the secondary ions with specific values of the mass over charge ratio. In particular, beams of protons with rigidities between 5 GV and 13 GV and A/Z = 2 ions with a rigidity of 40 GV were selected. The rigidities were known with an accuracy of 1.5%. The angular divergence of the beam was below 3 mrad so that the spread at the detector was ~1 cm. Beam intensities were in the range of 10^2 to 10^3 particles per spill.

To avoid backgrounds, the prototype was placed inside a light tight container and the set-up was complemented with a supporting structure that allowed changes in the relative distance between the radiator and the detection plane. The experimental set-up was completed with two scintillation counters to provide the a coincidence trigger and a double multiwire proportional chamber (MWPC) to measure the transverse coordinates of the particle trajectory with a submillimeter accuracy. The measurements reported below were performed on a sample of about 5 million events recorded in a 4 day run. Table 2.7 shows the different silica Aerogel radiators used during the test.

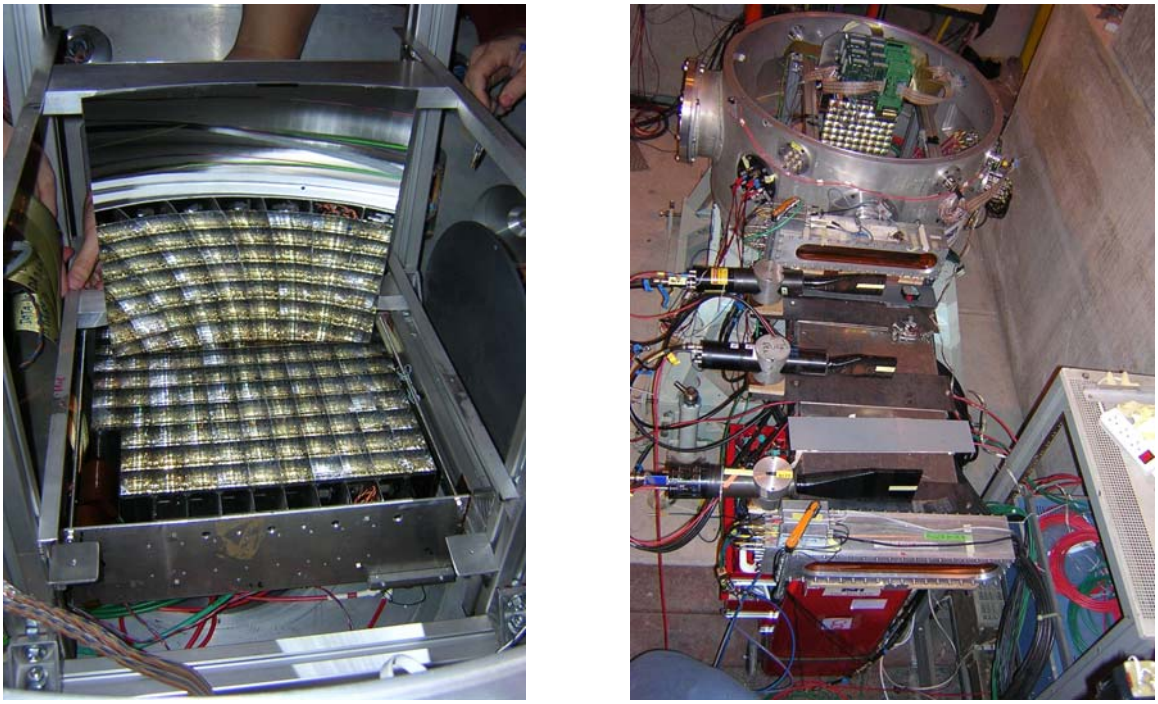

Figure 2.123: RICH prototype array of 9 x 11 cells (left), test beam set up (right).

Radiator	*n*	h (mm)	d (mm)	Stack
MEC	1.03	422.5	20	2
MEC	1.05	375.0	20	2
CIN	1.03	422.5	30	1
CIN	1.04	422.5	30	1

Table 2.7: Different silica Aerogels studied in the CERN SPS Test Beam, with refractive index, *n*, distance between the radiator and the detection plane, h, and sample thickness, d.

The reconstruction algorithms for the velocity and the electric charge of the incoming ions were the ones developed for the final detector with minor modifications to account for the particular configuration of the experimental set up, in particular the substitution of the data from MWPC for that from the Silicon Tracker. Using these track parameters, a velocity value can be associated to every single hit in the detection plane. These values are grouped into clusters and, as determined by a decision algorithm, the most significant one is associated to the particle (see Figure 2.124). The velocity is computed as the mean of the contributing hits, each one weighted with the corresponding signal in terms of photoelectrons. Finally, the track angular parameters are varied to optimize the cluster significance. The estimated velocity and the coordinates of the particle are used as inputs for the charge reconstruction. The algorithm computes, on an event-by-event basis, the expected number of detected photoelectrons for a Z = 1 particle (N_{exp}) with the same track parameters and velocity as the ones measured. This value is compared to the actual number of photoelectrons estimated from the signal of the most significant cluster (N_{ring}) and the charge of the particle charge is estimated as $Z_{meas} = \sqrt{N_{ring}/\, N_{exp}}$.

The measured distribution of charges in the beam is shown in Figure 2.125 where the structure of individual ion peaks up to Z = 26 (Fe) is clearly visible (protons have been suppressed). This spectrum has been fitted to a sum of Gaussian distributions and from their widths we have estimated the charge resolution for each of the ions. The results, consistent with what is expected from the simulation, are shown in Table 2.8 for the different radiators and incoming ions of Z = 1, 2 and 6.

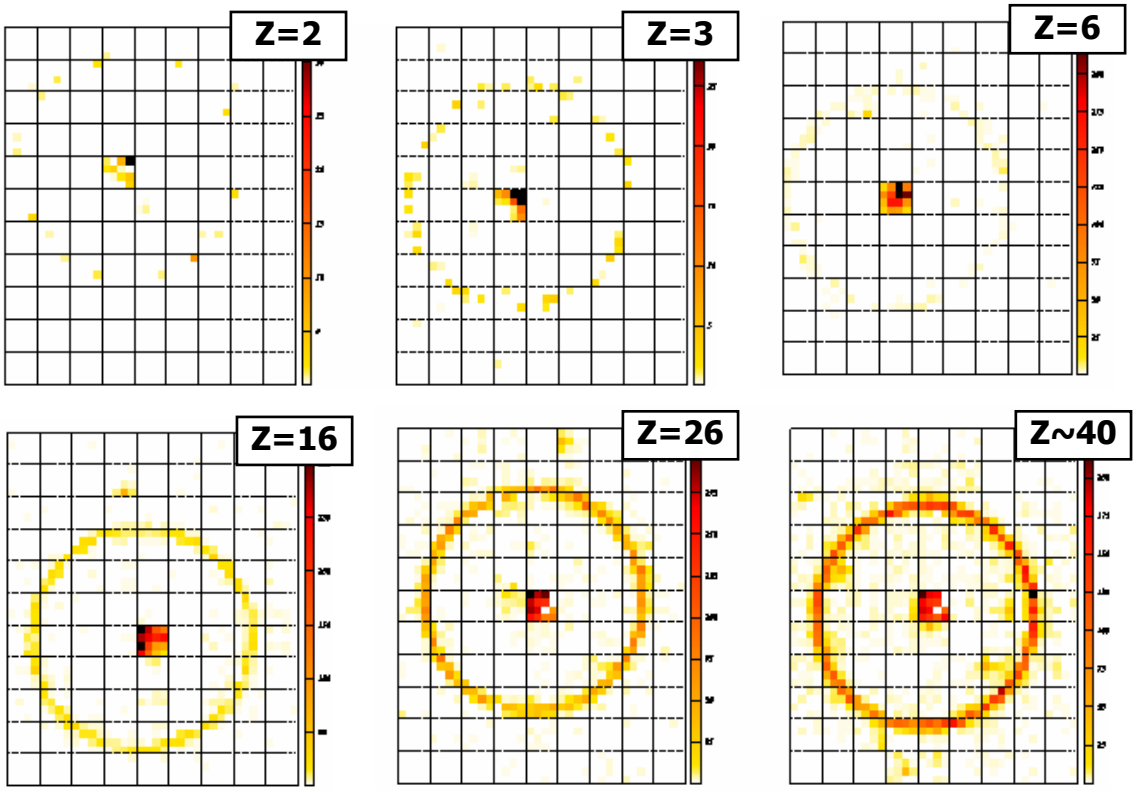

Figure 2.124: A sample of Cerenkov rings detected with single, A/Z = 2, ion events.

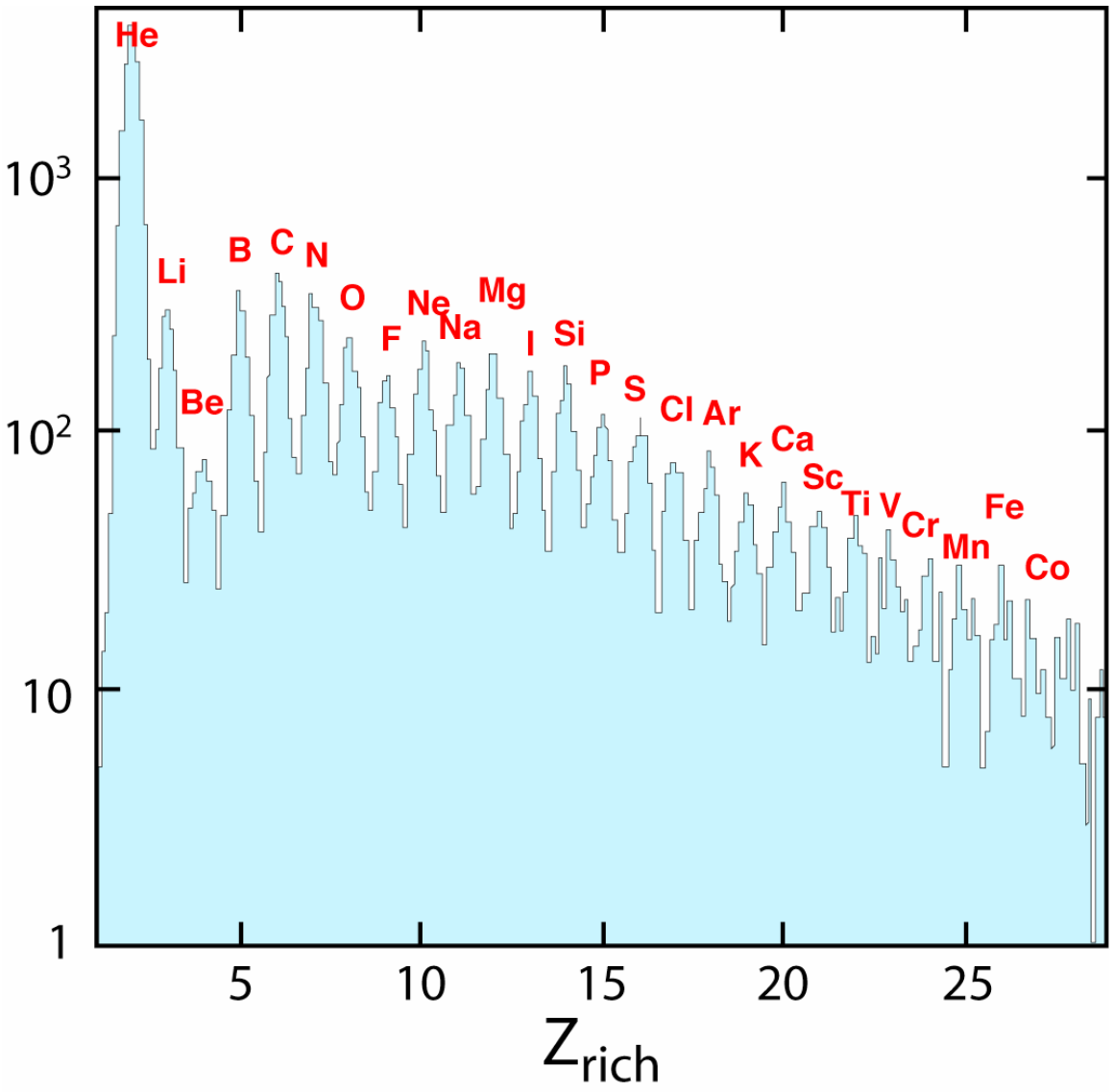

Figure 2.125: Measured distribution of charges (Z>1) for the CIN *n*=1.03 radiator.

Radiator	*n*	Z = 1	Z = 2	Z = 6
MEC	1.03	0.194 ± 0.001	0.227 ± 0.001	0.252 ± 0.004
MEC	1.05	0.189 ± 0.002	0.201 ± 0.001	0.228 ± 0.006
CIN	1.03	0.197 ± 0.003	0.199 ± 0.001	0.217 ± 0.006
CIN	1.04	0.198 ± 0.003	0.193 ± 0.003	0.232 ± 0.007

Table 2.8: Charge resolution for the different radiators and Z=1, 2 and 6 beams.

The accuracy in the determination of the velocity is estimated from the width of the normal distribution fitted to the reconstructed velocities for the different nuclei. In particular, the resolution obtained for helium nuclei is shown in Figure 2.126 and the values obtained for the different radiators under study are shown in Table 2.9 for protons and helium nuclei. The dependence of the resolution on the velocity as function of the charge of the particle is shown in Figure 2.127 for the CIN $n = 1.03$ radiator.

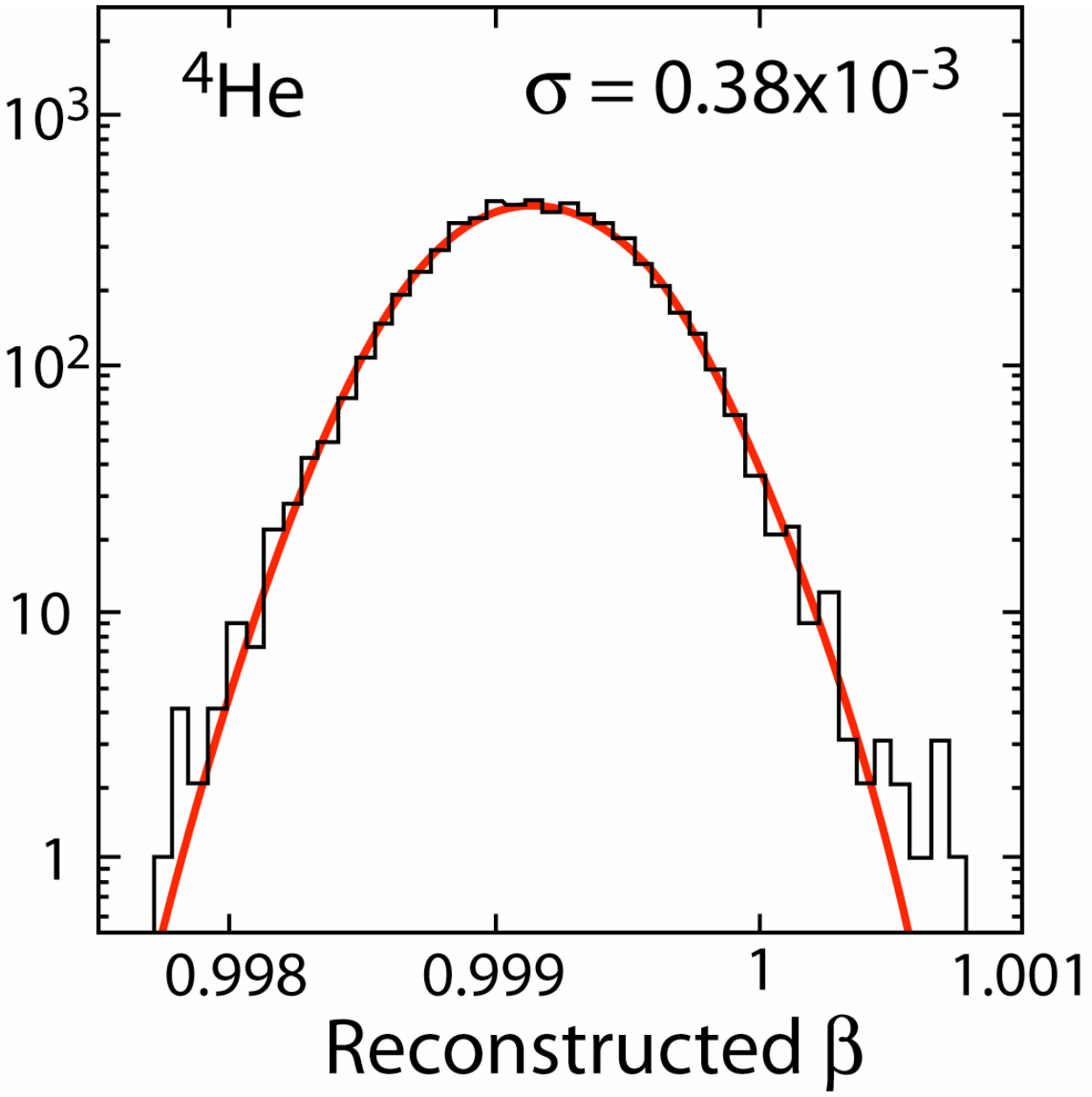

Figure 2.126: Velocity resolution for Helium nuclei from a fit to a Gaussian distribution for the CIN *n* = 1.03 radiator.

Radiator	*n*	Z = 1	Z = 2
MEC	1.03	0.71 ± 0.02	0.48 0.01
MEC	1.05	0.98 ± 0.05	0.55 ± 0.02
CIN	1.03	0.67 ± 0.01	0.382 ± 0.004
CIN	1.04	0.94 ± 0.08	0.382 ± 0.004

Table 2.9: Velocity resolution (per mil) for the different radiators for protons and helium nuclei.

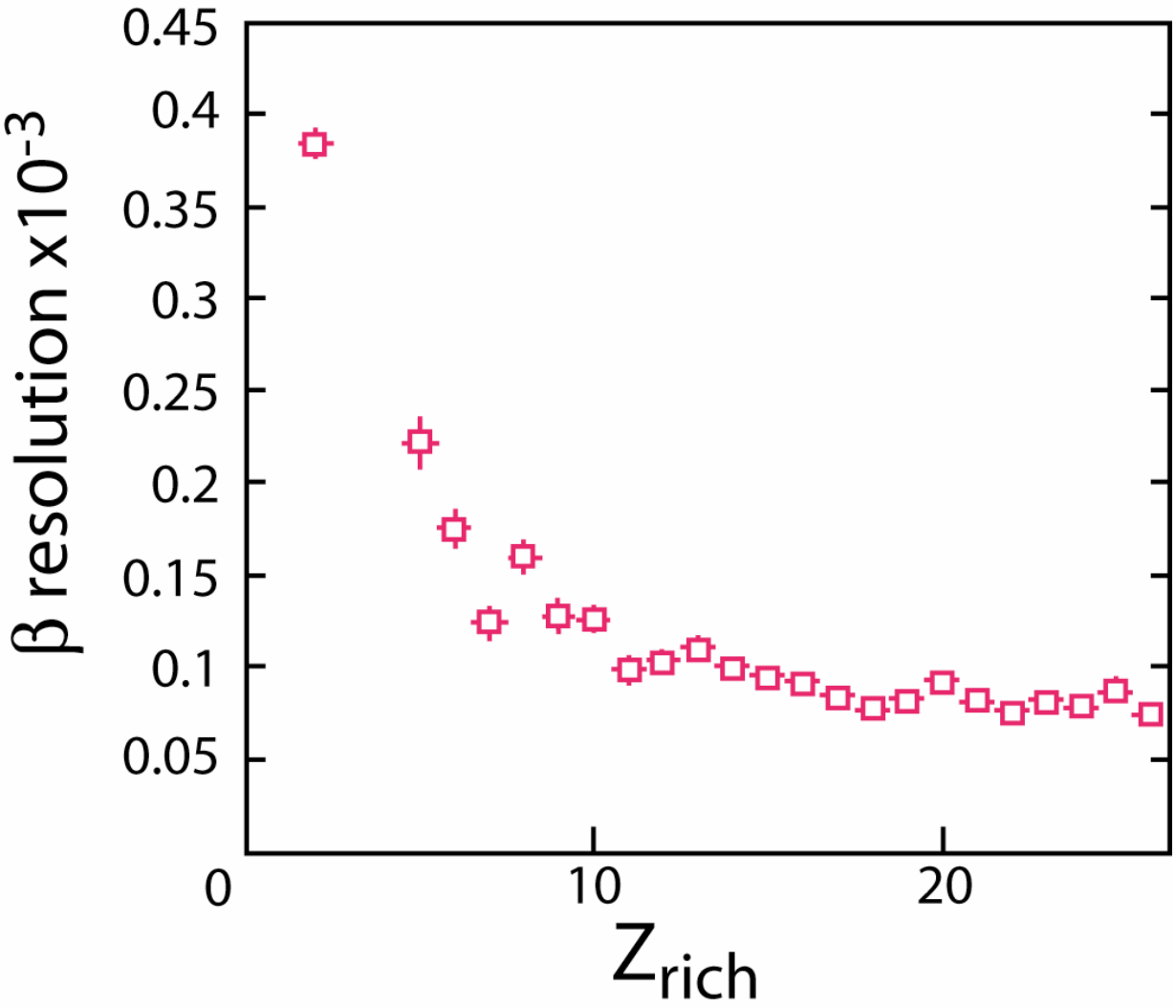

Figure 2.127: Dependence of the velocity resolution on the charge of the nuclei for the CIN *n* = 1.03 radiator.

2.7 Electromagnetic Calorimeter (ECAL)

The Electromagnetic Calorimeter (ECAL) of the AMS-02 experiment is a fine grained lead-scintillating fiber sampling calorimeter [1,2] that allows precise, 3-dimensional imaging of the longitudinal and lateral shower development, providing high ($\geq 10^6$) electron/hadron discrimination in combination with the other AMS-02 detectors [3] and good energy resolution. The calorimeter also provides a standalone photon trigger capability to AMS. The mechanical assembly has met the challenges of supporting the intrinsically dense calorimeter during launch and landing with minimum weight. The light collection system and electronics are optimized for the calorimeter to measure electromagnetic particles over a wide energy range, from GeV up to TeV. The ECAL is being provided by INFN-Pisa and Sienna, CALT, IHEP, LAPP and MIT. A full-scale ECAL qualification model was tested using electrons and protons beams with energies ranging from 3 to 180 GeV.

2.7.1 Calorimeter

The AMS-02 ECAL consists of a lead/scintillating fiber sandwich with an active area of 648 x 648 mm^2 and a thickness of 166.5 mm. The calorimeter is composed from "superlayers", each 18.5 mm thick and made of 11 grooved, 1 mm thick lead foils interleaved with layers of 1 mm diameter scintillating fibers and glued together with epoxy. The resulting composite structure is shown Figure 2.128. It has a relative lead-fiber-glue volume composition of 1:0.57:0.15 and an average density of 6.9±0.2 g/cm^3.

In each superlayer, fibers run in one direction only. The detector imaging capability is obtained by stacking superlayers with fibers alternatively parallel to the x-axis (4 layers) and y-axis (5 layers) (see Figure 2.129). The calorimeter has a total weight of 496 kg and a thickness corresponding to about 17 radiation lengths.

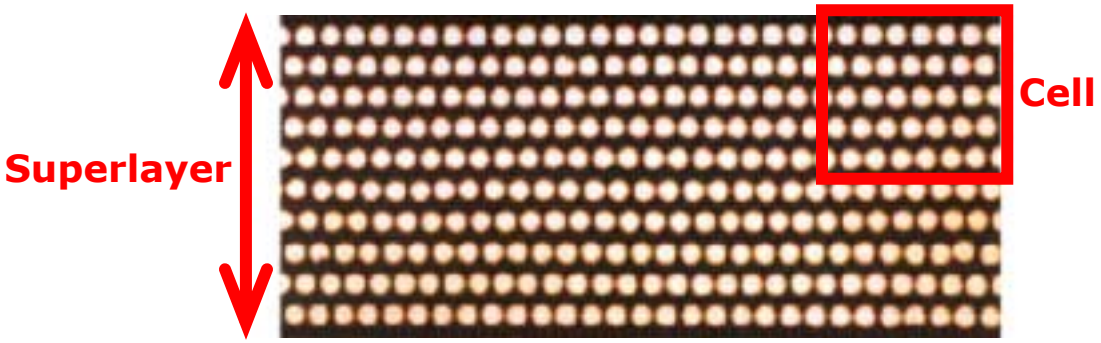

Figure 2.128: Cross section of the ECAL lead-fiber-glue composite structure.

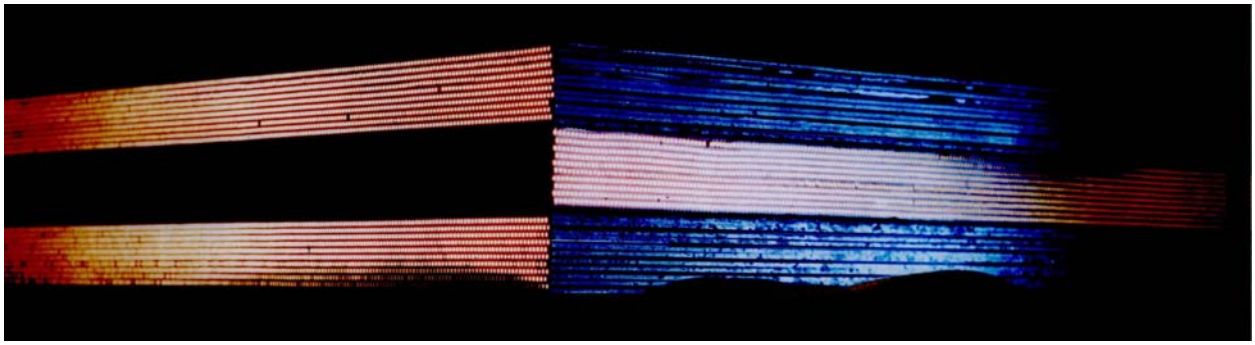

Figure 2.129: Assembly of three superlayers.

Fibers are read out, on one end only, by four anode Hamamatsu R7600-00-M4 photomultipliers (PMTs); each anode covers an active area of 9 x 9 mm^2, corresponding to 35 fibers, defined as a cell (see Figure 2.128). In total the ECAL is subdivided into 1296 cells (324 PMTs) and this allows a sampling of the longitudinal shower profile by 18 independent measurements.

2.7.2 Mechanical assembly

The ECAL mechanical assembly, shown in Figures 2.130 and 2.131, supports the calorimeter, PMTs and attached electronics. It is designed to minimum weight with a first resonance frequency above 50 Hz, a capability to withstand accelerations up to 14 g in any direction and thermal insulation limiting the gradient (the external temperature ranges from −40 to +50 °C).

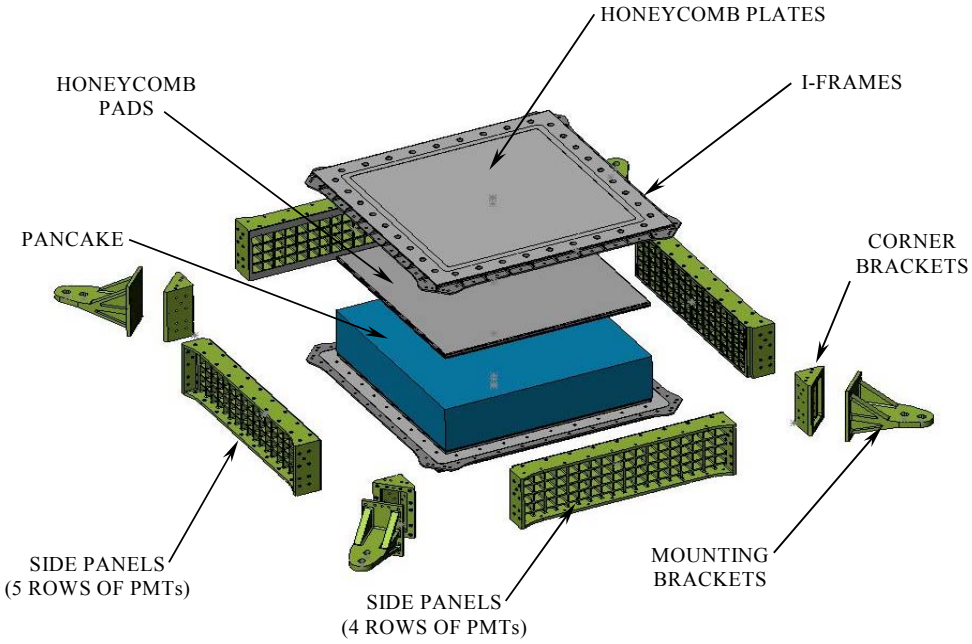

Figure 2.130: ECAL assembly.

Figure 2.131: ECAL mechanical support structure.

The optimization of the mechanical structure through finite element studies led to an aluminum alloy support frame, composed of four lateral panels which contain the PMTs and top and bottom honeycomb plates. The structural analysis was cross checked with a full scale, flight like qualification model at the Beijing Institute of Satellite Environment Engineering (BISEE). Sine-sweep and sine-burst data and stress measurements showed excellent agreement with the ECAL finite element model. In particular, the first resonance frequency was found to be higher than 60 Hz (see Figure 2.132).

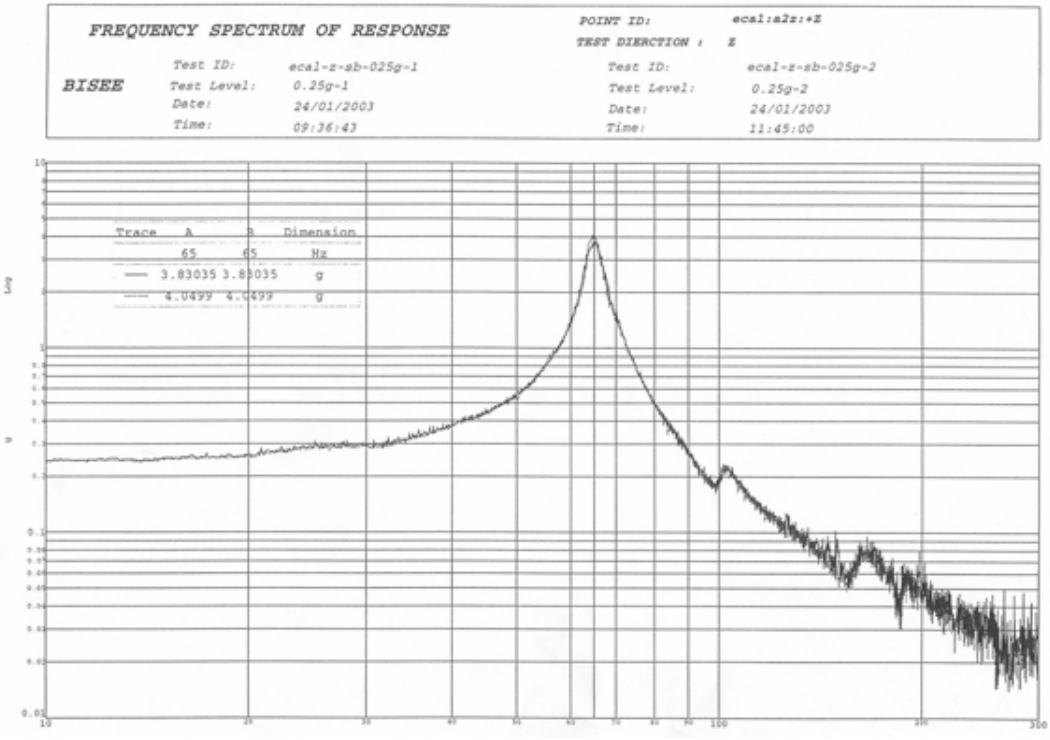

Figure 2.132: Typical z axis sine-sweep response (peak at 65 Hz).

2.7.3 Light collection

Each superlayer is read out by 36 PMTs, arranged alternately on the two opposite ends in order to read out each fiber (no dead areas). As shown in Figure 2.133, each PMT is surrounded by a magnetic shield which also contains light guides and the PMT base and front end (FE) electronics.

To maximize light yield and reduce cross-talk between cells, photons from the fibers are collected by means of individual Plexiglas light guides. As shown in Figure 2.134 each guide has a truncated pyramidal shape. They are wrapped in aluminum foil with Chromium and quartz coating and inserted inside a polycarbonate support tube. Silicone optical joints are positioned on both ends to ensure good optical transmission from the fibers to the PMTs, even when high mechanical stresses are applied.

To shield the residual magnetic field below 20 G, based on finite element calculations and measurements, the PMTs are positioned inside 1 mm thick soft iron square tubes with 30.5 mm sides and a length of 74 mm.

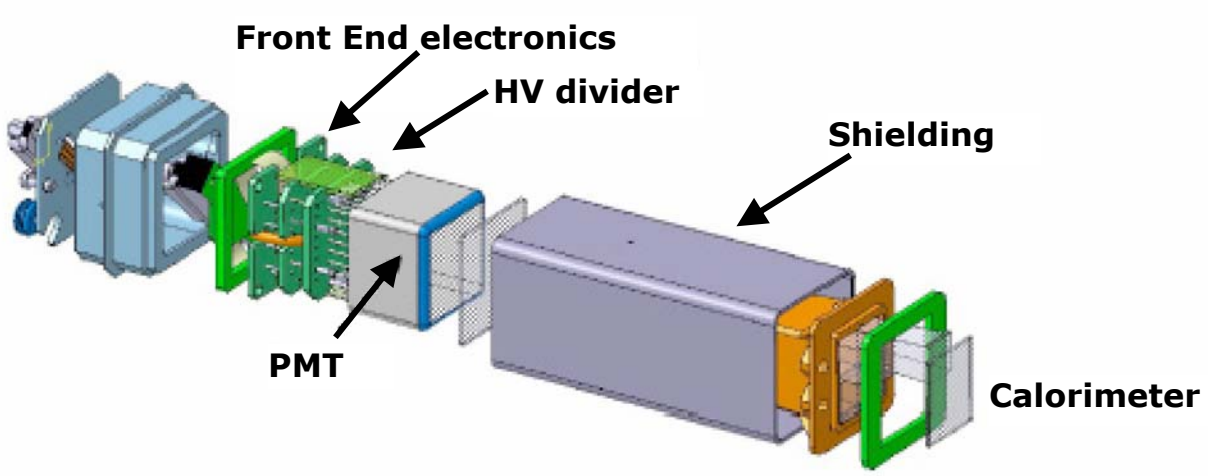

Figure 2.133: The light collection system for each PMT.

Figure 2.134: Light guides and polycarbonate support.

2.7.4 ECAL standalone gamma trigger

The excellent imaging capabilities of the AMS-02 electromagnetic calorimeter and the good energy resolution provided by the last dynode signals, as demonstrated in Figure 2.135, allow the implementation of a very efficient standalone trigger for photons with energies down to 2 GeV.

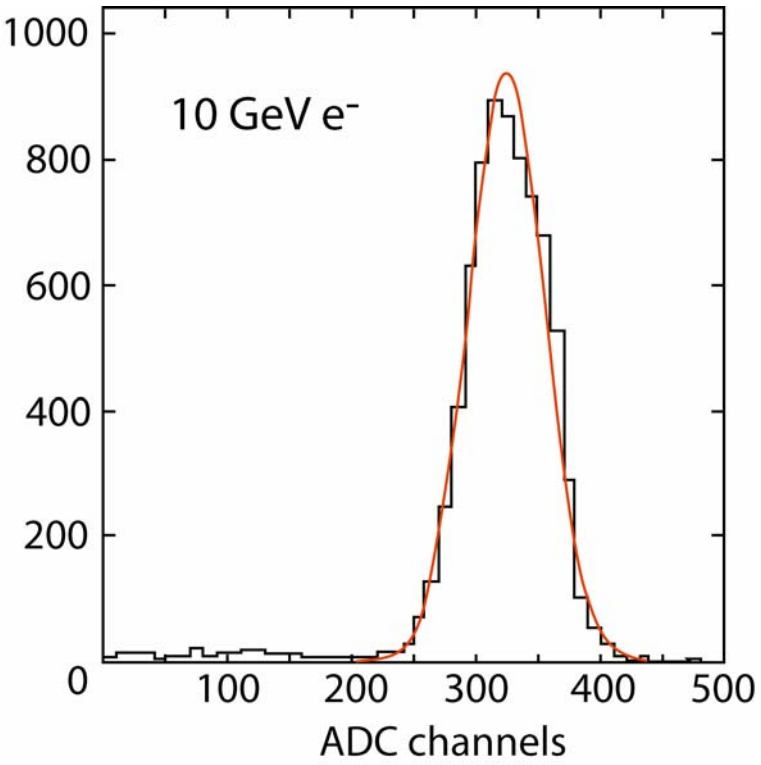

Figure 2.135: Test beam results for the summed dynode signals for 10 GeV electrons.

The trigger is made in 2 steps: a fast decision, available within 180 ns, given by the count of PMTs above threshold in the 6 central (2^{nd} to 7^{th}) superlayers of the calorimeter and a Level 1 trigger decision, well before 1 μs, obtained with a fast reconstruction of the particle direction. The fast trigger is realized by comparing the analog signal from the last dynode of each PMT to a threshold. The thresholds used are dependent only on the superlayer in order to exploit the longitudinal shape of the electromagnetic shower. The Level 1 trigger is determined by the particle direction, which is evaluated by taking, for each superlayer, the average position of the PMTs above threshold. The photon direction is calculated using the distances between the centers of gravity of the three superlayers belonging to the same projection. Particles with an inclination larger than 20 degrees are rejected, ensuring the trajectory passed cleanly through the other AMS-02 detectors.

The expected ECAL trigger efficiency in AMS-02 for unconverted photons of different energies is shown in Figure 2.136. The efficiency is 90% at 2 GeV and more than 99% for energies larger than 10 GeV. The trigger rates for photons and for the most relevant backgrounds, as deduced from Monte Carlo studies based the data collected by AMS-01 [4] and others [5], are shown in Figure 2.137. Particles firing the AMS charged trigger, which include converted photons, are not included in this background rate.

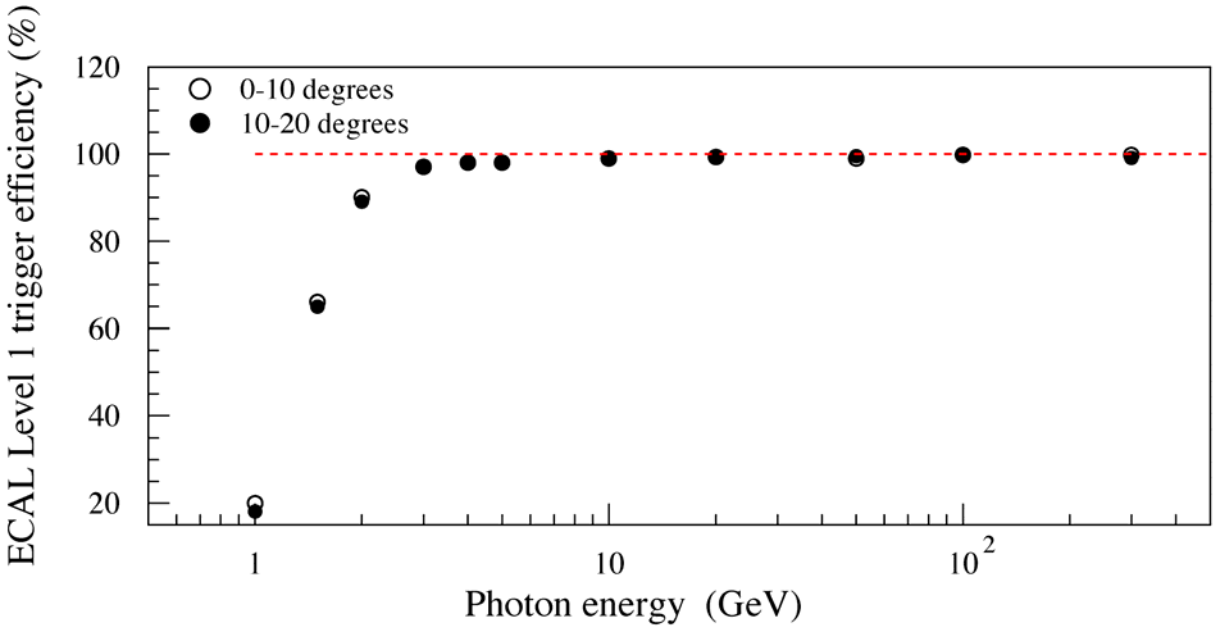

Figure 2.136: ECAL Level 1 trigger efficiency for different photon energies and angles.

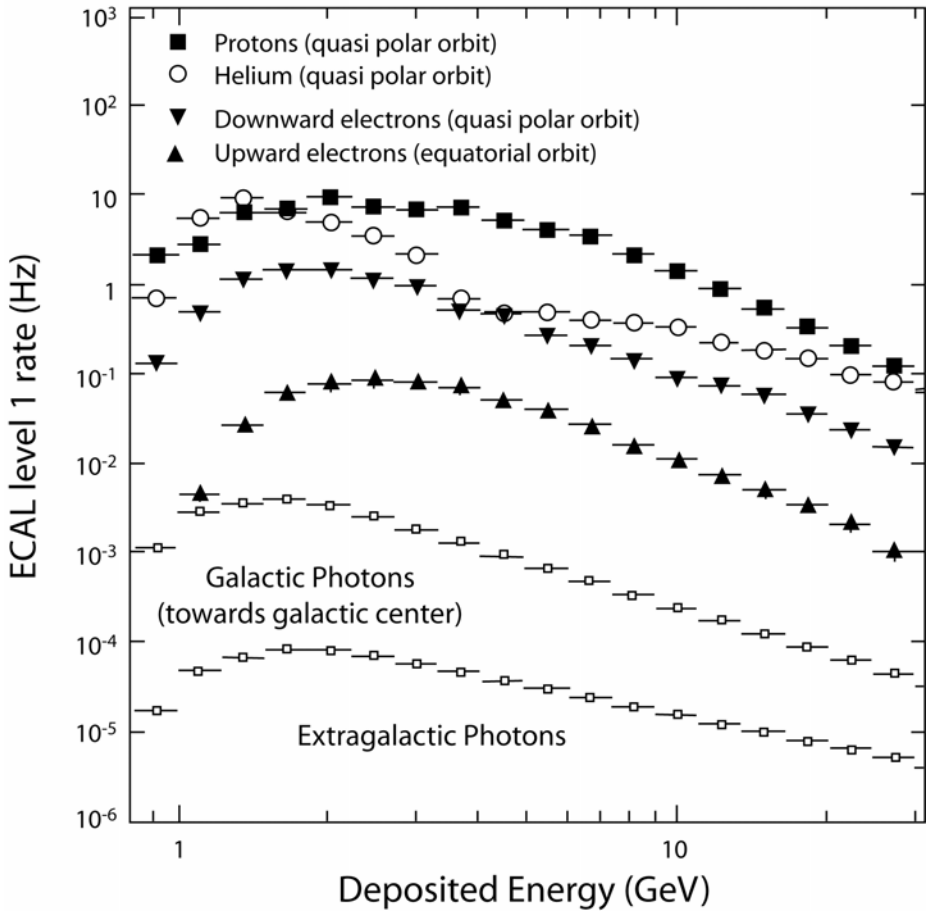

Figure 2.137: Expected ECAL stand alone trigger background and photon rates.

2.7.5 Electronics

In addition to the front end electronics mounted directly on the calorimeter, the ECAL is instrumented with several custom developed electronics subsystems for data acquisition, slow control and the ECAL trigger and to supply the high and low voltages. Except for the front end electronics, each board is composed of two completely independent sectors that are also separately powered but are capable of the same functionality. In case of any fault it is possible to switch from one sector to the other while maintaining full functionality of the ECAL.

i) Front End (FE) Electronics

The light collection and readout system must process signals with a good linearity over a wide dynamic range, from one minimum ionizing particle, which produces about 8 photoelectrons per cell, up to the 6 x 10^4 photoelectrons produced in one cell by the electromagnetic showering of a 1 TeV electron. To fulfil this requirement, the high voltages for the PMT are provided by a tapered resistor divider (1.5:1.5:1.5:1:1:1:1:1:1:2: 3.7) which also allows the power consumption to be reduced to 100 mW at the working point of 650 V. The PMT signals from the 4 anodes are split into two subranges by voltage dividers and read out by two electronics channels with a gain ratio of about 33 (Figure 2.138). This electronics was implemented in a dedicated ASIC chip [6] in BiCMOS 0.8 µm technology with very low power consumption (21 mW per PMT). The signal of the last dynode of the PMT is also read out and simultaneously sent to a low gain channel in the chip as a redundant measurement of the energy deposited and as input to a comparator. The signals in the 9 channels of the chip (2x4 anodes + 1 dynode) are shaped to give a peaking time around 2.2 µs and are held until they are read via a multiplexing circuit and sent sequentially to a serial ADC (AD7476A, also used by other sub-detectors). The HV dividers are implemented on two 26 x 26 mm^2 boards, and a third board, 30 x 30 mm^2 accommodates the ASIC and the ADC (Figure 2.139). All 3 boards are assembled together and mounted behind the PMT. The bases and the rear of the PMT are completely potted to avoid corona effects. The digitized outputs from 9 PMTs are sent via an intermediate board (EIB) to the off detector electronics. Except for the first and last superlayer, the comparator outputs from the last dynode signals are sent to the ECAL trigger.

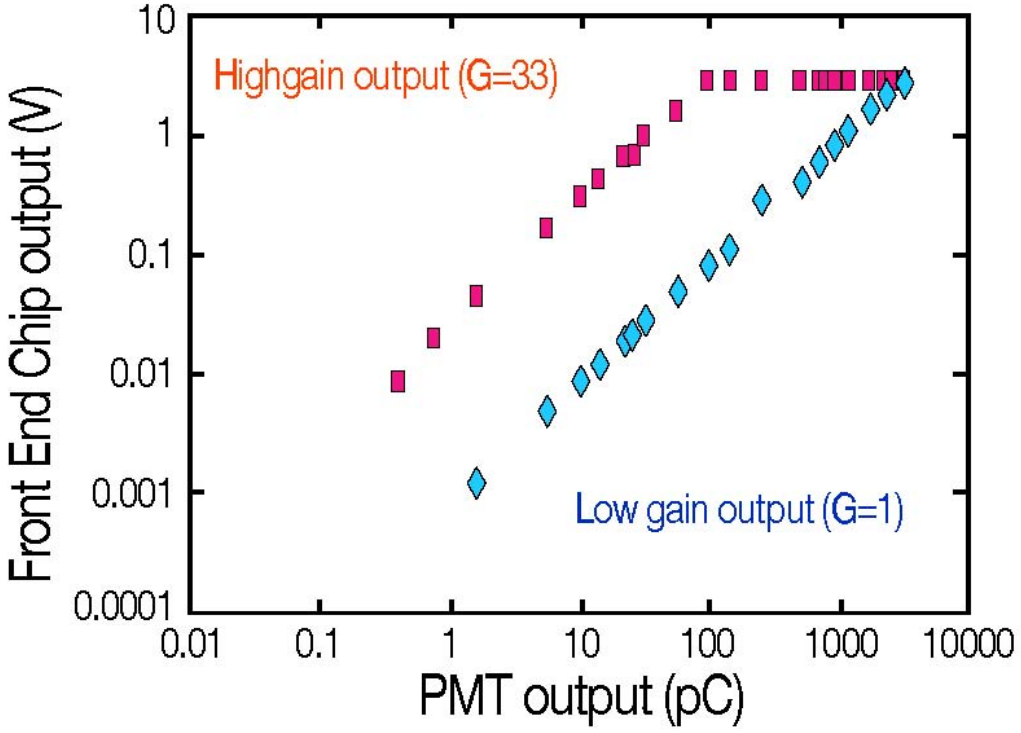

Figure 2.138: The dynamic range of front end chip.

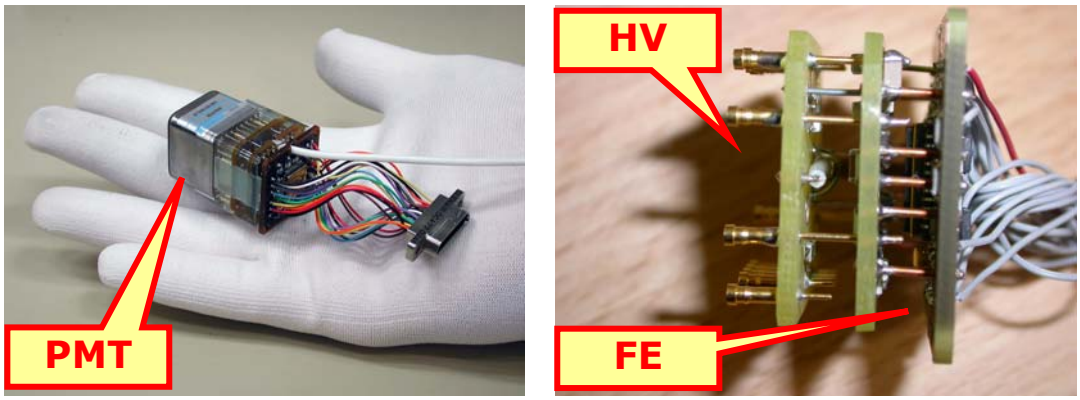

Figure 2.139: The potted HV divider and front end readout electronics mounted behind the PMT.

ii) DAQ System

The readout of the ECAL follows the AMS design. The DAQ node cloest to the front end is the EDR2 card based, as for the other subdetector electronics, on the common digital part (CDP). The EDR2 receives the digitized signals from 27 PMTs (3 EIB) over Low Voltage Differential Signaling (LVDS) lines, subtracts pedestals, suppresses zeros and sends the results over the backplane to the next node in the DAQ chain, the JINF. The EDR2 and JINF are mounted in two crates located at opposite corners of the detector, with each crate hosting 6 EDR2 and 1 JINF. As shown in Figure 2.140, the EDR2 also acts as a bridge for the front end electronics power (+3.5, −2.5 VDC) and control of the EIB using single ended TTL (5 V) signaling.

Each EDR2 is fully redundant, but it is connected to the non-redundant front end electronics. Special care was taken to avoid possible single point failures and interference at the junctions of the two sections. Each half of the EDR2 is protected by a solid state circuit breaker (SSF).

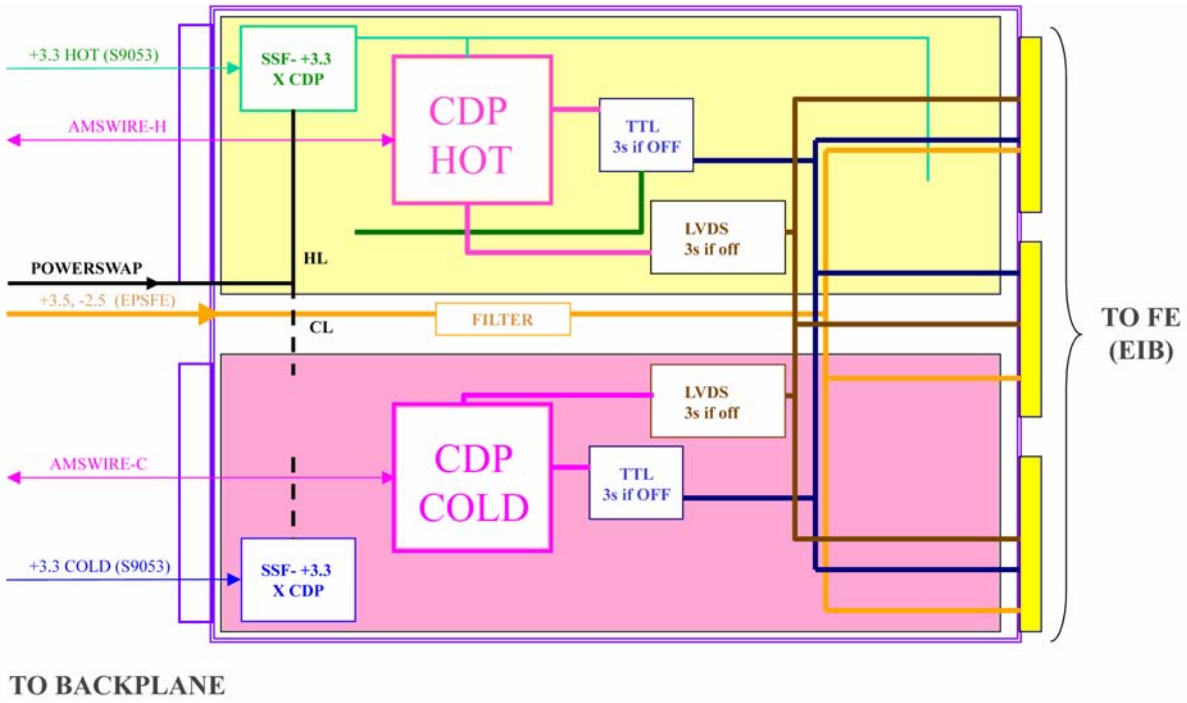

Figure 2.140: EDR2 schematic.

iii) Slow control

The main functions of the slow control system are to supervise the switching between the A and B ("hot" and "cold" or "H" and "C") redundant sections of each board and to set and monitor the high voltages. The overall concept, as shown in Figure 2.141, is to have two completely independent subsystems side by side, which are independently powered through highly reliable switches located in the Power Distribution System (PDS). In nominal operations only one subsystem is powered. In case of a fault, the working subsystem is switched off and the other turned on. In the unlikely occurrence of a second fault, both subsystems can be turned on and the individual sections of the boards can be switched off independently using the solid state circuit breakers (SSF). The primary slow control interface is also located on the JINF card which provides 8 serial buses using the LeCroy protocol which are attached to the HV bricks and low voltage control cards (EPSFE).

The high voltage controller boards, inside the high voltage brick, are directly capable of decoding the serial bus. All the other boards need standard single ended logic signals to switch between A and B sections, so a serial to parallel decoder was implemented on the EPSFE card. The EPSFE was introduced into the ECAL system to host the power switches for the front end electronics. Each group of 9 front ends (1 EIB) is powered through one of these switches, so that in case of a major failure a single section can be isolated from the full system. Three EPSFE cards are hosted in each crate.

The DC-DC converters which supply the low voltages (+3.8, −2.8 V and 3.3 V) are hosted inside the ERPD box. Each converter is dual redundant, supplying voltages to the hot (H) or cold (C) sides, as controlled by the power coming from the PDS. In total 4 dual DC-DC converters (1 S9053I and 3 S9057E) plus a dual 28V input/output filter are located in the ECAL (E) half of the ERPD.

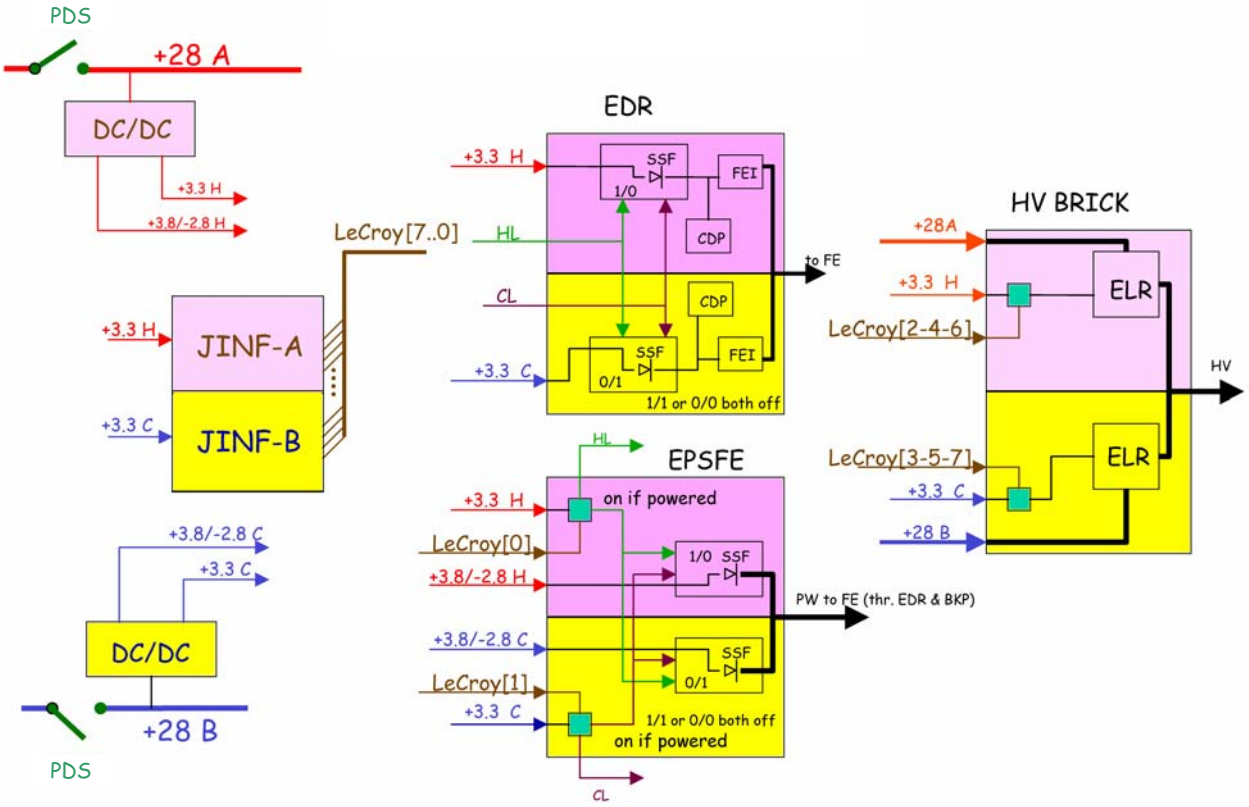

Figure 2.141: ECAL slow control architecture.

iv) ECAL Trigger

As described above, the trigger system analyzes the pulse generated by the last dynode in each PMT from 6 superlayers, for a total of 216 PMTs (108 for each x, y view). As shown in Figure 2.142, it is composed of an analog section located together with the FE electronics near the detector and a purely digital section which performs all the trigger algorithm computations and sends the final decision to the AMS global trigger (JLV1+JTBX, located in the JT-Crate). The analog section compares the signal of the last dynode, amplified by a factor of 10, of each PMT involved in the trigger to a given threshold set by a digital to analog converter (DAC). The output of the comparator is shaped (FF) to form a 100 ns pulse. These signals are sent to 2 trigger cards (ETRG), one for each view. The trigger card generates both the Fast and the ECAL-LV1 signals and includes the input data in the event data stream using the standard CDP. These signals can be used in the global trigger to override the anticoincidence counter trigger inputs for energetic events. The trigger algorithm has been implemented in an Actel FPGA and simulated (Figure 2.143). Each crate contains one ETRG card, each card processes the signals related to either the x or the y projection.

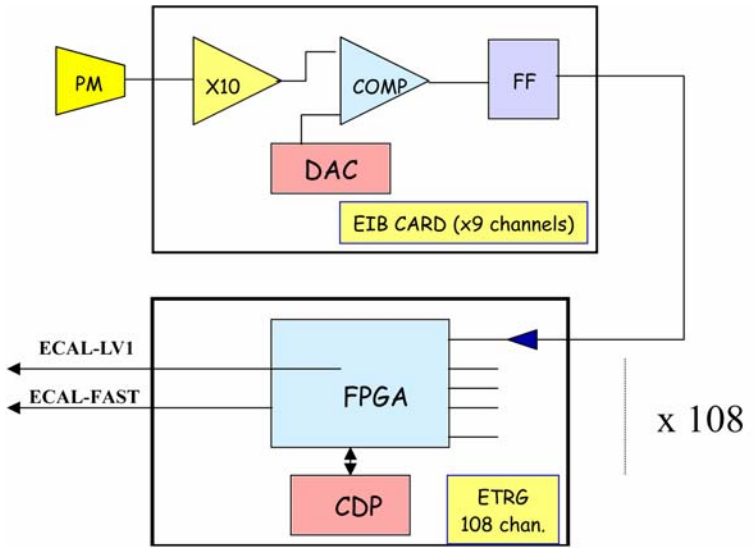

Figure 2.142: ECAL trigger circuit.

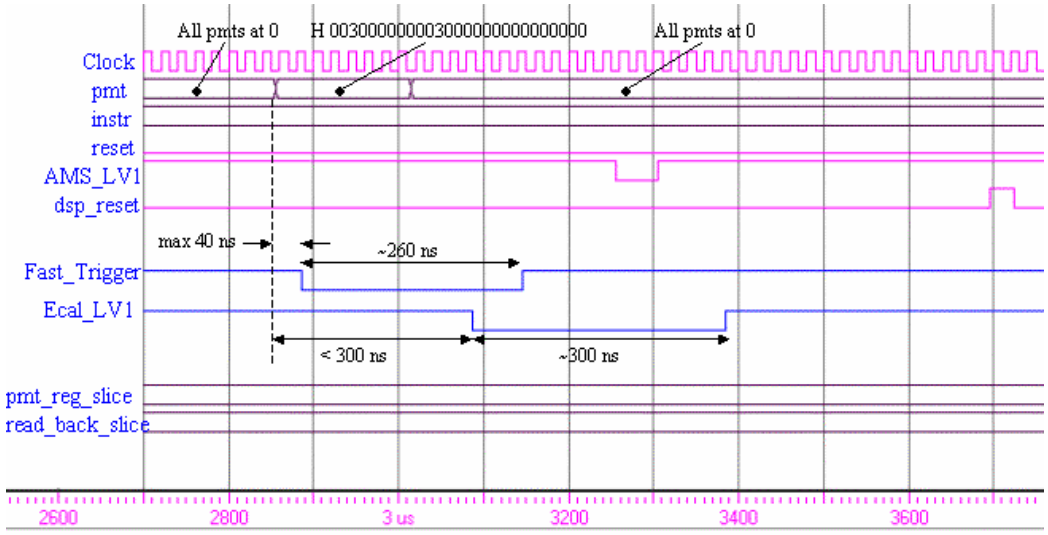

Figure 2.143: Simulation of the ECAL trigger firmware.

v) High voltage system

The high voltage system is composed of elevator, linear regulator (LR) and controller modules, see Figure 2.144. Each module is dual redundant. Each elevator is based on a 4 stage Cockcroft-Walton multiplier which raises the input 28 V to a high voltage in the range 500 to 1000 V. The linear regulators also provide an adjustment of the high voltage with 2 V steps through a discrete "series transistor". Eight regulators are installed in a module. Each elevator feeds 24 or 16 linear regulators; each linear regulator powers one or two PMTs. The controller module contains the digital to analog converters needed to regulate the system and all the slow control functions. All of these modules are mounted together within a HV Brick (EHV) made up of 1 controller, 2 elevator and 5 regulator modules, for a total of 40 regulated and independent channels supplying 55 PMTs. In total the 324 PMT ECAL will be equipped with 6 EHV. The power dissipation has been kept below 5 W per brick (worst case) by maintaining the efficiency at more then 90%. Space qualification tests of a HV Brick, Figure 2.145, are currently in progress.

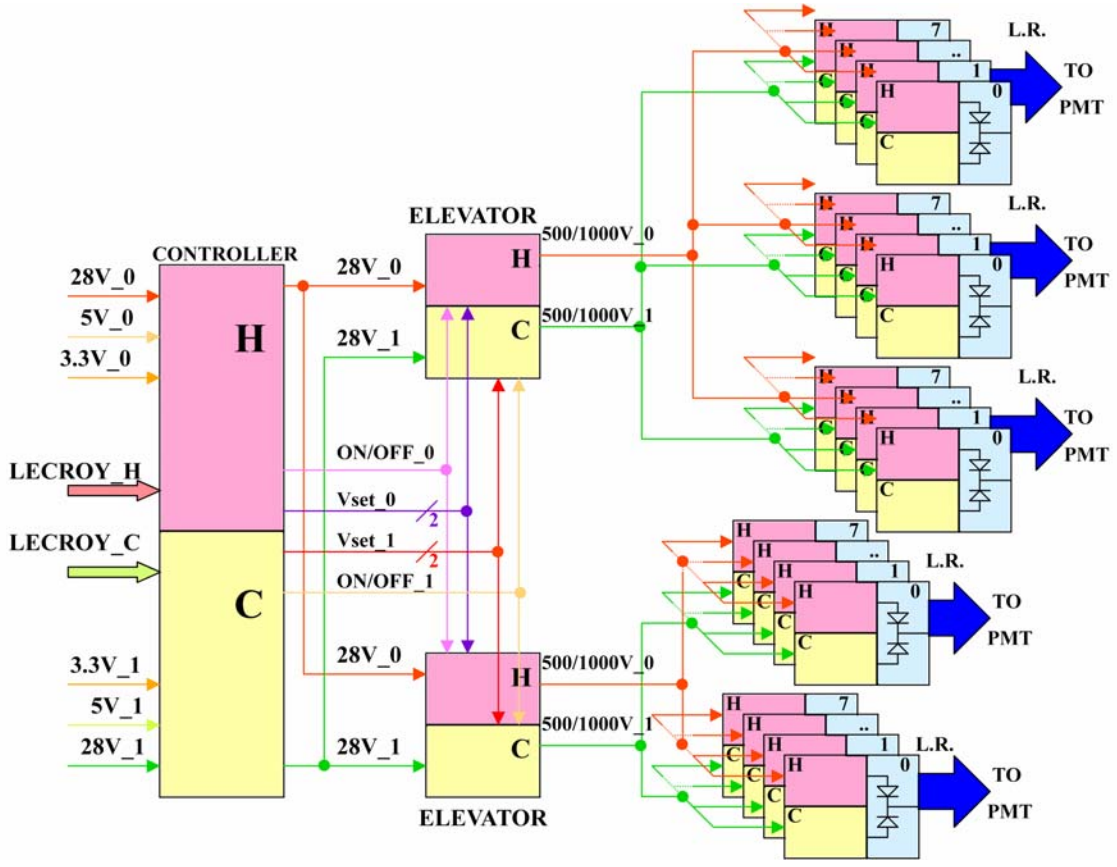

Figure 2.144: ECAL HV system schematic, one HV Brick (EHV).

Figure 2.145: Testing of a HV Brick (EHV).

2.7.6 ECAL performance

In July 2002, the ECAL qualification model was exposed to the CERN SPS beam line H6A with muons, 120 GeV protons and antiprotons and 3 to 180 GeV $e^{\pm}$. The calorimeter was partially equipped with 63 PMTs, covering a 126 x 126 mm^2 corner of the ECAL. The high voltage supply for each PMT was set individually to work at a gain of 2 x 10^5.

Two corrections were applied to the raw-data. First an attenuation function, measured by a scan with electrons and protons, was used to correct for the light attenuation along fibers, according to the relation $f(x) = 0.2\,e^{(-x/0.2\mathrm{m})} + 0.8\,e^{(-x/2.5\mathrm{m})}$, where x is the distance from the PMT. Next, an inter-calibration, or equalization, of the cell response was performed using the response to 50 GeV electrons. Based on a large statistical sample, the average cell response within each layer at equal distances from the shower axis was equalized, then a layer to layer equalization was applied by fitting the longitudinal profile of the showers to $dE/dt = E_0\, b^{(\alpha+1)}\, t^{\alpha}\, e^{-bt} / \Gamma(\alpha+1)$ [7], where E_0 is the initial $e^{\pm}$ energy, t is the layer depth (in radiation lengths) and α and b are the fit parameters. After equalization, specific analyses were devoted to: the measurement of the radiation length (X_0); the study of energy linearity and leakage corrections; the measurements of the energy and angular resolutions and the shower imaging and electron/hadron discrimination.

According to the formula cited, the shower maximum occurs at $t_{\max} = \alpha / b$. From the fit of the average longitudinal profile of each beam energy, as shown in Figure 2.146, the radiation length can be derived from the relation $t_{\max} = X_0 \log(E) + c$, where E is in GeV and c is a constant. From the data shown in Figure 2.147, a value of X_0 = 9.94±0.17 mm was found, implying that the total thickness of the ECAL is 16.7 X_0.

From the fits to the ECAL response at different energies (see Figure 2.148), good linearity was found up to 40 GeV (when longitudinal leakage is negligible), while deviations of the order of 5% at 80 GeV and of 13% at 180 GeV were observed. A leakage correction, based on the energy deposit in the last ECAL superlayer, was applied in order to estimate the total energy. The leakage corrected linearity plot, Figure 2.149, shows small residual deviations (<2% at 120 GeV and 5.3% at 180 GeV), due to the incomplete coverage of the lateral development of the shower in the test (63 of 324 PMTs) and to systematic errors in the equalization procedure.

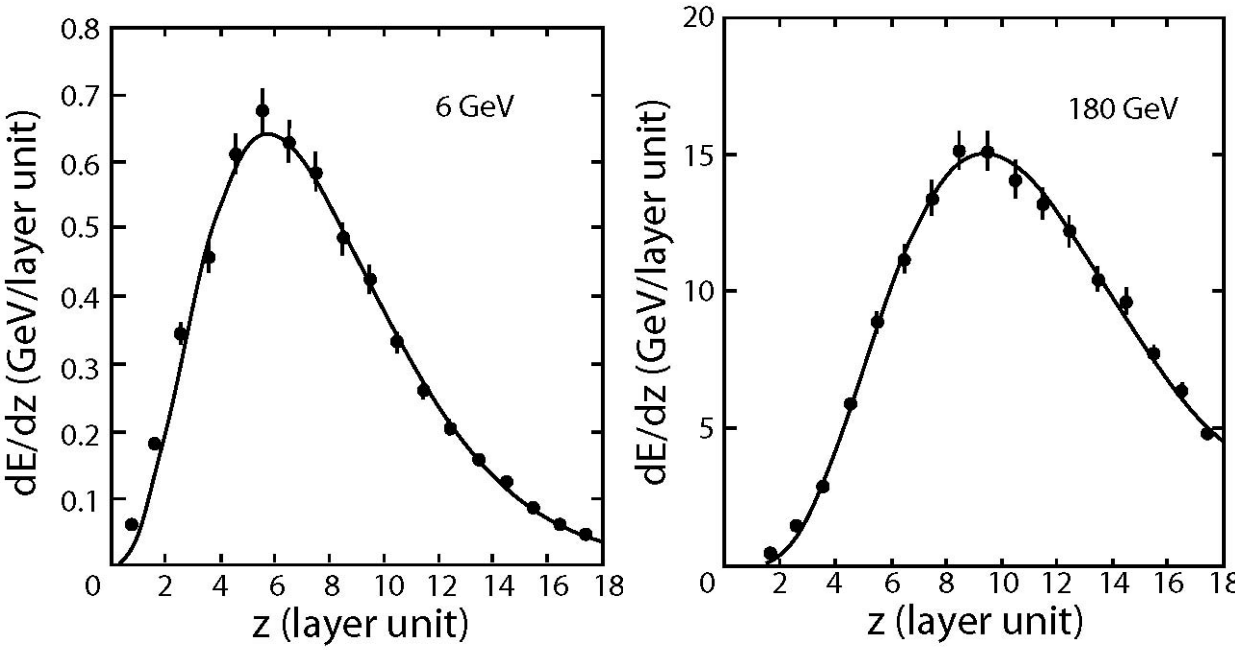

Figure 2.146: Typical longitudinal electromagnetic shower profiles.

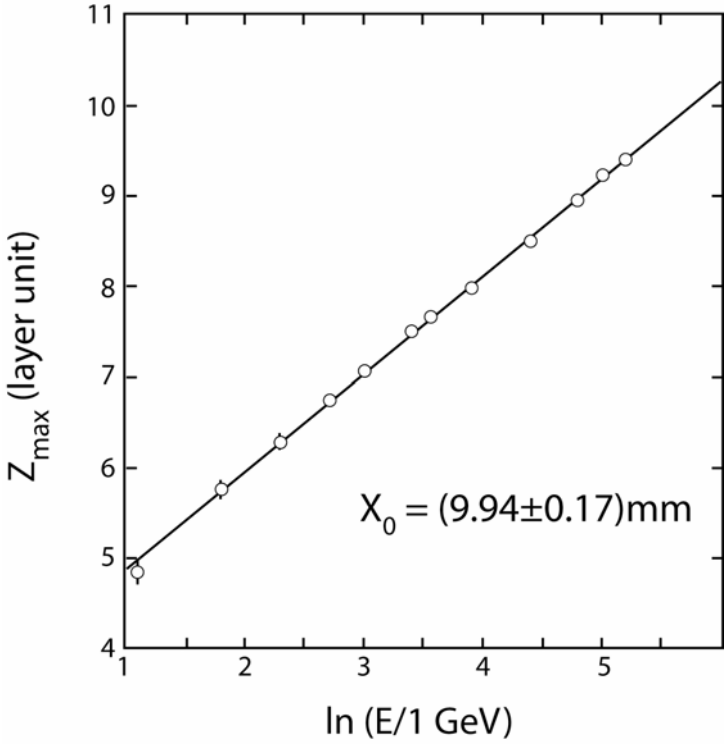

Figure 2.147: Shower maximum t_{max} (in layer units) vs. $e^{\pm}$ beam energy.

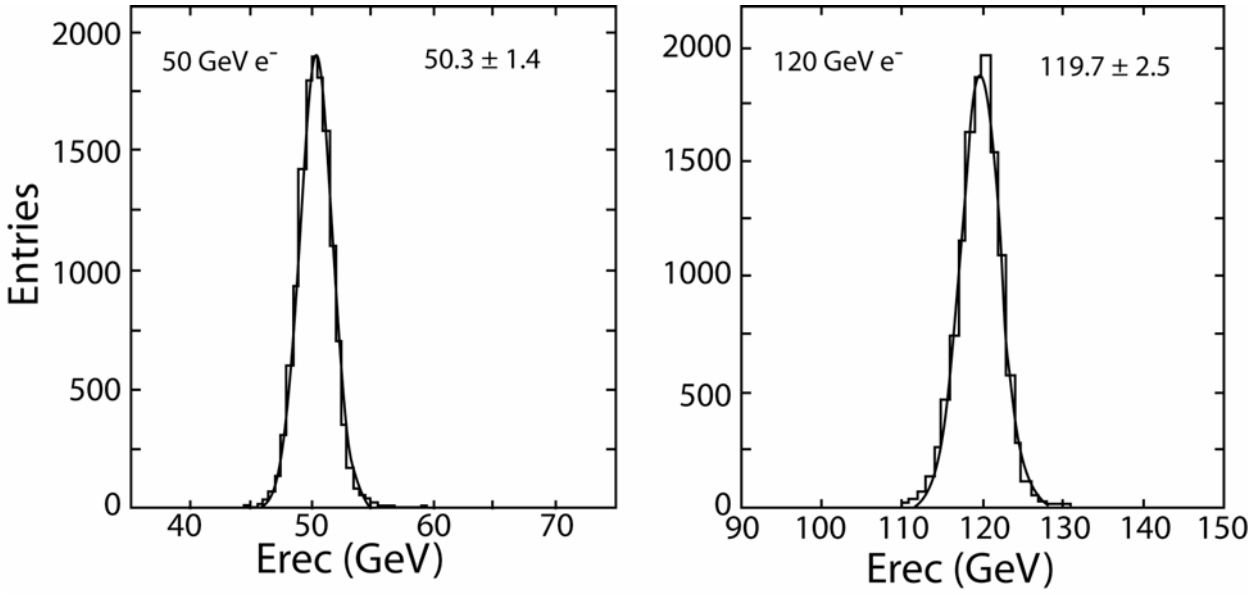

Figure 2.148: Typical ECAL energy measurements at the indicated beam energies. The mean reconstructed energy for 50 GeV e^- is 50.2 ± 1.4 GeV and for 120 GeV e^- is 119.7 ± 2.5 GeV.

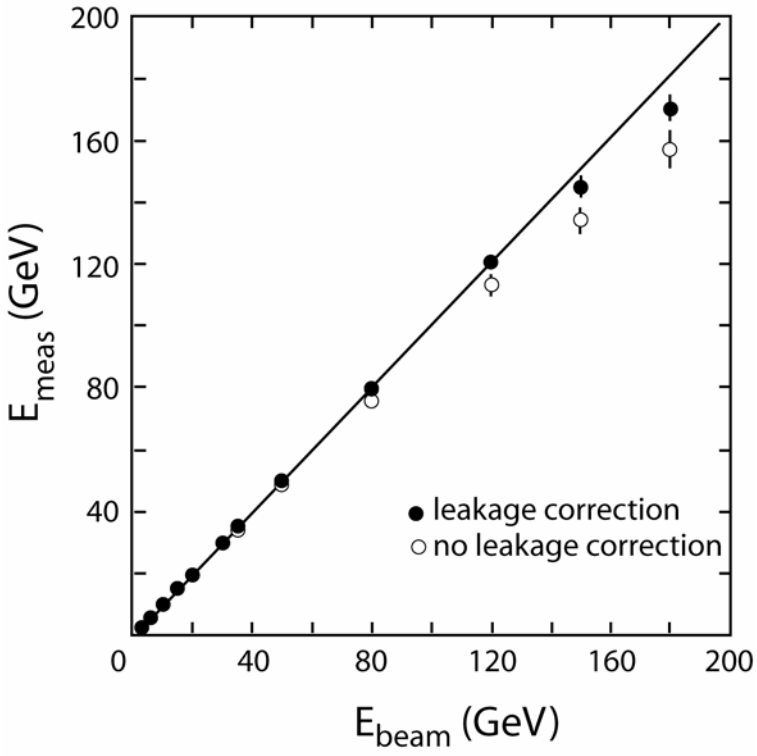

Figure 2.149: Leakage corrected linearity.

The calorimeter energy resolution is shown in Figure 2.150, where the fractional uncertainty in the energy measurement, $\sigma(E)/E$, is plotted as a function of the nominal beam energy, E (in GeV). The energy resolution is well parametrized by $\sigma(E)/E = (10.2 \pm 0.3)\% / \sqrt{E(\mathrm{GeV})} \oplus (2.3 \pm 0.1)\%$. This result was obtained for electrons entering ECAL at the center of the equipped region and is in good agreement with the Monte Carlo estimate $\sigma(E)/E = (10.0 \pm 0.3)\% / \sqrt{E(\mathrm{GeV})} \oplus (1.4 \pm 0.06)\%$ taking into consideration the errors due to the incomplete acceptance of the lateral shower development and to the calibration procedure.

The energy measurement and resolution were also studied for electrons impinging on ECAL near the edges. The energy measurement for electrons at 120 GeV are shown in Figure 2.151 as a function of the distance to the edge and for different incident angles. This study demonstrates that significant corrections (> 20%) are necessary when $e^{\pm}$ enter ECAL at distances less them 30 mm from the edge.

The angular resolution at a fixed energy is studied by using electrons impinging on ECAL at normal incidence. For each event the shower axis is calculated by means of standard center of gravity methods. At each energy the angular resolution is defined by the angular distance from the incoming beam that contains 68% of the events (see Figure 2.152).

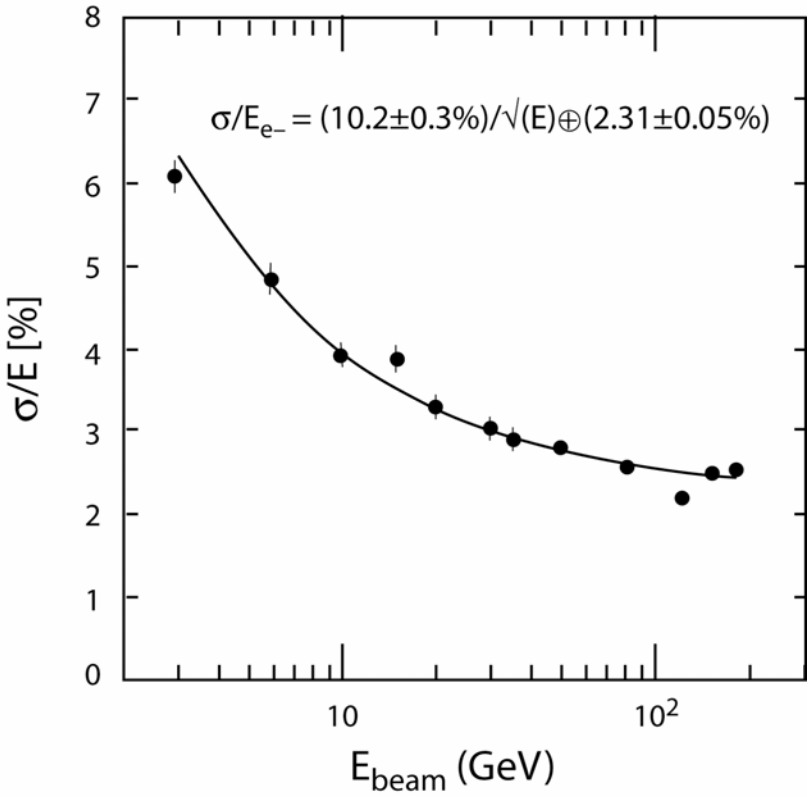

Figure 2.150: ECAL energy resolution.

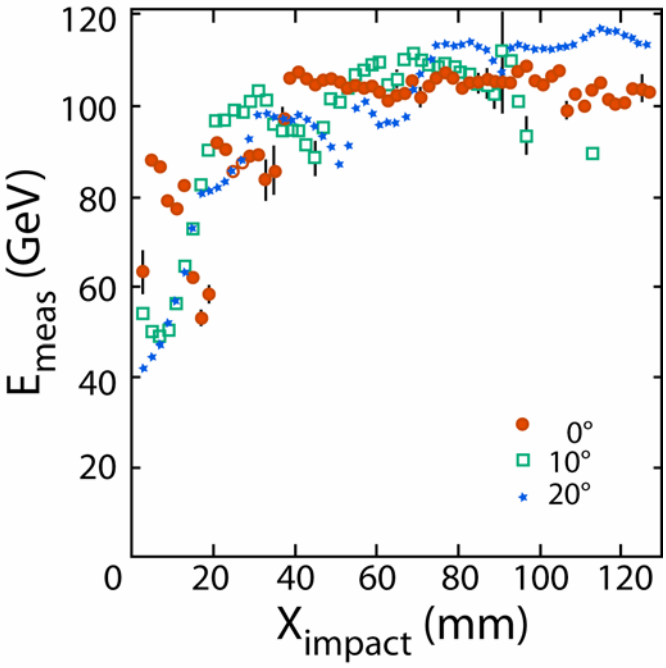

Figure 2.151: Energy measurement for 120 GeV electrons as a function of the distance to the edge and for different incident angles.

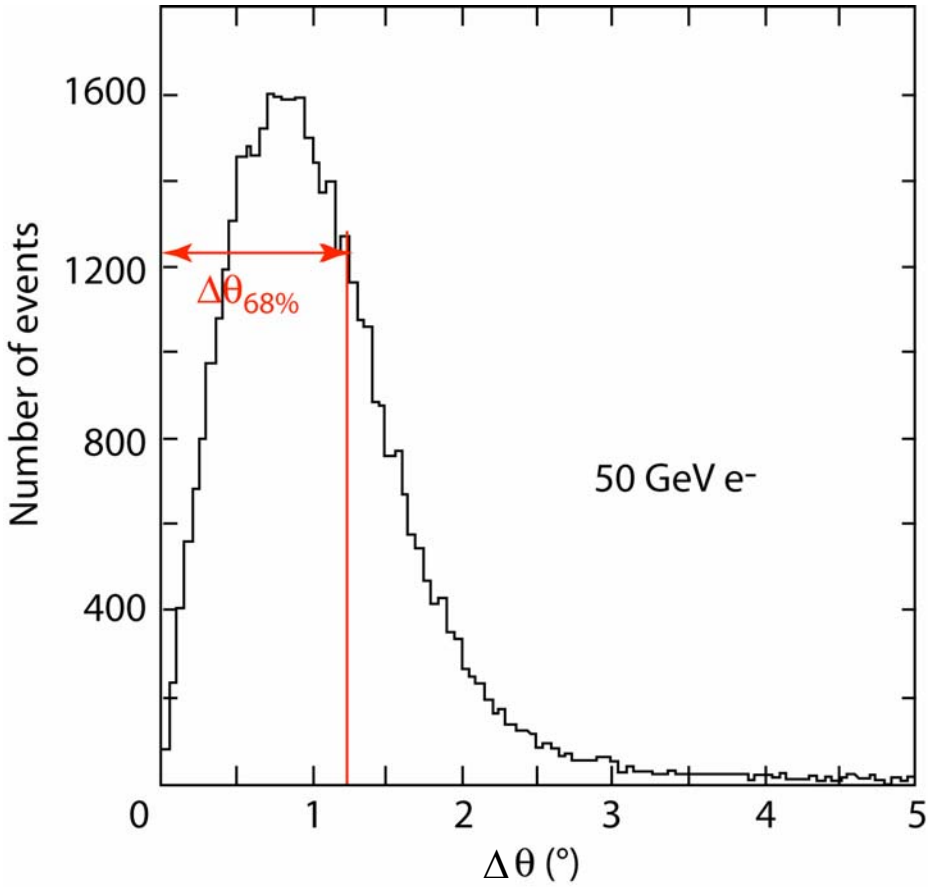

Figure 2.152: Angular resolution for 50 GeV electrons.

The angular resolution as a function of the electron energy, Figure 2.153, is well described by $\Delta\theta_{68\%} = (8.6 \pm 0.1)/\sqrt{E(\mathrm{GeV})} \oplus (0.57 \pm 0.04)$ (in degrees). Figure 2.154 shows the angular resolution when a 120 GeV electron beam enters ECAL at different incident angles.

To study the positron/proton rejection power with the test beam data, a neural network method was used which takes into account only the main shower characteristics (apex, depth, lateral and longitudinal profiles). Since the background to positrons of energy E_{e+} comes mostly from protons of energy $E_p \sim 2\ E_{e+}$, e^+/p discrimination is evaluated for positron data at 50 GeV and proton data at 120 GeV.

Monte Carlo calculations show that 75% of 120 GeV protons, misidentified as positrons have a visible energy in the range $40 < E_p < 60$ GeV, while 20% of them are in the range $20 < E_p < 40$ GeV. The ECAL discrimination power is shown in Figure 2.155, where the proton misidentification is plotted as a function of the efficiency for positron detection. The rejection can be improved by combining Tracker and ECAL information to determine the energy/momentum ratio (E/p). To evaluate the effectiveness of this procedure with the test beam data, the momentum was smeared according to the Tracker resolution and the matching requirement was applied with a cut E/p > 0.8, yielding a factor of 20 improvement in the discrimination power.

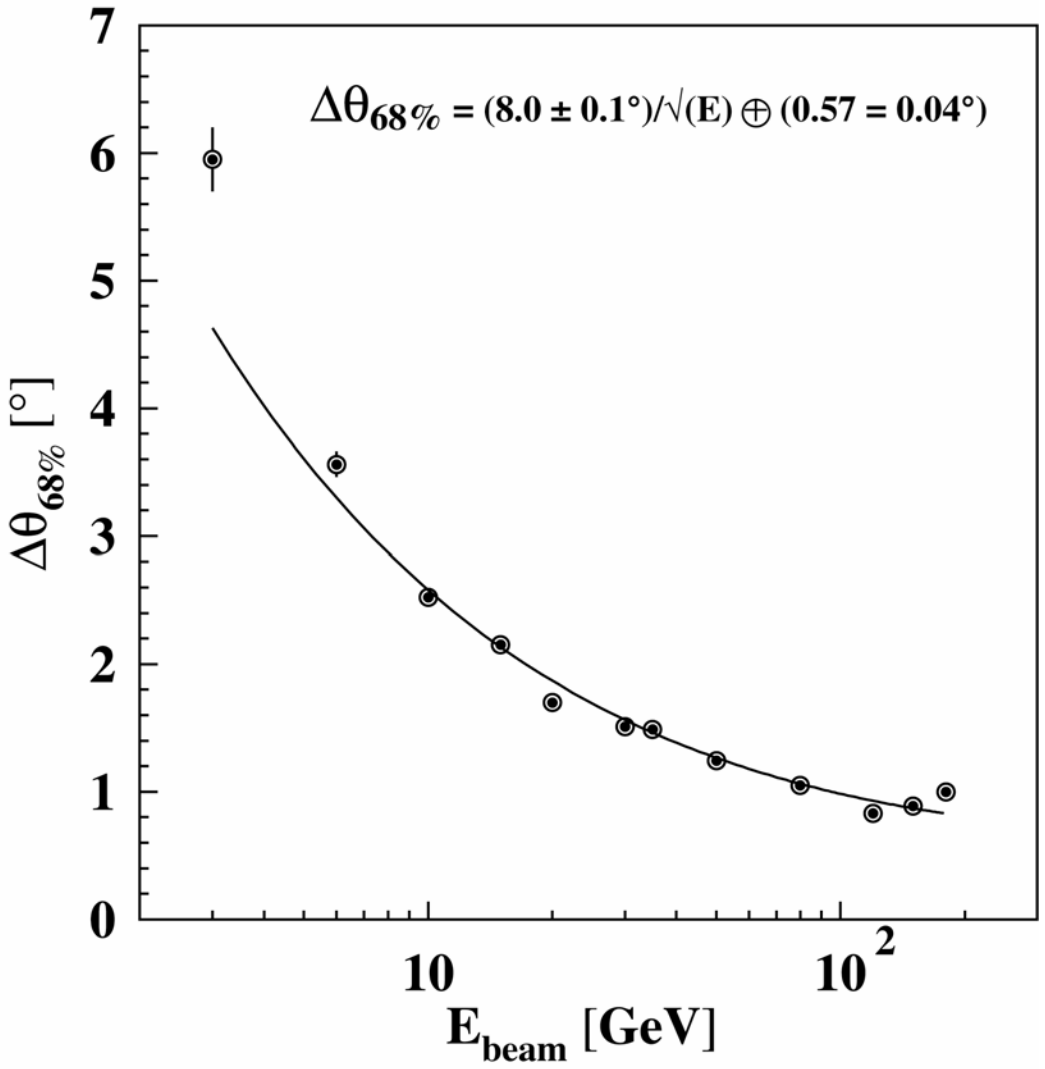

Figure 2.153: Angular resolution vs. electron energy.

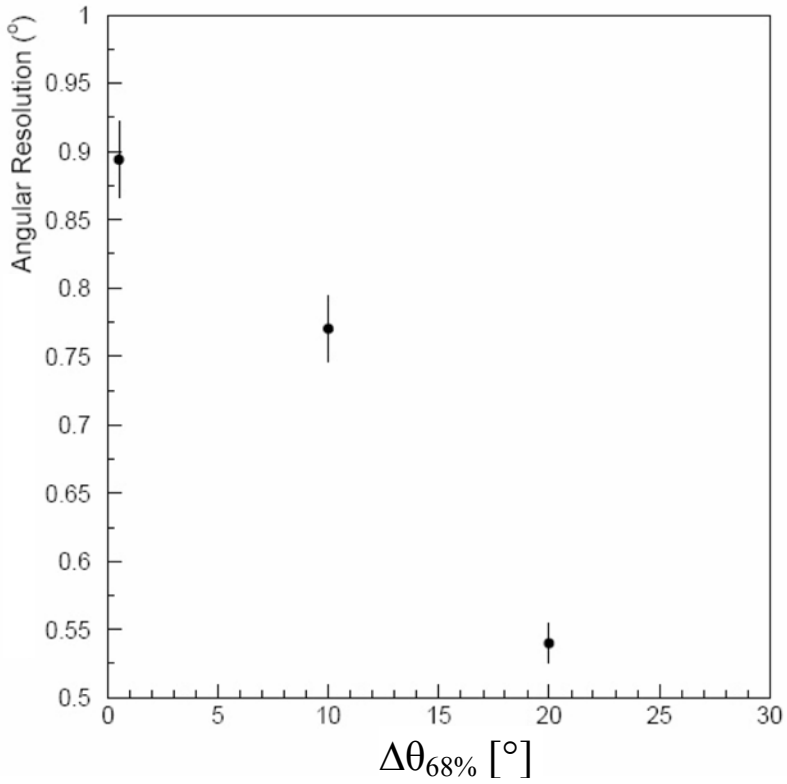

Figure 2.154: Angular resolution vs. incident angle for 120 GeV electrons.

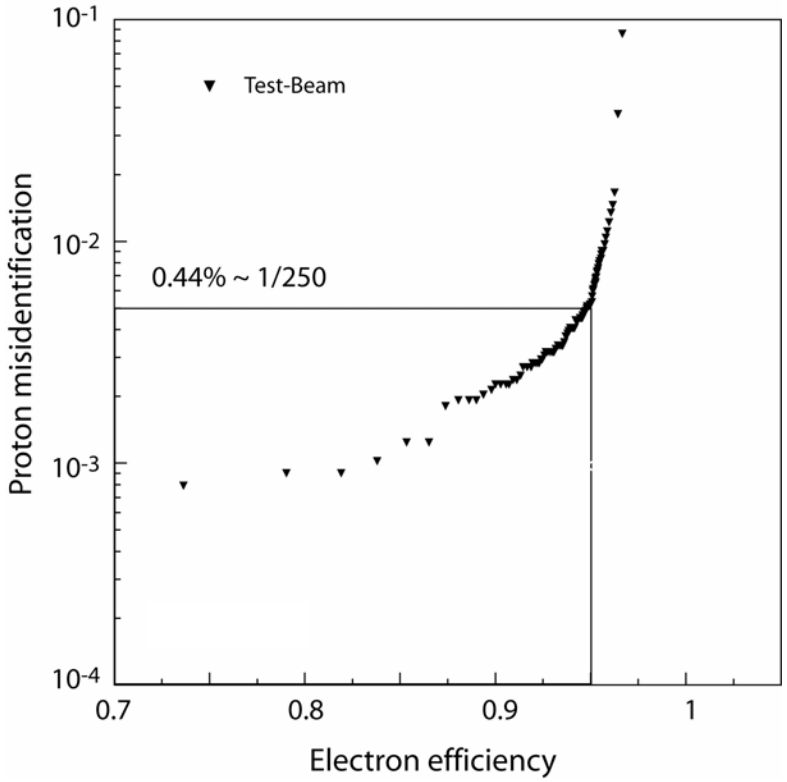

Figure 2.155: Misidentification of 120 GeV protons versus 50 GeV electron efficiency after the neural network selection (E/p matching not included).

2.7.7 References

[1] F. Cervelli et al., Nucl. Instr. and Method. A **490** (2002) 132.

[2] F. Cadoux et al., Nuclear Physics B (Proc. Suppl.) **113** (2002) 159.

[3] E.Choumilov et al., Nucl. Instr. and Method. A **426** (1999) 625.

[4] J. Alcaraz et al. (the AMS-01 Collaboration), Phys. Lett. B **472** (2000) 215;
J. Alcaraz et al. (the AMS-01 Collaboration), Phys. Lett. B **494** (2000) 193;
J. Alcaraz et al. (the AMS-01 Collaboration), Phys. Lett. B **484** (2000) 10;
J. Alcaraz et al. (the AMS-01 Collaboration), Phys. Lett. B **495** (2000) 440.

[5] P. Sreekumar et al., ApJ **494** (1998) 532-534.

[6] R. Hermel, 5th International Meeting on Front-End Electronics (2003).

[7] E.Longo and I.Sestili, Nucl. Instr. and Method. A **128** (1975) 283.

2.8 Electronics

For the electronics, AMS has taken the high performance technologies used in particle physics and implemented them for use in low Earth orbit. Figure 2.156 provides an overview of the AMS electronics elements and Figure 2.157 indicates the NASA provided interfaces on the ISS. A unified approach has been made to meet the requirements imposed by the different AMS subdetectors, by NASA and most importantly, by the physics goals. Particular effort has been made to ensure that the data acquisition and trigger electronics will meet the performance requirements on orbit during the 3-5 years of operation. The AMS crew operations post (ACOP) will archive the AMS data. Meeting the challenges of implementing high performance, space qualified electronics has been a key activity of the entire AMS collaboration.

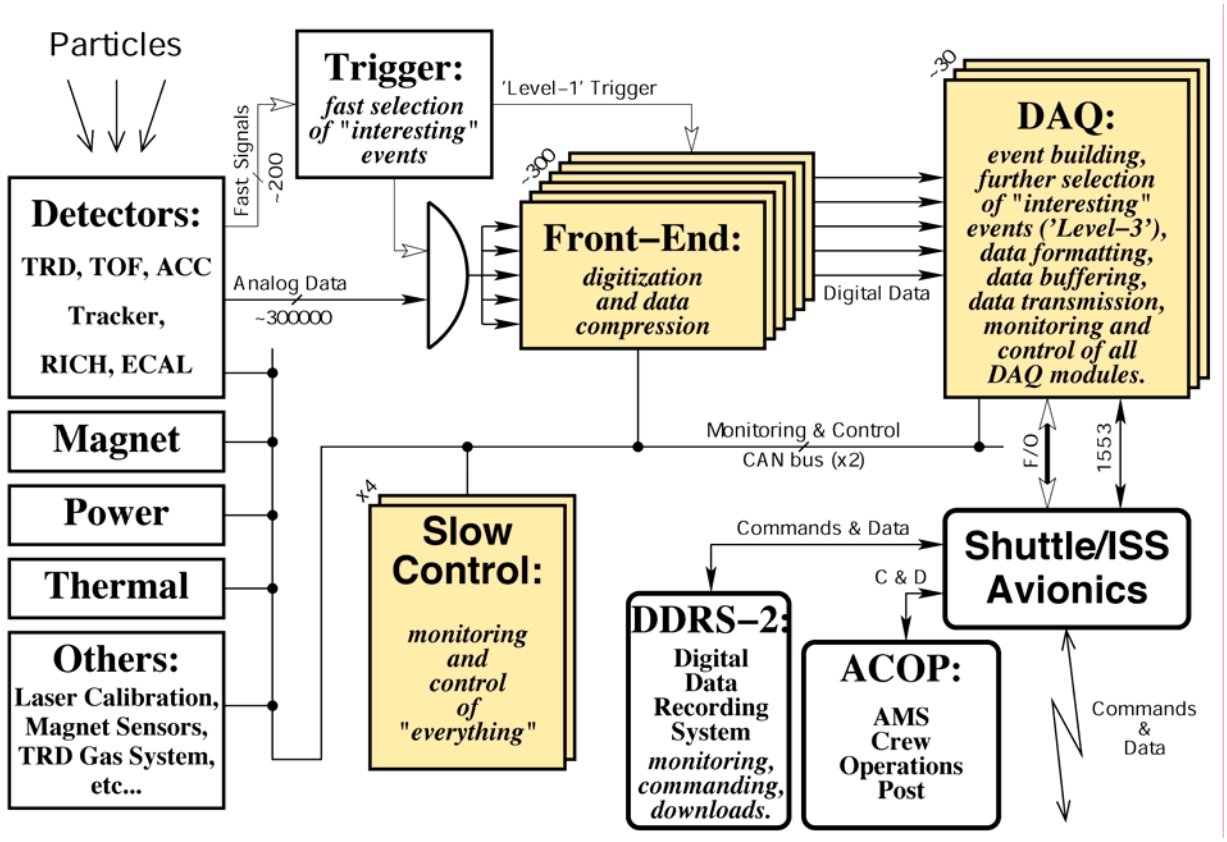

Figure 2.156: Overview of AMS-02 Electronics on the ISS and STS.

2.8.1 Interfaces

As indicated in Figure 2.157, NASA provides three electrical interfaces to AMS-02 on the ISS: power, Low Rate Data Link (LRDL) and High Rate Data Link (HRDL). The interfaces are physically located on the PAS within the Umbilical Mechanical Attachment (UMA) at bottom of the USS (see Figure 2.1). After AMS is mechanically installed on the ISS attach site, the UMA activates and mates the connectors. Then power is applied, the data links activated and experimental operations commence.

For operations during the shuttle (STS) flight to the ISS, NASA has provided the corresponding interfaces for power and low and high rate data transfer.

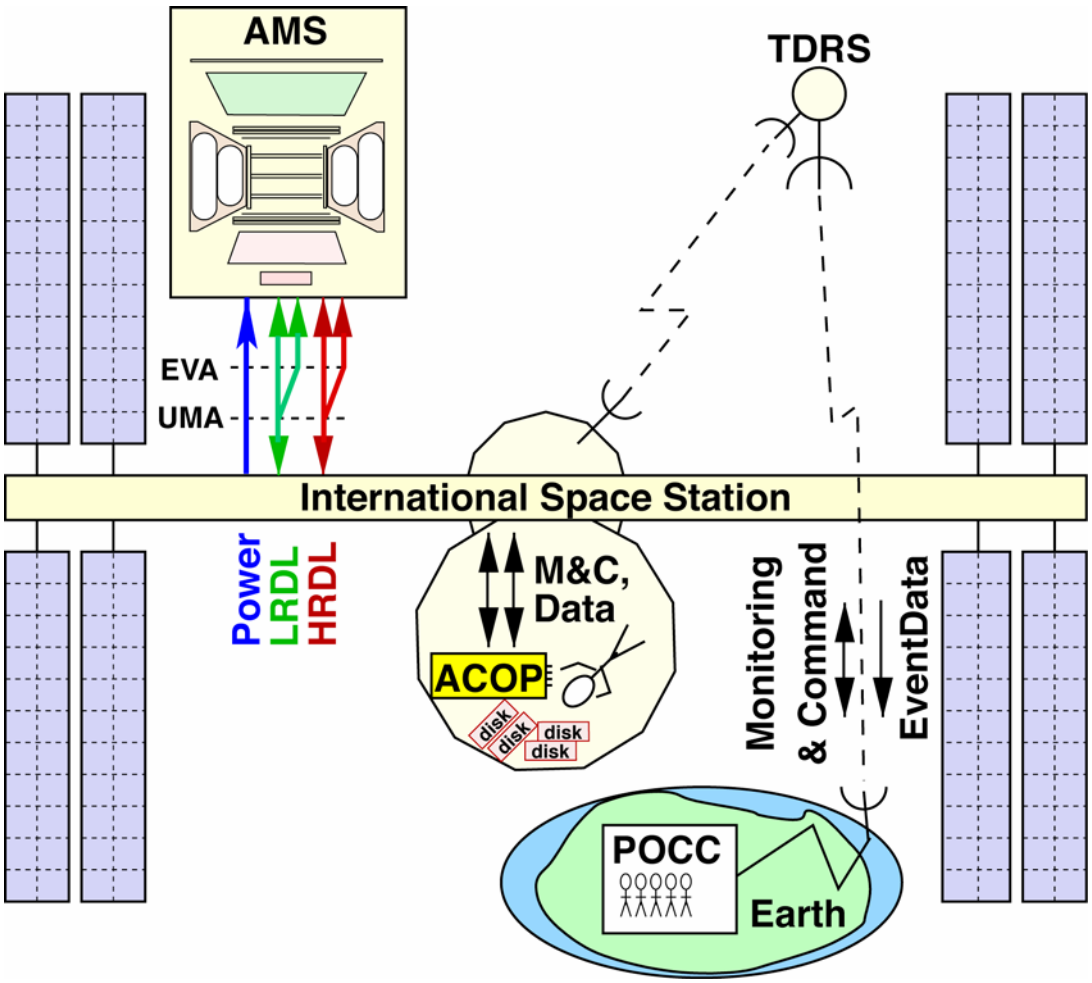

Figure 2.157: AMS electrical interfaces on ISS (TDRS: Tracking and Data Relay Satellite, POCC: Payload Operations and Control Center, M&C: Monitoring and Command).

i) Power Interface

Power on the ISS comes from the eight large solar arrays. AMS will have two power feeds, each one connected to one of the arrays. The power is provided at voltages ranging from 109 to 126 VDC with 120 VDC nominal. The maximum power draw allocated to AMS is 2000 W summed over both feeds, this limit being extended to 2300 W for the final 30 minutes of magnet charging. Stringent requirements are placed on AMS by NASA in terms of isolation, grounding, electromagnetic compatibility, inrush current and complex impedance.

To accommodate these requirements, and to maximize the overall power efficiency and system reliability, we have adopted the power architecture shown in Figure 2.158. For each of the two ISS feeds (A, B), the power distribution system (PDS) contains a thermal interlock, an electromagnetic interference filter (EMI), 11 heater control switches, a set of 120-28 V DC to DC converters, 32 solid state circuit breakers and numerous current and voltage sensors. The thermal interlock diverts power into the heaters within the PDS whenever AMS is turned on until the PDS temperature is within operational range. The filtering protects the rest of ISS from possible noise generated by the experiment and the experiment from other noise sources on the station. The heater switches allow the maximum power to be used to heat the experiment when it is turned on in cold cases. In other cases and in normal running all of this power is

allocated to operate the electronics. The converters provide the first isolation barrier and deliver a stable 28 VDC to each of the subsystem consumers. The 32 circuit breaker outputs from the A and B sides are OR'ed to allow each of the subsystem boxes to be supplied with power from either the ISS A or B feed, thus the overall consumption on the two feeds can be optimized with respect to other loads on the space station.

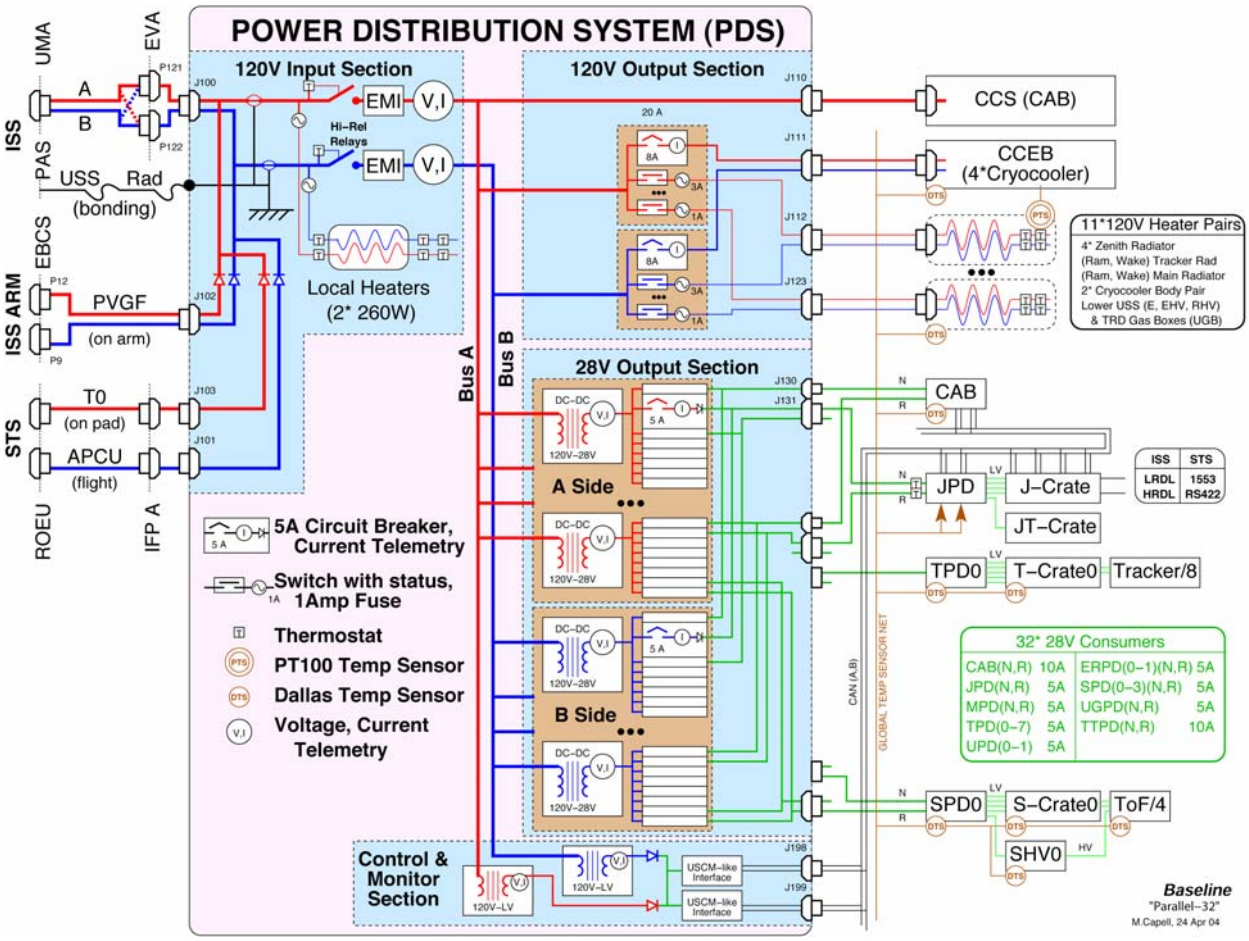

Figure 2.158: AMS-02 Power Distribution System (PDS).

Special provision has been made to feed the cryomagnet avionics box (CAB) and the cryocoolers directly with 120 VDC. A small amount of power is also directed though another pair of converters to run the control and monitoring section of the PDS, which is based around a pair of USCM (Universal Slow Control Modules) derived circuits run in hot redundancy.

This scheme attaches the minimum number of different units directly to the ISS feeds. It also provides full monitoring, protection and control of the power to each box. The large size (560 W) of the DC-DC converters allows a high efficiency (>90%) in the conversion to 28 V, while minimizing the voltage fluctuations and noise that could be induced into the sensitive detector electronics.

A typical consumer, shown in Figure 2.158, is the electronics for 1/8 of the silicon tracker (see also § 2.3.4). Power flows into one of eight Tracker Power Distribution (TPD) boxes, in which it is filtered and converted to several different low voltages, which flow into the electronics located in one of the eight T-Crates and 24 of the 192 tracker ladders. Thermal interlocking for this consumer is provided by monitoring the temperatures in the four-fold redundant main data acquisition computers (JMDC) located in the J-Crate, which has a dedicated hardware thermal interlock.

NASA planning indicates that no unscheduled interruptions will occur and that full power will be available for AMS about 364 days per year. However, given the lack of operational experience with the complete ISS to date, our systems are designed to survive reduced and zero power levels foreseen or not, for an extended interval.

ii) Low Rate Data Link (LRDL) Interface

The LRDL is based on the MIL STD 1553B dual serial bus, widely used in aircraft. This is split to each of the four JMDCs, one which is selected to actively manage the link. As the point of splitting is a possible single point failure, AMS has two such splitters which can be selected by an astronaut swapping a cable at the bottom of the experiment during an extra-vehicular activity (EVA). Figure 2.159 shows an astronaut practicing this intervention underwater on a mock up of AMS-02 in the Neutral Buoyancy Lab (NBL). The active JMDC receives commands and redistributes them within AMS, either to other software within that JMDC, to another JMDC or to the controllers of other electronics subsystems using either a dual CAN bus or a series of serial point to point links. The controllers in turn set, for example, switches and digital to analog converters (DACs) to control various experimental parameters such as voltages. They also monitor numerous temperatures, voltages and currents and report these values when requested to the active JMDC, where they are appropriately formatted and sent on to the LRDL.

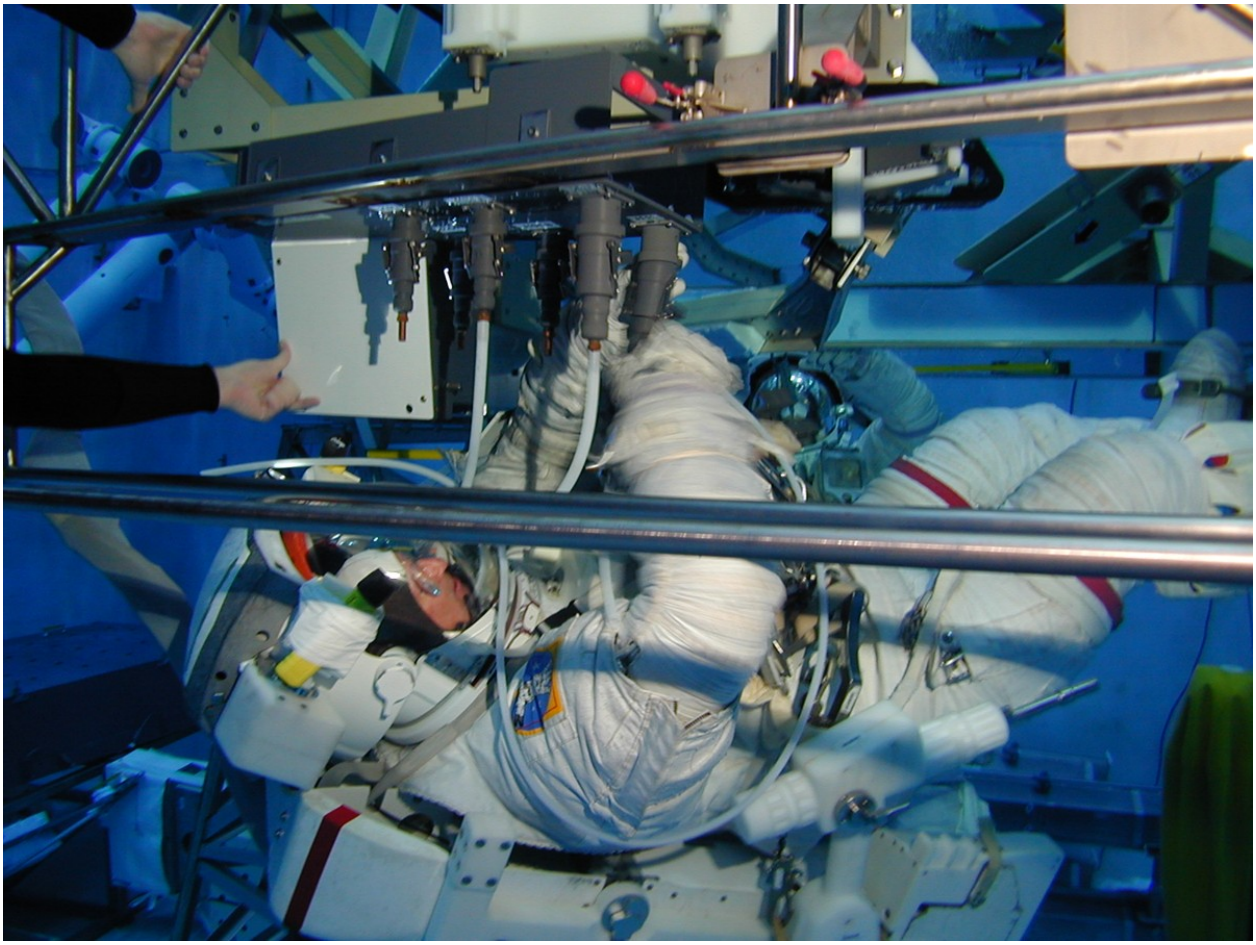

Figure 2.159: Practicing contingency EVA swap of AMS data cables at NBL.

As shown in Figure 2.160, this telemetry data then proceeds through a series of NASA units and then via radio beam to Earth, where it is routed to the AMS Payload Operation and Control Center (POCC). The NASA units involved include : the S-band with 50% duty cycle, the ACBSP S-band receiver, the Command and Control Multiplexer/Demultiplexer (C&C MDM), the Payload Multiplexer/Demultiplexer (P/L MDM), the Automated Payload Switch (APS), the High Rate Communications Outage Recorder (HCOR), the High Rate Frame Multiplexer & High Rate Modem (HRFM/HRM), the Ku-band system connecting the ISS via the Tracking and Data Relay Satellite (TDRS) through the White Sands Ground Complex (WSGC) to the Marshall Space Flight Center (MSFC) and the Johnson Space Center (JSC). Within the US Lab on the ISS, the astronaut crew has access to this data via their Portable Control System (PCS) laptops and via the AMS Crew Operations Post (ACOP).

In total AMS is allocated about 20 KBits/sec of data bandwidth on the LRDL, with an expected duty cycle of up to 70%. Ten highly summarized bytes per second of critical health data are transmitted with near to 100% duty cycle. Along the way the ISS crew and NASA ground controllers can monitor at this data and, should the need arise, have the facility to issue a few key commands, for example to put the experiment into a standby state. In nominal conditions, all commands originate in the POCC and follow the inverse path, the maximum command rate being about 1 Kbit/second.

As commanding and telemetry are critical to the operation of the experiment and as the NASA provisions for payloads are not fault tolerant, substantial effort has been made to implement a parallel set of data paths over the HRDL for both monitoring and commanding of AMS.

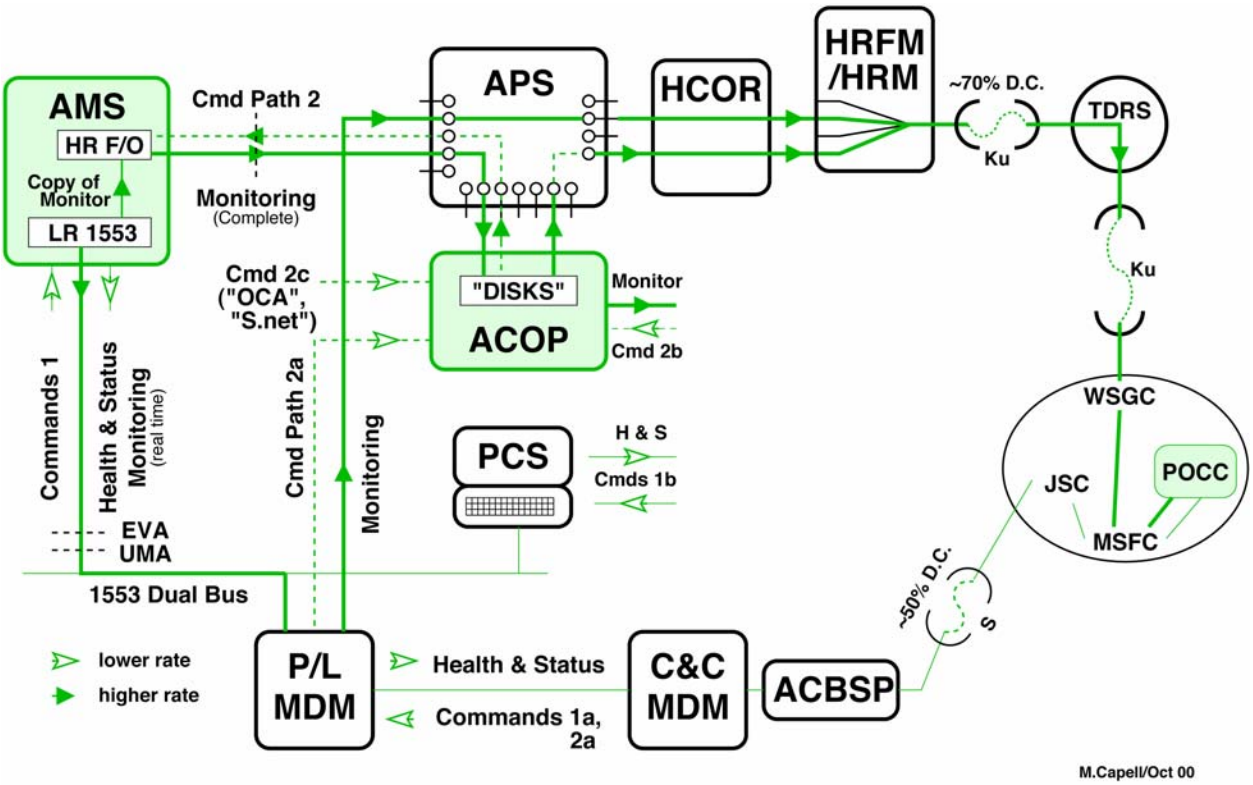

Figure 2.160: Monitoring and Command Data Flow over both the LRDL and HRDL.
The unshaded NASA supplied units are defined in the text.

iii) High Rate Data Link (HRDL) Interface

The HRDL is the main data conduit out of AMS. It is based on a NASA specific implementation of fiber optic communications. The link can move data on the ISS at speeds up to 90 MBit/sec, and the radio down link supports up to 43 Mbit/sec, again with an at best duty cycle of 70%. Of this AMS has been allocated an orbit average of 2 Mbit/sec. Within AMS, the data is collected by the data acquisition (DAQ) system to a buffer within the JMDCs. As for the LRDL, each of the four JMDC is connected to the HRDL and a cable swap during EVA avoids a possible single point of failure. On the HRDL the data flows over the paths shown in Figure 2.161. A key element in this path is ACOP, where the data is archived on disks. ACOP will be mounted in an Express Rack inside of an ISS Standard Payload Rack (ISPR). On the ground the data is routed to the AMS POCC and Science Operation Center.

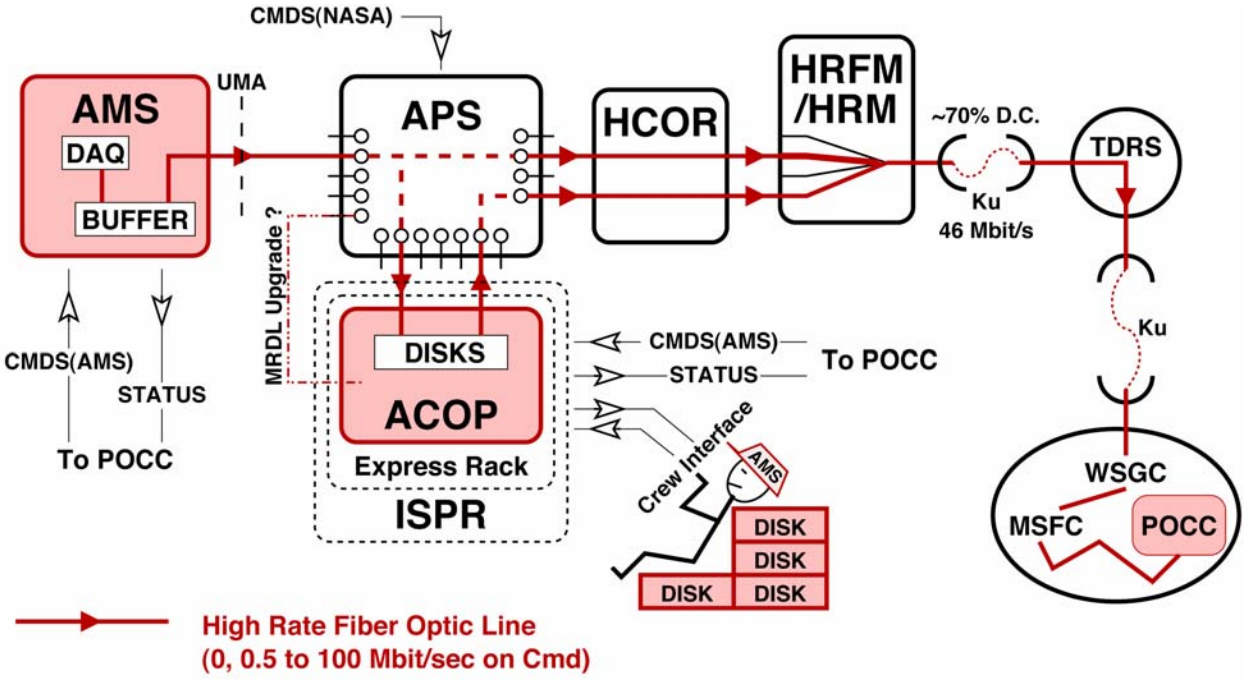

Figure 2.161: AMS Science data flow over the of High Rate Data Link.
The unshaded NASA supplied units are defined in the text.

2.8.2 Subdetector Electronics

Table 2.10 summarizes the electronics requirements of the different detectors described earlier in this chapter. The TRD requires the gas gain to be carefully controlled. The time of flight system requires relative timing accuracy of 100 picoseconds, the silicon microstrip tracker requires signals as small as a few femtocoulombs to be measured with a signal to noise suppression of 10^5. The RICH requires that single visible photons be measured. The ECAL requires a wide dynamic range of 60,000. In total there are ~300,000 separate subdetector detector channels producing 3.7 MBit of data for every trigger.

Subdetector	Critical Requirement	Channels	Raw Kbits
U: TRD	Gas gain	5,248	84
S: ToF+ACC	100 ps	48*4*8	49
T: Tracker	few fC	196,608	3,146
R: RICH	Single γ	680*16*2	348
E: ECAL	1:60,000	324*(4*2+1)	47
Σ Raw Kbits/event * Event Rate			3,674 * ≤ 2 Khz
= Total Raw Data Rate :			**~7 Gbit/sec**

Table 2.10: Subdetector electronics requirements and raw data volumes.

Though the detailed requirements imposed by the physics are different for each of the subdetectors, a unified approach has been adopted for their electronics. This approach is based on the successful experience gained with the AMS-01 engineering flight, updated for new technologies, for the subdetectors which were not installed on AMS-01 and for the tight resource requirements both on the ground (time, money, manpower) and on orbit (weight, power, data rate). This approach is shown in Figure 2.162. Analog signals from the detectors enter a detector specific Application Specific Integrated Circuit (ASIC) and are first shaped, and then held in response to a trigger, the trigger having been generated using signals from the detectors as shown in Figure 2.163. The held signals are then multiplexed with the ASIC. These are mounted close to the detector elements. Before or after digitization, typically with an ADC, the output is then sent over a cable into a CDP (common digital part) and buffered into memories. With multiplexing, each CDP collects data from up to 1000 different subdetector signals. A unified approach was also applied to the monitoring and control (M&C) of the subdetector parameters and to their power supplies. As discussed below, all of the components and circuits used in these unified approaches have gone through a rigorous process to ensure that they will meet the performance requirements and operate reliably in outer space.

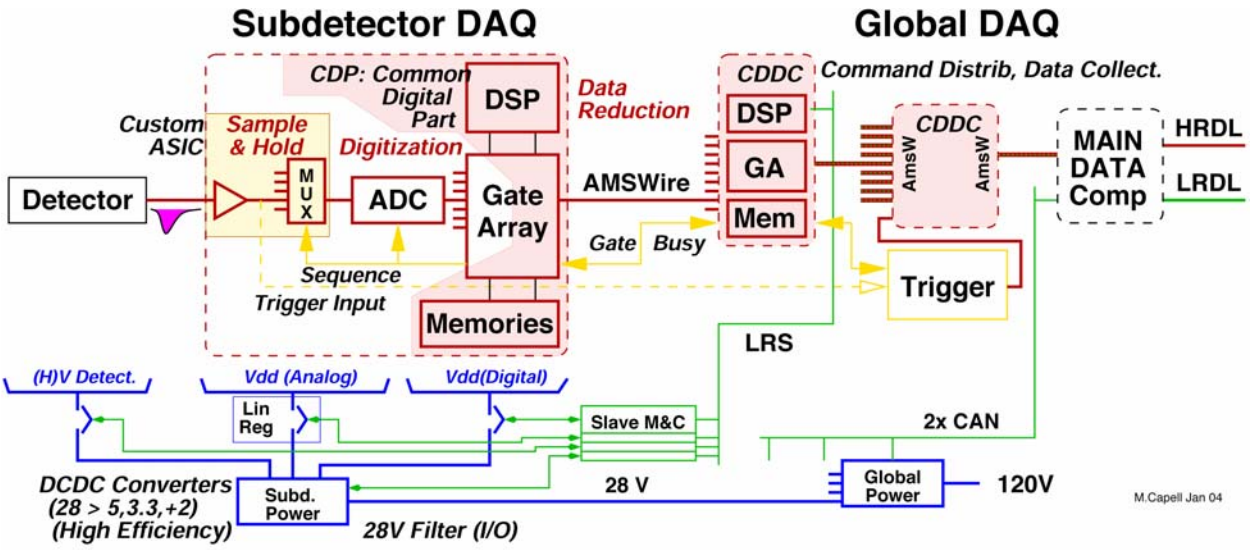

Figure 2.162: Unified approach to subdetector electronics for DAQ, Monitoring and Control (M&C) and power.

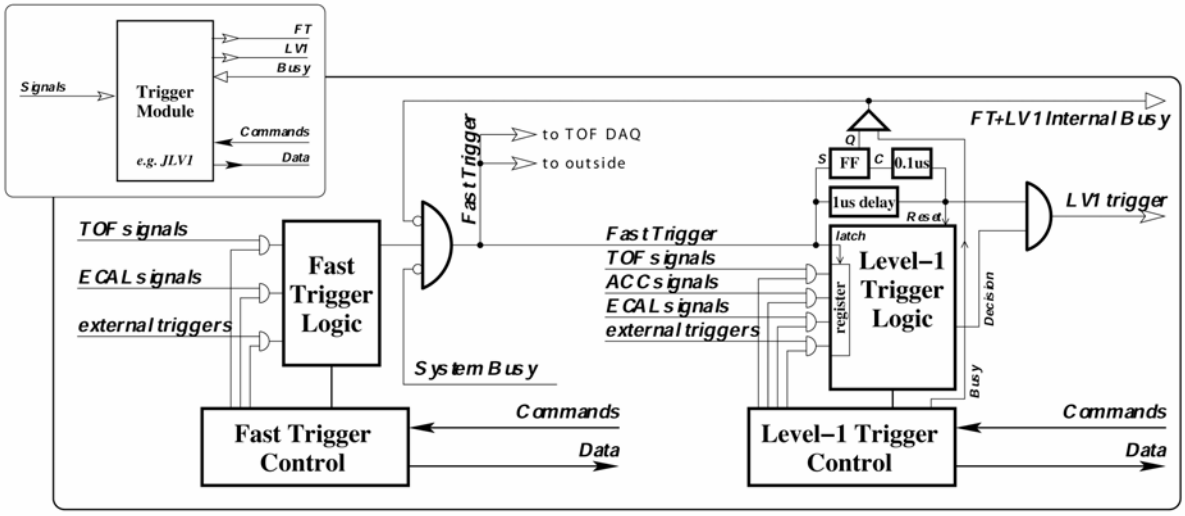

Figure 2.163: Fast (FT) and Level-1 (LV1) Trigger Scheme (FF - flip flop).

2.8.3 DAQ and Trigger Electronics

The physics data flow in the electronics is driven by the trigger system shown in Figure 2.163. This system recognizes when a charged particle has passed through the detector based on the coincidence of fast signals from the time of flight scintillators. It then looks at fast signals from the ACC and ECAL to check that the particle cleanly passed through the detector. In addition to charged particles, high energy gamma rays are also triggered when they pair produce electrons in the TRD. Unconverted photons above 1 GeV are also triggered based on stand-alone pattern recognition in the ECAL which rejects the primary background of off axis low energy protons. The total trigger rate is estimated from the measurements performed by AMS-01 to vary from 200 to 2000 Hz, depending on the geomagnetic latitude. The electronics system is being conservatively designed to perform precision physics at twice these rates.

Technically, two CDPs are located on one xDR board (see Figure 2.164), where x=E, R, S, T, U for the different subdetectors. For the RICH and Tracker, x=R, T, the two CDP are independent. For the ECAL, Scintillators and TRD, x=E, S, U, the two CDP are in cold redundancy. In all cases, once the raw data is stored into memory, the following DAQ circuitry is the same for all the subdetectors. Asynchronously with subsequent triggers, the data within a CDP is reduced using a subdetector specific algorithm in a digital signal processor (DSP) and rebuffered. When resources are available to receive it, this DSP output is shipped over a custom developed 10 MByte/sec serial link, AMSWire, into the global data acquisition tree. The next node in this tree, a Command Distributor and Data Concentrator (CDDC) circuit located on a JINF board, receives data from up to 24 CDP. The CDDC is in fact a CDP with modified front end and larger memories.

In the CDDC the data from an event is collated, buffered and, again using AMSWire links, sent to the top level CDDCs located on JINJ boards, collated, buffered and in turn passed into a JMDC. The JMDC receives the complete event and analyses it to ensure that it might contain interesting physics and also to monitor the detector performance. The selected events are then buffered and sent out the HRDL when it becomes available.

The extensive use of point to point serial links has made it straight forward to implement progressively higher levels of redundancy as the data travels higher up the DAQ tree, as shown in Figures 2.164 and 2.165.

From Table 2.10, the peak raw data rate is 7 GBit/sec. The extensive data reduction performed in parallel in the 284 front end DAQ modules combined with buffering through out the DAQ tree and in the JMDC, plus additional event filtering in the JMDC, allows this rate to be reduced to the allocated 2 MBit/sec orbit average.

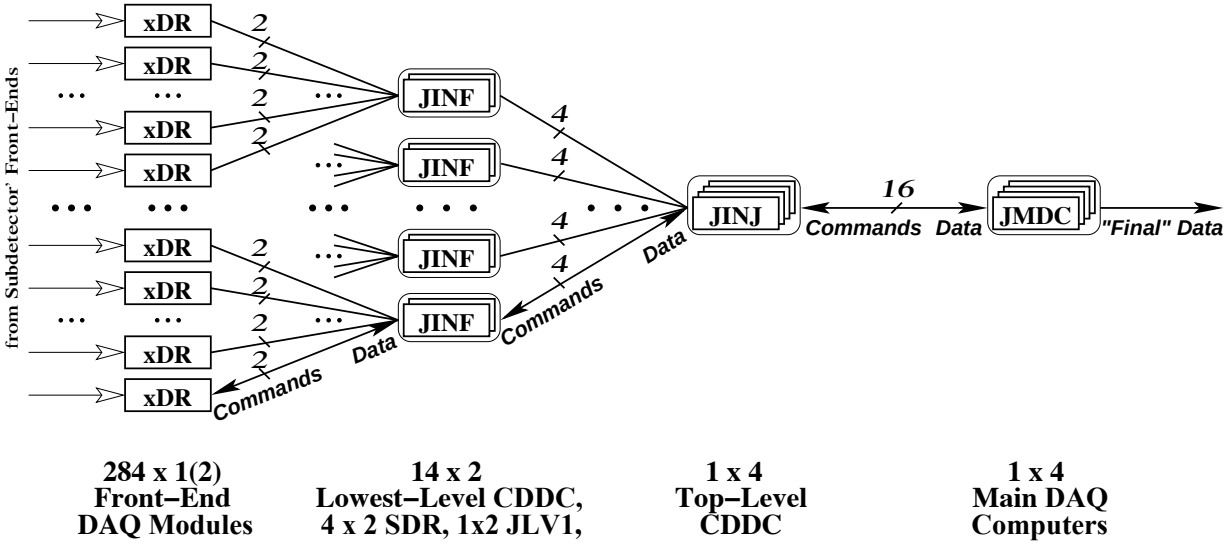

Figure 2.164: The DAQ tree. The number of redundant links at each level is indicated.

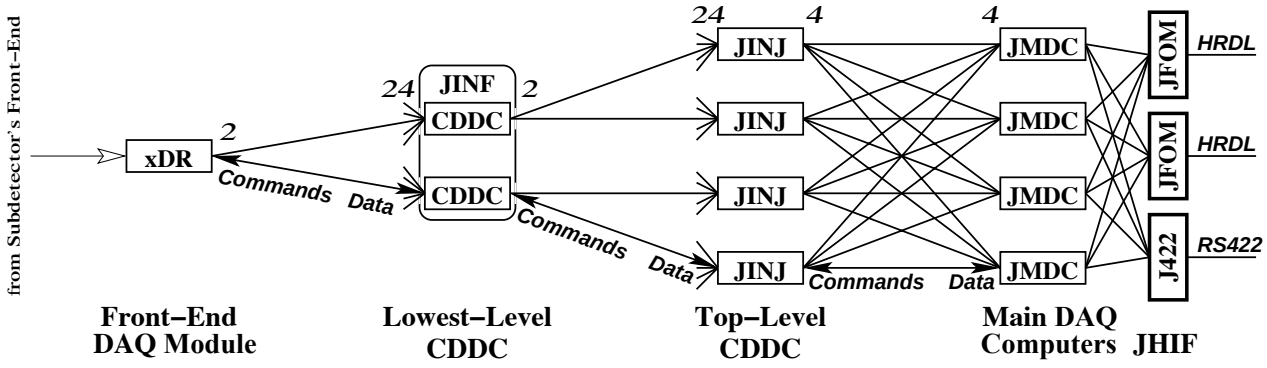

Figure 2.165: The DAQ tree. The number of redundant nodes at each level is shown.

The JMDC is based on a powerful recent microprocessor, the IBM PowerPC 750, implemented into a custom built computer using a compact PCI format bus (cPCI), with specific peripheral interfaces to a 2 GByte solid state memory buffer, which is required when the HRDL is not available, to the AMS CAN bus for monitoring and command transfers, to the DAQ AMSWire links and to the HRDL and LRDL and the equivalent data links for the shuttle. As for the subdetector electronics, the JMDC and peripherals have passed through an extensive space qualification process.

2.8.4 AMS Crew Operations Post (ACOP)

ACOP is a computer that is being specifically designed for AMS-02. In flight, the distinction between ACOP and the other electronics co-located with AMS is that ACOP is located inside the US lab module of the ISS and can be accessed by the astronaut crew, as shown in Figure 2.166, whereas the other flight electronics is located outside, under vacuum, next to the detectors on the S3 truss of ISS. The main function of ACOP is to archive the data from the experiment arriving from AMS-02 on the HRDL fiber optic data link. In addition, it allows the crew to monitor and, if necessary, command the experiment, as both on ACOP and within the AMS-02 JMDCs bi-directional fiber optic links are implemented.

ACOP is foreseen to be based on a CompactPCI format system in common with the AMS-02 JMDC systems. A conceptual design is shown in Figure 2.167. ACOP will contain a single board computer comparable to that of the JMDC but with extended memory and on-board peripherals. ACOP requires a custom developed interface for the High Rate Data Link (HRDL) and other peripheral devices, including Ethernet interfaces to support the Medium Rate Data Link (MRDL), a compact flash (CF) carrier to store the operating system and programs and digital input-output and video cards (DIO, VGA) which connect to a simple push button interface and a flight qualified LCD screen. ACOP will also contain four exchangeable hard disks used to archive the data and the necessary interfaces.

In addition to the ACOP system there will be stowage bag sent to ISS that will contain additional hard drives that can be exchanged with the hard drives in ACOP. From time to time the astronauts will perform this exchange enabling ACOP to record all of the AMS-02 data onto fresh hard drives. Exact hard disk capacity is under study, but without crew intervention ACOP should be able to archive the output of AMS for a month. With disk swapping this extends to six months. Once recorded, the data will not be overwritten; rather it will be transported to the ground as a permanent archive.

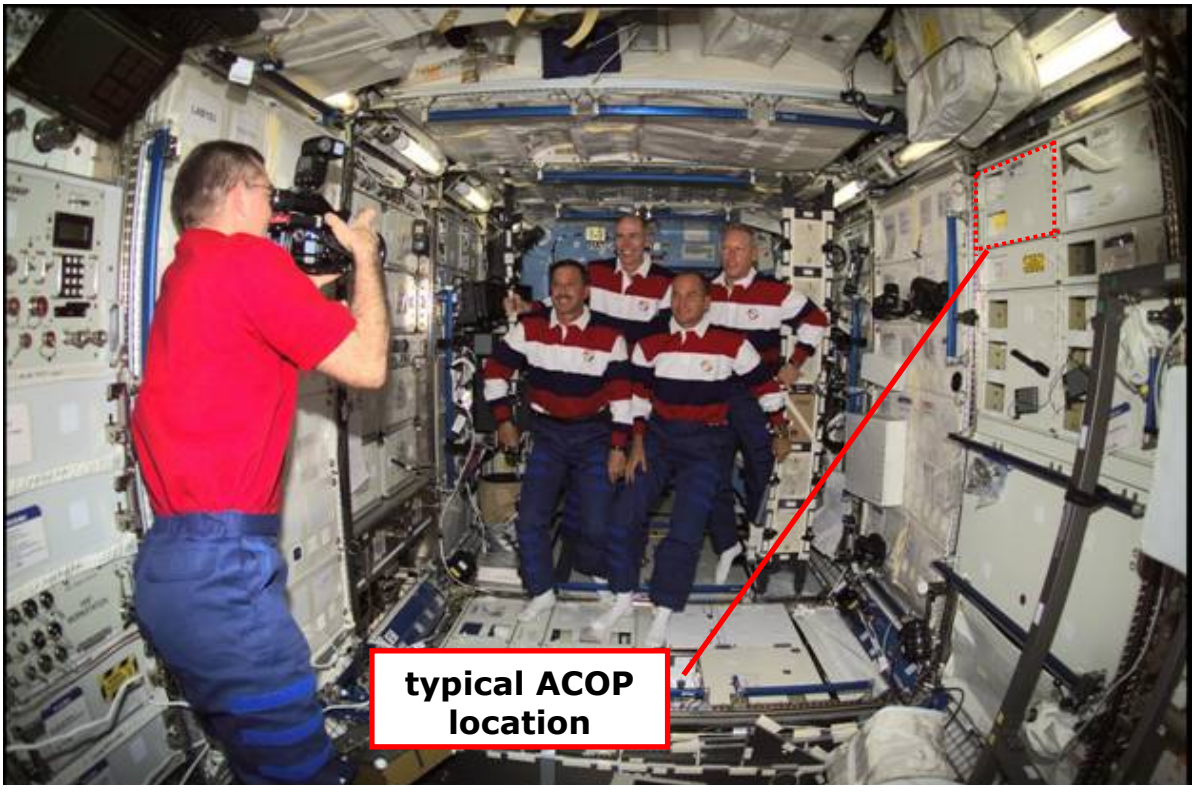

Figure 2.166: Typical ACOP location Inside the US Lab onboard the ISS.

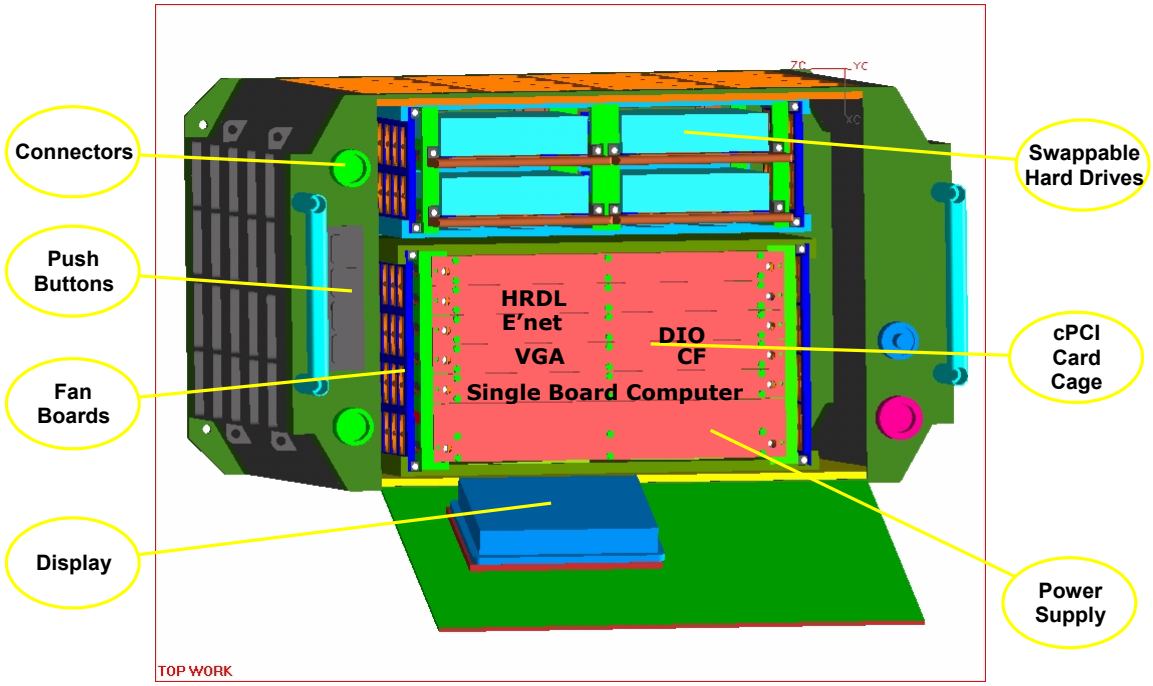

Figure 2.167: Conceptual design of ACOP.

AMS is expected to produce data at 2 Mbit/sec average, or 1+ GByte/hour. This continues 24 hours per day, 7 days per week, for the three year mission duration. Managing this data flow through the ISS systems will require substantial buffering and interaction and place a substantial load on the ISS systems. While the ISS high rate data systems have been demonstrated to operate to specification, they have not been used at high volume continuously for the weeks, months, years that AMS requires. ACOP will ensure that the critical output of AMS, the science data, is captured and accessible as securely as possible.

ACOP also provides a flexible and straight forward means for the astronauts to interact with AMS. One of most important resources on ISS is, of course, the crew. This makes this environment completely unique. In order to participate, the astronaut needs a means to monitor and control AMS-02. Certain key operations, like magnet charging, require the astronauts to continuously monitor AMS-02 and be prepared to exert control. ACOP is a flexible and powerful tool to monitor and control AMS-02.

ACOP also provides an alternate command path to AMS. The design of the ISS avionics systems has no tolerance for any failure of services with regard to payloads. There is a single path for commanding and monitoring a payload. If this fails there is no alternative but to repair the interface. This is the great thing about the space station; there is someone there to fix things. However the time to implement a repair is very high. Even the simplest repair can takes weeks or months – certainly an improvement over never, which is the alternative for non-manned systems. Since the super fluid helium will be boiling away while repairs are affected, significant data gathering capacity would be lost in the event of any failure. ACOP affords an alternate path from which commands can be sent from the ground to AMS-02.

2.8.5 Particle Physics Electronics in Space

Table 2.11 summarizes the challenges faced by the AMS collaboration in preparing particle physics electronics for use in space. The key point for AMS-02 electronics is derived from our extensive background in instrumentation of high energy physics detectors and our experience with AMS-01 and is rigorously tested all the way from the design prototyping and component screening through box level acceptance tests.

AMS has vastly more demanding requirements than those for usual space electronics, in terms of the performance, complexity and resources (power, weight, schedule). The requirements of each subsystem have been studied in detail and an optimized program to meet these requirements has been implemented. For example, in the Cryomagnet Avionics Box (CAB) it is not possible to connect completely redundant systems to the magnet, so heavy use is made of space grade components.

Challenge		**Solution**
Static Loads	40+10+10g	Mechanical Design & Test
Vibration	6.3 g_{rms}	
Depressurization	1 to 0 bar / 2 min	
Zero G	Floaters	Conformal coating
Vacuum	No Convection	Waste Heat Conduction
Thermal	−40, +80 °C Survival −30, +50 °C Operation	Parts Selection, Mech. Design & Testing
Radiation	~ 1 KRad /year	TID Testing
Heavy Ion	Latch Ups, Bit Flips	Beam Testing, Error D/C
Atomic O	Etching	Material Selection & Mechanical Shielding
Solar UV	Aging	
MM/OD	Punctures	More Shielding
EMC	Noise, Requirements	Ground, Filter, Screen
Mag. Field	Up to ~ 500 Gauss	Testing, Placement
Access	None for 3+ years	Reliability, Redundancy, Testing

Table 2.11: Challenges and solutions in flying state of the art electronics in low Earth orbit. Design and production follow processes validated with AMS-01.

In contrast the DAQ system primarily uses high grade commercial components and achieves reliability by interconnecting redundant elements. To ensure that these will work in space, a process has been developed leading from iterations of circuit design and component selection through mechanical design and material selection to the production, quality assurance and space qualification of a series of models. As indicated in Figure 2.168, candidate components are used to implement prototype circuits. These are then combined into functionally equivalent engineering models (EM). The EM are then reimplemented using high reliability components in to a series of qualification models (QM), which pass through a series of tests including vibration and thermal cycling at board level (QM1) and also thermal vacuum and electromagnetic compatibility (EMC) at box level (QM2). Figures 2.169 to 2.171 show the QM2 version of the crate containing the JMDC undergoing these tests. The QM2 boards are also used to completely iron out all kinks in the production process. The flight models and flight spares (FM, FS) are produced and qualified with vibration thermal cycling and thermal vacuum tests to the minimum levels required ensuring that each performs as the successful QM2 units.

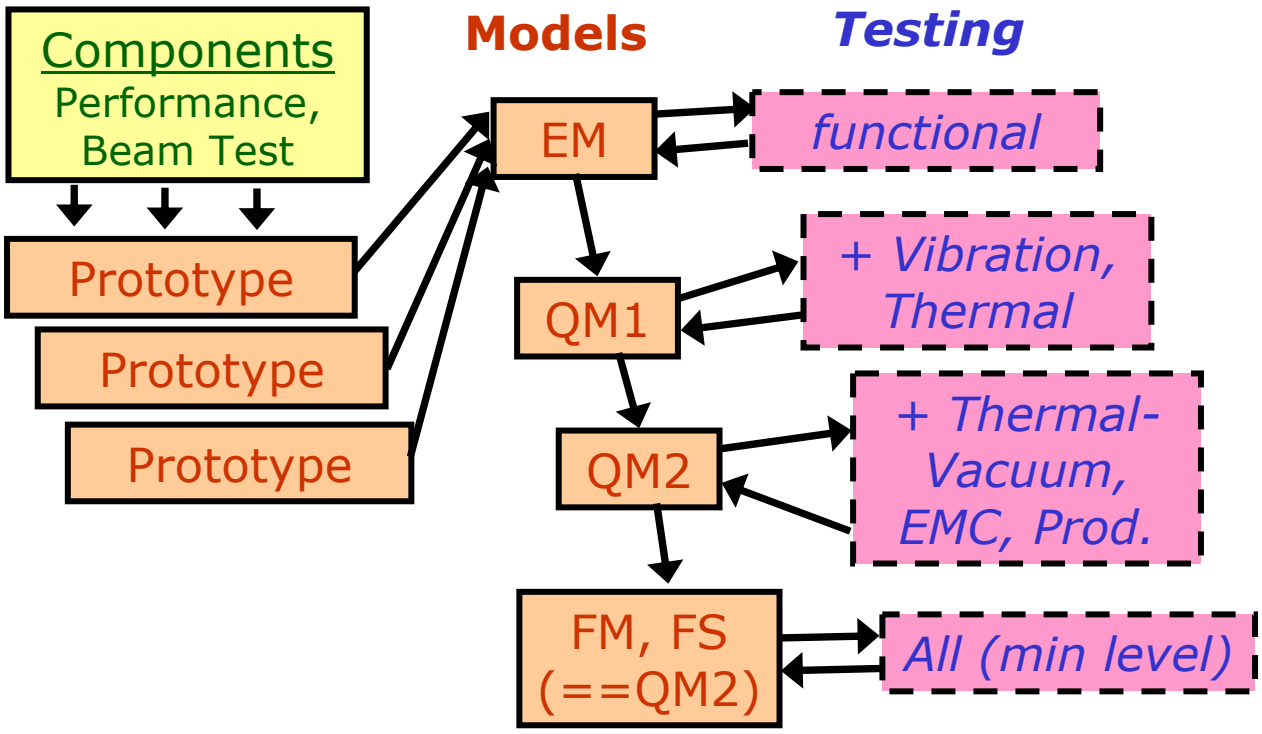

Figure 2.168: AMS-02 Process for producing space qualified electronics.

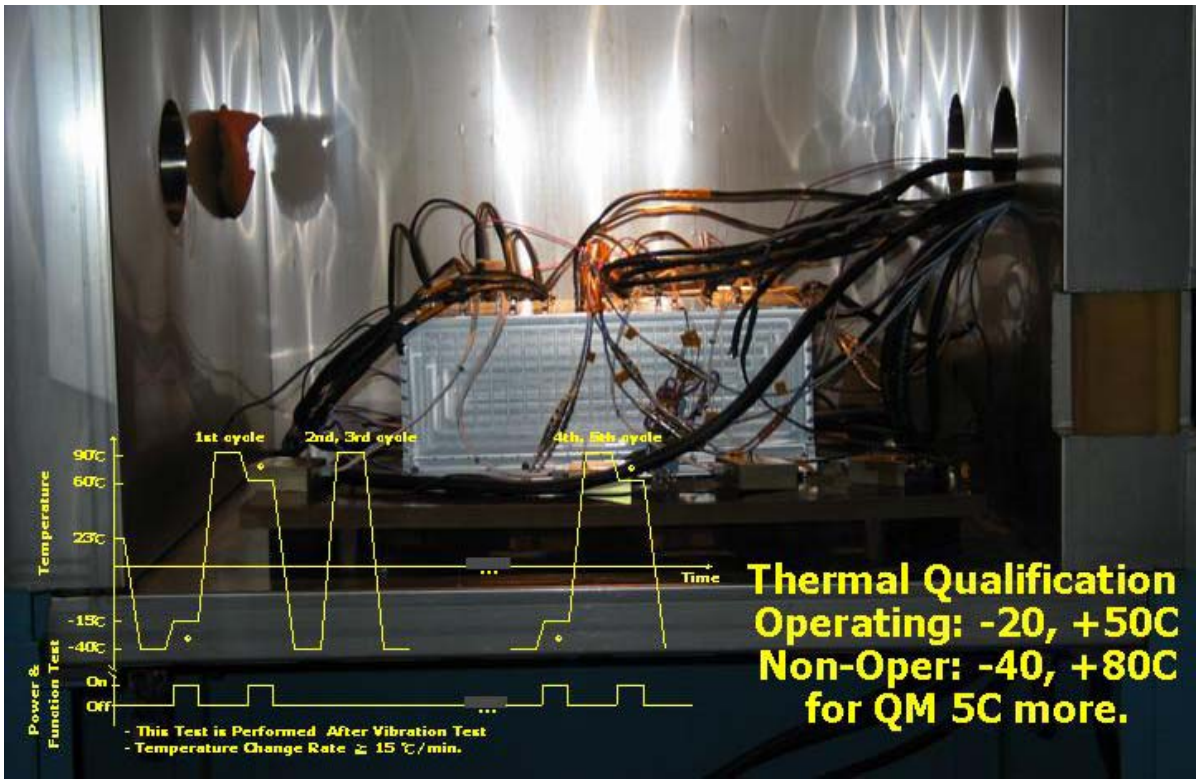

Figure 2.169: The JMDC crate under thermal cycling tests, with the test profile (10 cycles are performed before vibration and 5 afterwards).

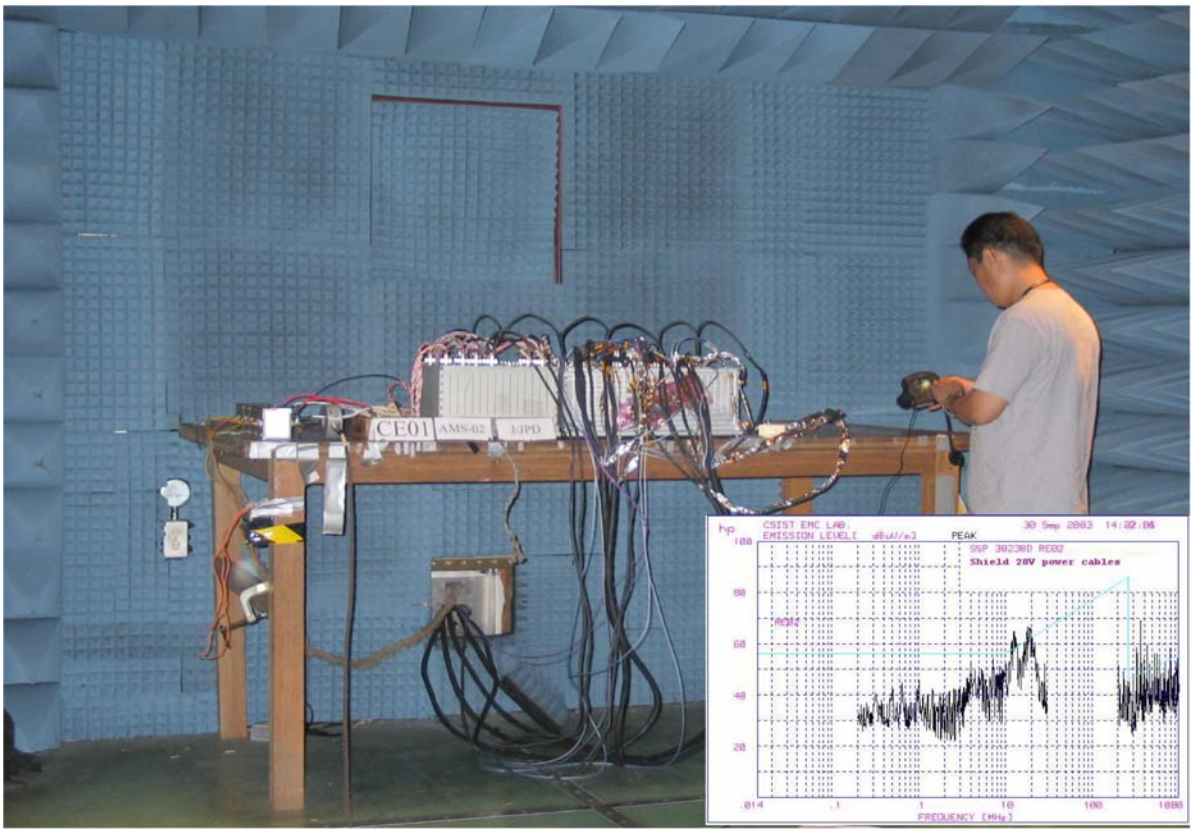

Figure 2.170: The JMDC crate during EMC testing and a typical result.

A key aspect in this process is the selection of components; particularly the measurement of cosmic ray heavy ion induced single event upsets and latch ups. Table 2.12 summarizes the results of the five heavy ion test beam campaigns led by the MIT team needed for the AMS electronics. Figure 2.172 shows the set up of one of the test campaigns and Figure 2.173 shows the test setup for the JMDC processor.

Date	**Location**	**Ions**	**LET** [MeV/mg/cm^2]	**Components Tested / Pass**
Nov'00	GSI, Darmstadt	Xe, Au, U	6 - 59	21 / 11
Nov'01	GSI, Darmstadt	Kr, Au	3 - 40	19 / 18
Dec'01	GSI, Darmstadt	U	19 - 30	7 / 4
May'02	GSI, Darmstadt	U	16 - 59	33 / 29
Feb'03	LNS, Catania	Kr	27 - 39	6 / 5

Table 2.12: Heavy ion test beam campaigns for AMS electronics component selection.

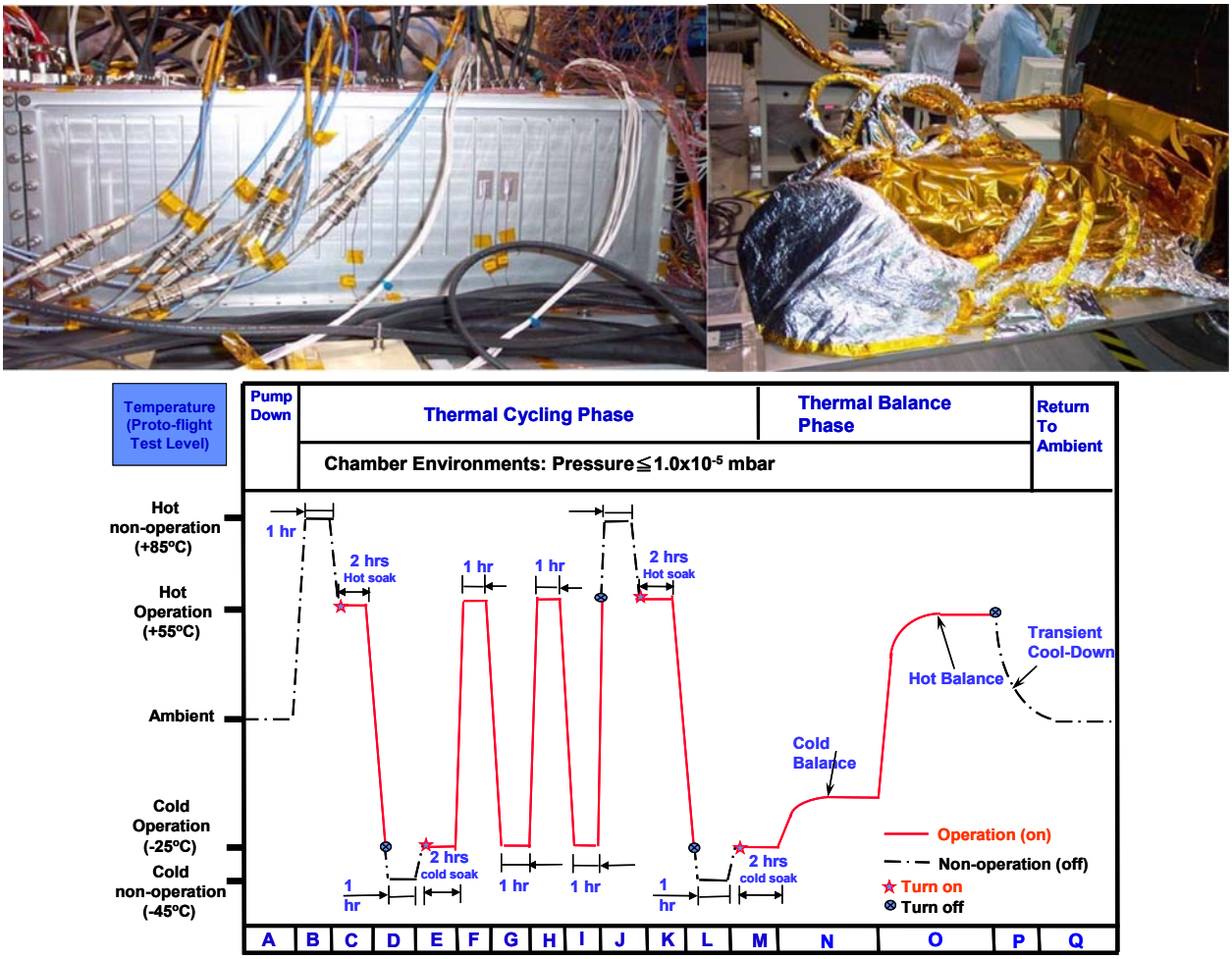

Figure 2.171: The JMDC crate before installation in the thermal vacuum chamber and the thermal vacuum test profile.

Figure 2.172: Radiation tests in heavy-ion beam for electronic component selection at the INFN Catania accelerator.

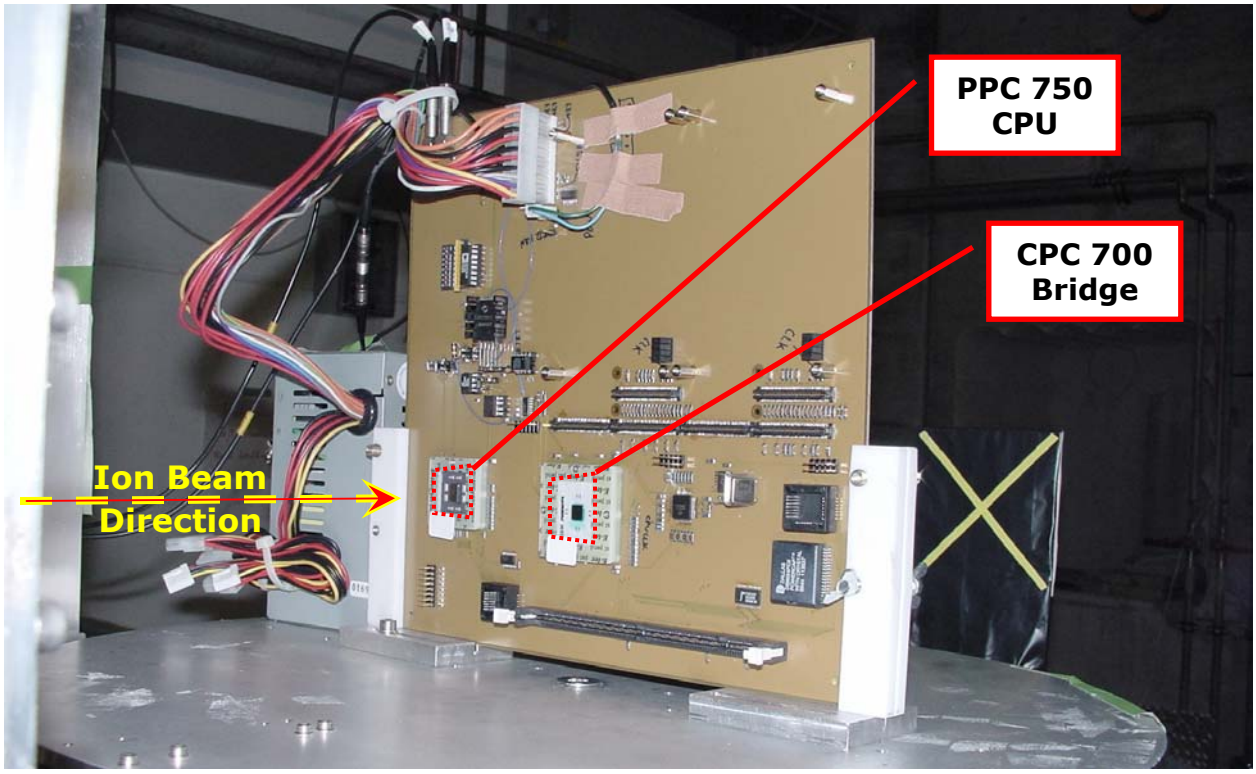

Figure 2.173: JMDC under beam test at GSI.

Many of the other challenges of operating particle physics electronics in space are met by the thermal and mechanical design of the electronics enclosures and thermal control system. As shown in Figure 2.174, the circuit boards are interconnected with backplanes and enclosed in crates and the DC to DC converters are enclosed in boxes. To cool the electronics and to minimize the heat flow into the cryogenics system, most of the electronics are mounted on the two large radiators shown in Figure 2.175. As summarized in Table 2.13, AMS has designed and built for flight over 600 such circuit boards of 70 different types which will be installed in 60 crates and boxes of a dozen types.

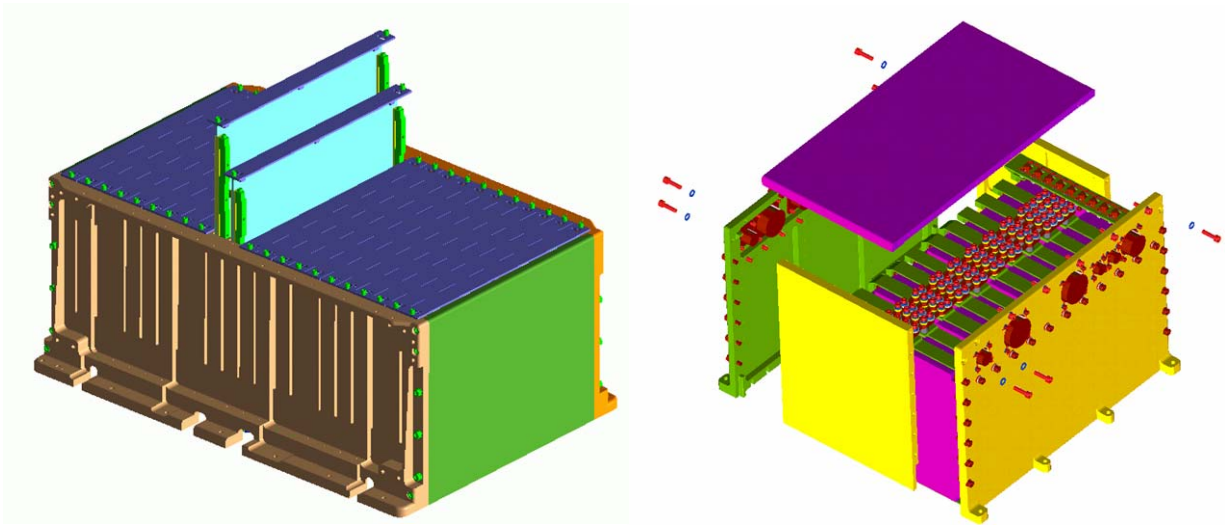

Figure 2.174: Electronics crates (left) and power distribution boxes (right).

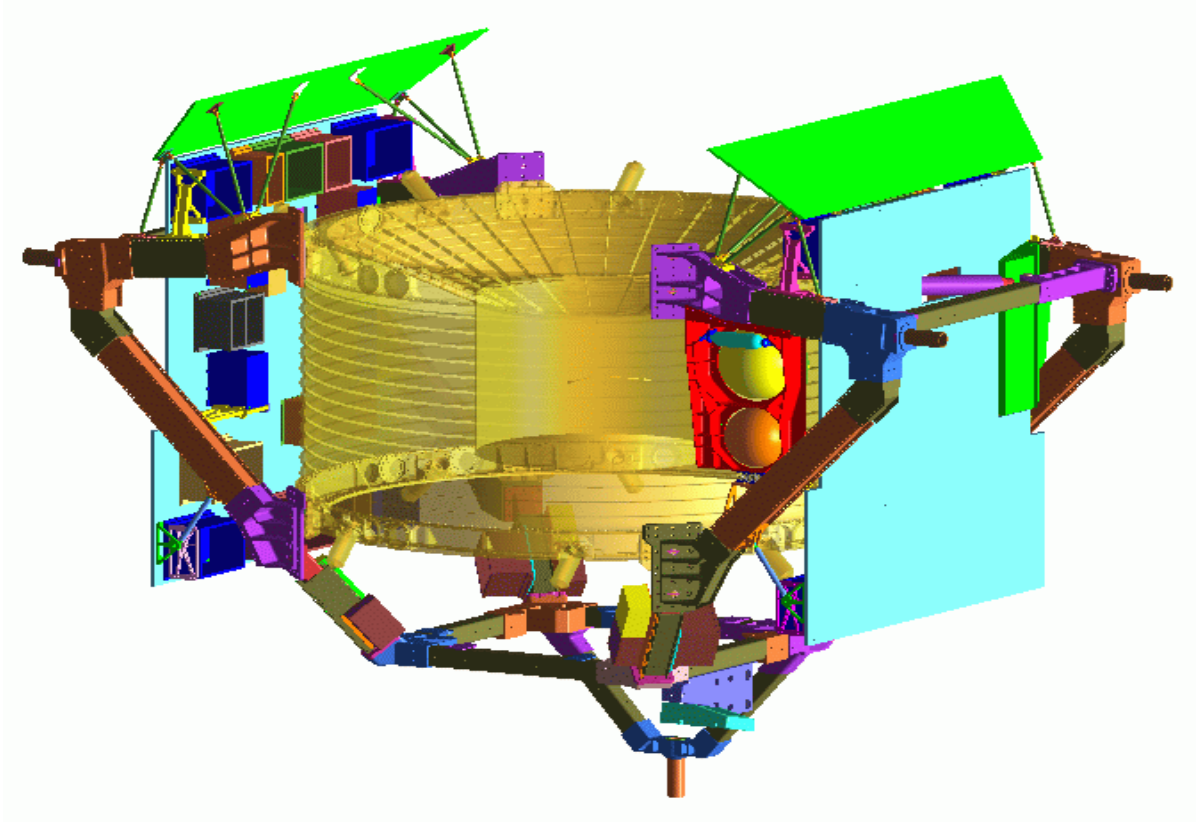

Figure 2.175: AMS-02 with electronics mounted on the main wake and ram radiators.

				Nominal Heat (W)				Weight (kg)	
Crate xPD	**Qty**	**Function (tot det)**	**Boards**	**Unit**	**Sum**	**extern.**	**Subsys**	**Unit**	**Subsys**
E-Crate	2	ECAL (324 PMT)	12	10.2	43.1	44.7	88	6.5	41.7
EHV			3*8	6.3				11.1	
EPD			5	5.0				3.3	
J-Crate	1	DAQ(MDC+JxIF)	23	28.0	50.5		50	14.2	29.1
JT-Crate		DAQ(Trig+JINJ)	8	3.8				5.6	
JPD		J+JT power	8	18.8				9.2	
M-Crate	1	Monitor, AST, GPS & Laser Align.	12	16.5	31.8	(ASTC +GPS)	46	6.8	8.7
MPD			3	15.4				1.9	
R elec	2	RICH (680 PMT)	12		31.9	30.0	62		19.4
RHV			2*8	7.2				6.6	
RPD			5	8.7				3.1	
S-Crate	4	Scint(34ToF+8ACC)	8	25.8	150.8	16.8	168	5.0	41.0
SHV			6	2.6				3.4	
SPD			3	9.4				1.9	
T-Crate	8	Tracker (192 Ladder)	20	37.7	502.1	138.3	640	11.1	140.9
TPD			10	25.1				6.5	
TT-Crate	1	Tracker Thermal Elec. (1H1C)	8	17.3	32.3	(TTCB)	136	4.5	7.6
TTPD			4	15.0				3.2	
U-Crate	2	TRD (82 Module)	17	19.1	71.4	19.4	91	9.0	29.6
UPD			9	16.6				5.8	
UG-Crate	1	TRD Gas Elec	12	13.2	18.7	(UGB)	83	6.5	11.3
UGPD			7	5.5				4.8	

Table 2.13: Electronics weight and power.

2.8.6 Software

Figure 2.176 shows the connections of the three types of processors used in AMS-02: the four fold redundant Main DAQ Computers (JMDC) based around a powerful PowerPC 750 processor, the hundreds of Digital Signal Processors (DSP) for science data handling and the microcontrollers for slow control (USCM). All of these processors require reliable programming. In addition, to test and develop this software and the hardware on which it runs, a large suite of additional software is required.

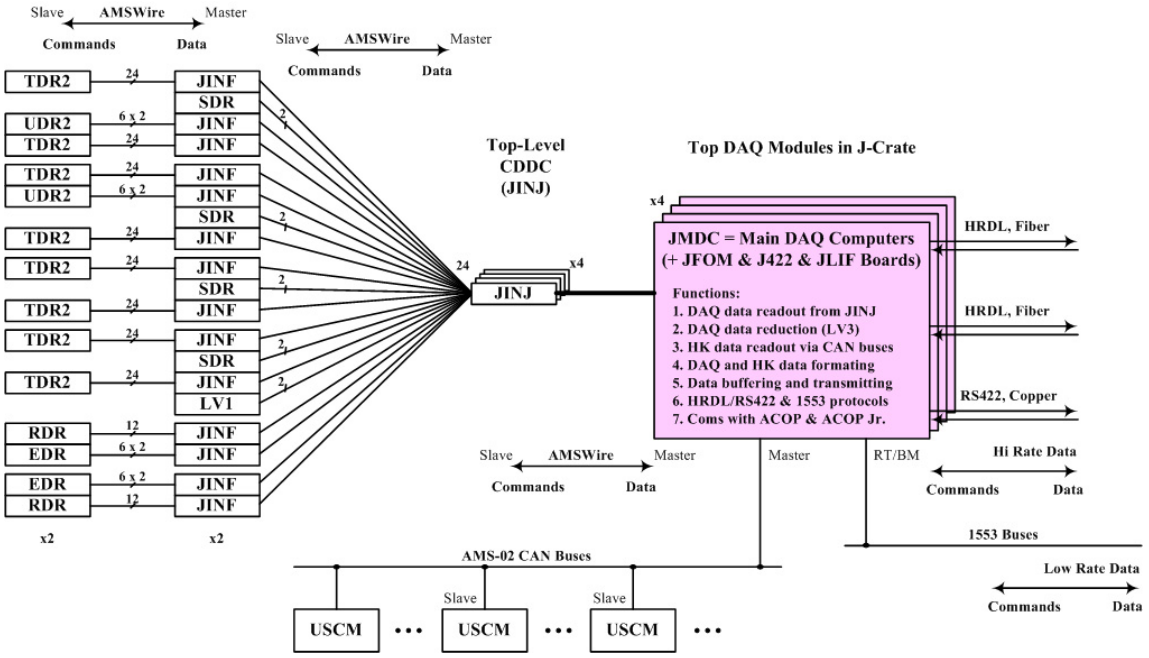

Figure 2.176: AMS-02 processors

In each of the processors the software is divided in two parts. A simple baseline program is loaded when the processor is booted. This fixed part provides minimal functionality and stored in a one time programmable memory. The other part is the main software with full functionality. It is upgradeable and stored in erasable flash memory or EEPROM.

The driving requirements for the software design come from main science data acquisition chain. The software has to be fast enough to receive the digitize data from the detector front-end electronics, reduce and collate the data and send it out to the ground at given rate. Figure 2.177 illustrates the rate requirements for the whole system. The input rate is about 7 Gbit/sec and the output rate limited by NASA to an average of 2 Mbit/sec. The primary function of the software in the different levels is to meet these requirements.

The system was modeled in detail to obtain the processing and transfer speeds, as well as the buffer depths, required. Figures 2.178 and 2.179 show some of the results which were used to define the major system software parameters.

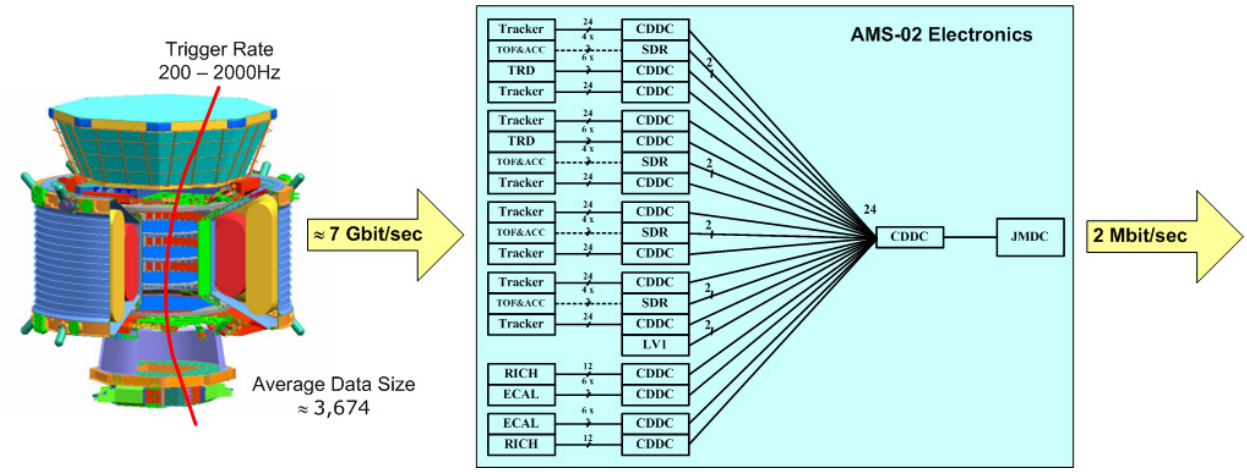

Figure 2.177: Input and Output Rates

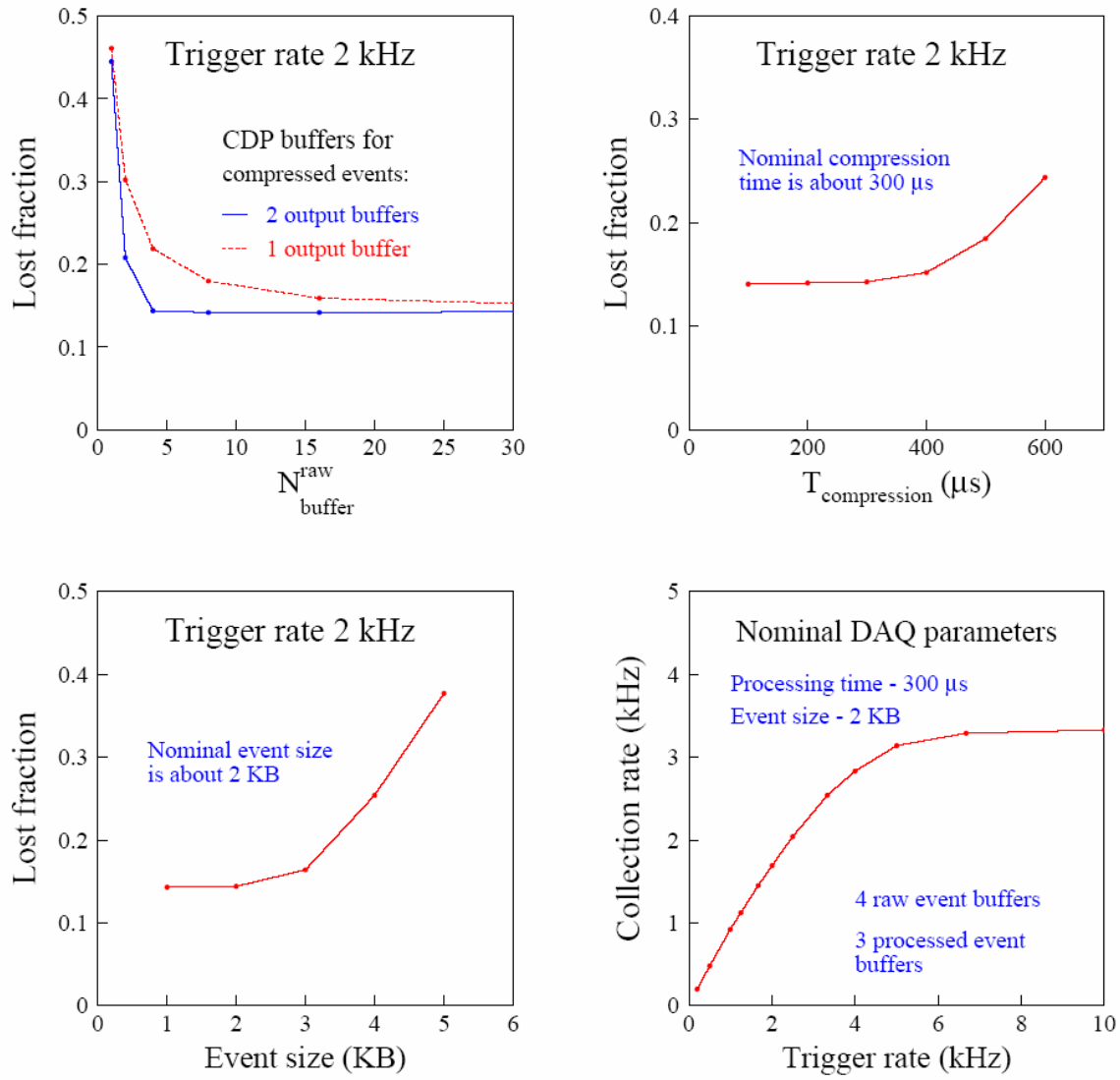

Figure 2.178: Study of Trigger Rate and Software Parameters.

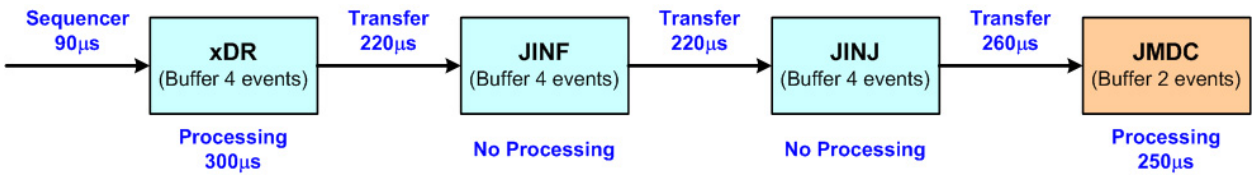

Figure 2.179: Time allotted at each step in the DAQ chain.

The DSPs are located on "xDR" boards (x = E, R, S, T & U for the different subdetectors). The software running in the DSPs must read in the data which the sequencer has written into the memory buffer, perform the data reduction and send the results to the next upper level upon request. Likewise, the JINF and JINJ software requests data from the xDRs, assembles the data together from an event and then sends that to the next upper level upon request. The software on the xDRs, JINF and JINJ has a similar structure; the only difference is the input source. The flow chart of this software is shown in Figure 2.180. After initialization, the software enters a loop on waiting for the input data. JINF and JINJ send out requests and wait for replies with the input data from each xDR, the xDRs wait for data from the sequencer. The input (RAW) FIFO and output (CMPR) FIFO status determines the xDR busy/ready status – if these buffers are allowed to fill then the data flow stops. When event data is available it is passed to the subdetector dependent routines which perform the data reduction. These routines are produced by the subdetector groups and fit into the overall structure shown.

The output data are placed in output FIFO and waiting for upper level requests to be transferred over AMSWire links. The software services and replies to all requests from upper level system.

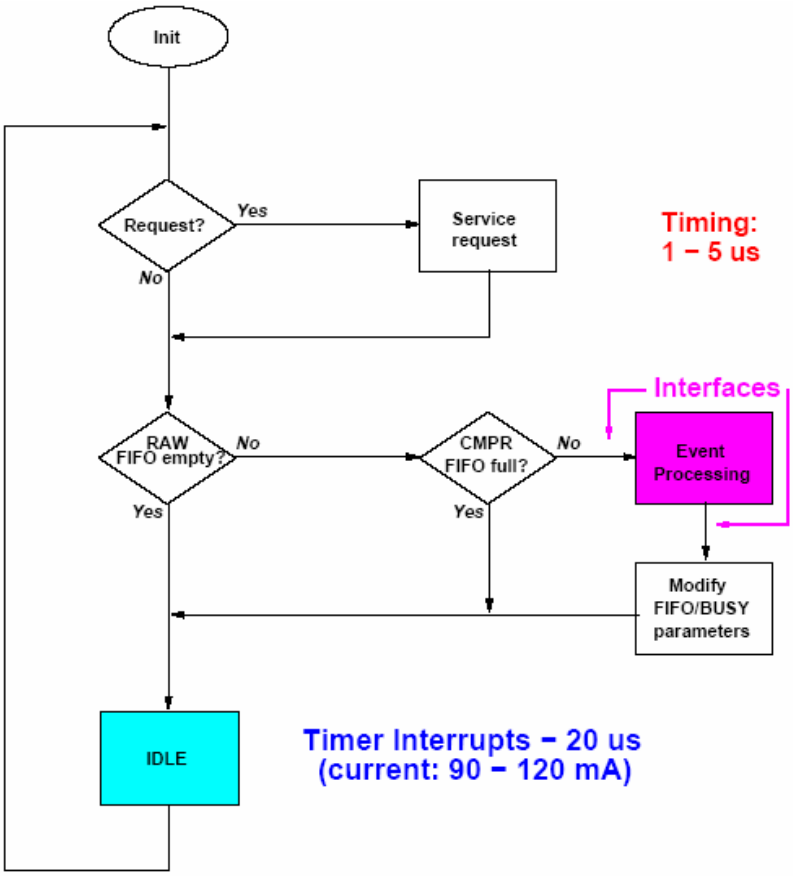

Figure 2.180. Flow Chart of DSP Software.

Currently, a working version of the DSP software for the common part has been used to implement the readout of the tracker, TRD and trigger system in qualification and beam tests. Both the common part and the subdetector parts are being continually improved in speed and reliability.

A different set of software runs in the JMDCs. Studies indicated that the processing power of one JMDC should be sufficient to handle the tasks assigned to this level, the other three are held in hot or cold redundancy. This level has three major functions: processing the science data, performing the housekeeping of the entire AMS detector and managing the external communications.

As indicated above, the data from an entire event is assembled in one of the four JINJ units. Upon request, this data is transferred, event by event, into the JMDC. A filter algorithm, Level-3, running on the JMDC runs a preliminary reconstruction of the event and selects those events that are physics interest based on the results for down linking.

Meanwhile, the software in the JMDC must perform the housekeeping of all the AMS systems. All mission critical systems are managed at the lowest level by hardware. However the performance is improved, the status reported and commands executed by the JMDC housekeeping software. Many parts of the detector are involved, including the monitor and control of the power systems, the HV and thresholds of the various subdetectors, oversight of the cryomagnet avionics, mixing and composition of the gas in the TRD, tracker and global thermal control, status of all the DAQ electronics and a summary status of all the information known as critical health data.

The third key function is managing the external communication. Data must be selected to be transmitted over the available links (HRDL and LRDL on the ISS and RS422 and 1553B busses on the shuttle) and formatted according to the requirements of that link. This data includes science data, the housekeeping data and the critical health data. Depending on the data generation rate and link availability the data must be buffered in the peripheral 2 GByte memory (JBU).

Final selection of the operating environment to fulfill these tasks is in progress. Either multiple processes or multiple threads within a monolithic process will be selected. For all cases, the software architecture is illustrated in Figure 2.181. The software has several layers. The base, or kernel, contains the device drivers which handle device I/O and interrupts. The next layer has link specific software agents to adapt the device driver handling to a common interface and convert the data to a common format. The upper layer contains the application tasks which actually process the data and pass on the results. A special task, the “dispatcher”, manages all commands and replies between agents and application tasks.

There are three distinct data flows within the JMDC – the science data (events), housekeeping data and command and reply pairs. The science and housekeeping data flows in one direction only, from the experiment through JMDC to the external communication interfaces. Events are requested from JINJ via the AMSWire agent, processed by the Level-3 task and sent to the telemetry manager. The telemetry data includes both the science and the house keeping data. Together they are sent to either the HRDL agent or 1553 agent and then transmitted on the HRDL or LRDL if AMS is on the station or the RS422 link or 1553 bus if AMS is in the shuttle. The third data flow for commands and replies. This flow always passes through the dispatcher. The data normally appears in request and reply pairs. If a request comes from an agent, it indicates a command has been received. The dispatcher parses the command and passes it to the corresponding task and then task passes a reply back to that agent via the dispatcher. If the request comes from a task, it indicates a command is being issued by the task. The dispatcher sends the request to the corresponding agent and passes back the reply to the task when it received from the agent.

The simplified, fixed version of the JMDC software, the ROM Monitor, includes the boot loader for the main software described above. It also supports file down loading and the most of the communication protocols. It can also process boot commands from most of the interfaces. It is a single process and single thread running without an operating system.

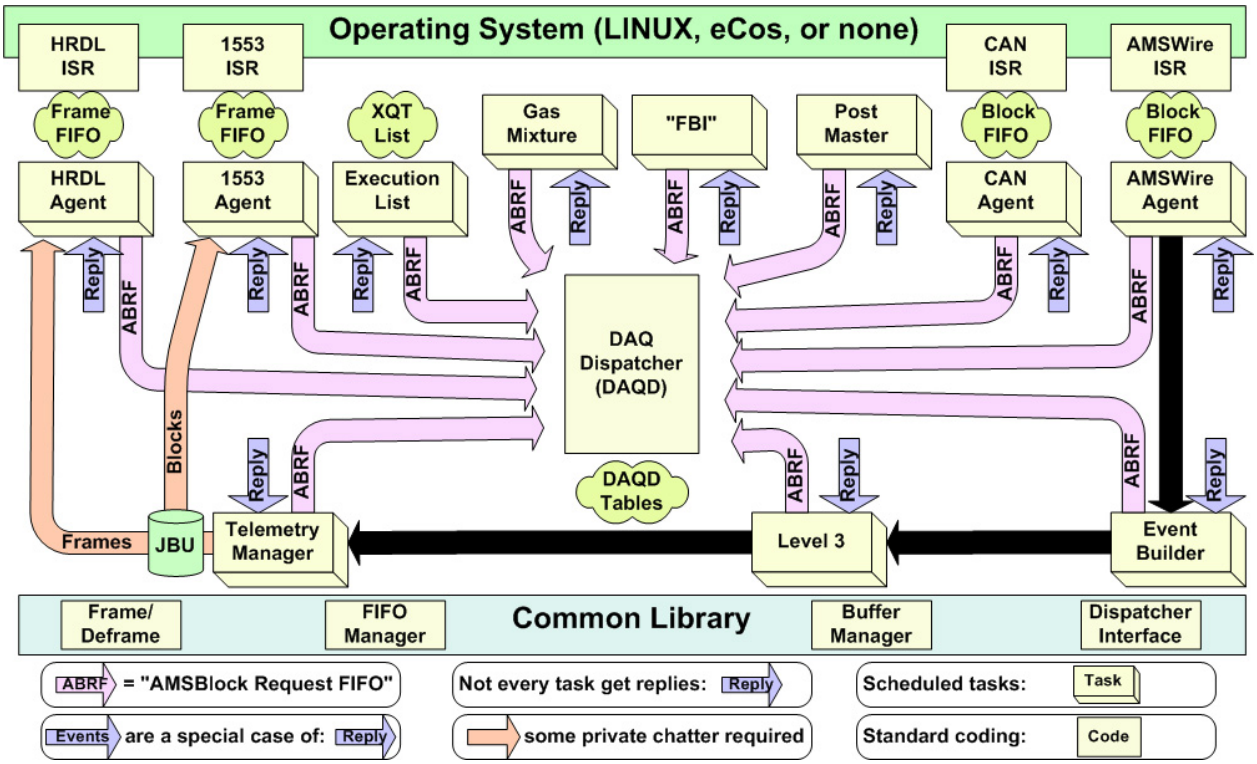

Figure 2.181: JMDC software architecture.

Currently, working versions of the ROM Monitor and three parallel developments of the main software are under development. The three parallel developments are a single process with multiple threads running under Linux or eCos operating systems and a multiple processes version running under Linux. The performance of the three developments will be evaluated and one version selected for further development, incorporating the lessons learned in the other two efforts.

Besides the software running inside AMS, the software to test the system components, the integrated system and to monitor and command the experiment is indicated in Figure 2.182. Figure 2.183 shows an example of the test environment for Main DAQ computers. The JMDCs receive power from the JPD which gets 28 V power either directly from a power supply or, as in flight, via the AMS-02 power distribution system (PDS). A data simulator, either a PC with a specially developed interface or the top level CDDC module, provides simulated event data as input to the JMDC. The high rate data is received either by ACOP via the HRDL link or by DDRS-2 via RS422 links. The 1553 bus, in either station or shuttle mode, is monitored and controlled by bus monitor and bus controller programs AMS has had to develop. In addition, an external CAN connection allows the direct (as opposed to via the JMDC) monitoring and controlling of the slow control modules directly as needed. The successful implementation of such a test environment requires the development of numerous different pieces of software.

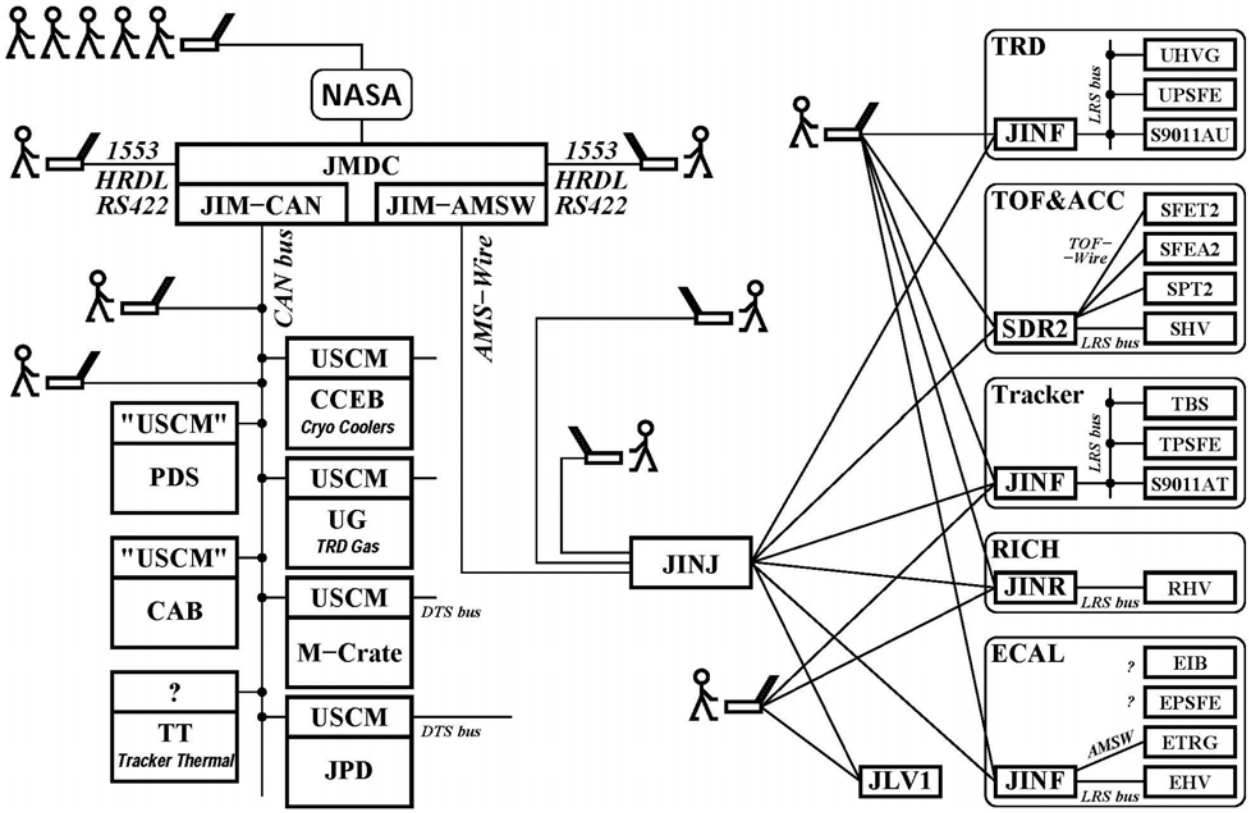

Figure 2.182: Software for test and flight use.

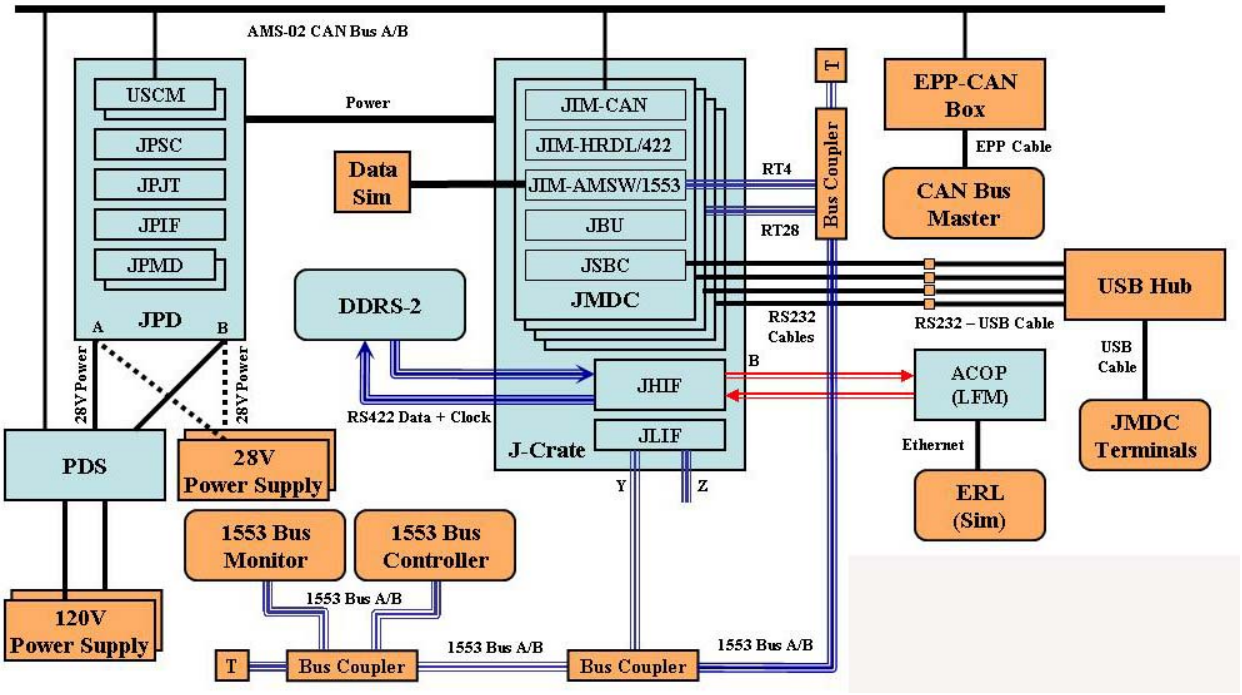

Figure 2.183: JMDC software test setup.

This test software will form the basis of the software used on the ground as the only way to monitor and control the experiment when it is in flight. In the development phase, we can control the JMDC software, and the experiment, via all the direct links which include the RS232 serial ports of the JMDC. In space, we have only high rate and low rate interfaces.

Each part of the JMDC housekeeping task requires a corresponding commanding and monitoring software on the ground. A simple example is the power supply for the J- and JT-Crates, which includes the four JMDC, one JHIF (high rate data interface), one JLIF (low rate data interface), the trigger system JL1 and four JINJ boards. The redundant parts of system may be switched off by software. The voltages and currents must be monitored. Tasks running in the JMDC to monitor and control these quantities require the corresponding commanding software running on ground. Figure 2.184 shows a screenshot of the JPD commanding software. It allows the any redundant part to be switched on or off, displays the voltages and currents of the supplies and the temperatures measured inside the JPD, J- and JT-Crates.

Many such dedicated programs will be required for the entire AMS-02 system, and some key systems are in development (TRD gas control, etc). A general scheme has been implemented and is ready for the delivery of the hardware for detailed implementation.

Besides commanding and monitoring, software is required for the functional testing and space qualification of the hardware as it is produced. This includes board and box level testing, thermal vacuum testing, a preliminary interface test (PIT) and a functional integration test (FIT). Each test requires special software to push the system outside of its normal operating conditions. Most of this software has been deployed, and is being continually updated and improved by the MIT group.

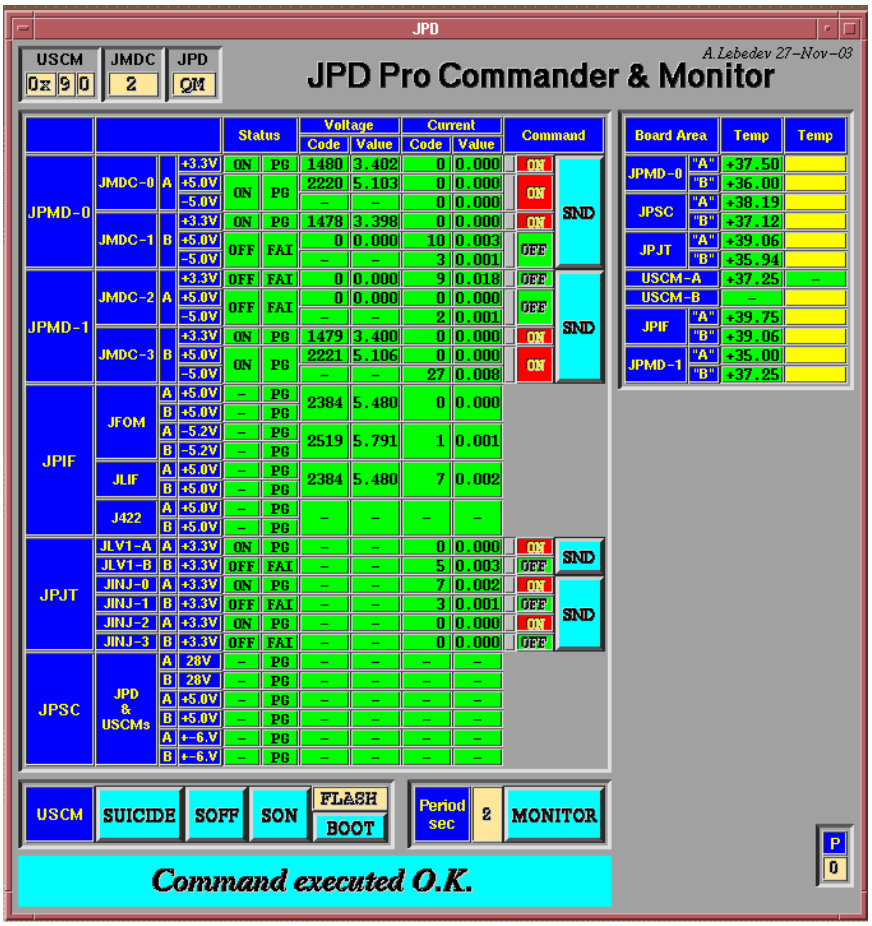

Figure 2.184: Screenshot of JPD Command & Monitor Software.

2.8.7 Electronics Process and Production

The total amount of electronics in AMS-02, ~300,000 channels, is equivalent to all of the ISS electronics combined. To ensure that this electronics, which is based on particle physics technology, can be reliably used in space, the design, manufacturing and space qualification follows a well established procedure developed for AMS-01. The production of the electronics is centered at the Chung-Shan Institute of Science & Technology (CSIST), which, as for AMS-01, is making available its extensive military grade design and production facilities, two examples of which are shown in Figure 2.185. The bulk of the electronics for AMS-02 is produced and tested at CSIST. Board level thermal studies and thermal vacuum testing is done at the Taiwanese National Space Program Office (NSPO).

Responsibilities for the subdetector electronics have been included in each chapter. In addition to the overall coordinating role played by the MIT team, IROE, Florence, is overseeing the development of the electronics for all the PMTs based detectors (TOF, ACC, RICH and ECAL).

The global data acquisition and trigger system has been developed by MIT and Taiwan and is under test at CSIST using parts procured by Academia Sinica, Taiwan and MIT. The JMDC computers are being designed directly by CSIST in close collaboration with MIT, especially as regards software.

The Italian aerospace company, Carlo Gavazzi Space (CGS), has made the thermal, mechanical and structural design of the crates and boxes under the supervision of MIT, and these designs are under fabrication at CSIST and AMS other institutes.

The Power Distribution System (PDS), is being developed under the leadership of the National Cheng Kung University, Taiwan.

The ACOP program is a joint collaboration between the Italian Space Agency and the National Chiao Tung University, Taiwan.

To be able to control and improve the proper functioning of the experiment, particularly the software, while it is in flight, Southeast University together with MIT, INFN-Perugia and the University of Geneva is developing the AMS Antimatter System (AIS) shown in Figure 2.186. This includes an exact replication of the key detector elements in the search for antimatter. The AMS Antimatter Simulator (AAS, indicated on the left) is based around refurbished elements from AMS-01, including the flight magnet, tracker ladders and TOF counters. The electronics is identical to the AMS-02 flight electronics. This will allow a precise simulation of the effects of any proposed changes to be investigated thoroughly on a high fidelity test bed before committing them to the hardware in flight.

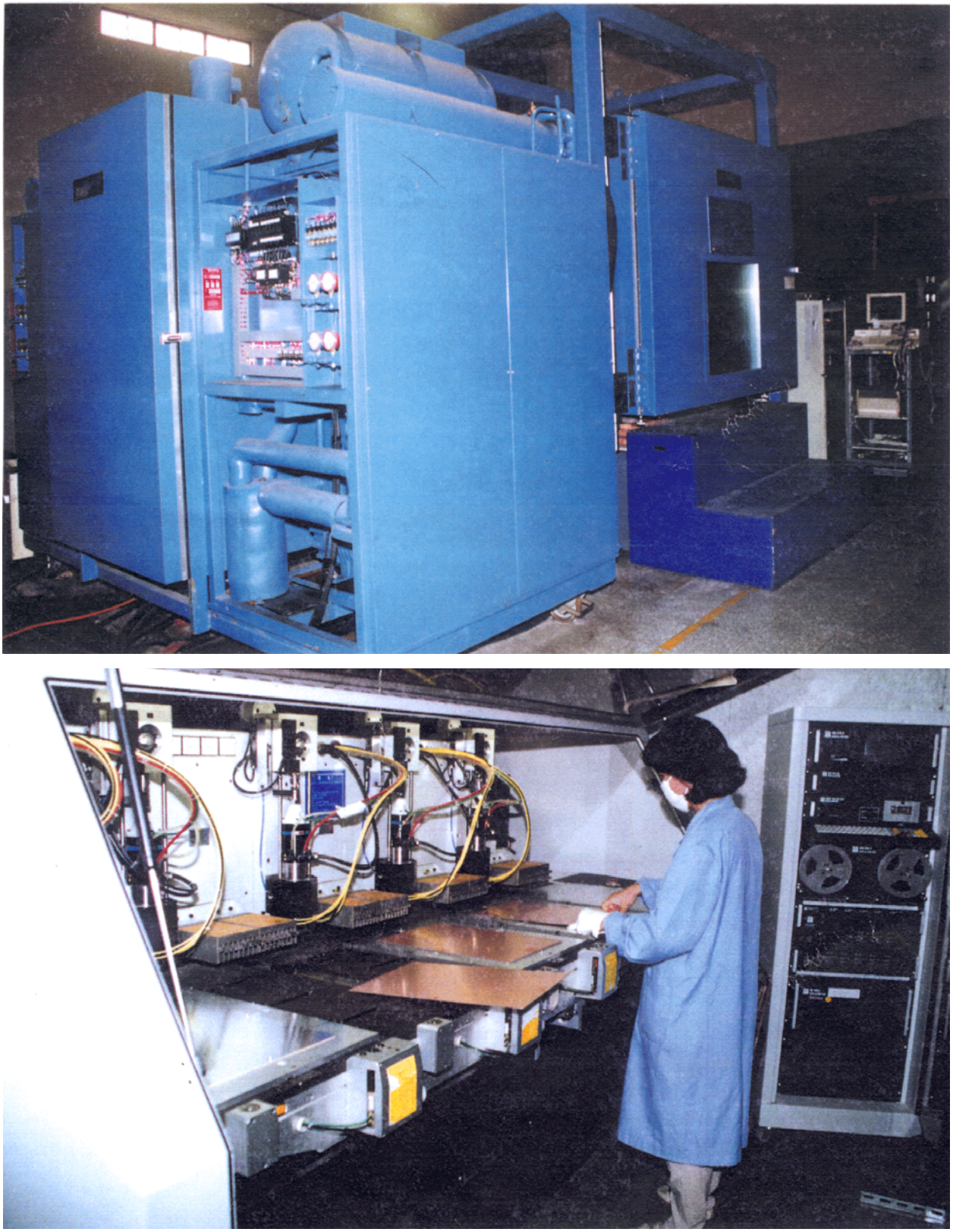

Figure 2.185: Thermal test chamber (upper) and PCB production facilities (lower) made available to AMS at CSIST.

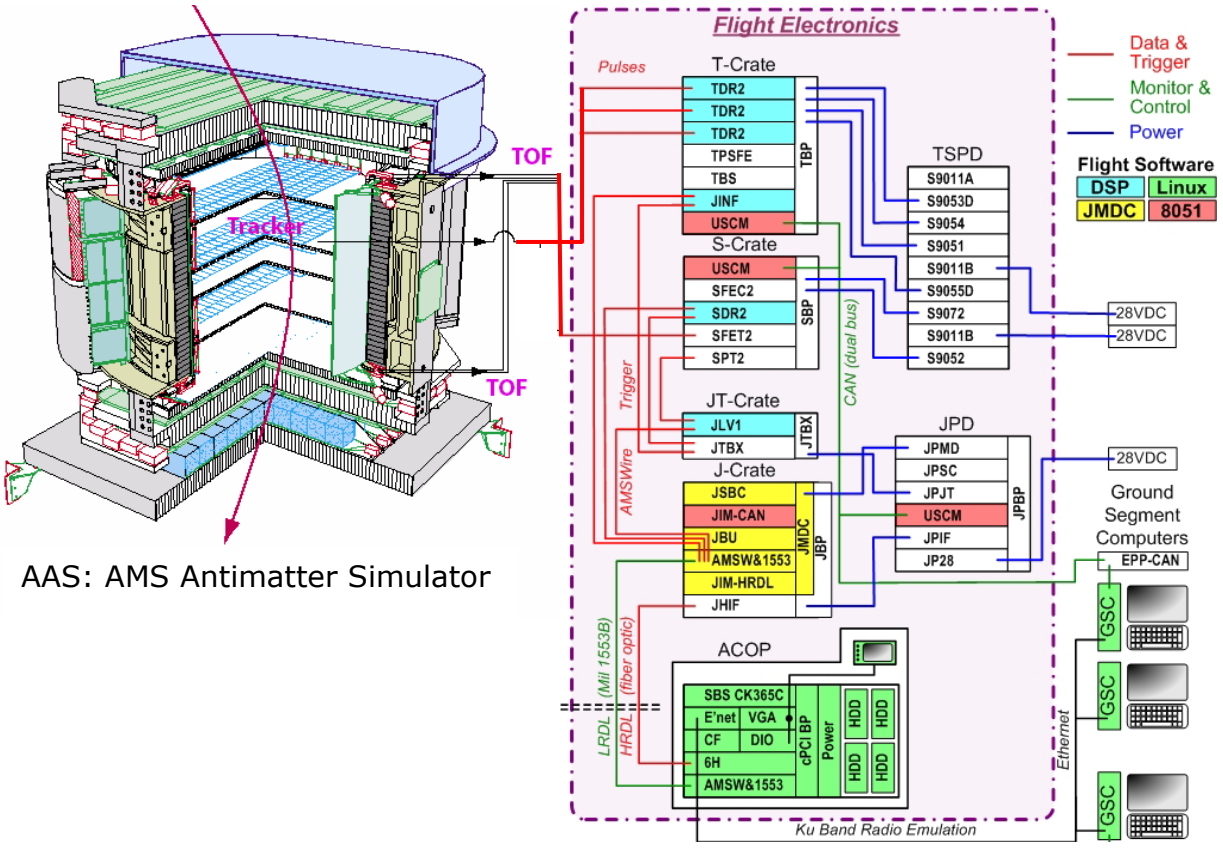

Figure 2.186: AMS Antimatter Investigation System (AIS).

2.8.8 Star Tracker

In addition to charged particles, the physics scope of AMS-02 is greatly broadened by the measurement of gamma rays. Unlike charged particles, which deflect in the solar, galactic and intergalactic magnetic fields, the direction from which neutral particles arrive indicates their point of origin. To correlate these sources with phenomena observed in other bands of the electromagnetic spectrum (radio, infrared, visible, UV and X-ray), it is necessary to have the precise direction in which the detector is pointing when the gamma ray arrived. Because the space station is a large and flexible structure it is necessary to make this measurement with a device attached directly to AMS-02. Within AMS, the highest angular precision is provided in the measurement of gamma rays which convert in the upper layers of the detector and the resulting e^+e^- pair is then measured in the silicon tracker. So, to avoid any systematic shifts, the measurement must be made directly attached to the silicon tracker structure. The AMICA (Astro Mapper for Instrument Check of Attitude) Star Tracker (AST), built by CARSO under contract to INFN-Perugia and ASI, provides this functionality. As shown in Figure 2.187, it consists of a pair of small optical telescopes mounted on either side of the upper silicon tracker which acquire the images of the stars and compare these with an on-board astrometric star catalogue. With this information, the attitude of AMS can be determined within an accuracy of a few arc seconds at rates up to 20 Hz.

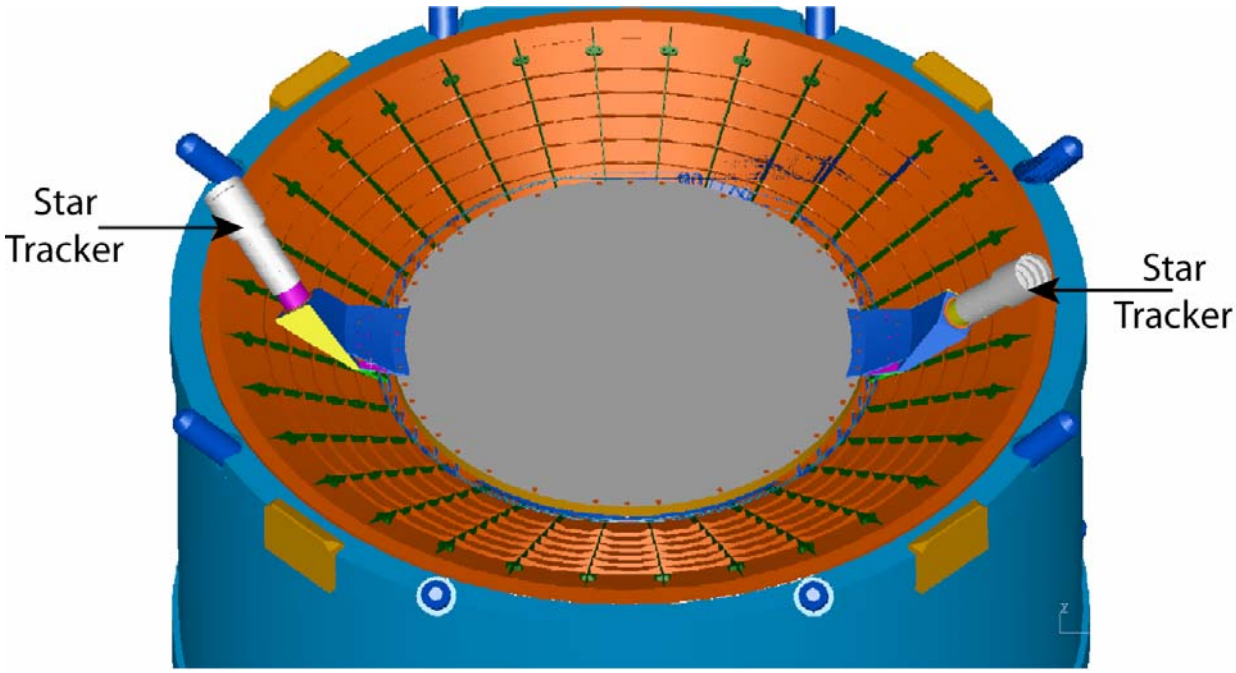

Figure 2.187: Star tracker telescopes mounted to the silicon tracker structure.

As shown in Figure 2.188, each telescope consists of an optics system, a low noise frame-transfer charge coupled device (CCD), a support and a baffle to limit reflected daylight. The optics contains an f/1.25 lens with 60 mm aperture and 75 mm focal length, filtered to pass 475 to 850 nm (transmission >70% 480 to 680 nm) for noise reduction and to prevent saturation, as well as protect from IR and UV. At the CCD, the field of view is 6.3° x 6.3° with an image scale of 0.36 μm/arcsec. The recently released CCD (type E2V CCD87-00) matches the traditional MPP technology aimed at reducing the thermal noise with the introduction of an innovative type of amplifier that allows to nearly cancel the read-out noise. It has 512 x 512 pixels, each 16 x 16 μm^2. To maintain the relative angular stability of the camera and the silicon tracker, a light weight support structure has been made of zero coefficient of thermal expansion reinforced carbon fiber composite, which, in addition to the usual finite element modeling of the response to launch and landing loads, has been through detailed thermo-elastic modeling. The support structure also houses the front end CCD electronics. To stabilize the temperature and further reduce any thermally induced deflections, both telescopes are thermally connected to the isothermal tracker thermal control system (§ 2.3.5). The baffle has a length of 369 mm, which determines the first avoidance angle of 14 degrees. It is tapered with an outer diameter of 104 mm at the camera end and 130 mm at the outer end. The baffles are thermally and structurally decoupled from the optics, CCD and their support and mount on the M-structure of the TRD.

The cameras have been oriented so as to maximize their view towards space, avoiding both the rotating solar panels as much as possible and attached radiators and the central parts of the space station. In addition, having two cameras pointing in opposite directions ensures that at least one will always have a clear view of space without solar interference.

The front end electronics uses a correlated double sampling technique. A gate array clocks the analog readout of the CCD, applies baseline suppression, and then uses a 12-bit ADC to digitize the results, which are transferred to the processor located in the M-Crate. At 10 °C, the readout noise is 22 μV/pixel (3.2 e^-/pixel). The processor electronics is centered around a floating point digital signal processor, AD-21020, specifically adapted to work in space. Programs and the star catalog are stored in a 2 MByte flash memory. Communication with the other AMS subsystems is implemented using the on chip RS-232 serial link and M-Crate USCMs.

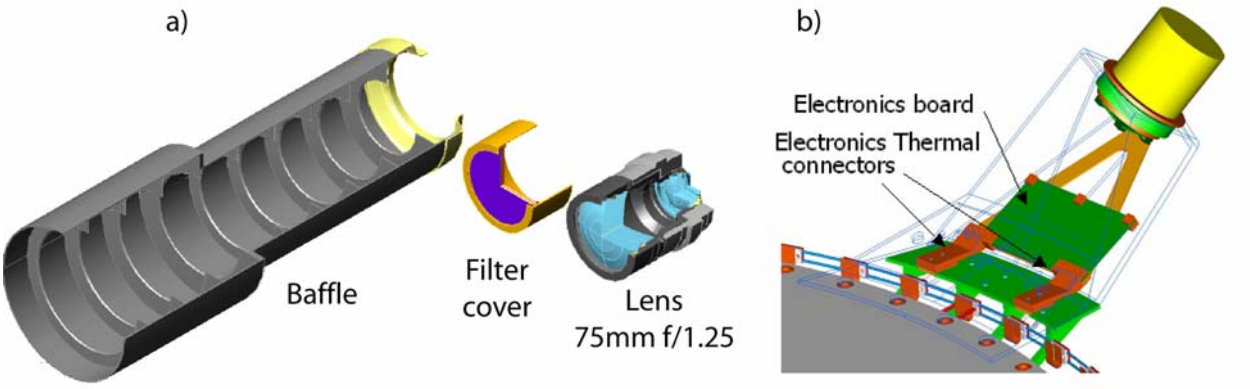

Figure 2.188: Star tracker optics (a) and support (b).

The AMICA on-board software selects the camera from which to perform the acquisition, and determines the threshold on the acquired image. Based on previous determinations, a seed direction provided from the space station or by scanning, it then determines the direction by loading a target star field from the catalog, projecting this on to the image plane and comparing this with the image obtained by the CCD. The program seeks a one-to-one correspondence between the measured angles between the imaged stars and the angles between stars in the catalog. The algorithm minimizes the distance between acquired stars and the corresponding ones determined from the catalog. The on-board star catalog is derived from the Smithsonian Astrophysical Observatory (SAO) catalog and contains 15945 stars brighter than magnitude 7. After recognition, the software transforms the camera reference system into the AMS system and interpolates the pointing trajectory to give the best attitude estimation among two acquisitions. Other software functions manage the serial communication with the USCM interface to exchange the attitude and housekeeping data and commands. It is also possible to upload a revised version of the software or star catalog.

2.8.9 GPS

In addition to the directional correlation provided by the star tracker, the physics accessible by measuring gamma rays also requires the precise, to a few microseconds, temporal correlation of measurements by AMS-02 and other instruments through out the electromagnetic spectrum. Timing information is provided by the space station, but owing to the limitations of the LRDL and the processing required within AMS, the reference time accuracy would be a few tenths of seconds, which is insufficient. Within AMS, short time intervals (up to a few seconds) can be measured accurately (with sub-microsecond precision) by the trigger system however they are subject to long term drift and lack an absolute reference, To redress these issues, a global positioning system (GPS) will be deployed on AMS-02.

The selected unit is an ALCATEL TOPSTAR 3000D, which has been successfully deployed on a variety of space based platforms, which will be integrated into AMS by IN2P3-Montpellier. Two patch type antennae (Sextant Avionique model 3407-79) will be mounted on an upper USS member pointing in different directions to ensure that the signals from a sufficient number of GPS satellites can always be acquired. Figure 2.189 shows the unit and an antenna. The unit contains a processor and a dedicated ASIC to convert the GPS signals and emit a timing pulse, which is used to reset a local timer within the trigger system. Interface electronics within the M-Crate then receive the precise time at which the pulse was emitted and this is included, along with the value of the local timer, in the event data. To reach the required accuracy, the software running in the unit has been specially developed to include all the corrections required when traveling in low earth orbit.

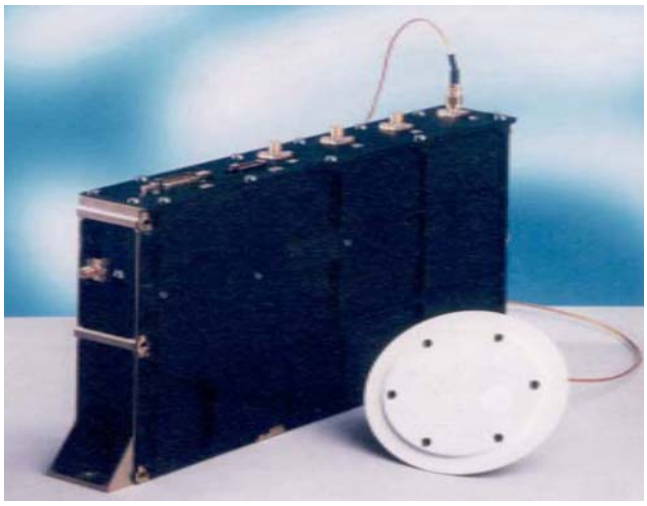

Figure 2.189: TOPSTAR 3000D unit and a GPS patch antenna.

2.8.10 AMS Ground Data Handling and Remote Commanding

The long duration of AMS-02 mission on the International Space Station (ISS) makes the operation of the ground data handling complex fundamentally different from that one of AMS-01. Data analysis will be performed during the flight on a continuous basis. Physicists will need access to scientific, calibration and monitoring data continuously.

Figure 2.190 shows the AMS-02 Ground Data Handling and Remote Commanding System. The ground based computing equipment can be conceptually divided into three functional units: the Ground Support Computers (GSC), the Payload Operations and Control Center (POCC) and the Science Operations Center (SOC).

The GSC receive control and science data from Huntsville Operations Science Center (HOSC) at MSFC; buffer science, housekeeping and NASA ancillary data for transmission to POCC and SOC. These computers will have to run unattended 24 hours per day, 7 days per week, thus system reliability is the vital issue. The system should be able to store about 2 weeks of data. Two identical systems will be installed and run simultaneously and independently. Thus, in case of a computer failure, the data transmission will be continued without interruption.

The POCC is where AMS operations will take place, including commanding, storage and analysis of housekeeping data and partial science data analysis for rapid quality control and feedback. The POCC computers will use the Telescience Resource Kit (TReK) software suite, developed by NASA, for commanding and slow control monitoring. After a check out period when AMS is first installed on the space station, the POCC will be located at CERN, with a backup location at MIT. Extensive data transmission tests with TReK between MSFC and MIT and between MSFC and CERN indicate that the Internet has ample bandwidth to accommodate AMS data. The commanding and detector control will be done from this one single place. However, detector monitoring programs can be run by experts from different geographical locations at their home institutes.

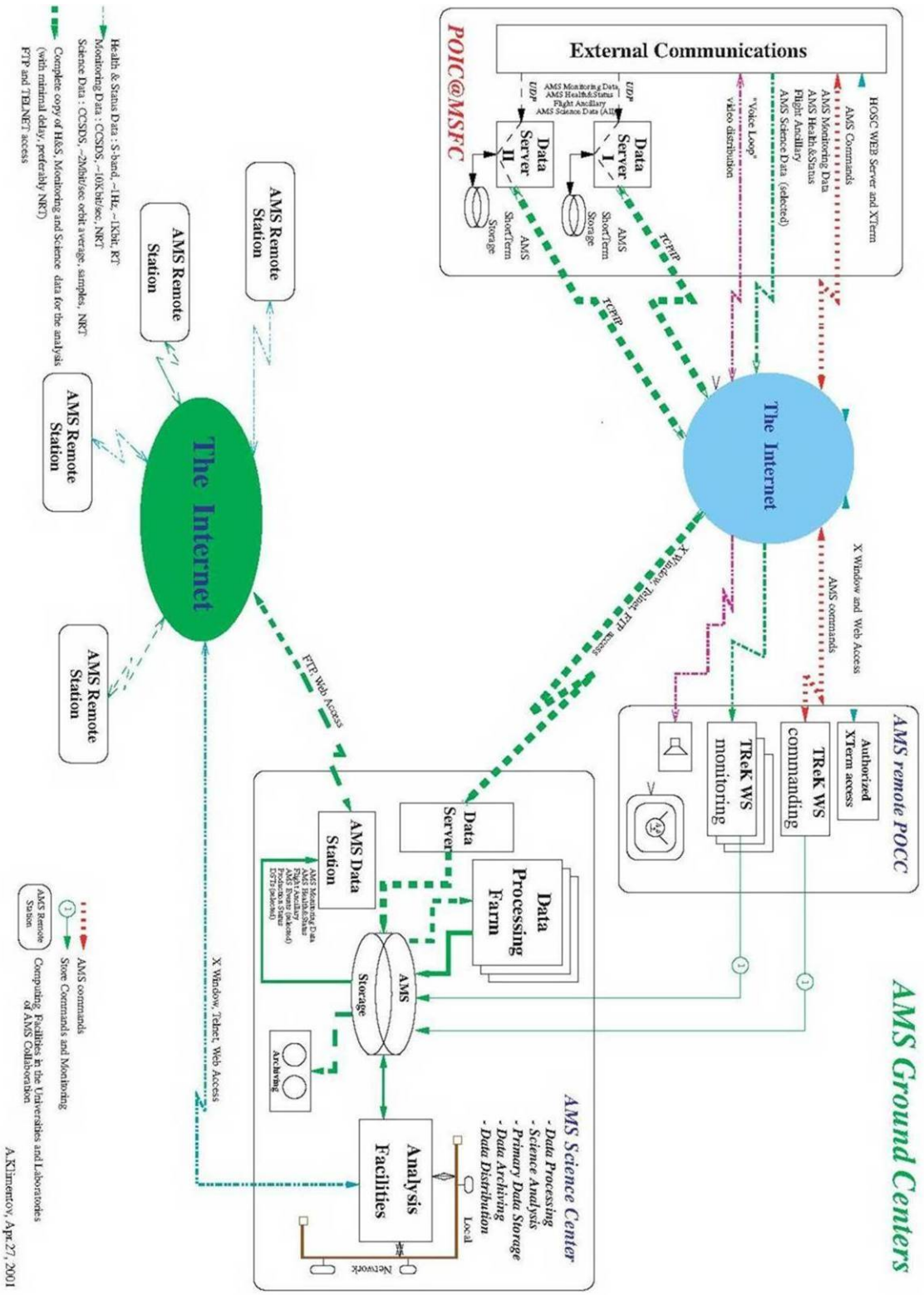

Figure 2.190: Data transmission from NASA-MSFC to AMS Ground Control Centers via the Internet.

The SOC, as shown in Figure 2.191, receives and stores all AMS science and housekeeping data, as well as ancillary data from NASA, ensures full science data reconstruction, calibration and alignment and keeps data available for physics analysis. All data is archived. The SOC will provide all facilities required to reconstruct AMS-02 science data, calibrate and align the detectors and store the results of reconstruction as well as Monte Carlo simulations. A SOC prototype has been setup at CERN and is in use for AMS-02 Monte Carlo simulation. The SOC event reconstruction facility will ensure the full reconstruction of about 10% of the input events with an average time delay of no more than half an hour and ensure the full reconstruction of 100% of the events with a typical delay time of less than one day.

The complete Ground Data Handling and Remote Commanding System is scheduled to be up and running six months before AMS launch to support AMS testing at KSC and the early installation of ACOP on the ISS.

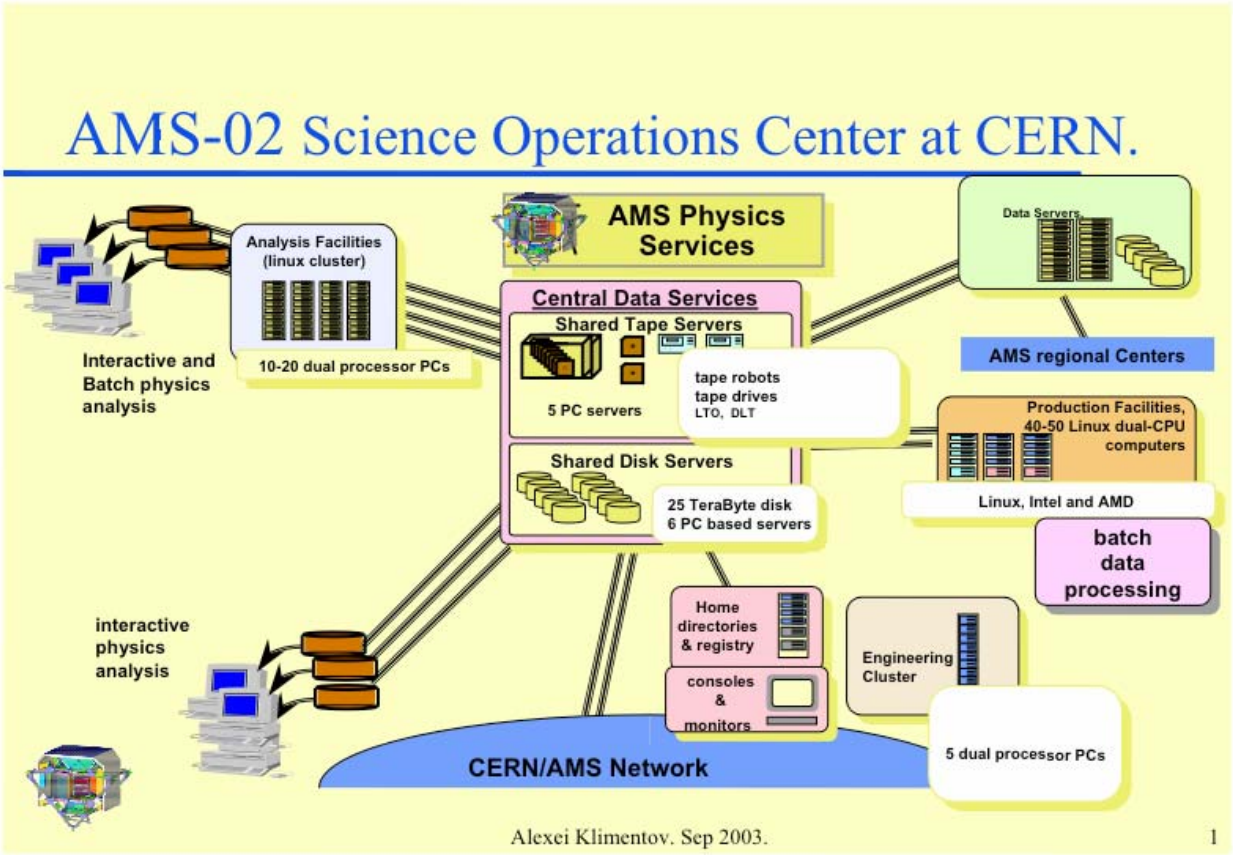

Figure 2.191: The AMS Science Operations Center (SOC) at CERN.

2.9 Thermal Control

The thermal environment in space is harsh. Different areas of the detector are subjected to rapidly varying direct solar illumination alternating with exposure to deep space, depending on the orbital parameters of the space station. Two kilowatts of power is dissipated within the experiment. Varying radiation from Earth must also be taken into account. The thermo-optical properties of the experiment change with time. In this environment, because the response of the different detectors is temperature dependent, their temperature must be kept not only within their different operational ranges but it must be kept stable over both time and volume. Most critically, the possibility of any heat leaking into the superfluid helium supply, which determines the duration of the experiment for many physics channels, must be minimized. For these reasons, the Thermal Control System (TCS) for AMS-02 has been designed and is under construction and testing by ETH Zürich, MIT, NSPO and Shandong University in collaboration with thermal contractors Carlo Gavazzi Space and OHB System. Extensive modeling and testing has been performed and the thermal control system will be validated in an overall Thermal Vacuum Test of the complete experiment supported by the European Space Agency (ESA).

2.9.1 Thermal environment

The primary external factor in the thermal environment is solar illumination. This depends primarily on the angle between the ISS orbital plane and the direction to the Sun. The "beta" angle is illustrated in Figure 2.192a. For the ISS orbital inclination (51.6°) and the tilt of the Earth's axis (23.5°), the beta angle varies between −75.1° and +75.1°, modulated by the seasons as shown in Figure 2.192b. For beta angles with magnitudes greater than 70° the orbit is entirely in sunlight, while for beta angles near 0° about 40% of the orbit is in the Earth's shadow (Figure 2.193a). For the majority of the time, the beta angle lies within −50° to +50° (Figure 2.193b). The intensity of the solar illumination, or solar constant, also varies annually with the distance to the sun, from 1322 to 1424 W/m^2 at closest approach (Figure 2.194a).

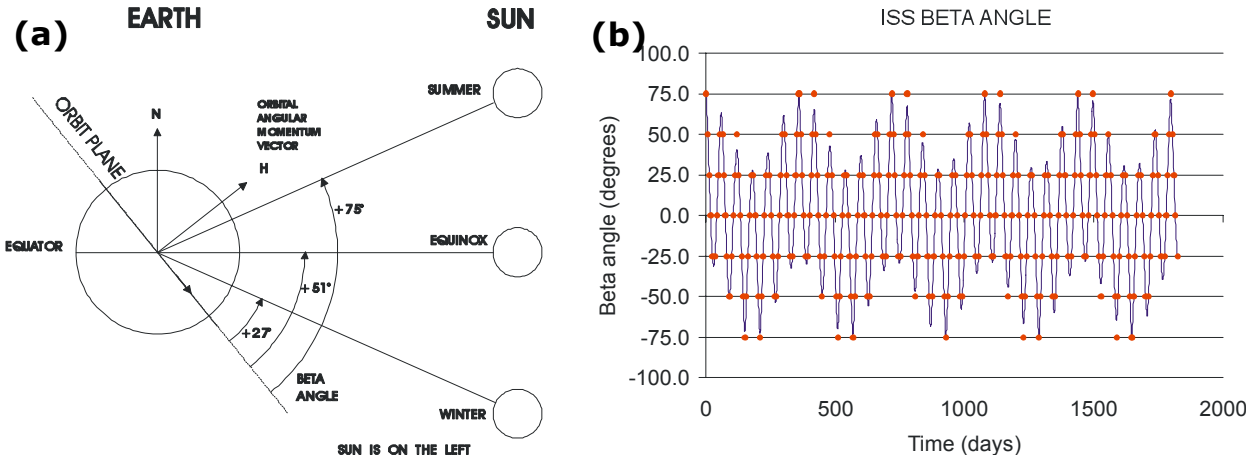

Figure 2.192: Beta angle definition (a) and variation (b).

Different parts of AMS are exposed to different amount of direct sunlight at different times, depending on the ISS attitude, which is expressed in the aeronautical coordinates of yaw, pitch and roll. These are expected to vary by up to ±20°. Complicating this is the shadowing, in some attitudes, of parts of the experiment by different parts of the space station and the radiation reflected onto different parts of the experiment by different space station elements. The ISS altitude can also vary from 277 to 500 km.

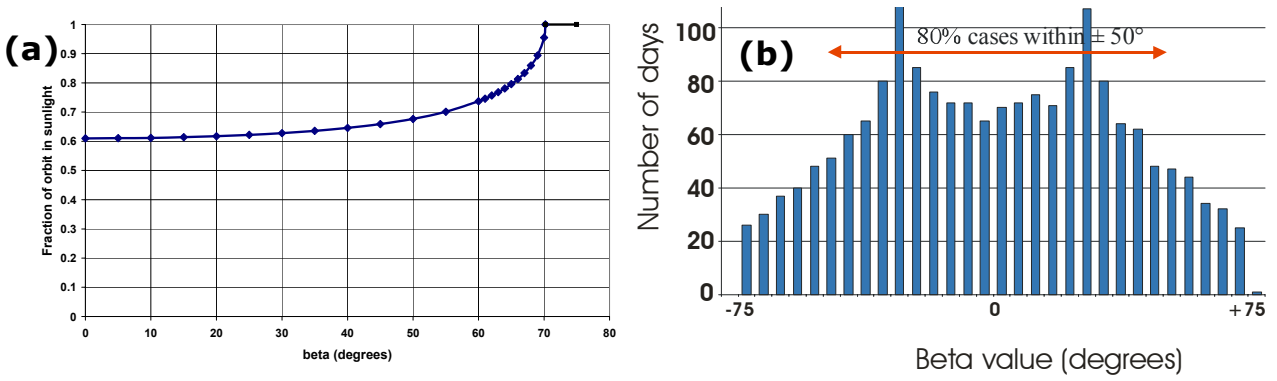

Figure 2.193: Fraction of orbit in sunlight vs. beta angle (a). Number of days per beta angle (b).

Heat from the Earth is accounted for in two ways. The temperature of the Earth as seen from space varies from 245 to 266 K (Figure 2.194b). The albedo constant, which is associated with reflected solar radiation also varies from 20 to 40% (Figure 2.194c).

In addition, the thermo-optical properties (emissivity and absorptivity) of the exposed experimental surfaces change with time. The evolution of a typical material property is shown in Figure 2.194d.

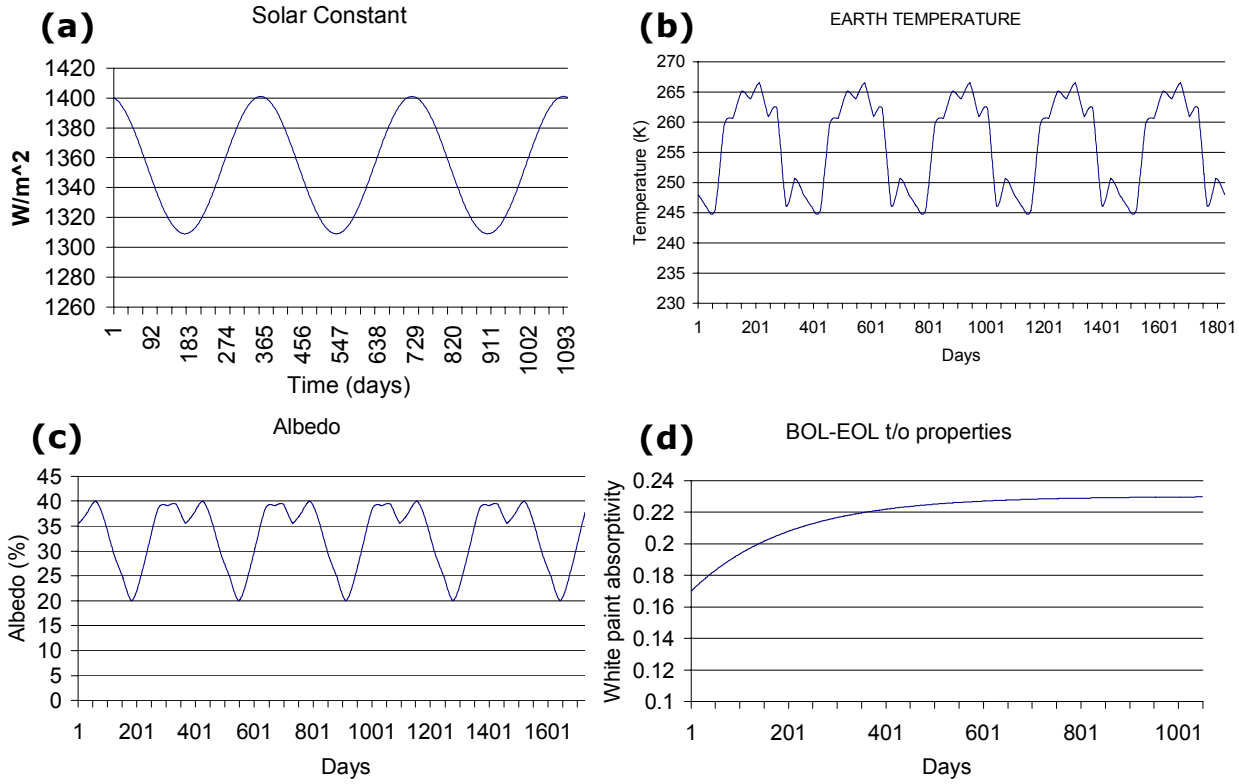

Figure 2.194: Factors effecting external thermal environment: Solar constant (a), Earth temperature (b), Albedo (c), Beginning of life (BOL) to End of life (EOL) properties of white paint (d) [1].

Internally to the experiment, the thermal environment is also complex, as shown in Figure 2.195. The magnet and surrounding tank of superfluid helium are at 1.8 K. At the vapor cooled shield closest to the outside of the toroidal vacuum case (VCS4, Figure 2.5) this has risen to about 68 K, maintained by the four cryocoolers which must radiate 400 W of input power plus the up to 32 W of heat lifted from the cryogenics system. The vacuum case temperature varies around 270 K. The tracker sits within the vacuum case annulus and dissipates 144 W. Above this are the Upper TOF and TRD, which together dissipate 23 W. Below are the Lower TOF (4 W), RICH (37 W) and the ECAL (72 W). All of the detectors must operate at or near 0 °C. The electronics, which must be located close to the detectors, dissipate the balance of the input power (~1500 W) though it does have a wider operational temperature range. All of these elements are thermally interconnected by radiation and conduction through common support structures and cabling.

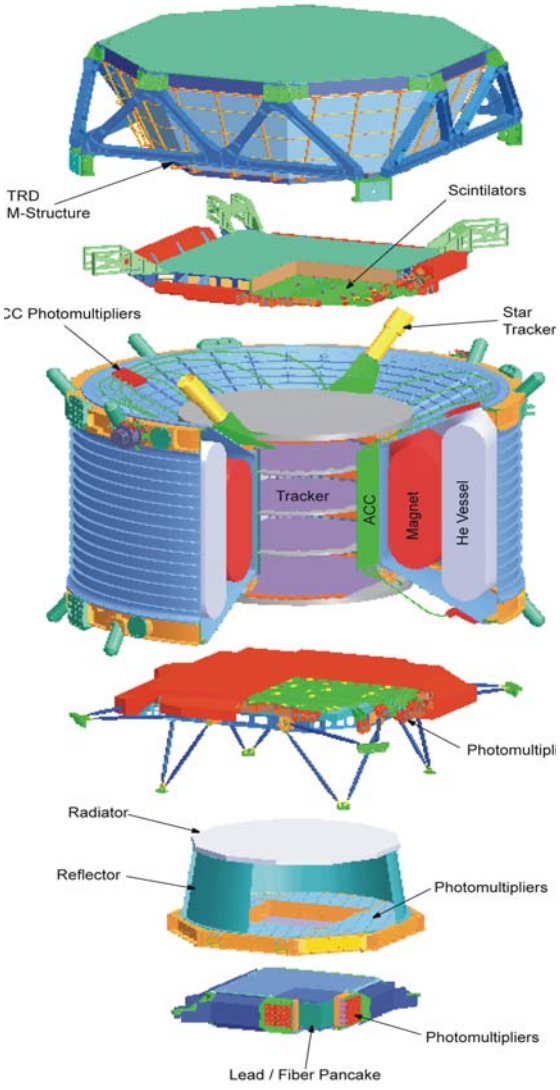

TRD (20 W): Indirect radiation, Enclosed in MLI

Upper TOF (3 W): Enclosed in MLI with TRD

ACC (1 W): Direct Radiation

Tracker (144 W): Dedicated pumped two phase loop.

Magnet+Cryocoolers (4x108 W): Capillary pumped loops to Zenith Rad.

Lower ToF (4 W): Direct Radiation

RICH (37 W): Direct Radiation

ECAL (72 W): Direct Radiation + Conduction to USS.

Figure 2.195: Thermal dissipation of AMS-02 detectors (MLI is multi-layer insulation).

2.9.2 Thermal requirements

Each of the detector elements has specific thermal requirements. The widest limits are the non-operational, or storage, limits. If the temperature of the elements is allowed to exceed these limits, they may be damaged. Within these limits are the operational limits that must be maintained for the proper function of the instruments. These are defined in terms of the absolute temperature range, in terms of the temperature variation (ΔT) over time and in terms of the variation over the volume of the element. Table 2.13 summarizes these limits for the major elements. In addition, the temperatures of the TRD gas tanks have to be kept above 17 °C for Xe and 31 °C for CO_2 to be able to determine the amount of gas remaining by measuring the pressure. Other elements (CAB, TTCB, etc) have their own ranges.

Element	Dissipation [W]	Non-Operational	Operational	Max ΔT per orbit	Max ΔT over detector volume
TRD	20	[−20, +40]	[+10, +25]	2	1
Tracker (silicon)	0	[−20, +40]	[−10, +25]	3 (10/day)	10
Tracker (hybrid)	144	[−20, +60]	[−10, +40]		
Vacuum Case		≤ +10			
Cryocoolers	432	[−10, +40]	[−10, +20]		
RICH	37	[−35, +60]	[−30, +50]	7	15 (among PMTs)
ECAL	72	[−40, +40]	[−20, +40]	5	10 (PMT to structure)
TOF	3+4	[−40, +60]	[−30, +55]	5	10 (PMT to structure)
ACC	1	[−20, +40]	[−20, +40]		
Electronics	1500	[−30, +55]	[−20, +50]		

Table 2.14: Summary of thermal requirements of major AMS-02 elements, in degrees Celsius.

In addition to these requirements, the heat flow into the cryomagnet must be minimized, so heat from nearby sources must be kept away. In particular, the tracker dissipation inside the vacuum case annulus must be collected, conducted outside the vacuum case and radiated. Likewise the dissipation of the four cryocoolers, which are mounted on the vacuum case, must be collected and transferred away. Radiative heat leaks from the other systems must be blocked with multi-layer insulation (MLI) and conductive leaks with insulating joints.

Beyond these requirements are design goals, which optimize the performance of the detectors and the endurance of the superfluid helium. As the response of all detectors depend on temperature, increased stability over time and volume can minimize the possibility of systematic shifts in the physics analysis. The tracker operates with less noise at lower temperatures. The electronics reliability is increased if it is operating at lower temperatures, though it is designed to work at the maximum temperature for the entire mission. The performance of the cryocoolers is a complicated function of the temperature at the interface of their cold tip with the vapor cooled shield, the body temperature and the input power. Optimum performance is obtained when the body of the cryocoolers is maintained at 0 °C. The time averaged temperature of the vacuum case must also be kept as low as possible.

Additional requirements are imposed by NASA to operate on the space station. Heat can not be rejected towards the station elements below AMS nor to the port and starboard sides of the experiment. Highly specular surfaces, which have extremely low absorption, cannot be used as they may dazzle the astronauts or optical instrumentation. The attitude of the station, and consequently AMS, is determined by other concerns than the AMS thermal environment, in particular the needs to keep the solar arrays maximally illuminated and to minimize the propulsion required.

2.9.3 Thermal design

Because of their differing thermal requirements, the overall thermal design approach has been to thermally separate, as much as possible, these different elements and arrive at a solution for each individually. The thermal control system for the tracker was described in § 2.3.5 and for the combined TRD plus Upper TOF element in § 2.2.4. The small amounts of heat from the Lower TOF, RICH and ECAL are rejected using small radiative surfaces attached directly to these detectors. The ECAL also uses the unique support structure (USS) beams to which it is attached as a heat sink. Heavy use is made of insulating shims between structural members and MLI between different volumes to maintain thermal separation and to avoid uncontrolled heat flow back into the magnet. For example, between the TRD plus Upper TOF and the vacuum case a 20-layer MLI blanket keeps the radiation load on the vacuum case below 3 W. The vacuum case temperature is controlled passively by surface treatment to achieve the required thermo-optical properties. In addition to the tracker system, the thermal systems for the cryocoolers and for the electronics have required the most study to meet their requirements. Figure 2.196 shows the radiators required for these three systems.

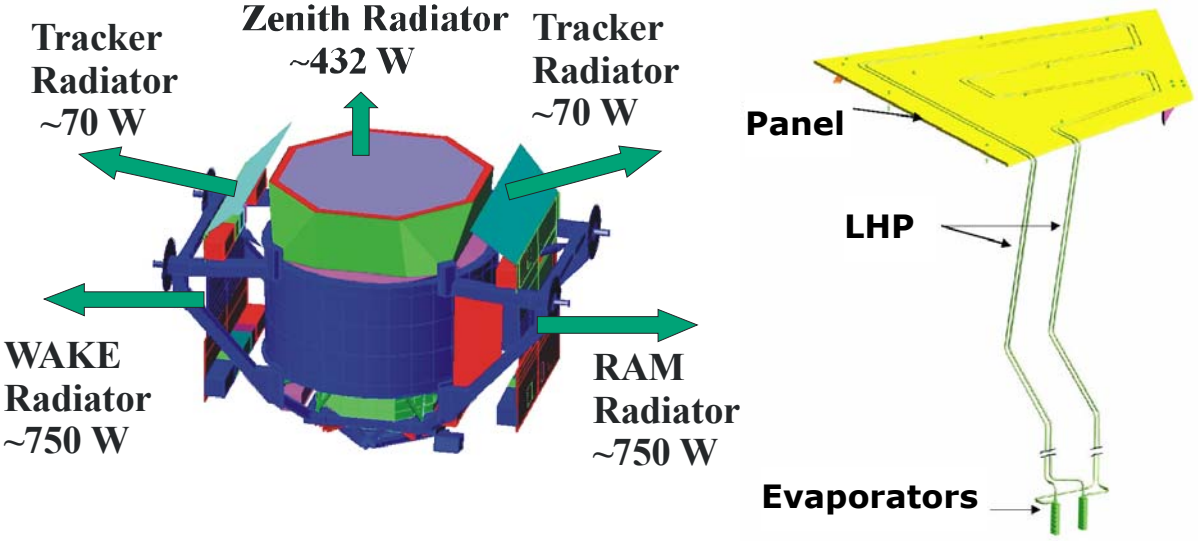

Figure 2.196: AMS-02 Radiators and loads (left).
Detail of Zenith ¼ panel and attached cooling loops (right).

The solution for the cryocoolers is to use capillary pumped loops to move the heat up to the zenith radiator. Each of the four cryocoolers is an independent, redundant system, with two evaporators mounted on the body of the cryocooler. As shown in Figure 2.196, each evaporator feeds a loop heat pipe (LHP) and the working fluid, ammonia, carries the heat up to the zenith radiator. The two loops from a cryocooler are brazed to a dedicated quarter panel (1 m^2) of the zenith radiator, from where the heat is rejected and the fluid condensed and recirculated by capillary pressure. Because the panels are in the aperture of the detector, they have been made as thin and uniform as possible (a sandwich of 1.6 mm Al, 10 mm of Rohacel and 0.3 mm Al) as have the condensing loops elements embedded with them (Al tubes of 3 mm outer diameter with 0.5 mm walls). The panels are mounted on fiber glass standoffs to insulate them from the TRD. Likewise the leak from cryocoolers to vacuum case is maintained at less than 5 W each.

As the electronics have a wide operating range and do not have strong stability requirements, the design of the thermal control system is simplified. On the other hand, altogether the dissipation is ~1500 W, a significant heat load that must be directed away from the other detector elements. The electronics is contained in the boxes shown Figure 2.197 located on the wake and ram sides of the

detector. On each side the boxes are mechanically linked to form a self supporting structure which spans the area between the four upper USS beams (see also Figure 2.1). The "main" radiators are mounted directly to the boxes. Heat from the electrical components is conducted from the printed circuit boards (PCBs) to the box walls or to frames which hold the boards. It is then conducted directly to the inside surface of the attached radiators, which are also made of an Al:Rohacel:Al sandwich. Ammonia heat pipes within the radiators ensure the transfer of the heat from the inside to the outside and also the distribution of the heat evenly over the entire area (4 m^2) of the radiator. Radiation back towards the detectors and vacuum case is blocked (<3%) by surface treatment of the inner radiator surfaces and MLI around the boxes.

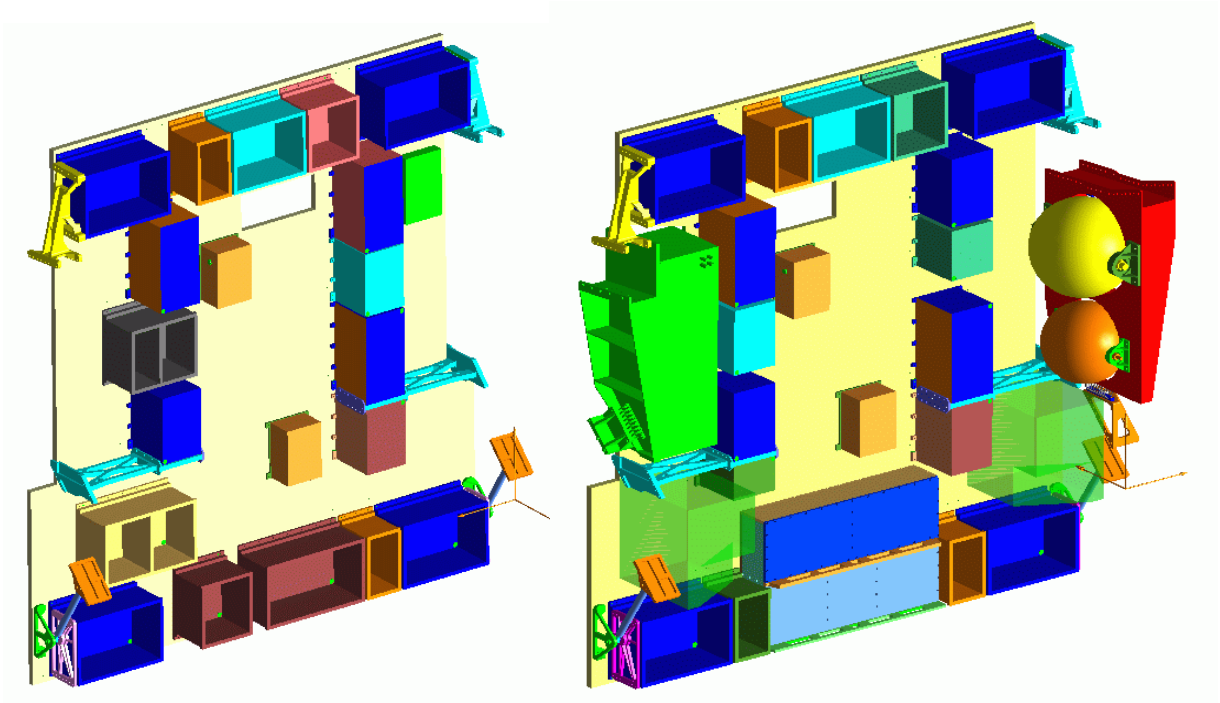

Figure 2.197: Main ram (right) and wake (left) radiators mounted on the structure of linked electronic boxes (ram refers to the ISS direction of travel, wake is opposite).

2.9.4 Thermal integration and modeling

Modeling of the thermal performance of AMS has been a multi-step, iterative procedure. First the experiment was split into the differing thermal elements described above and interfaces between these elements were defined. Detailed modeling is done for each element based on boundary conditions supplied from the overall thermal model. Results from the detailed modeling are then included back into the overall model in terms of heat flow across the interfaces, the overall model is reanalyzed and results supplied again to the detailed models. By design, the elements are as thermally independent as possible, so this procedure converges after just a few iterations. Based on the results, the thermal designs are adjusted and the procedure restarted until all the requirements are met and the design goals approached.

All of this modeling must be done in the varying external thermal environment. The main environmental factors, beta angle and ISS attitude are binned into 189 cases. For each element, the worst hot case, the worst cold case and, if required, the worst spatial variation case, are identified from these 189 cases using the appropriate worst ISS altitude, solar constant, Earth temperature, albedo and BOL-EOL properties. In addition, the operating range must be met when the element is dissipating and the

non-operating range met when it is not. The evolution of temperatures is studied over time using 12 sequential positions over each orbit. These dimensioning cases drive the thermal design which must balance the cooling required in the worst hot operating case with the heating required in the worst cold non-operating case. Owing to the different requirements of the detector elements and to the different environmental factors to which they are exposed, the dimensioning cases are different for each element. Typically, they occur at combinations of an extreme beta angle and an extreme yaw or roll angle.

Though of shorter duration, the thermal environments and thermal response when AMS is in the space shuttle payload bay and when it is being transferred from the space shuttle to the space station have also been examined. For some elements, the transfer phase had become the dimensioning cold non-operation case. To avoid this, the electrical design of the PDS (Figure 2.158) was modified to accept power from the space station arm to supply heaters.

Technically, the modeling is done by many different collaborators using the software most suited to their needs (ESATAN, SINDA/FLUINT, IDEAS-TMG, ad hoc Fortran codes, TRASYS). Significant effort has been required to establish a common data interchange format. In addition the complete model must be turned over to NASA for integration into their overall model of the space station. A reduced version of this model is provided by NASA to AMS in terms of fictitious "MERAT" (Mean Effective RAdiation Temperature) nodes, which mimic the local radiative environment for the 189 cases.

A simple example of the modeling is shown in Figure 2.198 for the temperature of the walls of one T-Crate located on the upper port side of the main ram radiator during its worst hot operating case. The wall temperatures are within the design requirements.

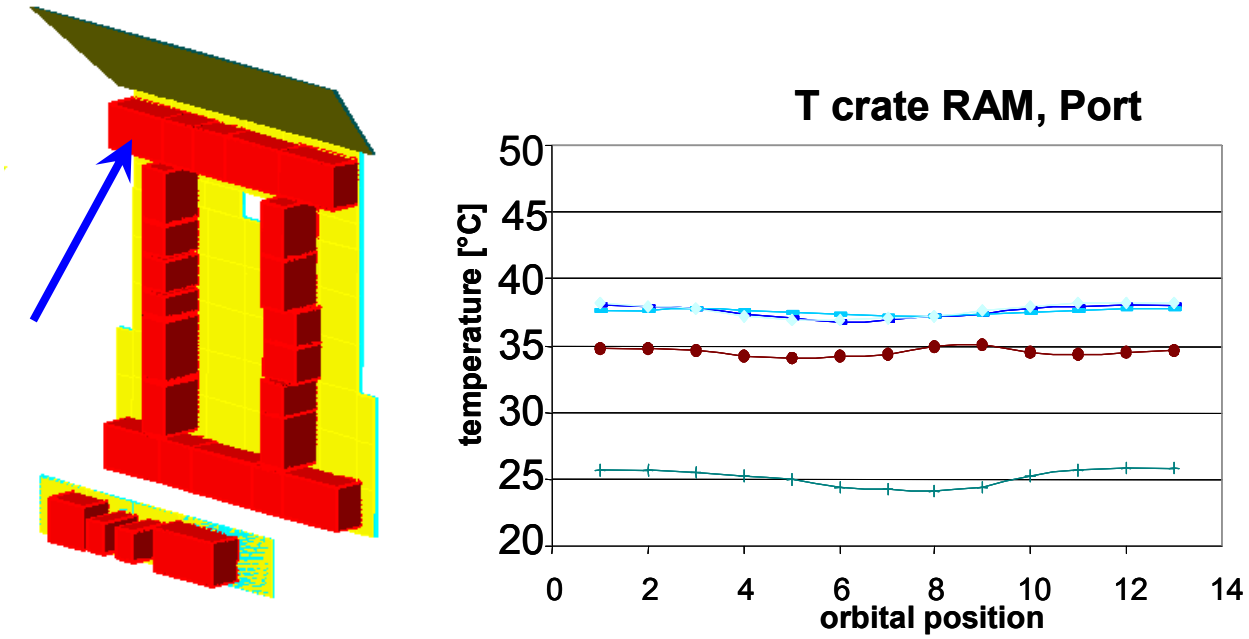

Figure 2.198: Model results for the indicated T-Crate.

A long term analysis was also performed using the space station "Minimum Propulsion Attitude", or MPA (yaw, pitch, roll = −2°, −10°, +1°) and nominal operating conditions. Figure 2.199 shows the results for the five radiator and the vacuum case temperatures. Despite some seasonal spikes, the radiators are kept within their target ranges. Likewise, over most of the mission, the average vacuum case temperature is kept well below 0 °C, meeting the design goal.

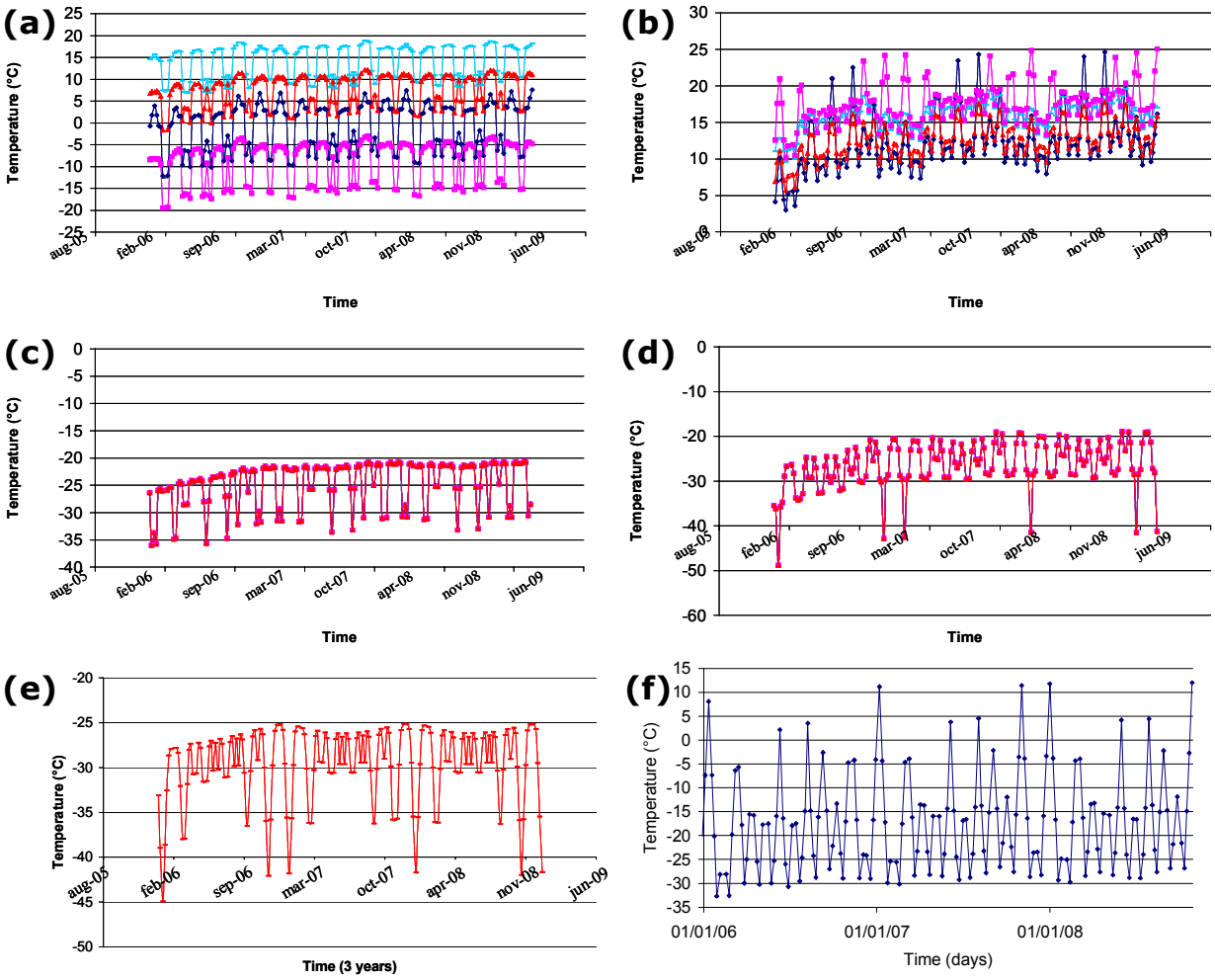

Figure 2.199: Temperatures from long term (3 year) transient analysis of radiator and vacuum case temperatures while in Minimum Propulsion Attitude: various points on main wake radiator (a), various points on main ram radiator (b), mean of tracker wake radiator (c), mean of tracker ram radiator (d), mean of zenith radiator (e), mean of vacuum case (f).

2.9.5 AMS Thermal Vacuum Test

Because of the complexity of the AMS detector, it is essential that an overall thermal vacuum and thermal balance test be performed after integration and before launch into space. The purposes of the test are to verify the functional performance of the experiment and its thermal control hardware under thermal vacuum conditions and to check that no degradation occurs during and after the test. The test will be coordinated with the support of Shandong University and will be conducted in the Large Space Simulator (Figure 2.200) at the European Space Agency ESTEC facility in the Netherlands. This is a 2500 m^3 thermal vacuum chamber with a solar beam simulator and walls which are temperature controlled by liquid or gaseous nitrogen. There will be a thermal vacuum test, during which the experiment will be taken to its hottest and coldest allowed non-operating temperatures (with power off), followed by four cycles in which the experiment will be taken to its hottest and coldest allowed operating temperatures (with power on). The purpose of this part of the test is to verify that all parts of the experiment continue to function under these conditions. The thermal vacuum test will be followed by a hot and cold thermal

balance test. During this test AMS will be held at a hot and cold operating temperature for a longer time, so that the validity of the thermal mathematical model of the experiment can be verified, as well as operation under space conditions. The solar beam will be turned on during the hot phase. The test will involve at least 30 days of operations inside the vacuum chamber with an additional 12 days of contingency because of the complexity of the cryogenic system for the magnet. Both the cryogenic system and the magnet will be operated during the test. Plans for the test are being coordinated with the ESA-ESTEC thermal testing group.

Figure 2.200: The Large Space Simulator (LSS) at ESTEC, site of the AMS thermal vacuum test.

2.9.6 Reference

[1] D. Gilmore, "SATELLITE THERMAL CONTROL HANDBOOK", Spacecraft Thermal Department, the Aerospace Corporation, 1994

2.10 Integration

The elements of the AMS-02 detector are assembled as shown in Figure 2.201 ("ram" refers to the ISS direction of flight, "wake" is opposite, "port" and "starboard" are transverse). The assembly takes place at a dedicated facility installed at CERN, with support from the entire collaboration, as indicated in Figure 2.202.

As shown in Figure 2.203, after all elements are integrated, the detector is calibrated in particle beams at CERN and GSI, Darmstadt for calibration. The detector undergoes a complete thermal vacuum test at the ESA Large Space Simulator at ESTEC, Noordwijk, the Netherlands.

After the instrument has been completely checked out it will be partially disassembled for transport and shipped to the Kennedy Space Center. There, after reassembly, it will be subjected to tests to verify that it is compliant with the NASA mechanical and electrical interfaces for both the space shuttle and the space station.

The experiment will then be installed in the shuttle and launched to the space station.

Assembly begins when Space Cryomagnetics delivers the completed and tested Magnet system, and the NASA Mission Management Office, supported by Lockheed Martin, delivers the unique support structure (USS) to CERN. The unique support structure is made up of three components: The USS main beam structure, the magnet vacuum case, and the lower USS. The vacuum case will have already been incorporated in the magnet system.

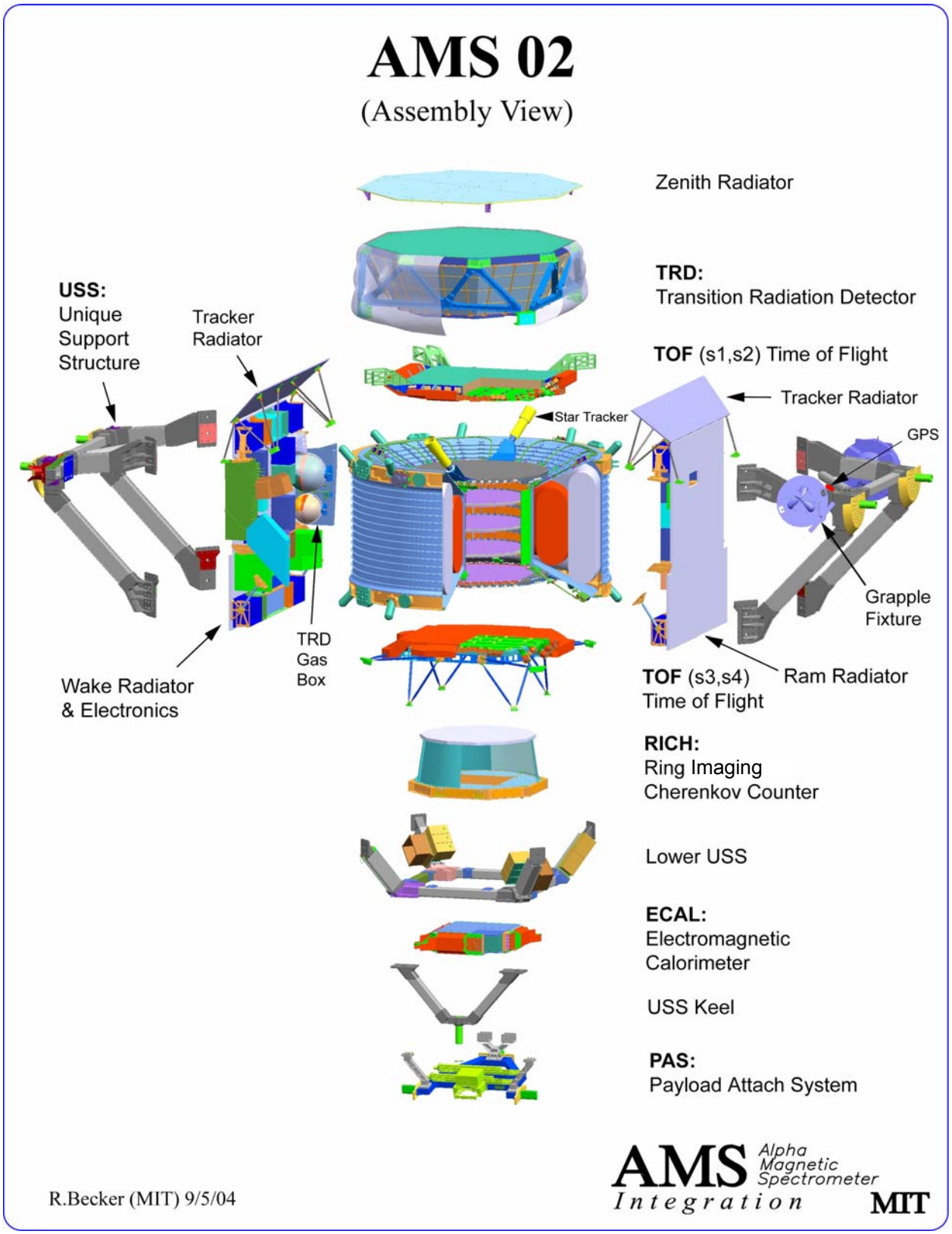

Figure 2.201: AMS-02 Assembly (Ram - ISS flight direction).

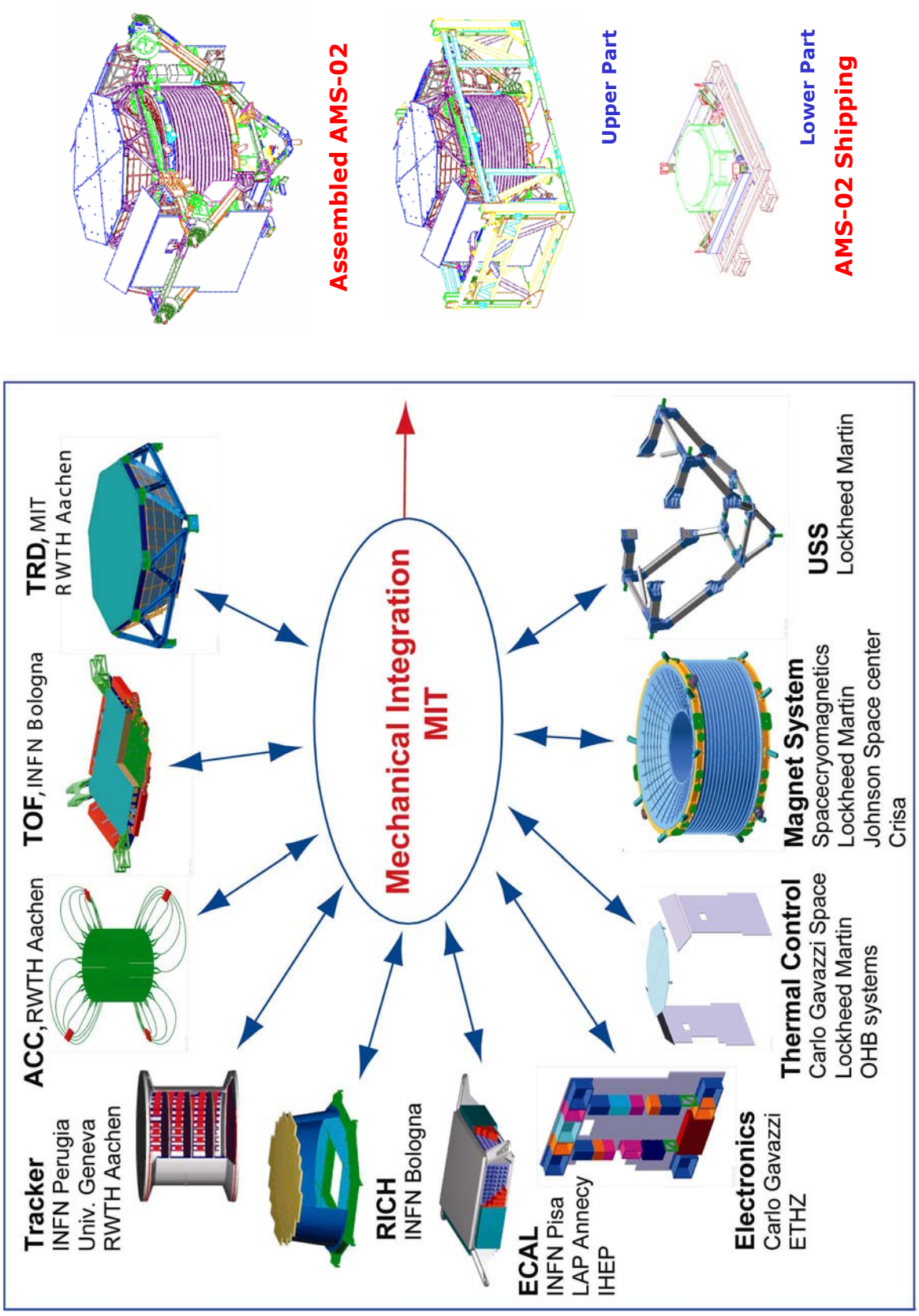

Figure 2.202: AMS-02 Mechanical Integration at CERN.

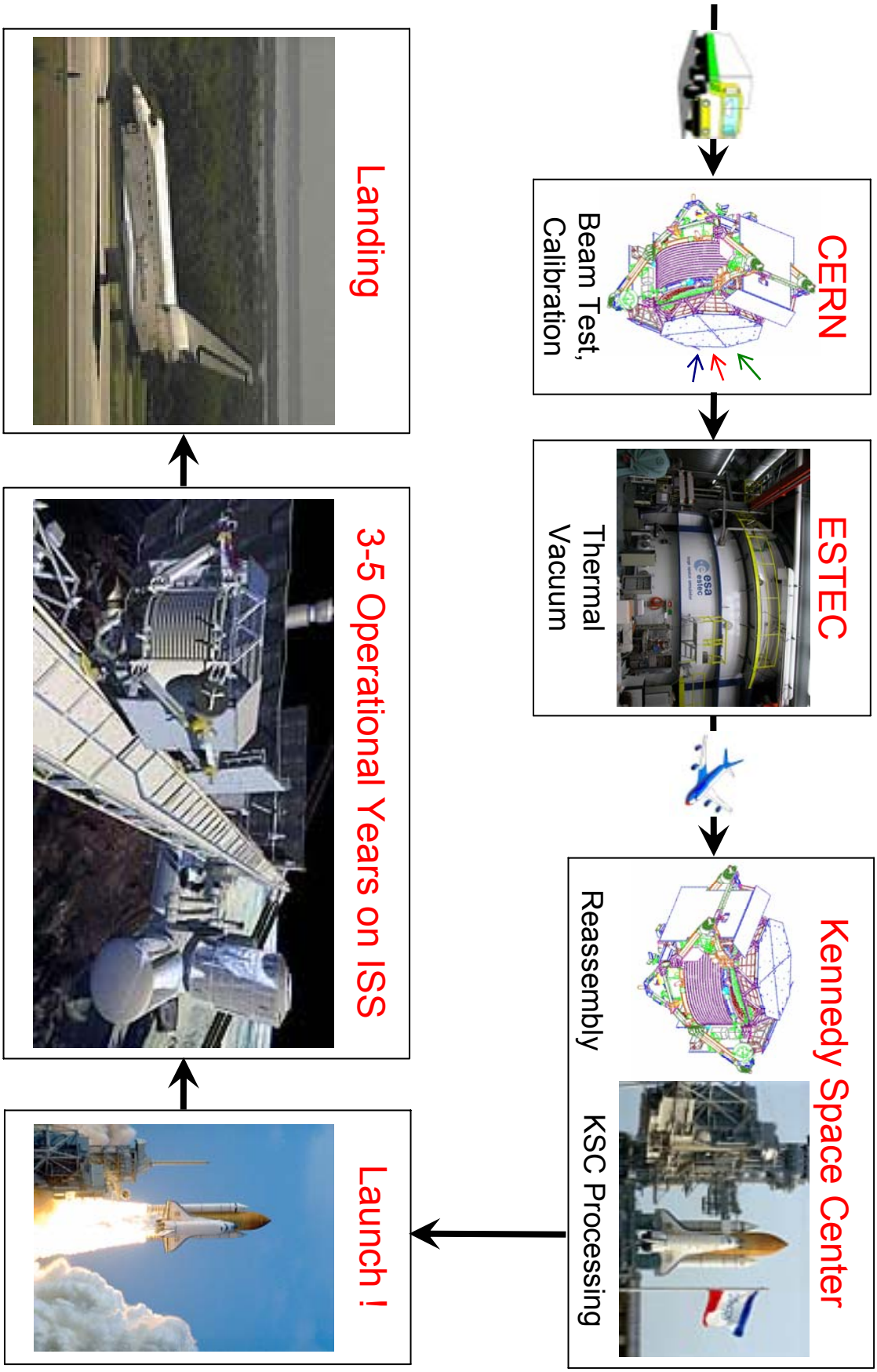

Figure 2.203: AMS-02 transportation flow.

2.10.1 USS and Magnet

The first step is bolting and pinning the USS main beam structure to the eight interface flanges of the magnet vacuum case forming the main USS structure (Figure 2.204). This structure is then mounted into a rotating and height adjustable assembly stand designed to hold AMS at the shuttle mechanical interfaces (trunnions). The magnet support boxes (the Cryomagnet Avionics Box (CAB), Cryo-valve box (CVB) and uninterruptible power source (UPS)) are mounted to the wake side of the USS and all interconnections between magnet and boxes are made.

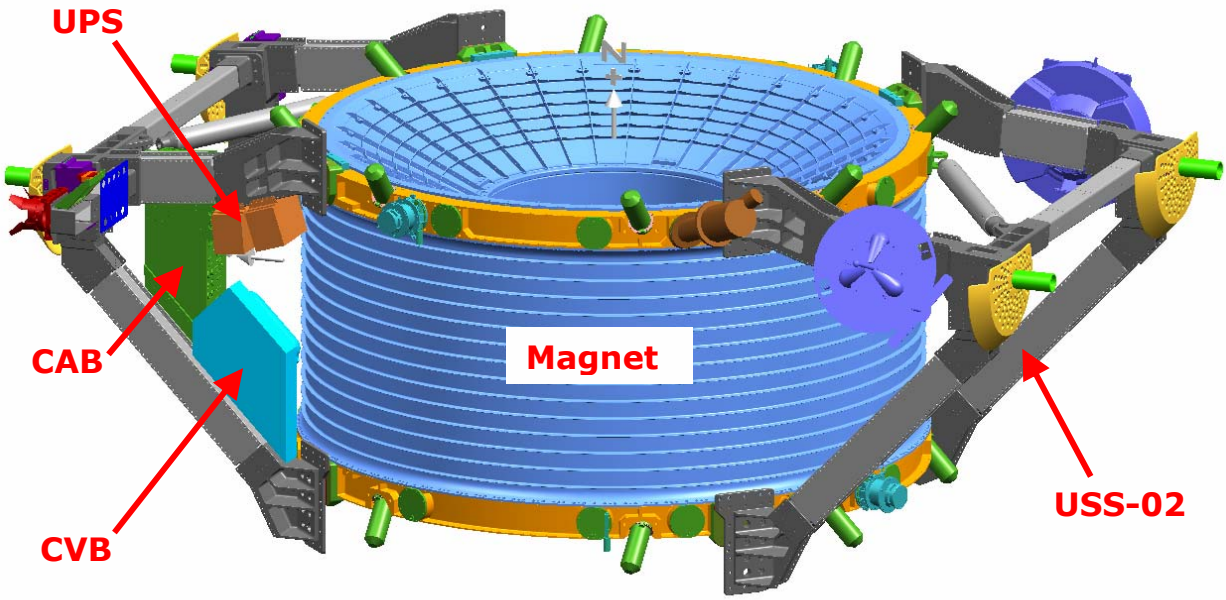

Figure 2.204: Main USS-02 structure and Magnet.

2.10.2 Anticoincidence Counters (ACC)

The first detector to be installed is the anticoincidence counter (ACC). It is composed of 16 scintillator paddles each individually mounted to the inner bore of the magnet Vacuum Case (VC). Once all paddles, fiber light guides and photomultiplier units have been inserted and mounted, they are secured with a carbon fiber composite cylinder (see Figure 2.205).

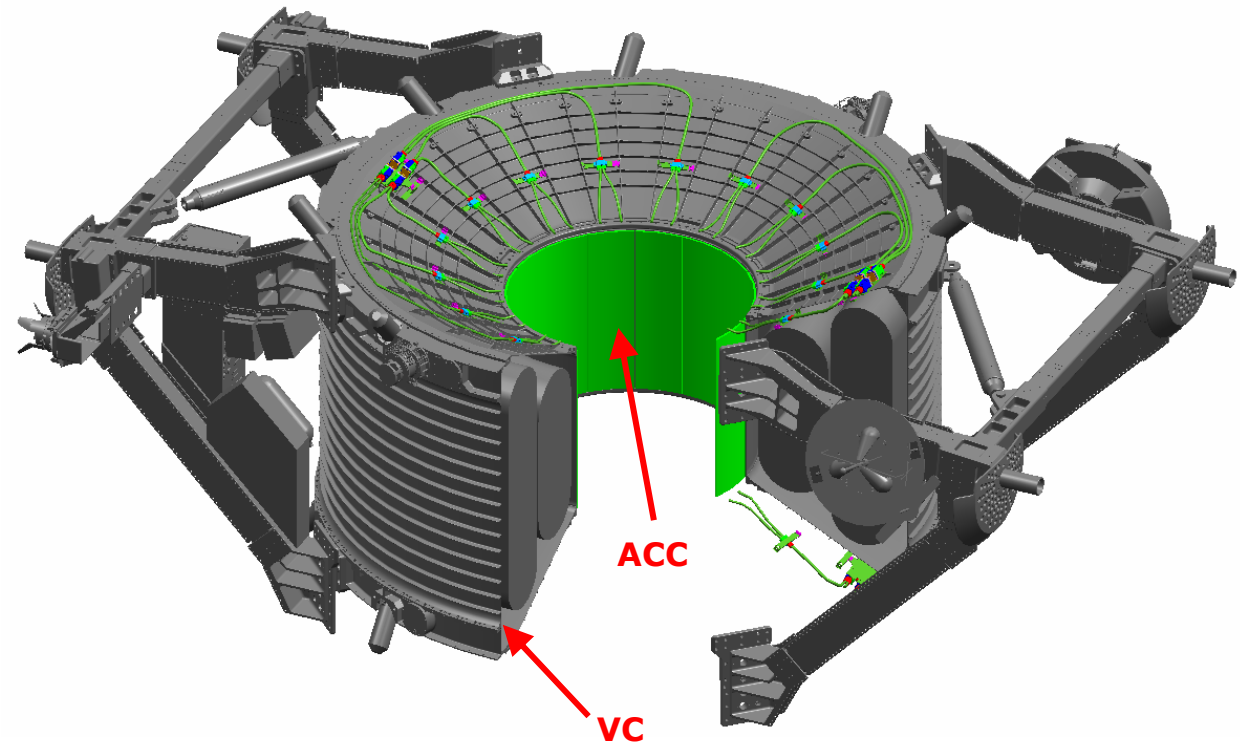

Figure 2.205: ACC installed.

2.10.3 Tracker & Star Tracker

Next, the tracker together with the star tracker is installed. The partially assembled tracker consisting of the cylindrical midsection with inner planes mounted together with the upper conical flange and star tracker structure and the upper four compliant tracker feet, which structurally connect the tracker to the Vacuum Case (VC), are lowered into the inner bore of the VC. The compliant tracker feet resting on the VC are then bolted. The lower conical flange is bolted to the tracker cylinder and another four compliant feet bolt to the tracker securing the lower end of the tracker to the VC. A large volume of cables from the inner silicon planes that were rolled and bundled for installation are now routed over the vacuum case to the 8 respective tracker crates (see Figure 2.206).

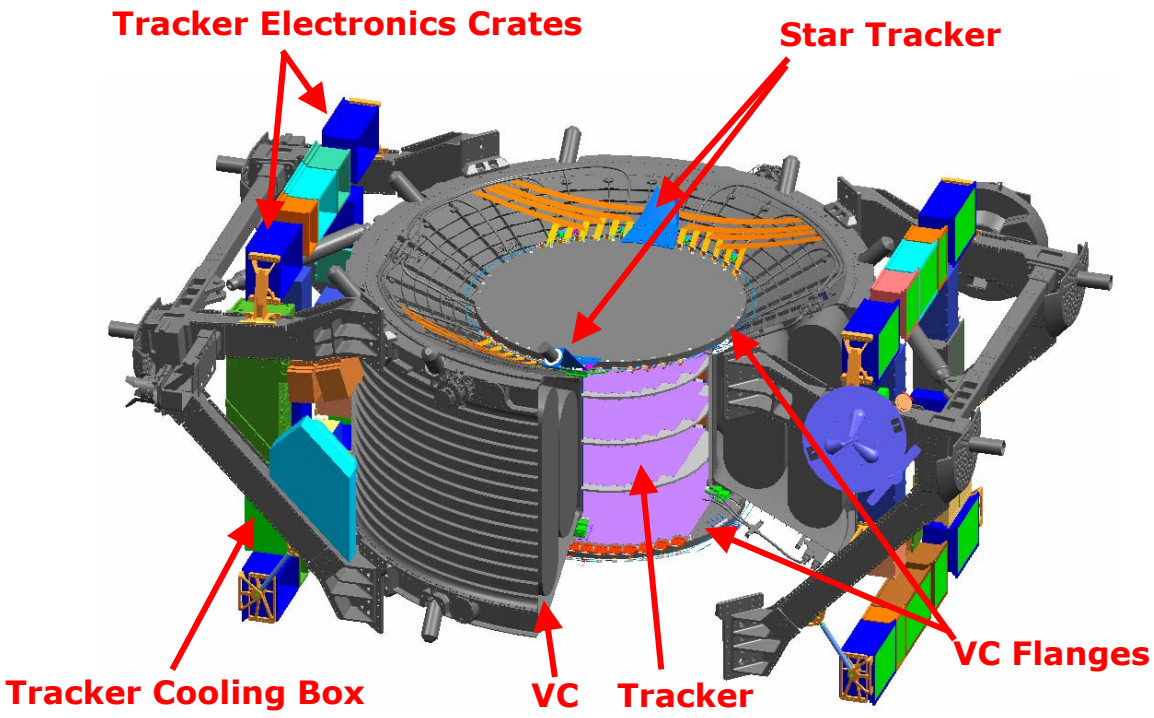

Figure 2:206: Tracker & Star Tracker with Electronics Boxes.

Next the tracker cooling system is installed. The tubing loops for cooling the inner planes and the two outer planes are inserted and attached to the front end electronics using a precision jig. The two boxes containing the "Tracker cooling box" and electronics are mounted on the wake side of the USS. Condensers that are to be attached to the backside of the tracker radiators are jigged in place and all tubing interconnecting the above components is routed and welded using a precision orbital welding machine.

Following this the upper and lower planes of the tracker are placed on the conical tracker flanges and bolted in place. The star tracker camera module is then bolted at the outer edge of the upper tracker plane and to the already installed star tracker structure.

Most electronics boxes are arranged and interlinked into rack-like structures that are mechanically self-supporting when complete. The tracker crates are the first to be installed within this self supporting arrangement and, due to their close proximity to the main USS, are the structural links to the USS (dark blue boxes near USS in Figure 2.206). These are installed together with a jig (not shown) that will hold most of other boxes in place during assembly.

2.10.4 Time of Flight (TOF) detector

The time of flight detector (TOF) is composed of two parts: the upper TOF containing two scintillator panel layers above the tracker, and another identical set of panel layers bellow the tracker, but supported by a different structure.

The upper TOF shares common attachment brackets with the TRD. First, they are bolted to the 4 interface flanges of the USS and then the TOF support arms are bolted to them, see Figure 2.207.

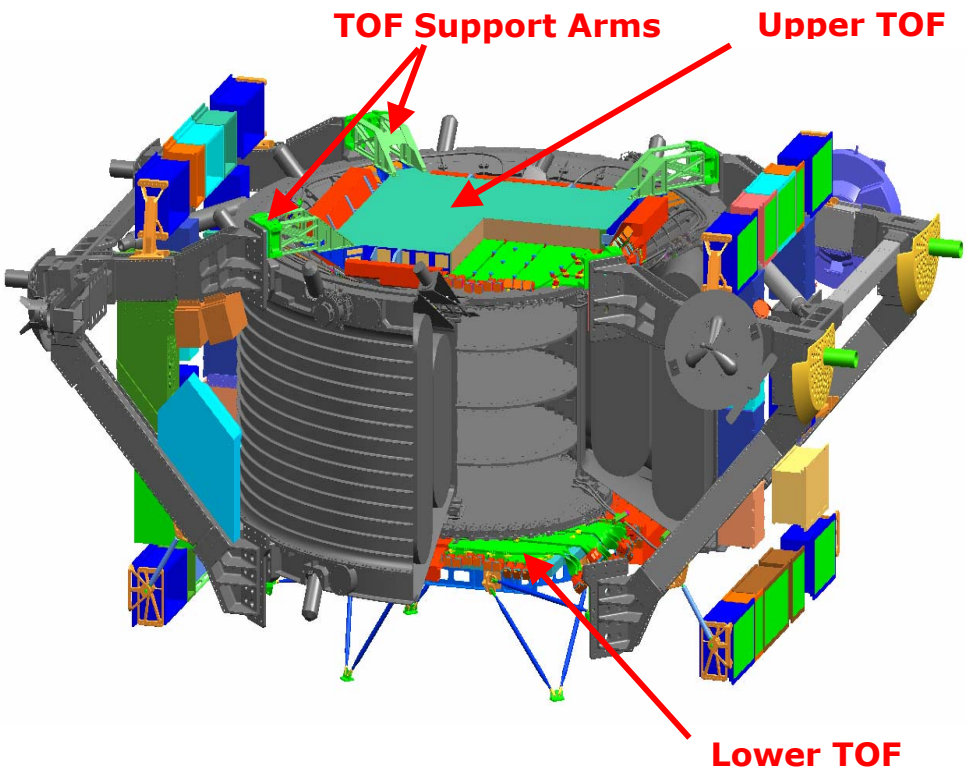

Figure 2.207: Upper and Lower Time of Flight Detectors (TOF).

2.10.5 Transition Radiation Detector (TRD)

The Transition Radiation Detector is installed by placing the corner of the TRD truss structure on the TOF common bracket and pinning and bolting it in place. The TRD gas supply and circulation system is hoisted and bolted to the upper wake, port side of the main USS structure. The 3mm diameter gas lines are routed to the detector, respective electronics boxes mounted and cabling routed. The TRD multi-layer insulation (MLI) enclosure is now wrapped and sealed around both the TRD and upper TOF detectors, see Figure 2.208.

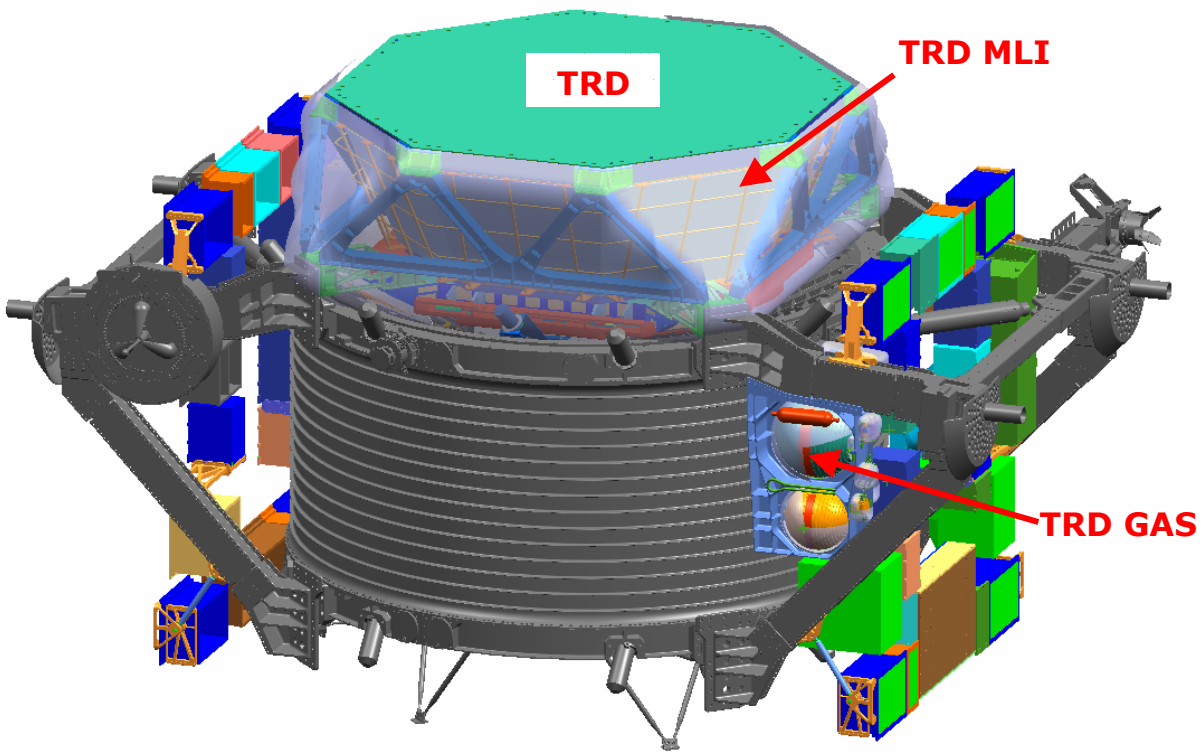

Figure 2.208: TRD installed with MLI enclosure.

2.10.6 RICH

The lower USS supporting the RICH and ECAL detectors are initially integrated separately from the rest of the experiment. The RICH detector is lowered onto the square structure where eight brackets secure it to the lower USS (Figure 2.209). Corresponding electronics crates are bolted to the radial arms and cables routed.

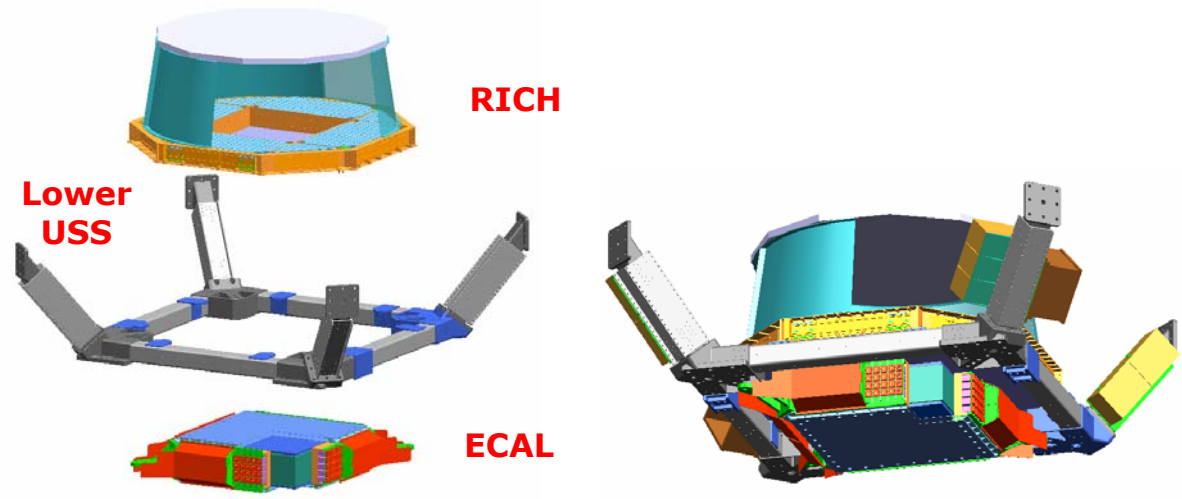

(a) Preassembly view (b) Assembled

Figure 2.209: Lower USS-02 with RICH and ECAL.

2.10.7 ECAL

To install the ECAL, the Lower USS with the RICH already attached is lifted and lowered onto the ECAL. The ECAL interfaces to the lower USS at the 4 corners of the square beam section (Figure 2.209). Again electronics are mounted on the radial corner beams and cabling routed.

2.10.8 Integration of the Upper and Lower Parts

The lower USS-02 part (carrying the RICH and the ECAL) is integrated with the Upper USS-02 part. The assembled and tested lower detectors and lower USS are rolled underneath the AMS upper part, crane lifted into position, and pinned and bolted into place. Electrical connections and testing follows, (see Figure 2.210).

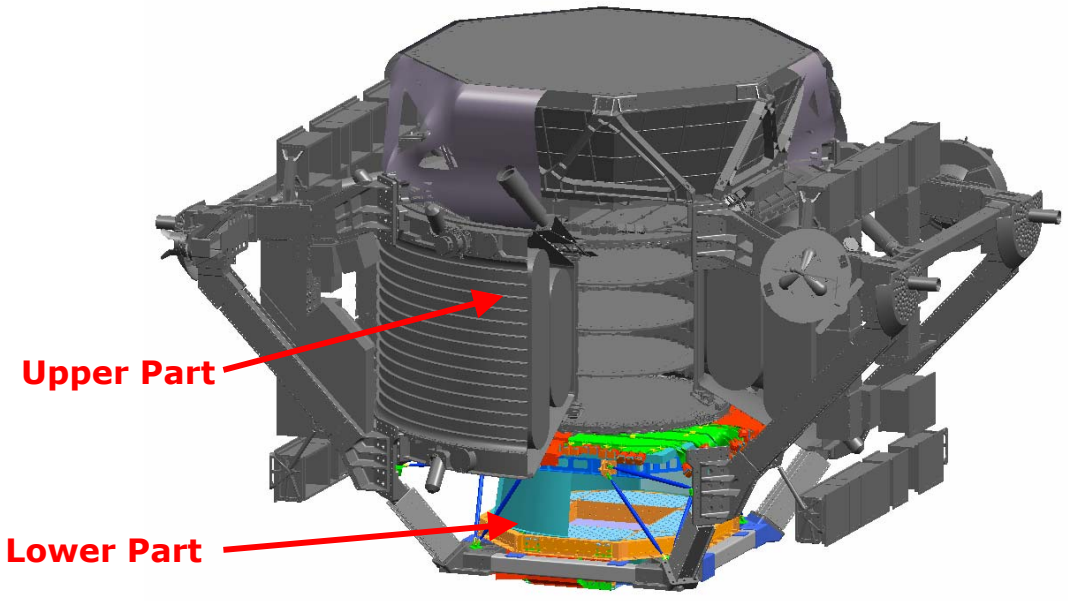

Figure 2.210: The Lower USS-02 integrated with the Upper USS-02.

2.10.9 Radiators & Electronics

For the installation of the main radiators, each is lifted in from below, positioned and then bolted to the crate structure. All electronics boxes are then grounded to the radiator via dedicated bonding straps, see Figure 2.211.

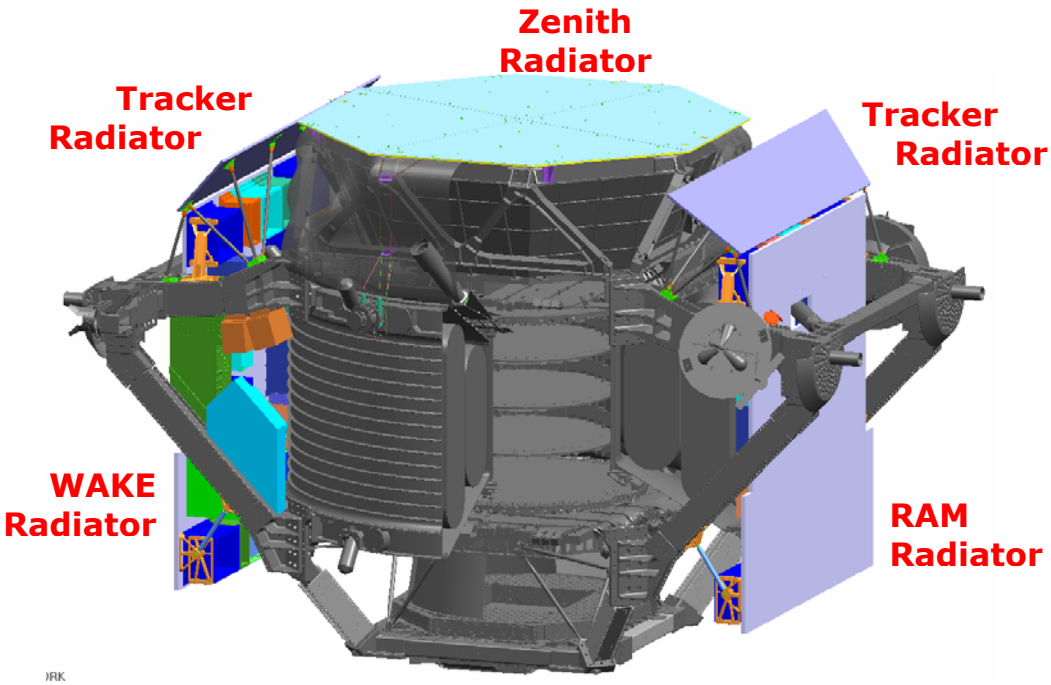

Figure 2.211: Radiators installed.

After the main ram and wake radiators have been installed, the GPS electronics box is mounted to the upper inside, ram, radiator and the GPS antennas bolted to the upper, ram, starboard, trunnion beam of the USS. Then the system is electrically interconnected and connected to rest of AMS.

Tracker radiators are then installed, lifting them into place and bolting the strut structures to the upper USS and vacuum case joints. The tracker cooling heat exchanger is bolted to the radiator and the jigs holding them removed.

The Zenith radiator, located on top of the TRD, is installed last. The radiator is composed of four quadrants, each panel cooling one of the four cryocoolers. Each radiator panel, with the lengthy pre-bent 3mm tubing and attached heat exchangers, is lowered onto the TRD. The tubing is then secured to designated bracketry and the heat exchangers bolted to their respective cryocoolers.

2.10.10 ISS Hardware

At Kennedy Space Center AMS will be fully completed with the addition of shuttle and ISS hardware. There, the USS Keel, and interface with shuttle and ISS will be installed (Figure 2.212).

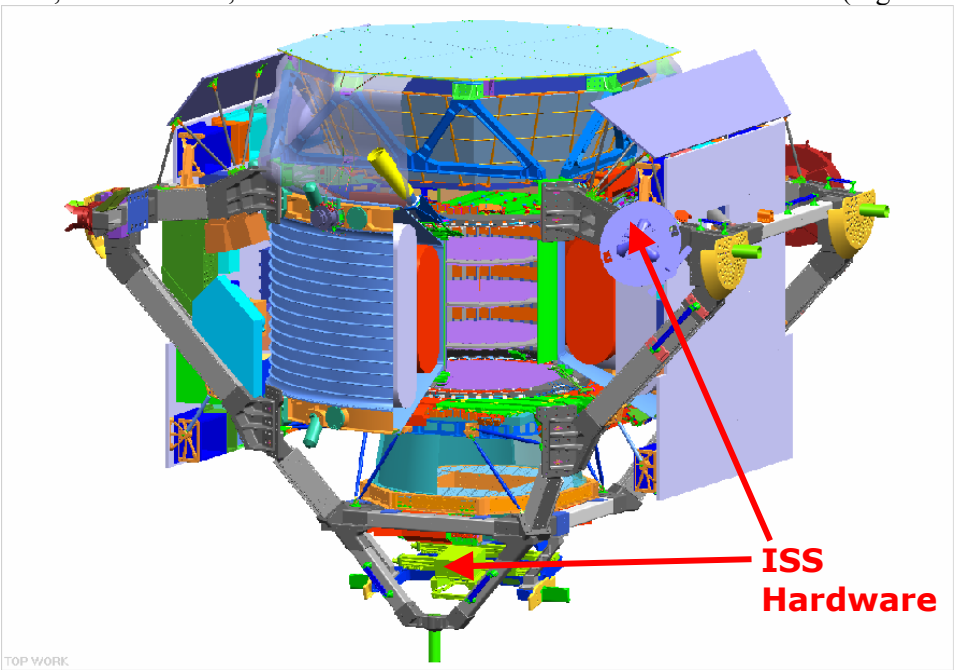

Figure 2.212: Complete assembly including shuttle & ISS hardware.

A full-scale mock up of AMS-02 has been built at CERN to develop and verify the assembly procedure, see Figure 2.213.

Figure 2.213: AMS-02 full-scale mock-up.

2.11 Operations

The operations of the AMS-02 experiment are divided into five distinct phases: Prelaunch, Ascent, STS on orbit, Transfer from STS to ISS and ISS on orbit. The AMS Crew Operations Post (ACOP) will have been launched to the station on a previous flight. During the intervening months it will be installed in the US Lab of the ISS and checked out to be ready for the arrival of AMS.

2.11.1 Prelaunch Operations

After the experiment has been turned over to NASA at KSC for processing, it is installed in the shuttle payload bay. Flight power and data connections to the shuttle are made via the Remotely Operated Electrical Umbilical (ROEU), see Figure 2.1. For prelaunch operations connections are also made through the ROEU to the tail of the shuttle and out through T-0 umbilical to equipment in the Mobile Launch Platform (MLP) underneath the shuttle. The flight connections are checked with a series of Interface Verification Tests (IVT) and End to End Tests.

During this prelaunch phase a vent pump mounted on AMS continuously removes boil off from the helium vessel. In addition, by using ground support computers located in the MLP, personnel monitor the 1553 Bus data for telemetry including temperature and pressure measurements and cryogenic system operating characteristics. The health and status of the Super Fluid Helium (SFHe) Tank are monitored by ground controllers and compared to established trend data. Depending on the thermal environment, the cryocoolers may be operational.

While on the launch pad the magnet will not be charged and is at zero field.

Shortly before the shuttle payload bay doors are closed at launch minus a few days, the cryogenic ground support equipment is used to top off the SFHe tank (§ 2.1.3.ix).

At launch minus 30 minutes, power to AMS over the T-0 is reduced to an absolute minimum and the vent pump turned off and the vent valve sealed.

Monitoring of the cryogenics and vacuum continue until at least launch minus nine minutes at which time ground controllers make a “Go/No Go” decision for launch based on the health and status of the SFHe Tank. After that, power to AMS may be cut off completely.

At launch, the T-0 umbilical is disconnected and control passes from KSC to JSC.

2.11.2 Ascent

While still under powered flight but when the pressure in the payload bay has approached zero (less than 20 mbar), a barometric switch opens a vent valve on the SFHe tank. This ensures that the superfluid helium is not in contact with the passive phase separator. The barometric switch is backed up with a time-tagged command issued from the shuttle Backup Flight System General Purpose Computer.

In the event of an ascent abort, the barometric switch will close the vent valve.

2.11.3 STS on orbit operations

Once on-orbit, the payload bay doors are opened. At about 2.5 hours after launch, AMS receives power from the APCU power supply and communication is established between AMS, the Digital Data Recording System (DDRS-2) in the orbiter and the ground. Control and monitoring of the cryogenics systems is reestablished and the cryocoolers activated. The subdetector elements are then checked out, either one by one or altogether, depending on thermal conditions. The magnet cannot be charged (see Figure 2.158) and remains at zero field. This continues for a couple of days until the shuttle approaches

the ISS, when certain key cryogenics valves are operated. After thermal conditioning, AMS is powered off.

2.11.4 STS to ISS transfer

Transfer operations commence when the space shuttle arm (SRMS) latches on to Flight Releasable Grapple Fixture (FRGF) mounted on AMS. Then the ROEU is disconnected, the Payload Retention Latch Actuators (PRLAs) and Active Keel Attachments are opened releasing the trunnions, and, as shown in Figure 2.214, the shuttle arm lifts AMS out of the shuttle payload bay. It is then maneuvered towards the space station where the station arm (SSRMS) latches on to the Power and Video Grapple Fixture (PVGF). The hand off is completed when the shuttle arm is disengaged. Power then flows through the station arm into AMS where it is used, as needed, to operate thermostatically controlled heaters which maintain the experiment elements in their operational ranges. The station arm then swings AMS over to the S3 station truss and, using the Berthing Cue System cameras, docks it in the upper, inboard payload attach site. The capture claw of the active Payload Attach System on the station then mechanically secures AMS to the station and then the Umbilical Mechanical Assembly (UMA) is driven activated and AMS is electrically mated to the station. Power from the arm to AMS is then cut off and the power through the UMA is activated. As the experiment has been kept in a good thermal condition by power from the station arm, it activates immediately and communication is established between AMS, ACOP and the ground. Then the station arm is disengaged and transfer operations are complete. In total, from power down in the space shuttle to power up on the space station, based on extensive simulations run by NASA, the transfer is estimated to take less than four hours.

2.11.5 ISS On-Orbit Operations

ISS on orbit operations start with the reestablishing of the health and status of the cryogenics system. The cryocoolers are activated. While preparations are being made for charging the magnet, the other experiment elements are checked out and some zero field data for calibration and alignment purposes may be taken. When the cryogenic systems are ready, all the other experimental elements are powered down and the CCS in the CAB (see Figure 2.22) is activated and the magnet is ramped to field, which will take two hours. Then the experimental elements are re-powered and nominal data taking proceeds.

Though all necessary protection is in place to accommodate reduced power levels from the ISS or even foreseen or unforeseen power outages, it is anticipated that the experiment will run continuously for three to five years, at which point the SFHe will be exhausted and the magnet will warm up and return to zero field. At this point the cryocoolers are turned off but, as detailed in the next section, a wealth of interesting physics data can still be obtained.

All critical interfaces (power, LRDL, HRDL) between AMS and ISS are redundant. If necessary, a contingency intervention (extra-vehicular activity or EVA), as shown in Figure 2.159, can be performed by the astronauts to swap cables between the redundant units.

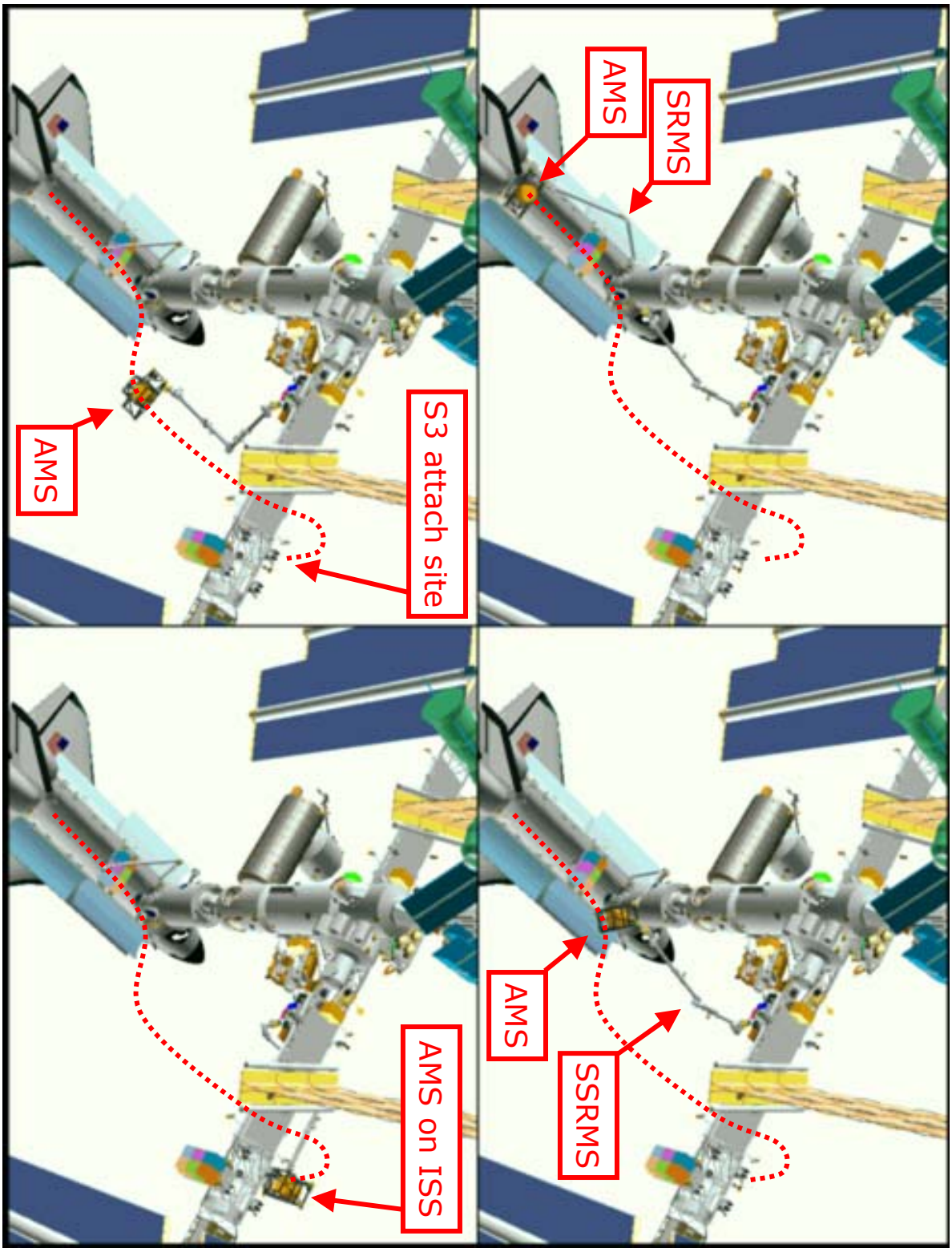

Figure 2.214: Transfer of AMS-02 from the space shuttle to the space station.

2.12 AMS-02 Physics Examples

AMS-02 will be the first major particle physics experiment on the Space Station. The physics goals of AMS are to search for antimatter [1] in the Universe at the level of 1 in 1 billion, to search for the origin of dark matter [2], to measure the spectrum of high energy gamma rays and to make high statistics measurements of the composition of cosmic rays up to the multi-TeV energy range.

In this chapter, examples of the physics capabilities of AMS-02 are presented. These studies were made using the AMS-02 simulation package which includes: a detailed description of the AMS-02 geometry, a simulation of the cosmic ray fluxes based on data collected with AMS-01, a complete simulation of the event using the GEANT 3 [3] package, a simulation of the trigger (Fast, Level-1 and Level-3), event reconstruction, visualization tools (event display, offline monitoring) and tools for Monte Carlo production.

2.12.1 AMS-02 Detector Simulation

The accurate simulation of the detector requires a complete description of the geometry, materials and response of all the experiment elements: the cryomagnet, the transition radiation detector (TRD), the silicon tracker, the time of flight and anticoincidence scintillators (TOF and ACC), the ring imaging Cerenkov detector (RICH) and the electromagnetic calorimeter (ECAL).

The superconducting magnet has the shape of a cylindrical shell with an inner diameter of 1.2 m and a length of 0.9 m. It produces a central dipole field of 0.86 Tesla across the magnet bore. The magnetic field map is included and the trajectories of particles in the field are simulated in detail.

The TRD is situated on the top of the spectrometer and consists of twenty layers of 20 mm thick fiber radiator interleaved with arrays of 6 mm diameter gas proportional tubes filled with a $Xe:CO_2$ mixture. It provides electron/hadron separation at energies up to 250 GeV as well as charged particle coordinate measurements.

The eight layers of double sided silicon tracker are arrayed transverse to the magnet axis. The tracker measures the trajectory of singly charged minimum ionizing particles (MIPs) with an overall accuracy of about 10 μm in the bending plane and 30 μm in the non-bending plane and provides measurements of the particle energy loss.

The time of flight system has four layers and measures singly charged particle transit times with an accuracy of 130 ps. It also provides energy loss and coordinate measurements. The anticoincidence scintillators flag particles entering or leaving the sensitive volume outside of the acceptance.

The RICH detector consists of two radiators (a 3 cm thick Aerogel radiator with refractive index of 1.03 and a central 0.5 cm thick NaF radiator with an area of 1156 cm^2 and a refractive index of 1.34), a mirror and an imaging plane matrix of pixel type photomultiplier tubes for light detection. It assures the measurement of the velocity of singly charged MIPs with an accuracy better than one per mil and the absolute magnitude of the charge as well as providing an unambiguous tag of the particle flight direction (upwards or downwards).

The ECAL is a 3D electromagnetic sampling calorimeter with total of 16.7 radiation lengths made of 1 mm diameter scintillating fibers sandwiched between grooved lead plates.

The simulated performance of the AMS subdetectors was checked against the AMS-01 flight and against test beam data and found to be in good agreement. In addition, to simulate real detector performance after 3 years on ISS, 1 to 2 per cent of the subdetector readout channels were assumed dead. The simulated events were triggered by the coincidence of signals in three out of four TOF plane and/or signals in the electromagnetic calorimeter.

To ensure a detailed evaluation of the AMS-02 physics performance, more than 10^{10} events, including protons, electrons, positrons, deuterons, antiprotons, He and other heavier nuclei, are being

simulated at different energies. To achieve this goal a collaboration wide effort has been undertaken. Figure 2.215 shows the 21 Monte-Carlo production centers. The current capacity, as measured during a long term (100 day) production run, is that 2×10^7 events (more than 30 GByte) can be simulated, collected and redistributed, on average, each day. The experimental sensitivity studies presented are based on these statistics.

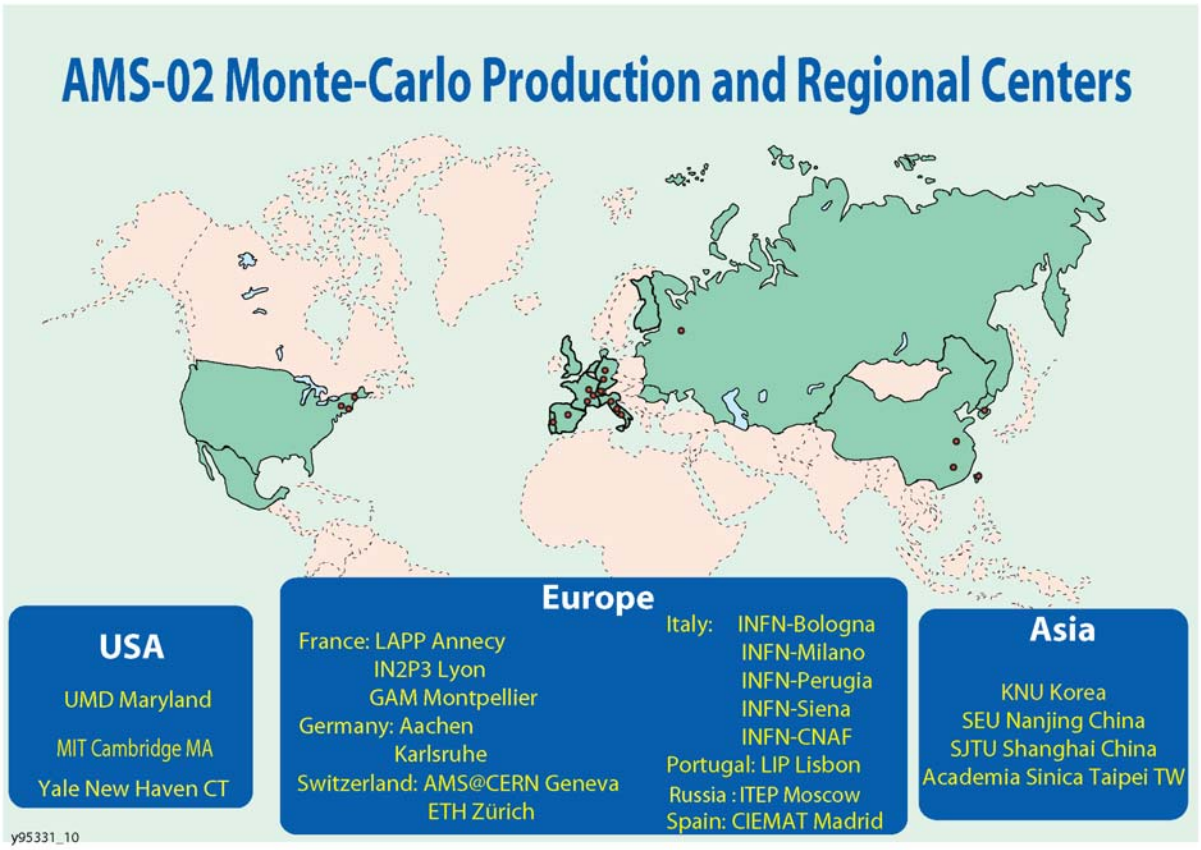

Figure 2.215: AMS Monte Carlo Production and Regional Analysis Centers. Each center participates in providing distributed computing resources, remote software development and physics analysis, new software tools for networking and interprocess communication and a working prototype of the ground data handling for the AMS-02 mission.

2.12.2 Antimatter search

The main backgrounds to a genuine $\overline{\text{He}}$ signal are He events which are either mismeasured or which interacted in the AMS detector. Using a selection procedure similar to that used in the AMS-01 antimatter search, the average AMS-02 acceptance for $\overline{\text{He}}$ events was estimated to be 0.4 m^2sr. The selection efficiency for $\overline{\text{He}}$ varies from 70% (from 2 to 100 GV) to 3% (around 1 TV). No He events survive the cuts. Projecting this result to a 3 year measurement, a $\overline{\text{He}}$/He limit of order of 10^{-9} will be obtained for rigidities up to 130−140 GV (Figure 2.216).

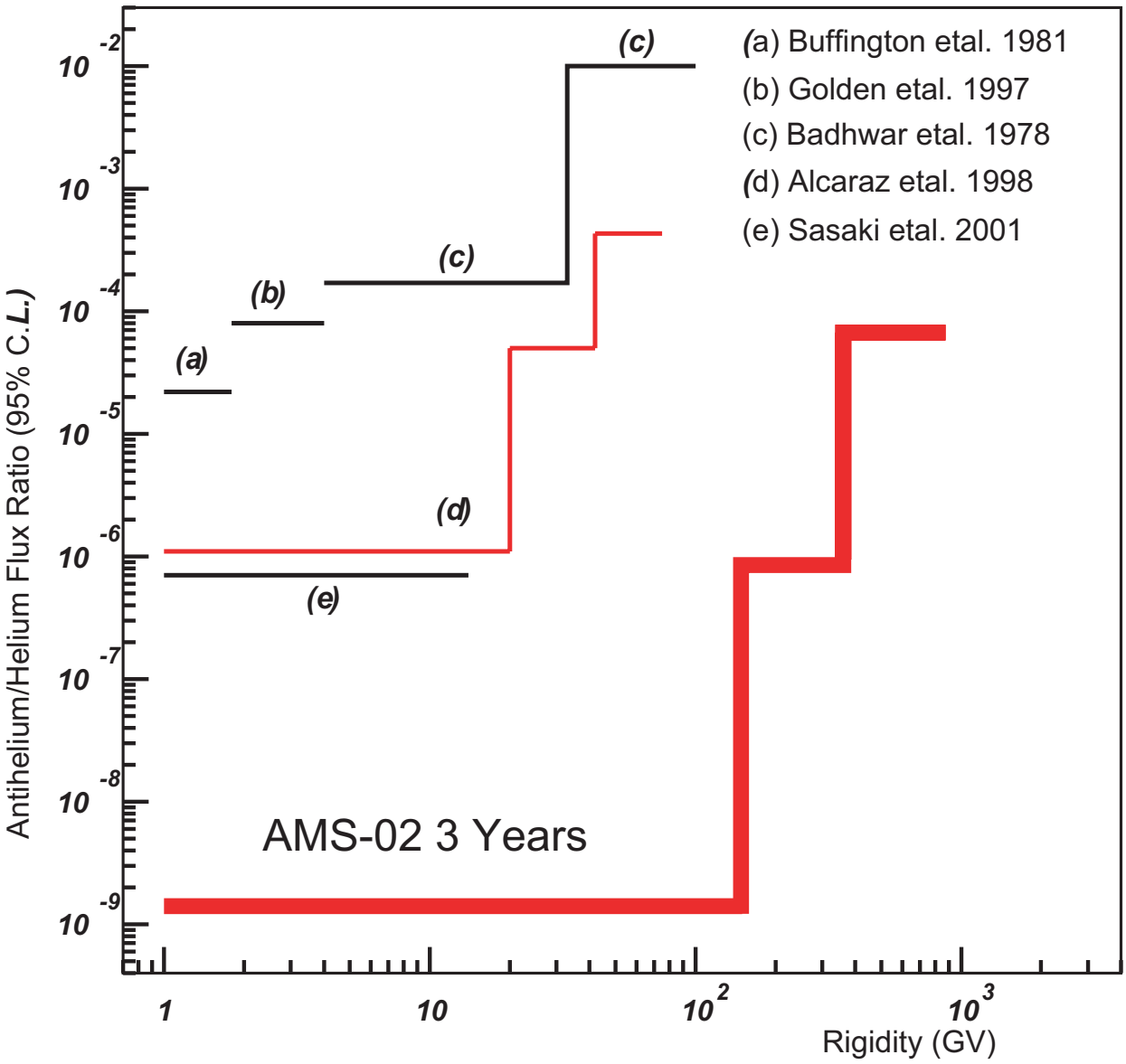

Figure 2.216: Projected AMS-02 limits on the $\overline{\text{He}}$/He flux ratio compared to previous measurements [4] including AMS-01 (d).

2.12.3 Dark matter search using the positron spectrum

According to SUSY theories, the leading dark matter candidate is the neutralino, χ. Neutralino annihilation in the galactic halo can produce $\bar{p}$, e^+ and γ via:

$$\chi + \chi \rightarrow \bar{p} + ...,$$
$$\rightarrow e^+ + ...,$$
$$\rightarrow \gamma + ... \text{ and}$$
$$\rightarrow \bar{D} + ...$$

The $\bar{p}$, e^+ and γ from these collisions produce deviations from smooth energy spectra [5]. Therefore, the precision and simultaneous measurement of the $\bar{p}$, e^+, γ and $\bar{D}$ spectra [6] will enable us to establish whether SUSY particles (for example neutralinos) are the origin of Dark Matter. The example in this section concentrates on positrons.

Two modes are used to detect positrons. Both use the TRD for electron/proton discrimination and the TOF+Tracker for charge magnitude and sign determination. The *low energy mode* relies on the RICH for the velocity measurement while *high energy mode* uses the ECAL to further improve the selection of positrons from the hadronic backgrounds. Using these two modes overall rejection factors of better than $1/10^6$ against protons and $1/10^4$ against electrons have been obtained [7]. This allows a clean measurement of the positron spectrum up to 350 GeV. Figure 2.217 shows the Monte Carlo comparison between the generated and reconstructed spectra. Figure 2.218 shows the anticipated AMS-02 measurement of the positron spectrum in the presence of dark matter annihilation.

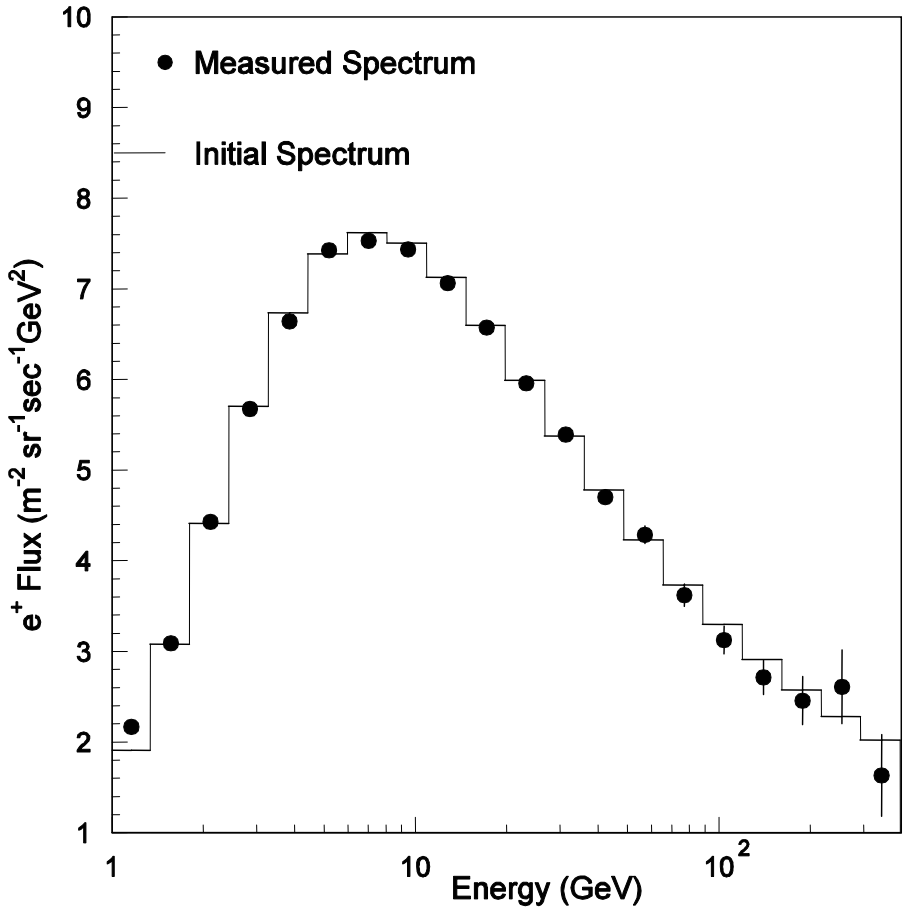

Figure 2.217: Secondary positron spectrum comparison predicted for AMS-02 .

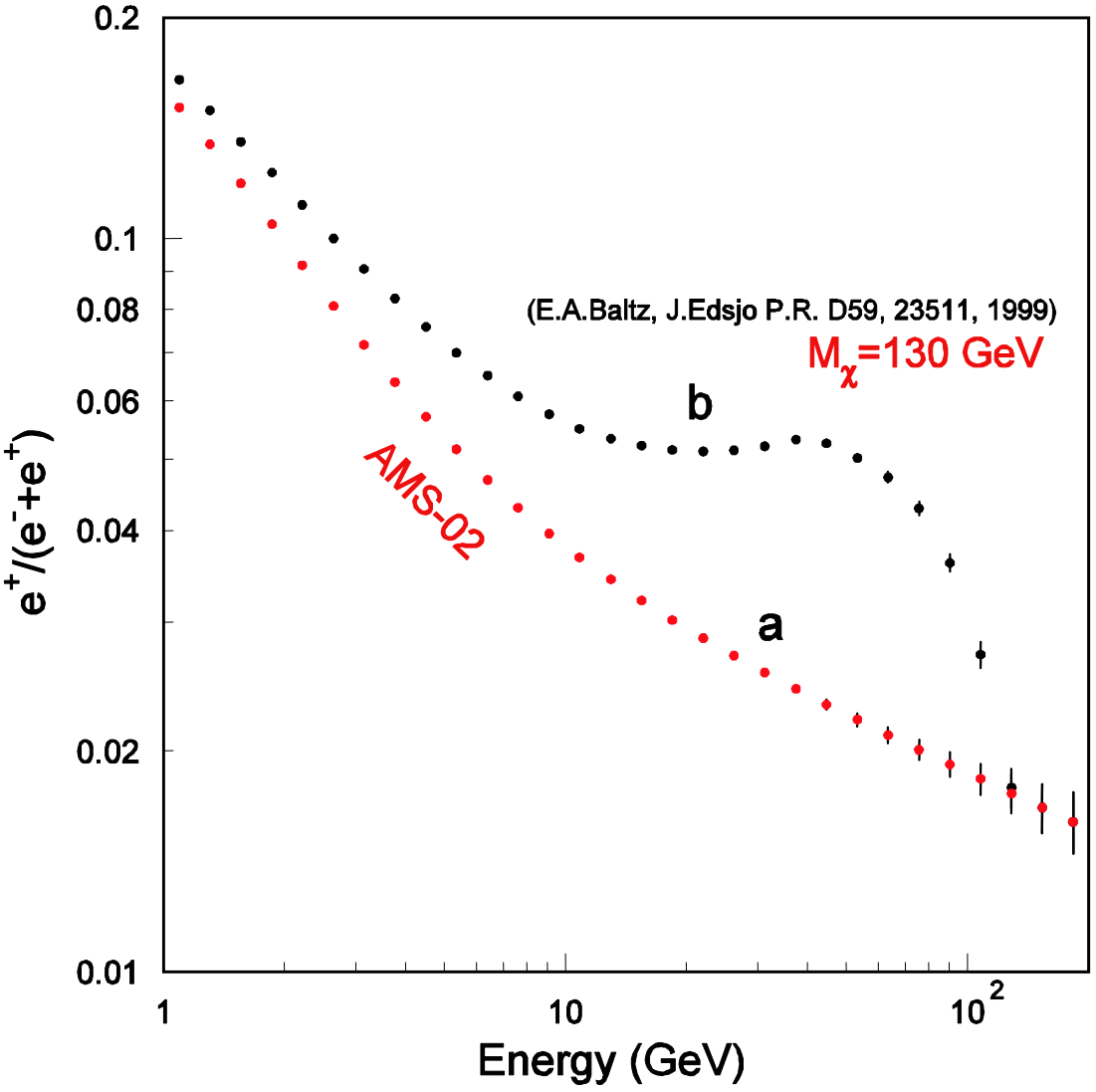

Figure 2.218: An example of AMS-02 positron spectrum measurement in the absence (a) or presence (b) of a neutralino with mass m_χ = 130 GeV.

2.12.4 Dark matter search using the antiproton spectrum

The main backgrounds to the antiproton signal are proton and electron events. Rejection factors better than 10^6 and 10^3 are correspondingly needed to allow the background free measurement of the antiproton spectrum up to energies of a few hundred GeV.

The proton background was rejected using the rigidity measurement in the tracker, while the TRD, RICH and ECAL were used to reject electrons. Figure 2.219 shows the rejection factors obtained [8]. Figure 2.220 shows the simulated antiproton spectrum measurement obtained with AMS-02 in 3 years of data taking.

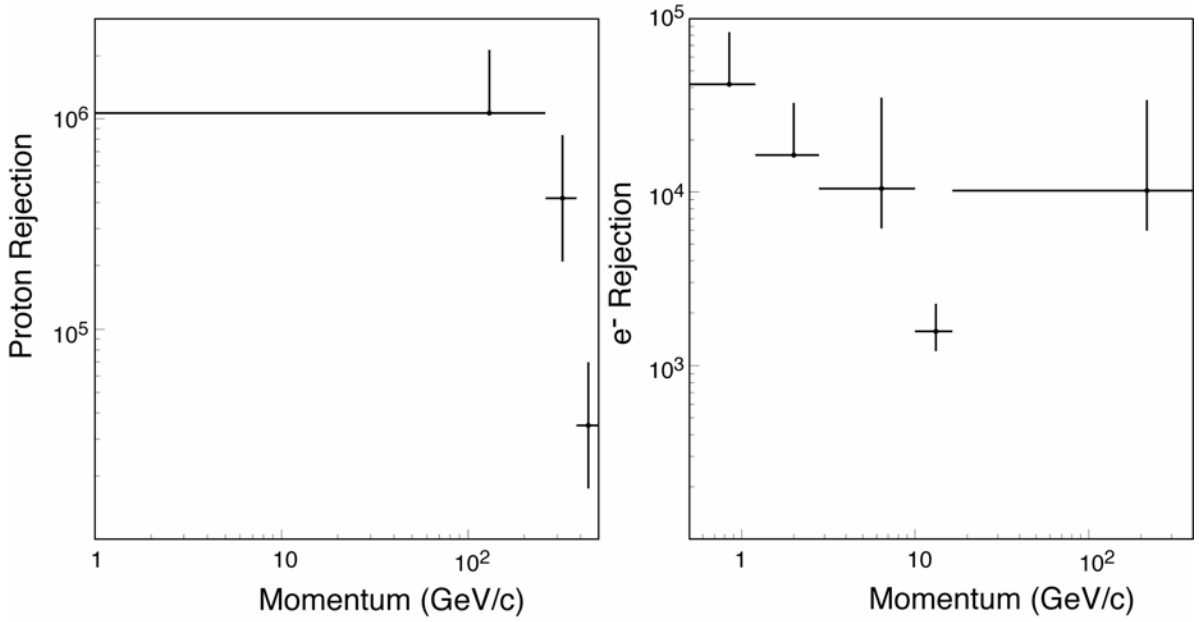

Figure 2.219: Estimated proton (left) and electron (right) rejection factors for the AMS-02 antiproton flux measurement.

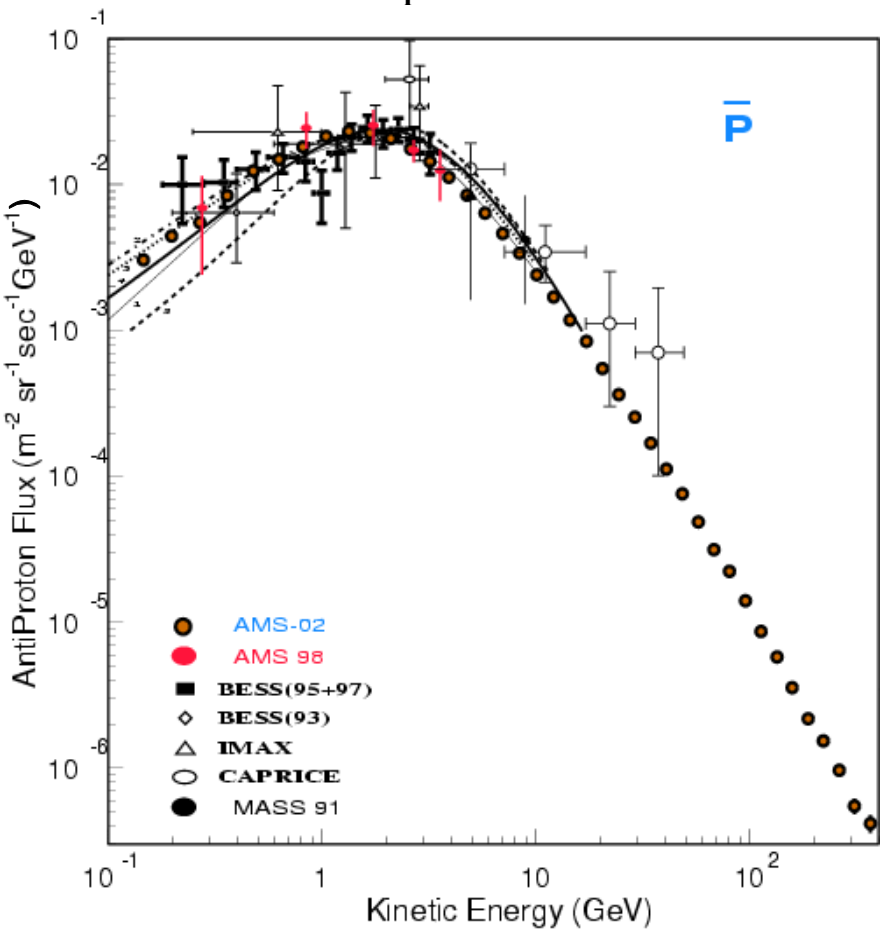

Figure 2.220: Example of a AMS-02 antiproton flux measurement together with recent experimental data [9].

2.12.5 Gamma ray spectra

Precise measurement of diffuse gamma ray fluxes may also reveal the origin of dark matter, while gamma rays originating from different sources such as active galactic nuclei (AGN) and gamma ray bursts may provide information about possible quantum gravity effects. AMS-02 will be able to measure the galactic and extragalactic diffuse gamma ray spectra up to 1 TeV [10]. In addition, up to 10 gamma ray bursts and about 500 AGN per year will be recorded.

The main backgrounds to gamma ray signals are the proton and electron (positron) events. Two distinct gamma ray signatures were exploited to estimate the capability of AMS-02 to detect gamma rays: low energy mode and high energy mode.

In low energy mode, the photon is converted in top of AMS and an electron-positron pair is detected in the AMS tracker . This method of studying cosmic γ rays is similar to the method used at DESY to study $\gamma + N \rightarrow N + e^+e^-$ reactions [11]. From the measurement of the production angles and energies of the e^+, e^- pair, QED provides excellent information on the initial direction of γ ray. In this mode photons may be detected from 1 to 200 GeV with excellent pointing accuracy, shown in Figure 2.221.

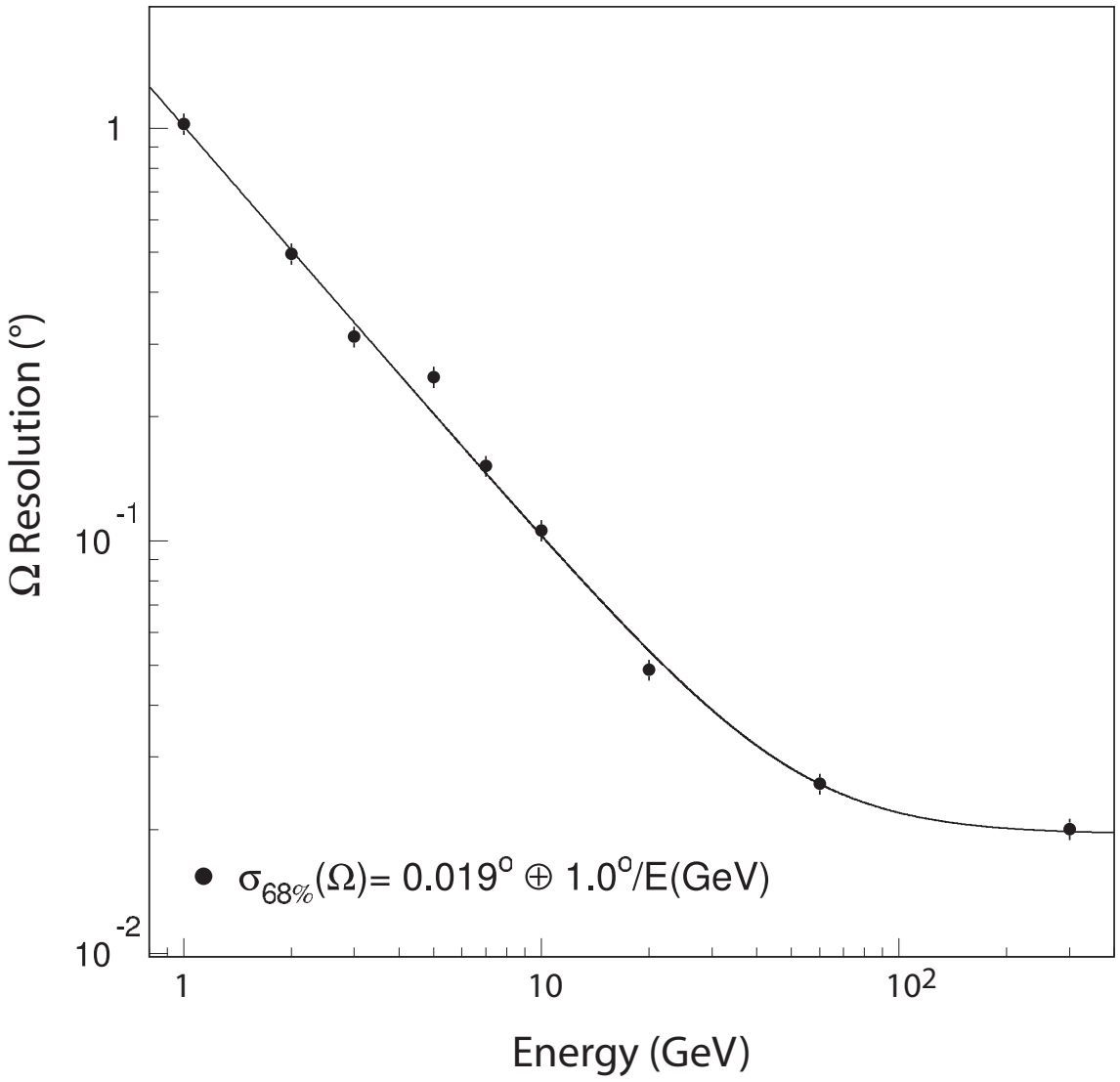

Figure 2.221: Estimated AMS-02 photon angular resolution vs. energy.

In high energy mode, the photon is detected by its characteristic shower in the electromagnetic calorimeter and an absence of charged tracks in the rest of the detector. In this mode photons may be detected from a few GeV up to TeV with an energy resolution of a few per cent and a typical angular resolution of 1 degree. Figure 2.222 shows the Monte Carlo comparison between the generated and reconstructed spectra of galactic and extragalactic γ rays up to energy of 1 TeV.

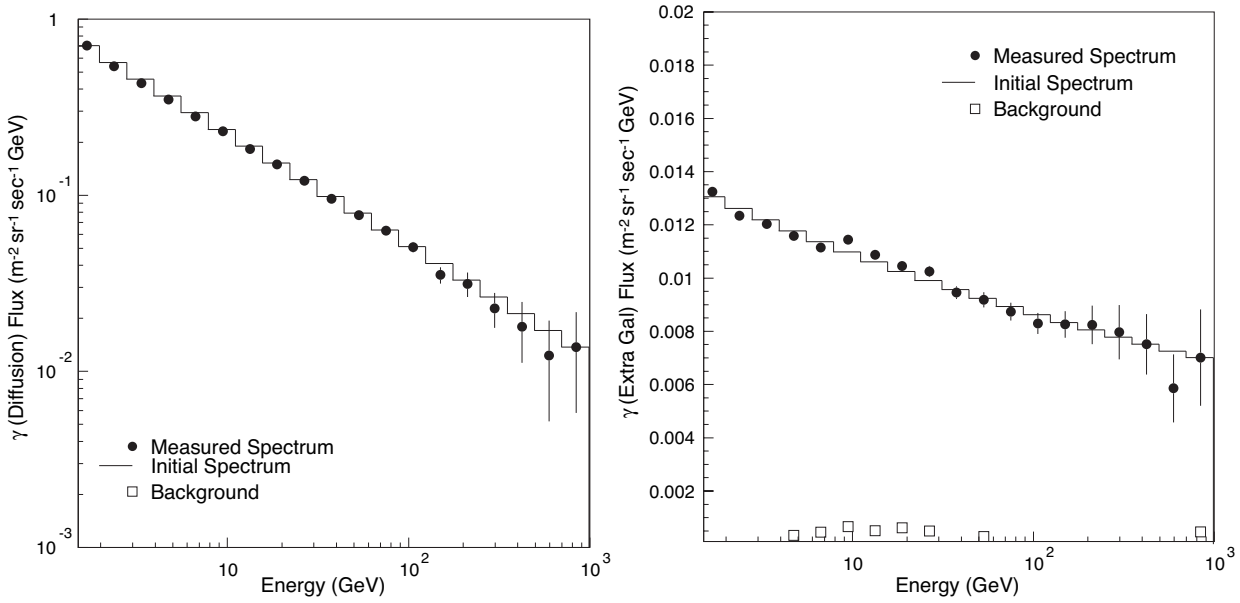

Figure 2.222: Projected AMS-02 measurements of the diffuse galactic (left) and extra-galactic (right) gamma flux [7]. Photons up to 1 TeV will be detected.

2.12.6 Cosmic Ray Spectra

AMS-02 will precisely determine the fluxes of individual elements with charge magnitude at up to at least 26 (Fe) in the energy range from 100 MeV/nucleon to 1 TeV/nucleon. Figures 2.223, 2.224 and 2.225 show the projected AMS-02 measurements of the proton, electron and He fluxes [12].

Independently of the magnet and silicon tracker, low and high energy parts of cosmic ray spectra will also be measured by the RICH and TRD respectively. Figures 2.226 and 2.227 show the AMS-02 measurements of the carbon spectrum using the RICH and of the iron spectrum based on the TRD data.

High statistics measurements of the heavy nuclei detected by AMS-02 will allow the precise measurement of the boron to carbon ratio, as shown in Figure 2.228.

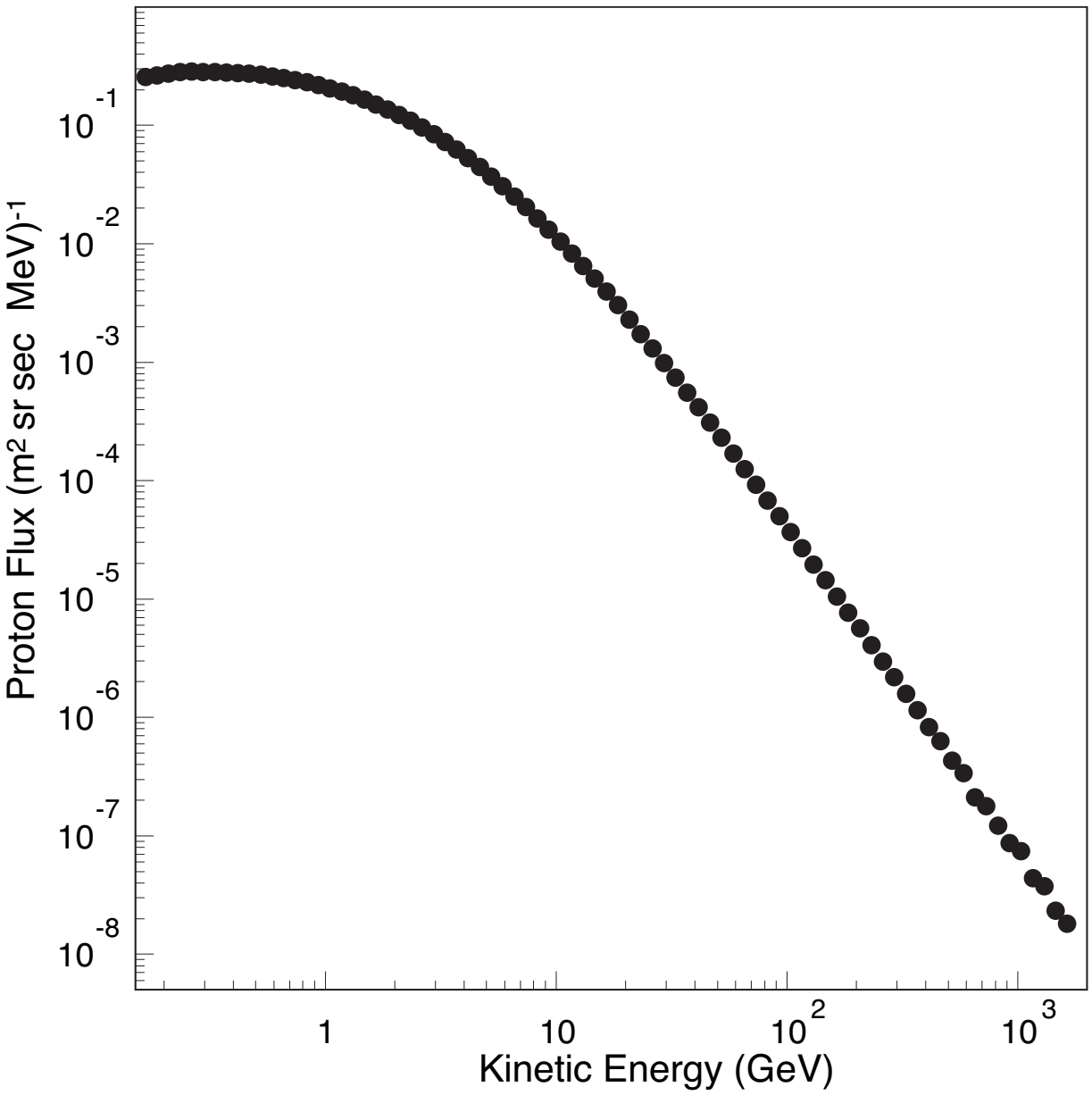

Figure 2.223: Projected AMS-02 proton flux measurement in 1 week (statistical errors not visible).

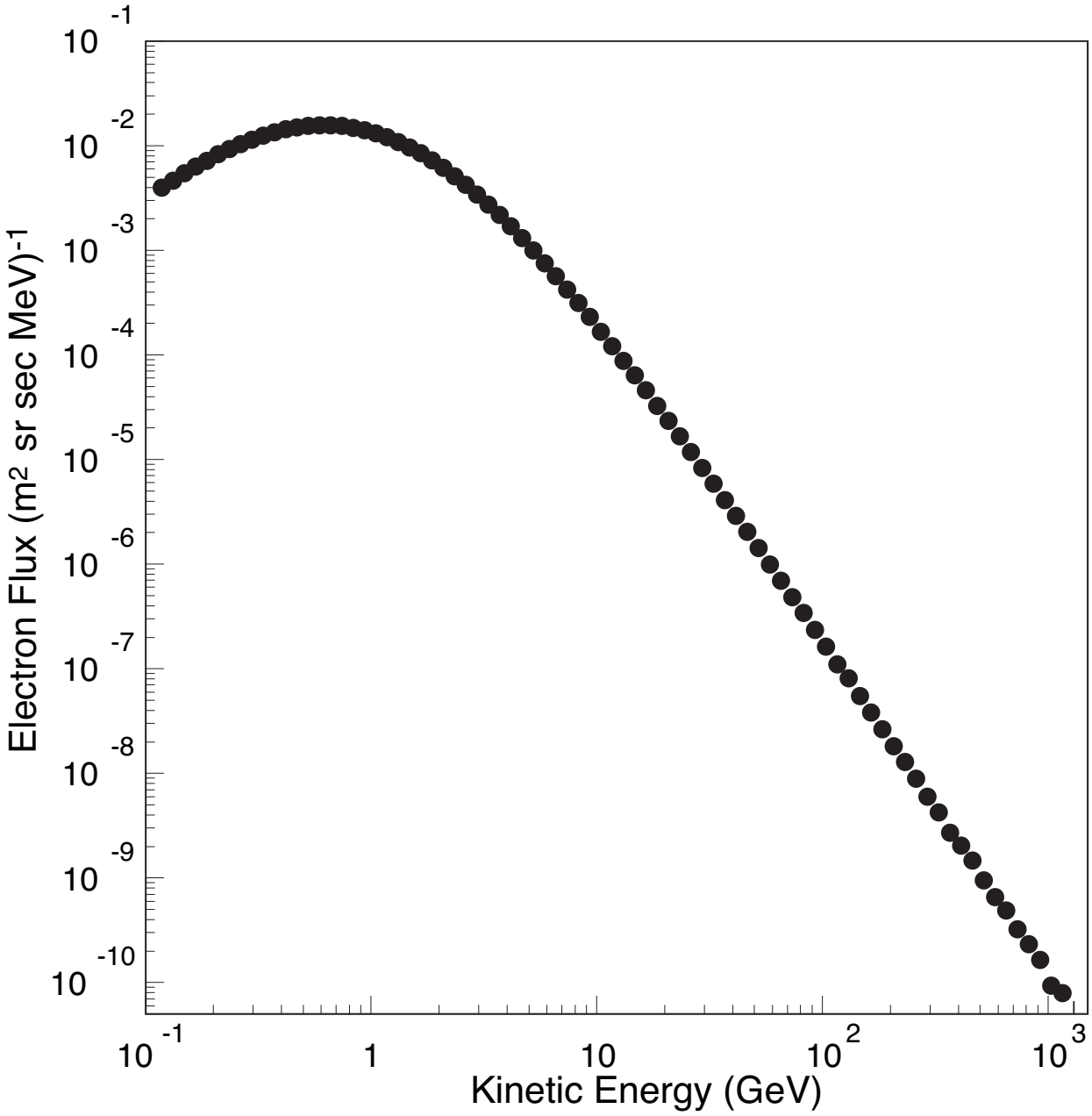

Figure 2.224: Projected AMS-02 measurement of the electron cosmic ray spectrum over 3 years.

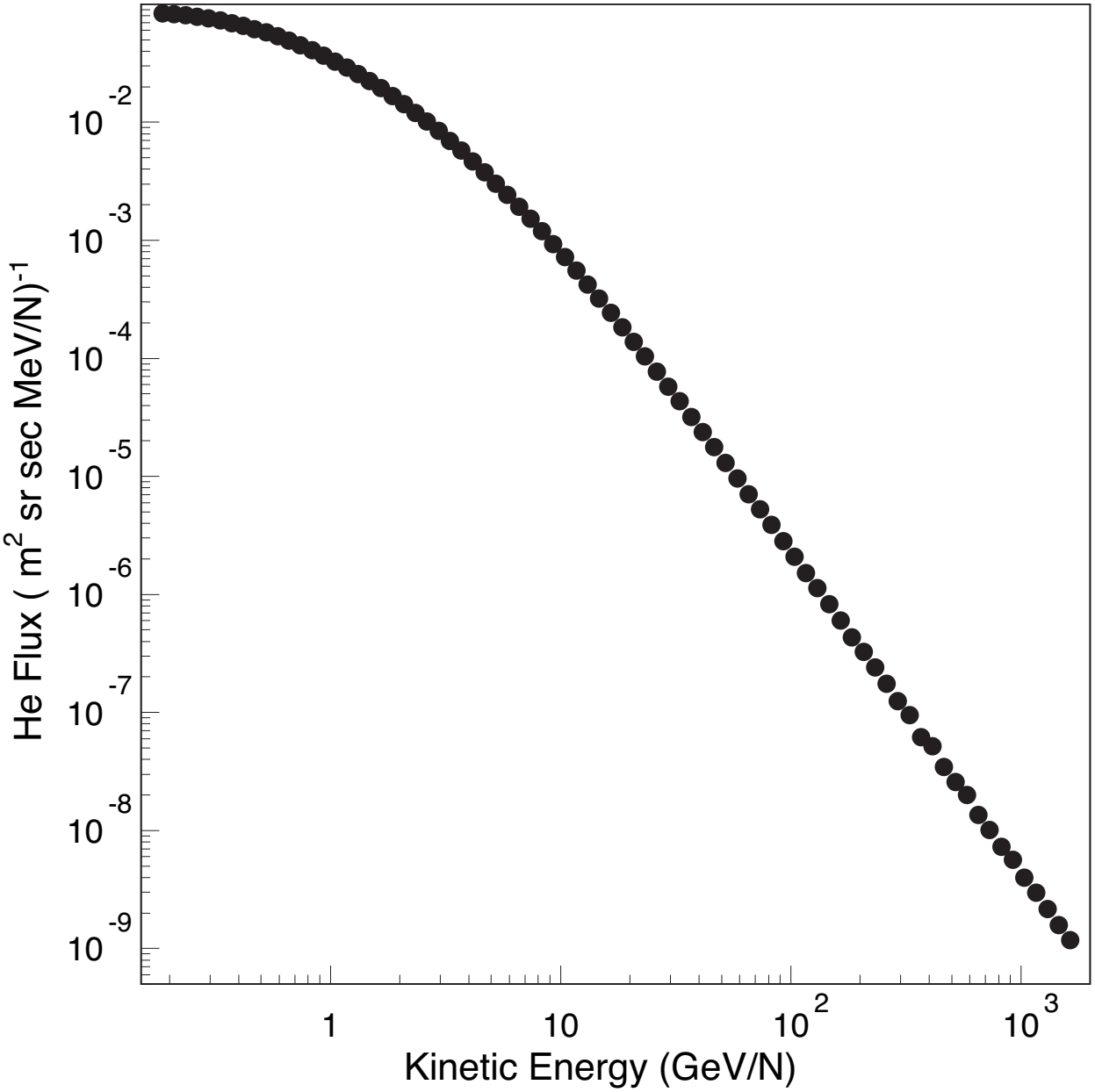

Figure 2.225: Projected AMS-02 measurement of the He flux over 1 month.

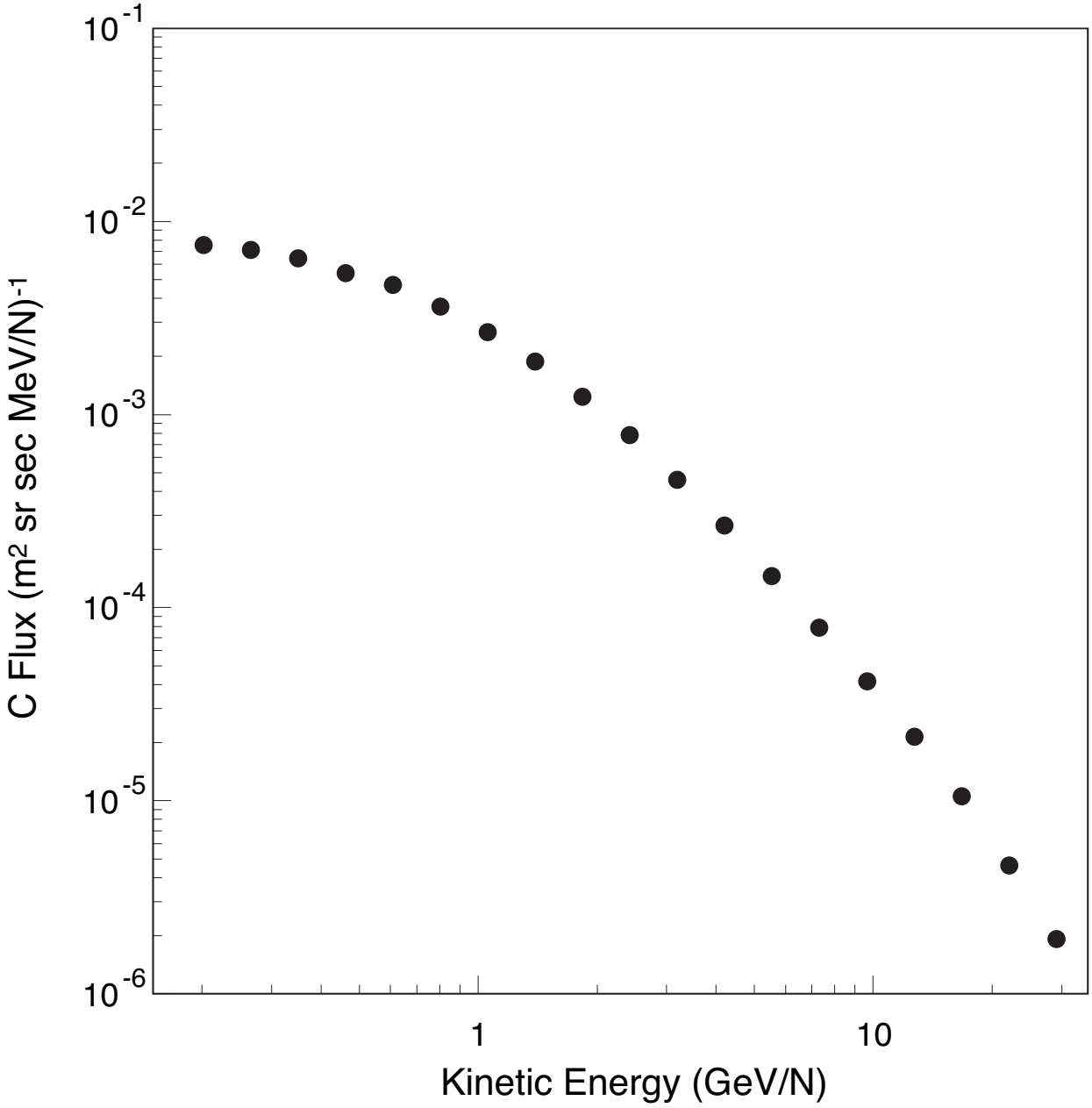

Figure 2.226: Projected AMS-02 10 day measurement of the carbon flux using the RICH. This measurement may be performed with the magnet at zero field.

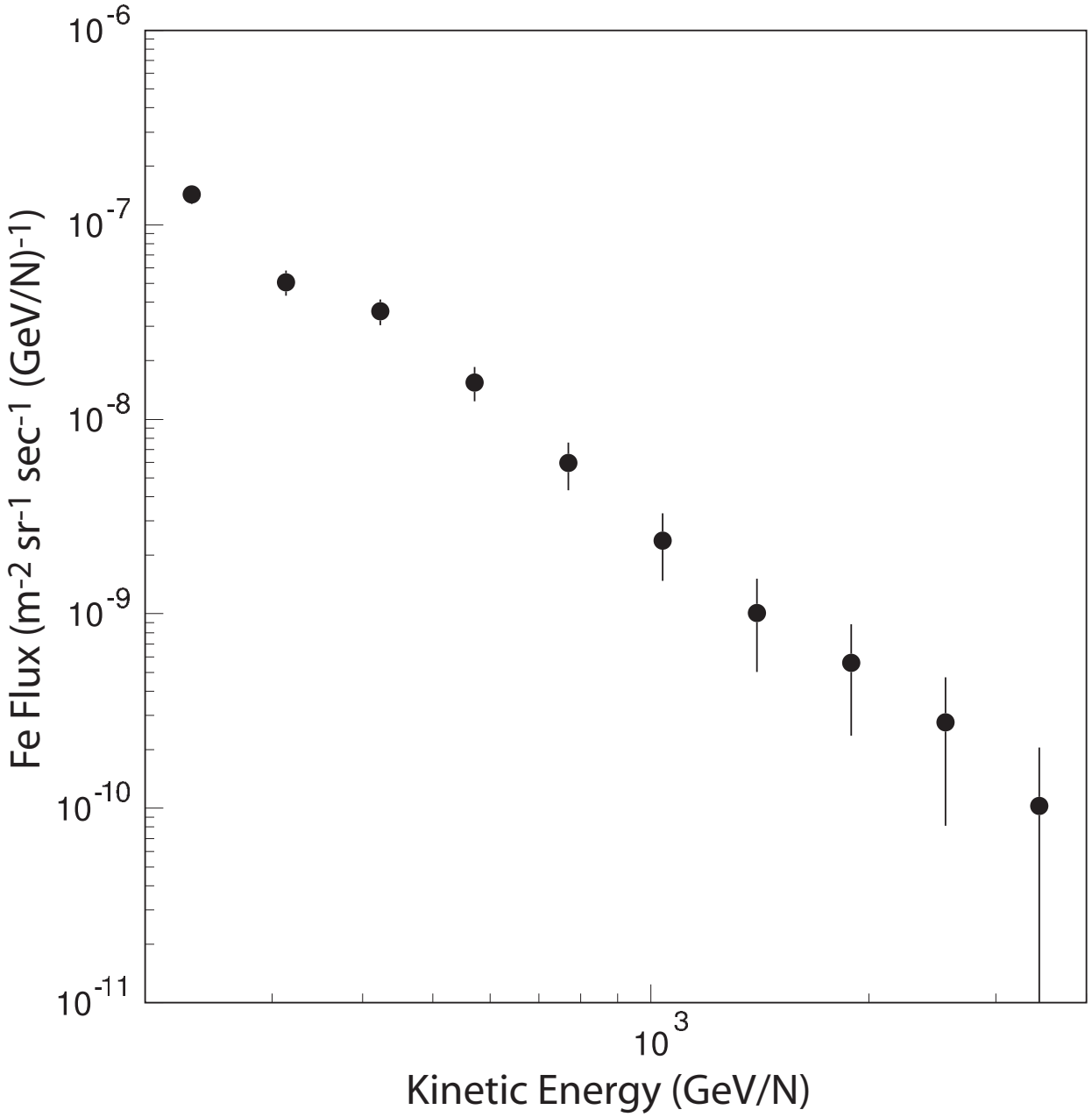

Figure 2.227: Projected AMS-02 1 year measurement of the iron flux using the TRD. This measurement may be performed with the magnet at zero field.

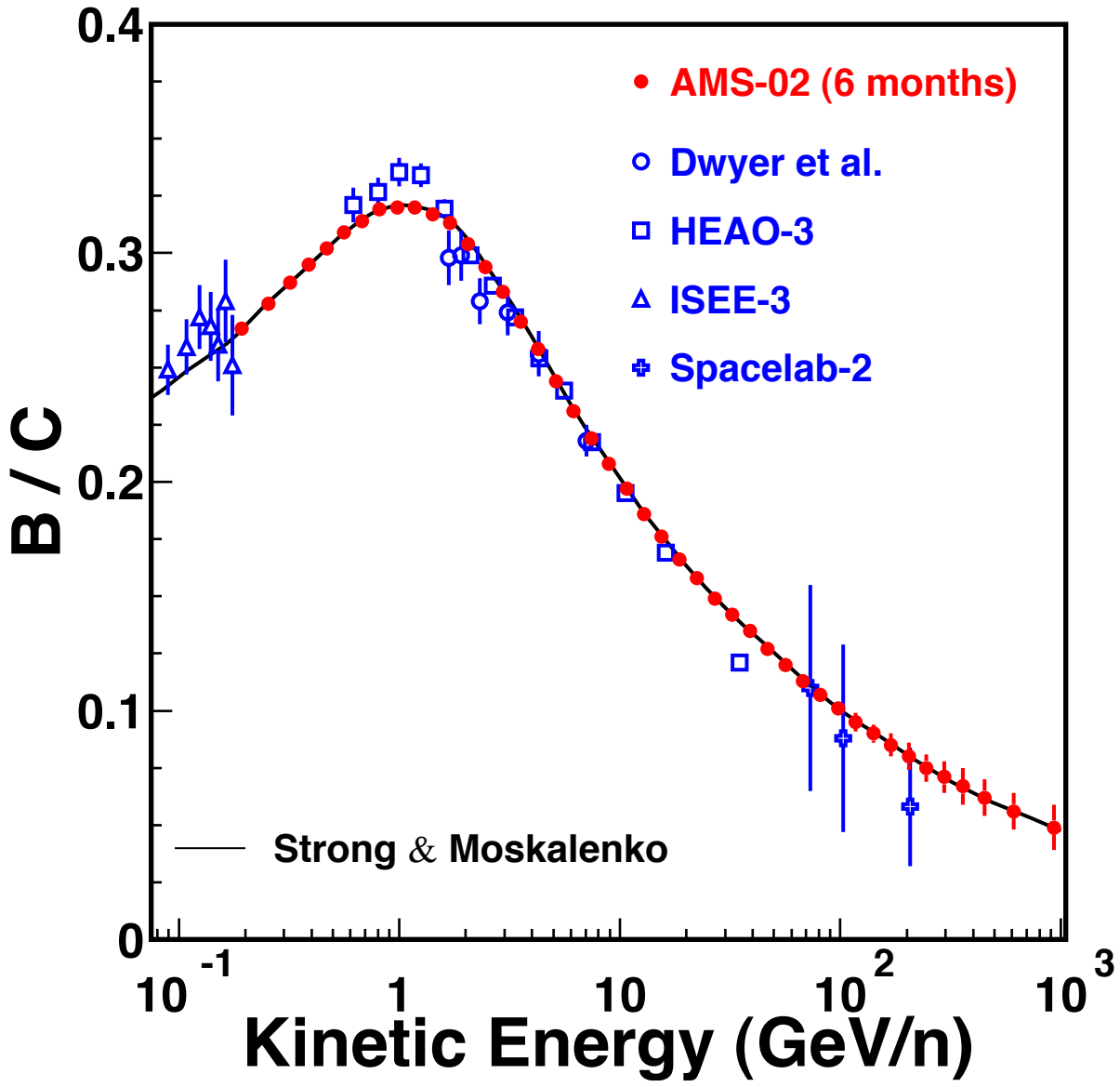

Figure 2.228: Projected AMS-02 6 month measurement of the Boron to Carbon ratio, together with recent data from different experiments [13].

2.12.7 Search for anomalously heavy nuclei

Numerous searches for anomalously heavy nuclei in cosmic rays and in the atmosphere have been conducted over the past years using balloon and satellite-born experiments as well as laser spectroscopy and geosismology [14]. A few candidate events have been found and limits on the possible flux of such events established. One of the motivations for such searches is the possible existence of strange quark matter in the form of strangelets [15]. Using more than four million He events collected with the AMS-01 detector during the STS-91 flight in June 1998, a search was performed for doubly charged anomalously heavy nuclei [16]. As shown in Figure 2.229, one event candidate was found with Z/A around 0.11. The background probability of such event is estimated at 0.1%. With the large acceptance of AMS-02 and more than 1,000 days of data collection, AMS-02 will be able to detect more than 200 such events and discover stranglets if they exist.

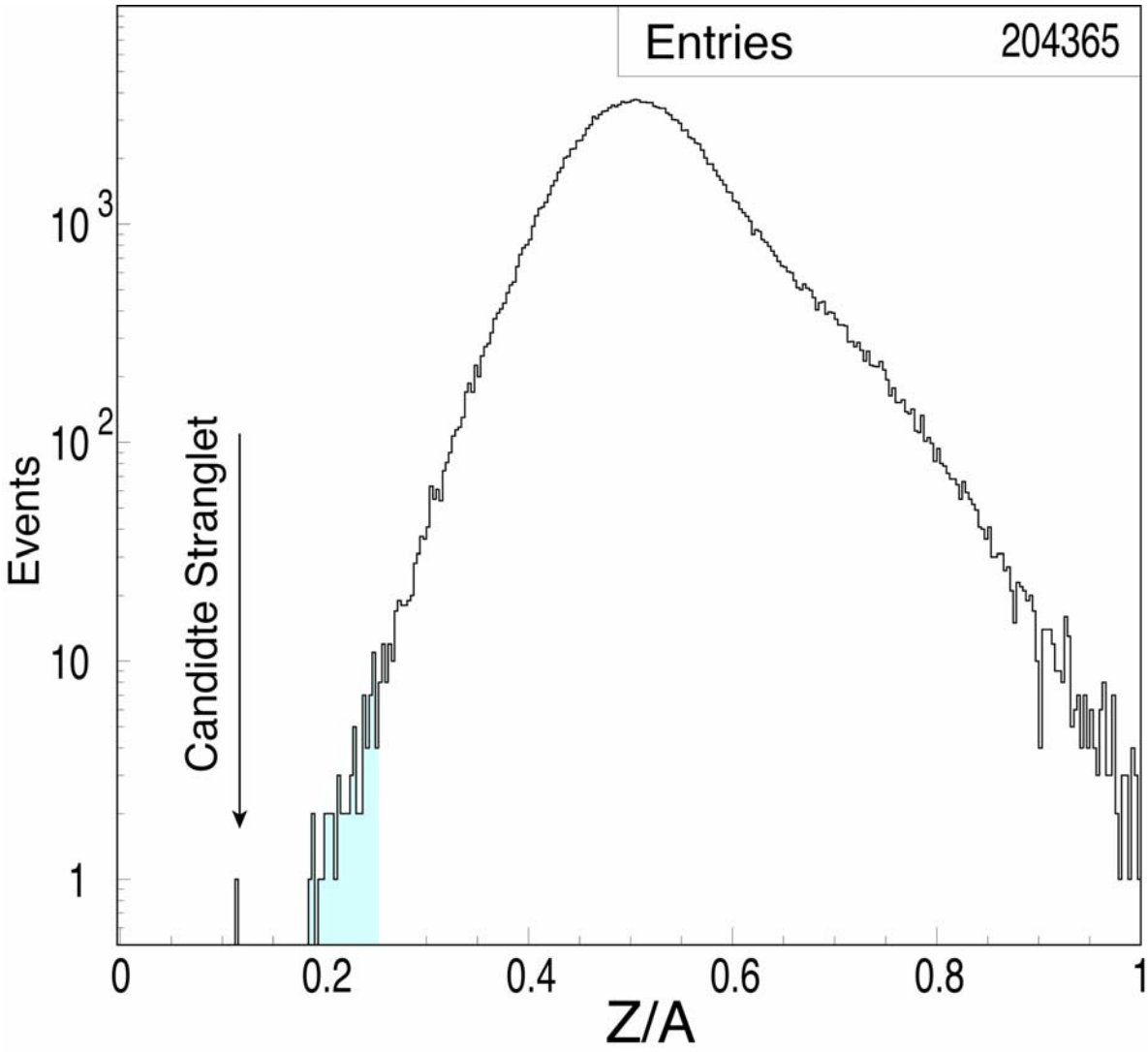

Figure 2.229: Measurement of Z/A using AMS-01 data for selected He events.

2.12.8 Measurement of $^{10}Be/^{9}Be$ ratio

The velocity resolution of the RICH measured with test beams can be seen in Figure 2.127. This implies an excellent capability for AMS-02 to separate beryllium isotopes. This ability to make a high statistics determination of the $^{10}Be/^{9}Be$ ratio would enable AMS-02 to perform one of the most important measurements in cosmic ray physics: a highly accurate determination of the cosmic ray confinement time in the galaxy and a determination of the mean density of interstellar material traversed by cosmic rays. Figure 2.230 shows the result projected using the AMS-02 RICH over one year of data taking.

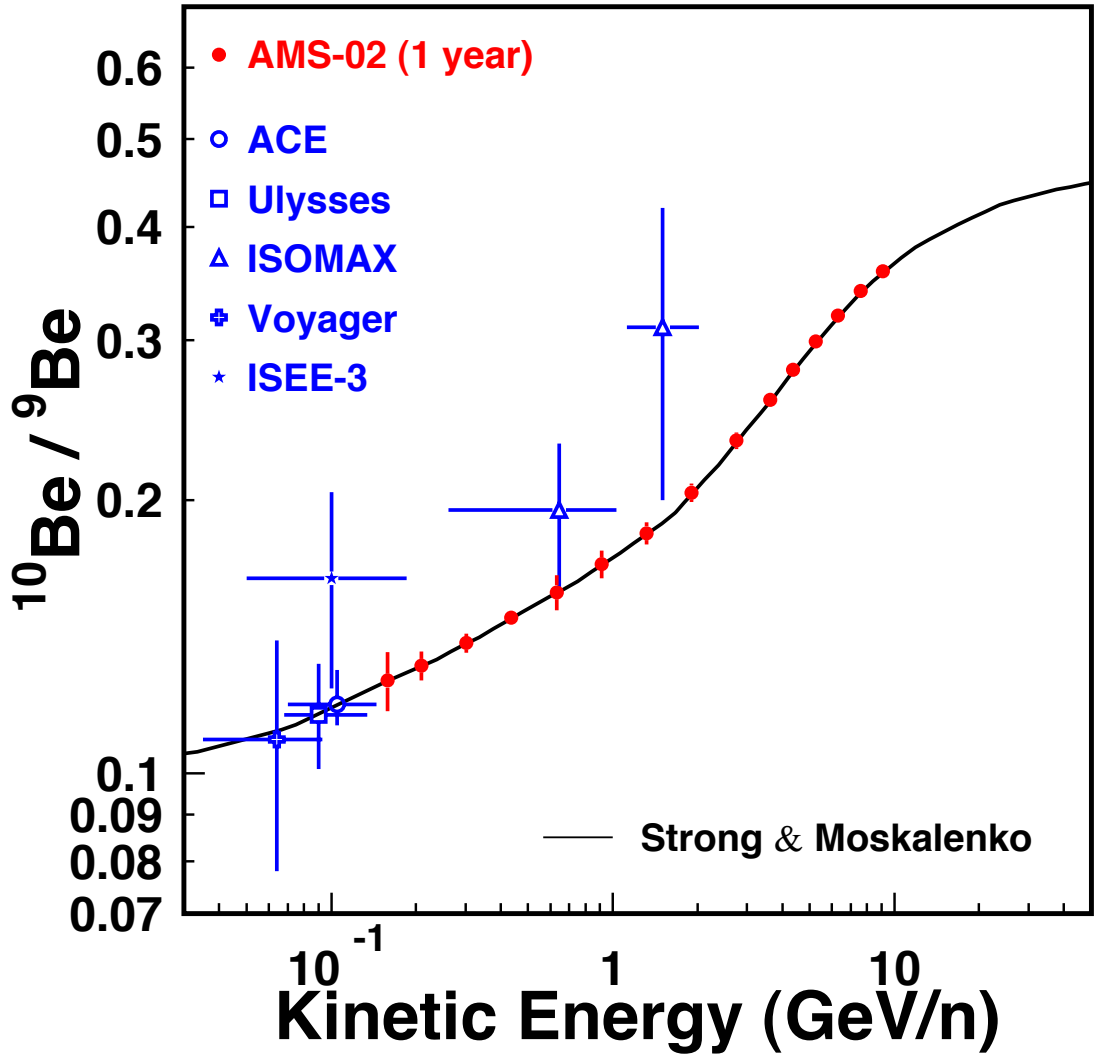

Figure 2.230: Projected AMS-02 1 year measurement of the ^{10}Be / ^{9}Be ratio energy dependence compared with a diffusion/convection model prediction (curve) together with the results from satellite measurements [17].

2.12.9 References

[1] A.D. Sakharov, JETP Letters **5** (1967) 24;
A.D. Dolgov and Ya.B. Zeldovich *et al.*, Rev. Mod. Phys. **53** (1981) 1;
E.W. Kolb and M.S. Turner, Ann. Rev. Nucl. Part. Sci. **33** (1983) 645;
A.D. Dolgov, Phys. Rep. **222** (1992) 309;
D. Comelli *et al.*, Nucl. Phys. **B412** (1994) 441;
A.D. Dolgov and J. Silk, Phys. Rev. **D47** (1993) 4244;
M.Yu. Khlopov, Gravitation and Cosmology **4** (1998) 69-72;
A.G. Cohen *et al.*, Ap. J. **495** (1998) 539-549;
J. Rehm and K. Jedamzik *et al.*, Phys. Rev. Lett. **81** (1998) 3307-3310;
A.D. Dolgov, Lec.at 25th ITEP Winter School, (1997), hep-ph/9707419;
W. Kinney *et al.*, Phys. Rev. Lett. **79** (1997) 2620;
M.Yu. Khlopov *et al.*, Phys. Rev. **D62** (2000) 83-505;
J. Rehm and K. Jedamzik *et al.*, (2000) arXiv:astro-ph/0006381.

[2] L.Bergström, Rep. Prog. Phys. **63**(2000) 793-841;
J. Ellis *et al.*, Phys. Lett. **B214** (1998) 3;
M. Turner and F. Wilczek, Phys. Rev. **D42** (1990) 4;
E.A. Baltz and J. Edsjo, Phys. Rev. **D59** (1999) 23511;
T. Moroi and L. Randall, Nuc. Phys. **B570** (2000) 455.

[3] R. Brun *et al.*, GEANT3, *CERN-DD/EE/* **84-1** (Revised 1987).

[4] G. Badhwar *et al.*. Nature **274** (1978) 137;
A. Buffington *et al.*, Ap. J. **248** (1981) 1179;
R.L. Golden *et al.*, Ap. J .**479** (1997) 992;
J. Alcaraz *et al.*, Phys. Lett. **B461** (1999) 387;
M. Sasaki *et al.*, 27th ICRC (2001) 1711;
Juan Garcia-Bellido, private communication, gratefully received.

[5] E.A. Balitz, J.Edsjo, Phys. Rev. **D59** (1999) 23511;
S.W. Barwick *et al.,* Ap. J. Lett. **482** (1997) L191;
S.Coutu *et al.,* Astropart.Phys. **11** (1999) 429;
S.Coutu *et al.,* 27th ICRC (2001).

[6] P. Salati, *et al.*, Nucl.Phys.Proc.Suppl. **81** (2000) 37.

[7] V. Choutko, G. Lamanna and A. Malinine, Int. J. Modern Phys. **A17** (2002) 1817.

[8] V. Choutko, Nucl. Phys. **B** (Proc. Suppl.) **113** (2002) 170.

[9] K. Yoshimura *et al.*, Phys. Rev. Lett. **75** (1995) 3792;
M. Hof *et al*., Ap. J. **467** (1996) 33;
H. Matsunaga *et al.*, Phys. Rev. Lett. **81** (1998) 4052;
S. Orito *et al.*, Phys. Rev. Lett. **84** (2000) 1078;
J.W. Mitchell *et al*., Phys. Rev. Lett. **76** (1996) 3057;
M. Boezio *et al.*, Ap. J. **487** (1997) 415;
M. Boezio *et al.*, Ap. J. **561** (2001) 787;
J. Alcaraz *et al.*, Phys. Rep. **366/6** (2002) 331.

[10] R. Battiston *et al.*, Astropart.Phys. **13** (2000) 51.

[11] J.G. Asbury *et al.,* Phys. Rev. Lett. **18**, 2 (1967) 65;
J.G. Asbury *et al.,* Phys. Rev. Lett. **19**, 15 (1967) 869;
U. Becker *et al.,* Phys. Rev. Lett. **21**, 21 (1968) 1504;
H. Alvensleben *et al.,* Phys. Rev. Lett. **27**, 13 (1971) 888.

[12] G.D Badwar and P.M. O'Neill, Adv. Space res. **17/2** (1996) 7;
A.J. Tylka, W.F. Dietrich, and P.R. Boberg, IEEE Transactions Nuc. Sci. **44** (1997) 2140.
B. Wiebel-Sooth, P.L. Biermann and H. Meyer, A & A **330** (1998) 389.

[13] R. Dwyer, P. Meyer, Ap. J. **322** (1987) 981;
J.J. Engelmann *et al.*, A&A **96** (1990) 223;
K.E. Krombel, M.E. Wiedenbeck, Ap. J. **328** (1988) 940;
S.P. Swordy *et al.*, Ap. J. **349** (1990) 625;
A.W. Strong and I. Moskalenko, ApJ **509** (1998) 212.

[14] W.R. Binnis *et al.*, Ap. J. **347** (1989) 997;
P.H. Fowler *et al.*, Ap. J. **314** (1987) 739;
M. Ichimura *et al.*, Nuovo Cimento **106A** (1993) 843;
P. Muller *et al.*, (2003) arXiv:nucl-ex/0302025;
P.B. Price *et al.*, Phys. Rev. **D18** (1978) 1382;
T. Saito *et al.*, Phys. Rev. Lett. **65** (1990) 2094;
E.K. Shirk and P.B. Price, Ap. J. **220** (1978) 719;
David P. Anderson *et al.*, (2002) arXiv:astro-ph/0205089.

[15] P.H. Fowler *et al.*, Ap. J. **314** (1987) 739;
J. Madsen, Phys. Rev. Lett. **87** (2001) 172;
J. Sandweiss J. Phys. G **30** (2004) 51

[16] V. Choutko, 28th ICRC **4** (2003) 1765.

[17] W.R. Binns *et al.*, 26th ICRC **3** (1999) 9;
J.J. Connell, 1998, Ap. J. **501** (1998) L59;
G.A. de Nolfo *et al.*, 27th ICRC **5** (2001) 1659;
T. Hams *et al.*, 27th ICRC **5** (2001) 1655;
A. Lukasiak *et al.*, 26th ICRC **3** (1999) 41;
M.E. Wiedenbeck, 19th ICRC **2** (1985) 84.

Conclusion

AMS-02 is the first precision particle physics experiment on the space station. With its acceptance, resolution and ability to study different particles and nuclei over 3 to 5 years of data taking, it provides an opportunity to accurately explore new regions of physics.

Acknowledgements

The construction of AMS-02 is an undertaking of many individuals and organizations. The support of NASA and the U.S. Dept. of Energy has been vital in the inception, development and fabrication of the experiment. The interest and support of Daniel S. Goldin, former NASA Administrator, A. Yu. Rumyantsev, head of the Federal Agency for Atomic Energy, Russia, Xu Guanhua, Minister of Science and Technology, China, and Jörg Feustel-Büechl, European Space Agency is gratefully acknowledged. The dedication of Dr. John O'Fallon, Dr. Robin Staffin, Dr. A. Byon-Wagner and Dr. P.K. Williams of U.S. DOE, our Mission Management team, Dr. Douglas P. Blanchard, Mr. Mark J. Sistilli and Mr. James R. Bates, NASA, Mr. Kenneth Bollweg and Mr. T. Martin, Lockheed-Martin, the support of the space agencies from Germany (DLR)[1], Italy (ASI), France (CNES), Spain (CDTI) and China (CALT) and the support of CSIST, Taiwan, have made the construction possible.

The support of GSI-Darmstadt, particularly of Dr. Reinhard Simon made it possible for us to test electronics components for radiation effects. The support ESA, including Martin Zell, Jean Jamar and Wolfgang Supper, will enable the overall thermal vacuum test at ESTEC.

The support of INFN, Italy, IN2P3, Region Rhône-Alpes and Haute Savoie, France, CIEMAT and CICYT, Spain, LIP, Portugal, CHEP, Korea, the Chinese Academy of Sciences, the National Natural Science Foundation and the Ministry of Science and Technology of China, Academia Sinica, Taiwan, the U.S. NSF, M.I.T., ETH-Zűrich, the University of Geneva, National Central University, National Space Program Office, National Chaio Tung University and National Cheng Kung University, Taiwan, Moscow State University, Southeast University, Nanjing, Shanghai Jiao Tong University, Sun Yat-sen University, Guangzhou, Shandong University, Jinan, RWTH-Aachen, the University of Turku and the University of Technology of Helsinki, is gratefully acknowledged.

We are also grateful for the strong support and interest shown from the private sector, including Dr. E. Ettlinger, Linde, Dr. R. Herzog, ILK, Dresden, Mr. J. Ross, Mr. S. Milward and Mr. S. Harrison of SCL, Culham, UK, Mr. M. Molina, CGS, Milan, Mr. F. Petroni, CAEN, Viareggio, Mr. A. Posada, CRISA (Astrium), Madrid, Ing. A. Pontetti, G&A Engineering, Italy, Dr. E.A. Werner and Dr. J. Krieger, ISATEC, Aachen, and Dr. H. Bieri, Bieri Engineeering, Switzerland.

We thank Professors A. De Rujula, J. Ellis, A. Guth, L. Maiani, for many interesting discussions and support.

[1] Including support under 1KZ 50 009902 4.

Appendix A: Acronyms and Abbreviations

A	Ampere, (in combination) one of a set of redundant elements
AAS	AMS Antimatter Simulator
ACBSP	ISS S-Band receiver
ACC	Anti Coincidence Counters
ACOP	AMS (or Astronaut, depreciated) Crew Operations Post
ADC	Analog to Digital Converter
AIS	Antimatter Investigation System
AMS	Alpha Magnetic Spectrometer
AMS-01	AMS engineering flight on the space shuttle
AMS-02	AMS mission on the ISS
APCU	Assembly Power & Control Unit
APS	Automated Payload Switch
ASIC	Application Specific Integrated Circuit
AST	Amica Star Tracker
ASTE	Amica Star Tracker Electronics board
ASTE	AST Electronics
ASTP	Amica Star Tracker Power board
AUX	Auxiliary
AWG	American Wire Gauge
B	sometimes Byte, sometimes Bit
BCS	Berthing Cue System, also EBCS
BOL	Beginning of Life
C	Cryomagnet (in combination), Cold (in combination)
C & D	Commands and Data
CAB	Cryomagnet Avionics Box
CAEN	Costruzioni Apparecchiature Elettroniche Nucleari , S.p.A.
CAN	Controller Area Network
CC	Cryocooler (in combination)
CCBPC	CCEB Backplane, Control
CCBPP	CCEB Backplane, Power
CCBT	CC 3D Hall Probe and PTS readout
CCDC	CC DC-DC Converter board
CCEB	Cryocooler Electronics Box
CCIF	CC Interface Board
CCMDM	Command & Control MDM
CCMO	CC Monitor & Oscillator
CCPA	CC Power Amplifier
CCS	Cryomagnet Charging System
CCSC	Cryomagnet Controller and Signal Conditioner
CDD	Cryomagnet Dump Diodes
CDDC	Command Distributor, Data Concentrator
CDP	Common Digital Part
CERN	European Center for Nuclear Research
CGS	Carlo Gavazzi Space SpA, I-Milano
CGSE	Cyrogenic Ground Support Equipment
CL, C.L.	Confidence Limit
CP	Charge Parity
cPCI	Compact PCI bus format
CRISA	Computadoras, Redes e Ingenieria, S.A.
CSP	Cryomagent Self Protection circuits
CVB	Cryomagent Valve Box

D	deuteron
DAC	Digital to Analog Converter
DAQ	Data Acquisition
DC	Direct Current
DC-DC	DC to DC converter
DDRS	Digital Data Recording System
dE/dX	Energy loss when traversing matter
DESY	Deutsches Elektronen-Synchrotron
DSP	Digital Signal Processor
DTS	Digital Temperature Sensor (e.g. DS18S20)
E	ECAL (in combination)
E-Crate	ECAL Crate
EBCS	External Berthing Cue System
EBP	E-Crate Backplane
ECAL	Electromagnetic Calorimeter
EDR2	ECAL Data Reduction board (contains two EDR)
EHV	ECAL HV Brick
EM	Engineering Model
EMC	Electromagnetic Compatibility
EMI	Electromagnetic Interference
EOL	End of Life
EPD	ECAL Power Distribution box
EPSFE	ECAL Power Supply for Front End board
ESA	European Space Agency
ESTEC	ESA European Space Research and Technology Centre
ETRG	ECAL Trigger board
EVA	Extravehicular Activity
F/O	Fiber optic
FE	Front End
FIFO	First In, First out
FM	Flight Model
FS	Flight Spare
G	Gauss (0.1 mT)
g	9.8 m/s/s, gram
GPS	Global Positioning System
GPSE	Interface for GPS (Topstar 3000D ?)
GSC	Ground Support Computers
GSE	Ground Support Equipment
GSFC	Goddard Space Flight Center
GSI	Geschellschaft für Schwerionenforschung
H	Hot (in combination)
HCOR	HRDL Communication Outage Recorder
HOSC	Huntville Operations and Science Center
HRDL	High Rate Data Link
HRFM	HRDL Frame Multiplexer
HRM	HRDL Modem
HV	High Voltage
I	Current
ICD	Interface Control Document
IFP A	Interface Panel A
ISPR	ISS Standard Payload Rack
ISS	International Space Station

IVT	Interface Verification Test
J	DAQ or Global (in combination)
J-Crate	Main Computer and Interface Crate
JBP	J-Crate Backplane
JBU	JMDC 2*1GB Memory Buffer
JHIF	Redund HRDL (ISS)=JFOM + single RS422(STS)=J422 Interfaces
JIM-AMSW&1553	JMDC Interface to AMSWire & LRDL via JLIF (ISS) & 1553 (STS)
JIM-CAN	JMDC Interface to CAN
JIM-HRDL/422	JMDC Interface to HRDL (ISS) or RS422 (STS) via JHIF
JINF	DAQ Intermediate Node, Front End
JINJ	DAQ Intermediate Node
JINR	DAQ Intermediate Node, RICH
JLIF	Redundant LRDL (1553)=J1553 Interfaces
JLV1	Level-1 trigger processor
JMDC	Main DAQ Computer
JPBP	JPD backplane
JPD	J- and JT-Crate Power Distribution box
JPIF	DC-DC & M&C for JHIF & JLIF
JPJT	DC-DC & M&C for JT
JPMD	DC-DC & M&C for 2 JMDC's
JPSC	DC-DC & M&C for USCM, JPD internals
JSBC	JMDC Single Board Computer
JSC	Johnson Space Center
JT-Crate	Trigger & DAQ Crate
JTBP	JT-Crate Backplane
JTBX	fast trigger signal fan in/out & logic.
JTPD	Trigger Power Distributor (suppressed)
K	degrees Kelvin
KSC	Kennedy Space Center
kW	1000 Watt
l	liter, litre
LCTL	Laser Alignment control board (was LAC)
LDDR	Laser Alignment driver boards (was LAD)
LM	Lockheed-Martin
LHe	Liquid helium
LHP	Looped Heat Pipe
LN	Liquid nitrogen
LRDL	Low Rate Data Link
LSS	Large Space Simulator
LV	Low Voltage
LVDS	LV Differential Signaling
M	Mass, Monitor & Control (in combination)
M-Crate	Monitor & Control Crate
M&C	Monitor and Control
MDM	Multiplexer/Demulitplexer
MIP	Minimum Ionizing Particle
MLI	Multi-Layer Insulation
MLP	Mobile Launch Platform
MMO	NASA AMS Mission Management Office
MOSFET	Metal Oxide on Silicon Field Effect Transistor
MPD	Monitor & Control Power Distributor
MSFC	Marshall Space Flight Center

NASA	National Aeronautics and Space Agency
NBL	Neutral Buoyancy Lab
P	momentum, pressure, probability, (in combination) Power, Port, Primary
p	proton, momentum
PAS	Payload Attach System
PCA	Printed Circuit Assembly
PCB	Printed Circuit Board
PCS	Portable Control System laptops
PDB	Power Distribution Box (disfavored) – see PDS
PDS	Power Distribution System
PLMDM	Payload MDM
PMT	Photo Multiplier Tube
POCC	Payload Operations and Control Center
PPS	Passive Phase Separator
PRLA	Payload Retention Latch Actuator
PTS	Platinum Temperature Sensor (e.g. PT100)
PVGF	Power and Video Grapple Fixture
Q	charge
QM	Qualification Model
R	Rigidity, RICH (in combination), Ram
R-Crate	RICH Crate
RD	Reference Document
REPD	RICH & ECAL Power Distribution box (contain EPD & RPD)
RHV	RICH HV Brick
RICH	Ring Imaging Cerenkov detector
ROEU	Remotely Operated Electrical Umbilical
RPD	RICH Power Distribution
RPDA	Remote Power Distribution Assembly
S	(in combination) Scintillator (i.e. TOF and ACC), Starboard, Secondary
S-Crate	Scintillator (TOF & ACC) Crate
S9048	dual DC-DC(+-2.5V)
S9051	dual DC-DC(+-2.5V, +5.6V)
S9052	dual DC-DC(+-5.6V)
S9053	dual DC-DC(+-3.4V), MOSFETed
S9053I	dual DC-DC(+-3.4V)
S9053U	dual DC-DC(+-3.8V), Dioded
S9054	dual DC-DC(+5.2V)
S9054D	dual DC-DC(+5.2V), Dioded
S9055	dual DC-DC(+-6V,+120V), Dioded
S9056	dual DC-DC(+-5V,+120V)
S9057	dual DC-DC(+3.6V,-2.6V)
S9057E	dual DC-DC(+3.8V,-2.8V)
S9074	dual DC-DC(+3.4V,+5.6V)
SBP	S-Crate Backplane
SCL	Space Cryomagnetics Ltd
SDR2	FE DAQ for S-Crate, 2 Redund, CDP.
SFEA2	Scintillator FE, time measure of ACC & TOF, board
SFEC	Scintillator FE, charge measurement, board
SFET2	Scintillator FE, time measurement TOF, quad, board
SFHe	Superfluid helium
SHV	Scintilator HV Brick
SOC	Science Operations Center

SPD	Scintillator Power Distribution box
SPOE	Standard Payload Outfitting Equipment
SPT2	ToF pretrigger
sr	steradian
SRMS	Shuttle Remote Manipulator System (arm)
SSRMS	Space Station Remote Manipulator System (arm)
STS	Space Transportation System (a.k.a. Space Shuttle)
T	Tesla, Silicon Tracker (in combination)
T-0	Instant of lift off, also electrical connection between Shuttle & Earth, disconnected at time T-0.
T-Crate	Tracker Crate
TBC	To Be Confirmed
TBD	To Be Defined
TBP	T-Crate Backplane (S9015)
TBR	To Be Reviewed
TBS	Tracker Bias supply regulator (12 ladders) (S9068)
TCS	Thermal Control System
TDC	Time to Digital Converter
TDR2	FE DAQ for 2* (Tracker ladders on non-redund CDP) (S9018)
TDRS	Tracking and Data Relay Satellite
TFE	Tracker FE boards (hybrids) for –S and –K sides
TMP	Themo-Mechanical Pump
TOF	Time of Flight detector
TPD	Tracker Power Distributor
TPSFE	FE Tracker LV regulator, 6 ch per ladders S and 6 K (S9067)
TRD	Transition Radiation Detector
TReK	Telescience Resource Kit
TT	Tracker Thermal System (in combination)
TT-Crate	Tracker Thermal Control Electronics
TTBP	TT-Crate Backplane
TTCB	Tracker Thermal Control Box
TTCS	Tracker Thermal Control System
TTEC	Tracker Thermal Sensor & Actuator Electronics Controller
TTEI	Tracker Thermal Sensor & Actuator Electronics Interfaces
TTPC	Tracker Thermal Pump Controller
TTPD	Tracker Thermal Control Power Distributor
TTPT	Tracker Thermal PTS Readout, dual redundant
U	TRD (in combination, from *Ubergangstrahlung*)
U-Crate	TRD Crate
UBP	U-Crate Backplane (S9058)
UDR2	FE DAQ for 7 TDR towers, 2 Redund, Exclusive CDP (S9043)
UG	TRD Gas (in combination)
UG-Crate	TRD Gas Electronics
UGBC	TRD Gas Box C (Circulation), Electronics board for
UGBP	UG-Crate Backplane
UGBS	TRD Gas Box S (Supply), Electronics board for
UGFV	M&C Elec for TRD Gas Flip Valv & Manif Pressure sensors
UGPD	TRD Gas Box Power Distributor
UHVG	TRD HV 2*(7 redund generators)
UMA	Umbilical Mechanical Assembly
UPD	TRD Power Distributor
UPS	Uninterruptible Power Supply
UPSFE	FE TRD LV Regulators, 7 ch "dig"+ 7 ch "ana" (S9070)
USCM	Universal Slow Control Monitor

USCM	Universal Slow Control Module
USS	Unique Support Structure
V	Volts
VC	Vacuum Case
VCS	Vapo(u)r Cooled Shield
VDC	Volts DC
VLSI	Very Large Scale Integrated circuit
W	Watt, Wake
WSGC	White Sands Ground Complex
X_0	Radiation length
Z	charge

Appendix B: AMS Principal Publications

1. J. Alcaraz *et al.*, “Search for Antihelium in Cosmic Rays”, Phys. Lett. **B461** (2 Sep 1999) 387-396, hep-ex/0002048.
2. J. Alcaraz *et al.*, “Protons in Near Earth Orbit”, Phys. Lett. **B472** (26 Jan 2000) 215-226, hep-ex/0002049.
3. J. Alcaraz *et al.*, “Leptons in Near Earth Orbit”, Phys. Lett. **B484** (27 Jun 2000) 10-22; Erratum Phys. Lett. **B495** (14 Dec 2000) 440.
4. J. Alcaraz *et al.*, “Cosmic Protons”, Phys. Lett. **B490** (28 Sep 2000) 27-35.
5. J. Alcaraz *et al.*, “Helium in Near Earth Orbit", Phys. Lett. **B494** (30 Nov 2000) 193-202.
6. M.Aguilar *et al.*, “The Alpha Magnetic Spectrometer (AMS) on the International Space Station, Part I, Results from the test flight on the Space Shuttle”, Physics Reports, **vol. 366/6** (Aug.2002), 331-404; Erratum ibid 380 (2003) 97-98.

Appendix C: Collaborating Institutes and Universities

Institute	Location	Contact
I. Physikalisches Institut, RWTH	Aachen	St. Schael
III. Physikalisches Institut, RWTH	Aachen	G. Flügge
University of Aarhus	Aarhus	J. Madsen
National Institute for Nuclear Physics and High Energy Physics (NIKHEF)	Amsterdam	B. Verlaat
Laboratoire d'Annecy-Le-Vieux de Physique des Particules	Annecy-Le-Vieux	J.P. Vialle
Johns Hopkins University	Baltimore, MD	A. Pevsner
Beijing Institute of Satellite Environment Engineering (BISEE)	Beijing	Xiang Shuhong
China Academy of Launch Vehicle Technology (CALT)	Beijing	Li Ning
Institute of Electrical Engineering (IEE), Chinese Academy of Sciences	Beijing	Kong Li
Institute of High Energy Physics (IHEP), Chinese Academy of Sciences	Beijing	Chen Heshen
University of Bologna and INFN-Sezione di Bologna	Bologna	F. Palmonari
University of Bucharest and Institute for Space Science (ISS)	Bucharest	A. Mihul
Massachusetts Institute of Technology (MIT)	Cambridge, MA	U. Becker
National Central University	Chung Li	Yuan Hann Chang
University of Maryland, Department of Physics	College Park, MD	E.S. Seo
University of Maryland, East-West Space Science Center	College Park, MD	R. Sagdeev
Kyungpook National University	Daegu	D. Son
National Aerospace Laboratory (NLR)	Emmeloord	J. van Es
Istituto di Ricerca sulle Onde Elettromagnetiche (IROE)	Florence	G. Castellini
Max-Plank-Institut (MPI) für Extraterrestrische Physik	Garching	J. Truemper
Université de Genève, D.P.N.C.	Geneva	M. Pohl
NASA Goddard Space Flight Center (GSFC)	Greenbelt	S. Breon
Laboratoire de Physique Subatomique et de Cosmologie (LPSC)	Grenoble	M. Buenerd
Sun Yat-sen University (SYSU)	Guangzhou	He Zhenhui
NASA Johnson Space Center (JSC)	Houston	S. Porter
National Chiao Tung University (NCTU)	Hsinchu	C.Y. Chang
National Space Program Office (NSPO)	Hsinchu	Lou-Chuan Lee
Shandong University (SDU)	Jinan	Li Kang
University of Karlsruhe, Institute for Experimental Nuclear Physics	Karlsruhe	W. De Boer
Helsinki University of Technology, Metsahovi Radio Observatory	Kylmala	A. Mujunen
Laboratory of Instrumentation and Experimental Particle Physics	Lisbon	F. Barao
Chung Shan Institute of Science and Technology (CSIST)	Lung Tan	Yuan-Tzu Ting
Centro de Investigaciones Energeticas Medioambientales y Technologicas (CIEMAT)	Madrid	M. Aguilar
Universidad Nacional Autonoma de Mexico (UNAM)	Mexico City	A. Menchaca Rocha
University of Milano and INFN-Sezione di Milano	Milan	P.G. Rancoita
Groupe d'Astroparticules de Montpellier (GAM), IN2P3, Universite Montpellier II	Montpellier	A. Jacholkowska

Institute	Location	Contact
Institute of Theoretical and Experimental Physics (ITEP)	Moscow	Y. Galaktionov
Institute of Space Research (IKI)	Moscow	I. Mitrafonov
Russian Research Centre, Kurchatov Institute	Moscow	N. Chernoplekov
Skobeltsyn Institute of Nuclear Physics, Moscow State University	Moscow	M. Panasyuk
Southeast University (SEU)	Nanjing	Luo Junzhou
Yale University, Department of Physics	New Haven, CT	J. Sandweiss
European Space Agency, European Space and Technology Centre (ESTEC)	Noordwijk	M. Zell
University of Perugia and INFN-Sezione di Perugia	Perugia	R. Battiston
University of Pisa and INFN-Sezione di Pisa	Pisa	F. Cervelli
Italian Space Agency (ASI)	Roma	S. Di Pippo
University of Roma "La Sapienza" and INFN-Sezione di Roma	Roma	B. Borgia
EWHA Women's University	Seoul	J. Yang
Shanghai Jiaotong University (SJTU)	Shanghai	Ye Qinghao
University of Siena and INFN-Sezione di Siena	Siena	P.S. Marrocchesi
National Cheng Kung University (NCKU)	Tainan	Chin E. Lin
Academia Sinica, Institute of Physics	Taipei	Shih-Chang Lee
Florida A&M University	Tallahassee, FL	R. O'Neal
Instituto de Astrofisica de Canarias (IAC)	Tenerife	R.C. Garica Lopez
Center for Advanced Research in Space Optics (CARSO), University of Trieste	Trieste	P. Trampus
University of Turku, Space Research Laboratory	Turku	J. Torsti
Eidgenössische Technische Hochschule (ETH) Zürich, Lab. f.Hochenergiephysik	Zurich	H. Hofer